Haim Abramovich

ADVANCED AEROSPACE MATERIALS

ALUMINUM-BASED AND COMPOSITE STRUCTURES

Haim Abramovich

Advanced Aerospace Materials

Also of interest

Intelligent Materials and Structures
Abramovich, 2016
ISBN 978-3-11-033801-0, e-ISBN 978-3-11-033802-7

Advanced Materials
van de Ven, Soldera (Eds.), 2019
ISBN 978-3-11-053765-9, e-ISBN 978-3-11-053773-4

Nanoscience and Nanotechnology
Advances and Developments in Nano-sized Materials
Van de Voorde (Ed.), 2018
ISBN 978-3-11-054720-7, e-ISBN 978-3-11-054722-1

Space Technology
A Compendium for Space Engineering
Mütsch, Kowalski, 2016
ISBN 978-3-11-041321-2, e-ISBN 978-3-11-041322-9

Haim Abramovich

Advanced Aerospace Materials

Aluminum-Based and Composite Structures

DE GRUYTER

Author
Prof. Dr. Haim Abramovich
Technion-Israel Inst. of Technology
Aerospace Structural Laboratory
Technion City
32000 Haifa
Israel

Preface

Advanced Aerospace Materials aims at dissemination of advanced engineering topics using isotropic and composite materials. The present book was written to provide students and scholars a good understanding of new emerging technologies using composite materials, mainly in the aerospace sector. It can serve as an introductory book for graduate students wishing to study about composite made structures, enabling them to acquire the necessary physical and mathematical tools to understand the various aspects of composite based structures as compared to isotropic ones.

The book is based on the various researches and investigations performed during the years by the author on metal and composite structures.

The present book aims at providing a textbook to a graduate or graduate–undergraduate course on thin walled structures. It also can serve as a reference for engineers and scientists working in industry or academia.

The book starts with an extended introductory on thin walled structures, characterizing aerospace and aeronautical structures. It stresses the transition from aluminum-based structures to laminated composite ones, to save weight. An introductory to elasticity topics and equations of motion is also presented to enable the understanding of structural analysis of aerospace-aeronautical structures. Chapter 2 is devoted to laminated composite materials, and presents the classical lamination theory and the first order shear deformation theory. This chapter aims at providing mathematical and physical insight of composite materials. To complement this topic, higher order theories are also displayed. The first two chapters are therefore suitable for an introduction on aluminum and/or composite materials for aerospace/aeronautical structures to the graduate or undergraduate students.

The third chapter is devoted to some design formulas to be used by engineers on solving various problems of thin walled structures. Fatigue issues are presented in chapter four of the book. This chapter presents introductory topics in this well documented subject of engineering Crack propagation subject is described and reviewed in the fifth chapter of the book, thus complementing the topics presented in Chapter four, enabling the reader to understand and use the various equations to predict the life of a single structural component.

The sixth chapter displays various issues for the buckling for columns and plates, using isotropic and laminated composite materials. A complementary chapter, chapter seven, presents the vibrational aspects for the structures presented in the previous chapter.

Another important topic in the analysis of thin walled structure, the dynamic buckling of structural components due to pulse loading, is described and presented in detail in chapter eight, highlighting both analytical and experimental aspects of the subject.

The two last chapters of the book, optimization of thin-walled structures in chapter nine, and structural health monitoring in chapter ten, aim at presenting the readers with two emerging engineering topics, by providing the basic definitions and the present state of the art.

I wish that this book, together with other books and the huge numbers of references existing in the literature, would enable readers to become familiar with the treatment of thin walled structures, and how to investigate and calculate their structural behavior.

I would like to thank all my former graduate students for their dedicated research in the field of composite based structures, Mr. Joshua Harris for his involvement in Chapter 9 and Mr. Osher Shapira for his contribution to Chapter 10.

I want to thank, my wife, Dorit and my children, Chen, Oz, Shir and Or for their support, understanding, love and devotion. Their continuous support throughout the writing period enabled the publishing of the present book.

Haifa, June 2019
Haim Abramovich

Contents

1 Introduction

1.1 Introduction

This chapter aims at presenting the reader with aerospace structures, its basic structural parts and the transfer from aluminum to laminated composite materials, as a main way of saving weight. To be able to analyze those aerospace structures, which are thin-walled structures, basic elasticity equations will be derived and presented. The following chapters will present additional topics and equations regarding the behavior of thin-walled structures and how to analyze it.

1.2 Aerospace structures

Prior to defining the structures itself, one has to define the word *AEROSPACE*. As it is defined, aerospace combines the science, engineering and business of flying vehicles in the earth atmosphere, leading to the word *AERONAUTICS*, while flying in the surrounding space is called *ASTRONAUTICS*. The vehicles used for aerospace traveling are called *Aerospace Structures*.

The machine or the vehicle such as an airplane, helicopter, glider or any autonomous device capable of flying in the earth atmosphere is denoted as *aircraft*. Its main parts are schematically presented in Fig. 1.1.

The vehicle, capable of flying in the space, like a satellite, space station or any other machine, would be named as *spacecraft*.

Figure 1.2 presents one of the old famous aircrafts, the Lockheed Vega, a Lockheed Corporation six-passenger high-wing monoplane, used to break flight records. The famous Amelia Earhart used this aircraft to fly the Atlantic. From structural point of view, one should note the wooden monologue fuselage and the plywood-covered wings [1]. With increasing the performance of the aircraft, the wood was replaced by aluminum, as the basic material to manufacture the structural parts of the aircraft. A typical metal skin aircraft fuselage assembly is shown in Fig. 1.3, depicting the frames and their clips and the longitudinal riveted stringers. The wings would be made of an assembly of spars giving the aerodynamic shape to the wing, ribs connecting the spars and all covered by skin panels. A space aircraft has similar structural design, like an aircraft (see Fig. 1.4) if it has to return to earth. If the space device is designed to spend its life in space, like satellites, solar panels and/or space antennas (see Figs. 1.5, 1.6), then its shape and the adjacent structure would be according to the loads expected to be applied on it during its space mission.

The aerospace structures aim at providing operational demands and safety within a minimum weight. These structures comprise thin load skins, frames,
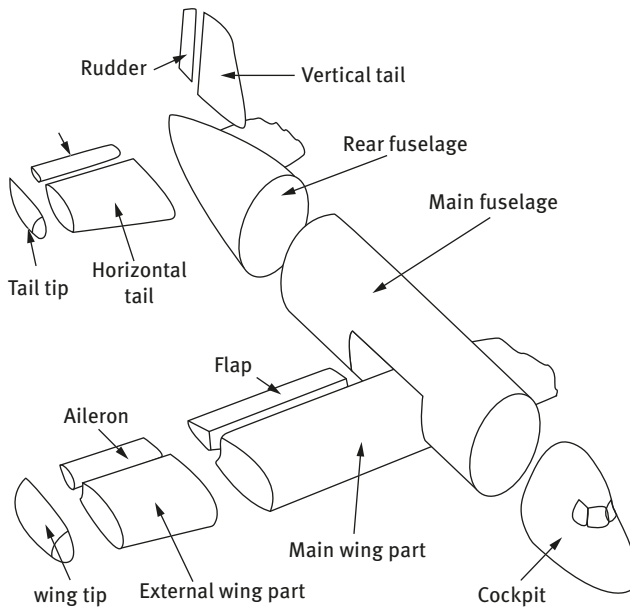
Fig. 1.1: Main parts of a typical aircraft.

Lockheed vega

Wing Span: 16 m.
Length: 14 m.
Max. Speed: 298 km/h

Amelia Earhart's Lockheed Vega

National Air and Space Museum Smithsonian Institute
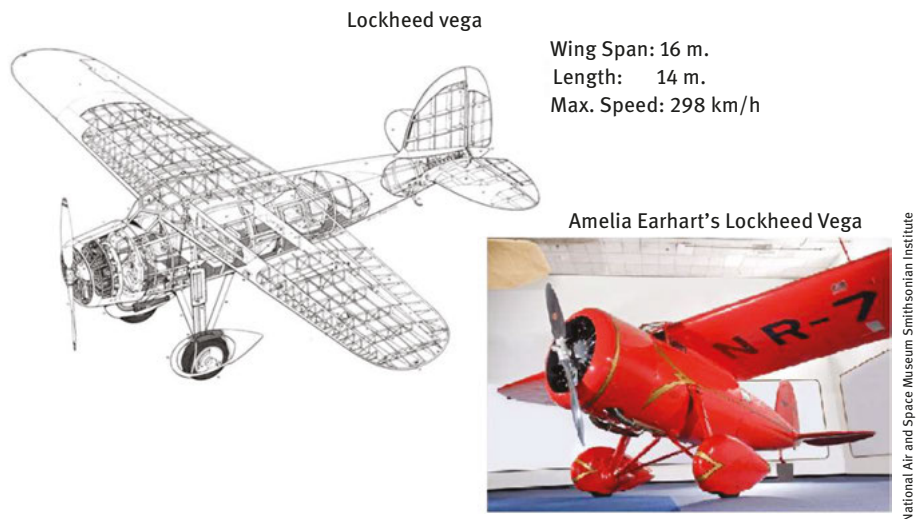
Fig. 1.2: Lockheed Vega aircraft.

stiffeners and spars, all made of high strength and stiffness materials to comply with
the minimum weight criterion. To be able to design and calculate those structures,
three basic structures, namely beams (or column for buckling and rods for tension),
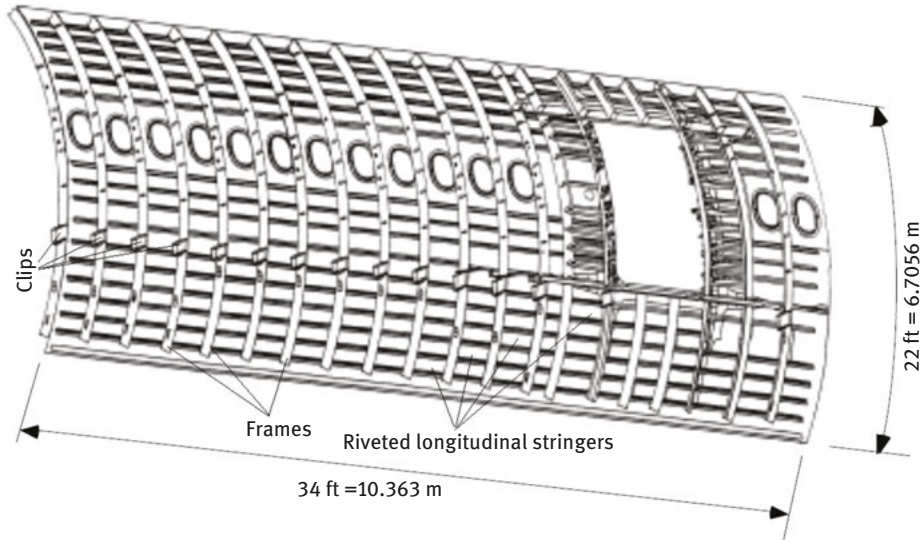
Fig. 1.3: Typical metal skin aircraft fuselage assembly (from NASA CR4730, Ref. [2]).
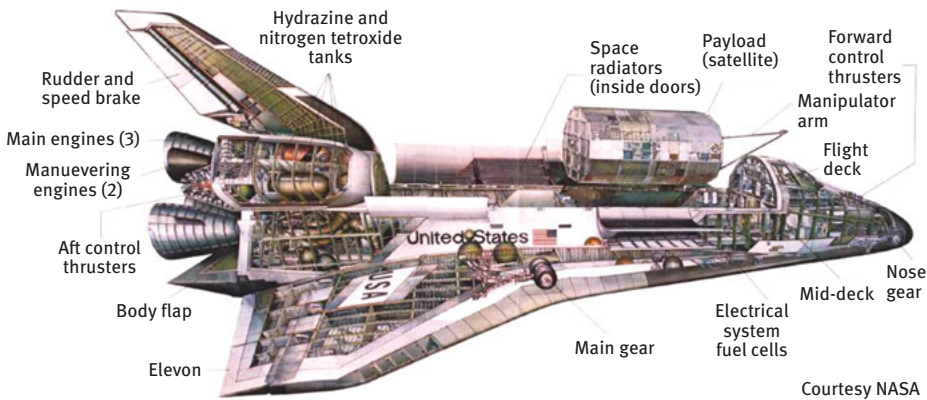
Fig. 1.4: A spacecraft – the NASA Shuttle.

plates and shells have to be analyzed and their behavior under various types of loads be understood (Fig. 1.7). As shown, a beam is a 1D structure (h, $b \ll L$), a thin plate is considered as a 2D structure (a, $b \gg t$), while a cylindrical shell forms a 3D thin-walled structure.

Many books and articles have been written on aerospace structures, how to analyze and calculate their response to static and dynamic loads. Typical references and their contents can be found in [2–6].
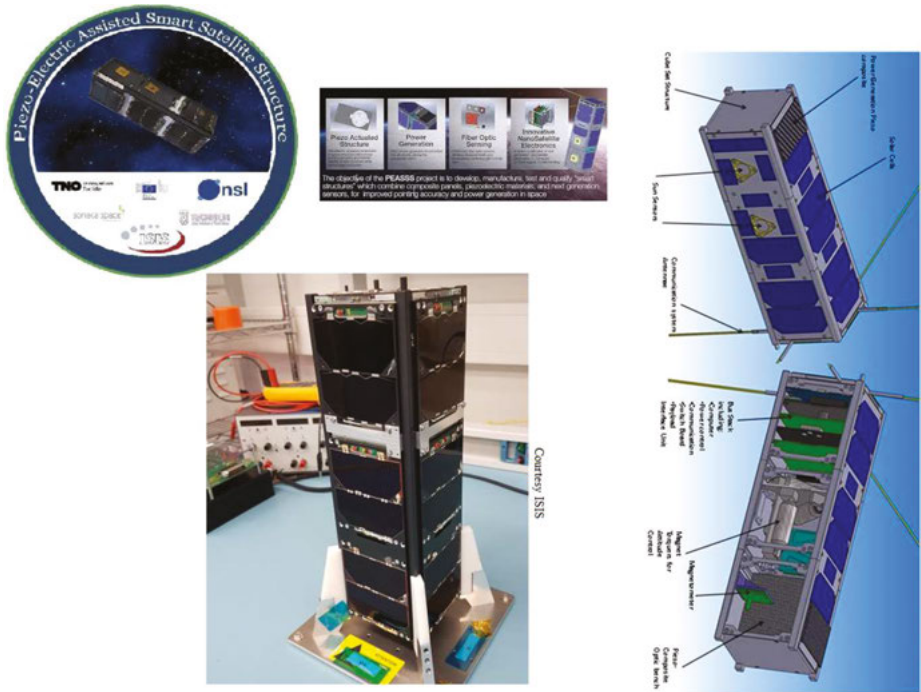
Fig. 1.5: The PEASSS (*Piezo*Electric-*A*ssisted *S*mart *S*atellite *S*tructure) nanosatellite structure launched on 15 February 2017 by an Indian PLSV rocket together with other 103 nanosatellites.

Space antennas
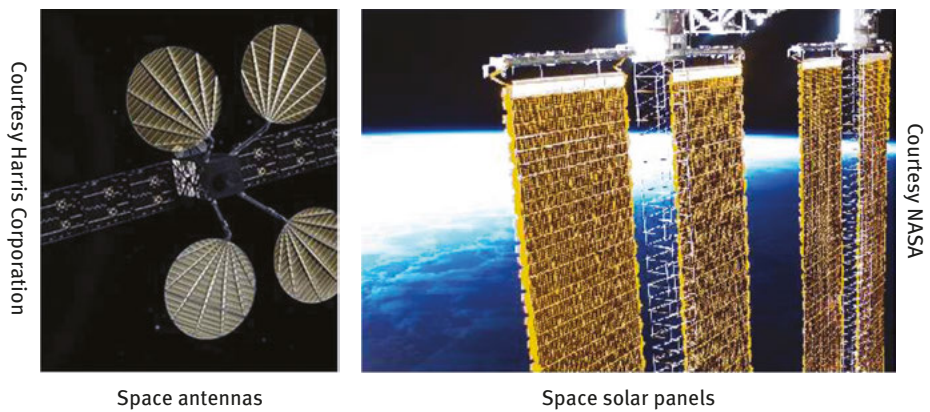
Space solar panels

Fig. 1.6: Space antennas and solar panels.
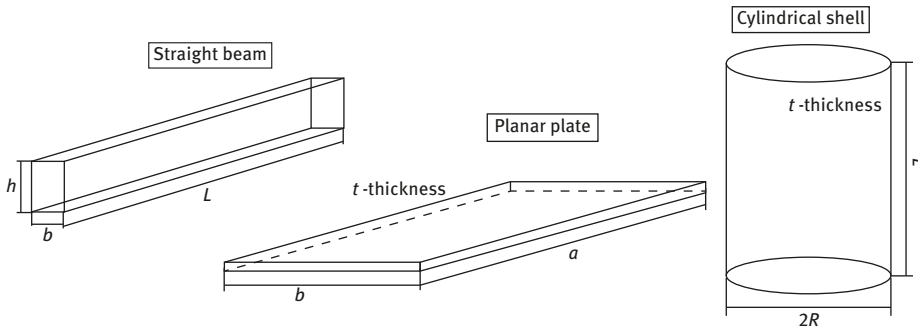
Fig. 1.7: Schematic drawings of the three basic structures: a straight beam, a planar plate and a cylindrical shell.

1.3 Aerospace structures – transition to composite materials

The constant strive to improve efficiency, increase performance of the aircrafts in parallel with the need to reduce their development and operating costs is the moto of the aircraft industry [7]. Using composite materials for primary aircraft structures and thus reducing the aircraft weight may be the answer to improve aircraft efficiency and performance.

Intensive investigation had been performed on introduction of composite materials in commercial and military aircrafts [8–11]. Figures 1.8 and 1.9 present the realization
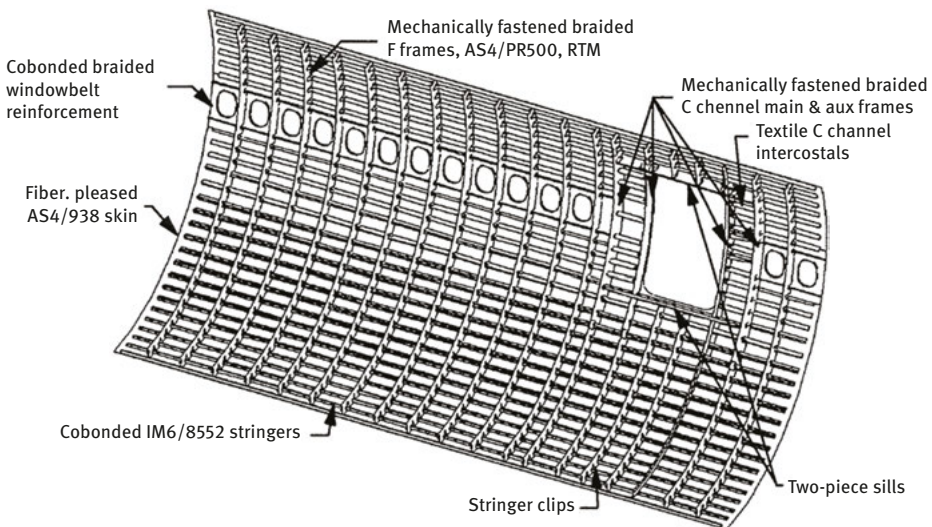
Fig. 1.8: Typical skin-stringer-frame side design composite concept (from NASA CR4735, ref. [11]).

Cobonded braided RTM AS4/PR500 J frames

Textile intercoslals

Mechanically fastened
C-chennel braided edge frames

Mechanically
fastened metallic
window frame

Cobonded braided
Aux frames

Cobonded
floor
attach. Blade

0.5 in, 8.0 pcf HRP Core

Two-piece sills

Fiber-pleced AS4/8552 facesheets
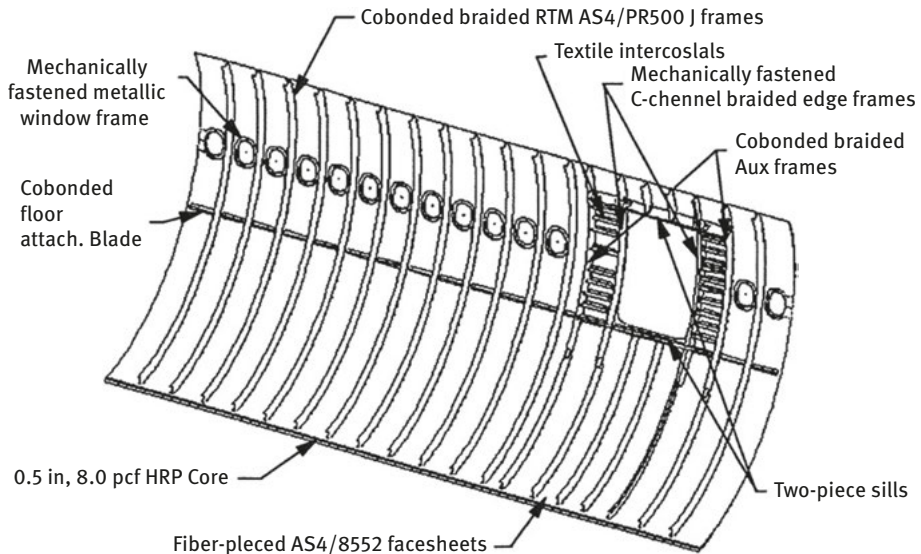
Fig. 1.9: Typical sandwich-frame side design composite concept (from NASA CR4735 [11]).

of a fuselage panel, originally manufactured from aluminum (see Fig. 1.3), using either laminated graphite epoxy stringers (Fig. 1.8) or laminated graphite epoxy sandwich faces (Fig. 1.9).

One should note that the composite structure depicted in Fig. 1.9 does not have any stringers. The fibers have been oriented to support the loads normally carried by stringers, as in Figs. 1.3 and 1.8.

The reduction in the panel weight in comparison with the aluminum baseline model is presented in Fig. 1.10 from [8]. One can observe that using skin-stringer or sandwich structures would reduce the total weight by 24% or 13%, respectively.

It is interesting to note that already in the 1950s composite materials were first used on commercial aircraft, and 2% of the Boeing 707 was made of fiberglass (see Fig. 1.11). Airbus introduced composite materials in its aircraft in the 1980s, using 5% composites on the A310-300.

This trend continued, and by the turn of the century, the advancements made in composite manufacturing allowed both Boeing and Airbus to significantly increase their use of composite. Boeing jumped from 12% on the Boeing 777 to 50% on the Boeing 787, better known as the "Dreamliner" (see Fig. 1.12), while Airbus moved from 10% on the A340 to 25% on the A380 (see Fig. 1.13) and finally to 53% on the A350XWB (Fig. 1.14).

Weight per shipset, lbs

Weight per shipset, lbs

Legend:
- Skin-stringer
- Sandwich
- Aluminum baseline

X-axis categories: Skin | Stringers/core | Frames | Window belt | Skin panel ass'y | Door reinforc. fab | Pass floor details | Splice details | Assembly | Total

Total values: 1,984 · 2,247 · 2,592
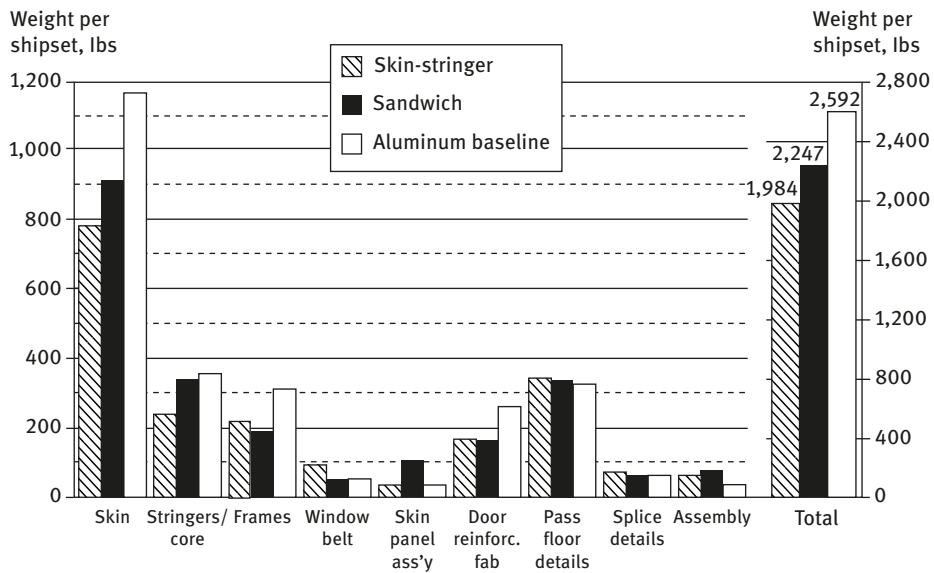
Fig. 1.10: Weight comparison of side panel designs (from NASA CR4730 [8]).

Boeing 707-120

143 seats; 600 mph = 965 km/h

Clipper America — PAN AMERICAN — N710PA

From Pan Am–An airline and its aircrafts, by Ron Davies
Mike M achat drawing
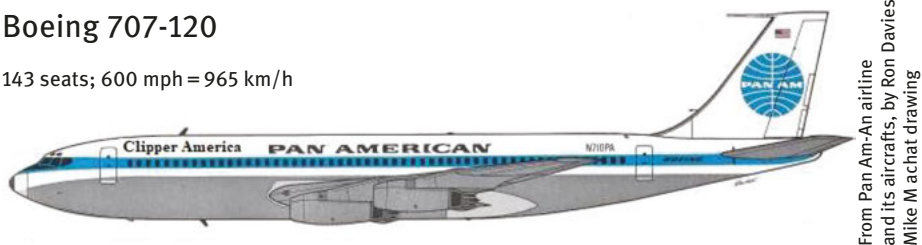
Name changed later to "Jet Clipper Caroline"
Pratt & Whitney JT3C-6 (13,500 lb thrust) × 4 • 124 tons max. gross take-off weight • 3000 stature miles range

P.St. John Turner

Fig. 1.11: Boeing 707-120 from PAN AMERICAN airlines.

Boeing 787 "Dreamliner" composite structure

Materials used in 787 body

- Fiberglass
- Aluminum
- Carbon laminate composite
- Carbon sandwich composite
- Aluminum/steel/titanium

Total materials used
By weight

- Composites 50%
- Aluminum 20%
- Titanium 15%
- Steel 10%
- Other 5%

By comparison, the 777 uses 12 percent composites and 50 percent aluminum.

Aft flaps
- Outboard (graphite)
- Inboard (graphite/fiberglass)

Rudder (graphite)

Flap support fairings
- Fwd segment (graphite/Kevlar + non-woven Kevlar mat)
- Aft segment (graphite/fiberglass)

Tip fairings (fiberglass)

Fixed trailing edge panels (graphite/Kevlar + non-woven Kevlar mat)

Ailerons (graphite)

Elevators (graphite)

Fixed trailing edge panels upper (graphite/fiberglass) lower (graphite/Kevlar + non-woven Kevlar mat)

Engine strut fairings (Kevlar/fiberglass)

Auxiliary power inlet (graphite)

Environmental control system ducts (Kevlar)

Fixed trailing edge panels (graphite/Kevlar + non-woven Kevlar mat)

Nose landing gear doors (graphite)

Spoilers (graphite)

Wing leading edge lower panels (Kevlar/fiberglass)

Wing-to-body fairings (graphite/Kevlar/fiberglass) and (graphite/Kevlar + non-woven Kevlar mat)

Cowl components (graphite)

- Body main landing gear doors (graphite)
- Trunnion fairings and wing landing gear doors (graphite/Kevlar)
- Brakes (structural carbon)

Fig. 1.12: Boeing 787 "Dreamliner" composite components.

With its 787 "Dreamliner," Boeing became the first airliner to launch a full-size commercial aircraft using composite materials for the almost full fuselage, upper and lower wing skin, radom, wing flaps, elevators, ailerons, vertical fin and horizontal stabilizer (Fig. 1.12). One should note that the use of composites in the Boeing 787 is 80% by volume and 50% by weight.

Chapter 2 of this book is devoted to composite materials and their use. Additional information regarding composite materials can be found in [12, 13].

Model aeroplane
A380 composite components

Carbon fibre
Aramid fibre
Glass fibre
Hybrid (carbon + glass)

Outer wing
Wing box
Ailerons
Flap-track fairings
Outer flap
Fixed leading-edge upper and lower panels
Belly fairing skins
Radome
Nose landing-gear doors
Main and centre landing-gear doors
Central torsion box
Main landing-gear leg-fairing door
Nacelle cowlings
Over wing panel
Pressure bulkhead
Keel beam
Vertical stabiliser
Tail cone
Horizontal stabiliser outer boxes
Trailing-edge upper and lower panels and shroud-box
Spoilers
Pylon fairings

Fig. 1.13: Airbus A380 composite components.

Boeing 787 Dreamliner

Passengers
210 – 250
Cabin width
5.49 m

60.0 m

Airbus A350 XWB

Passengers
314
Cabin width
5.61 m

64.8 m
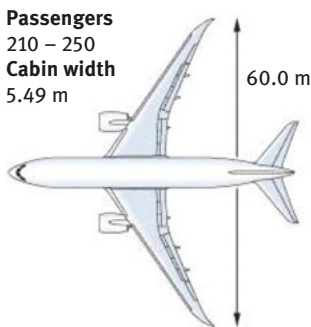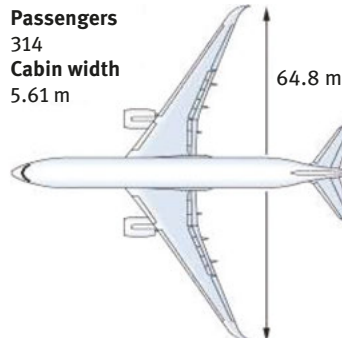
Fig. 1.14: Boeing 787 versus Airbus A350 XWB.

1.4 Basic topics in elasticity

1.4.1 Stresses, strains and rigid body rotations

To be able to calculate the structural behavior of basic and complicate components of aerospace structures, the basic concepts of elasticity will next be presented. More in-depth notions can be found in [14].

In a 3D structure, the components of the mechanical stress (defined as force per unit area) are presented in Fig. 1.15 for a cubic point in a structural continuum (for a Cartesian coordinate system).
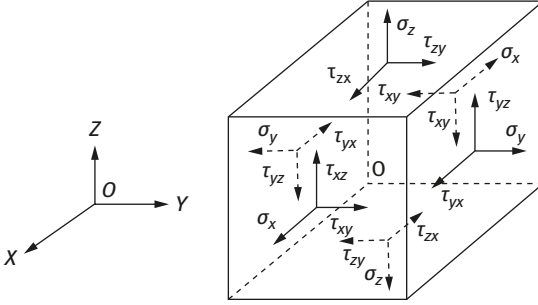
Fig. 1.15: Mechanical stresses in a Cartesian coordinate system.

The expressions with only one index, $\sigma_x, \sigma_y, \sigma_z$, are normal stresses acting in the directions x, y and z, respectively. Positive values will mean tension stress, while a negative value will stand for compression stress. The other expressions $\tau_{xz}, \tau_{zx}, \tau_{yz}, \tau_{zy}, \tau_{xy}, \tau_{yx}$ are shear stresses, where the first index denotes the normal of the surface on which the shear stress acts, while the second index denotes the direction of the stress. One should note that due to equilibrium, the following identities hold for the shear stresses:

$$\tau_{xz} = \tau_{zx}, \qquad \tau_{yz} = \tau_{zy}, \qquad \tau_{xy} = \tau_{yx}. \tag{1.1}$$

The stress tensor will have the following form:

$$\begin{bmatrix} \sigma_x & \tau_{xy} & \tau_{xz} \\ \tau_{yx} & \sigma_y & \tau_{yz} \\ \tau_{zx} & \tau_{zy} & \sigma_z \end{bmatrix} = \begin{bmatrix} \sigma_x & \tau_{xy} & \tau_{xz} \\ \tau_{xy} & \sigma_y & \tau_{yz} \\ \tau_{xz} & \tau_{yz} & \sigma_z \end{bmatrix} \tag{1.2}$$

The stresses in cylindrical coordinate system (r, θ, z) (see Fig. 1.16) are presented in Fig. 1.17. The normal stresses are $\sigma_r, \sigma_\theta, \sigma_z$. All the other stresses $\tau_{rz}, \tau_{zr}, \tau_{\theta z}, \tau_{z\theta}, \tau_{r\theta}, \tau_{\theta r}$ would stand for shear stresses:

$$\tau_{r\theta} = \tau_{\theta r}, \qquad \tau_{rz} = \tau_{zr}, \qquad \tau_{\theta z} = \tau_{z\theta}. \tag{1.3}$$

The stress tensor will have the following form:

$$\begin{bmatrix} \sigma_r & \tau_{r\theta} & \tau_{rz} \\ \tau_{\theta r} & \sigma_\theta & \tau_{\theta z} \\ \tau_{zr} & \tau_{z\theta} & \sigma_z \end{bmatrix} = \begin{bmatrix} \sigma_r & \tau_{r\theta} & \tau_{rz} \\ \tau_{r\theta} & \sigma_\theta & \tau_{\theta z} \\ \tau_{rz} & \tau_{\theta z} & \sigma_z \end{bmatrix} \tag{1.4}$$

$$x = rSin\,\theta Cos\phi$$
$$y = rSin\,\theta Cos\phi$$
$$z = rCos\theta$$
$$r = \sqrt{(x^2 + Y^2 + z^2)}$$
$$Tan\theta = \left(\sqrt{(x^2 + Y^2 + z^2)}/z\right)$$
$$Tan\phi = (Y/x)$$

Spherical coordinates

$$x = rCos\theta$$
$$y = rSin\,\theta$$
$$r = \sqrt{(x^2 + Y^2)}$$
$$Tan\theta = (Y/x)$$

Cylindrical coordinates
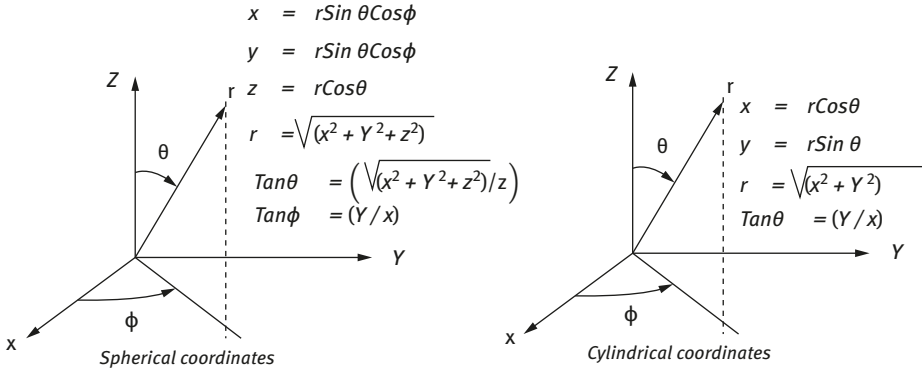
Fig. 1.16: Spherical and cylindrical coordinate systems.
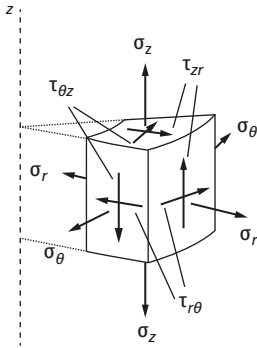
Fig. 1.17: Mechanical stresses in cylindrical coordinate system.

One should note that a polar coordinate system (r, θ) is a 2D planar system, with only three stresses $\sigma_r, \sigma_\theta, \tau_{r\theta}$.

Writing the stresses in spherical coordinates (see Fig. 1.16) yields

$$\begin{bmatrix} \sigma_r & \tau_{r\theta} & \tau_{r\phi} \\ \tau_{\theta r} & \sigma_\theta & \tau_{\theta\phi} \\ \tau_{\phi r} & \tau_{\phi\theta} & \sigma_\phi \end{bmatrix} = \begin{bmatrix} \sigma_r & \tau_{r\theta} & \tau_{r\phi} \\ \tau_{r\theta} & \sigma_\theta & \tau_{\theta\phi} \\ \tau_{r\phi} & \tau_{\theta\phi} & \sigma_\phi \end{bmatrix} \qquad (1.5)$$

The associated strains for a Cartesian coordinate system are defined as

$$\varepsilon_x = \frac{\partial u}{\partial x}, \qquad \varepsilon_y = \frac{\partial v}{\partial y}, \qquad \varepsilon_z = \frac{\partial w}{\partial z}$$

$$\gamma_{xy} = \frac{\partial u}{\partial y} + \frac{\partial v}{\partial x}, \qquad \gamma_{yz} = \frac{\partial v}{\partial z} + \frac{\partial w}{\partial y}, \qquad \gamma_{xz} = \frac{\partial u}{\partial z} + \frac{\partial w}{\partial x} \qquad (1.6)$$

where u, v and w are the displacements in the x, y and z directions, respectively; $\varepsilon_x, \varepsilon_y$ and ε_z are the tension/compression strains in the x, y and z directions,

respectively, while the shear strains are represented by $\gamma_{xy} = \gamma_{yx}$, $\gamma_{yz} = \gamma_{zy}$ and $\gamma_{xz} = \gamma_{zx}$. In matrix notation, the strains are written as

$$\begin{bmatrix} \varepsilon_x & \varepsilon_{xy} & \varepsilon_{xz} \\ \varepsilon_{xy} & \varepsilon_y & \varepsilon_{yz} \\ \varepsilon_{xz} & \varepsilon_{yz} & \varepsilon_z \end{bmatrix} = \begin{bmatrix} \varepsilon_x & 0.5\gamma_{xy} & 0.5\gamma_{xz} \\ 0.5\gamma_{xy} & \varepsilon_y & 0.5\gamma_{yz} \\ 0.5\gamma_{xz} & 0.5\gamma_{yz} & \varepsilon_z \end{bmatrix} \tag{1.7}$$

For a cylindrical coordinate system, having the displacements u_r, u_θ and u_z in the r, θ, and z directions, respectively, the strains are defined as follows:

$$\varepsilon_r = \frac{\partial u_r}{\partial r}, \qquad \varepsilon_\theta = \frac{u_r}{r} + \frac{1}{r}\frac{\partial u_\theta}{\partial \theta}, \qquad \varepsilon_z = \frac{\partial u_z}{\partial z}$$

$$\gamma_{r\theta} = \gamma_{\theta r} = \frac{\partial u_\theta}{\partial r} + \frac{1}{r}\frac{\partial u_r}{\partial \theta} - \frac{u_\theta}{r}, \; \gamma_{\theta z} = \gamma_{z\theta} = \frac{1}{r}\frac{\partial u_z}{\partial \theta} + \frac{\partial u_\theta}{\partial z}, \; \gamma_{zr} = \gamma_{rz} = \frac{\partial u_r}{\partial z} + \frac{\partial u_z}{\partial r}$$

$$\tag{1.8}$$

The matrix notation would be

$$\begin{bmatrix} \varepsilon_r & \varepsilon_{r\theta} & \varepsilon_{rz} \\ \varepsilon_{r\theta} & \varepsilon_\theta & \varepsilon_{\theta z} \\ \varepsilon_{rz} & \varepsilon_{\theta z} & \varepsilon_z \end{bmatrix} = \begin{bmatrix} \varepsilon_r & 0.5\gamma_{r\theta} & 0.5\gamma_{rz} \\ 0.5\gamma_{r\theta} & \varepsilon_\theta & 0.5\gamma_{\theta z} \\ 0.5\gamma_{rz} & 0.5\gamma_{\theta z} & \varepsilon_z \end{bmatrix} \tag{1.9}$$

where $\varepsilon_r, \varepsilon_\theta$ and ε_z are the tension/compression strains in the r, θ and z directions, respectively, while the shear strains are represented by $\gamma_{r\theta} = \gamma_{\theta r}, \gamma_{\theta z} = \gamma_{z\theta}$ and $\gamma_{zr} = \gamma_{rz}$.

For a spherical coordinate system, having the displacements u_r, u_θ and u_ϕ in the r, θ and ϕ directions, respectively, the strains are defined as follows:

$$\varepsilon_r = \frac{\partial u_r}{\partial r}; \quad \varepsilon_\theta = \frac{u_r}{r} + \frac{1}{r}\frac{\partial u_\theta}{\partial \theta}; \quad \varepsilon_\phi = \frac{1}{r\sin\theta}\frac{\partial u_\phi}{\partial \phi} + \frac{u_r}{r} + \frac{u_\theta \cot\theta}{r}$$

$$\gamma_{r\theta} = \gamma_{\theta r} = r\frac{\partial}{\partial r}\left(\frac{u_\theta}{r}\right) + \frac{1}{r}\frac{\partial u_r}{\partial \theta} = \frac{\partial u_\theta}{\partial r} - \frac{u_\theta}{r} + \frac{1}{r}\frac{\partial u_r}{\partial \theta}$$

$$\gamma_{\theta\phi} = \gamma_{\phi\theta} = \frac{\sin\theta}{r}\frac{\partial}{\partial\theta}\left(\frac{u_\phi}{\sin\theta}\right) + \frac{1}{r\sin\theta}\frac{\partial u_\theta}{\partial\phi} = \frac{1}{r}\frac{\partial u_\phi}{\partial\theta} - \frac{u_\phi}{r}\cot\theta + \frac{1}{r\sin\theta}\frac{\partial u_\theta}{\partial\phi}$$

$$\gamma_{r\phi} = \gamma_{\phi r} = \frac{1}{r\sin\theta}\frac{\partial u_r}{\partial\phi} + r\frac{\partial}{\partial r}\left(\frac{u_\phi}{r}\right) = \frac{1}{r\sin\theta}\frac{\partial u_r}{\partial\phi} + \frac{\partial u_\phi}{\partial r} - \frac{u_\phi}{r}$$

$$\tag{1.10}$$

where $\varepsilon_r, \varepsilon_\theta$ and ε_ϕ are the tension/compression strains in the r, θ and ϕ directions, respectively, while the shear strains are represented by $\gamma_{r\theta} = \gamma_{\theta r}, \gamma_{\theta\phi} = \gamma_{\phi\theta}$ and $\gamma_{\phi r} = \gamma_{r\phi}$. The matrix of the strains in spherical coordinates has the following form:

$$\begin{bmatrix} \varepsilon_r & \varepsilon_{r\theta} & \varepsilon_{r\phi} \\ \varepsilon_{r\theta} & \varepsilon_\theta & \varepsilon_{\theta\phi} \\ \varepsilon_{r\phi} & \varepsilon_{\theta\phi} & \varepsilon_\phi \end{bmatrix} = \begin{bmatrix} \varepsilon_r & 0.5\gamma_{r\theta} & 0.5\gamma_{r\phi} \\ 0.5\gamma_{r\theta} & \varepsilon_y & 0.5\gamma_{\theta\phi} \\ 0.5\gamma_{r\phi} & 0.5\gamma_{\theta\phi} & \varepsilon_z \end{bmatrix} \tag{1.11}$$

One should note that during deforming, an element on a given body would change its shape, translate and rotate. So, beside strains, one can write the rigid body rotations as a function of the assumed displacements. For a Cartesian coordinate system, these rotations are defined as (see also [14])

$$\omega_x = \frac{1}{2}\left(\frac{\partial w}{\partial y} - \frac{\partial v}{\partial z}\right), \quad \omega_y = \frac{1}{2}\left(\frac{\partial u}{\partial z} - \frac{\partial w}{\partial x}\right), \quad \omega_z = \frac{1}{2}\left(\frac{\partial v}{\partial x} - \frac{\partial u}{\partial y}\right)$$

and

$$\omega_{zy} = -\omega_{yz} \equiv \omega_x, \quad \omega_{xz} = -\omega_{zx} \equiv \omega_y, \quad \omega_{yx} = -\omega_{xy} \equiv \omega_z$$

(1.12)

The definitions for the rotations in a cylindrical coordinate system will have the following expressions:

$$\omega_r = \frac{1}{2}\left(\frac{1}{r}\frac{\partial u_z}{\partial \theta} - \frac{\partial u_\theta}{\partial z}\right), \quad \omega_\theta = \frac{1}{2}\left(\frac{\partial u_r}{\partial z} - \frac{\partial u_z}{\partial r}\right), \quad \omega_z = \frac{1}{2r}\left[\frac{\partial}{\partial r}(r \cdot u_\theta) - \frac{\partial u_r}{\partial \theta}\right]$$

and

$$\omega_{z\theta} = -\omega_{\theta z} \equiv \omega_r, \quad \omega_{rz} = -\omega_{zr} \equiv \omega_\theta, \quad \omega_{\theta r} = -\omega_{r\theta} \equiv \omega_z$$

(1.13)

while for a spherical coordinate system, these rotations will be given by

$$\omega_r = \frac{1}{2r^2 \sin\theta}\left[\frac{\partial}{\partial \theta}(r \cdot u_\phi \cdot \sin\theta) - \frac{\partial}{\partial \phi}(r \cdot u_\theta)\right]$$

$$\omega_\theta = \frac{1}{2r \sin\theta}\left[\frac{\partial u_r}{\partial \phi} - \frac{\partial}{\partial r}(r \cdot u_\phi \cdot \sin\theta)\right], \quad \omega_\phi = \frac{1}{2r}\left[\frac{\partial}{\partial r}(r \cdot u_\theta) - \frac{\partial u_r}{\partial \theta}\right]$$

(1.14)

and

$$\omega_{\phi\theta} = -\omega_{\theta\phi} \equiv \omega_r, \quad \omega_{r\phi} = -\omega_{\phi r} \equiv \omega_\theta, \quad \omega_{\theta r} = -\omega_{r\theta} \equiv \omega_\phi$$

Assuming Hook's law for isotropic materials, one can write the strain–stress relations in a Cartesian coordinate system yielding the following expressions:

$$\varepsilon_x = \frac{1}{E}\left[\sigma_x - v(\sigma_y + \sigma_z)\right], \quad \varepsilon_y = \frac{1}{E}\left[\sigma_y - v(\sigma_x + \sigma_z)\right]$$

$$\varepsilon_z = \frac{1}{E}\left[\sigma_z - v(\sigma_x + \sigma_y)\right]$$

$$\gamma_{xy} = \frac{\tau_{xy}}{G}, \quad \gamma_{yz} = \frac{\tau_{yz}}{G}, \quad \gamma_{xz} = \frac{\tau_{xz}}{G}$$

(1.15)

where E, $G = \frac{E}{2(1+v)}$ and v are the Young's modulus, the shear modulus and the Poisson's ratio, respectively. For a cylindrical coordinate system, the strain–stress relations can be written as

$$\varepsilon_r = \frac{1}{E}[\sigma_r - \nu(\sigma_\theta + \sigma_z)], \quad \varepsilon_\theta = \frac{1}{E}[\sigma_\theta - \nu(\sigma_r + \sigma_z)],$$

$$\varepsilon_z = \frac{1}{E}[\sigma_z - \nu(\sigma_r + \sigma_\theta)], \tag{1.16}$$

$$\gamma_{r\theta} = \frac{\tau_{r\theta}}{G}, \quad \gamma_{\theta z} = \frac{\tau_{\theta z}}{G}, \quad \gamma_{rz} = \frac{\tau_{rz}}{G}$$

In a similar way, the strain–stress relations for a spherical coordinate system can be shown to have the following expressions:

$$\varepsilon_r = \frac{1}{E}\left[\sigma_r - \nu(\sigma_\theta + \sigma_\phi)\right], \quad \varepsilon_\theta = \frac{1}{E}\left[\sigma_\theta - \nu(\sigma_r + \sigma_\phi)\right]$$

$$\varepsilon_\phi = \frac{1}{E}\left[\sigma_\phi - \nu(\sigma_r + \sigma_\theta)\right] \tag{1.17}$$

$$\gamma_{r\theta} = \frac{\tau_{r\theta}}{G}, \quad \gamma_{\theta\phi} = \frac{\tau_{\theta\phi}}{G}, \quad \gamma_{r\phi} = \frac{\tau_{r\phi}}{G}$$

The stress–strain relations, namely the stresses being expressed as a function of the strains, for Cartesian, cylindrical and spherical coordinate systems are presented in eqs. (1.18), (1.19) and (1.20), respectively

$$\sigma_x = \frac{E}{(\nu + 1)(1 - 2\nu)}\left[(1 - \nu)\varepsilon_x + \nu(\varepsilon_y + \varepsilon_z)\right]$$

$$\sigma_y = \frac{E}{(\nu + 1)(1 - 2\nu)}\left[(1 - \nu)\varepsilon_y + \nu(\varepsilon_x + \varepsilon_z)\right] \tag{1.18}$$

$$\sigma_z = \frac{E}{(\nu + 1)(1 - 2\nu)}\left[(1 - \nu)\varepsilon_z + \nu(\varepsilon_x + \varepsilon_y)\right]$$

$$\tau_{xy} = G\gamma_{xy}, \quad \tau_{yz} = G\gamma_{yz}, \quad \tau_{xz} = G\gamma_{xz}$$

$$\sigma_r = \frac{E}{(\nu + 1)(1 - 2\nu)}\left[(1 - \nu)\varepsilon_r + \nu(\varepsilon_\theta + \varepsilon_z)\right]$$

$$\sigma_\theta = \frac{E}{(\nu + 1)(1 - 2\nu)}\left[(1 - \nu)\varepsilon_\theta + \nu(\varepsilon_r + \varepsilon_z)\right] \tag{1.19}$$

$$\sigma_z = \frac{E}{(\nu + 1)(1 - 2\nu)}\left[(1 - \nu)\varepsilon_z + \nu(\varepsilon_r + \varepsilon_\theta)\right]$$

$$\tau_{r\theta} = G\gamma_{r\theta}, \quad \tau_{\theta z} = G\gamma_{\theta z}, \quad \tau_{rz} = G\gamma_{rz}$$

$$\sigma_r = \frac{E}{(\nu + 1)(1 - 2\nu)} \left[(1 - \nu)\varepsilon_r + \nu(\varepsilon_\theta + \varepsilon_\phi) \right]$$

$$\sigma_\theta = \frac{E}{(\nu + 1)(1 - 2\nu)} \left[(1 - \nu)\varepsilon_\theta + \nu(\varepsilon_r + \varepsilon_\phi) \right]$$

(1.20)

$$\sigma_\phi = \frac{E}{(\nu + 1)(1 - 2\nu)} \left[(1 - \nu)\varepsilon_\phi + \nu(\varepsilon_r + \varepsilon_\theta) \right]$$

$$\tau_{r\theta} = G\gamma_{r\theta}, \quad \tau_{\theta\phi} = G\gamma_{\theta\phi}, \quad \tau_{r\phi} = G\gamma_{r\phi}$$

1.4.2 Equilibrium and compatibility equations in elasticity

For a Cartesian coordinate system, the equilibrium equations have the following form:

$$\frac{\partial \sigma_x}{\partial x} + \frac{\partial \tau_{xy}}{\partial y} + \frac{\partial \tau_{xz}}{\partial z} + \bar{X} = 0$$

$$\frac{\partial \tau_{xy}}{\partial x} + \frac{\partial \sigma_y}{\partial y} + \frac{\partial \tau_{yz}}{\partial z} + \bar{Y} = 0$$

(1.21)

$$\frac{\partial \tau_{xz}}{\partial x} + \frac{\partial \tau_{yz}}{\partial y} + \frac{\partial \sigma_z}{\partial z} + \bar{Z} = 0$$

while $\bar{X}$, $\bar{Y}$ and $\bar{Z}$ being body forces in the x, y and z directions, respectively.

Similarly, for a cylindrical coordinate system, the three equilibrium equations would read

$$\frac{\partial \sigma_r}{\partial r} + \frac{1}{r}\frac{\partial \tau_{r\theta}}{\partial \theta} + \frac{\partial \tau_{rz}}{\partial z} + \frac{\sigma_r - \sigma_\theta}{r} + \bar{R} = 0$$

$$\frac{\partial \tau_{r\theta}}{\partial r} + \frac{1}{r}\frac{\partial \sigma_\theta}{\partial \theta} + \frac{\partial \tau_{\theta z}}{\partial z} + \frac{2\tau_{r\theta}}{r} + \bar{\Theta} = 0$$

(1.22)

$$\frac{\partial \tau_{rz}}{\partial r} + \frac{1}{r}\frac{\partial \tau_{\theta z}}{\partial \theta} + \frac{\partial \sigma_z}{\partial z} + \frac{\tau_{rz}}{r} + \bar{Z} = 0$$

with $\bar{R}$, $\bar{\Theta}$ and $\bar{Z}$ being body forces in the r, θ and z directions, respectively.

Finally, the equilibrium equations in a spherical coordinate system can be written as

$$\frac{\partial \sigma_r}{\partial r} + \frac{1}{r}\frac{\partial \tau_{r\theta}}{\partial \theta} + \frac{1}{r \cdot \sin\theta}\frac{\partial \tau_{r\phi}}{\partial \phi} + \frac{1}{r}\left(2\sigma_r - \sigma_\theta - \sigma_\phi + \tau_{r\theta}\cot\theta\right) + \bar{R} = 0$$

$$\frac{\partial \tau_{r\theta}}{\partial r} + \frac{1}{r}\frac{\partial \sigma_\theta}{\partial \theta} + \frac{1}{r \cdot \sin\theta}\frac{\partial \tau_{\theta\phi}}{\partial \phi} + \frac{1}{r}\left[(\sigma_\theta - \sigma_\phi)\cot\theta + 3\tau_{r\theta}\right] + \bar{\Theta} = 0$$

(1.23)

$$\frac{\partial \tau_{r\phi}}{\partial r} + \frac{1}{r}\frac{\partial \tau_{\theta\phi}}{\partial \theta} + \frac{1}{r \cdot \sin\theta}\frac{\partial \sigma_\phi}{\partial \phi} + \frac{1}{r}\left(3\tau_{r\phi} + 2\tau_{\theta\phi}\right) + \bar{\Phi} = 0$$

with $\bar{R}, \bar{\Theta}$ and $\bar{\Phi}$ being body forces in the r, θ and ϕ directions, respectively.

With the strains and the stresses being interconnected through the Hook's law, the question remains how to get the displacements if the expressions for the strains are known. To ensure a unique solution for the displacements, once the strains are given, the compatibility equations should be satisfied. These equations, for a Cartesian coordinate system, are given in a compact form as

$$\varepsilon_{ij,kl} + \varepsilon_{kl,ij} - \varepsilon_{ik,jl} - \varepsilon_{jl,ik} = 0$$

where (1.24)

$$i,j,k,l = x,y,z$$

The compact form of eq. (1.24) transforms in the following six equations, which have to be fulfilled to ensure a unique solution for the displacement field, for a prescribed strain field:

$$\frac{\partial^2 \varepsilon_x}{\partial y^2} + \frac{\partial^2 \varepsilon_y}{\partial x^2} = 2\frac{\partial^2 \varepsilon_{xy}}{\partial x \partial y}$$

$$\frac{\partial^2 \varepsilon_x}{\partial z^2} + \frac{\partial^2 \varepsilon_z}{\partial x^2} = 2\frac{\partial^2 \varepsilon_{xz}}{\partial x \partial z}$$

$$\frac{\partial^2 \varepsilon_y}{\partial z^2} + \frac{\partial^2 \varepsilon_z}{\partial y^2} = 2\frac{\partial^2 \varepsilon_{yz}}{\partial y \partial z}$$

(1.25)

$$\frac{\partial^2 \varepsilon_x}{\partial y \partial z} + \frac{\partial^2 \varepsilon_{yz}}{\partial x^2} = \frac{\partial^2 \varepsilon_{xz}}{\partial x \partial y} + \frac{\partial^2 \varepsilon_{xy}}{\partial x \partial z}$$

$$\frac{\partial^2 \varepsilon_y}{\partial x \partial z} + \frac{\partial^2 \varepsilon_{xz}}{\partial y^2} = \frac{\partial^2 \varepsilon_{yz}}{\partial x \partial y} + \frac{\partial^2 \varepsilon_{xy}}{\partial y \partial z}$$

$$\frac{\partial^2 \varepsilon_z}{\partial x \partial y} + \frac{\partial^2 \varepsilon_{xy}}{\partial z^2} = \frac{\partial^2 \varepsilon_{xz}}{\partial y \partial z} + \frac{\partial^2 \varepsilon_{yz}}{\partial x \partial z}$$

where

$$\varepsilon_{xy} \equiv 0.5\gamma_{xy}, \quad \varepsilon_{xz} \equiv 0.5\gamma_{xz}, \quad \varepsilon_{yz} \equiv 0.5\gamma_{yz}$$

(1.26)

$$\varepsilon_{yx} \equiv 0.5\gamma_{yx}, \quad \varepsilon_{zx} \equiv 0.5\gamma_{zx}, \quad \varepsilon_{zy} \equiv 0.5\gamma_{zy}$$

Equation (1.25) can be written in terms of stresses and are usually referred to as the compatibility equations in terms of stress, or the Beltrami–Michell (see [14, 15]) compatibility equations. Before presenting these compatibility equations it is instructive to present the equilibrium equations presented in eq. (1.21), using the assumed Cartesian displacements. These are called the equilibrium equations in terms of displacement or the Navier's equations. Their form is given as

$$(\lambda + G)\frac{\partial \varepsilon}{\partial x} + G\nabla^2 u + F_x = 0$$

$$(\lambda + G)\frac{\partial \varepsilon}{\partial y} + G\nabla^2 v + F_y = 0 \qquad (1.27)$$

$$(\lambda + G)\frac{\partial \varepsilon}{\partial z} + G\nabla^2 w + F_z = 0$$

where the Laplace operator, ∇^2, is defined (for a Cartesian coordinate system[1]) as

$$\nabla^2 \equiv \frac{\partial^2}{\partial x^2} + \frac{\partial^2}{\partial y^2} + \frac{\partial^2}{\partial z^2}$$

and $\qquad (1.28)$

$$\varepsilon \equiv \varepsilon_x + \varepsilon_y + \varepsilon_z = \frac{\partial u}{\partial x} + \frac{\partial v}{\partial y} + \frac{\partial w}{\partial z}$$

and the body forces F_x, F_y and F_z are defined according to the body forces defined in eq. (1.21), yielding

$$F_x \equiv \bar{X}, \qquad F_y \equiv \bar{Y}, \qquad F_z \equiv \bar{Z} \qquad (1.29)$$

Finally, the constants λ and G, also called the Lame's constants, are defined as

$$G \equiv \frac{E}{2(1 + v)} \qquad \lambda = \frac{vE}{(1 + v)(1 - 2v)}. \qquad (1.30)$$

where v and E are the Poisson's ratio and the Young's modulus, respectively.

The Navier's equations in a cylindrical coordinate system can be presented as

$$(\lambda + 2G)\frac{\partial H_\varepsilon}{\partial r} - 2G\left(\frac{1}{r}\frac{\partial \rho_z}{\partial \theta} - \frac{\partial \rho_\theta}{\partial z}\right) + F_r = 0$$

$$(\lambda + 2G)\frac{\partial H_\varepsilon}{r\partial \theta} - 2G\left(\frac{\partial \rho_r}{\partial z} - \frac{\partial \rho_z}{\partial r}\right) + F_\theta = 0 \qquad (1.31)$$

$$(\lambda + 2G)\frac{\partial H_\varepsilon}{\partial z} - 2G\left(\frac{\partial (r\rho_\theta)}{\partial r} - \frac{\partial \rho_r}{\partial \theta}\right) + F_z = 0$$

where, according to eq. (1.22), the body forces are defined as

$$F_r \equiv \bar{R}, \qquad F_\theta \equiv \bar{\Theta}, \qquad F_z \equiv \bar{Z} \qquad (1.32)$$

and

---

1 For a cylindrical coordinates system: $\nabla^2 \equiv \frac{\partial^2}{\partial r^2} + \frac{1}{r}\frac{\partial}{\partial r} + \frac{1}{r^2}\frac{\partial^2}{\partial \theta^2} + \frac{\partial^2}{\partial z^2}$, while for a spherical one the expression is: $\nabla^2 \equiv \frac{\partial^2}{\partial r^2} + \frac{2}{r}\frac{\partial}{\partial r} + \left(\frac{1}{r\sin(\phi)}\right)^2\frac{\partial^2}{\partial \theta^2} + \frac{1}{r^2}\frac{\partial^2}{\partial \phi^2} + \frac{1}{r^2\tan(\phi)}\frac{\partial}{\partial \phi}$.

$$H_\varepsilon \equiv \frac{1}{r}\frac{(ru_r)}{\partial r} + \frac{1}{r}\frac{\partial u_\theta}{\partial \theta} + \frac{\partial u_z}{\partial z}$$

$$\rho_r \equiv \frac{1}{2}\left[\frac{1}{r}\frac{\partial u_z}{\partial \theta} - \frac{\partial u_\theta}{\partial z}\right]$$

$$\rho_\theta \equiv \frac{1}{2}\left[\frac{\partial u_r}{\partial z} - \frac{\partial u_z}{\partial r}\right] \tag{1.33}$$

$$\rho_z \equiv \frac{1}{2}\left[\frac{\partial (ru_\theta)}{\partial r} - \frac{\partial u_r}{\partial \theta}\right]$$

while for a spherical coordinate system, the relevant expressions are

$$(\lambda + 2G)\frac{\partial \overline{H}_\varepsilon}{\partial r} - \frac{2G}{r\sin\theta}\left[\frac{\partial\left(\overline{\rho}_\phi \sin\theta\right)}{\partial\theta} - \frac{\partial\overline{\rho}_\theta}{\partial\phi}\right] + \overline{F}_r = 0$$

$$(\lambda + 2G)\frac{\partial \overline{H}_\varepsilon}{r\partial\theta} - \frac{2G}{r}\left[\frac{1}{\sin\theta}\frac{\partial(\overline{\rho}_r)}{\partial\phi} - \frac{\partial\left(r\overline{\rho}_\phi\right)}{\partial r}\right] + \overline{F}_\theta = 0 \tag{1.34}$$

$$\frac{(\lambda + 2G)}{r\sin\theta}\frac{\partial \overline{H}_\varepsilon}{\partial\phi} - \frac{2G}{r}\left[\frac{\partial\left(r\overline{\rho}_\theta\right)}{\partial r} - \frac{\partial(r\overline{\rho}_r)}{\partial\theta}\right] + \overline{F}_\phi = 0$$

where, according to eq. (1.23), the body forces are defined as

$$\overline{F}_r \equiv \overline{R}, \qquad \overline{F}_\theta \equiv \overline{\Theta}, \qquad \overline{F}_z \equiv \overline{\Phi} \tag{1.35}$$

and

$$\overline{H}_\varepsilon \equiv \frac{1}{r^2}\frac{\partial(r^2 u_r)}{\partial r} + \frac{1}{r\sin\theta}\frac{\partial(u_\theta \sin\theta)}{\partial\theta} + \frac{1}{r\sin\theta}\frac{\partial u_\phi}{\partial\phi}$$

$$\overline{\rho}_r \equiv \frac{1}{2r\sin\theta}\left[\frac{\partial\left(u_\phi \sin\theta\right)}{\partial\theta} - \frac{\partial u_\theta}{\partial\phi}\right]$$

$$\overline{\rho}_\theta \equiv \frac{1}{2}\left[\frac{1}{r\sin\theta}\frac{\partial u_r}{\partial\phi} - \frac{1}{r}\frac{\partial\left(ru_\phi\right)}{\partial r}\right] \tag{1.36}$$

$$\overline{\rho}_z \equiv \frac{1}{2r}\left[\frac{\partial(ru_\theta)}{\partial r} - \frac{\partial u_r}{\partial\theta}\right]$$

The Beltrami–Michell compatibility equations are given in a compact form[2] as

$$\sigma_{ij,kk} + \frac{1}{1+\nu}\sigma_{kk,uj} = -\frac{\nu}{1-\nu}F_{k,k}\delta_{ij} - F_{i,j} - F_{j,i} \tag{1.37}$$

---

2 δ_{ij} is the Kronecker delta defined as: $\delta_{ij} = 0$ *if* $i \neq j$; and $\delta_{ij} = 1$ *if* $i = j$.

Expanding eq. (1.32) leads to the following six equations (for a Cartesian system)

$$\nabla^2\sigma_x + \frac{1}{1+v}\frac{\partial^2\Lambda}{\partial x^2} = -\frac{1}{1-v}\left[\frac{\partial F_x}{\partial x} + \frac{\partial F_y}{\partial y} + \frac{\partial F_z}{\partial z}\right] - 2\frac{\partial F_x}{\partial x}$$

$$\nabla^2\sigma_y + \frac{1}{1+v}\frac{\partial^2\Lambda}{\partial y^2} = -\frac{1}{1-v}\left[\frac{\partial F_x}{\partial x} + \frac{\partial F_y}{\partial y} + \frac{\partial F_z}{\partial z}\right] - 2\frac{\partial F_y}{\partial y}$$

$$\nabla^2\sigma_z + \frac{1}{1+v}\frac{\partial^2\Lambda}{\partial z^2} = -\frac{1}{1-v}\left[\frac{\partial F_x}{\partial x} + \frac{\partial F_y}{\partial y} + \frac{\partial F_z}{\partial z}\right] - 2\frac{\partial F_z}{\partial z}$$

$$\nabla^2\tau_{yz} + \frac{1}{1+v}\frac{\partial^2\Lambda}{\partial y\partial z} = -\left(\frac{\partial F_z}{\partial y} + \frac{\partial F_y}{\partial z}\right)$$

$$\nabla^2\tau_{zx} + \frac{1}{1+v}\frac{\partial^2\Lambda}{\partial z\partial x} = -\left(\frac{\partial F_x}{\partial z} + \frac{\partial F_z}{\partial x}\right)$$

$$\nabla^2\tau_{xy} + \frac{1}{1+v}\frac{\partial^2\Lambda}{\partial x\partial y} = -\left(\frac{\partial F_y}{\partial x} + \frac{\partial F_x}{\partial y}\right)$$

(1.38)

where $\quad \Lambda \equiv \sigma_x + \sigma_y + \sigma_z$

For a cylindrical coordinate system, the strain compatibility equations have the following form (see derivation in [16]):

$$\frac{1}{r}\frac{\partial^2\varepsilon_r}{\partial\theta^2} + \frac{\partial}{\partial r}\left\{r\frac{\partial\varepsilon_\theta}{\partial r} - (\varepsilon_r - \varepsilon_\theta)\right\} = \frac{\partial}{\partial\theta}\left\{\frac{\partial\gamma_{r\theta}}{\partial r} + \frac{\gamma_{r\theta}}{r}\right\}$$

$$\frac{1}{r^2}\frac{\partial^2\varepsilon_z}{\partial\theta^2} + \frac{\partial^2\varepsilon_\theta}{\partial z^2} + \frac{1}{r}\frac{\partial\varepsilon_z}{\partial r} = \frac{1}{r}\frac{\partial}{\partial z}\left\{\frac{\partial\gamma_{\theta z}}{\partial\theta} + \gamma_{rz}\right\}$$

$$\frac{\partial^2\varepsilon_z}{\partial r^2} + \frac{\partial^2\varepsilon_r}{\partial z^2} = \frac{\partial^2\gamma_{rz}}{\partial r\partial z}$$

$$\frac{2}{r}\frac{\partial^2\varepsilon_r}{\partial\theta\partial z} = \frac{1}{r}\frac{\partial}{\partial r}\left\{r\frac{\partial\gamma_{r\theta}}{\partial z} - \gamma_{\theta z}\right\} + \frac{\partial}{\partial r}\left\{\frac{1}{r}\frac{\partial\gamma_{rz}}{\partial\theta} - \frac{\partial\gamma_{\theta z}}{\partial r}\right\} + \frac{1}{r}\frac{\partial\gamma_{r\theta}}{\partial z} + \frac{\gamma_{\theta z}}{r^2}$$

$$2\frac{\partial}{\partial z}\left\{\frac{\partial\varepsilon_\theta}{\partial r} - \left(\frac{\varepsilon_r - \varepsilon_\theta}{r}\right)\right\} = \frac{1}{r}\frac{\partial}{\partial\theta}\left\{\frac{\partial\gamma_{\theta z}}{\partial r} - \frac{1}{r}\frac{\partial\gamma_{rz}}{\partial\theta} + \frac{\partial\gamma_{r\theta}}{\partial z}\right\} + \frac{1}{r^2}\frac{\partial\gamma_{\theta z}}{\partial\theta}$$

$$\frac{2}{r}\frac{\partial}{\partial\theta}\left\{\frac{\partial\varepsilon_z}{\partial r} - \frac{\varepsilon_z}{r}\right\} = \frac{\partial}{\partial z}\left\{\frac{\partial\gamma_{\theta z}}{\partial r} + \frac{1}{r}\frac{\partial\gamma_{rz}}{\partial\theta} - \frac{\partial\gamma_{r\theta}}{\partial z} - \frac{\gamma_{\theta z}}{r}\right\}$$

(1.39)

where the various strain components were defined in eq. (1.8).

The associated Beltrami–Michell compatibility equations given for a cylindrical coordinate system are given as

$$\frac{1}{r}\frac{\partial}{\partial r}\left(r\frac{\partial \sigma_r}{\partial r}\right) + \frac{1}{r^2}\frac{\partial \sigma_r}{\partial \theta^2} + \frac{\partial^2 \sigma_r}{\partial z^2} + \frac{1}{1+\nu}\frac{\partial^2 \Omega}{\partial r^2} = -\frac{1}{1-\nu}\frac{1}{r}\left[\frac{\partial(rF_r)}{\partial r} + \frac{\partial F_\theta}{\partial \theta} + \frac{r\partial F_z}{\partial z}\right] - 2\frac{\partial F_r}{\partial r}$$

$$\frac{1}{r}\frac{\partial}{\partial r}\left(r\frac{\partial \sigma_\theta}{\partial r}\right) + \frac{1}{r^2}\frac{\partial \sigma_\theta}{\partial \theta^2} + \frac{\partial^2 \sigma_\theta}{\partial z^2} + \frac{1}{1+\nu}\frac{\partial^2 \Omega}{\partial \theta^2} = -\frac{1}{1-\nu}\frac{1}{r}\left[\frac{\partial(rF_r)}{\partial r} + \frac{\partial F_\theta}{\partial \theta} + \frac{r\partial F_z}{\partial z}\right] - 2\frac{\partial F_\theta}{\partial \theta}$$

$$\frac{1}{r}\frac{\partial}{\partial r}\left(r\frac{\partial \sigma_z}{\partial r}\right) + \frac{1}{r^2}\frac{\partial \sigma_z}{\partial \theta^2} + \frac{\partial^2 \sigma_z}{\partial z^2} + \frac{1}{1+\nu}\frac{\partial^2 \Omega}{\partial z^2} = -\frac{1}{1-\nu}\frac{1}{r}\left[\frac{\partial(rF_r)}{\partial r} + \frac{\partial F_\theta}{\partial \theta} + \frac{r\partial F_z}{\partial z}\right] - 2\frac{\partial F_z}{\partial z}$$

$$\frac{1}{r}\frac{\partial}{\partial r}\left(r\frac{\partial \sigma_{\theta z}}{\partial r}\right) + \frac{1}{r^2}\frac{\partial \sigma_{\theta z}}{\partial \theta^2} + \frac{\partial^2 \sigma_{\theta z}}{\partial z^2} + \frac{1}{1+\nu}\frac{\partial^2 \Omega}{\partial \theta \partial z} = -\left(\frac{\partial F_\theta}{\partial z} + \frac{\partial F_z}{\partial \theta}\right)$$

$$\frac{1}{r}\frac{\partial}{\partial r}\left(r\frac{\partial \sigma_{rz}}{\partial r}\right) + \frac{1}{r^2}\frac{\partial \sigma_{rz}}{\partial \theta^2} + \frac{\partial^2 \sigma_{rz}}{\partial z^2} + \frac{1}{1+\nu}\frac{\partial^2 \Omega}{\partial r \partial z} = -\left(\frac{\partial F_z}{\partial r} + \frac{\partial F_r}{\partial z}\right)$$

$$\frac{1}{r}\frac{\partial}{\partial r}\left(r\frac{\partial \sigma_{r\theta}}{\partial r}\right) + \frac{1}{r^2}\frac{\partial \sigma_{r\theta}}{\partial \theta^2} + \frac{\partial^2 \sigma_{r\theta}}{\partial z^2} + \frac{1}{1+\nu}\frac{\partial^2 \Omega}{\partial r \partial \theta} = -\left(\frac{\partial F_r}{\partial \theta} + \frac{\partial F_\theta}{\partial r}\right)$$

where $\quad \Omega \equiv \sigma_r + \sigma_\theta + \sigma_z$

$$(1.40)$$

The strain compatibility equations in a spherical coordinate system, defined in eq. (1.10), have the following form (for clarity, the expressions for the various strains are not presented using the three assumed displacements u_r, u_θ and u_ϕ in the directions r, θ, ϕ, respectively)

$$\frac{\partial^2 \varepsilon_r}{\partial \theta^2} + \frac{\partial^2 \varepsilon_\theta}{\partial r^2} - 2\frac{\partial^2 \varepsilon_{r\theta}}{\partial r \partial \theta} = 0$$

$$\frac{\partial^2 \varepsilon_\theta}{\partial \phi^2} + \frac{\partial^2 \varepsilon_\phi}{\partial \theta^2} - 2\frac{\partial^2 \varepsilon_{\theta\phi}}{\partial \theta \partial \phi} = 0$$

$$\frac{\partial^2 \varepsilon_\phi}{\partial r^2} + \frac{\partial^2 \varepsilon_r}{\partial \phi^2} - 2\frac{\partial^2 \varepsilon_{\phi r}}{\partial \phi \partial r} = 0$$

$$\frac{\partial^2 \varepsilon_r}{\partial \theta \partial \phi} + \frac{\partial^2 \varepsilon_{\theta\phi}}{\partial r^2} - \frac{\partial^2 \varepsilon_{r\theta}}{\partial r \partial \phi} - \frac{\partial^2 \varepsilon_{r\phi}}{\partial r \partial \theta} = 0$$

$$\frac{\partial^2 \varepsilon_\theta}{\partial \phi \partial r} + \frac{\partial^2 \varepsilon_{\phi r}}{\partial \theta^2} - \frac{\partial^2 \varepsilon_{\theta\phi}}{\partial \theta \partial r} - \frac{\partial^2 \varepsilon_{\theta r}}{\partial \theta \partial \phi} = 0$$

$$\frac{\partial^2 \varepsilon_\phi}{\partial r \partial \theta} + \frac{\partial^2 \varepsilon_{r\theta}}{\partial \phi^2} - \frac{\partial^2 \varepsilon_{\phi r}}{\partial \phi \partial \theta} - \frac{\partial^2 \varepsilon_{\phi\theta}}{\partial \phi \partial r} = 0$$

$$(1.41)$$

where

$$\varepsilon_{r\theta} \equiv 0.5\gamma_{r\theta}, \qquad \varepsilon_{r\phi} \equiv 0.5\gamma_{r\phi}, \qquad \varepsilon_{\theta\phi} \equiv 0.5\gamma_{\theta\phi}$$

$$\varepsilon_{\theta r} \equiv 0.5\gamma_{\theta r}, \qquad \varepsilon_{\phi r} \equiv 0.5\gamma_{\phi r}, \qquad \varepsilon_{\phi\theta} \equiv 0.5\gamma_{\phi\theta}$$

$$(1.42)$$

Finally, the associated Beltrami–Michell compatibility equations given for a spherical coordinate system are given as

$$\frac{1}{r^2}\frac{\partial}{\partial r}\left(r^2\frac{\partial\sigma_r}{\partial r}\right) + \frac{1}{r^2\sin\theta}\frac{\partial}{\partial\theta}\left(\sin\theta\frac{\partial\sigma_r}{\partial\theta}\right) + \frac{1}{r^2\sin^2\theta}\frac{\partial^2\sigma_r}{\partial\phi^2} + \frac{1}{1+\nu}\frac{\partial^2\Psi}{\partial r^2} =$$

$$-\frac{1}{1-\nu}\frac{1}{r}\left[\frac{1}{r}\frac{\partial(r^2F_r)}{\partial r} + \frac{1}{\sin\theta}\frac{\partial}{\partial\theta}(\sin\theta\cdot F_\theta) + \frac{1}{\sin\theta}\frac{\partial F_\phi}{\partial\phi}\right] - 2\frac{\partial F_r}{\partial r}$$

$$\frac{1}{r^2}\frac{\partial}{\partial r}\left(r^2\frac{\partial\sigma_\theta}{\partial r}\right) + \frac{1}{r^2\sin\theta}\frac{\partial}{\partial\theta}\left(\sin\theta\frac{\partial\sigma_\theta}{\partial\theta}\right) + \frac{1}{r^2\sin^2\theta}\frac{\partial^2\sigma_\theta}{\partial\phi^2} + \frac{1}{1+\nu}\frac{\partial^2\Psi}{\partial\theta^2} =$$

$$-\frac{1}{1-\nu}\frac{1}{r}\left[\frac{1}{r}\frac{\partial(r^2F_r)}{\partial r} + \frac{1}{\sin\theta}\frac{\partial}{\partial\theta}(\sin\theta\cdot F_\theta) + \frac{1}{\sin\theta}\frac{\partial F_\phi}{\partial\phi}\right] - 2\frac{\partial F_\theta}{\partial\theta}$$

$$\frac{1}{r^2}\frac{\partial}{\partial r}\left(r^2\frac{\partial\sigma_\phi}{\partial r}\right) + \frac{1}{r^2\sin\theta}\frac{\partial}{\partial\theta}\left(\sin\theta\frac{\partial\sigma_\phi}{\partial\theta}\right) + \frac{1}{r^2\sin^2\theta}\frac{\partial^2\sigma_\phi}{\partial\phi^2} + \frac{1}{1+\nu}\frac{\partial^2\Psi}{\partial\phi^2} =$$

$$-\frac{1}{1-\nu}\frac{1}{r}\left[\frac{1}{r}\frac{\partial(r^2F_r)}{\partial r} + \frac{1}{\sin\theta}\frac{\partial}{\partial\theta}(\sin\theta\cdot F_\theta) + \frac{1}{\sin\theta}\frac{\partial F_\phi}{\partial\phi}\right] - 2\frac{\partial F_\phi}{\partial\phi}$$

$$\frac{1}{r^2}\frac{\partial}{\partial r}\left(r^2\frac{\partial\sigma_{\theta\phi}}{\partial r}\right) + \frac{1}{r^2\sin\theta}\frac{\partial}{\partial\theta}\left(\sin\theta\frac{\partial\sigma_{\theta\phi}}{\partial\theta}\right) + \frac{1}{r^2\sin^2\theta}\frac{\partial^2\sigma_{\theta\phi}}{\partial\phi^2} + \frac{1}{1+\nu}\frac{\partial^2\Psi}{\partial\theta\partial\phi} =$$

$$-\left(\frac{\partial F_\theta}{\partial\phi} + \frac{\partial F_\phi}{\partial\theta}\right)$$

$$\frac{1}{r^2}\frac{\partial}{\partial r}\left(r^2\frac{\partial\sigma_{r\phi}}{\partial r}\right) + \frac{1}{r^2\sin\theta}\frac{\partial}{\partial\theta}\left(\sin\theta\frac{\partial\sigma_{r\phi}}{\partial\theta}\right) + \frac{1}{r^2\sin^2\theta}\frac{\partial^2\sigma_{r\phi}}{\partial\phi^2} + \frac{1}{1+\nu}\frac{\partial^2\Psi}{\partial\theta\partial\phi} =$$

$$-\left(\frac{\partial F_r}{\partial\phi} + \frac{\partial F_\phi}{\partial r}\right)$$

$$\frac{1}{r^2}\frac{\partial}{\partial r}\left(r^2\frac{\partial\sigma_{r\theta}}{\partial r}\right) + \frac{1}{r^2\sin\theta}\frac{\partial}{\partial\theta}\left(\sin\theta\frac{\partial\sigma_{r\theta}}{\partial\theta}\right) + \frac{1}{r^2\sin^2\theta}\frac{\partial^2\sigma_{r\theta}}{\partial\phi^2} + \frac{1}{1+\nu}\frac{\partial^2\Psi}{\partial r\partial\theta} =$$

$$-\left(\frac{\partial F_r}{\partial\theta} + \frac{\partial F_\theta}{\partial r}\right)$$

(1.43)

where $\quad \Psi \equiv \sigma_r + \sigma_\theta + \sigma_\phi$

1.4.3 Plane stress and plane strain (2D representations)

Often 3D elasticity problems can be reduced to only 2D representations, thus enabling an easier solution. These cases are either called *plane stress* and/or *plane strain* problems.

1.4.3a Plane stress problems

Three-dimensional cases for which 1D is much smaller than the other two, like in the case of thin flat plates, can be approximated using the plane stress assumption. For these cases, the plate thickness would be in the z direction, with loads being applied perpendicular to it. Then, under these assumptions, all stress components having a subscript z are assumed to be zero. The remaining stress components are then assumed to be functions of only x and y coordinates. This will transform the 3D equations, presented in eq. (1.15) (for a Cartesian coordinate system) into the following simplified 2D form:

$$\varepsilon_x = \frac{1}{E}\left[\sigma_x - v\sigma_y\right], \qquad \varepsilon_y = \frac{1}{E}\left[\sigma_y - v\sigma_x\right]$$

$$\varepsilon_z = -\frac{1}{E}\left[v\left(\sigma_x + \sigma_y\right)\right] \tag{1.44}$$

$$\gamma_{xy} = \frac{\tau_{xy}}{G}, \qquad \gamma_{yz} = 0, \qquad \gamma_{xz} = 0$$

Accordingly, for a cylindrical coordinate system, we will get the following equations (based on eq. (1.16), under the assumption that there is no z dependence), which are also known as *polar* representation

$$\varepsilon_r = \frac{1}{E}[\sigma_r - v\sigma_\theta], \qquad \varepsilon_\theta = \frac{1}{E}[\sigma_\theta - v\sigma_r]$$

$$\varepsilon_z = -\frac{1}{E}[v(\sigma_r + \sigma_\theta)] \tag{1.45}$$

$$\gamma_{r\theta} = \frac{\tau_{r\theta}}{G}, \qquad \gamma_{\theta z} = 0, \qquad \gamma_{rz} = 0$$

The inverse equations, namely the stresses as a function of the strains, are next presented[3]

$$\sigma_x = \frac{E}{(1-v^2)}\left[\varepsilon_x + v\varepsilon_y\right]$$

$$\sigma_y = \frac{E}{(1-v^2)}\left[\varepsilon_y + v\varepsilon_x\right] \tag{1.46}$$

$$\sigma_z = 0 = \left[(1-v)\varepsilon_z + v\left(\varepsilon_x + \varepsilon_y\right)\right]$$

$$\tau_{xy} = G\gamma_{xy}, \qquad \tau_{yz} = 0, \qquad \tau_{xz} = 0$$

---

3 One should note that the strain in the z direction, $\varepsilon_z \neq 0$!

$$\sigma_r = \frac{E}{(1 - v^2)} [\varepsilon_r + v\varepsilon_\theta]$$

$$\sigma_\theta = \frac{E}{(1 - v^2)} [\varepsilon_\theta + v\varepsilon_r]$$

$$\sigma_z = 0 = [(1 - v)\varepsilon_z + v(\varepsilon_r + \varepsilon_\theta)]$$

$$\tau_{r\theta} = G\gamma_{r\theta}, \quad \tau_{\theta z} = 0, \quad \tau_{rz} = 0$$

(1.47)

The strains compatibility equations, as presented in eq. (1.25), will have the following compact form for the plane stress case for a Cartesian system:

$$\frac{\partial^2 \varepsilon_x}{\partial y^2} + \frac{\partial^2 \varepsilon_y}{\partial x^2} = 2\frac{\partial^2 \varepsilon_{xy}}{\partial x \partial y}$$

$$\frac{\partial^2 \varepsilon_z}{\partial x^2} = 0$$

$$\frac{\partial^2 \varepsilon_z}{\partial y^2} = 0$$

$$\frac{\partial^2 \varepsilon_z}{\partial x \partial y} = 0$$

(1.48)

Note that the last three equations in eq. (1.48) might cause some difficulties for plane stress problems. For a cylindrical coordinate system, the strain compatibility equations would be (see eq. (1.39) for the 3D case)

$$\frac{1}{r}\frac{\partial^2 \varepsilon_r}{\partial \theta^2} + \frac{\partial}{\partial r}\left\{ r\frac{\partial \varepsilon_\theta}{\partial r} - (\varepsilon_r - \varepsilon_\theta) \right\} = \frac{\partial}{\partial \theta}\left\{ \frac{\partial \gamma_{r\theta}}{\partial r} + \frac{\gamma_{r\theta}}{r} \right\}$$

$$\frac{1}{r}\frac{\partial^2 \varepsilon_z}{\partial \theta^2} + \frac{\partial \varepsilon_z}{\partial r} = 0$$

$$\frac{\partial^2 \varepsilon_z}{\partial r^2} = 0$$

$$\frac{\partial}{\partial \theta}\left\{ \frac{\partial \varepsilon_z}{\partial r} - \frac{\varepsilon_z}{r} \right\} = 0$$

(1.49)

1.4.3b Plane strain problems

Three-dimensional cases for which 1D is much larger than the other two, as in the case of long cylindrical bodies or water dam-type structures, can be approximated using the plane strain assumption. For these cases, the larger dimension would be in the z direction, and for any x–y plane (perpendicular to z) it is assumed that the loads are independent of z. Then, under these assumptions, all strain components

having a subscript *z* are assumed to be zero. The remaining strain components are then assumed to be functions of only *x* and *y* coordinates.[4] This will transform the 3D equations presented in eq. (1.15) (for a Cartesian coordinate system) into the following simplified 2D form:

$$\varepsilon_x = \frac{1}{E}\left[\sigma_x - v(\sigma_y + \sigma_z)\right], \quad \varepsilon_y = \frac{1}{E}\left[\sigma_y - v(\sigma_z + \sigma_x)\right]$$

$$\varepsilon_z = 0 = \frac{1}{E}\left[\sigma_z - v(\sigma_x + \sigma_y)\right] \tag{1.50}$$

$$\gamma_{xy} = \frac{\tau_{xy}}{G}, \quad \gamma_{yz} = 0, \quad \gamma_{xz} = 0$$

Accordingly, for a cylindrical coordinate system, we will obtain

$$\varepsilon_r = \frac{1}{E}\left[\sigma_r - v(\sigma_\theta + \sigma_z)\right], \quad \varepsilon_\theta = \frac{1}{E}\left[\sigma_\theta - v(\sigma_z + \sigma_r)\right]$$

$$\varepsilon_z = 0 = -\frac{1}{E}\left[\sigma_z - v(\sigma_r + \sigma_\theta)\right] \tag{1.51}$$

$$\gamma_{r\theta} = \frac{\tau_{r\theta}}{G}, \quad \gamma_{\theta z} = 0, \quad \gamma_{rz} = 0$$

The inverse equations, namely the stresses as a function of the strains, are next presented:

$$\sigma_x = \frac{E}{(1+v)(1-2v)}\left[(1-v)\varepsilon_x + v\varepsilon_y\right]$$

$$\sigma_y = \frac{E}{(1+v)(1-2v)}\left[(1-v)\varepsilon_y + v\varepsilon_x\right] \tag{1.52}$$

$$\sigma_z = \frac{E}{(1+v)(1-2v)}\left[v(\varepsilon_x + \varepsilon_y)\right]$$
$$\tau_{xy} = G\gamma_{xy}, \quad \tau_{yz} = 0, \quad \tau_{xz} = 0$$

$$\sigma_r = \frac{E}{(1+v)(1-2v)}\left[(1-v)\varepsilon_r + v\varepsilon_\theta\right]$$

$$\sigma_\theta = \frac{E}{(1+v)(1-2v)}\left[(1-v)\varepsilon_\theta + v\varepsilon_r\right] \tag{1.53}$$

$$\sigma_z = \frac{E}{(1+v)(1-2v)}\left[v(\varepsilon_r + \varepsilon_\theta)\right]$$
$$\tau_{r\theta} = G\gamma_{r\theta}, \quad \tau_{\theta z} = 0, \quad \tau_{rz} = 0$$

The strain compatibility equations, as presented in eq. (1.25), will have the following compact form for the plane strain case for a Cartesian system:

---

4 Note that in this case $\sigma_z \neq 0$!

$$\frac{\partial^2 \varepsilon_x}{\partial y^2} + \frac{\partial^2 \varepsilon_y}{\partial x^2} = 2\frac{\partial^2 \varepsilon_{xy}}{\partial x \partial y}$$

$$\frac{\partial^2 \varepsilon_z}{\partial x^2} = 0$$

$$\frac{\partial^2 \varepsilon_z}{\partial y^2} = 0 \tag{1.54}$$

$$\frac{\partial^2 \varepsilon_z}{\partial x \partial y} = 0$$

Note that the last three equations in eq. (1.54) might complicate the solutions for plane strain problems (the same as for the plane stress case, presented above). For a cylindrical coordinate system, the strain compatibility equations would be (see eq. (1.39) for the 3D case)

$$\frac{1}{r}\frac{\partial^2 \varepsilon_r}{\partial \theta^2} + \frac{\partial}{\partial r}\left\{r\frac{\partial \varepsilon_\theta}{\partial r} - (\varepsilon_r - \varepsilon_\theta)\right\} = \frac{\partial}{\partial \theta}\left\{\frac{\partial \gamma_{r\theta}}{\partial r} + \frac{\gamma_{r\theta}}{r}\right\}$$

$$\frac{1}{r}\frac{\partial^2 \varepsilon_z}{\partial \theta^2} + \frac{\partial \varepsilon_z}{\partial r} = 0$$

$$\frac{\partial^2 \varepsilon_z}{\partial r^2} = 0 \tag{1.55}$$

$$\frac{\partial}{\partial \theta}\left\{\frac{\partial \varepsilon_z}{\partial r} - \frac{\varepsilon_z}{r}\right\} = 0$$

1.4.4 The Airy function $\phi(x, y)$

One of the most efficient ways to solve 2D problems in elasticity is to introduce a new variable, known as the Airy stress function, $\phi(x, y)$, suggested by sir George Airy in 1862.[5] According to his idea, the stresses are defined as a function of the new variable leading to a new differential equation, which can be shown to be solvable in a much easier way compared to the solution of the equations of equilibrium, the Navier's equations (see eq. (1.27)). This leads to the following expressions for the three planar stresses (for a Cartesian coordinate system):

---

5 Sir George Biddeli Airy (1801–1892), English astronomer and mathematician (https://en.wikipe dia.org/wiki/George_Biddell_Airy)

$$\sigma_x(x,y) \equiv \frac{\partial^2 \phi(x,y)}{\partial y^2}$$

$$\sigma_y(x,y) \equiv \frac{\partial^2 \phi(x,y)}{\partial x^2} \tag{1.56}$$

$$\tau_{xy}(x,y) \equiv -\frac{\partial^2 \phi(x,y)}{\partial x \partial y}$$

Having the stresses expressed by the Airy function, $\phi(x,y)$, we can substitute eq. (1.56) into eq. (1.54) yielding the compatibility equation for a state of plane strain, with no body forces, where the unknown is the Airy function:

$$\frac{\partial^4 \phi(x,y)}{\partial x^4} + 2\frac{\partial^4 \phi(x,y)}{\partial x^2 \partial y^2} + \frac{\partial^4 \phi(x,y)}{\partial y^4} \equiv \nabla^4 \phi(x,y) = 0 \tag{1.57}$$

Equation (1.57) is also known as the biharmonic equation or $\nabla^4 \phi(x,y) = 0$.

For a cylindrical coordinate system, the biharmonic equation has the following form:

$$\nabla^4 \phi(r,\theta) \equiv \nabla^2 \left[\nabla^2 \phi(r,\theta) \right] =$$
$$\left(\frac{\partial^2}{\partial r^2} + \frac{1}{r}\frac{\partial}{\partial r} + \frac{1}{r^2}\frac{\partial^2}{\partial \theta^2} \right) \left(\frac{\partial^2 \phi(r,\theta)}{\partial r^2} + \frac{1}{r}\frac{\partial \phi(r,\theta)}{\partial r} + \frac{1}{r^2}\frac{\partial^2 \phi(r,\theta)}{\partial \theta^2} \right) = 0 \tag{1.58}$$

where the stress components are defined as

$$\sigma_r(r,\theta) \equiv \frac{1}{r}\frac{\partial \phi(r,\theta)}{\partial r} + \frac{1}{r^2}\frac{\partial^2 \phi(r,\theta)}{\partial \theta^2}$$

$$\sigma_\theta(r,\theta) \equiv \frac{\partial^2 \phi(r,\theta)}{\partial r^2} \tag{1.59}$$

$$\tau_{r\theta}(r,\theta) \equiv -\frac{1}{r}\frac{\partial^2 \phi(r,\theta)}{\partial r \partial \theta} + \frac{1}{r^2}\frac{\partial \phi(r,\theta)}{\partial \theta}$$

Often, there are problems in which the applied loads have an axisymmetric distribution, namely there is no dependence on the θ variable, and all derivatives with respect to it would vanish. This results in the following stress field: $\sigma_r(r), \sigma_\theta(r)$ and $\sigma_{r\theta}(r) = 0$. For the axisymmetric stress distribution, the biharmonic function (eq. (1.58)) reduces to

$$\nabla^4 \phi(r) \equiv \left(\frac{\partial^2}{\partial r^2} + \frac{1}{r}\frac{\partial}{\partial r} \right) \left(\frac{\partial^2 \phi(r)}{\partial r^2} + \frac{1}{r}\frac{\partial \phi(r)}{\partial r} \right) =$$
$$\frac{d^4 \phi(r)}{dr^4} + \frac{2}{r}\frac{d^3 \phi(r)}{dr^3} - \frac{1}{r^2}\frac{d^2 \phi(r)}{dr^2} + \frac{1}{r^3}\frac{d\phi(r)}{dr} = 0 \tag{1.60}$$

The solution for eq. (1.60) has the following form:

$$\phi(r) = A_1 + A_2 \log r + A_3 r^2 + A_4 r^2 \log r \tag{1.61}$$

and according to eq. (1.59) the expressions for the stresses are

$$\sigma_r(r) \equiv \frac{1}{r} \frac{d\phi(r)}{dr} = \frac{A_2}{r^2} + 2A_3 + A_4(2\log r + 1)$$

$$\sigma_\theta(r) \equiv \frac{d^2\phi(r,\theta)}{dr^2} = -\frac{A_2}{r^2} + 2A_3 + A_4(2\log r + 3) \tag{1.62}$$

$$\tau_{r\theta}(r,\theta) \equiv 0$$

where A_1, A_2, A_3 and A_4 are constants to be determined from the boundary conditions of the given problem.

For the case of plane stress, it can be shown that for the case of no body forces with symmetrically distributed applied loads, the Airy stress function $\phi(x,y)$ has the following form:

$$\phi(x,y) \equiv \psi(x,y) - \frac{vz^2}{2(1+v)r^2} \nabla^2 \psi(x,y) \tag{1.63}$$

where $\psi(x,y)$ is the solution of the following biharmonic function $\nabla^2\psi(x,y)$. Assuming the condition for the plane strain, namely, z is a very small quantity leads to $\phi(x,y) \approx \psi(x,y)$, which makes also the plane stress cases being solved by the biharmonic equation presented above.

In conclusion, the use of the Airy stress function representation reduces the problem of solving the stresses for an elastic body to that of finding a solution for the biharmonic partial differential equation, $\nabla^4\phi(x,y) = 0$, whose derivatives would satisfy certain boundary conditions, according to the posed problem.

1.4.5 Thermal field

All the previous equations were derived assuming the temperature of the given structure is constant, without any changes. However, for an unconstrained body, changing the uniform temperature, either by heating or by cooling, would cause the body to expand or contract, leading to normal strains. Preventing the expansion or the contraction would give rise to thermal stresses inside the structure.

To take this effect into consideration, one must redefine the stress–strain relationships, superimposing the thermal strains onto the mechanical one. Assuming the change in temperature is given spatially by $T(x, y)$, the corresponding change in the length would be written by

$$\Delta L = \alpha L T(x,y) \tag{1.64}$$

where α is the linear thermal expansion coefficient. The associated thermal strain is then defined as

$$\varepsilon_t = \frac{\Delta L}{L} = \alpha T(x, y) \tag{1.65}$$

Adding thermal strains to the mechanical ones (see, e.g., eq. (1.44)) leads for the plane stress case to

$$\varepsilon_x = \frac{1}{E}\left[\sigma_x - \nu\sigma_y\right] + \alpha T, \quad \varepsilon_y = \frac{1}{E}\left[\sigma_y - \nu\sigma_x\right] + \alpha T, \quad \gamma_{xy} = \frac{\tau_{xy}}{G} \tag{1.66}$$

Expressing strains as a function of strains leads to

$$\sigma_x = \frac{E}{(1 - \nu^2)}\left[\varepsilon_x + \nu\varepsilon_y\right] - \frac{E\alpha T}{(1 - \nu)}$$

$$\sigma_y = \frac{E}{(1 - \nu^2)}\left[\varepsilon_y + \nu\varepsilon_x\right] - \frac{E\alpha T}{(1 - \nu)} \tag{1.67}$$

$$\tau_{xy} = G\gamma_{xy}$$

Similar expressions can also be obtained for the plane strain case.

The biharmonic equation in the presence of a temperature field, $T(x, y)$, can be shown to have the following form:

$$\nabla^4\phi(x, y) + \alpha E\nabla^2 T(x, y) = 0 \tag{1.68}$$

This equation is true for both the plane stress and plane strains, provided the body forces can be assumed to be negligible.

References

[1] Francillon, René J. Lockheed Aircraft since, Naval Institute Press, Annapolis, Maryland, 1913, 1987, ISBN 0-85177-835-6.
[2] Niu, M. C.-Y. Airframe Structural Design –Practical Design Information and Data on Aircraft Structures, CONMILIT Press Ltd., ©, 1988, 607.
[3] Bruhn, E.F. Analysis and Design of Flight Vehicle Structures, Jacobs Publication ©, 1973, 650.
[4] Megson, T.H.G. Aircraft Structures for Engineering Students, 4th Edition, Butterworth-Heinemann (an imprint of Elsevier Ltd.,) ©, 2007, 804.
[5] Gran, B. Bruhn Errata- a Companion to Analysis of Flight Vehicle Structures, GRAN Corporation, 2nd Edition, 2008, 309.
[6] Weisshaar, T.A. Aerospace Structures- an Introduction to Fundamental Problems, Purdue University, USA, 28th of July,, 2011, 197.
[7] Kalanchiam, M., and Chinnasamy, M. Advantages of Composite Materials in Aircraft Structures, International Journal of Aerospace and Mechanical Engineering, 6(11), 2012, 2428–2432.

[8] Polland, D.R., Finn, S.R., Griess, K.H., Hafenrichter, J. L., Hanson, C.T., Ilsewicz, L.B., Metschan, S.L., Scholz, D.B., and Smith, P.J. Global Cost Weight Evaluation of Fuselage Panel Design Concepts, NASA, CR4730, April 1997, 319.

[9] Walker, T.H., Minguet, P.J., Flynn, B,W., Carbery, D.J., Swanson, G.D., and Ilsewicz, L.B Advanced Technology Composite Fuselage-Structural Performance, NASA CR4732, April 1997, 101.

[10] Flynn, B,W., Bodine, J.B., Dopker, B., Finn, S.R., Griess, K.H., Hanson, C.T., Harris, C.G., Nelson, K.M., Walker, T.H., Kennedy, T.C., and Nahan, M.F Advanced Technology Composite Fuselage-Repair and Damage Assessment Supporting Maintenance, NASA CR4733, April 1997, 154.

[11] Willden, K.S., Harris, C.G., Flynn, B.W., Gessel, M.G., Scholz, D.B., Stawski, S., and Winson, V. Advanced Technology Composite Fuselage-Manufacturing, NASA CR4735, April 1997, 189.

[12] Birch, H. Aerospace Materials-Changing Planes, Chemistry World, Oct, 2013, 60–63.

[13] Abramovich, H. Stability and Vibrations of Thin Walled Composite Structures, ©, Elsevier Ltd, Woodhead Publishing Limited, The Officers' Mess Business Centre, Royston Road, Duxford, CB22 4QH, United Kingdom; 50 Hampshire Street, 5th Floor, Cambridge, MA 02139, United States; The Boulevard, Langford Lane, Kidlington, OX5 1GB, United Kingdom, 2017, 778.

[14] Timoshenko, S.P., and Goodier, J.N. Theory of Elasticity, 3rd Ed, International Student Edition, McGraw-Hill Book Company, Kögakusha Company, Ltd, Tokyo, Japan, ©, 1970, McGraw-Hill Inc, 567.

[15] Chou, P.C., and Pagano, N.J. ELASTICITY Tensor, Dyadic and Engineering Approaches, Dover Publications, Inc, New York, 1992, 290.

[16] Carlucci, D., Payne, N., and Mehmedagic, I. Small Strain Compatibility Conditions of an Elastic Solid in Cylindrical Coordinates, Technical Report ARDSM-TR-12001, U.S. Army Armament Research, Development and Engineering Center, Munitions Engineering Technology Center, Picatinny Arsenal, New Jersey, USA, April 2013, 14.

2 Composite materials

2.1 Introduction

2.1.1 General introduction

One of the common definitions for a composite material, usually made of two constituents,one being the fiber (the reinforcement) and the other the glue (the matrix) states that a combination of the two materials would result in better properties than those of the individual components when they are used alone. The main advantages of composite materials over other existing materials, like metals or plastics, are their high strength and stiffness, combined with low density, allowing for a weight reduction in the finished part. The various types of composites are usually referred in the literature, as a block diagram, as depicted in Fig. 2.1 In this chapter when we are talking about a composite material, we restrict ourselves to only continuous fibers (reinforcements) being embedded into a carrying matrix formed from an adequate glue.

Examples of such continuous reinforcements include unidirectional, woven cloth and helical winding (see Fig. 2.2). Continuous-fiber composites are often made into laminates by stacking single sheets of continuous fibers in different orientations to obtain the desired strength and stiffness properties with fiber volumes as high as 60–70%. Fibers produce high-strength composites because of their small diameter; they contain far fewer defects (normally surface defects) compared to the material produced in bulk. On top of it, due to their small diameter the fibers are flexible and suitable for complicated manufacturing processes, such as small radii or weaving. Materials like glass, graphite, carbon or aramid are used to produce fibers (see typical properties in Table 2.1). The today's usage of composite materials is mainly driven by the aerospace sector, with large percentage of the modern airplane structures, like Boeing 787 or Airbus A380 (see Fig. 2.3), being manufactured from carbon, glass and aramid fibers. The main material for the matrix is a polymer, which has low strength and stiffness. The main functions of the matrix are to keep the fibers in the proper orientation and spacing and providing protection to the fiber from abrasion and the environment. In polymer matrix composites, the good and strong bond between the matrix and the reinforcement allows the matrix to transmit the outside loads from the matrix to the fibers through shear loading at the interface. Two types of polymer matrices are available: thermosets and thermoplastics. A thermoset starts as a low-viscosity resin that reacts and cures during processing, forming a solid. A thermoplastic is a high-viscosity resin that is processed by heating it above its melting temperature. Because a thermoset resin sets up and cures during processing, it cannot be reprocessed by reheating. A thermoplastic can be reheated above its melting temperature for additional processing.
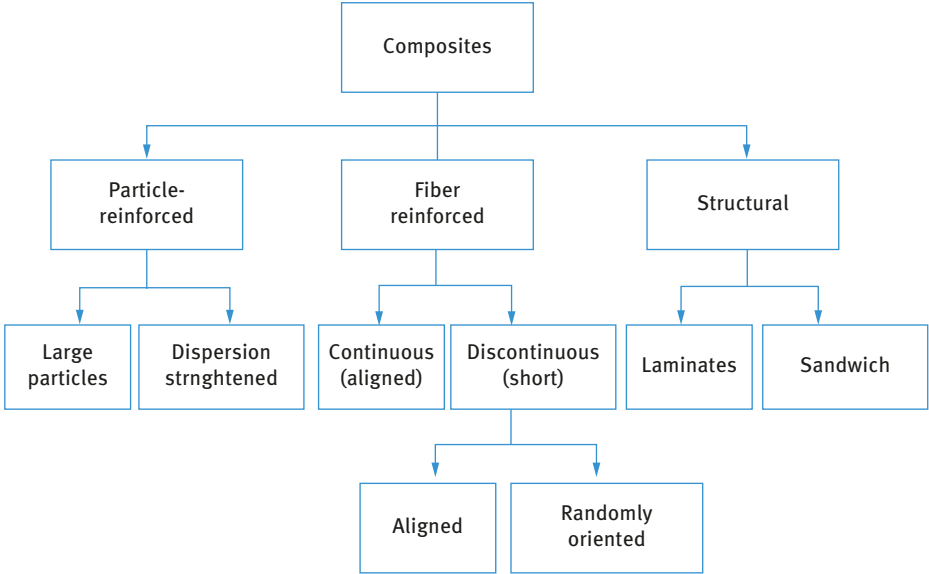
Fig. 2.1: Typical composite materials.
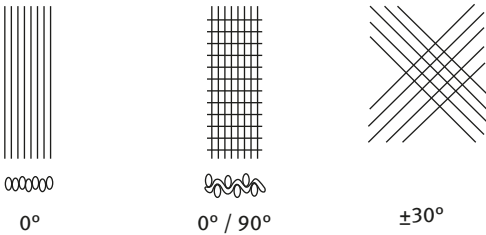
Fig. 2.2: Typical composite materials.

2.2 Unidirectional composites

Unidirectional composites are usually composed of two constituents, the fiber and the matrix (which is the glue holding together the two components). Based on the rule of mixtures one can calculate the properties of the unidirectional layer based on the properties of the fibers and the matrix and their volume fracture. The assumption to be made when applying the rule of mixtures is that the two constituents are bonded together and they behave like a single body. The longitudinal modulus (or the major modulus), E_{11}, of the layer can be written as

$$E_{11} = E_f V_f + E_m V_m \tag{2.1}$$

Table 2.1: Typical properties of mostly used reinforced continuous fibers (from [1] and [2]).

Material	Trade name	Density, ρ (kg/m^2)	Typical fiber diameter (µm)	Young's modulus, E (GPa)	Tensile strength (GPa)
α-Al$_2$O$_3$ (aluminum oxide)	FP (US)	3,960	20	385	1.8
Al$_2$O$_3$ + SiO$_2$ + B$_2$O$_3$ (mullite)	Nextel480 (USA)	3,050	11	224	2.3
Al$_2$O$_3$ + SiO$_2$ (alumina–silica)	Altex (Japan)	3,300	10–15	210	2.0
Boron (CVD* on tungsten)	VMC (Japan)	2,600	140	410	4.0
Carbon (PAN** precursor)	T300 (Japan)	1,800	7	230	3.5
Carbon (PAN** precursor)	T800 (Japan)	1,800	5.5	295	5.6
Carbon (pitch*** precursor)	Thorne IP755 (USA)	2,060	10	517	2.1
SiC (+O) (silicon carbide)	Nicalon (Japan)	2,600	15	190	2.5–3.3
SiC (low O) (silicon carbide)	Hi-Nicalon (Japan)	2,740	14	270	2.8
SiC (+O + Ti) (silicon carbide)	Tyranno (Japan)	2,400	9	200	2.8
SiC (monofilament) (silicon carbide)	Sigma	3,100	100	400	3.5
E-glass (silica)		2,500	10	70	1.5–2.0
E-glass (silica)		2,500	10	70	1.5–2.0
Quartz(silica)		2,200	3–15	80	3.5
Aromatic polyamide	Kevlar 49 (USA)	1,500	12	130	3.6
Polyethylene (UHMW)†	Spectra 100 (USA)	970	38	175	3.0
High carbon steel	E.g., piano wire	7,800	250	210	2.8

Table 2.1 (continued)

Material	Trade name	Density, ρ (kg/m^2)	Typical fiber diameter (µm)	Young's modulus, E (GPa)	Tensile strength (GPa)
Aluminum	Electrical wire	2,680	1670	75	0.27
Titanium	Wire	4,700	250	115	0.434

[*]CVD, chemical vapor deposition.
[**] PAN, polyacrylonitrile. About 90% of the carbon fibers produced are made from PAN.
[***] Pitch is a viscoelastic material that is composed of aromatic hydrocarbons. Pitch is produced via the distillation of carbon-based materials, such as plants, crude oil and coal.
[†] UHMW, ultra-high-molecular-weight polyethylene (or polyethene, the most common plastic produced in the world) is a subset of the thermoplastic polyethylene.

where E_f and E_m are the longitudinal moduli for the fibers and the matrix, respectively, and V_f and V_m are their volume fractions.[1]

The major Poisson's coefficient, ν_{12}, is given by

$$\nu_{12} = \nu_f V_f + \nu_m V_m \tag{2.2}$$

where ν_f and ν_m are the longitudinal moduli for the fibers and the matrix, respectively.

One should note that the minor Poisson's coefficient, ν_{21}, will be calculated to be

$$\frac{\nu_{12}}{E_{11}} = \frac{\nu_{21}}{E_{22}} \Rightarrow \nu_{21} = \nu_{12}\frac{E_{22}}{E_{11}} \tag{2.3}$$

The transverse modulus (or the minor modulus), E_{22}, of the layer is given as

$$\frac{1}{E_{22}} = \frac{V_f}{E_f} + \frac{V_m}{E_m} \Rightarrow E_{22} = \frac{E_m}{V_f\frac{E_m}{E_f} + V_m} = \frac{E_m}{V_f\frac{E_m}{E_f} + (1 - V_f)} \tag{2.4}$$

The shear modulus of the layer, G_{12}, is given as

$$\frac{1}{G_{12}} = \frac{V_f}{G_f} + \frac{V_m}{G_m} \Rightarrow G_{12} = \frac{G_m}{V_f\frac{G_m}{G_f} + V_m} = \frac{G_m}{V_f\frac{G_m}{G_f} + (1 - V_f)} \tag{2.5}$$

where G_f and G_m are the shear moduli for the fibers and the matrix, respectively.

To be able to assess the differences between the properties of the fiber and to compare to those of the matrix, the reader is referred to Table 2.2 (from [1]).

---

1 Note that $V_f + V_m = 1$.
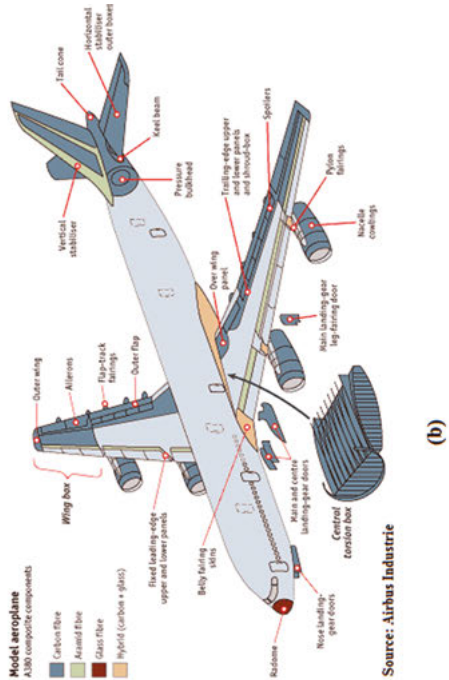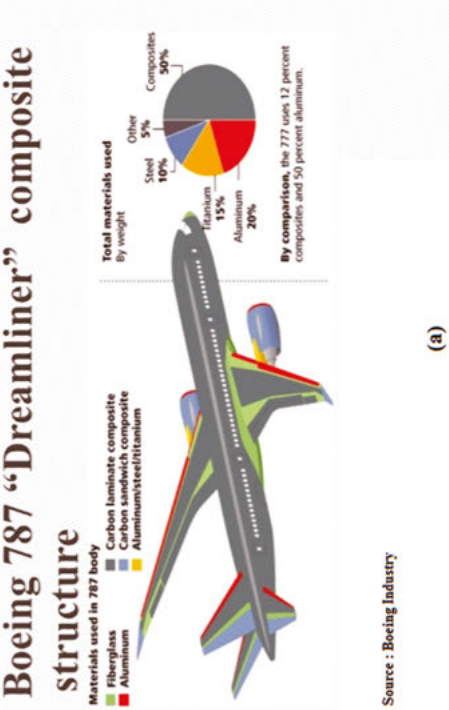
Fig. 2.3: Usage of composite materials in aerospace structures: (a) Boeing 787 and (b) Airbus A380.

Table 2.2: Typical properties of T300 carbon fibers and 914 epoxy resin.

Property	T300 carbon fibers	914 epoxy resin matrix
Young's modulus, E (GPa)	220	3.3
Shear modulus, G (GPa)	25	1.2
Poisson's ratio, v	0.15	0.37

As described in [1], the simple micromechanics model used in the rule of mixtures predict well the values of the four variables, E_{11}, E_{22}, G_{12} and $v12$, when compared to experimental values, as mentioned in Table 2.3.

Table 2.3: Predictions of unidirectional composite properties by simple micromechanic models (adapted from [1]).

Equation	Relationship	Predicted values (moduli in GPa)	Experimental values (moduli in GPa)
2.1	$E_{11} = E_f V_f + E_m(1 - V_f)$	124.7	125.0
2.4	$\frac{1}{E_{22}} = \frac{V_f}{E_f} + \frac{(1 - V_f)}{E_m}$	7.4	9.1
2.5	$\frac{1}{G_{12}} = \frac{V_f}{G_f} + \frac{(1 - V_f)}{G_m}$	2.6	5.0
2.2	$v_{12} = v_f V_f + v_m(1 - V_f)$	0.25	0.34

2.3 Properties of a single ply

A ply has two major dimensions and one, the thickness, is very small as compared to the two major ones. Therefore, the 3D presentation of an orthotropic material will be simplified to a 2D presentation (plane stress) by assuming that $\sigma_{33} = 0$ [1, 2]. This leads to a reduced compliance matrix for the ply, in the form:

$$\begin{Bmatrix} \varepsilon_{11} \\ \varepsilon_{22} \\ \gamma_{12} \end{Bmatrix} = \begin{bmatrix} \dfrac{1}{E_1} & -\dfrac{v_{21}}{E_2} & 0 \\ -\dfrac{v_{12}}{E_1} & \dfrac{1}{E_2} & 0 \\ 0 & 0 & \dfrac{1}{G_{12}} \end{bmatrix} \begin{Bmatrix} \sigma_{11} \\ \sigma_{22} \\ \sigma_{12} \end{Bmatrix} \tag{2.6}$$

a third equation, for the strain in the thickness direction, ε_{33}, which is seldom used has the form

$$\varepsilon_{33} = -\frac{\gamma_{13}}{E_1}\sigma_{11} - \frac{\gamma_{23}}{E_2}\sigma_{22} \tag{2.7}$$

And the remaining two equations for the shear strains are written as

$$\left\{ \begin{array}{c} \gamma_{23} \\ \gamma_{13} \end{array} \right\} = \begin{bmatrix} \dfrac{1}{G_{23}} & 0 \\ 0 & \dfrac{1}{G_{13}} \end{bmatrix} \left\{ \begin{array}{c} \sigma_{23} \\ \sigma_{13} \end{array} \right\} \tag{2.8}$$

Calculation of the stresses as a function of strains would yield (by the use of eqs. (2.6) and (2.8)):

$$\left\{ \begin{array}{c} \sigma_{11} \\ \sigma_{22} \\ \sigma_{12} \end{array} \right\} = \begin{bmatrix} Q_{11} & Q_{12} & 0 \\ Q_{21} & Q_{22} & 0 \\ 0 & 0 & Q_{66} \end{bmatrix} \left\{ \begin{array}{c} \varepsilon_{11} \\ \varepsilon_{22} \\ \gamma_{12} \end{array} \right\} = \begin{bmatrix} \dfrac{E_1}{(1 - v_{12}v_{21})} & \dfrac{v_{21}E_1}{(1 - v_{12}v_{21})} & 0 \\ \dfrac{v_{12}E_2}{(1 - v_{12}v_{21})} & \dfrac{E_2}{(1 - v_{12}v_{21})} & 0 \\ 0 & 0 & G_{12} \end{bmatrix} \left\{ \begin{array}{c} \varepsilon_{11} \\ \varepsilon_{22} \\ \gamma_{12} \end{array} \right\} \tag{2.9}$$

with $Q_{12} = Q_{21}$ and $v_{12} \neq v_{21}$

$$\left\{ \begin{array}{c} \sigma_{23} \\ \sigma_{13} \end{array} \right\} = \begin{bmatrix} Q_{23} & 0 \\ 0 & Q_{13} \end{bmatrix} \left\{ \begin{array}{c} \gamma_{23} \\ \gamma_{13} \end{array} \right\} = \begin{bmatrix} G_{23} & 0 \\ 0 & G_{13} \end{bmatrix} \left\{ \begin{array}{c} \gamma_{23} \\ \gamma_{13} \end{array} \right\} \tag{2.10}$$

2.4 Transformation of stresses and strains

Consider the two coordinate systems described in Fig. 2.4. The one with indexes 1 and 2 describes the ply orthotropic coordinate system, while the other one (x, y) is an arbitrary one, rotated at a given angle θ relative to the 1, 2 system. The transformation of the stresses and the strains from the 1, 2 coordinate system to the x, y coordinate system is done by multiplication of both the stresses and the strains at the ply level by the transformation matrix **T** as given by[2]

$$\left\{ \begin{array}{c} \sigma_1 \\ \sigma_2 \\ \tau_{12} \end{array} \right\}^k = [T] \left\{ \begin{array}{c} \sigma_x \\ \sigma_y \\ \tau_{xy} \end{array} \right\}^k \tag{2.11}$$

$$\left\{ \begin{array}{c} \varepsilon_1 \\ \varepsilon_2 \\ \dfrac{\gamma_{12}}{2} \end{array} \right\}^k = [T] \left\{ \begin{array}{c} \varepsilon_x \\ \varepsilon_y \\ \dfrac{\gamma_{xy}}{2} \end{array} \right\}^k \tag{2.12}$$

---

2 See, for example, ref. [1]: Primer on Composite Materials: Analysis by J. E. Ashton and J.C. Halpin, TECHNOMIC Publishing Co., Inc., 750 Summer St., Stamford, Conn. 06901, USA, 1969.
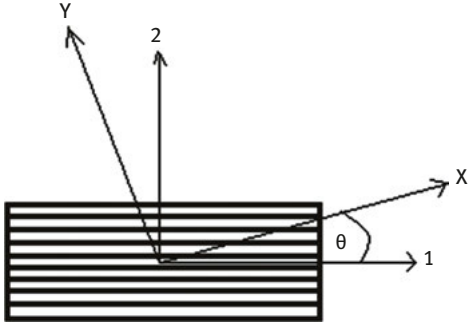
Fig. 2.4: Two coordinate systems: 1, 2 the ply orthotropic axis; *X, Y* arbitrary axis.

where k is the number of the ply, for which the transformation of strains and stresses is performed.[3] The transformation matrix T is given by

$$[T] = \begin{bmatrix} c^2 & s^2 & 2cs \\ s^2 & c^2 & -2cs \\ -cs & cs & c^2 - s^2 \end{bmatrix} \quad \text{where} \quad \begin{matrix} c \equiv \cos\theta \\ s \equiv \sin\theta \end{matrix} \tag{2.13}$$

To obtain the inverse of the matrix T one needs simply to insert $-\theta$ instead of θ in eq. (2.13) to yield

$$[T]^{-1} = [T(-\theta)] = \begin{bmatrix} c^2 & s^2 & -2cs \\ s^2 & c^2 & 2cs \\ cs & -cs & c^2 - s^2 \end{bmatrix} \tag{2.14}$$

The ply (or lamina) strain–stress relationships transformed to the laminate references axis (x, y) is written as

$$\begin{Bmatrix} \sigma_1 \\ \sigma_2 \\ \tau_{12} \end{Bmatrix}^k = [T]^{-1}[Q]^k[T] \begin{Bmatrix} \varepsilon_x \\ \varepsilon_y \\ \gamma_{xy} \end{Bmatrix}^k \tag{2.15}$$

where

$$[Q]^k = \begin{bmatrix} Q_{11} & Q_{12} & 0 \\ Q_{12} & Q_{22} & 0 \\ 0 & 0 & 2Q_{66} \end{bmatrix}^k$$

and the expressions for Q_{11}, Q_{12}, Q_{22} and Q_{66} are given in eq. (2.9). Performing the matrix multiplication in eq. (2.15) yields

---

3 Note that $\sigma_{11} \equiv \sigma_1$; $\sigma_{22} \equiv \sigma_2$; $\varepsilon_{11} \equiv \varepsilon_1$; $\varepsilon_{22} \equiv \varepsilon_2$.

$$\left\{ \begin{array}{c} \sigma_1 \\ \sigma_2 \\ \tau_{12} \end{array} \right\}^k = \left[\overline{Q} \right]^k \left\{ \begin{array}{c} \varepsilon_x \\ \varepsilon_y \\ \gamma_{xy} \end{array} \right\}^k$$

(2.16)

where

$$\left[\overline{Q} \right]^k = \begin{bmatrix} \overline{Q_{11}} & \overline{Q_{12}} & \overline{Q_{16}} \\ \overline{Q_{12}} & \overline{Q_{22}} & \overline{Q_{26}} \\ \overline{Q_{16}} & \overline{Q_{26}} & \overline{Q_{66}} \end{bmatrix}^k$$

where

$$\overline{Q_{11}} = Q_{11}\cos^4\theta + 2(Q_{12} + 2Q_{66})\sin^2\theta\cos^2\theta + Q_{22}\sin^4\theta$$

$$\overline{Q_{12}} = (Q_{11} + Q_{22} - 4Q_{66})\sin^2\theta\cos^2\theta + Q_{12}(\sin^4\theta + \cos^4\theta)$$

$$\overline{Q_{22}} = Q_{11}\sin^4\theta + 2(Q_{12} + 2Q_{66})\sin^2\theta\cos^2\theta + Q_{22}\cos^4\theta$$

$$\overline{Q_{16}} = (Q_{11} - Q_{12} - 2Q_{66})\sin\theta\cos^3\theta + (Q_{12} - Q_{22} + 2Q_{66})\sin^3\theta\cos\theta$$

$$\overline{Q_{26}} = (Q_{11} - Q_{12} - 2Q_{66})\sin^3\theta\cos\theta + (Q_{12} - Q_{22} + 2Q_{66})\sin\theta\cos^3\theta$$

$$\overline{Q_{66}} = (Q_{11} + Q_{22} - 2Q_{12} - 4Q_{66})\sin^2\theta\cos^2\theta + Q_{12}(\sin^4\theta + \cos^4\theta)$$

(2.17)

Another useful way of presenting the various terms of the matrix $\left[\overline{Q} \right]^k$ is the invariant procedure suggested by Tsai & Pagano, described in details in [2]:

$$\overline{Q_{11}} = U_1 + U_2\cos(2\theta) + U_3\cos(4\theta)$$

$$\overline{Q_{12}} = U_4 - U_3\cos(4\theta)$$

$$\overline{Q_{22}} = U_1 - U_2\cos(2\theta) + U_3\cos(4\theta)$$

$$\overline{Q_{16}} = -\frac{1}{2}U_2\sin(2\theta) - U_3\sin(4\theta)$$

$$\overline{Q_{26}} = -\frac{1}{2}U_2\sin(2\theta) + U_3\sin(4\theta)$$

$$\overline{Q_{66}} = U_5 - U_3\cos(4\theta)$$

where

$$U_1 = \frac{1}{8}[3Q_{11} + 3Q_{22} + 2Q_{12} + 4Q_{66}]$$

$$U_2 = \frac{1}{2}[Q_{11} - Q_{22}]$$

$$U_3 = \frac{1}{8}[Q_{11} + Q_{22} - 2Q_{12} - 4Q_{66}]$$

$$U_4 = \frac{1}{8}[Q_{11} + Q_{22} + 6Q_{12} - 4Q_{66}]$$

$$U_5 = \frac{1}{8}[Q_{11} + Q_{22} - 2Q_{12} + 4Q_{66}]$$

(2.18)

Note that the terms U_1, U_4 and U_5 are invariant to a rotation relative to the 3 axis (perpendicular to the 1–2 plane).

2.5 The classical lamination theory

Now we shall present the addition of the properties of each lamina to form a laminate, which is the structure to be investigated when we apply loads, using the classical lamination theory (CLT), which is based on Kirchhoff–Love plate theory [3–5].

Referring to Fig. 2.5, one can write the displacement in the x-direction of a point at a z-distance from the mid-plane as follows (where w is the displacement in the z direction):

$$u = u_0 - z\frac{\partial w}{\partial x} \tag{2.19}$$

Similarly the displacement in the y direction will be

$$v = v_0 - z\frac{\partial w}{\partial y} \tag{2.20}$$

Then the strains (ε_x, ε_y and y_{xy}) and the curvatures (κ_x, κ_y and κ_{xy}) can be written as

$$\varepsilon_x \equiv \frac{\partial u}{\partial x} = \frac{\partial u_0}{\partial x} - z\frac{\partial^2 w_0}{\partial x^2} = \varepsilon_x^0 + z\kappa_x$$

$$\varepsilon_y \equiv \frac{\partial v}{\partial y} = \frac{\partial v_0}{\partial y} - z\frac{\partial^2 w_0}{\partial y^2} = \varepsilon_y^0 + z\kappa_y \tag{2.21}$$

$$\gamma_{xy} \equiv \frac{\partial u}{\partial y} + \frac{\partial v}{\partial x} = \frac{\partial u_0}{\partial y} + \frac{\partial v_0}{\partial x} - 2z\frac{\partial^2 w}{\partial x \partial y} = \gamma_{xy}^0 + z\kappa_{xy}$$
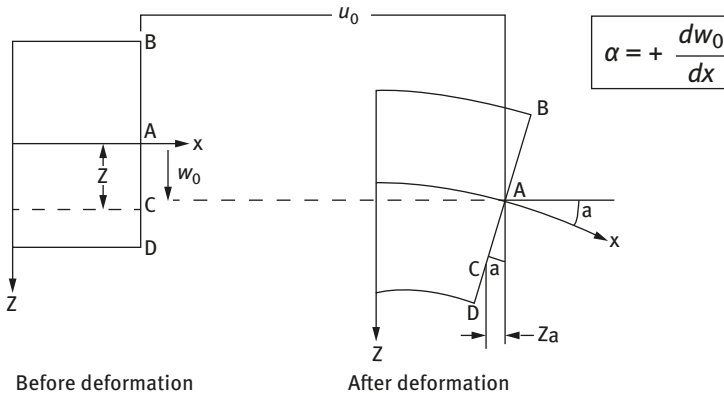
Fig. 2.5: The plate cross section before and after the deformation (CLT approach).

where $\varepsilon_x^0, \varepsilon_y^0, \gamma_{xy}^0$ are the strains at the neutral plane. In matrix notation, eq. (2.21) can be presented as

$$\left\{ \begin{array}{c} \varepsilon_x \\ \varepsilon_y \\ \gamma_{xy} \end{array} \right\} = \left\{ \begin{array}{c} \varepsilon_x^0 \\ \varepsilon_y^0 \\ \gamma_{xy}^0 \end{array} \right\} + z \left\{ \begin{array}{c} \kappa_x \\ \kappa_y \\ \kappa_{xy} \end{array} \right\} \Rightarrow \quad \{\varepsilon\} = \{\varepsilon^0\} + z\{\kappa\} \tag{2.22}$$

Then the stresses at the lamina level will be written as

$$\{\sigma\}^k = \left[\overline{Q}\right]^k \{\varepsilon^0\} + z\left[\overline{Q}\right]^k [\kappa] \tag{2.23}$$

Now we shall deal with force (N_x, N_y, N_{xy}) and moment (M_x, M_y, M_{xy}) resultants, per unit width (b in Fig. 2.6). Their definitions are given as (h is the total thickness of the laminate) follows:
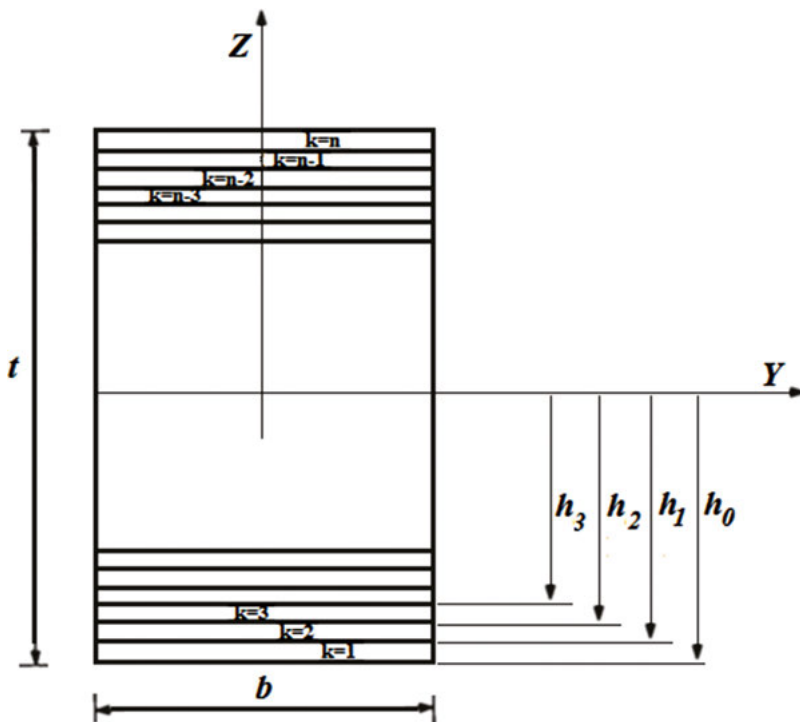
Fig. 2.6: Lamina notations within a given laminate.

$$N_x \equiv \int_{-h/2}^{h/2} \sigma_x dz, \quad N_y \equiv \int_{-h/2}^{h/2} \sigma_y dz, \quad N_{xy} \equiv \int_{-h/2}^{h/2} \tau_{xy} dz$$

$$M_x \equiv \int_{-h/2}^{h/2} \sigma_x z dz, \quad M_y \equiv \int_{-h/2}^{h/2} \sigma_y z dz, \quad M_{xy} \equiv \int_{-h/2}^{h/2} \tau_{xy} z dz \qquad (2.24)$$

Substituting the expressions of the stresses, one obtains expressions for the force and moments resultants as a function of the strain on the mid-plane, ε^0 and the curvature κ (see also [2]). The short written expressions are

$$\left\{ \begin{array}{c} \{N\} \\ \{M\} \end{array} \right\} = \left[\begin{array}{cc} [A] & [B] \\ [B] & [D] \end{array} \right] \left\{ \begin{array}{c} \{\varepsilon^0\} \\ \{\kappa\} \end{array} \right\}$$

or

$$\left\{ \begin{array}{c} \left\{ \begin{array}{c} N_x \\ N_y \\ N_{xy} \end{array} \right\} \\ \left\{ \begin{array}{c} M_x \\ M_y \\ M_{xy} \end{array} \right\} \end{array} \right\} = \left[\begin{array}{cc} \left[\begin{array}{ccc} A_{11} & A_{12} & A_{16} \\ A_{12} & A_{22} & A_{26} \\ A_{16} & A_{26} & A_{66} \end{array} \right] & \left[\begin{array}{ccc} B_{11} & B_{12} & B_{16} \\ B_{12} & B_{22} & B_{26} \\ B_{16} & B_{26} & B_{66} \end{array} \right] \\ \left[\begin{array}{ccc} B_{11} & B_{12} & B_{16} \\ B_{12} & B_{22} & B_{26} \\ B_{16} & B_{26} & B_{66} \end{array} \right] & \left[\begin{array}{ccc} D_{11} & D_{12} & D_{16} \\ D_{12} & D_{22} & D_{26} \\ D_{16} & D_{26} & D_{66} \end{array} \right] \end{array} \right] \left\{ \begin{array}{c} \left\{ \begin{array}{c} \varepsilon_x^0 \\ \varepsilon_y^0 \\ \gamma_{xy}^0 \end{array} \right\} \\ \left\{ \begin{array}{c} \kappa_x \\ \kappa_y \\ \kappa_{xy} \end{array} \right\} \end{array} \right\} \qquad (2.25)$$

where the various constants are defined as

$$A_{ij} \equiv \int_{-h/2}^{h/2} \overline{Q}_{ij}^k dz = \sum_{k=1}^{n} \overline{Q}_{ij}^k (h_k - h_{k-1})$$

$$B_{ij} \equiv \int_{-h/2}^{h/2} \overline{Q}_{ij}^k z dz = \frac{1}{2} \sum_{k=1}^{n} \overline{Q}_{ij}^k (h_k^2 - h_{k-1}^2) \qquad (2.26)$$

$$D_{ij} \equiv \int_{-h/2}^{h/2} \overline{Q}_{ij}^k z^2 dz = \frac{1}{3} \sum_{k=1}^{n} \overline{Q}_{ij}^k (h_k^3 - h_{k-1}^3)$$

where $i, j = 1, 1; 1, 2; 2, 2; 1, 6; 2, 6; 6, 6$.

The way the sum is performed in eq. (2.26) is according to the notations in Fig. 2.6. The passage from integral over the thickness of the laminate to the sum over the thickness is dictated by the fact that the individual plies are very thin and the properties within each lamina are assumed constant in the thickness direction.

Finally the equations of motion for a general case, applied to a thin plate made of laminated composite plies, using the CLT, are given as [1, 2] follows:

$$\frac{\partial N_x}{\partial x} + \frac{\partial N_{xy}}{\partial y} = I_1 \frac{\partial^2 u_0}{\partial t^2} - I_2 \frac{\partial^2}{\partial t^2}\left(\frac{\partial w_0}{\partial x}\right)$$

$$\frac{\partial N_{xy}}{\partial x} + \frac{\partial N_y}{\partial y} = I_1 \frac{\partial^2 v_0}{\partial t^2} - I_2 \frac{\partial^2}{\partial t^2}\left(\frac{\partial w_0}{\partial y}\right)$$

$$\frac{\partial^2 M_x}{\partial x^2} + 2\frac{\partial^2 M_{xy}}{\partial x \partial y} + \frac{\partial^2 M_y}{\partial y^2} + \frac{\partial}{\partial x}\left[N_{xx}\frac{\partial w_0}{\partial x} + N_{xy}\frac{\partial w_0}{\partial y}\right] + \tag{2.27}$$

$$\frac{\partial}{\partial y}\left[N_{yy}\frac{\partial w_0}{\partial y} + N_{xy}\frac{\partial w_0}{\partial x}\right] = -p_z + I_1\frac{\partial^2 w_0}{\partial t^2}$$

$$- I_3\frac{\partial^2}{\partial t^2}\left(\frac{\partial^2 w_0}{\partial x^2} + \frac{\partial^2 w_0}{\partial y^2}\right) + I_2\frac{\partial^2}{\partial t^2}\left(\frac{\partial w_0}{\partial x} + \frac{\partial w_0}{\partial y}\right)$$

where p_z is the load per unit area in the z direction[4] and the subscript 0 represents the values at the mid-plane of the cross section. N represents the in-plane loads and the various moments of inertia, I_1, I_2 and I_3 are given by (ρ is the mass/unit length)

$$I_j = \int_{-h/2}^{h/2} \rho z^{j-1} dz; \quad j = 1, 2, 3 \tag{2.28}$$

To obtain the equations for a beam, one can use eq. (2.27), while all the derivations with respect with y are identically zero. This yields a 1D equation in the following form:

$$\frac{\partial^2 M_x}{\partial x^2} + \frac{\partial}{\partial x}\left(N_{xx}\frac{\partial w_0}{\partial x}\right) = -p_z + I_1\frac{\partial^2 w_0}{\partial t^2} - I_3\frac{\partial^4 w_0}{\partial t^2 \partial x^2} + I_2\frac{\partial^3 w_0}{\partial t^2 \partial x} \tag{2.29}$$

where N_x is the axial (in-plane, in the direction of the length of the beam) load. Remembering the relationship between transverse deflection, w, and the bending moment, we can rewrite eq. (2.29) in terms of w_0 only to yield

$$-D_{11}\frac{\partial^2 w_0}{\partial x^2} = M_x \Rightarrow$$

$$-\frac{\partial^2}{\partial x^2}\left(D_{11}\frac{\partial^2 w_0}{\partial x^2}\right) + \frac{\partial}{\partial x}\left(N_{xx}\frac{\partial w_0}{\partial x}\right) = -p_z + I_1\frac{\partial^2 w_0}{\partial t^2} - I_3\frac{\partial^4 w_0}{\partial t^2 \partial x^2} + I_2\frac{\partial^3 w_0}{\partial t^2 \partial x} \tag{2.30}$$

with its associated boundary conditions:

$$\text{Geometric: specify either } w_0 \text{ or } \frac{\partial w_0}{\partial x}$$

$$\text{Natural: specify either } Q \equiv \frac{\partial M}{\partial x} \text{ or } M \tag{2.31}$$

---

4 Note that the z coordinate is normally used for the thickness direction, while x and y coordinates define the plate area.

Typical boundary conditions normally used in the literature are in the following form:

$$\text{Simply supported}: \ w = 0 \ \text{ and } \ M = 0$$

$$\text{Clamped}: \ \ w = 0 \ \text{and} \ \frac{\partial w}{\partial x} \ = 0$$

$$\text{Free}: \ Q \equiv \frac{\partial M}{\partial x} \ = 0 \ \text{and} \ M \ = 0$$

(2.32)

The reader should be aware of thermal issues associated with the manufacturing of composite structures due to the differential thermal contraction during the post-curing phase and also as a consequence of any temperature changes during the service life of the structure. This issue is caused by the relatively small axial thermal expansion coefficient of the modern reinforcing fibers (for carbon fibers it is even slightly negative), while the resin matrix has a large thermal coefficient. When cooling from a typical curing temperature, like 140 °C to room temperature, the fibers of the laminate composite will be in compression, while the matrix will show tension stresses [1]. Typical residual stresses due to thermal mismatch between the two components of the laminate are presented in Table 2.4.

Table 2.4: Typical thermal stresses in some common unidirectional composites (from [1]).

Matrix	Fiber	% Fiber volume, V_f	Temperature range ΔT (°K)	Fiber residual stress (MPa)	Matrix residual stress (MPa)
Epoxy (high T cure)	T300 carbon	65	120	−19	36
Epoxy (low T cure)	E glass	65	100	−15	28
Epoxy (low T cure)	Kevlar-49	65	100	−16	30
Borosilicate glass	T300 carbon	50	520	−93	93
CAS* glass-ceramic	Nicalon SiC	40	1,000	−186	124

*CAS, CaO–Al$_2$O$_3$–SiO$_2$.

Another important data for design is the experimental tension and compression strength as measured during various laboratory tests, as presented in Table 2.5 [1].

Finally, a table with a list of the main manufacturers of various composite materials is presented in Table 2.6.

Table 2.5: Typical experimental tension and compression strengths for common composite materials (from [1]).

Material	Lay-up	% Fiber volume, V_f	Tensile strength, σ_t (GPa)	Compression strength, σ_c (GPa)	Ratio σ_c/σ_t
GRP	ud (unidirectional)	60	1.3	1.1	0.85
CFRP	ud (unidirectional)	60	2.0	1.1	0.55
KFRP	ud (unidirectional)	60	1.0	0.4	0.40
HTA/913 (CFRP)	$\left[\left(\pm 45^0, 0^0_2\right)_2\right]_S$	65	1.27	0.97	0.77
T800/924 (CFRP)	$\left[\left(\pm 45^0, 0^0_2\right)_2\right]_S$	65	1.42	0.90	0.63
T800/ 5245(CFRP)	$\left[\left(\pm 45^0, 0^0_2\right)_2\right]_S$	65	1.67	0.88	0.53
SiC/CAS (CMC*)	ud (unidirectional)	37	334	1,360	4.07
SiC/CAS (CMC)	$\left[0^0, 90^0\right]_{3S}$	37	210	463	2.20

* CMC, ceramic matrix composites.

Table 2.6: List of the main manufacturers of various composite materials and resins.

Types of composite	Company	Company website
Thermoplastic composites	Milliken Tegris	tegris.milliken.com
Thermoplastic composites	Polystrand, Inc.	www.polystrand.com
Nonwoven fabrics (PolyWeb™) and foam	Wm. T. Burnett & Co.	www.williamtburnett.com
Thermoplastic composites	Schappe Techniques	www.schappe.com
Thermoplastic composites	TechFiber	www.fiber-tech.net
Thermoplastic composites	TenCate	www.tencate.com
Thermoplastic composites	Thercom	www.thercom.com
Thermoplastic composites	Vectorply	www.vectorply.com
Composite materials:resins and fibers	SF composites	www.sf-composites.com
Formulation and manufacture of epoxy-based systems	SICOMIN	www.sicomin.com

Table 2.6 (continued)

Types of composite	Company	Company website
Composite materials + resin, composite laminates	Lamiflex SPA	www.lamiflex.il
Composite materials + polyester	AMP Composite	www.amp-composite.il
Infusion, pultrusion, wet lay-up, prepreg, filament winding	Applied Poleramic Inc.	www.appliedpoleramic.com
Epoxy and polyurethane	Endurance Technologies	www.epoxi.com
Composite materials	Gurit	www.gurit.com
Advanced thermoset resins	Huntsman Advanced Materials	www.huntsman.com/advanced_materials/a/Home
Advanced thermoset resins	Lattice Composites	www.latticecomposites.com
Kevlar	DuPont™ Kevlar®	www.dupont.com/products-and-services/fabrics-fibers-nonwovens/fibers/brands/kevlar.html
UHMWPE – ultra-high-molecular-weight, high-performance polyethylene material	DuPont™ Tenslyon™	www.dupont.com
Innegra™ HMPP (polypropylene), high-performance fiber	Innegra Technologies	www.innegratech.com
Spread tow fabrics	TeXtreme	www.textreme.com/b2b
Adhesives and sealants	3M	solutions.3m.com
Prepreg and resins	Axiom Materials Inc.	www.axiommaterials.com
Fabrics, resins, composite materials	Barrday Advanced Materials Solutions	www.barrday.com
Carbon prepreg	Hankuk Carbon Co., Ltd.	www.hcarbon.com/eng/product/overview.asp
Carbon fibers and prepregs	Hexcel®	www.hexcel.com/Products/Industries/ICarbon-Fiber
Prepregs and compounds	Pacific Coast Composites	www.pccomposites.com
Prepregs and compounds	Quantum Composites	www.quantumcomposites.com

2.6 First-order shear deformation theory

Unlike isotropic materials, the ratio between the shear and the bending in orthotropic material, like laminated composite structures, is not negligible. The need to remove the somehow restricting assumptions from the CLT which, as stated above, are based on Kirchhoff–Love plate theory [3–5], like neglecting the influence of the shear strains and the fact that a plane before deformation remains plane after the deformation, led to derivation of more advanced bending theories for plates, like Mindlin theory of plates [6–8], which includes in-plane shear strains and is an extension of Kirchhoff–Love plate theory incorporating first-order shear effects.

Mindlin's theory assumes that there is a linear variation of displacement across the plate thickness but the plate thickness does not change during deformation. An additional assumption is that the normal stress through the thickness is ignored, an assumption that is also called the plane stress condition. The Mindlin theory is often called the FSDT of plates, and its application to composite materials is next presented. Under the assumptions and restrictions of Mindlin's theory (which has a similarity to Timoshenko's theory for beams [9–12]), the displacement field has five unknowns (u_0, v_0, w_0 – the displacements of the mid-plane in the x, y and z directions, respectively, and ϕ_x, ϕ_y – the rotations due to shear about x and y directions, respectively) and is given by (see also Fig. 2.7, which is similar to Fig. 2.5, but for FSDT approach)

$$u(x,y,z,t) = u_0(x,y,t) + z\phi_x(x,y,t)$$
$$v(x,y,z,t) = v_0(x,y,t) + z\phi_y(x,y,t) \tag{2.33}$$
$$w(x,y,z,t) = w_0(x,y,t)$$

The associated strains [13][5] assuming nonlinear terms are

$$\varepsilon_x = \frac{\partial u_0}{\partial x} + \frac{1}{2}\left(\frac{\partial w_0}{\partial x}\right)^2 + z\frac{\partial \phi_x}{\partial x}$$

$$\varepsilon_x = \frac{\partial v_0}{\partial y} + \frac{1}{2}\left(\frac{\partial w_0}{\partial y}\right)^2 + z\frac{\partial \phi_y}{\partial y}$$

$$\varepsilon_z = 0, \quad \gamma_{xz} = \frac{\partial w_0}{\partial x} + \phi_x, \quad \gamma_{yz} = \frac{\partial w_0}{\partial y} + \phi_y \tag{2.34}$$

$$\gamma_{xy} = \left(\frac{\partial u_0}{\partial y} + \frac{\partial v_0}{\partial x} + \frac{\partial^2 w_0}{\partial x \partial y}\right) + z\left(\frac{\partial \phi_x}{\partial y} + \frac{\partial \phi_y}{\partial x}\right)$$

---

5 Note that the assumption of constant shear strains across the height of the laminate is a rough approximation of the true strain distribution, which is at least quadratic through the thickness. However, although the rough approximation, the results of the application of Mindlin's plate theory present very good results when compared with experimental ones.
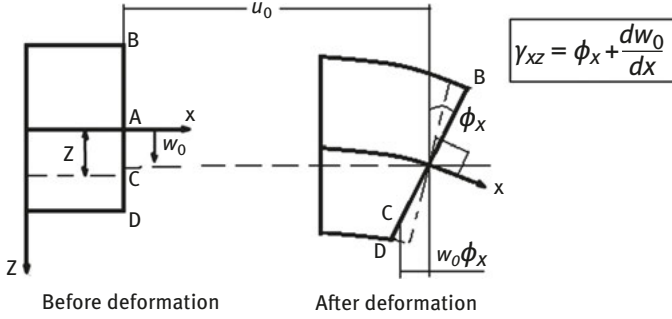
Fig. 2.7: The plate cross section before and after the deformation (FSDT approach).

Multiplying eq. (2.34) by the stiffness matrix $\boxed{Q}$ and integrating through the thickness of the laminate, yields the force and moments resultants (as in eq. (2.23)), with two additional terms, the shear resultants, being defined by

$$
\begin{Bmatrix} Q_x \\ Q_y \end{Bmatrix} = \kappa \int_{-h/2}^{h/2} \begin{Bmatrix} \tau_{xz} \\ \tau_{yz} \end{Bmatrix} dz
\tag{2.35}
$$

where κ is called the shear correction coefficient and is defined by the ratio between the shear strain energies calculated by the actual shear distribution and the constant distribution assumed in the FSDT theory. The value of κ is taken as 5/6 for a rectangular cross section.[6]

The equations of motion will then have the following form:

$$
\frac{\partial N_x}{\partial x} + \frac{\partial N_{xy}}{\partial y} = I_1 \frac{\partial^2 u_0}{\partial t^2} + I_2 \frac{\partial^2 \phi_x}{\partial t^2}
$$

$$
\frac{\partial N_{xy}}{\partial x} + \frac{\partial N_y}{\partial y} = I_1 \frac{\partial^2 v_0}{\partial t^2} + I_2 \frac{\partial^2 \phi_y}{\partial t^2}
$$

$$
\frac{\partial Q_x}{\partial x} + \frac{\partial Q_y}{\partial y} + \frac{\partial}{\partial x}\left[N_{xx}\frac{\partial w_0}{\partial x} + N_{xy}\frac{\partial w_0}{\partial y} \right]
$$

$$
+ \frac{\partial}{\partial y}\left[N_{yy}\frac{\partial w_0}{\partial y} + N_{xy}\frac{\partial w_0}{\partial x} \right] = -p_z + I_1 \frac{\partial^2 w_0}{\partial t^2}
\tag{2.36}
$$

$$
\frac{\partial M_x}{\partial x} + \frac{\partial M_{xy}}{\partial y} - Q_x = I_3 \frac{\partial^2 \phi_x}{\partial t^2} + I_1 \frac{\partial^2 u_0}{\partial t^2}
$$

$$
\frac{\partial M_{xy}}{\partial x} + \frac{\partial M_y}{\partial y} - Q_y = I_3 \frac{\partial^2 \phi_y}{\partial t^2} + I_1 \frac{\partial^2 v_0}{\partial t^2}
$$

6 The accurate value is $\kappa = \frac{10(1+v)}{12+11v}$ for a rectangular cross section and $\kappa = \frac{6(1+v)}{7+6v}$ for a solid circular cross section.

where p_z is the load per unit area in the z direction.[7] N_{xx}, N_{yy} and N_{xy} represent the in-plane loads, and the various moments of inertia, I_1, I_2 and I_3, are given by (ρ is the mass/unit length) eq. (2.28).

One should note that in addition to eq. (2.25), which describes the resultants of the force and the moment as a function of the stiffness coefficients A_{ij}, B_{ij} and D_{ij}, the shear resultants Q_x and Q_y are defined as

$$
\left\{ \begin{array}{c} Q_y \\ Q_x \end{array} \right\} = \kappa \begin{bmatrix} A_{44} & A_{45} \\ A_{45} & A_{55} \end{bmatrix} \left\{ \begin{array}{c} \frac{\partial w_0}{\partial y} + \phi_y \\ \frac{\partial w_0}{\partial x} + \phi_x \end{array} \right\} \tag{2.37}
$$

where

$$
A_{44} \equiv \kappa \int_{-h/2}^{h/2} \overline{Q}_{44}^k dz = \kappa \sum_{k=1}^{n} \overline{Q}_{44}^k (h_k - h_{k-1})
$$

$$
A_{45} \equiv \kappa \int_{-h/2}^{h/2} \overline{Q}_{45}^k dz = \kappa \sum_{k=1}^{n} \overline{Q}_{45}^k (h_k - h_{k-1}) \tag{2.38}
$$

$$
A_{55} \equiv \kappa \int_{-h/2}^{h/2} \overline{Q}_{55}^k dz = \kappa \sum_{k=1}^{n} \overline{Q}_{55}^k (h_k - h_{k-1})
$$

and

$$
\overline{Q}_{44} = Q_{44}\cos^2\theta + Q_{55}\sin^2\theta
$$

$$
\overline{Q}_{45} = (Q_{55} - Q_{44})\cos\theta\sin\theta
$$

$$
\overline{Q}_{55} = Q_{44}\sin^2\theta + Q_{55}\cos^2\theta \tag{2.39}
$$

$$
\text{where} \quad Q_{44} = G_{23}; \quad \text{and} \quad Q_{55} = G_{13}
$$

Substituting the resultants defined in terms of the five unknown displacements (u_O, v_O, w_O, ϕ_x, ϕ_y), we get [13] five differential equations for the five unknown displacements:

---

[7] Note that the coordinate z is normally used for the thickness direction, while x and y coordinates define the plate area.

$$A_{11}\left[\frac{\partial^2 u_0}{\partial x^2} + \frac{\partial^3 w_0}{\partial x^3}\right] + A_{12}\left[\frac{\partial^2 v_0}{\partial x\partial y} + \frac{\partial^3 w_0}{\partial x\partial y^2}\right] +$$

$$A_{16}\left[2\frac{\partial^2 u_0}{\partial x\partial y} + \frac{\partial^2 v_0}{\partial x^2} + 3\frac{\partial^3 w_0}{\partial x^2\partial y}\right] + A_{26}\left[\frac{\partial^2 v_0}{\partial y^2} + \frac{\partial^3 w_0}{\partial y^3}\right] +$$

$$A_{66}\left[\frac{\partial^2 u_0}{\partial y^2} + \frac{\partial^2 v_0}{\partial x\partial y} + 2\frac{\partial^3 w_0}{\partial x\partial y^2}\right] + B_{11}\frac{\partial^2 \phi_x}{\partial x^2} + B_{12}\frac{\partial^2 \phi_y}{\partial x\partial y} +$$

$$B_{16}\left[2\frac{\partial^2 \phi_x}{\partial x\partial y} + \frac{\partial^2 \phi_y}{\partial x^2}\right] + B_{26}\frac{\partial^2 \phi_y}{\partial y^2} + B_{66}\left[\frac{\partial^2 \phi_x}{\partial y^2} + \frac{\partial^2 \phi_y}{\partial x\partial y}\right] = I_1\frac{\partial^2 u_0}{\partial t^2} + I_2\frac{\partial^2 \phi_x}{\partial t^2} \qquad (2.40)$$

$$A_{22}\left[\frac{\partial^2 v_0}{\partial y^2} + \frac{\partial^3 w_0}{\partial y^3}\right] + A_{12}\left[\frac{\partial^2 u_0}{\partial x\partial y} + \frac{\partial^3 w_0}{\partial x^2\partial y}\right] +$$

$$A_{16}\left[\frac{\partial^2 u_0}{\partial x^2} + \frac{\partial^3 w_0}{\partial x^3}\right] + A_{26}\left[\frac{\partial^2 u_0}{\partial y^2} + 2\frac{\partial^2 v_0}{\partial x\partial y} + 3\frac{\partial^3 w_0}{\partial x\partial y^2}\right] +$$

$$A_{66}\left[\frac{\partial^2 u_0}{\partial x\partial y} + \frac{\partial^2 v_0}{\partial x^2} + 2\frac{\partial^3 w_0}{\partial x^2\partial y}\right] + B_{22}\frac{\partial^2 \phi_y}{\partial y^2} + B_{12}\frac{\partial^2 \phi_x}{\partial x\partial y} +$$

$$B_{16}\frac{\partial^2 \phi_x}{\partial x^2} + B_{26}\left[\frac{\partial^2 \phi_x}{\partial y^2} + 2\frac{\partial^2 \phi_y}{\partial x\partial y}\right] + B_{66}\left[\frac{\partial^2 \phi_y}{\partial x^2} + \frac{\partial^2 \phi_x}{\partial x\partial y}\right] = I_1\frac{\partial^2 v_0}{\partial t^2} + I_2\frac{\partial^2 \phi_y}{\partial t^2} \qquad (2.41)$$

$$\kappa A_{55}\left[\frac{\partial^2 w_0}{\partial x^2} + \frac{\partial \varphi_x}{\partial x}\right] + \kappa A_{45}\left[2\frac{\partial^2 w_0}{\partial x\partial y} + \frac{\partial \varphi_y}{\partial x} + \frac{\partial \varphi_x}{\partial y}\right] + \kappa A_{44}\left[\frac{\partial^2 w_0}{\partial y^2} + \frac{\partial \varphi_y}{\partial y}\right] +$$

$$\frac{\partial}{\partial x}\left[N_{xx}\frac{\partial w_0}{\partial x} + N_{xy}\frac{\partial w_0}{\partial y}\right] + \frac{\partial}{\partial y}\left[N_{yy}\frac{\partial w_0}{\partial y} + N_{xy}\frac{\partial w_0}{\partial x}\right] = -p_z + I_1\frac{\partial^2 w_0}{\partial t^2} \qquad (2.42)$$

$$B_{11}\left[\frac{\partial^2 u_0}{\partial x^2} + \frac{\partial^3 w_0}{\partial x^3}\right] + B_{12}\left[\frac{\partial^2 v_0}{\partial x\partial y} + \frac{\partial^3 w_0}{\partial x\partial y^2}\right] +$$

$$B_{16}\left[2\frac{\partial^2 u_0}{\partial x\partial y} + \frac{\partial^2 v_0}{\partial x^2} + 3\frac{\partial^3 w_0}{\partial x^2\partial y}\right] + B_{26}\left[\frac{\partial^2 v_0}{\partial y^2} + \frac{\partial^3 w_0}{\partial y^3}\right] +$$

$$B_{66}\left[\frac{\partial^2 u_0}{\partial y^2} + \frac{\partial^2 v_0}{\partial x\partial y} + 2\frac{\partial^3 w_0}{\partial x\partial y^2}\right] + D_{11}\frac{\partial^2 \phi_x}{\partial x^2} + D_{12}\frac{\partial^2 \phi_y}{\partial x\partial y} + \qquad (2.43)$$

$$D_{16}\left[2\frac{\partial^2 \phi_x}{\partial x\partial y} + \frac{\partial^2 \phi_y}{\partial x^2}\right] + D_{26}\frac{\partial^2 \phi_y}{\partial y^2} + D_{66}\left[\frac{\partial^2 \phi_x}{\partial y^2} + \frac{\partial^2 \phi_y}{\partial x\partial y}\right] -$$

$$\kappa A_{55}\left[\frac{\partial w_0}{\partial x} + \phi_x\right] - \kappa A_{45}\left[\frac{\partial w_0}{\partial y} + \phi_y\right] = I_3\frac{\partial^2 u_0}{\partial t^2} + I_3\frac{\partial^2 \phi_x}{\partial t^2}$$

$$B_{22}\left[\frac{\partial^2 v_0}{\partial y^2} + \frac{\partial^3 w_0}{\partial y^3}\right] + B_{12}\left[\frac{\partial^2 u_0}{\partial x \partial y} + \frac{\partial^3 w_0}{\partial x^2 \partial y}\right] +$$

$$B_{16}\left[\frac{\partial^2 u_0}{\partial x^2} + \frac{\partial^3 w_0}{\partial x^3}\right] + B_{26}\left[\frac{\partial^2 u_0}{\partial y^2} + 2\frac{\partial^2 v_0}{\partial x \partial y} + 3\frac{\partial^3 w_0}{\partial x \partial y^2}\right] +$$

$$B_{66}\left[\frac{\partial^2 u_0}{\partial x \partial y} + \frac{\partial^2 v_0}{\partial x^2} + 2\frac{\partial^3 w_0}{\partial x^2 \partial y}\right] + D_{22}\frac{\partial^2 \phi_y}{\partial y^2} + D_{12}\frac{\partial^2 \phi_x}{\partial x \partial y} + \tag{2.44}$$

$$D_{16}\frac{\partial^2 \phi_x}{\partial x^2} + D_{26}\left[\frac{\partial^2 \phi_x}{\partial y^2} + 2\frac{\partial^2 \phi_y}{\partial x \partial y}\right] + D_{66}\left[\frac{\partial^2 \phi_y}{\partial x^2} + \frac{\partial^2 \phi_x}{\partial x \partial y}\right] -$$

$$\kappa A_{44}\left[\frac{\partial w_0}{\partial y} + \phi_y\right] - \kappa A_{45}\left[\frac{\partial w_0}{\partial x} + \phi_x\right] = I_1\frac{\partial^2 v_0}{\partial t^2} + I_2\frac{\partial^2 \phi_y}{\partial t^2}$$

To solve the five differential equations, 10 boundary conditions should be supplied in the form of geometric and natural boundary conditions.[8]

To obtain the equations of motion for a beam, using FSDT, presented before for a plate, one should assume that all the derivations in the y direction should vanish, and v and ϕ_y should be identically zero. This yields for the general case, three coupled equations of motion having the following form (assuming constant properties along the beam):

$$A_{11}\frac{\partial^2 u_0}{\partial x^2} + B_{11}\frac{\partial^2 \phi_x}{\partial x^2} = I_1\frac{\partial^2 u_0}{\partial t^2} + I_2\frac{\partial^2 \phi_x}{\partial t^2}$$

$$B_{11}\frac{\partial^2 u_0}{\partial x^2} + D_{11}\frac{\partial^2 \phi_x}{\partial x^2} - \kappa A_{55}\left[\frac{\partial w_0}{\partial x} + \phi_x\right] = I_3\frac{\partial^2 u_0}{\partial t^2} + I_3\frac{\partial^2 \phi_x}{\partial t^2} \tag{2.45}$$

$$\kappa A_{55}\left[\frac{\partial^2 w_0}{\partial x^2} + \frac{\partial \varphi_x}{\partial x}\right] + N_{xx}\frac{\partial^2 w_0}{\partial x^2} = -p_z + I_1\frac{\partial^2 w_0}{\partial t^2}$$

with the following boundary conditions:

$$A_{11}\frac{\partial u_0}{\partial x} + B_{11}\frac{\partial \phi_x}{\partial x} = -N_{xx} \quad \underline{\text{or}} \quad u_0 = 0$$

$$A_{55}\left(\phi_x + \frac{\partial w_0}{\partial x}\right) - N_{xx}\frac{\partial w_0}{\partial x} = 0 \quad \underline{\text{or}} \quad w_0 = 0 \tag{2.46}$$

$$B_{11}\frac{\partial u_0}{\partial x} + D_{11}\frac{\partial \phi_x}{\partial x} = 0 \quad \underline{\text{or}} \quad \phi_x = 0$$

The reader is referred to refs. [14–20], as typical sources for solving buckling and natural frequencies of beams using the FSDT approach.

---

8 For further discussion about the types of boundary conditions to be imposed, the reader is referred to ref. [13].

2.7 Higher order theories

The need for higher order shear deformation theories stems from the fact that although the FSDT approach presents accurate results, it does not fulfill the shear free boundary conditions on the top and bottom sides of the beam or a plate. One should remember that the FSDT approach would need far less computer efforts as compared with any higher order theories, which are known as demanding large computer memory.

One of the higher order shear deformation theory was proposed by Reddy [13] and involves a third-order shear deformation theory (TSDT), which will be presented next.

Based on the kinematics of the problem (Fig. 2.8), the displacement field has the following components:

$$u(x,y,z,t) = u_0(x,y,t) + z\alpha_x(x,y,t) + z^2\beta_x(x,y,t) + z^3\delta_x(x,y,t)$$

$$v(x,y,z,t) = v_0(x,y,t) + z\alpha_y(x,y,t) + z^2\beta_y(x,y,t) + z^3\delta_y(x,y,t) \qquad (2.47)$$

$$w(x,y,z,t) = w_0(x,y,t)$$
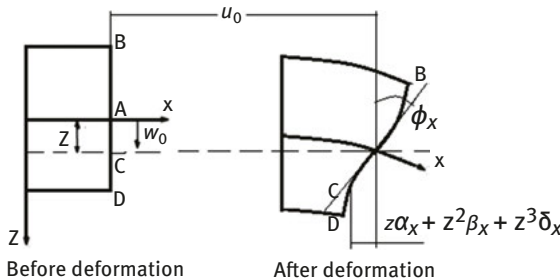
Fig. 2.8: The plate cross section before and after the deformation (TSDT approach).

The various terms in eq. (2.47), like α_x, α_y, β_x, β_y, δ_x and δ_y, are functions to be determined, having the following values at $z = 0$:

$$\alpha_x = \left[\frac{\partial u}{\partial z}\right], \quad \alpha_y = \left[\frac{\partial v}{\partial z}\right], \quad \beta_x = \frac{1}{2}\left[\frac{\partial^2 u}{\partial z^2}\right]$$

$$\beta_y = \frac{1}{2}\left[\frac{\partial^2 v}{\partial z^2}\right], \quad \delta_x = \frac{1}{6}\left[\frac{\partial^3 u}{\partial z^3}\right], \quad \delta_y = \frac{1}{6}\left[\frac{\partial^3 v}{\partial z^3}\right] \qquad (2.48)$$

Accordingly, nine independent unknowns are to be found from nine second-order partial differential equations. However, the number of independent unknowns can

be reduced for certain boundary conditions, like traction-free boundary conditions on the top and bottom layers of the plate [13], namely[9]

$$\tau_{xz}\left(x,y,+\frac{h}{2},t\right)=0\,,\quad \tau_{xz}\left(x,y,-\frac{h}{2},t\right)=0$$

$$\tau_{yz}\left(x,y,+\frac{h}{2},t\right)=0\,,\quad \tau_{yz}\left(x,y,-\frac{h}{2},t\right)=0$$

$$(2.49)$$

For arbitrary values of Q_{55}, Q_{45} and Q_{44} (see also eqs. (2.37)–(2.39)), one can show that the boundary equations in eq.. (2.49) can be written in terms of the shear strains (see also [13]), using the following expressions:

$$\gamma_{xz}\left(x,y,+\frac{h}{2},t\right)=0\,;\quad \gamma_{xz}\left(x,y,-\frac{h}{2},t\right)=0\,;$$

$$\gamma_{yz}\left(x,y,+\frac{h}{2},t\right)=0\,;\quad \gamma_{yz}\left(x,y,-\frac{h}{2},t\right)=0\,.$$

$$(2.50)$$

Performing the necessary derivations to express the shear strains using the assumed strain field (eq.. (2.47)), one gets

$$\gamma_{xz}\equiv\frac{\partial w}{\partial x}+\frac{\partial u}{\partial z}=\frac{\partial w_0}{\partial x}+\alpha_x+2z\beta_x+3z^2\delta_x$$

$$\gamma_{yz}\equiv\frac{\partial w}{\partial y}+\frac{\partial v}{\partial z}=\frac{\partial w_0}{\partial y}+\alpha_y+2z\beta_y+3z^2\delta_y$$

$$(2.51)$$

Substituting the boundary conditions from eq. (2.50) into eq. (2.51), we get the following four equations:

$$@z=+\frac{h}{2}\quad \gamma_{xz}=\frac{\partial w_0}{\partial x}+\alpha_x+h\beta_x+\frac{3h^2}{4}\delta_x=0,\quad \gamma_{yz}=\frac{\partial w_0}{\partial y}+\alpha_y+h\beta_y+\frac{3h^2}{4}\delta_y=0$$

$$@z=-\frac{h}{2}\quad \gamma_{xz}=\frac{\partial w_0}{\partial x}+\alpha_x-h\beta_x+\frac{3h^2}{4}\delta_x=0,\quad \gamma_{yz}=\frac{\partial w_0}{\partial y}+\alpha_y-h\beta_y+\frac{3h^2}{4}\delta_y=0$$

$$(2.52)$$

Solving eq. (2.52) yields the following expressions:

$$\beta_x=0,\quad \delta_x=-\frac{4}{3h^2}\left(\alpha_x+\frac{\partial w_o}{\partial x}\right)$$

$$\beta_y=0,\quad \delta_y=-\frac{4}{3h^2}\left(\alpha_y+\frac{\partial w_o}{\partial y}\right)$$

$$(2.53)$$

---

9 h being the total height of the beam (or plate), x-axis is along the beam's (or plate's) length, while y and z are perpendicular to it.

Back-substituting the expression in eq. (2.53) into eq. (2.47) provides the strain field for the posed problem:

$$u(x,y,z,t) = u_0(x,y,t) + z\alpha_x(x,y,t) - z^3\frac{4}{3h^2}\left[\alpha_x(x,y,t) + \frac{\partial w_0(x,y,t)}{\partial x}\right]$$

$$v(x,y,z,t) = v_0(x,y,t) + z\alpha_y(x,y,t) - z^3\frac{4}{3h^2}\left[\alpha_y(x,y,t) + \frac{\partial w_0(x,y,t)}{\partial y}\right] \qquad (2.54)$$

$$w(x,y,z,t) = w_0(x,y,t)$$

One should notice that the number of unknowns had been reduced to only 5, similar to the case of FSTD approach being applied to a rectangular plate.

For the case of small strains and moderate rotations the strain-displacement relations can be shown to be

$$\varepsilon_{xx} = \frac{\partial u}{\partial x} + \frac{1}{2}\left(\frac{\partial w}{\partial x}\right)^2, \quad \varepsilon_{yy} = \frac{\partial v}{\partial y} + \frac{1}{2}\left(\frac{\partial w}{\partial y}\right)^2, \quad \varepsilon_{zz} = \frac{\partial w}{\partial z}$$

$$\varepsilon_{xy} = \frac{1}{2}\left(\frac{\partial u}{\partial y} + \frac{\partial v}{\partial x} + \frac{\partial^2 w}{\partial x \partial y}\right), \quad \varepsilon_{xz} = \frac{1}{2}\left(\frac{\partial u}{\partial z} + \frac{\partial w}{\partial x}\right), \quad \varepsilon_{yz} = \frac{1}{2}\left(\frac{\partial v}{\partial z} + \frac{\partial w}{\partial y}\right) \qquad (2.55)$$

Substituting the displacement field, defined by eq. (2.54), into the nonlinear strain-displacement equations, eq. (2.55) yields the following expressions:

$$\begin{Bmatrix} \varepsilon_{xx} \\ \varepsilon_{yy} \\ \gamma_{xy} \end{Bmatrix} = \begin{Bmatrix} \dfrac{\partial u_0}{\partial x} + \dfrac{1}{2}\left(\dfrac{\partial w_0}{\partial x}\right)^2 \\[2mm] \dfrac{\partial v_0}{\partial y} + \dfrac{1}{2}\left(\dfrac{\partial w_0}{\partial y}\right)^2 \\[2mm] \dfrac{\partial u_0}{\partial y} + \dfrac{\partial v_0}{\partial x} + \dfrac{\partial^2 w_0}{\partial x \partial y} \end{Bmatrix} + z\begin{Bmatrix} \dfrac{\partial \alpha_x}{\partial x} \\[2mm] \dfrac{\partial \alpha_y}{\partial y} \\[2mm] \dfrac{\partial \alpha_x}{\partial y} + \dfrac{\partial \alpha_y}{\partial x} \end{Bmatrix} - z^3\left(\dfrac{4}{3h^2}\right)\begin{Bmatrix} \dfrac{\partial \alpha_x}{\partial x} + \dfrac{\partial^2 w_0}{\partial x^2} \\[2mm] \dfrac{\partial \alpha_y}{\partial y} + \dfrac{\partial^2 w_0}{\partial y^2} \\[2mm] \dfrac{\partial \alpha_x}{\partial y} + \dfrac{\partial \alpha_y}{\partial x} + 2\dfrac{\partial^2 w_0}{\partial x \partial y} \end{Bmatrix}$$

$$\begin{Bmatrix} \gamma_{xz} \\ \gamma_{yz} \end{Bmatrix} = \begin{Bmatrix} \alpha_x + \dfrac{\partial w_0}{\partial x} \\[2mm] \alpha_y + \dfrac{\partial w_0}{\partial y} \end{Bmatrix} - z^2\left(\dfrac{4}{h^2}\right)\begin{Bmatrix} \alpha_x + \dfrac{\partial w_0}{\partial x} \\[2mm] \alpha_y + \dfrac{\partial w_0}{\partial y} \end{Bmatrix} \quad \text{and} \quad \varepsilon_{zz} = 0$$

$$\qquad (2.56)$$

where

$$\gamma_{xy} \equiv 2\varepsilon_{xy}, \quad \gamma_{xz} \equiv 2\varepsilon_{xz}, \quad \gamma_{yz} \equiv 2\varepsilon_{yz} \qquad (2.57)$$

The relationship stress resultants–strains can be shown to have the following form (see also [13]):

$$
\left\{ \begin{array}{c} \{N\} \\ \{M\} \\ \{T\} \end{array} \right\} = \begin{bmatrix} [A] & [B] & [E] \\ [B] & [D] & [F] \\ [E] & [F] & [G] \end{bmatrix} \left\{ \begin{array}{c} \{\varepsilon^{(a)}\} \\ \{\varepsilon^{(b)}\} \\ \{\varepsilon^{(c)}\} \end{array} \right\}
\tag{2.58}
$$

$$
\left\{ \begin{array}{c} \{Q\} \\ \{S\} \end{array} \right\} = \begin{bmatrix} [A] & [D] \\ [D] & [F] \end{bmatrix} \left\{ \begin{array}{c} \{\gamma^{(a)}\} \\ \{\gamma^{(b)}\} \end{array} \right\}
\tag{2.59}
$$

where the terms $\{T\}$ and $\{S\}$ are higher order stress resultants, stemmed from the present TSDT. The various matrix terms for eq. (2.58) are defined in the following way:

$$
A_{ij} = \sum_{k=1}^{N} \int_{z_k}^{z_{k+1}} \bar{Q}_{ij} dz = \sum_{k=1}^{N} \bar{Q}_{ij}^{(k)} [z_{k+1} - z_k]
$$

$$
B_{ij} = \sum_{k=1}^{N} \int_{z_k}^{z_{k+1}} \bar{Q}_{ij} z\, dz = \frac{1}{2} \sum_{k=1}^{N} \bar{Q}_{ij}^{(k)} \left[(z_{k+1})^2 - (z_k)^2 \right]
$$

$$
D_{ij} = \sum_{k=1}^{N} \int_{z_k}^{z_{k+1}} \bar{Q}_{ij} z^2 dz = \frac{1}{3} \sum_{k=1}^{N} \bar{Q}_{ij}^{(k)} \left[(z_{k+1})^3 - (z_k)^3 \right] \qquad \text{while} \quad i,j = 1,2,6
$$

$$
E_{ij} = \sum_{k=1}^{N} \int_{z_k}^{z_{k+1}} \bar{Q}_{ij} z^3 dz = \frac{1}{4} \sum_{k=1}^{N} \bar{Q}_{ij}^{(k)} \left[(z_{k+1})^4 - (z_k)^4 \right]
\tag{2.60}
$$

$$
F_{ij} = \sum_{k=1}^{N} \int_{z_k}^{z_{k+1}} \bar{Q}_{ij} z^4 dz = \frac{1}{5} \sum_{k=1}^{N} \bar{Q}_{ij}^{(k)} \left[(z_{k+1})^5 - (z_k)^5 \right]
$$

$$
G_{ij} = \sum_{k=1}^{N} \int_{z_k}^{z_{k+1}} \bar{Q}_{ij} z^6 dz = \frac{1}{7} \sum_{k=1}^{N} \bar{Q}_{ij}^{(k)} \left[(z_{k+1})^7 - (z_k)^7 \right]
$$

while for eq. (2.59) their definition is

$$
A_{lm} = \sum_{k=1}^{N} \int_{z_k}^{z_{k+1}} \bar{Q}_{lm} dz = \sum_{k=1}^{N} \bar{Q}_{lm}^{(k)} [z_{k+1} - z_k]
$$

$$
D_{lm} = \sum_{k=1}^{N} \int_{z_k}^{z_{k+1}} \bar{Q}_{lm} z^2 dz = \frac{1}{3} \sum_{k=1}^{N} \bar{Q}_{lm}^{(k)} \left[(z_{k+1})^3 - (z_k)^3 \right] \qquad \text{while} \quad l,m = 4,5
$$

$$
F_{lm} = \sum_{k=1}^{N} \int_{z_k}^{z_{k+1}} \bar{Q}_{lm} z^4 dz = \frac{1}{5} \sum_{k=1}^{N} \bar{Q}_{lm}^{(k)} \left[(z_{k+1})^5 - (z_k)^5 \right]
\tag{2.61}
$$

where

$$
\left\{ \varepsilon^{(a)} \right\} \equiv
\begin{Bmatrix}
\dfrac{\partial u_0}{\partial x} + \dfrac{1}{2}\left(\dfrac{\partial w_0}{\partial x}\right)^2 \\[2ex]
\dfrac{\partial v_0}{\partial y} + \dfrac{1}{2}\left(\dfrac{\partial w_0}{\partial y}\right)^2 \\[2ex]
\dfrac{\partial u_0}{\partial y} + \dfrac{\partial v_0}{\partial x} + \dfrac{\partial^2 w_0}{\partial x \partial y}
\end{Bmatrix},
\quad
\left\{ \varepsilon^{(b)} \right\} \equiv
\begin{Bmatrix}
\dfrac{\partial \alpha_x}{\partial x} \\[2ex]
\dfrac{\partial \alpha_y}{\partial y} \\[2ex]
\dfrac{\partial \alpha_x}{\partial y} + \dfrac{\partial \alpha_y}{\partial x}
\end{Bmatrix},
$$

$$
\left\{ \varepsilon^{(c)} \right\} \equiv -\left(\dfrac{4}{3h^2}\right)
\begin{Bmatrix}
\dfrac{\partial \alpha_x}{\partial x} + \dfrac{\partial^2 w_0}{\partial x^2} \\[2ex]
\dfrac{\partial \alpha_y}{\partial y} + \dfrac{\partial^2 w_0}{\partial y^2} \\[2ex]
\dfrac{\partial \alpha_x}{\partial y} + \dfrac{\partial \alpha_y}{\partial x} + 2\dfrac{\partial^2 w_0}{\partial x \partial y}
\end{Bmatrix}
\tag{2.62}
$$

$$
\left\{ \gamma^{(a)} \right\} \equiv
\begin{Bmatrix}
\alpha_x + \dfrac{\partial w_0}{\partial x} \\[2ex]
\alpha_y + \dfrac{\partial w_0}{\partial y}
\end{Bmatrix},
\quad
\left\{ \gamma^{(b)} \right\} \equiv -\left(\dfrac{4}{h^2}\right)
\begin{Bmatrix}
\alpha_x + \dfrac{\partial w_0}{\partial x} \\[2ex]
\alpha_y + \dfrac{\partial w_0}{\partial y}
\end{Bmatrix}
$$

Finally, the equations of motion, expressed in stress resultants, for a TSDT can be written as [13]

$$
\frac{\partial N_{xx}}{\partial x} + \frac{\partial N_{xy}}{\partial y} = I_0 \ddot{u}_0 + \left(I_1 - \frac{4}{3h^2}I_3\right)\ddot{\alpha}_x - \frac{4}{3h^2}I_3 \frac{\partial \ddot{w}_0}{\partial x}
\tag{2.63a}
$$

$$
\frac{\partial N_{xy}}{\partial x} + \frac{\partial N_{yy}}{\partial y} = I_0 \ddot{v}_0 + \left(I_1 - \frac{4}{3h^2}I_3\right)\ddot{\alpha}_y - \frac{4}{3h^2}I_3 \frac{\partial \ddot{w}_0}{\partial y}
\tag{2.63b}
$$

$$
\frac{\partial \bar{Q}_x}{\partial x} + \frac{\partial \bar{Q}_y}{\partial y} + \frac{\partial}{\partial x}\left(N_{xx}\frac{\partial w_0}{\partial x} + N_{xy}\frac{\partial w_0}{\partial y}\right) + \frac{\partial}{\partial y}\left(N_{xy}\frac{\partial w_0}{\partial y} + N_{yy}\frac{\partial w_0}{\partial y}\right)
$$

$$
+ \frac{4}{3h^2}\left(\frac{\partial^2 T_{xx}}{\partial x^2} + 2\frac{\partial^2 T_{xy}}{\partial x \partial y} + \frac{\partial^2 T_{yy}}{\partial y^2}\right) + q = I_0 \ddot{w}_0 - \frac{16}{9h^4}I_6\left(\frac{\partial^2 \ddot{w}_0}{\partial x^2} + \frac{\partial^2 \ddot{w}_0}{\partial y^2}\right)
\tag{2.63c}
$$

$$
+ \frac{4}{3h^2}\left[I_3\left(\frac{\partial \ddot{w}_0}{\partial x} + \frac{\partial \ddot{w}_0}{\partial y}\right) + \left(I_4 - \frac{4}{3h^2}I_6\right)\left(\frac{\partial \ddot{\alpha}_x}{\partial x} + \frac{\partial \ddot{\alpha}_y}{\partial y}\right)\right]
$$

$$
\frac{\partial \bar{M}_{xx}}{\partial x} + \frac{\partial \bar{M}_{xy}}{\partial y} - \bar{Q}_x =
$$

$$
\left(I_1 - \frac{4}{3h^2}I_3\right)\ddot{u}_0 + \left(I_2 - \frac{8}{3h^2}I_4 + \frac{16}{9h^4}I_6\right)\ddot{\alpha}_x - \frac{4}{3h^2}\left(I_4 - \frac{4}{3h^2}I_6\right)\frac{\partial \ddot{w}_0}{\partial x}
\tag{2.63d}
$$

$$\frac{\partial \bar{M}_{xy}}{\partial x} + \frac{\partial \bar{M}_{yy}}{\partial y} - \bar{Q}_y =$$

$$\left(I_1 - \frac{4}{3h^2}I_3\right)\ddot{v}_0 + \left(I_2 - \frac{8}{3h^2}I_4 + \frac{16}{9h^4}I_6\right)\ddot{\alpha}_y - \frac{4}{3h^2}\left(I_4 - \frac{4}{3h^2}I_6\right)\frac{\partial \ddot{w}_0}{\partial y}$$

(2.63e)

where

$$I_0 = \sum_{k=1}^{N}\int_{z_k}^{z_{k+1}}\rho^{(k)}dz, \quad I_1 = \sum_{k=1}^{N}\int_{z_k}^{z_{k+1}}\rho^{(k)}zdz, \quad I_2 = \sum_{k=1}^{N}\int_{z_k}^{z_{k+1}}\rho^{(k)}z^2dz$$

$$I_3 = \sum_{k=1}^{N}\int_{z_k}^{z_{k+1}}\rho^{(k)}z^3dz, \quad I_4 = \sum_{k=1}^{N}\int_{z_k}^{z_{k+1}}\rho^{(k)}z^4dz$$

(2.64)

$$I_5 = \sum_{k=1}^{N}\int_{z_k}^{z_{k+1}}\rho^{(k)}z^5dz, \quad I_6 = \sum_{k=1}^{N}\int_{z_k}^{z_{k+1}}\rho^{(k)}z^6dz$$

and

$$\bar{M}_{xx} = M_{xx} - \frac{4}{3h^2}T_{xx}, \quad \bar{M}_{xy} = M_{xy} - \frac{4}{3h^2}T_{xy}, \quad \bar{M}_{yy} = M_{yy} - \frac{4}{3h^2}T_{yy}$$

$$\bar{Q}_x = Q_4 - \frac{4}{h^2}S_4, \quad \bar{Q}_y = Q_5 - \frac{4}{h^2}S_5$$

(2.65)

Solution of eqs. (2.63a)–(2.63e) will lead to the finding of the five unknowns, namely displacements u_0, v_0, w_0 and rotations α_x, α_y. Reddy [13] presents simplified results of the third-order theory, by neglecting the higher order terms (T_{xx}, T_{xy}, T_{yy}), while keeping the other higher order terms (S_x, S_y); however, the resulting theory comes out to be inconsistent in the energy sense.

A simpler high-order theory, a second-order shear deformation, was developed and presented by Khdeir and Reddy [21]. They propose the following displacement field:

$$u(x,y,z,t) = u_0(x,y,t) + z\alpha_x(x,y,t) + z^2\beta_x(x,y,t)$$

$$v(x,y,z,t) = v_0(x,y,t) + z\alpha_y(x,y,t) + z^2\beta_y(x,y,t)$$

(2.66)

$$w(x,y,z,t) = w_0(x,y,t)$$

For the case of linear strains the strain-displacement relations can be shown to be written as

$$\varepsilon_{xx} \equiv \frac{\partial u}{\partial x} = \frac{\partial u_0}{\partial x} + z \frac{\partial \alpha_x}{\partial x} + z^2 \frac{\partial \beta_x}{\partial x}, \quad \varepsilon_{yy} \equiv \frac{\partial v_0}{\partial y} + z \frac{\partial \alpha_y}{\partial y} + z^2 \frac{\partial \beta_y}{\partial y}, \quad \varepsilon_{zz} \equiv \frac{\partial w}{\partial z} = 0$$

$$\varepsilon_{xy} \equiv \frac{1}{2}\left(\frac{\partial u}{\partial y} + \frac{\partial v}{\partial x} \right) = \frac{1}{2}\left[\left(\frac{\partial u_0}{\partial y} + \frac{\partial v_0}{\partial x} \right) + z \left(\frac{\partial \alpha_x}{\partial y} + \frac{\partial \alpha_y}{\partial x} \right) + z^2 \left(\frac{\partial \beta_x}{\partial y} + \frac{\partial \beta_y}{\partial x} \right) \right]$$

$$\varepsilon_{xz} \equiv \frac{1}{2}\left(\frac{\partial u}{\partial z} + \frac{\partial w}{\partial x} \right) = \frac{1}{2}\left[\left(\alpha_x + \frac{\partial w_0}{\partial x} \right) + 2z\beta_x \right]$$

$$\varepsilon_{yz} \equiv \frac{1}{2}\left(\frac{\partial v}{\partial z} + \frac{\partial w}{\partial y} \right) = \frac{1}{2}\left[\left(\alpha_y + \frac{\partial w_0}{\partial x} \right) + 2z\beta_y \right]$$

(2.67)

The seven equations of motion presented in stress resultant terms, for the seven unknown displacements (u_0, v_0, w_0, α_x, α_y, β_x and β_y), assumed for the second-order shear deformation theory can be written as (see also [21])

$$\frac{\partial N_{xx}}{\partial x} + \frac{\partial N_{xy}}{\partial y} = I_1\ddot{u}_0 + I_2\ddot{\alpha}_x + I_3\ddot{\alpha}_y \qquad (2.68a)$$

$$\frac{\partial N_{xy}}{\partial x} + \frac{\partial N_{yy}}{\partial y} = I_1\ddot{v}_0 + I_2\ddot{\beta}_x + I_3\ddot{\beta}_y \qquad (2.68b)$$

$$\frac{\partial Q_x}{\partial x} + \frac{\partial Q_y}{\partial y} + q = I_1\ddot{w}_0 \qquad (2.68c)$$

$$\frac{\partial M_{xx}}{\partial x} + \frac{\partial M_{xy}}{\partial y} - Q_x = I_2\ddot{u}_0 + I_3\ddot{\alpha}_x + I_4\ddot{\alpha}_y \qquad (2.68d)$$

$$\frac{\partial M_{xy}}{\partial x} + \frac{\partial M_{yy}}{\partial y} - Q_y = I_2\ddot{v}_0 + I_3\ddot{\beta}_x + I_4\ddot{\beta}_y \qquad (2.68e)$$

$$\frac{\partial T_{xx}}{\partial x} + \frac{\partial T_{xy}}{\partial y} - 2S_x = I_3\ddot{u}_0 + I_4\ddot{\alpha}_x + I_5\ddot{\alpha}_y \qquad (2.68f)$$

$$\frac{\partial T_{xy}}{\partial x} + \frac{\partial T_{yy}}{\partial y} - 2S_y = I_3\ddot{v}_0 + I_4\ddot{\beta}_x + I_5\ddot{\beta}_y \qquad (2.68g)$$

where

$$I_1 = \sum_{k=1}^{N} \int_{z_k}^{z_{k+1}} \rho^{(k)} dz, \quad I_2 = \sum_{k=1}^{N} \int_{z_k}^{z_{k+1}} \rho^{(k)} z\, dz, \quad I_3 = \sum_{k=1}^{N} \int_{z_k}^{z_{k+1}} \rho^{(k)} z^2 dz$$

$$I_4 = \sum_{k=1}^{N} \int_{z_k}^{z_{k+1}} \rho^{(k)} z^3 dz, \quad I_5 = \sum_{k=1}^{N} \int_{z_k}^{z_{k+1}} \rho^{(k)} z^4 dz$$

(2.69)

The stress resultants–strains relationships, based on the above second-order displacement field, can be written as

$$
\left\{ \begin{array}{c} \{N\} \\ \{M\} \\ \{T\} \end{array} \right\} = \left[\begin{array}{ccc} [A] & [B] & [D] \\ [B] & [D] & [E] \\ [D] & [E] & [F] \end{array} \right] \left\{ \begin{array}{c} \{\varepsilon^{(a)}\} \\ \{\varepsilon^{(b)}\} \\ \{\varepsilon^{(c)}\} \end{array} \right\}
\tag{2.70}
$$

$$
\left\{ \begin{array}{c} \{Q\} \\ \{S\} \end{array} \right\} = \left[\begin{array}{cc} [A] & [B] \\ [B] & [D] \end{array} \right] \left\{ \begin{array}{c} \{\gamma^{(a)}\} \\ \{\gamma^{(b)}\} \end{array} \right\}
\tag{2.71}
$$

where for eq. (2.70), the components are defined as

$$
A_{ij} = \sum_{k=1}^{N} \int_{z_k}^{z_{k+1}} \bar{Q}_{ij} dz = \sum_{k=1}^{N} \bar{Q}_{ij}^{(k)} [z_{k+1} - z_k]
$$

$$
B_{ij} = \sum_{k=1}^{N} \int_{z_k}^{z_{k+1}} \bar{Q}_{ij} z \, dz = \frac{1}{2} \sum_{k=1}^{N} \bar{Q}_{ij}^{(k)} \left[(z_{k+1})^2 - (z_k)^2 \right]
$$

$$
D_{ij} = \sum_{k=1}^{N} \int_{z_k}^{z_{k+1}} \bar{Q}_{ij} z^2 dz = \frac{1}{3} \sum_{k=1}^{N} \bar{Q}_{ij}^{(k)} \left[(z_{k+1})^3 - (z_k)^3 \right] \qquad \text{while} \quad i,j = 1,2,6 \quad (2.72)
$$

$$
E_{ij} = \sum_{k=1}^{N} \int_{z_k}^{z_{k+1}} \bar{Q}_{ij} z^3 dz = \frac{1}{4} \sum_{k=1}^{N} \bar{Q}_{ij}^{(k)} \left[(z_{k+1})^4 - (z_k)^4 \right]
$$

$$
F_{ij} = \sum_{k=1}^{N} \int_{z_k}^{z_{k+1}} \bar{Q}_{ij} z^4 dz = \frac{1}{5} \sum_{k=1}^{N} \bar{Q}_{ij}^{(k)} \left[(z_{k+1})^5 - (z_k)^5 \right]
$$

while for eq. (2.71) their definition is

$$
A_{lm} = \sum_{k=1}^{N} \int_{z_k}^{z_{k+1}} \bar{Q}_{lm} dz = \sum_{k=1}^{N} \bar{Q}_{lm}^{(k)} [z_{k+1} - z_k]
$$

$$
B_{lm} = \sum_{k=1}^{N} \int_{z_k}^{z_{k+1}} \bar{Q}_{lm} z \, dz = \frac{1}{2} \sum_{k=1}^{N} \bar{Q}_{lm}^{(k)} \left[(z_{k+1})^2 - (z_k)^2 \right] \qquad \text{while} \quad l,m = 4,5
$$

$$
(2.73)
$$

$$
D_{lm} = \sum_{k=1}^{N} \int_{z_k}^{z_{k+1}} \bar{Q}_{lm} z^2 dz = \frac{1}{3} \sum_{k=1}^{N} \bar{Q}_{lm}^{(k)} \left[(z_{k+1})^3 - (z_k)^3 \right]
$$

where

$$
\left\{\varepsilon^{(a)}\right\} \equiv \left\{
\begin{array}{c}
\dfrac{\partial u_0}{\partial x} \\[2mm]
\dfrac{\partial v_0}{\partial y} \\[2mm]
\dfrac{\partial u_0}{\partial y} + \dfrac{\partial v_0}{\partial x}
\end{array}
\right\}, \quad
\left\{\varepsilon^{(b)}\right\} \equiv \left\{
\begin{array}{c}
\dfrac{\partial \alpha_x}{\partial x} \\[2mm]
\dfrac{\partial \alpha_y}{\partial y} \\[2mm]
\dfrac{\partial \alpha_x}{\partial y} + \dfrac{\partial \alpha_y}{\partial x}
\end{array}
\right\}, \quad
\left\{\varepsilon^{(c)}\right\} \equiv \left\{
\begin{array}{c}
\dfrac{\partial \beta_x}{\partial x} \\[2mm]
\dfrac{\partial \beta_y}{\partial y} \\[2mm]
\dfrac{\partial \beta_x}{\partial y} + \dfrac{\partial \beta_y}{\partial x}
\end{array}
\right\}
$$

$$
\left\{\gamma^{(a)}\right\} \equiv \left\{
\begin{array}{c}
\alpha_x + \frac{\partial w_0}{\partial x} \\[2mm]
\alpha_y + \frac{\partial w_0}{\partial y}
\end{array}
\right\}, \quad
\left\{\gamma^{(b)}\right\} \equiv 2 \left\{
\begin{array}{c}
\beta_x \\[1mm]
\beta_y
\end{array}
\right\}
$$

$$(2.74)$$

and

$$
\gamma_{xy} \equiv 2\varepsilon_{xy}, \quad \gamma_{xz} \equiv 2\varepsilon_{xz}, \quad \gamma_{yz} \equiv 2\varepsilon_{yz}
$$

$$(2.75)$$

The equations of motion (2.68a)–(2.68g) can be expressed using the seven unknown displacements to yield [21]:

$$
A_{11} \frac{\partial^2 u_0}{\partial x^2} + A_{66} \frac{\partial^2 u_0}{\partial y^2} + (A_{12} + A_{66}) \frac{\partial^2 v_0}{\partial x \partial y} + 2B_{16} \frac{\partial^2 \alpha_x}{\partial x \partial y} + B_{16} \frac{\partial^2 \beta_x}{\partial x^2}
$$

$$(2.76a)$$

$$
B_{26} \frac{\partial^2 \beta_x}{\partial y^2} + D_{11} \frac{\partial^2 \alpha_y}{\partial x^2} + D_{66} \frac{\partial^2 \alpha_y}{\partial y^2} + (D_{12} + D_{66}) \frac{\partial^2 \beta_y}{\partial x \partial y} = I_1 \ddot{u}_0 + I_3 \ddot{\alpha}_y
$$

$$
A_{22} \frac{\partial^2 v_0}{\partial y^2} + A_{66} \frac{\partial^2 v_0}{\partial x^2} + (A_{12} + A_{66}) \frac{\partial^2 u_0}{\partial x \partial y} + B_{16} \frac{\partial^2 \alpha_x}{\partial x^2} + B_{26} \frac{\partial^2 \alpha_x}{\partial y^2}
$$

$$(2.76b)$$

$$
2B_{26} \frac{\partial^2 \beta_x}{\partial x \partial y} + D_{22} \frac{\partial^2 \beta_y}{\partial y^2} + D_{66} \frac{\partial^2 \beta_y}{\partial x^2} + (D_{12} + D_{66}) \frac{\partial^2 \alpha_y}{\partial x \partial y} = I_1 \ddot{v}_0 + I_3 \ddot{\beta}_y
$$

$$
A_{55} \left(\frac{\partial \alpha_x}{\partial x} + \frac{\partial^2 w_0}{\partial x^2} \right) + A_{44} \left(\frac{\partial \beta_x}{\partial y} + \frac{\partial^2 w_0}{\partial y^2} \right) + 2B_{45} \left(\frac{\partial \beta_y}{\partial x} + \frac{\partial \alpha_y}{\partial y} \right) + q = I_1 \ddot{w}_0 \quad (2.76c)
$$

$$
2B_{16} \frac{\partial^2 u_0}{\partial x \partial y} + B_{16} \frac{\partial^2 v_0}{\partial x^2} + B_{26} \frac{\partial^2 v_0}{\partial y^2} + D_{11} \frac{\partial^2 \alpha_x}{\partial x^2} + D_{66} \frac{\partial^2 \alpha_x}{\partial y^2} + (D_{12} + D_{66}) \frac{\partial^2 \beta_x}{\partial x \partial y}
$$

$$(2.76d)$$

$$
+ 2E_{16} \frac{\partial^2 \alpha_y}{\partial x \partial y} + E_{16} \frac{\partial^2 \beta_y}{\partial x^2} + E_{26} \frac{\partial^2 \beta_y}{\partial y^2} - A_{55} \left(\alpha_x + \frac{\partial w_0}{\partial x} \right) - 2B_{45} \beta_y = I_3 \ddot{\alpha}_x
$$

$$2B_{26}\frac{\partial^2 v_0}{\partial x \partial y} + B_{16}\frac{\partial^2 u_0}{\partial x^2} + B_{26}\frac{\partial^2 u_0}{\partial y^2} + D_{22}\frac{\partial^2 \beta_x}{\partial y^2} + D_{66}\frac{\partial^2 \beta_x}{\partial x^2} + (D_{12} + D_{66})\frac{\partial^2 \alpha_x}{\partial x \partial y}$$

$$+ E_{26}\frac{\partial^2 \alpha_y}{\partial y^2} + 2E_{26}\frac{\partial^2 \beta_y}{\partial x \partial y} + E_{16}\frac{\partial^2 \alpha_y}{\partial x^2} - A_{44}\left(\alpha_x + \frac{\partial w_0}{\partial y}\right) - 2B_{45}\alpha_y = I_3\ddot{\beta}_x$$

(2.76e)

$$D_{11}\frac{\partial^2 u_0}{\partial x^2} + D_{66}\frac{\partial^2 u_0}{\partial y^2} + (D_{12} + D_{66})\frac{\partial^2 v_0}{\partial x \partial y} + 2E_{16}\frac{\partial^2 \alpha_x}{\partial x \partial y} + E_{16}\frac{\partial^2 \beta_x}{\partial x^2} + E_{26}\frac{\partial^2 \beta_x}{\partial y^2}$$

$$+ F_{11}\frac{\partial^2 \alpha_y}{\partial x^2} + F_{66}\frac{\partial^2 \alpha_y}{\partial y^2} + (F_{12} + F_{66})\frac{\partial^2 \beta_y}{\partial x \partial y} - 2B_{45}\left(\beta_x + \frac{\partial w_0}{\partial y}\right) - 4D_{55}\alpha_y = I_3\ddot{u}_0 + I_5\ddot{\alpha}_y$$

(2.76f)

$$D_{22}\frac{\partial^2 v_0}{\partial y^2} + D_{66}\frac{\partial^2 v_0}{\partial x^2} + (D_{12} + D_{66})\frac{\partial^2 u_0}{\partial x \partial y} + 2E_{26}\frac{\partial^2 \beta_x}{\partial x \partial y} + E_{16}\frac{\partial^2 \alpha_x}{\partial x^2} + E_{26}\frac{\partial^2 \alpha_x}{\partial y^2}$$

$$+ F_{221}\frac{\partial^2 \beta_y}{\partial y^2} + F_{66}\frac{\partial^2 \beta_y}{\partial x^2} + (F_{12} + F_{66})\frac{\partial^2 \alpha_y}{\partial x \partial y} - 2B_{45}\left(\alpha_x + \frac{\partial w_0}{\partial x}\right) - 4D_{44}\beta_y = I_3\ddot{v}_0 + I_5\ddot{\beta}_y$$

(2.76g)

The solution in [21] is given for a case of an antisymmetric angle-ply-laminated rectangular plate, with two opposite edges having simply supported boundary conditions (in the *x* direction), while the other two (in the *y* direction) may have any arbitrary combinations of free, clamped or simply supported edge conditions. The natural frequencies of such a plate are calculated using a generalized Lèvy-type solution, namely selecting the assumed deflections and rotations to fulfill in *x* direction, the simply supported boundary conditions (these functions will be dependent only on *x*), while in the perpendicular direction, having arbitrary boundary conditions, the functions will be dependent only on *y*. These functions (in the y direction) will now be the seven unknowns of the problem, after fulfillment of the prescribed boundary conditions in the *y* direction.

Another approach for using high-order approximation is known in the literature as "the Zig-Zag" (ZZ) theory, as in [22–35]. This approach is best summarized and reviewed by Carrera in [25] The idea behind this approach is to describe a piecewise continuous displacement field for basic elements like beams, plates and shells in the thickness direction and fulfill interlaminar continuity (IC) of the transverse stresses at each layer interface. One should note that in the literature the piecewise assumption of stresses and displacement fields is often referred to as ZZ and IC, respectively, while the theories applying both assumptions are named as ZZ theories. As Carrera [25] pointed out in his review, Lekhnitskii [36] was the first to suggest a theory for multilayered structures, followed by other fundamental contributors like Ambartsumian [37, 38] and Reisner [39, 40]. In the present context, we shall present only Lekhnitskii's approach to highlight the ZZ theory.

Figure 2.9 presents the multilayered beam model as suggested by Lekhnitskii. It consists of a beam having the length L, total height H and width b. The cantilevered beam is loaded by a concentrated load P and a bending moment M. The beam consists of N_L layers. The coordinate system, as presented in Fig. 2.9, shows the Y coordinate along the length of the beam, with the Y–Z plane being perpendicular to it. The various Z coordinates of each layer is denoted by h_i, while the thickness of each layer is given by t_i. The black dots on the drawing stand for the interface surfaces.
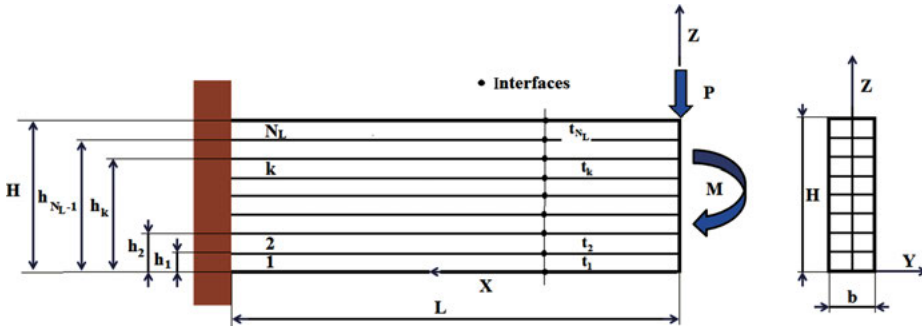
Fig. 2.9: Lekhnitskii's cantilever multilayered beam model – geometry and notations.

We shall denote the stresses for the k layer as $\sigma_{xx}^k, \tau_{xz}^k, \sigma_{zz}^k$, while its displacements are written as u^k, w^k, with E^k, v^k, G^k being the kth-layer Young's modulus, the Poisson's ratio and the shear modulus, respectively. As can be seen the problem involves the X–Z plane, and it is a plane-stress problem which can be solved using stress functions φ^k for each layer k, defined as

$$\sigma_{xx}^k = \frac{\partial^2 \varphi^k}{\partial z^2}, \quad \sigma_{zz}^k = \frac{\partial^2 \varphi^k}{\partial x^2}, \quad \tau_{xz}^k = -\frac{\partial^2 \varphi^k}{\partial x \partial z} \tag{2.77}$$

The problem is then defined by demanding the compatibility of the resulted strains due to the applied loading, which can be written as

$$\frac{\partial^4 \varphi^k}{\partial x^4} + \frac{\partial^4 \varphi^k}{\partial x^2 \partial z^2} + \frac{\partial^4 \varphi^k}{\partial z^4} = 0 \tag{2.78}$$

Now Lekhnitskii assumed the following stress function:

$$\varphi^k(x,z) = \frac{\alpha^k}{6} z^3 + \frac{\beta^k}{2} z^2 + x \left[\frac{A^k}{3} z^3 + \frac{B^k}{2} z^2 + X^k z \right] \tag{2.79}$$

with $\alpha^k, \beta^k, A^k, B^k, X^k$ being constants to be latter determined from the boundary conditions and the continuity demands at the interface between two layers.

Using eq. (2.77), one can find the three plane stresses as

$$\sigma_{xx}^k \equiv \frac{\partial^2 \varphi^k}{\partial z^2} = \alpha^k z + \beta^k + x\left[2A^k z + B^k\right] \tag{2.80}$$

$$\sigma_{zz}^k \equiv \frac{\partial^2 \varphi^k}{\partial x^2} = 0 \tag{2.81}$$

$$\tau_{xz}^k \equiv -\frac{\partial^2 \varphi^k}{\partial x \partial z} = -A^k z^2 - B^k z - X^k \tag{2.82}$$

As shown in eqs. (2.80)–(2.82), the longitudinal stresses σ_{xx}^k are linear in both the longitudinal (x direction) and thickness (z direction) directions, and the stresses in the thickness direction, σ_{zz}^k, are zero throughout the X–Z plane, while the shear stresses τ_{xz}^k, have a parabolic distribution in the z direction. The above results, stemming from Lekhnitskii's assumption of the stress function, $\varphi^k(x, z)$(eq. (2.79)), lead to a stress distribution that is acceptable for a beam theory.

To obtain the $5xN_L$ unknown constants, $\alpha^k, \beta^k, A^k, B^k, X^k$, the following relations must be satisfied and then solved:

The strain–stress relation, expressed using the two displacements, u^k, w^k, can be written as (using the Hook's law)

$$\varepsilon_{xx}^k \equiv \frac{\partial u^k}{\partial x} = \frac{\sigma_{xx}^k}{E^k} - v^k \frac{\sigma_{zz}^k}{E^k}$$

$$\varepsilon_{zz}^k \equiv \frac{\partial w^k}{\partial z} = \frac{\sigma_{zz}^k}{E^k} - v^k \frac{\sigma_{xx}^k}{E^k} \tag{2.83}$$

$$\gamma_{xz}^k \equiv \frac{\partial u^k}{\partial z} + \frac{\partial w^k}{\partial x} = \frac{\tau_{xz}^k}{G^k}$$

The continuity (or compatibility) conditions for the displacements and the transverse stresses have to be satisfied at the laminar interfaces (namely the ZZ phenomenon) according to the following equations

$$u^k = u^{k-1} \text{ and } w^k = w^{k-1} \text{ for } k = 2, ..., N_L \tag{2.84}$$

$$\sigma_{yy}^k = \sigma_{yy}^{k-1} \text{ and } \sigma_{xy}^k = \sigma_{xy}^{k-1} \text{ for } k = 2, ..., N_L \tag{2.85}$$

Next the various boundary conditions have to be fulfilled. The upper and lower planes of the beam are free of stresses. This can be written as

$$\text{At } Z = 0, H \quad \sigma_{yy}^1 = 0; \ \sigma_{yy}^{N_L} = 0 \text{ and } \sigma_{xy}^1 = 0; \ \sigma_{xy}^{N_L} = 0 \tag{2.86}$$

Finally, equilibrium between the applied load (P and M) and the stresses should also be demanded, namely

$$b \sum_1^{N_L} \int_{h_{k-1}}^{h_k} \sigma_{zz}^k dz = 0$$

$$b \sum_1^{N_L} \int_{h_{k-1}}^{h_k} \sigma_{xx}^k z dz = \frac{M - Px}{H}$$ (2.87)

$$b \sum_1^{N_L} \int_{h_{k-1}}^{h_k} \sigma_{xz}^k dz = -\frac{P}{H}$$

Using expressions for stresses, as presented in eqs (2.80)–(2.82), substituting it in eq. (2.83) and then integrating in the X and Y directions yields the following expressions for the displacements:

$$u^k = \int \frac{\sigma_{xx}^k}{E^k} dx = \frac{1}{E^k}\left[\left(\alpha^k z + \beta^k\right)x + \frac{x^2}{2}\left(2A^k z + B^k\right)\right] + f(z)$$

$$w^k = -\int \frac{v^k \sigma_{xx}^k}{E^k} dz = -\frac{v^k}{E^k}\left[\left(\alpha^k \frac{z^2}{2} + \beta^k z\right) + x\left(A^k z^2 + B^k z\right)\right] + f_1(x)$$ (2.88)

where $f(z)$ and $f_1(x)$ are functions to be determined using the last equation in eqs. (2.83), namely

$$\gamma_{xz} \equiv \frac{\partial u^k}{\partial z} + \frac{\partial w^k}{\partial z} = \tau_{xz} = -\frac{1}{G^k}\left[A^k z^2 + B^k z + X^k\right]$$ (2.89)

Substituting the expressions for u^k and w^k into eq. (2.89) yields

$$\frac{1}{E^k}\left[\alpha^k x + x^2 A^k\right] + \frac{\partial f(z)}{\partial z} - \frac{v^k}{E^k}\left[A^k z^2 + B^k z\right] + \frac{\partial f_1(x)}{\partial x} = -\frac{1}{G^k}\left[A^k z^2 + B^k z + X^k\right]$$ (2.90)

Equation (2.90) can be rearranged to yield the following form:

$$F(x) = \frac{1}{E^k}\left[\alpha^k x + x^2 A^k\right] + \frac{\partial f_1(x)}{\partial x} \equiv e^k$$

$$G(z) = \left[\frac{1}{G_{xz}} - \frac{v^k}{E^k}\right]\left[A^k z^2 + B^k z\right] + \frac{\partial f(z)}{\partial z} \equiv d^k$$ (2.91)

$$K = -\frac{X^k}{G_{xz}}$$

and

$$e^k + d^k = K = -\frac{X^k}{G^k} \Rightarrow e^k = -\left(\frac{X^k}{G^k} + d^k\right)$$ (2.92)

It is clear from eq. (2.90) that if the sum of the two functions $F(x)$ and $G(z)$ is equal to a constant, K, for every x and z, then each of those functions must be a constant, e^k and d^k, respectively (see eqs. (2.91) and (2.92)). Now we can proceed to integrate the functions presented in eq. (2.91) to yield the two functions $f(z)$ and $f_1(x)$. From eq. (2.92) we can see that

$$\frac{df(z)}{dz} = d^k - \left(\frac{1}{G^k} - \frac{v^k}{E^k}\right)\left[A^k z^2 + B^k z\right]$$

$$\frac{df_1(x)}{dx} = e^k - \frac{1}{E^k}\left[x\alpha^k + x^2 A^k\right] \tag{2.93}$$

$$= -\left(\frac{X^k}{G^k} + d^k\right) - \frac{1}{E^k}\left[x\alpha^k + x^2 A^k\right]$$

Integrating the equations presented in eq. (2.93) yields

$$f(z) = d^k \cdot z - \left(\frac{1}{G^k} - \frac{v^k}{E^k}\right)\left[\frac{A^k z^3}{3} + B^k \frac{z^2}{2}\right] + d_1^k$$

$$f_1(x) = -\left(\frac{X^k}{G^k} + d^k\right)x - \frac{1}{E^k}\left[\frac{x^2}{2}\alpha^k + \frac{x^3}{3}A^k\right] + e_1^k \tag{2.94}$$

where d_1^k and e_1^k, e_1 are additional constants besides the constant d^k (see eq. (2.93)) defined earlier. Substituting the two functions from eq. (2.94), $f(z)$ and $f_1(x)$ into eq. (2.88) provides the expression for the two displacements u^k, w^k,

$$u^k = \frac{1}{E^k}\left[\left(\alpha^k z + \beta^k\right)x + \frac{x^2}{2}\left(2A^k z + B^k\right)\right] + d^k \cdot z - \left(\frac{1}{G^k} - \frac{v^k}{E^k}\right)\left[\frac{A^k z^3}{3} + B^k \frac{z^2}{2}\right] + d_1^k$$

$$w^k = -\frac{v^k}{E^k}\left[\left(\alpha^k \frac{z^2}{2} + \beta^k z\right) + x\left(A^k z^2 + B^k z\right)\right] - \left(\frac{X^k}{G^k} + d\right)x - \frac{1}{E^k}\left[\frac{x^2}{2}\alpha^k + \frac{x^3}{3}A^k\right] + e_1^k$$

$$\tag{2.95}$$

Having the two expressions for the displacements u^k, w^k, the requirements listed in eqs. (2.84)–(2.87) are used to obtain all the unknowns, including the constants d, d_1 and e_1. This results in the following relations [25]:

$$\frac{\alpha^k}{E^k} = \frac{\alpha^{k-1}}{E^{k-1}}, \quad \frac{A^k}{E^k} = \frac{A^{k-1}}{E^{k-1}}$$

$$\frac{A^k}{E^k}h_{k-1} + \frac{B^k}{2E^k}h_{k-1} = \frac{A^{k-1}}{E^{k-1}}h_{k-1} + \frac{B^{k-1}}{2E^{k-1}}h_{k-1}$$

$$\frac{\alpha^k h_{k-1} + \beta^k}{E^k} = \frac{\alpha^{k-1}h_{k-1} + \beta^{k-1}}{E^k}$$

$$X^1 = 0, \quad A^{N_L}h_{N_L}^2 + B^{N_L}h_{N_L} + X^{N_L} = 0$$

$$A^k h_{k-1}^2 + B^k h_{k-1} + X^k = A^{k-1}h_{k-1}^2 + B^{k-1}h_{k-1} + X^{k-1}$$

$$-\left(\frac{1}{G^{k-1}} - \frac{v^k}{E^{k-1}}\right)\left[\frac{A^k h_{k-1}^3}{3} + B^k \frac{h_{k-1}^2}{2}\right] - d^k h_{k-1} + d_1^k =$$

$$= \left(\frac{1}{G^k} - \frac{v^{k-1}}{E^k}\right)\left[\frac{A^{k-1}h_{k-1}^3}{3} + B^{k-1}\frac{h_{k-1}^2}{2}\right] - d^{k-1}h_{k-1} + d_1^{k-1}$$

$$\frac{v^k}{E^k}\left(A^k h_{k-1}^2 + B^k h_{k-1}\right) - \frac{X^k}{G^k} + d^k = \frac{v^{k-1}}{E^{k-1}}\left(A^{k-1}h_{k-1}^2 + B^{k-1}h_{k-1}\right) - \frac{X^{k-1}}{G^{k-1}} + d^{k-1}$$

$$-\frac{v^k}{E^k}\left(\frac{\alpha^k}{2}h_{k-1}^2 + \beta^k h_{k-1}\right) + e_1^k = -\frac{v^{k-1}}{E^{k-1}}\left(\frac{\alpha^{k-1}}{2}h_{k-1}^2 + \beta^{k-1}h_{k-1}\right) + e_1^{k-1} \tag{2.96}$$

As a result of the expressions presented in eq. (2.96), the following recursive equations can be obtained:

$$A^k = \frac{A^1 E^k}{E^1}, \quad B^k = \frac{B^1 E^k}{E^1}, \quad \alpha^k = \frac{\alpha^1 E^k}{E^1}, \quad \beta^k = \frac{\beta^1 E^k}{E^1}$$

$$X^k = \frac{1}{E^1}\left\{A^1\left[\sum_{t=1}^{k-1}(h_t^2 - h_{t-1}^2)E^t - h_{k-1}E^k\right] + B^1\left[\sum_{t=1}^{k-1}(h_t - h_{t-1})E^t - h_{k-1}E^k\right]\right\}$$
$$k = 2, 3, N_{L-1} \tag{2.97}$$

with

$$X^1 = 1 \quad \text{and} \quad C_{N_L} = \frac{E^k}{E^1}\left[A^1 h_{N_L}^2 + B^1 h_{N_L}\right] \tag{2.98}$$

The other constants can be written as

$$A^1 = \frac{6PE^1}{\delta b}, \quad B^1 = -\frac{6PE^1}{\delta b}\delta_2, \quad \alpha^1 = -\frac{12ME^1}{\delta b}\delta_1, \quad \beta^1 = -\frac{12ME^1}{\delta b}\delta_2$$

where

$$\delta = 4\sum_{i=1}^{N_L}\left[h_i^3 - h_{i-1}^3\right]E^i + \sum_{i=1}^{N_L}[h_i - h_{i-1}]E^i - 3\left[\sum_{i=1}^{N_L}\left[h_i^2 - h_{i-1}^2\right]E^i\right]^2$$

$$\delta_1 = \sum_{i=1}^{N_L}\left[h_i^3 - h_{i-1}^3\right]E^i, \quad \delta_2 = \sum_{i=1}^{N_L}\left[h_i^2 - h_{i-1}^2\right]E^i$$

(2.99)

One should remember that $h_0 = 0$ and $h_{N_L} = H$.

Finally, the expression for the stresses can be written as

$$\sigma_{xx}^k = \frac{6E^k}{\delta b}[Px + M)]\,[2\delta_1 z - \delta_2], \quad k = 1, 2, \ldots, N_L$$

$$\sigma_{zz}^k = 0, \quad k = 1, 2, \ldots, N_L$$

$$\sigma_{xz}^k = \frac{6P}{\delta b}\left\{\delta_1\left[\sum_{t=1}^{k-1}\left(h_t^2 - h_{t-1}^2\right)E^t + \left(z^2 - h_{t-1}^2\right)E^k\right]\right\}$$

$$- \left\{\delta_2\left[\sum_{t=1}^{k-1}\left(h_t - h_{t-1}\right)E^t + \left(z - h_{t-1}\right)E^k\right]\right\}, \quad k = 2, 3, \ldots, N_{L-1}$$

(2.100)

with

$$\sigma_{xz}^1 = -\frac{6PE^1}{\delta b}z[\delta_1 z - \delta_2], \quad \sigma_{xz}^{N_L} = -\frac{6PE^{N_L}}{\delta b}\left(h_{N_L} - z\right)\left[\delta_2 - \left(h_{N_L} + z\right)\delta_1\right]$$

With all the constants being determined, the expressions for the two displacements u^k, w^k can now be evaluated using eq. (2.95).

For other formulations of the various ZZ theories and the assumed stress functions, one can address references [22–34] and similar available studies in the open literature.

References

[1]   Harris, B. Engineering composite materials, The Institute of Materials, London, UK, 1999, 193.
[2]   Jones, R. M. Mechanics of composite materials, 2nd edition, Taylor & Francis, Philadelphia, PA 19106, USA, 1999, 519.
[3]   Love, A. E. H. On the small free vibrations and deformations of elastic shells, Philosophical trans. of the Royal Society (London), 1888, série A, N°, Vol. 17, 491–549.
[4]   Reddy, J. N. Theory and analysis of elastic plates and shells, CRC Press, Taylor and Francis, 2007.
[5]   Timoshenko, S., and Woinowsky-Krieger, S. Theory of plates and shells, McGraw-Hill, New York, 1959.
[6]   Mindlin, R. D. Influence of rotatory inertia and shear on flexural motions of isotropic, elastic plates, ASME Journal of Applied Mechanics, 18, 1951, 31–38.
[7]   Reddy, J. N. Theory and analysis of elastic plates, Taylor and Francis, Philadelphia, 1999.

[8] Lim, G. T., and Reddy, J. N On canonical bending relationships for plates, International Journal of Solids and Structures, 40, 2003, 3039–3067.

[9] Timoshenko, S. P. On the correction factor for shear of the differential equation for transverse vibrations of bars of uniform cross-section, Philosophical Magazine, 1921, 744.

[10] Timoshenko, S. P. On the transverse vibrations of bars of uniform cross-section, Philosophical Magazine, 1922, 125.

[11] Rosinger, H. E., and Ritchie, I. G. On Timoshenko's correction for shear in vibrating isotropic beams, Journal of Physics D: Applied Phys, 10, 1977, 1461–1466.

[12] Timoshenko, S. P., and Gere, J. M. Mechanics of Materials, Van Nostrand Reinhold Co, 1972.

[13] Reddy, J.N. Mechanics of Laminated Composite Plates and Shells-Theory and Analysis, CRC Press LLC, Boca Raton, Florida, 33431 USA, 2nd Edition, 2004.

[14] Chandrashekhara, K., Krishnamurthy, K., and Roy, S. Free vibration of composite beams including rotary inertia and shear deformation, Composite Structures, 14(4), 1990, 269–279.

[15] Singh, G., and Venkateswara, R. Analysis of the nonlinear vibrations of unsymmetrically laminated composite beams, AAIA Journals, 29(10), October 1991.

[16] Abramovich, H., and Livshits, A. Free vibrations of non-symmetric cross-ply laminated composite beams, Journal of Sound and Vibration, 176(5), 6 October 1994, 597–612.

[17] Abramovich, H., Eisenberger, M., and Shulepov, O. Vibrations and buckling of non-symmetric laminated composite beams via the exact element method, AAIA Journals, 1995, http://arc.aiaa.org/doi/abs/10.2514/6.1995-1459.

[18] Abramovich, H., Eisenberger, M., and Shulepov, O. Vibrations and Buckling of Cross-Ply Nonsymmetric Laminated Composite Beams, AAIA Journals, 34(5), May, 1996.

[19] Li, J., Wu, Z., Kong, X., Li, X., and Wu, W. Comparison of various shear deformation theories for free vibration of laminated composite beams with general lay-ups, Composite Structures, 108, February 2014, 767–778.

[20] Abadi, M.M., and Daneshmehr, A.R. An investigation of modified couple stress theory in buckling analysis of micro composite laminated Euler–Bernoulli and Timoshenko beams, International Journal of Engineering Science, 75, February 2014, 40–53.

[21] Khdeir, A.A., and Reddy, J.N. Free vibrations of laminated composite plates using second-order shear deformation theory, Computers and Structures, 71(6), June 1999, 617–626.

[22] Li, X., and Liu, D. Zigzag theory for composite laminates, AIAA Journal, 33(6), 1995, 1163–1165.

[23] Cho, Y. B., and Averill, R.C. First-order zig-zag sublaminate plate theory and finite element model for laminated composite and sandwich panels, Composite Structures, 50, 2000, 1–15.

[24] Fares, M.E., and Elmarghany, M. Kh. A refined zigzag nonlinear first-order shear deformation theory of composite laminated plates, Composite Structures, 82, 2008, 71–83.

[25] Carrera, E. Historical review of Zig-Zag theories for multilayered plates and shells, Applied Mechanics Reviews, 56(3), May 2003, 287–308.

[26] Demasi, L. ∞^6 mixed plate theories based on the generalized unified formulation. Part I: Governing equations, Composite Structures, 87, 2009, 1–11.

[27] Demasi, L. ∞^6 mixed plate theories based on the generalized unified formulation. Part II: Layerwise theories, Composite Structures, 87, 2009, 12–22.

[28] Demasi, L. ∞^6 mixed plate theories based on the generalized unified formulation. Part III: Advanced mixed high order shear deformation theories, Composite Structures, 87, 2009, 183–94.

[29] Demasi, L. ∞^6 mixed plate theories based on the generalized unified formulation. Part IV: Zig-zag theories, Composite Structures, 87, 2009, 195–205.

[30] Demasi, L. ∞^6 mixed plate theories based on the generalized unified formulation. Part V: Results, Composite Structures, 88, 2009, 1–16.

[31] Sahoo, R., and Singh, B.N. A new inverse hyperbolic zigzag theory for the static analysis of composite and sandwich plates, Composite Structures, 105, 2013, 385–397.

[32] Tessler, A. Refined zigzag theory for homogenous, laminated composite, and sandwich plates: A homogenous limit methodology for zigzag function selection, NASA/TP-2010-216214, March 2010.

[33] Barut, A., Madenci, E. and Tessler, A. C°- continuous triangular plate element for laminated composite and sandwich plates using the {2,2}-, Refined Zigzag Theory, Composite Structures, 106(2013), 835–853.

[34] Sahoo, R. and Singh, B.N. A new trigonometric zigzag theory for buckling and free vibration analysis of laminated composite and sandwich plates, Composite Structures, 117, 2014, 316–332.

[35] Sahoo, R., and Singh, B.N. A new trigonometric zigzag theory for static analysis of laminated composite and sandwich plates, Aerospace Science and Technology, 35, 2014, 15–28.

[36] Lekhnitskii, S.G. Strength calculation of composite beams, Vestnik inzhen i tekhnikov, 9, 1935.

[37] Ambartsumian, S.A. Analysis of two-layer orthotropic shells, Investiia Akad Nauk SSSR, Ot Tekh Nauk, (7), 1957.

[38] Ambartsumian, S.A. Two analysis method for two-layer orthotropic shells, Izv An Arm SSR Seiya Fiz-Matem nauk X(2), 1957.

[39] Reissner, E. On a certain mixed variational theory and a proposed application, International Journal of Numerical Methods in Engineering, 20, 1984, 1366–1368.

[40] Reissner, E. On a mixed variational theorem and on a shear deformable plate theory, International Journal of Numerical Methods in Engineering, 23, 1986, 193–198.

3 Design formulas

3.1 Introduction

This chapter aims at presenting the reader with useful design formulas to analyze aerospace structures and predict their structural behavior. First, some Airy functions will be presented, followed by the strength of materials' formulas and natural frequencies for various structures.

3.2 Airy functions

To solve directly the equations of elasticity for a posed problem is not an easy task. Therefore, the use of the Airy solutions (described in detail in Chapter 1 and in [1]) might provide a way to obtain elasticity solutions. One of those functions can be obtained by a combination of polynomials, which must satisfy the biharmonic equation (see eqs. (1.57) and (1.58)) and having at least a second degree to prevent obtaining a zero-stress solution. Some typical examples are presented in Table 3.1.

One should note that for Case #1 in Table 3.1, assuming a rectangular plate, if $a = b = 0$, one gets simple constant tension in the x direction, while for $b = 0$, we would get constant tension in both x and y directions, and for $a = c = 0$, the result would represent a constant pure shear stress. For Case #2, if one assumes, for example, $a = b = c = 0$, the resulting stress $\sigma_x = 6dy$ would be linear, namely representing a pure bending of a rectangular plate.

3.3 Distribution of the shear forces, moments, deflections and slopes for beams

One of the basic elements to be used in any complex structure is a beam. Beam may be straight or curved, according to the required design. Loading a beam in bending and finding the appropriate reactions at its boundaries can be obtained by demanding equilibrium for all the forces and moments acting on it [2]. By the distribution of shear forces, V, and the moments M, along a beam, loaded in bending, one can either use the section method [2] or the summation method, based on the next relations

$$\frac{dV}{dx} = -p \quad \frac{dM}{dx} = -V \Rightarrow \quad \frac{d^2M}{dx^2} = +p \tag{3.1}$$

where p is the load per unit length, acting on the beam (see Fig. 3.1). One should note the definitions of positive external loading, as depicted in Fig. 3.1.

Table 3.1: Typical Airy functions and their resulting stresses.

Case #	Airy function	σ_x or σ_r	σ_y or σ_θ	τ_{xy} or $\sigma_{r\theta}$
1	$\phi(x,y) = ax^2 + bxy + cy^2$	$2c$	$2a$	$-b$
2	$\phi(x,y) = ax^3 + bx^2y + cxy^2 + dy^3$	$2cx + 6dy$	$6ax + 2by$	$-2(b+c)$
3	$\phi(x,y) = ax^4 + bx^3y + cx^2y^2 + dxy^3 + ey^{4*}$	$-6(a+e)x^2 +$ $6dxy + 12ey^2$	$12ax^2 + 6bxy$ $-6(a+e)y^2$	$-3bx^2 - 3dy^2$ $+12(a+e)xy$
4	$\phi(r,\theta) = Ar^2(1 - \cos 2\theta)$	$2A(1 + \cos 2\theta)$	$2A(1 - \cos 2\theta)$	$-A\sin 2\theta$

*If the relation $3(a + e) = -c$ holds, then eq. (1.57) in Chapter 1 is fulfilled.
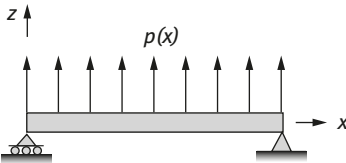
Fig. 3.1: A schematic beam on simply supported ends under load per unit length $p(x)$.

Establishing the relation in eq. (3.1), one can write the relations among the bending moment, M, the shear force, V, and the load per unit length p and the deflection W, for the case of small deflections, to be

$$EI\frac{d^2W(x)}{dx^2} = M(x), \quad EI\frac{d^3W(x)}{dx^3} = -V(x), \quad EI\frac{d^4W(x)}{dx^4} = +p\,(x) \tag{3.2}$$

Solutions for deflections, slopes and reactions for beams on various boundary conditions and loadings are presented in Table 3.2.

3.4 Natural frequencies for common basic structures
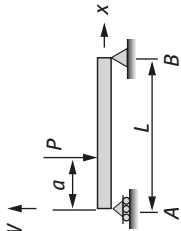
For a single degree of freedom system, consisting of a mass, m, and a spring, k, the equation of motion solving the natural frequency is known to be [3]

$$m\ddot{x} + kx = 0 \tag{3.3}$$

where x is a coordinate and $\ddot{x}$ is the acceleration of the mass. Then the single natural frequency can be written as
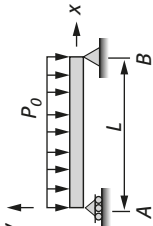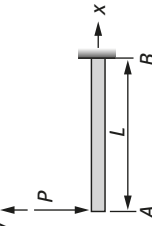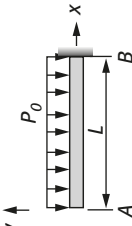
$$\omega_n = \sqrt{\frac{k}{m}} \Rightarrow f_n = \frac{1}{2\pi}\sqrt{\frac{k}{m}} \tag{3.4}$$

Table 3.2: Reactions, deflections and slopes for typical loaded beams.

#	Loading	Boundary conditions		Reactions	Deflection and slope
		Left A	**Right B**		
1		Simply supported	Simply supported	$R_A = P\left(1-\dfrac{a}{L}\right); M_A = 0$ $R_B = P \cdot \dfrac{a}{L}; M_B = 0$	For $\quad 0 \le x \le a$ $W(x) = \dfrac{1}{EI}\left[P\left(1-\dfrac{a}{L}\right)\dfrac{x^3}{6}+A_1 x\right]$ $\theta(x) = \dfrac{1}{EI}\left[P\left(1-\dfrac{a}{L}\right)\dfrac{x^2}{2}+A_1\right]$ For $\quad a \le x \le L$ $W(x) = \dfrac{1}{EI}\left[P\dfrac{ax^2}{2}\left(1-\dfrac{x}{3L}\right)+B_1 x+B_2\right]$ $\theta(x) = \dfrac{1}{EI}\left[Pax - P\dfrac{a}{L}\dfrac{x^2}{2}+B_1\right]$ where $A_1 = \dfrac{Pa^2}{6}\left\{3-2\dfrac{L}{a}\left[1+\left(\dfrac{a}{L}\right)^2\left(1+\dfrac{a}{L}\right)\right]\right\}$ $B_1 = -\dfrac{PaL}{3}\left[1+\left(\dfrac{a}{L}\right)^2\left(1+\dfrac{a}{L}\right)\right]$ $B_2 = \dfrac{Pa^3}{3}\left(1+\dfrac{a}{L}\right)$

(continued)

Table 3.2 (continued)

#	Loading	Boundary conditions		Reactions	Deflection and slope
		Left A	**Right B**		
2		Simply supported	Simply supported	$R_A = \dfrac{p_0 L}{2}; M_A = 0$ $R_B = \dfrac{p_0 L}{2}; M_B = 0$	For $0 \le x \le L$ $W(x) = \dfrac{p_0}{24EI}\left[2Lx^3 - x^4 - xL^3\right]$ $\theta(x) = \dfrac{p_0}{24EI}\left[6Lx^2 - 4x^3 - L^3\right]$
3		Free	Clamped	$R_A = 0; M_A = 0$ $R_B = P; M_B = -PL$	For $0 \le x \le L$ $W(x) = \dfrac{P}{6EI}\left[3L^2 x - x^3 - 2L^3\right]$ $\theta(x) = \dfrac{P}{6EI}\left[3L^2 - 3x^2\right]$
4		Free	Clamped	$R_A = 0; M_A = 0$ $R_B = p_0 L; M_B = -p_0 \dfrac{L^2}{2}$	For $0 \le x \le L$ $W(x) = \dfrac{p_0}{24EI}\left[4L^3 x - x^4 - 3L^4\right]$ $\theta(x) = \dfrac{p_0}{6EI}\left[L^3 - x^3\right]$

5
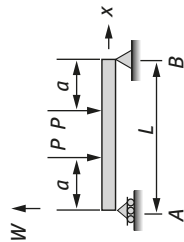
Simply supported

Simply supported

$R_A = P; M_A = 0\text{-}$
$R_B = P; M_B = 0$

For $\quad 0 \leq x \leq a$

$W(x) = \frac{1}{EI}\left[\frac{Px^3}{6} + A_1 x\right]$

$\theta(x) = \frac{1}{EI}\left[\frac{Px^2}{2} + A_1\right]$

For $\quad a \leq x \leq (L-a)$

$W(x) = \frac{1}{EI}\left[\frac{Pax^2}{2} + B_1 x + B_2\right]$

$\theta(x) = \frac{1}{EI}[Pax + B_1]$

For $\quad (L-a) \leq x \leq L$

$W(x) = \frac{1}{EI}\left[P\frac{ax^2}{2} - P\frac{x^3}{6} + P(L-a)\frac{x^2}{2} + C_1 x + C_2\right]$

$\theta(x) = \frac{1}{EI}\left[Pax - P\frac{x^2}{2} + P(L-a)x + C_1\right]$

where

$A_1 = \frac{P}{6}\left(\frac{a}{L}\right)\left[3aL + 2(a^2 - L^2)\right]$
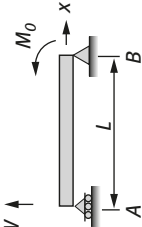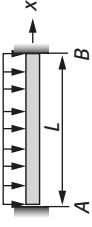
$B_1 = \frac{Pa}{3L}(a^2 - L^2) \quad B_2 = -\frac{Pa^3}{6}$

$C_1 = \frac{Pa^3}{3L} - \frac{P}{2}(a^2 + L^2)$

$C_2 = \frac{P(L-a)^3}{6} - \frac{Pa^3}{6}$

(continued)

Table 3.2 (continued)

#	Loading	Boundary conditions		Reactions	Deflection and slope
		Left A	**Right B**		
6		Simply supported	Simply supported	$R_A = \dfrac{M_0}{L}; M_A = 0$ $R_B = -\dfrac{M_0}{L}; M_B = M_0$	For $\quad 0 \le x \le L$ $W(x) = \dfrac{M_0 x}{6EIL}\left[x^2 - L^2\right]$ $\theta(x) = \dfrac{M_0}{6EIL}\left[3x^2 - L^2\right]$
7		Clamped	Clamped	$R_A = \dfrac{p_0 L}{2}; M_A = -\dfrac{p_0 L^2}{12}$ $R_B = \dfrac{p_0 L}{2}; M_B = -\dfrac{p_0 L^2}{12}$	For $\quad 0 \le x \le L$ $W(x) = \dfrac{p_0 x^2}{24EI}\left[2Lx - x^2 - L^2\right]$ $\theta(x) = \dfrac{p_0 x}{12EIL}\left[3Lx - 2x^2 - L^2\right]$
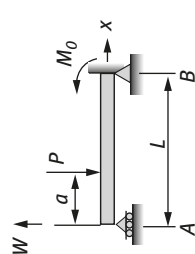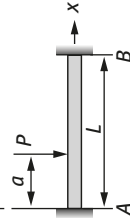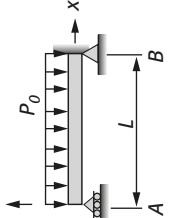
8

Simply supported

Clamped

$R_A = P - \dfrac{P}{2}\left(\dfrac{a}{L}\right)\left[\left(\dfrac{a}{L}\right)^2 + 3\right]$;

$M_A = 0$

$R_B = \dfrac{P}{2}\left(\dfrac{a}{L}\right)\left[\left(\dfrac{a}{L}\right)^2 + 3\right]$;

$M_B = \dfrac{Pa}{2}\left[\left(\dfrac{a}{L}\right)^2 + 1\right]$

For $\quad 0 \le x \le a$

$W(x) = \dfrac{1}{EI}\left[R_A \dfrac{x^3}{6} + A_1 x\right]$

$\theta(x) = \dfrac{1}{EI}\left[R_A \dfrac{x^2}{2} + A_1\right]$

For $\quad a \le x \le L$

$W(x) = \dfrac{1}{EI}\left[R_A \dfrac{x^3}{6} - \dfrac{Px^3}{6} + \dfrac{Pax^2}{2} + B_1 x + B_2\right]$

$\theta(x) = \dfrac{1}{EI}\left[R_A \dfrac{x^2}{2} - \dfrac{Px^2}{2} + Pax + B_1\right]$

where

$A_1 = B_1 + \dfrac{Pa^2}{2}$

$B_1 = \dfrac{PL^2}{4}\left(\dfrac{a}{L}\right)\left[\left(\dfrac{a}{L}\right)^2 + 3\right] - PaL$

$B_2 = + \dfrac{Pa^3}{6}$

(continued)
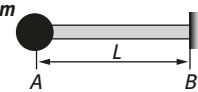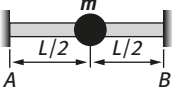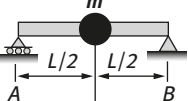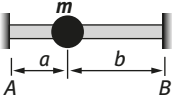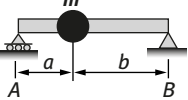
Table 3.2 (continued)

#	Loading	Boundary conditions		Reactions	Deflection and slope
		Left A	**Right B**		
9		Clamped	Clamped	$R_A = P + 3P\left(\frac{a}{L}\right)^2\left(1 - \frac{3a}{2L}\right)$; $M_A = Pa + P(2L - 3a)\left(\frac{a}{L}\right)^2$ $R_B = 3P\left(\frac{a}{L}\right)^2\left(\frac{3a}{2L} - 1\right)$; $M_B = P\left(\frac{a}{L}\right)^2\left(\frac{3a}{2} - L\right)$	For $0 \le x \le a$ $W(x) = \frac{1}{EI}\left[R_A\frac{x^3}{6} - M_A\frac{x^2}{2}\right]$ $\theta(x) = \frac{1}{EI}\left[R_A\frac{x^2}{2} - M_A x\right]$ For $a \le x \le L$ $W(x) = \frac{1}{EI}\left[-R_B\frac{x^3}{6} - (M_A - Pa)\frac{x^2}{2} + B_1 x + B_2\right]$ $\theta(x) = \frac{1}{EI}\left[-R_B\frac{x^2}{2} - (M_A - Pa)x + B_1\right]$ where $B_1 = -\frac{Pa^2}{2}$, $B_2 = +\frac{Pa^3}{2}$
10		Simply supported	Clamped	$R_A = \frac{3p_0L}{8}$; $M_A = 0$ $R_B = \frac{5p_0L}{8}$; $M_B = -\frac{p_0L^2}{8}$	For $0 \le x \le L$ $W(x) = \frac{p_0 x}{48EI}\left[3Lx^2 - 2x^3 - L^3\right]$ $\theta(x) = \frac{p_0}{48EIL}\left[9Lx^2 - 8x^3 - L^3\right]$

where f_n is the natural frequency in Hz, and $\omega_n = 2\pi f_n$ (the circular frequency expressed in rad/s).

For cases where the spring is provided by the deflection of a beam, the resulting natural frequencies are presented in Table 3.3, while the mass of the beam is negligible compared to the mass m, and in Table 3.5, when this assumption is removed.

Table 3.3: Natural frequencies for a concentrated mass resting on a massless beam.

#	Case	Boundary conditions		Natural frequency f_n (Hz)
		Left A	Right B	
1		Free	Clamped	$\dfrac{1}{2\pi}\sqrt{\dfrac{3EI}{mL^3}}$
2		Clamped	Clamped	$\dfrac{1}{2\pi}\sqrt{\dfrac{192EI}{mL^3}}$
3		Simply supported	Simply supported	$\dfrac{1}{2\pi}\sqrt{\dfrac{48EI}{mL^3}}$
4		Clamped	Clamped	$\dfrac{1}{2\pi}\sqrt{\dfrac{3EIL^3}{ma^3b^3}}$
5		Simply supported	Simply supported	$\dfrac{1}{2\pi}\sqrt{\dfrac{3EIL}{ma^2b^2}}$

Note that in Table 3.3, E represents the Young's modulus of the beam, I is the cross-sectional area moment of inertia, L is the beam's length and m is the concentrated mass.

For the case of an isotropic continuous beam, the equation of motion to find its natural frequencies has the following form:

$$\frac{\partial^2}{\partial x^2}\left(EI\frac{\partial^2 w(x,t)}{\partial x^2}\right) + \rho A\frac{\partial^2 w(x,t)}{\partial t^2} = 0 \tag{3.5}$$

Assuming constant structural properties along the beam, and using the following expression

$$w(x,t) = W(x)e^{i\omega t} \tag{3.6}$$

equation (3.5) transforms in the following regular differential equation

$$EI\frac{d^4 W(x)}{dx^4} - \rho A\omega^2 W(x) = 0 \tag{3.7}$$

having the following solution:

$$W(x) = C_1\cos(\lambda x) + C_2\sin(\lambda x) + C_3\cosh(\lambda x) + C_4\sinh(\lambda x)$$

where

$$\lambda^4 = \frac{\rho A\omega^2}{EI} \Rightarrow \omega = \lambda^2\sqrt{\frac{EI}{\rho A}} \tag{3.8}$$

where (ρA) is the mass per unit length of the beam, A being the cross section of the beam and ρ its density, EI is the bending stiffness of the beam and C_1, C_2, C_3 and C_4 are constants to be determined by imposing boundary conditions at both ends of the beam. This leads to an eigenvalue problem, from which the natural frequencies of the beam are calculated together with their associated mode shapes. The values for the expression $(\lambda L)^2$, where L is the beam's length, for typical configurations of a beam are given in Table 3.4.

When a concentrated mass is added to a beam, its first natural frequency is lowered. Typical values are presented in Table 3.5.

The classical equation of motion for the transverse deflection, w, of thin plates [4] can be written as

$$D\nabla^4 w + \overline{m}\frac{\partial^2 w}{\partial t^2} = 0 \tag{3.9}$$
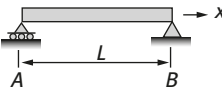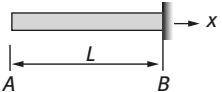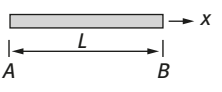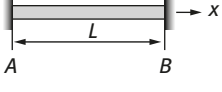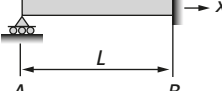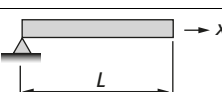
where the expression for D, the flexural rigidity of the plate, is given as

$$D = \frac{Eh^3}{12(1 - \nu^2)} \tag{3.10}$$

where $\overline{m}$ is the mass density per unit area of the plate, E is the Young's modulus, h the plate thickness, ν the Poisson's ratio, t the time and ∇^4 the Laplacian (∇^2) squared, defined in Cartesian coordinates as

$$\nabla^4 \equiv \left[\frac{\partial^2}{\partial x^2} + \frac{\partial^2}{\partial y^2}\right]^2 = \frac{\partial^4}{\partial x^4} + 2\frac{\partial^4}{\partial x^2\partial y^2} + \frac{\partial^4}{\partial y^4} \tag{3.11}$$

Table 3.4: Natural frequencies for typical beams.

#	Case	Boundary conditions		$(\lambda L)^2$		
		Left A	Right B	First mode	Second mode	Third mode
1		Simply supported	Simply supported	9.87	39.5	88.9
2		Free	Clamped	3.52	22.4	61.7
3		Free	Free	0	22.40	61.7
4		Clamped	Clamped	22.40	61.7	121.0
5		Simply supported	Clamped	15.40	50.0	104.0
6		Simply supported	Free	0	15.4	50.0

In polar coordinates (r, θ), the expression for ∇^4 is written as
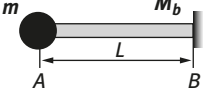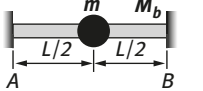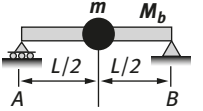
$$\nabla^4 \equiv \left[\frac{\partial^2}{\partial r^2} + \frac{1}{r}\frac{\partial}{\partial r} + \frac{1}{r^2}\frac{\partial^2}{\partial \theta^2} \right]^2 \tag{3.12}$$

while for skew coordinates (ξ, η) that are related to x, y Cartesian coordinates are (where α is the angle between y and η coordinates)

$$\xi = x - y \tan \alpha$$
$$\eta = \frac{y}{\cos \alpha} \tag{3.13}$$

the expression for ∇^4 is given as

Table 3.5: Natural frequencies for a concentrated mass resting on a beam with a mass of M_b.

#	Case	Boundary conditions		Natural frequency f_n (Hz)
		Left A	Right B	
1		Free	Clamped	$\dfrac{1}{2\pi}\sqrt{\dfrac{3EI}{(m+0.23M_b)L^3}}$
2		Clamped	Clamped	$\dfrac{1}{2\pi}\sqrt{\dfrac{196EI}{(m+0.35M_b)L^3}}$
3		Simply supported	Simply supported	$\dfrac{1}{2\pi}\sqrt{\dfrac{48EI}{(m+0.5M_b)L^3}}$

$$\nabla^4 \equiv \left[\frac{1}{\cos^2\alpha}\left(\frac{\partial^2}{\partial\xi^2} - 2\sin\alpha \frac{\partial^2}{\partial\xi\partial\eta} + \frac{\partial^2}{\partial\eta^2} \right) \right]^2 \tag{3.14}$$

For transforming the partial differential equation (3.9) into an ordinary differential equation as for free vibration of beams, presented above, the following expression is used:

$$w = We^{i\omega t} \tag{3.15}$$

which leads to

$$D\nabla^4 W - \overline{m}\omega^2 W = 0 \tag{3.16}$$

where ω is the circular frequency (in rad/s) and W is a function only of the position coordinates.

Typical values for the eigenvalues, λ, of various circular plates with different boundary conditions are presented in Table 3.6 (from [4]).

For rectangular plates, the natural frequencies can be obtained analytically only for a plate on simply supported boundary conditions for all four edges. This expression is given as

$$\omega_{m,n} = \sqrt{\frac{D}{\overline{m}}}\left[\left(\frac{m\pi}{a} \right)^2 + \left(\frac{n\pi}{b} \right)^2 \right] \tag{3.17}$$

Table 3.6: Values of $\lambda^2 = \omega R^2 \sqrt{m/D}$ for a circular plate with a radius R.

s n	0	1	2	3	4
All around clamped circular plate at $r = R$					
0	10.2168	21.26	34.88	51.04	69.6659
1	39.771	60.82	84.68	111.01	140.1079
2	89.104	120.08	163.81	190.30	229.5186
3	168.183	199.06	242.71	289.17	338.4113
All around simply supported circular plate at $r = R$, $\nu = 0.3$					
0	4.977	13.94	25.65	–	–
1	29.76	48.51	70.14	–	–
2	74.20	102.80	134.33	–	–
3	138.34	176.84	218.24	–	–
Completely free circular plate, $\nu = 0.33$					
0	–	–	5.253	12.23	21.6
1	9.084	20.52	35.25	52.91	73.1
2	38.55	59.86	83.9	111.3	142.8
3	87.80	119.0	154.0	192.1	232.3

where a and b are the length and width of the plate, respectively; and m and n are half-waves in the longitudinal and lateral directions, respectively. For other boundary conditions, various approximate methods have been used to determine the natural frequencies. Table 3.7 presents the results obtained using the Rayleigh method, where the assumed function is given in Table 3.7, and the natural frequency is calculated assuming the following expression (for $\nu = 0.25$, see [4]):

$$\omega = \frac{\pi^2}{a^2} \sqrt{\frac{D\alpha}{\overline{m}\beta}}$$

(3.18)

3.5 Torsion of bars

When a bar is held at one side and being rotated at the other side by a torque T (see Fig. 3.2), the bar will be under torsion, leading to shear stresses. The calculation of the stresses for bars having circular cross section assumes that the cross section rotates and remains planar, leading to the following expression:

$$\tau = \frac{Tr}{J} \Rightarrow \tau_{\max} = \frac{TR}{J}$$

(3.19)

Table 3.7: Frequency coefficients for eq. (3.18) and various mode shapes at $u = 0.25$.
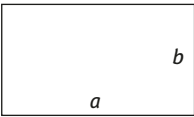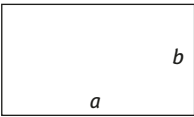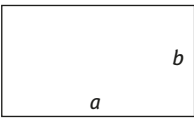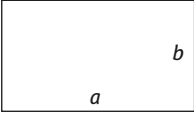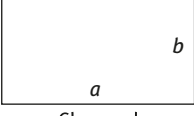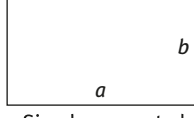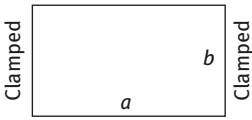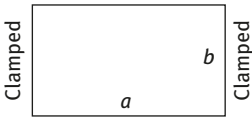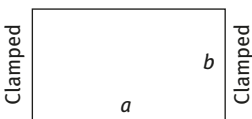
Boundary conditions	Deflection function or mode shape	α	β
Clamped; Clamped; Clamped; Clamped; a, b	$\left(\cos\dfrac{2\pi x}{a} - 1\right)$ $\left(\cos\dfrac{2\pi y}{b} - 1\right)$	$12 + 8\left(\dfrac{a}{b}\right)^2 + 12\left(\dfrac{a}{b}\right)^4$	2.25
Simply supported; Simply supported; Simply supported; Simply supported; a, b	$\sin\dfrac{\pi x}{a}\sin\dfrac{\pi y}{b}$	$\dfrac{1}{4} + \dfrac{1}{2}\left(\dfrac{a}{b}\right)^2 + \dfrac{1}{4}\left(\dfrac{a}{b}\right)^4$	0.25
Free; Simply supported; Simply supported; Free; a, b	$\sin\dfrac{\pi x}{a}$	$\dfrac{1}{2}$	0.50
Free; Clamped; Free; Free; a, b	$1 - \cos\dfrac{\pi x}{2a}$	0.0313	0.2268
Free; Clamped; Clamped; Free; a, b	$\left(1 - \cos\dfrac{\pi x}{2a}\right)$ $\left(1 - \cos\dfrac{\pi y}{2b}\right)$	$0.0071 + 0.024\left(\dfrac{a}{b}\right)^2$ $+ 0.071\left(\dfrac{a}{b}\right)^4$	0.0514
Simply supported; Clamped; Simply supported; Simply supported; a, b	$\left(\cos\dfrac{3\pi x}{2a} - \cos\dfrac{\pi x}{2a}\right)$ $\sin\dfrac{\pi y}{b}$	$1.28 + \dfrac{5}{4}\left(\dfrac{a}{b}\right)^2 + \dfrac{1}{2}\left(\dfrac{a}{b}\right)^4$	0.50

Table 3.7 (continued)

Boundary conditions	Deflection function or mode shape	α	β
Free / Clamped / Clamped / Free (sides a, b)	$\cos\dfrac{2\pi x}{a} - 1$	1.5	1.50
Simply supported / Clamped / Clamped / Simply supported (sides a, b)	$\left(\cos\dfrac{2\pi x}{a} - 1\right)\sin\dfrac{\pi y}{b}$	$4 + 2\left(\dfrac{a}{b}\right)^2 + \dfrac{3}{4}\left(\dfrac{a}{b}\right)^4$	0.75
Free / Clamped / Clamped / Simply supported (sides a, b)	$\left(\cos\dfrac{2\pi x}{a} - 1\right)\dfrac{y}{b}$	$2.67 + 0.304\left(\dfrac{a}{b}\right)^2$	0.50
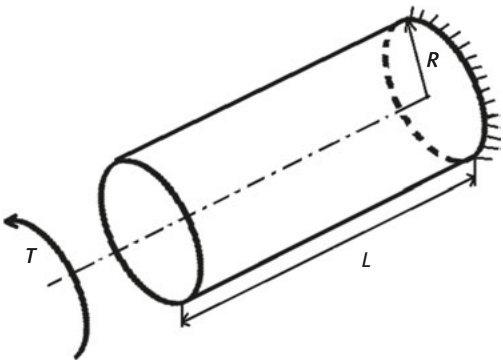
Fig. 3.2: A circular bar with a radius R and length L under a torque T.

where τ is the shear stress at an intermediate radius r, T is the applied torque and J being the polar moment of inertia expressed in m^4. The maximal shear stress $\tau_{\max}$ will appear at $r = R$. The angle of rotation, θ, is calculated according to the following equation:

$$\theta = \frac{TL}{GJ} \tag{3.20}$$

where G is the shear modulus and L is the length of the bar. Note that for isotropic materials G can be expressed using the Young's modulus E and the Poisson's ratio, υ, to yield

$$G = \frac{E}{2(1+\upsilon)} \tag{3.21}$$

For noncircular cross sections, the behavior of the bars is nonsymmetric when a torque is applied and the plane sections do not remain plane. Note that the distribution of stress in a noncircular cross section is not necessarily linear as for circular cross sections. Typical expressions for the polar moment of inertia and the associated maximal shear stresses are presented in Table 3.8. For additional cases, the reader is addressed to ref. [5].

Table 3.8: Polar moment of inertia and maximal shear stresses.
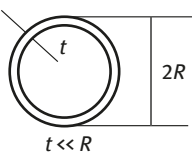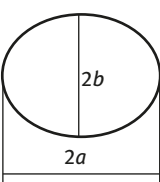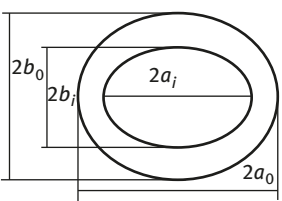
Type of cross section	Polar moment of inertia, J	Maximal shear stress, τ_{max}
circle, $2R$	$\dfrac{\pi R^4}{2}$	$\dfrac{2T}{\pi R^3}$
hollow circle, $2b$ $2a$	$\dfrac{\pi a^4}{2} - \dfrac{\pi b^4}{2}$	$\dfrac{2Ta}{\pi(a^4 - b^4)}$
thin tube, t, $2R$, $t \ll R$	$2\pi R^3 t$	$\dfrac{T}{2\pi R^2 t}$
ellipse, $2b$, $2a$	$\dfrac{\pi a^3 b^3}{(a^2 + b^2)}$	$\dfrac{2T}{\pi a b^2}$ @ ends of minor axis
hollow ellipse, $2b_0$ $2b_i$ $2a_i$ $2a_0$	$\dfrac{\pi a^3 b^3}{(a^2 + b^2)}\left(1 - \kappa^4\right)$ $\kappa \equiv \dfrac{a_i}{a_o} = \dfrac{b_i}{b_o}$	$\dfrac{2T}{\pi a b^2 (1 - \kappa^4)}$

Table 3.8 (continued)
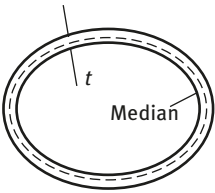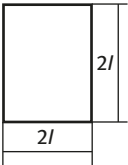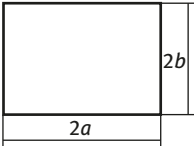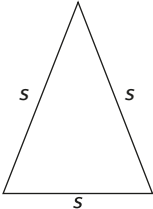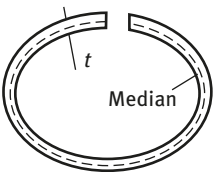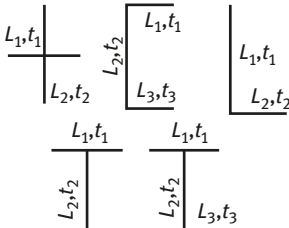
Type of cross section	Polar moment of inertia, J	Maximal shear stress, τ_{max}
	$\dfrac{4A^2t}{L'}$, A = area enclosed by the median, L' = length of median	$\dfrac{T}{2tA}$
	$\dfrac{9l^4}{4}$	$\dfrac{0.601T}{l^3}$ @ mid of each edge.
	$ab^3\left[\dfrac{16}{3} - 3.36\dfrac{b}{a}\left(1 - \dfrac{1}{12}\left(\dfrac{b}{a}\right)^4\right)\right]$	$\dfrac{3T}{8ab^2}\left\{1 + 0.6095\left(\dfrac{b}{a}\right) + 0.8865\left(\dfrac{b}{a}\right)^2\right.$ $\left. - 1.8023\left(\dfrac{b}{a}\right)^3 + 0.9100\left(\dfrac{b}{a}\right)^4\right\}$ @ mid of each edge a
	$\dfrac{\sqrt{3}s^4}{80}$	$\dfrac{20T}{s^3}$ @ mid of each edge s
	$\dfrac{L't^2}{3}$, $'L$ = length of median	$\dfrac{T(3L' + 1.8t)}{t^2(L')^2}$ @ mid of each edge s

Table 3.8 (continued)

Type of cross section	Polar moment of inertia, J	Maximal shear stress, τ_{max}
Thin-walled profiles $L_i \gg t_i$	$\frac{1}{3}\sum_{i=1}^{n}(L_i)^3 t_i$	$\frac{T L_{max}}{\frac{1}{3}\sum_{i=1}^{n}(L_i)^3 t_i}$ @ mid-way along t_{max} element

L_1, t_1 L_2, t_2 L_1, t_1 L_1, t_1

L_2, t_2 L_3, t_3 L_2, t_2

L_1, t_1 L_1, t_1

L_2, t_2 L_2, t_2 L_3, t_3

L_i = length of element
t_i = thickness of element

References

[1]   Timoshenko, S.P., and Goodier, J.N. Theory of Elasticity, 3rd Ed., International Student Edition, McGraw-Hill Book Company, Kōgakusha Company, Ltd., Tokyo, Japan, © 1970, McGraw-Hill Inc., 567.

[2]   Popov, E.P. Introduction to Mechanics of Solids, Prentice-Hall, Inc., Englewood Cliffs, N.J., 1968, 571.

[3]   Thompson, W.T. Vibration Theory and Applications, George Allen & Unwin Ltd., Ruskin House, 40 Museum Street, W. C. 1, London, UK, 1965, 384.

[4]   Leissa, A.W. Vibration of Plates, NASA SP-160, 1969, 350.

[5]   Young, W.C., and Budynas, R. G. Roark's Formulas for Stress and Strain, 7th Edition, Mc-Graw Hill, New York, NY 10121-2298, USA., 2002, 852.

4 Introduction to fatigue

4.1 Introduction

This chapter presents the behavior of structures under fatigue. The structures can be made of metals or laminated composite materials. The issue of crack propagation, normally associated with the fatigue phenomenon will be presented in Chapter 5.

4.2 Definition of fatigue

Fatigue (coming from the French word fatigué = tired) of metal structures had been identified already in 1840 in the English railway industry, mainly on train axle failures, as people thought that the materials became "tired" and weak due to cyclic repeated loading [1]. The name *fatigue* was then introduced to describe those structural failures due to repeated stresses and continued to be used until today to describe failures, mainly caused by fracture of the structure due to cycling loadings (see Fig. 4.1 for typical fatigue failures).

Most of the structural parts of movable machines are susceptible to fatigue; therefore, it is very important to assure that those parts will not fail due to repetitive stresses, which might be expected to reach at least a few million load cycles. The aerospace sector, the automotive and train sector, the wind-power turbines sector and the maritime sector are the main domains of engineering that are heavily influenced by the fatigue. Fatigue of various aerospace, mechanical and civil structures had been investigated in depth during the past years, with numerous books trying to address the issue (see typical books in [1–19]). Apart from books, the literature is full of dedicated manuscripts covering all the aspects of fatigue and the ways to prevent failures due to it [20–34].

4.2.1 Basic fatigue concepts

The various factors causing fatigue failure of a given structural member can be listed as
  – High value of tensile stresses
  – A large number of variations and changes of the applied stresses
  – A sufficient large number of the applied stress cycles
  – The metallurgical structure or material characteristics
  – Stress concentration
  – Corrosion
  – Residual stress

(a)   (b)
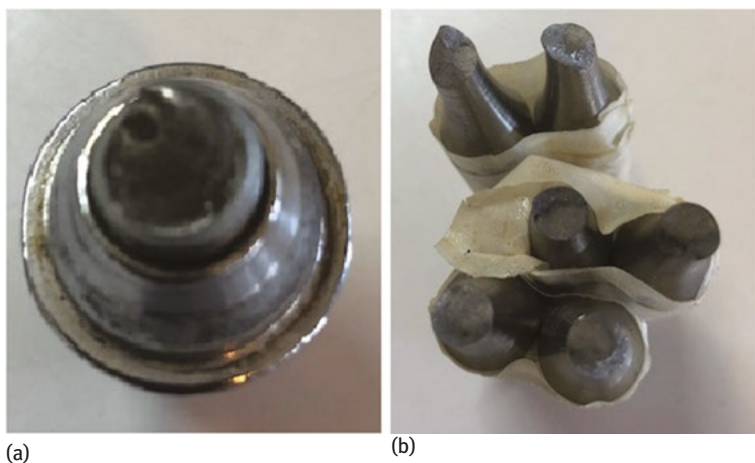
Fig. 4.1: Cross section after fatigue failure: (a) wheel car bolt and (b) test specimens.

- Combined stresses
- Temperature
- Overloading the structure

One should note that under the point "The metallurgical structure and material characteristics" the following attributes could be found[1]:

a. Due to the way the part was fabricated:
  - Method of fabrication
    - Shaping method: ground, turned, broached, milled, EDM,[2] chemical milling
    - Bending, spinning, stretching
    - Welding
    - Heat treatment
  - Finishing process
    - Surface finish: polished, as-cast surface, as-machined surface (with maximal surface roughness)
    - Special treatments like cold working, case hardening, plating, anodized within specified thickness

---

1 Note that the material attributes are normally controlled by the material specifications such as *SAE/AMS* (*S*ociety of *A*utomotive *E*ngineering/*A*erospace *M*aterial *S*pecification) number, part drawing, the manufacturing company standards and by the way the part is fabricated.
2 *EDM* , *e*lectrical *d*ischarge *m*achining.

b. Due to the SAE/AMS number, part drawing and company standards:
   – The material itself
     – The chemical composition
     – The cleanliness of the process (like commercial quality), the melting method (in air vs. in vacuum) and so on
   – Forming the material and its processing
     – Casting, un-HIP[3]'d or HIP'd (location in the casting form)
     – Forging, bar, extrusion, plate sheet (its texture and cold working process)
     – Type of the metal powder
     – Microstructure (the size of the grain)
     – The overall size of the part
     – Heat treatment
     – Hardness

The fluctuating stresses acting on the structure can be either sinusoidal above the time axis, as presented in Fig. 4.2, meaning the stresses are only tensile, or completely reversed cycle of stress, in which the sinusoidal curve passes the time axis, leading to alternating tensile and compressive stresses. The alternating stresses can also appear in irregular or random form. One should note that tensile stresses are positive, with negative values being attributed to the compression ones.
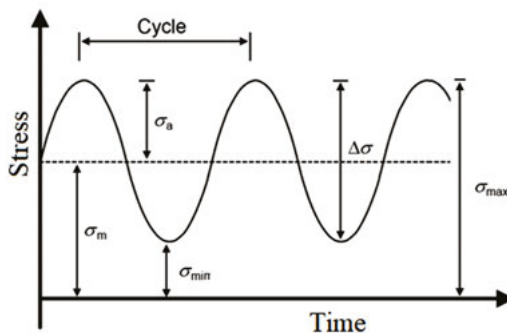
Fig. 4.2: Schematic definition of various expressions for cyclic stress.

The definition of the various expressions is displayed in Fig. 4.2 and the additional ones are depicted in Table 4.1.

One should note that a structure undergoing cyclic or fluctuating stresses might fail at loads lower than the static ones. It was noted that almost 90% of all the failure

---

3 *HIP* , *h*ot *i*sostatic *p*ressing.

Table 4.1: Definition of various expressions connected with cyclic stresses.

No.	Name	Equation/notation
1	Maximum stress	σ_{max}
2	Minimum stress	σ_{min}
3	Stress range	$\Delta\sigma \equiv \sigma_r = \sigma_{max} - \sigma_{min}$
4	Fluctuating stress	$\sigma_a \equiv \dfrac{\Delta\sigma}{2} = \dfrac{\sigma_{max} - \sigma_{min}}{2}$
5	Average stress	$\sigma_m \equiv \dfrac{\sigma_{max} + \sigma_{min}}{2}$
6	Stress ratio	$R \equiv \dfrac{\sigma_{min}}{\sigma_{max}}$
7	Amplitude ratio	$A \equiv \dfrac{\sigma_a}{\sigma_m} = \dfrac{1-R}{1+R}$

of metallic components, like aircraft, bridges and machine parts, are attributed to fatigue. The fatigue failure is sudden and catastrophic, and has the nature of brittle-type failure, even in normally ductile-type materials.

The behavior of the two types of materials, brittle versus ductile ones, is presented in Fig. 4.3, where the relevant curves of the stress versus the strain are plotted. It is evident that a brittle material presents no yield point and its failure is a sudden breakage into pieces due to the application of tensile stresses. A ductile material exhibits a well- defined yield point with failure in the plastic strain regime.
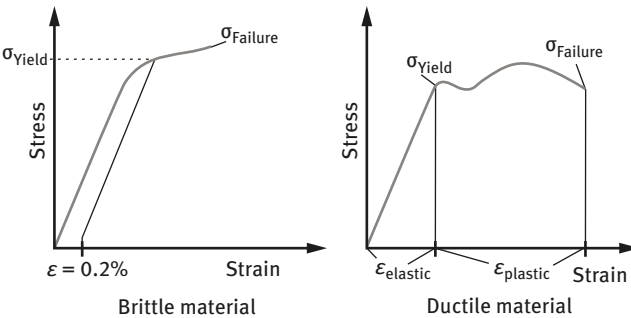
Fig. 4.3: Brittle versus ductile materials.

4.2.2 The four steps of fatigue failure

One of the basic questions related to fatigue is "why the structural component would fatigue fail if the working stress is below the yield stress?". The answer to this query is microscopic plasticity behavior at fatigue failure, occurring below the

yield stress, and another important factor connected to damage accumulation on the time axis is the many load cycles being applied on the structural component. Roughly, four steps can be identified up to the failure:

1. Crack initiation on external and internal surfaces of the specimen due to slip process. This will take part within the first 10% of the total component life.
2. First stage of the crack growth along planes under high shear stresses, a continuation of the slip process encountered in the first step. This causes the deepening of the crack.
3. Second stage of the crack growth, which is characterized by a crack growth along high tensile stresses. This is called transgranular crack propagation.
4. Ductile failure of the component due to the crack propagation, which leads to the reduction in the load-bearing area.

4.3 The *S–N* curve

The well-known curve, the *S–N* curve, known also as Wöhller[4] curve, is the basic representation of engineering fatigue data, in which the stress, *S*, versus the number of cycles, *N*, is drawn (see Fig. 4.4). The *y*-axis, the stress, can be one of the following values (see Table 4.1):, σ_{max} or σ_{min}, while mentioning the σ_m, *R* or *A*.
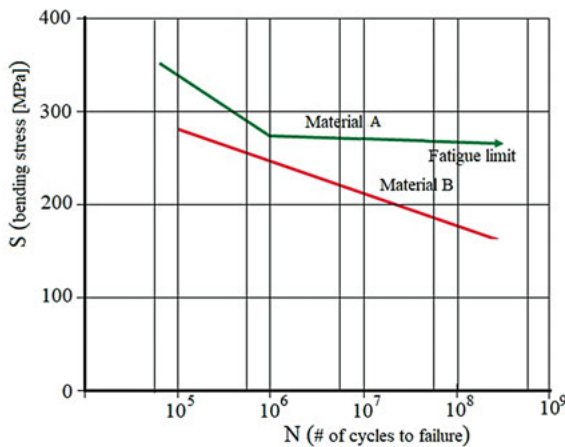
Fig. 4.4: A schematic *S–N* curve.

---

[4] August Wöhller (1819–1914) was a German railway engineer who investigated in-depth metal fatigue failures of railway axles.

On the graph presented in Fig. 4.4, material "A" displays a threshold value called *"fatigue limit"* or *"endurance limit"* in the range of 10^7 or 10^8 cycles. Below this limit, the material presumably can endure an infinite number of cycles before failure. Materials like mild steel (St) and titanium (Ti) show this property. The second graph, in Fig. 4.4, material "B," shows no fatigue limit, a property attributed to nonferrous materials like aluminum (Al), magnesium (Mg) and copper (Cu), for which the fatigue strength is defined at 10^8 cycles. Another interesting property appearing in the *S–N* curve is the regime named *fatigue failure at high numbers of cycles* or *high cycle fatigue (HCF)* defined as $N > 10^5$ cycles, while the region $N < 10^5$ cycles is called *low cycle fatigue (LCF)*. Note that the value of N would increase with the decrease in the stress level. In addition, the HCF is characterized by low strains, while LCF would display high strains. The *S–N* curve for the HCF region is sometimes analytically described by the Basquin equation [35], having the following form:

$$\sigma_{max} = \alpha N_f^\beta \tag{4.1}$$

where α and β are model fitting constants, σ_{max} is the stress amplitude at $N < 10^6$ and N_f is the number of cycles at failure. To determine the constants, the following procedure is performed: taking the log of eq. (4.1) yields

$$\log(\sigma_{max}) = \log(\alpha) + \beta(N_f) \tag{4.2}$$

Assuming that σ_{max} at low number of cycles, let say $N = 1,000$, is 90% of the ultimate strength of the tested material, σ_{ul}, and that for $N = 10^6$ $\sigma_{max} = \sigma_\infty$(where σ_∞ stands for stress at fatigue limit), thus yielding indefinite fatigue life, which leads to the following equations:

$$\log(0.9\sigma_{ul}) = \log(\alpha) + \beta(1,000) = \log(\alpha) + 3\beta$$
$$\log(\sigma_\infty) = \log(\alpha) + \beta(1,000,000) = \log(\alpha) + 6\beta \tag{4.3}$$

from which, the two constants, α and β, can be determined to yield

$$\alpha = \frac{\sigma_{F.L.}}{10^{6\beta}}; \quad \beta = \frac{\log(\sigma_\infty) - \log(0.9S_{ul})}{3}. \tag{4.4}$$

To determine the N_f, for a given stressσ_{max}, once the constants α and β were calculated (see eq. (4.4)), eq. (4.1) is changed to yield

$$N_f = \left[\frac{\sigma_{max}}{\alpha}\right]^{\frac{1}{\beta}} \tag{4.5}$$

Another well-known description of the *S–N* curve carries the name of Weibull distribution [36], which suggested the following expression:

$$\frac{\sigma_{max} - \sigma_\infty}{\sigma_{ul} - \sigma_\infty} = 1 - \varphi[\alpha \log N_f + \beta] \tag{4.6}$$

where $\sigma_{\max}$ is the maximal applied stress, σ_{ul} is the ultimate tensile strength stress, σ_{∞} stands for the fatigue limit stress, α, β are model fitting parameters, N_{f} the number of cycles at failure and φ is a Gaussian error function. Based on eq. (4.6), Weibull proposed an *S–N* curve model having the following expression:

$$\sigma_{\max} = (\sigma_{\mathrm{ul}} - \sigma_{\infty})e^{\left[-\alpha\left(\log N_{\mathrm{f}}\right)^{\beta}\right]} + \sigma_{\infty} \tag{4.7}$$

which includes both the ultimate strength stress (σ_{ul}) and the fatigue limit stress (σ_{∞}). The two fitting parameters (α and β) in eq. (4.7) can be determined by taking log on both sides of the equation, namely

$$\frac{\sigma_{\max} - \sigma_{\infty}}{\sigma_{\mathrm{ul}} - \sigma_{\infty}} = e^{\left[-\alpha\left(\log N_{\mathrm{f}}\right)^{\beta}\right]} \tag{4.8}$$

One should note that based on the characterization of the materials using the *S–N* curves, some designed philosophies were used. The old design standard, also known as infinite life design, was based on the empirical information of the fatigue life presented by the *S–N* curves, adding to it a large safety factor, and requesting the retiring of parts and components at the preset life limit value of $N_{\mathrm{failure}} = 10^{7}$. Today, the American air force (but not the navy) adopted a standard based on the damage-tolerant design, which accepts the presence of cracks in the various components of a structure. The determination of the structural life is based on the prediction of the crack growth rate (see Chapter 5).

The experimental construction of the *S–N* is usually done using 8–12 test specimens. Normally, the tests would start at a stress $\sigma = 2/3\sigma_{\mathrm{static\ tensile\ strength}}$ of the tested material and the stress is lowered until the specimens do not fail at about 10^{7} cycles. As expected, a considerable scatter in the experimental data can be expected, with adoption of statistical approach to define the fatigue limit. Usually a logarithmic normal distribution of the fatigue life is assumed for the region with failure probability of $0.10 < P < 0.90$ (P = probability).

Note also that the increase in the mean stress applied to a component would decrease its fatigue strength.

One should be aware of the great influence of the stress ratio, R, as depicted in Fig. 4.5, on the fatigue life of the tested specimens. The largest fatigue life would be obtained at $R = -1$, while the minimal one at $R = +1$, with a large drop in the interval $-1 < R < +1$.

4.3.1 The probability distributions for fatigue life

The log-normal distribution [37] is one of the most useful probability distributions to model failure times of materials and structures undergoing fatigue. Its probability density function (PDF) has the following form:
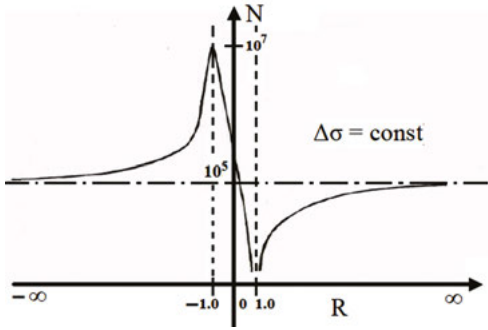
Fig. 4.5: The schematic of the influence of stress ratio, R, on the fatigue life of samples.

$$f(x) = \frac{1}{\sqrt{2\pi} \cdot \sigma} e^{\left[-\frac{1}{2}\frac{(x-\mu)^2}{\sigma^2} \right]}, \quad -\infty < x < +\infty; \tag{4.9}$$

where $\quad x = \log N_f$

Note that if the fatigue life N_f has a log normal, the logarithm of N_f, namely, x, has a normal distribution. This conclusion is very important as one can use the theoretical results and the equation of normal distribution, while applying the log-normal distribution. The cumulative distribution function (CDF) of the log-normal distribution has the following form:

$$F(x) = \int_{-\infty}^{x} f(t)dt \tag{4.10}$$

where the variable t is the integration one, and $f(t) = f(x)$ is given by eq. (4.9). Note that the integral in eq. (4.10) has no closed-form solution and a numerical algorithm is needed to evaluate it. Next, the evaluation of the two variables has to be estimated using the following relationships:

$$\mu = \frac{1}{n}\sum_{i=1}^{n} x_i; \quad \sigma = \sqrt{\frac{\sum (x_i - \mu)^2}{n-1}}. \tag{4.11}$$

for a fatigue data obtained with n samples with $x_i = \log(N_i)$, $i = 1,\ldots,n$.

Another very popular model, successfully applied for fatigue issues, is the Weibull distribution [37], having the following PDF form:

$$f(x) = \frac{\beta}{\Omega} \left(\frac{x-x_0}{\Omega}\right)^{\beta-1} e^{-\left(\frac{x-x_0}{\Omega}\right)^{\beta}} \tag{4.12}$$

where β is the shape parameter changing the shape of the PDF curve and it can have the following values:

a. If $\beta < 1$, PDF shape is similar to an exponential distribution.
b. If $1 < \beta < 3$, the PDF shape is positively skewed.
c. If $\beta > 3$, the PDF is symmetrical.

The symbol Ω in eq. (4.12) is the scale parameter or the dispersion of the distribution, affecting both the mean and standard deviation. The third parameter, x_0, the location parameter for the Weibull distribution, is defined as $x_0 = \log N_0$, where N_0 is a lower fatigue life, namely no fatigue failure will happen under this value. If $x_0 = 0$, the three-parameter Weibull distribution will be reduced to two-parameter Weibull distribution, with the previous one providing the best fitting capacity. The CDF of Weibull distribution has an explicit expression with the following form:

$$F(x) = 1 - e\left(-\left(\frac{x - x_0}{\Omega}\right)^{\beta}\right), \quad x \geq x_0 \tag{4.13}$$

To estimate the three parameters in the Weibull distribution, the most used method is to fit the experimental points in a linear regression line in the form $y = a + bx$, using the least square method. Using eq. (4.13) one obtains

$$\log\left[\log\left(\frac{1}{1 - F(x)}\right)\right] = -\beta \log(\Omega) + \beta \log(x_i - x_0) \tag{4.14}$$

Applying the least-square fit yields

$$\begin{aligned}
y_i &= \log\left[\log\left(\frac{1}{1 - F(x_i)}\right)\right] \\
x_i &= \log(N_i) \\
a &= \beta \\
b &= -\beta \log(\Omega)
\end{aligned} \tag{4.15}$$

For a Weibull distribution, an approximated straight line could be drawn, with the parameter β being the slope of the graph, and the parameter Ω is estimated for a point of the straight line corresponding to 63.2% failure, namely $F(x_i) = 0.632$. The third parameter, x_0, is estimated using an iteration procedure (no closed form is available).

4.3.2 Fatigue life for various combinations of alternating and mean stresses

When plotting the alternating stress σ_a versus the mean stress σ_m, as shown in Fig. 4.6, various lines can be achieved and compared with test results. Those lines have the following expressions (note that σ_e is the fatigue limit stress for a completely reversible loading ($R = -1$):
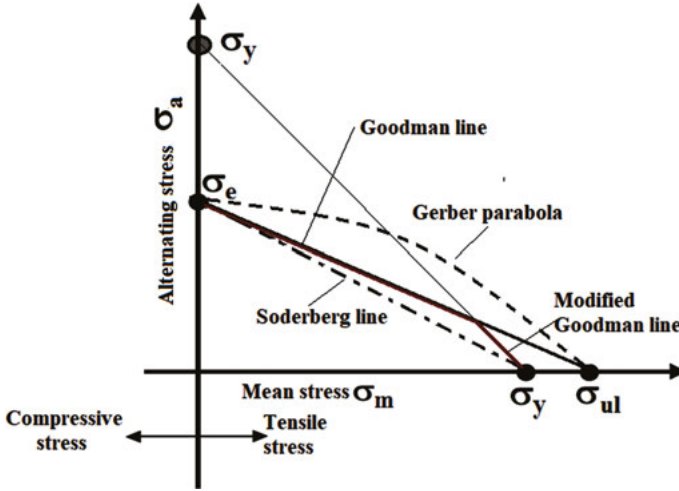
Fig. 4.6: Constant life diagrams: combinations of σ_a and σ_m leading to the same fatigue life.

a. Goodman line – a linear approximation

$$\left(\frac{\sigma_m}{\sigma_{ul}}\right) + \left(\frac{\sigma_a}{\sigma_e}\right) = 1 \tag{4.16}$$

b. Soderberg line – a linear approximation as in eq. (4.16) with the σ_{ul} being replaced by σ_y, the yield strength of the material to give

$$\left(\frac{\sigma_m}{\sigma_y}\right) + \left(\frac{\sigma_a}{\sigma_e}\right) = 1 \tag{4.17}$$

c. Gerber's parabola line – a nonlinear approximation with the following form:

$$\left(\frac{\sigma_m}{\sigma_{ul}}\right)^2 + \left(\frac{\sigma_a}{\sigma_e}\right) = 1 \tag{4.18}$$

d. Modified Goodman line – starts at the yield strength σ_y for the mean stress σ_m continues along the yield line [$(\sigma_m = \sigma_y,0),(0, \sigma_a = \sigma_y)$] (see Fig. 4.6) till it intercepts the Goodman line. From that point, it continues along the Goodman line.

One should note that any combination of mean and alternating stresses under the corresponding lines (depending on which theory is chosen) would lead to the required number of cycles, and all those points above the lines would expect to fail earlier.

Appendix A provides an example for the use of Fig. 4.6 and its associated eqs. (4.16), (4.17) and (4.18).

4.4 Miner rule – the cumulative damage

In real life, a component or a structure might experience loads at variable amplitudes. Designing of fatigue for those structures is performed by the famous approach called Miner's rule or Miner's linear damage rule [38]. According to it, the fatigue damage D is found using the following equation:

$$D = \frac{n_1}{N_1} + \frac{n_2}{N_2} + \frac{n_3}{N_3} + \cdots + \frac{n_i}{N_i} = \sum_{i=1}^{k} \frac{n_i}{N_i} \leq 1.0 \qquad (4.19)$$

where $n_1, n_2, n_3, \ldots, n_i$ are the number of cycles at stresses $S_1, S_2, S_3, \ldots, S_i$ expected during the life of the component, while $N_1, N_2, N_3, \ldots, N_i$ are the number of cycles at failure under constant load amplitude (see Fig. 4.7 for a typical example). For values less and/or equal to unity, no failure is expected. Values above unity will mean failure due to fatigue. Note that the failure cycle N_i should be obtained from a relevant component design S–N curve.
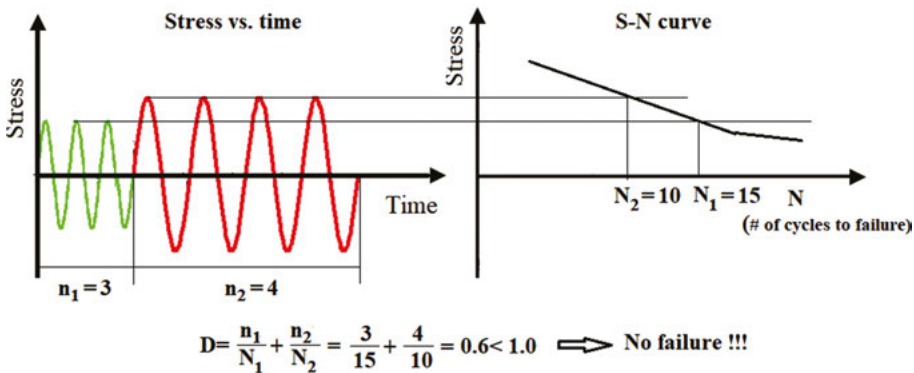
Fig. 4.7: Schematic application of the Miner's rule.

One should be aware that the Miner's rule does not account for the sequence of the stress ranges, but only for the number of stress ranges. To take this issue into account the design of the component should be more conservative, thus reducing the limiting damage to a value less than unity.

4.5 Fatigue of composite materials

Although laminated composite materials experience high static strength and stiffness together with a low specific mass (in the order of 15–1.6 g/cm^3), showing an almost fully elastic behavior up to failure, as described by Schijve [11], it seems that

fatigue problems might appear also for this type of material. This is reflected in the numerous articles dealing with fatigue of composite materials. References [27–33] are only typical for those papers dealing with the behavior of fiberglass-type materials under fatigue, while [39–45] address the way the graphite/epoxy-type materials (used mainly in the aerospace sector) behave under fatigue loads.

In considering fatigue damage and failure, it is generally agreed that fatigue damage consists of various combinations of matrix cracking, fiber–matrix debonding, delamination, void growth and local fiber breakage. Moreover, mechanism, type and distribution of damage would depend upon the material system (combination of fiber and matrix material), stacking sequence of plies, fabrication techniques, geometry, stress state and loading history. Finally, it can be stated that those mechanisms are sensitive to one or more parameters, including type of loading, frequency of cyclic loading, temperature and moisture.

Already in 1979, Rosenfeld and Huang [39] investigated the fatigue behavior of graphite/epoxy laminates under compression for $R = 0, -\infty, -1$. They reported a significant life reduction for the load cases $R = -1$ and $R = -\infty$. The mechanism causing failure is reported to be the failure of the matrix near a stress riser, leading to fiber split that caused a progressive delamination yielding the buckling of the fibers followed by the laminate failure. Rotem [40] reports the behavior of orthotropic laminates under applying tension–compression loading. He investigated two types of laminates: $L_1 = [0^0, \pm 45^0, 0^0]_{2s}$ and $L_2 = [90^0, \pm 45^0, 90^0]_{2s}$. Both laminates started their failure due to delamination, with the L_1 laminate failing in compression due to delamination between 0° and 45° laminae, while L_2 failed under tension caused by the delamination between +450 and −450 laminae. Typical results for both laminates are shown in Fig.4.8.
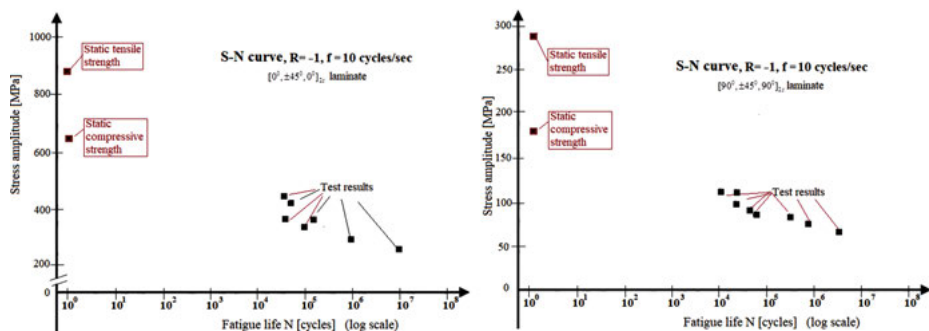
Fig. 4.8: Typical test results (adapted from [40]).

Another team of researchers, Caprino and D'Amore [41], also investigated the fatigue life of graphite/epoxy laminates subjected to tension–compression loading, using the two-parameter model they developed earlier for random glass fiber

reinforced plastics loaded in tension. This model assumes that a continuous decrease in the material strength will be experienced with the increasing number of cycles N, according to the following equation [41]:

$$\frac{d\sigma_{tN}}{dN} = -a_t \cdot N^{-b_t} \tag{4.20}$$

where σ_{tN} is the residual tensile materials strength after N cycles; a_t and b_t are two positive constants to be determined from tests. It was further assumed that the constant a_t can be written as

$$a_t = a_{0t} \cdot (\sigma_{max} - \sigma_{min}) \tag{4.21}$$

with a_{0t} being a constant. Integrating eq. (4.20) using the boundary condition $N = 1 \rightarrow \sigma_{tN} = \sigma_{t0}$, where σ_{t0} is the monotonic tensile strength of the virgin material one obtains

$$\sigma_{tN} = \sigma_{t0} - \alpha_t \cdot \sigma_{max} \cdot (1 - R) \cdot \left(N^{\beta_t} - 1\right)$$

where

$$\alpha_t = \frac{\alpha_{0t}}{1 - b_t}, \quad \beta_t = 1 - b_t \tag{4.22}$$

Finally, the critical number of cycles to failure, N_t, is calculated using the following expression:

$$N_t = \left[1 + \frac{\sigma_{t0} - \sigma_{max}}{\alpha_t \cdot (\sigma_{max} - \sigma_{min})}\right]^{\frac{1}{\beta_t}} \tag{4.23}$$

To enable the use of the above-developed expressions also for the compression case, eqs. (4.20) and (4.23) were modified by Caprino and D'Amore [41] to yield

$$\frac{d\sigma_{cN}}{dN} = +a_c \cdot N^{-b_c} \tag{4.24}$$

$$N_c = \left[1 + \frac{\sigma_{min} - \sigma_{c0}}{\alpha_c \cdot (\sigma_{max} - \sigma_{min})}\right]^{\frac{1}{\beta_c}} \tag{4.25}$$

The main conclusions from the research presented in [41] claim that the two-constant model is capable of describing accurately the classical S–N curve for composites. The experimental calculation of the two constants seems to be sensitive to the loads applied and yields different values for tension–tension and tension–compression cases. Also, a reasonable agreement was found between the prediction and the experimental results.

Minak et al. [42] present another interesting research addressing the fatigue residual strength of graphite/epoxy circular plates damaged by low velocity impact

and undamaged specimens. Good experimental data are presented and discussed. Williams et al. [43] investigated Hercules As/3501-6 graphite fiber epoxy composite using an eight-ply $[0^0, \pm 45^0, 0^0]_2$ laminate. The specimens were subjected to a sinusoidal flexural fatigue in a cantilever mode, with the load varying between +73.5 and −73.5 N at 30 Hz at room temperature. The structural state of the specimens was measured using ultrasonic 4.0 MHz attenuation method. The method could measure the void volume fraction. They report that beyond 10,000 cycles, the flexural stiffness of the tested specimens decreased with the number of fatigue cycles and the ultrasonic through transmission attenuation increased with the number of fatigue cycles. Minak [44] presents an interesting research on the determination of fatigue life of specimens manufactured from graphite-epoxy, by measuring the temperature variation of the tested specimens throughout the alternating loads. Two types of laminates were tested: type A $[0^0, \pm 45^0, 90^0, \pm 45^0, 0^0]$ and type B $[90^0, \pm 45^0, 0^0, \pm 45^0, 90^0]_2$. The load ratio applied was $R = 0.1$, with three levels of frequencies 5, 10 and 15 Hz being used throughout the tests. Measuring the temperature of the external ply and in parallel the variation of the specimen's variation enabled the author to conclude, "dissipated energy-life relation could be used as an alternative method for CFRP components life prediction" [44].

Finally, Jamison and Reifsnider [45] performed a very comprehensive research to establish the character and sequence of development of advanced damage resulting from tension–tension cyclic loading of graphite/epoxy laminates. They defined the advanced damage development as the damage produced by the part of the loading history, which is applied subsequent to the development of the characteristic damage state for matrix cracking.

Three laminate types, $[0^0, 90^0_2]_s$, $[0^0, \pm 45^0]_s$ and $[0^0, 90^0, \pm 45^0]_s$, manufactured from T300/5208 graphite/epoxy material, representing a broad range of intralaminar and interlaminar stress conditions were subjected to tensile fatigue loading. Post-fatigue analysis was performed by both nondestructive and destructive (microscopic) means. During the tests, the dynamic secant modulus was continuously computed with any changes in this quantity serving as an indication of damage in the specimen. The work presents a large data of experimental results for graphite/epoxy specimens.

The authors discovered local delamination regions near interior matrix cracks and they claim that internal stress redistributions are much larger than previously suspected and can be large enough to cause strength reductions of as much as 30–50%, levels that are commonly observed in long-term cyclic loading. It appears that fiber failure is much less consequential in these large strength reductions than has been suggested in the literature, and that the acceleration of damage quite near the end of life for laminates of this type is caused by a localization of damage, primarily secondary matrix cracking and local delamination. No evidence of accelerating fiber fracture in that region was found. It seems that the most important strength

reduction mechanism for the tested laminated composite material is the redistribution of the internal stresses.

Another important conclusion states, "matrix cracks in off-axis plies of angle-ply laminates seem to be important for long-term fatigue behavior primarily in the sense that they act as initiation points of fiber failure and local delamination". This means that while matrix cracks alone do not reduce the residual strength during cyclic loading, the events associated with and nucleated by their presence are the main drive to the development of subsequent damage that does reduce the strength, stiffness and life of composite laminates.

Moreover, the longitudinal engineering modulus of composite laminates seems to change during long-term cyclic loading, in large, systematic and reproducible ways, which are directly and quantitatively related to the details of the micro-events that influence the residual properties of such laminates. This change can be measured using nondestructive techniques to characterize the internal damage for a specific specimen. Using the measured internal damage one can apply adequate models to predict actual longitudinal engineering stiffness, normally yielding an excellent agreement (within a few percent) with experimentally measured values.

References

[1]   Stephens, R.I., Fatemi, A., Stephens, R.R., and Fuchs, H.O. Metal Fatigue in Engineering, John Wiley and Sons, 2000, 496.

[2]   Rolfe, S.T., and Barsom, J.M. Fracture and Fatigue Control in Structures: Applications of Fracture Mechanics, ASTM International, 1977, Technology & Engineering, 562.

[3]   Almar-Naess, A. Fatigue Handbook: Offshore Steel Structures, Tapir, 1985, 520.

[4]   Mann, J.Y. Bibliography on the Fatigue of Materials, Components and Structures, Science Direct, Elsevier Ltd., 1990, 509.

[5]   Radaj, D. Design and Analysis of Fatigue Resistant Welded Structures, Woodhead Publishing Series in Welding and Other Joints Technologies, 1990, 378.

[6]   Reifsnider, K.L. editor, Fatigue of composite materials, Vol. 4, Composite Materials Series, 1st, Elsevier Science, 1991, 518.

[7]   Maddox, S.J. Fatigue Strength of Welded Structures, 2nd, Woodhead Publishing, 1991, 208.

[8]   Gurney, T.R. Fatigue of Thin Walled Joints under Complex loading, 1st, Abington Publishing, 1997, 222.

[9]   Etube, L. Fatigue and Fracture Mechanics of Offshore Structures, Wiley, 2000, 164.

[10]   Lassen, T., and Recho, N. Fatigue Life Analyses of Welded Structures: Flaws, Wiley ISTE, 2006, 407.

[11]   Schijve, J. Fatigue of Structures and Materials, Springer, 2009, 623.

[12]   Maranian, P. Reducing Brittle and Fatigue Failures in Steel Structures, American Society of Civil Engineers, 2010, 196.

[13]   Nussbaumer, A., Borges, L., and Davaine, L. Fatigue Design of Steel and Composite Structures: Eurocode 3: Design of Steel Structures, Part 1-9 Fatigue; Design of Composite Steel and Concrete Structures, Wiley, 2011, 334.

[14]   Campbell, F.C. Fatigue and Fracture: Understanding the Basics, ASM International, 2012, 685.

[15]   Radaj, D., and Vormwald, M. Advanced Methods of Fatigue Assessment, Springer, 2013, 481.

[16] Dowling, N.E. Mechanical Behavior of Materials: Engineering Methods for Deformation, Fracture, and Fatigue, Pearson Education Ltd., 2013, 954.

[17] Bathias, C., and Pineau, A. Eds. Fatigue of Materials and Structures: Fundamentals, Wiley, 2013, 511.

[18] Bathias, C., and Pineau, A. Eds. Fatigue of Materials and Structures: Application to Design and Analysis, Wiley, 2013, 344.

[19] Lotsberg, I. Fatigue Design of Marine Structures, Cambridge University Press, March 2016.

[20] Mikhailov, S.E., and Namestnikova, I.V. Fatigue strength and durability analysis by normalized equivalent stress functionals, in Proc. of the 9th International Conference on the Mechanical Behavior of Materials, ICM9, 2003, Geneva, Switzerland, 10.

[21] Ritchie, R.O. Mechanisms of fatigue crack propagation in metals, ceramics and composites: Role of crack tip shielding, Material Sciences and Engineering A, 103, 1988, 15–28.

[22] DET NORSKE VERITAS AS. Fatigue design of offshore steel structures, Recommended Practice DNV-RP-C203, 2012, 178.

[23] Azeez, A.A. Fatigue failure and testing method, M.Sc. thesis, Mechanical Engineering and Production technology, Mechatronics, HAMK University of Applied Sciences, Riihimäki, Finland, 2013, 32.

[24] Santecchia, E., Hamouda, A.M.S., Musharavati, F., Zalnezhad, E., Cabibbo, M. El Mehmedi, M., and Spigarelli, S. A review on fatigue life predictions methods for metals Advances in Materials Science and Engineering, 2016, 2016, Article ID 9573524. 26. doi: 10.1155/2016/9573524.

[25] Özdeş, H., Tiryakioğlu, M., Eason, P.D. On estimating axial high cycle fatigue behavior by rotating beam fatigue testing: Application to A356 Aluminum alloy castings, Materials Science and Engineering A, 697, 2017, 95–100. doi. 10.1016/j.msea.2017.05.008.

[26] Zhang, Z., Ma, H., Zheng, R., Hu, Q., Nakatani, M., Ota, M., Chen, G., Chen, X., Ma, C., and Ameyama, K. Fatigue behavior of a harmonic structure designed austenitic stainless steel under uniaxial stress loading, Materials Science and Engineering A, 707, 2017, 287–294. doi. 10.1016/j.msea.2017.05.008.

[27] Freire Jr., R.C.S, and de Aquino, E.M.F. Fatigue damage mechanism and failure prevention in fiberglass reinforce plastic, Materials Research, 8(1), 2005, 45–49.

[28] Ellyin, F, Xia, Z., and Li, C.-S. Fatigue damage of particle reinforce metal matrix composites, WIT Transaction on State of the Art in Science and Engineering, 21, 2005(4), 73–103.

[29] Zhou, A., Post, N., Pingry, R., Cain, J., Lesko, J.J., and Case S.W. Durability of composite under fatigue loads, Durability of composites for civil structural applications, Karbhari, V.M. ed., Woodhead Publishing, Boca Raton, FL., 2007, Ch, Vol. 7, 126–149.

[30] Brighenti, R., Carpinteri, A., and Scorza, D. Fatigue crack propagation simulating fiber debonding in cyclically loaded composites, Procedia Materials Science, 3, 2014, 357–362.

[31] Mouhoubi, S., and Azouaoui, K. Residual properties of composite plates subjected to impact fatigue, Journal of Composite Materials, 53(6), 2018, 799–817. doi: 10.1177/0021998318791324.

[32] Deveci, H.A., and Artem, H.S. On the estimation and optimization capabilities of the fatigue life prediction models in composite laminates, Reinforced Plastics and Composites, 37(21), 2018, 1304–1321. doi: 10.1177/0731684418791231.

[33] Burhan, I., and Kim, H.S. S-N curve models for composite materials characterization: An evaluative review, Journal of Composite Science, 2(38), 2018, 29, doi: 10.3390/jcs2030038.

[34] Klevtsov, G. V., and Klevtsova, N. A. Influence of stress ratio R on the fatigue strength and fatigue crack path in metal materials, Proc. of the International Conference on Crack Paths (CP2009), University of Padua, Vicenza, Italy, 23-25 Sept. 2009, pp. 359–365.

[35] Basquin, O. H. The exponential law of endurance test, Proceedings of the American Society for Testing and Materials, 10, 1910, 625–630.

[36] Weibull, W. The statistical aspect of fatigue failures and its consequences, Fatigue and Fracture of Metals, A Symposium Held at the Massachusetts Institute of Technology, June 19-22,1950, Murray, W.M. editor, John Wiley & Sons, New York, NY, USA, 1952, 182–196.

[37] Li, H., Wen, D., Lu, Z., Wang, Y., and Deng, F. Identifying the probability distribution on fatigue using the maximum entropy principle, Entropy, 18(111), 2016, 19, doi: 10.3390/e18040111.

[38] Ballio, G., and Castiglioni, C. A. A unified approach for the design of steel structures under low and/or high cycle fatigue, Journal of Constructional Steel Research, 34, 1995, 75–101.

[39] Rosenfeld, M.S., and Huang, S.L. Fatigue characteristics of graphite/epoxy laminates under compression loading, Journal of Aircraft, 15(5), 1978, 264–268.

[40] Rotem, A. The fatigue behavior of orthotropic laminates under-tension-compression loading, International Journal of fatigue, 13(3), 1991, 209–215.

[41] Caprino, G., and D'Amore, A. Fatigue life of graphite/epoxy laminates subjected to tension-compression loading, Mechanics of Time-dependent Materials, 4, 2000, 139–154.

[42] Minak, G., Morreli, P., and Zucchelli, A. Fatigue residual strength of circular laminate graphite-epoxy composite plates damaged by transverse load, Composite Science and Technology, 69, 2009, 1358–1363.

[43] Williams, J.H. Jr., Yuce, H., and Lee, S.S. Ultrasonic and mechanical characterizations of fatigue states of graphite epoxy composite laminates, NASA CR, 3504, January 1982, 26.

[44] Minak, G. On the determination of the fatigue life of laminated graphite-epoxy composite by means of temperature measurement, Journal of Composite Materials, 44(14), 1739-1752, 2010. doi: 10.1177/0021998309359815.

[45] Jamison, R.D., and Reifsnider, K.L. Advanced fatigue damage development in graphite-epoxy laminates, ADA130190, AFWAL TR-82-3130, Flight Dynamic Laboratory, Air Force Wright Aeronautical Laboratories, Air Force Systems Command, Wright Patterson Air Force Base, Ohio, 45433, USA, December 1982, 222.

Appendix A: Application of Fig. 4.6 and its associated equations

Determine the diameter of a 4340 steel rod undergoing alternating axial load, which varies from a maximal value of 350 kN tension to a minimal compression of 150 kN, taking into account a safety factor S.F. = 2.5.

The mechanical properties of 4340 steel are:

$\sigma_{ul} = 1{,}092$ MPa; $\sigma_y = 1{,}005$ MPa; $\sigma_e = 520$ MPa (for the safety factor of 1.0)

Solution:

Assuming that the cross-sectional area of the road is given by the variable A, with d standing for the rod diameter:

$$A = \frac{\pi}{4}d^2 \Rightarrow d = \sqrt{\frac{4A}{\pi}}$$

We can write the following expressions:

$$\sigma_{max} = \frac{0.35}{A}[\text{MPa}], \quad \sigma_{min} = -\frac{0.15}{A}[\text{MPa}]$$

$$\Rightarrow \sigma_{mean} \equiv \sigma_m = \frac{\sigma_{max} + \sigma_{min}}{2} = \frac{0.35 - 0.15}{2A} = \frac{0.1}{A}[\text{MPa}]$$

$$\sigma_a = \frac{\sigma_{max} - \sigma_{min}}{2} = \frac{0.35 + 0.15}{2A} = \frac{0.25}{A}[\text{MPa}]$$

Using eq. (4.16), namely

$$\left(\frac{\sigma_m}{\sigma_{ul}}\right) + \left(\frac{\sigma_a}{\sigma_e}\right) = 1$$

and substituting for σ_m and σ_a, taking into account the safety factor, S.F. = 2.5 yields

$$\sigma_e = \frac{520}{2.5} = 208[\text{MPa}]$$

$$\left(\frac{0.1}{A \cdot 1,092}\right) + \left(\frac{0.25}{A \cdot 208}\right) = 1 \Rightarrow A = \left(\frac{0.1}{1,092}\right) + \left(\frac{0.25}{208}\right) = 1293[\text{mm}]^2$$

Therefore, the diameter of the rod will be

$$\Rightarrow d = \sqrt{\frac{4A}{\pi}} = \sqrt{\frac{4 \cdot 1293}{\pi}} = 40.58 \, [\text{mm}]$$

5 Introduction to crack propagation analysis

5.1 Introduction

This chapter presents the crack behavior of various materials under repeated loading. This is a continuation of Chapter 4, and presents the crack propagation philosophy associated with fatigue behavior of components.

5.2 Foundations of fracture mechanics

5.2.1 Introductory concepts

Fracture mechanics deals with the appearance of a crack in an engineering material, be it metal or composite, trying to provide answers to two key issues:

a. The failure criteria
b. Determination of strain and stress fields and the deformation in the vicinity of the geometrical singularity of the crack tip

Griffith [1] was the first to lay the foundations of fracture mechanics already in 1921. He suggested using the following relation to find the σ_f, the stress at the fracture and the length of the crack (see Fig. 5.1):

$$\sigma_f \cdot \sqrt{a} \approx \mathrm{Const} = \sqrt{\frac{2E\Psi}{\pi}} \tag{5.1}$$

where E is the Young's modulus of the material and Ψ is its surface energy density (having the value of 1 J/m^2 for glass).

In 1939, Westergaard [2] presented a solution for the stress field around a crack in the form (Fig. 5.2)

$$\sigma_{xx} = \sigma_{yy} = \frac{\sigma_{\mathrm{inf.}}}{\sqrt{1 - \left(\frac{a}{x}\right)^2}} \tag{5.2}$$

It is clear that the stresses would tend to infinity at the crack tip and would get the value $\sigma_{\mathrm{inf.}}$ at a far distance from it.

Irwin [3] started the extension of the discipline in 1957, by modifying Griffith's equation (eq. (5.1)) and suggested to include also a plastic energy dissipation, leading to the following relation:

$$\sigma_\mathrm{f} \cdot \sqrt{a} = \sqrt{\frac{EG}{\pi}}, \quad G = 2\Psi + G_\mathrm{p} \tag{5.3}$$
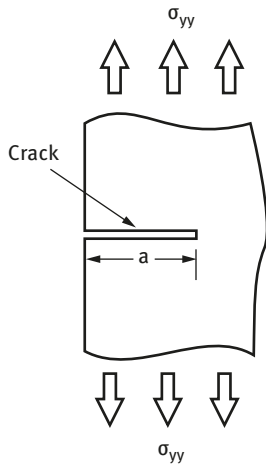
Fig. 5.1: A schematic drawing of a crack (Griffith's model).
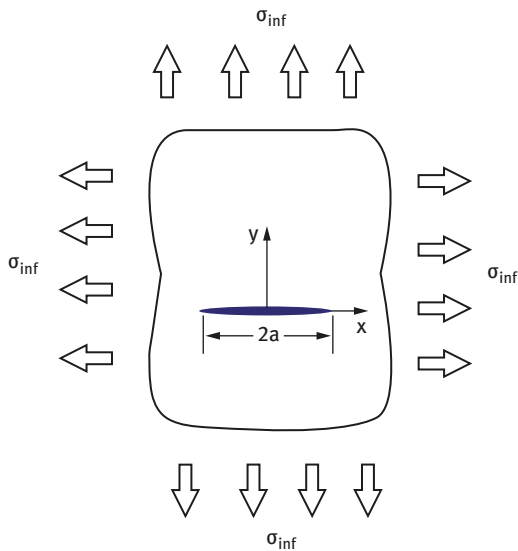
Fig. 5.2: A schematic drawing of a crack having the length 2*a* under tensile stresses at infinity,σ_{inf}..

where G is the total energy dissipation and G_{p} is the plastic part of it. One should note that for glass (a brittle material), the term Ψ would dominate leading to $G \approx 2\Psi = 2 \, \text{J/m}^2$, while for ductile materials (metals like steel and some aluminum alloys) we will obtain $G \approx G_p = 1,000 \, \text{J/m}^2$.

As can be deducted from eq. (5.2), in the vicinity of the crack tip, a stress concentration is observed. To visualize this phenomenon, flow lines are depicted in Fig. 5.3
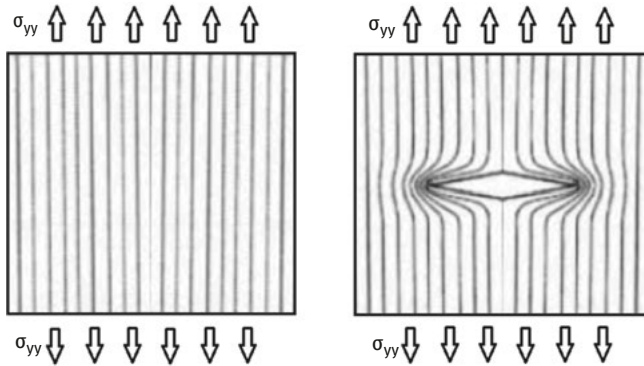
Fig. 5.3: Concentration of flow lines in the vicinity of the crack tip compared with a virgin specimen − a schematic drawing.

for a virgin specimen in comparison with the same specimen with a central crack, which experiences a concentration of the flow lines at its tips.

Today the fracture mechanics includes nonlinear problems due to their geometric and material variations. The topic of crack bifurcation in mixed loading modes has also been extensively researched over the last decade. In the last decade, the fracture mechanics had been applied to composites using numerical algorithms and FE (Finite Element) codes. (see typical references in [4–24]).

5.2.2 Basic failure modes

The basic failure modes due to cracking are presented in Fig. 5.4. The first failure mode called in the literature *Mode I (opening mode)* is presenting the opening of the crack lips in a perpendicular direction to its propagation. The second mode, *Mode II* (*sliding mode*), is an in-plane shear with the crack propagation being parallel to the crack lip displacements. The third and last mode, *Mode III* (*tearing mode*), is an out-of-plane shear (torsion type) in which the crack lip displacements are perpendicular to its propagation. Note that in real cases, a combination of more than one type of crack failure might occur. To determine, after fracture, what type of failure mode occurred, one should carefully examine the topography of the failure. In general cases, a smooth zone characteristically to crack propagation by fatigue may be observed in ductile materials, while brittle one would show a crystalline and/or apparent grains along the fracture boundary.
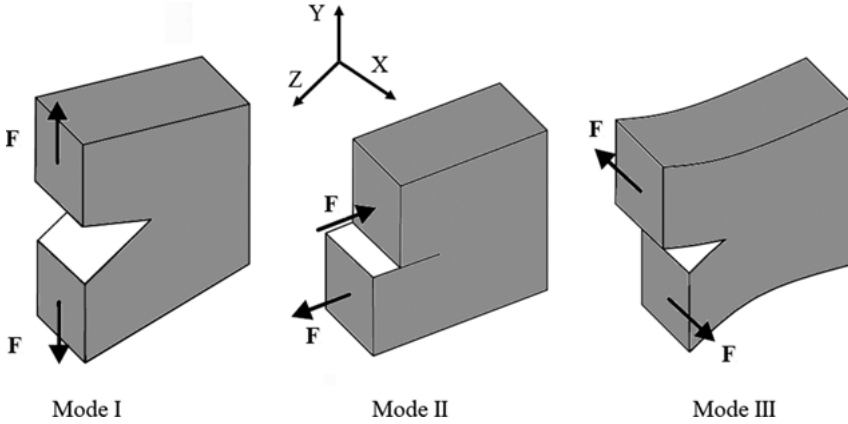
Fig. 5.4: The three crack modes.

5.2.3 The stress intensity factor, *K*

Irwin [3] presented expressions for the displacements *u, v* along the *X, Y* axes (see Fig. 5.4) and the various stresses in the singular zone of the crack tip (which presents a singularity in the form of $1/\sqrt{r}$) using parameters called stress intensity factors, K_I, K_{II} and K_{III}, for the three modes of failure presented earlier. These expressions are

$$u = \frac{K_I}{2H}\sqrt{\frac{r}{2\pi}}\cos\frac{\theta(k - \cos\theta)}{2} + \frac{K_{II}}{2H}\sqrt{\frac{r}{2\pi}}\sin\frac{\theta(k + \cos\theta + 2)}{2}$$

$$v = \frac{K_I}{2H}\sqrt{\frac{r}{2\pi}}\sin\frac{\theta(k - \cos\theta)}{2} - \frac{K_{II}}{2H}\sqrt{\frac{r}{2\pi}}\cos\frac{\theta(k + \cos\theta - 2)}{2}$$

(5.4)

$$\sigma_x = \frac{K_I}{\sqrt{2\pi r}}\cos\frac{\theta}{2}\left(1 - \sin\frac{\theta}{2}\sin\frac{3\theta}{2}\right) - \frac{K_{II}}{\sqrt{2\pi r}}\sin\frac{\theta}{2}\left(2 + \cos\frac{\theta}{2}\cos\frac{3\theta}{2}\right)$$

$$\sigma_y = \frac{K_I}{\sqrt{2\pi r}}\cos\frac{\theta}{2}\left(1 + \sin\frac{\theta}{2}\sin\frac{3\theta}{2}\right) + \frac{K_{II}}{\sqrt{2\pi r}}\sin\frac{\theta}{2}\cos\frac{\theta}{2}\cos\frac{3\theta}{2}$$

(5.5)

$$\tau_{xy} = \frac{K_I}{\sqrt{2\pi r}}\cos\frac{\theta}{2}\sin\frac{\theta}{2}\cos\frac{3\theta}{2} + \frac{K_{II}}{\sqrt{2\pi r}}\cos\frac{\theta}{2}\left(1 - \sin\frac{\theta}{2}\sin\frac{3\theta}{2}\right)$$

where

$k = 3 - 4\nu$ for plane strain; $k = \frac{3 - \nu}{1 + \nu}$ for plane stress; $H \equiv \frac{E}{2(1 + \nu)}$ is the shear modulus, *E* is the Young's modulus, ν is the Poisson's ratio and *r*, θ are the radius and angle for polar coordinates (see Fig. 5.5).

Note that for out-of-plane tractions, the *Z* displacement component, *w*, is considered and has the following form:
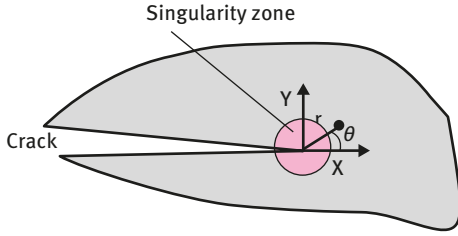
Fig. 5.5: A schematic drawing of the crack and its singularity zone.

$$w = \frac{2K_{\text{III}}}{\text{H}} \sqrt{\frac{r}{2\pi}} \sin\frac{\theta}{2} \tag{5.6}$$

The associated stress components are

$$\tau_{xz} = -\frac{2K_{\text{III}}}{\sqrt{2\pi r}} \sin\frac{\theta}{2};$$

$$\tau_{yz} = -\frac{2K_{\text{III}}}{\sqrt{2\pi r}} \cos\frac{\theta}{2} \tag{5.7}$$

The definitions of the stress intensity factors, K_{I}, K_{II} and K_{III}, are

$$K_{\text{I}} \equiv \lim_{r \to 0} \left[\frac{E}{8\alpha} \sqrt{\frac{2\pi}{r}} (v) \right]$$

$$K_{\text{II}} \equiv \lim_{r \to 0} \left[\frac{E}{8\alpha} \sqrt{\frac{2\pi}{r}} (u) \right] \tag{5.8}$$

$$K_{\text{III}} \equiv \lim_{r \to 0} \left[\frac{E}{8(1+v)} \sqrt{\frac{2\pi}{r}} (w) \right]$$

with $\alpha = 1$ for in-plane stress, $\alpha = 1 - v^2$ for in-plane strain, and u, v and w are the expressions for the displacements of the crack lips. As can be deducted from eq. (5.8), the three stress concentration factors independent of the coordinates r, θ, depend only on the applied tractions and the crack geometry and proportional to the displacements of the crack lips.

5.2.4 The energy release rate, *G*

Griffith [1] presented in its seminal work the issue of bodies containing cracks using an energy approach and introducing a variable *G*, the energy release rate, defined as

$$G \equiv - \frac{dW}{d(a)} = - \frac{W_{\text{ext.}} + W_{\text{elastic}}}{d(a)}$$

where $\qquad$ (5.9)

$$W_{\text{elastic}} = \int\limits_{\text{Volume}} \left(\int \sigma_{ij} d\varepsilon_{ij} \right) dV, \quad i, j = x, y, z$$

while $W_{\text{ext.}}$ is the potential energy of the external tractions and a is half of the crack length. The formal wording definition for G is *the energy needed to extend the front (tip) of the crack by a unit length da*, and from the energy point of view *it corresponds to the reduction (the reason for the minus sign of G) of the total energy W of a body containing a crack passing from an initial crack length 2a to (2a + da).*

The energy release rate G can also be defined in the following way:

$$G \equiv \frac{(K_{\text{I}}^2 + K_{\text{II}}^2)}{\Gamma} + \frac{K_{\text{III}}^2}{2H}$$ (5.10)

where $\Gamma = E$ for an in-plane stress case; $\Gamma = \frac{E}{1 - \nu^2}$ for an in-plane strain case.

For a simple case of a crack in a thin rectangular plate, with the traction being perpendicular to the notch, we can get the criterion for a crack propagation as

If G ≥ Gc the crack will propagate
where

$$G = \frac{\pi \sigma^2 a}{E}, \quad G_{\text{c}} = \frac{\pi \sigma_{\text{f}}^2 a}{E}$$ (5.11)

Note that eq. (5.11) is true for in-plane stress, while for the case of in-plane strain instead of E one would use the expression $E/(1 - \nu^2)$.

For mode I, one can write the fracture toughness K_{I}, for a center-cracked infinite plate as

$$K_{\text{I}} = \sigma \sqrt{\pi a};$$

$$K_{\text{Ic}} = \sqrt{EG_{\text{c}}} \text{ in-plane stress}$$ (5.12)

$$K_{\text{Ic}} = \sqrt{\frac{EG_{\text{c}}}{1 - \nu^2}} \text{ in-plane strain}$$

Note that fracture will occur if $K_{\text{I}} \geq K_{\text{Ic}}$. To take into account the geometry of the specimen, eq. (5.12) is multiplied by a dimensionless correction factor f which is a function of the crack length and width, b, of the specimen. In the case of a plate with finite width denoted $\overline{W}$ and a through-thickness crack of length $2a$, this factor will have the following form:

$$f\left(\frac{a}{\overline{W}}\right) = \sqrt{\sec\left(\frac{\pi a}{\overline{W}}\right)} \tag{5.13}$$

while for a plate with a finite width $\overline{W}$ and a through-thickness edge crack of length a the correction factor will be

$$f\left(\frac{a}{\overline{W}}\right) = 1.12 - \frac{0.41}{\sqrt{\pi}}\frac{a}{\overline{W}} + \frac{18.7}{\sqrt{\pi}}\left(\frac{a}{\overline{W}}\right)^2 - \cdots \tag{5.14}$$

5.2.5 The *J*-integral

A new interpretation to characterize the singularity of the stress field in the vicinity of a notch (crack) was proposed in 1968 by Rice [23] by defining an integral of a contour defined as

$$J \equiv \int_{\Gamma}\left(W dy - T\frac{\partial \vec{u}}{\partial x}\,ds\right)$$

where $\tag{5.15}$

$$W = W(x,y) = W(\vec{e}) = \int_0^{\varepsilon} \sigma_{ij}d\varepsilon_{ij}$$

where $\vec{e} = [\varepsilon_{ij}]$ is an infinitesimal strain tensor, Γ(see Fig. 5.6) is a closed curve surrounding the tip of the crack and the integral should be evaluated in a counterclockwise direction starting from the lower flat part of the crack surface and continuing along the path Γ to the upper flat surface; T is the traction vector defined according to the outward normal $\vec{n}$ along Γ; $T_i = \sigma_{ij}n_j$; $\vec{u}$ is the displacement vector and ds is an arc length element along Γ. Note that the J-integral is path independent [23].
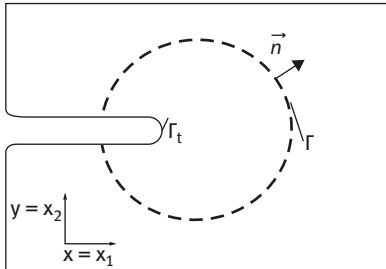
Fig. 5.6: The integral path for the *J*-integral-flat 2D-surfaced notch (crack) deformation field. Γ is any curve surrounding the crack tip, while Γ_t denotes the curved crack tip.

Rice interpreted the J-integral as the difference in potential energy W of two cracked bodies submitted to the same boundary conditions, with lengths of crack differing by a length Δa, expressing it by the following relation:

$$J \equiv -\lim_{\Delta a \to 0} \frac{W(a + \Delta a) - W(a)}{\Delta a} = -\frac{dW}{\Delta a} \tag{5.16}$$

Assuming a case of an elastic material near the crack zone, we can write

$$J = G = -\frac{dW}{\Delta a} \tag{5.17}$$

5.2.6 The crack opening displacement

The COD is a variable used to model crack propagation. It is the vector for the displacement at the crack tip. It represents the displacement that makes the crack propagate. Normally, measurements of the COD are limited to the crack of mode I, which propagates along a fixed direction, which corresponds to the axis of the initial crack.

When treating a mixed mode, these measurements would be based on the vector CTD (crack tip displacement), which is defined in the literature as a combination of CTOD (crack tip opening displacement) at loading in mode I and of CTSD (crack tip sliding displacement) which is the vector of displacement due to the slip of crack lips corresponding to the loading in mode II.

5.2.7 Some closure notes

Note that the above-described parameters of fracture mechanics K, G, J and COD are used to predict the direction of crack propagation under loadings in mixed mode, being limited to the failure in linear elastic medium. Their applications lead to very good predictions for fragile elastic materials containing a real crack.

However, for cases with ductile material, or when the load is alternating like in fatigue and/or in the presence of overloading or residual stresses, the applications of these criteria would lead to less good predictions.

5.3 Fatigue crack propagation

5.3.1 Introductory concepts

In Chapter 4, the fatigue process till failure of the component was described as being composed of four steps all connected to cracks, their initiation, growth, propagation and failure. Once the crack has been formed, its growth can be divided into two steps:

1. First step in which growth is done along slip bands due to shear stresses, leading to formation of intrusions or crack deepening. During this step, the crack would extend by only few grain diameter at a rate of a few nanometers per cycle.
2. Second step is associated with a much faster crack growth at a rate of microns per cycle, being dictated by the normal stress applied on the specimen. This stage would show also fatigue striations[1] produced by a cycle of stress. The formation of the striations is explained in the literature by three consecutive laps, starting with formation of double notch concentrating slip at $45°$ due to a tensile stress, followed by a crack widening, with the third lap being crack tip extension and its blunting. From the fatigue failure point of view, the second step is the most important, as at this step the component can be replaced before the crack would reach its critical value.

5.3.2 The Paris law

In 1963, Paris and Erdogan [4] proposed the following relation, to be known in the literature as Paris–Erdogan rule, or in short Paris law:

$$\frac{da}{dN} = C \cdot (\Delta K)^{\alpha} \tag{5.18}$$

where a is the length of the crack, C is a constant in region II (see Fig. 5.7) of the graph and α is a constant, both to be empirically determined (usually, $\alpha \approx 3$ for steel-type materials and $\alpha \approx 3 - 4$ for aluminum alloys). ΔK has the following form[2]:

$$\Delta K \equiv K_{\max} - K_{\min} = \sigma_{\max}\sqrt{\pi a} - \sigma_{\min}\sqrt{\pi a} = \Delta\sigma\sqrt{\pi a} \tag{5.19}$$

As shown in Fig. 5.7, the graph has three distinct regions. Region I is characterized by a slow and negligible crack growth, with a large influence of microstructure mean stress environment [11], with $\Delta K_{\mathrm{incep}}$ being the threshold of ΔK beyond which the crack will start to grow considerably. The second region, II, also called the Paris domain, due to the Paris law, presents stable crack growth with a linear behavior between crack growth rate and log of the stress intensity factor range ($\log(\Delta K)$). This region shows the primary mechanism of the crack, the development of striations, very small influence of the microstructure thickness and the large influence

---

1 Striations: a word coming from geology, meaning ridges, furrows or linear marks due to movement of parts.
2 One should use a range of ΔK due to the fatigue-loading mode and this makes the link between fatigue and fracture mechanics. Note that K is not defined for compression mode and it is taken as zero.
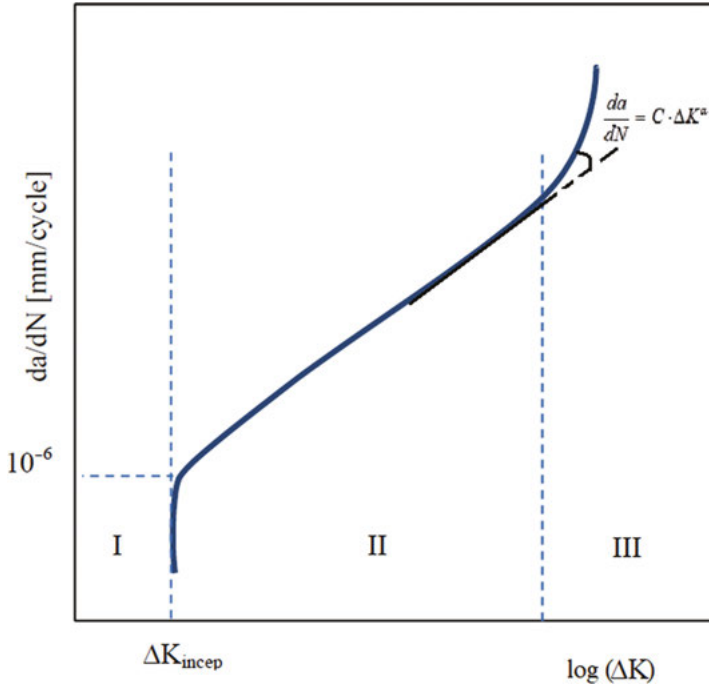
Fig. 5.7: Schematic description of the Paris law.

of mean stress, fatigue frequency and certain combinations of environment [11]. Region III, the third and the last region, presents an unstable growth of the crack leading to failure, as $K_{max} > K_c$ of the certain material. Ritchie [11] calls this region "the static mode mechanisms" as it shows cleavage, intergranular and fibrous mechanisms. The region presents a large influence of the microstructure, mean stress and thickness, with very little influence of the environment [11].

Note that the fatigue life of a specimen can be obtained by integrating Paris law (eq. (5.18)) to yield the following expression:

$$\frac{da}{dN} = C \cdot (\Delta K)^{\alpha} \Rightarrow N_{final} = \int_0^{N_{final}} dN = \int_{a_{start}}^{a_{final}} \frac{da}{C \cdot (\Delta K)^{\alpha}} \tag{5.20}$$

Introducing the relation between the stress intensity factor and the crack length + stress, together with the function f (see eq. (5.14)) one obtains the following expression:

$$N_{final} = \frac{1}{C(f\Delta\sigma\sqrt{\pi})^{\alpha}} \left(\frac{1}{0.5\alpha - 1} \right) \left[\frac{1}{a_{start}^{0.5\alpha - 1}} - \frac{1}{a_{final}^{0.5\alpha - 1}} \right] \tag{5.21}$$

Note that the correction factor f was introduced in eq. (5.21) after integration as it is an empirical value.

5.3.3 Experimental fracture mechanics

5.3.3a Experimental determination of the Paris law

The geometry of the samples is according to ASTM E399 [25] with the variables w and B (Fig. 5.8) being $W = 1''$ (25.4 mm) and $B = \frac{1}{2}''$ (12.7 mm) (more details in [24]).

Fig. 5.8: Schematic drawing of the crack propagation specimen.

The tests were performed on an MTS hydraulic fatigue tensile machine equipped with a 100 kN load cell. At the end of the crack, an MTS COD gage was placed and it measured the crack opening value at each load cycle (Fig. 5.9). For tests on solid specimens, a crack length gage Vishay TK-09-CPA01-005/DP was bonded to the specimen (Fig. 5.10). The gage has 20 wires at 0.25 mm distance between two adjacent ones and as the crack propagates, the wires tear thus indicating the crack length.

5.3.3b Experimental determination of the Paris law constants

The sample was installed on the loading machine, which applied a 10 Hz sinusoidal load at $R = 0.1$ (i.e., the machine applies only tensile force). During the test, every 10 cycles, a sample of the crack length gage and a sample of the COD gage were taken

Fig. 5.9: COD implementation.
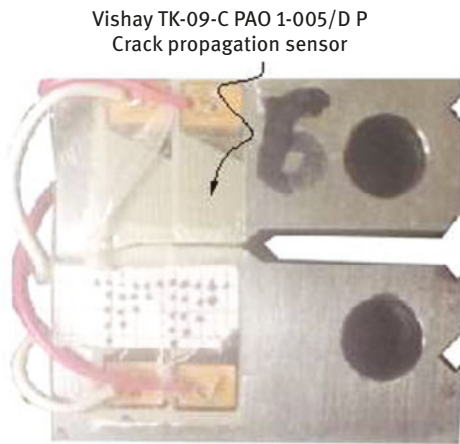
Fig. 5.10: Crack propagation sensor implementation.

and stored. The output measurements include the maximum and minimum forces at each cycle and the amplitude of the COD gage and the readings of the crack propagation sensor. The large database is then filtered to reduce its size for further processing, by keeping only the data when the crack length changes its value by a unit.

For each cycle, the stiffness of the tested specimen is determined using the following relation:

$$k_s = \frac{\text{Force}_{\text{max}} - \text{Force}_{\text{min}}}{\text{COD}_{\text{length}}} \tag{5.22}$$

After calculating the stiffness of the specimen with respect to the crack length, a polynomial expression is curve fitted between the crack length and the stiffness defined in eq. (5.22). A typical graph of the crack length versus the specimen's stiffness is presented in Fig. 5.11.
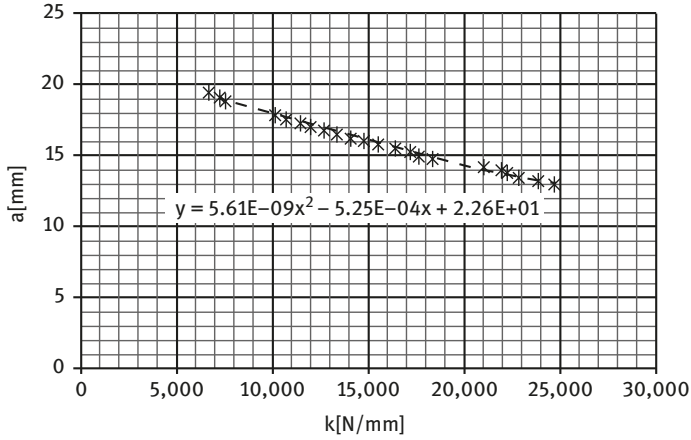
Fig. 5.11: Typical experimental graph of crack length (a) versus specimen's stiffness (k).

Knowing the crack length and the applied load yields, the ΔK_1 values for the entire data as well as the crack length rate da/dN (a is the crack length and N stands for the number of cycles) lead to a graph of the crack length rate versus ΔK_1 (Fig. 5.12). ΔK_1 is calculated using the following expression:

$$\Delta K_1 = \frac{\Delta P}{B \cdot \sqrt{W}} \cdot f\left(\frac{a}{W}\right) \tag{5.23}$$

where
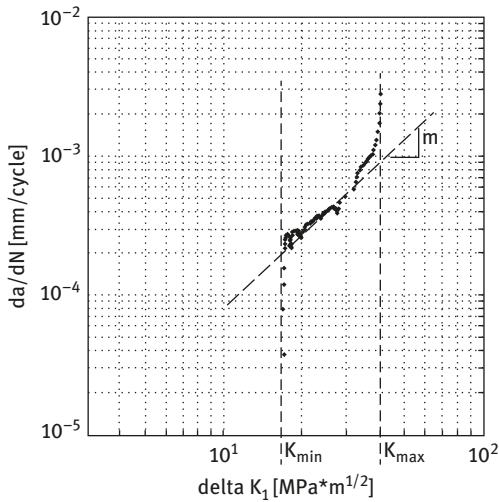
Fig. 5.12: Typical experimental graph of (da/dN) versus ΔK_1.

$$f(\chi) = \frac{2 + \chi}{(1 - \chi)^{3/.2}} \Gamma$$

$$\Gamma \equiv \left[0.886 + 4.64(\chi) - 13.32(\chi)^2 + 14.72(\chi)^3 - 5.6(\chi)^4 \right] \qquad (5.24)$$

$$\chi \equiv \frac{a}{W}$$

ΔP is the load amplitude, a is the crack length, W and B are dimensions as presented in Fig. 5.8. The graph depicted in Fig. 5.8 enables to find the Paris coefficients C and α appearing in Paris law (see eqs. (5.18) and (5.19)) as expressed by the following equations

$$\frac{da}{dN} = C \cdot \Delta K^\alpha \qquad (5.25)$$

where

$$\Delta K = K_{max} - K_{min} \qquad (5.26)$$

One should note that for the typical graph shown in Fig. 5.12, the following values were obtained: $\alpha = 1.86$, $K_{min} = 17 \left[\text{MPa} \cdot \sqrt{m} \right]$, $K_{max} = 40 \left[\text{MPa} \cdot \sqrt{m} \right]$ and $C = 6.92 \cdot 10^{-21} [m^{0.5}/(\text{cycle} \cdot \text{MPa})]$. For the case $da/dN \to \infty$, $K_{max} \to K_{1C}$ and sometimes K_{min} is also named ΔK_{th}, occurred at lower threshold value of da/dN, below which no crack propagation would occur (see also Fig. 5.7).
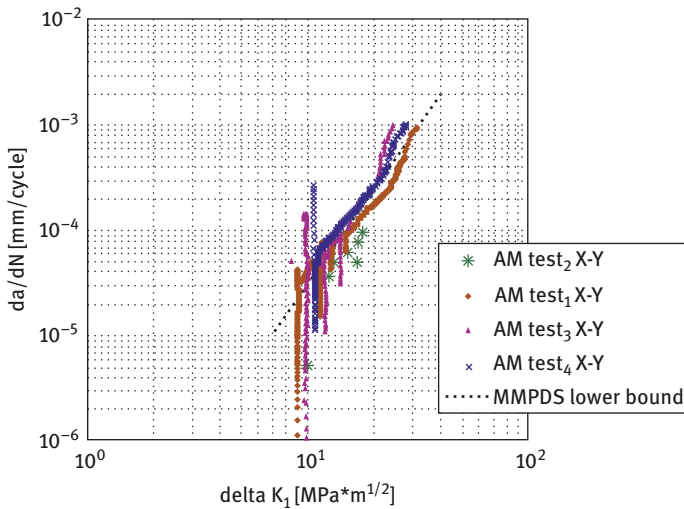
Fig. 5.13: Experimental results for four additive manufactured specimens printed in the x–y plane direction [24].

It seems that the results in Fig. 5.13 are in close agreement with the results presented in the Metallic Materials Properties Development and Standardization Scientific Report [25].

References

[1]   Griffith, A.A. The phenomena of rupture and flow in solids, Philosophical Transactions of the Royal Society, series A, 221, 1921, 163–197, doi.org/10.1098/rsta.1921.0006.

[2]   Westergaard, H.M. Bearing pressures and cracks, Journal of Applied Mechanics, 6, 1939, A49–53.

[3]   Irwin, G. Analysis of stresses and strains near the end of a crack traversing a plate, Journal of Applied Mechanics, Transactions of ASME, 24, 1957, 361–364.

[4]   Paris, P. and Erdogan, F. A critical analysis of crack propagation laws, Journal Basic Engineering, 85(4), 1963, 528–533.

[5]   Tomkins, B. Fatigue crack propagation – an analysis, Journal Philosophical Magazine, Vol. 18, Issue 155, 1968, pp. 1041–1066.

[6]   Engle, R.M. Jr. CRACKS, A Fortran IV digital computer program for crack propagation analysis, Technical Report AFFDL-TR-70-107, Air force Flight Dynamics Laboratory, Air Force Systems Command, Wright-Patterson Air Force Base, Ohio, USA, 1970, 61.

[7]   Jaske, C.E., Feddersen, C.E., Davies, K.B. and Rice, R.C. Analysis of fatigue, fatigue-crack propagation and fracture data, NASA CR-132332, 1973, 188.

[8]   Engelder, T. Brittle crack propagation, Chapter 3 in *Continental Tectonics*, Hancock, P, Editor, Pergamon Press, Oxford, 1994, 43–52.

[9]   Ortiz, M. and Pandolfi, A. Finite-deformation irreversible cohesive elements for three-dimensional crack-propagation analysis, International Journal for Numerical Methods in Engineering, 444, 1999, 1267–1282.

[10] Kerans, R. J. and Parthasarathy, T.A. Crack deflection in ceramic composites and fiber coating design criteria, Composites Part A: Applied Science and Manufacturing, 30(4), 1999, 521–524.

[11] Ritchie, R.O. Mechanisms of fatigue-crack propagation in ductile and brittle solids, International Journal of Fracture, 100, 1999, 55–83.

[12] Scheider, I. Cohesive model for crack propagation analyses of structures with elastic-plastic material behavior-Foundations and implementation, Technical report, GKSS Research Center, Internal report No. WMS/2000/19, 2001, 41.

[13] Scheider, I., Schödel, M., Brocks, W. and Schönfeld, W. Crack propagation analyses with CTOA and cohesive model: comparison and experimental validation, Engineering Fracture Mechanics, 73, 2006, 252–263.

[14] Patrício, M. and Mattheij, R. M. M. Crack propagation analysis, CASA-Report, Vol. 0723, 2007, Eindhoven, Technische Universiteit Eindhoven, The Netherlands, 25.

[15] Souiyah, M., Muchtar, A., Alshoaibi, A. and Ariffin, A.K. Finite element analysis of the crack propagation for solid materials, American Journal of Applied Sciences, 6(7), 2009, 1396–1402.

[16] Kostson, E. and Fromme, P. Fatigue crack monitoring in multi-layered aircraft structures using guided ultrasonic waves, Journal of Physics: Conference series, 195, 2009, Article Id: 012003, 10. doi: 10.1088/1742-6596/195/1/012003.

[17] Chin, P. L. Stress analysis, crack propagation and stress intensity factor computation of a Ti-6Ai-4V aerospace bracket using ANSYS and FRANC3D, Master Thesis, Rensselaer Polytechnic Institute, Hartford, Connecticut, USA, 2011, 65.

[18]   Okada, H., Kawai, H., Tokuda, T. and Fukui, Y. Fully automated mixed mode crack propagation analyses based on tetrahedral finite element and VCCM (virtual crack closure-integral method), International Journal of Fatigue, 50, 2013, 33–39.

[19]   Dassios, K.G., Kordatos, E.Z., Aggelis, D.G. and Matikas, T.E. Crack growth monitoring in ceramic matrix composites by combined infrared thermography and acoustic emission, Journal of the American Ceramic Society, 97(1), 2014, 251–257. doi: 10.1111/jace.12592.

[20]   Dündar, H. and Ayhan, A.O. Three-dimensional fracture and fatigue crack propagation analysis in structures with multiple cracks, Computers and Structures, 158, 2015, 259–273.

[21]   Jensen, B.E.W. Numerical analysis of crack propagation and lifetime estimation, Master thesis, Aalborg University Esbjerg, Denmark, 2015, 94.

[22]   Hashtroodi, S. Crack propagation analysis of a pre-stressed L-shaped spandrel parking garage beam, Master thesis in Civil Engineering, The University of Toledo, Toledo, Ohio, US, 2015, 120.

[23]   Rice, J.R. A path independent integral and the approximate analysis of strain concentrations by notches and cracks, Journal of Applied Mechanics, 35, 1968, 379–386.

[24]   Abramovich, H., Broitman, N. and Shirizly, A. Investigation of crack propagation properties of additive manufacturing products, 31st Congress of the International Council of the Aeronautical Sciences, Belo Horizonte, Brazil, Sept. 9–14, 2018, 9.

[25]   Standard Test Methods for Measurement of Fatigue. Crack Growth Rates. ASTM E647. 100 Barr Harbor Dr. West Conshohocken, PA 19428, USA, 1999.

6 Buckling of thin-walled structures

6.1 Introduction

This chapter presents the behavior of thin-walled structures like columns and plates. The thin-walled structures can be either isotropic or orthotropic, and their critical loads will be analytically evaluated for applicable cases. Finally, some approximate energy methods will also be highlighted, enabling the calculation of buckling loads for cases where no closed-form solutions are available.

6.2 Buckling of columns

6.2.1 Euler buckling

To find the buckling[1] load of a column, having the length L, and stiffness EI[2] resting on simply-supported, or hinged–hinged[3] boundary conditions and being compressed by a compressive load P (see Fig. 6.1), one needs to write the moment at a chosen axial coordinate, x, and equate it to the known expression of EId^2z/dx^2. One should note that in Fig. 6.1, the column is described after its deformation in an exaggerated manner. The result is [1, 2]

$$EI\frac{d^2z(x)}{dx^2} = -Pz(x) \tag{6.1}$$

Rearranging eq. (6.1) and dividing by EI, one obtains

$$\frac{d^2z(x)}{dx^2} + k^2z(x) = 0, \quad k^2 = \frac{P}{EI} \tag{6.2}$$

The general solution for eq. (6.2) is given by

$$z(x) = A\sin(kx) + B\cos(kx) \tag{6.3}$$

while A and B are constants to be determined from the boundary conditions of the problem. For the hinged–hinged column case, the boundary conditions would

---

1 "Buckling" phenomenon has various definitions. One of those definitions *describe* it as the state of a compressed column, when slight increase in the compressive load would induce sudden large lateral (unbounded) deformation of structure, whereas before that compressive load (critical load), the column had experienced little, if any, lateral deformation.
2 E, Young's modulus; I, moment of inertia of the cross section (for a rectangular cross, having a height of h and width of b, $I = bh^3/12$).
3 In some of the books and manuscripts, these boundary conditions are referred to as *pinned–pinned* boundary conditions.
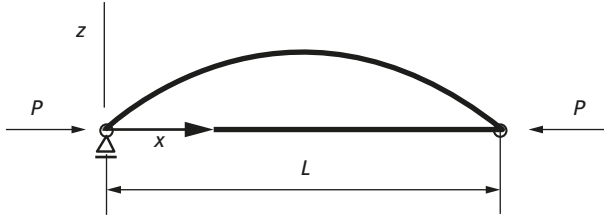
Fig. 6.1: A hinged–hinged column under compressive loads P.

require the lateral displacement and the moment to vanish at its both ends. One should note that for the equation of motion displayed in eq. (6.1), the natural boundary conditions, namely the moment is inherently fulfilled. Therefore, we are left with only two geometric boundary conditions, which lead to

$$z(0) = 0 \Rightarrow B = 0$$
$$z(L) = 0 \Rightarrow A\sin(kL) = 0 \tag{6.4}$$
$$A \neq 0 \quad \text{and} \quad \sin(kL) = 0 \Rightarrow kL = n\pi, \quad n = 1, 2, 3, \ldots$$

The mathematical result from eq. (6.4) is that the calculation of the buckling of a column leads to an eigenvalue problem. Substituting the expression for k (see eq. (6.2)) and taking $n = 1$ leads to the expression for what it is called the *Euler buckling load*:

$$k^2 \equiv \frac{P}{EI} = \left(\frac{n\pi}{L}\right)^2 \Rightarrow P = \left(\frac{n\pi}{L}\right)^2 EI, \quad P_{n=1} \equiv P_{\text{Euler}} = \frac{\pi^2 EI}{L^2} \tag{6.5}$$

For other boundary conditions (besides hinged–hinged), incorporating both geometrical and natural boundary conditions, the equation of motion would have the following form[4]:

$$\frac{d^4 z(x)}{dx^4} + k^2 \frac{d^2 z}{dx^2}(x) = 0, \quad k^2 = \frac{P}{EI} \tag{6.6}$$
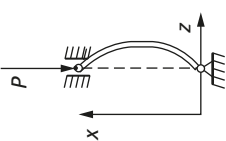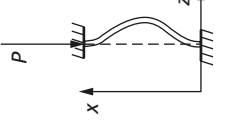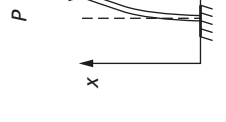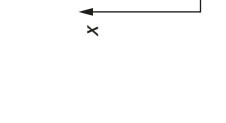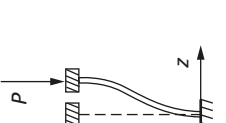
The general solution for eq. (6.6) is then given by

$$z(x) = A\sin(kx) + B\cos(kx) + Cx + D \tag{6.7}$$

Application of various boundary conditions (see Table 6.1 for the most used one) would provide the relevant buckling load and its associated mode. For an enhanced understanding of the buckling phenomenon, which is a stability issue, the reader is referred to refs. [1–6].

---

4 The theory leading to eq. (6.6) is usually denoted in the literature as the *Bernoulli–Euler* theory.

Table 6.1: Buckling factors and associated modes.

Hinged–hinged	Clamped–clamped	Clamped–free	Hinged–guided	Clamped–guided	Clamped–hinged
$z(0) = z(L) = 0$ $z''(0) = z''(L) = 0$	$z(0) = z(L) = 0$ $z'(0) = z'(L) = 0$	$z(0) = z'(0) = 0$ $z''(L) = 0$ $z'''(L) + k^2 z'(L) = 0$	$z(0) = z''(0) = 0$ $z'(L) = 0$ $z'''(L) + k^2 z'(L) = 0$	$z(0) = z'(0) = 0$ $z'(L) = 0$ $z'''(L) + k^2 z'(L) = 0$	$z(0) = z(L) = 0$ $z'(0) = z''(L) = 0$
$K = 1$	$K = 4$	$K = 0.25$	$K = 0.25$	$K = 1$	$K = 2.045$
$z(x) =$ $\sin\left(\dfrac{\pi x}{L}\right)$	$z(x) =$ $1 - \cos\left(\dfrac{2\pi x}{L}\right)$	$z(x) =$ $1 - \cos\left(\dfrac{\pi x}{2L}\right)$	$z(x) =$ $1 - \cos\left(\dfrac{\pi x}{2L}\right)$	$z(x) =$ $1 - \cos\left(\dfrac{\pi x}{2L}\right)$	$z(x) =$ $\sin(\alpha x) +$ $\alpha L\left[1 - \cos(\alpha x) - \dfrac{x}{L}\right]$ $\alpha = 1.4318\dfrac{\pi}{L}$
$L_{eff} = L$	$L_{eff} = 0.5L$	$L_{eff} = 2L$	$L_{eff} = 2L$	$L_{eff} = L$	$L_{eff} = 0.7L$

Note that $z'(x) \equiv \dfrac{dz(x)}{dx}$; $z''(x) \equiv \dfrac{d^2 z(x)}{dx^2}$; $z'''(x) \equiv \dfrac{d^3 z(x)}{dx^3}$. $P_{(any)}$ BC $= K P_{(Euler)} = K \dfrac{\pi^2 EI}{L^2}$, $0 < K \le 4$.

L_{eff} (effective length) of a column = the distance between two successive inflection points.

6.2.2 Rankin–Gordon formula

The buckling formulas derived in the previous section dealt with what is called "slender" columns. Slenderness ratio of a column (λ is defined as the ratio of the effective length of a column (L_{eff} – see last row in Table 6.1) and the least radius of gyration (r) about the axis under consideration. Consequently, this can be expressed as

$$\lambda \equiv \frac{L_{\text{eff}}}{r}, \quad r = \sqrt{\frac{I}{A}} \tag{6.8}$$

where A is the cross-sectional area of the column and I is its moment of inertia.

The Euler buckling formula, developed in the previous section, is not suitable for short stubby columns. There are a few formulas to be used for relatively low slenderness ratio, with the Johnson's parabola [7] and the Rankine–Gordon[5] semi-empirical formula, being the most known ones.

Johnson's parabola [7] is given by the following expression (see also Fig. 6.2):
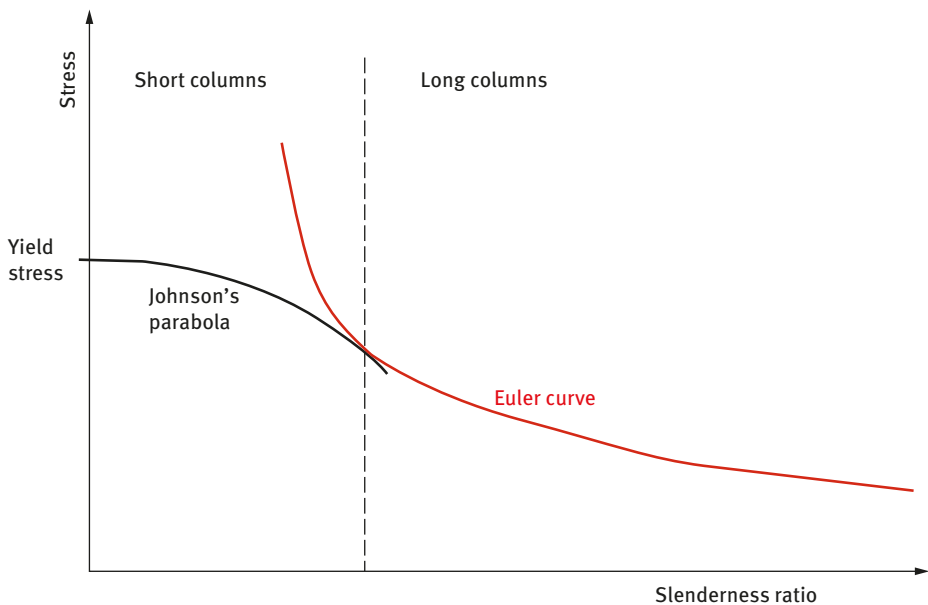
Fig. 6.2: Schematic diagram presenting Euler curve and Johnson's parabola.

---

5 William John Macquorn Rankine (1820–1872) and Perry Hugesworth Gordon (1894–1966).

$$\sigma \equiv \sigma_y - \frac{1}{E}\left(\frac{\sigma_y}{2\pi}\right)^2\left(\frac{L_{eff}}{r}\right)^2 = \sigma_y - \frac{1}{E}\left(\frac{\sigma_y}{2\pi}\right)^2\lambda^2 \tag{6.9}$$

where σ_y is the yield stress for a given material.

Rankine–Godman semiempirical formula can be written as

$$\frac{1}{P_{R-G}} \equiv \frac{1}{P_{Euler}} + \frac{1}{P_{Crush}} \tag{6.10}$$

where $P_{Crush} \equiv \sigma_y \cdot A$ is the crushing load or yield point load in compression for a given material. Equation (6.10) can be rearranged to show the stress in the column according to Rankine–Godman approach to yield

$$\sigma_{R-G} = \frac{\sigma_y}{1 + \dfrac{\sigma_y}{\pi^2 E}\left(\dfrac{L_{eff}}{r}\right)^2} = \frac{\sigma_y}{1 + \dfrac{\sigma_y}{\pi^2 E}\lambda^2} \tag{6.11}$$

A schematic diagram presenting the Euler curve and the Rankine–Godman curve is shown in Fig. 6.3.
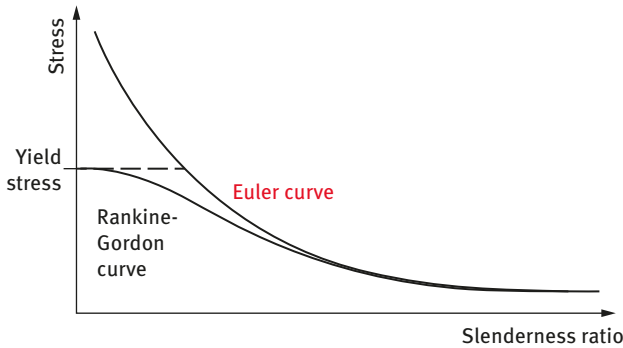
Fig. 6.3: Schematic diagram presenting Euler curve and Rankine–Gordon curve.

One can see from Fig. 6.3 that for short columns the stress predicted by the Rankine–Gordon curve is tending to the yield stress, while for long columns, both curves would coincide.

6.2.3 Composite columns – CLT approach

Buckling of laminated composite columns (see Chapter 2), which are considered as 1D elements (see Fig. 6.4) can be derived for a general laminate using the classical lamination theory (CLT), to yield the following equations of motion:
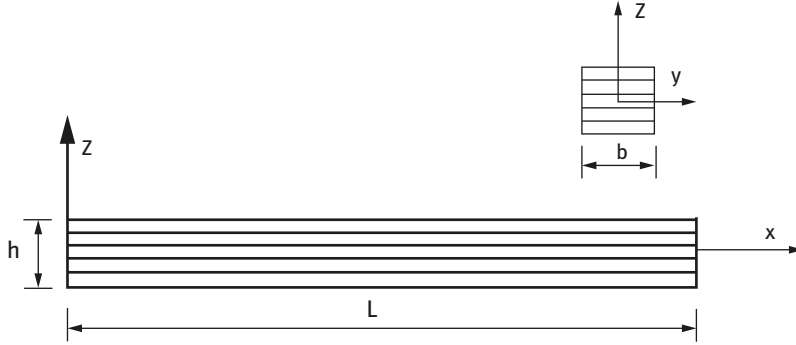
Fig. 6.4: The laminated composite column model.

$$A_{11}\left(\frac{d^2u_0}{dx^2} + \frac{d^3w_0}{dx^3}\right) - B_{11}\frac{d^3w_0}{dx^3} = 0 \tag{6.12}$$

$$-B_{11}\left(\frac{d^3u_0}{dx^3} + \frac{d^4w_0}{dx^4}\right) + D_{11}\frac{d^4w_0}{dx^4} + \overline{N}_{xx}\frac{d^2w_0}{dx^2} = 0 \tag{6.13}$$

while A_{11}, B_{11} and D_{11} are the stretching, coupled stretching–bending and bending stiffness, accordingly and $\overline{N}_{xx}$ stands for the axial compression per unit width (b) and it is assumed to be independent of the coordinate x. The two coupled equations of motion (eqs. (6.12) and (6.13)) can be decoupled to yield one single equation having the following form:

$$\left(D_{11} - \frac{B_{11}^2}{A_{11}}\right)\frac{d^4w_0}{dx^4} + \overline{N}_{xx}\frac{d^2w_0}{dx^2} = 0 \tag{6.14}$$

or

$$\frac{d^4w_0}{dx^4} + \frac{\overline{N}_{xx}}{\left(D_{11} - \frac{B_{11}^2}{A_{11}}\right)}\frac{d^2w_0}{dx^2} = 0 \tag{6.15}$$

6.2.3a Symmetric laminate ($B_{11} = 0$)

For the case of symmetric laminate, $B_{11} = 0$, and where, and w_b being the buckling deflection, one obtains

$$\frac{d^4w_b}{dx^4} + \frac{P}{E_{xx} \cdot I_{yy}}\frac{d^2w_b}{dx^2} = 0 \tag{6.16}$$

where

$$b \cdot D_{11} = E_{xx} \cdot I_{yy} \quad \text{and} \quad b \cdot \overline{N}_{xx} = P \tag{6.17}$$

One should note that eq. (6.16) is exactly the Bernoulli–Euler equation of buckling for columns (see eq. (6.6)).

Now we shall present the general solution for eq. (6.16), applicable to the buckling of symmetric laminated composite columns ($B_{11} = 0$). Rearranging eq. (6.16) we obtain

$$\frac{d^4 w_b}{dx^4} + \lambda^2 \frac{d^2 w_b}{dx^2} = 0, \quad \lambda^2 = \frac{\overline{N}_{xx}}{D_{11}} \tag{6.18}$$

The solution of eq. (6.18) has the following general form (which is identical to eq. (6.7) applied for Bernoulli–Euler columns):

$$w_b(x) = C_1 \sin(\lambda x) + C_2 \cos(\lambda x) + C_3 x + C_4 \tag{6.19}$$

where C_1, C_2, C_3 and C_4 are constants to be determined using four boundary conditions of a given problem. For example, assuming a simply-supported column having a length L, one can write its boundary conditions as

$$
\begin{aligned}
w_b(0) = 0; \quad M_{yy}(0) = 0 \quad &\Rightarrow \quad \frac{d^2 w_b(0)}{dx^2} \equiv w_b''(0) = 0 \\
w_b(L) = 0; \quad M_{yy}(L) = 0 \quad &\Rightarrow \quad \frac{d^2 w_b(L)}{dx^2} \equiv w_b''(L) = 0
\end{aligned}
\tag{6.20}
$$

Substituting the boundary conditions in eq. (6.19) yields a set of four equations with four unknowns, which can be written in a 4 × 4 matrix while the right-hand side of the four equations are identically zero. To obtain a unique solution, the determinant of the matrix must vanish. This leads to the following characteristic equation:

$$\sin(\lambda L) = 0 \quad \Rightarrow \quad \lambda L = n\pi, \quad n = 1, 2, 3, 4, \ldots \tag{6.21}$$

The critical buckling load of the column (the lowest one, $n = 1$) will then be

$$\left(\overline{N}_{xx}\right)_{cr} = \frac{\pi^2}{L^2} D_{11} \tag{6.22}$$

One should remember that that the term in eq. (6.22) should be multiplied by the width of the beam, b, to obtain P_{cr} [N]. One can see that the buckling load for a laminated symmetric composite column (eq. (6.22)) is exactly the same as for the Bernoulli–Euler column presented in eq. (6.5).

The column buckling shape (the eigenfunction) has the following form (this is obtained by back substituting the eigenvalue from eq. (6.21) into the matrix form):

$$w_b(x) = C_1 \sin(\lambda x) = C_1 \sin\left(\frac{\pi x}{L}\right) \tag{6.23}$$

Tables 6.2 and 6.3[6] present some of the most encountered column cases, while the schematic drawings of the various out-of-plane boundary conditions are presented in Fig. 6.5. One should note that only the out-of-plane boundary conditions can influence the critical buckling load and the shape at buckling (see also Appendix A).

Table 6.2: Buckling of laminated composite columns: out-of-plane boundary conditions – CLT approach.

No.	B.C. Name	Out-of-plane boundary conditions	
		$x = 0$	$x = L$
1	SS-SS*	$w_{\mathrm{b}} = 0; \dfrac{d^2 w_{\mathrm{b}}}{dx^2} = 0$	$w_{\mathrm{b}} = 0; \dfrac{d^2 w_{\mathrm{b}}}{dx^2} = 0$
2	C-C**	$w_{\mathrm{b}} = 0; \dfrac{d w_{\mathrm{b}}}{dx} = 0$	$w_{\mathrm{b}} = 0; \dfrac{d w_{\mathrm{b}}}{dx} = 0$
3	C-F***	$w_{\mathrm{b}} = 0; \dfrac{d w_{\mathrm{b}}}{dx} = 0$	$\dfrac{d^2 w_{\mathrm{b}}}{dx^2} = 0; \dfrac{d^3 w_{\mathrm{b}}}{dx^3} + \lambda^2 \dfrac{d w_{\mathrm{b}}}{dx} = 0$
4	F-F	$\dfrac{d^2 w_{\mathrm{b}}}{dx^2} = 0; \dfrac{d^3 w_{\mathrm{b}}}{dx^3} + \lambda^2 \dfrac{d w_{\mathrm{b}}}{dx} = 0$	$\dfrac{d^2 w_{\mathrm{b}}}{dx^2} = 0; \dfrac{d^3 w_{\mathrm{b}}}{dx^3} + \lambda^2 \dfrac{d w_{\mathrm{b}}}{dx} = 0$
5	SS-C	$w_{\mathrm{b}} = 0; \dfrac{d^2 w_{\mathrm{b}}}{dx^2} = 0$	$w_{\mathrm{b}} = 0; \dfrac{d w_{\mathrm{b}}}{dx} = 0$
6	SS-F	$w_{\mathrm{b}} = 0; \dfrac{d^2 w_{\mathrm{b}}}{dx^2} = 0$	$\dfrac{d^2 w_{\mathrm{b}}}{dx^2} = 0; \dfrac{d^3 w_{\mathrm{b}}}{dx^3} + \lambda^2 \dfrac{d w_{\mathrm{b}}}{dx} = 0$
7	G****-F	$\dfrac{d w_{\mathrm{b}}}{dx} = 0; \dfrac{d^3 w_{\mathrm{b}}}{dx^3} + \lambda^2 \dfrac{d w_{\mathrm{b}}}{dx} = 0$	$\dfrac{d^2 w_{\mathrm{b}}}{dx^2} = 0; \dfrac{d^3 w_{\mathrm{b}}}{dx^3} + \lambda^2 \dfrac{d w_{\mathrm{b}}}{dx} = 0$
8	G-SS	$\dfrac{d w_{\mathrm{b}}}{dx} = 0; \dfrac{d^3 w_{\mathrm{b}}}{dx^3} + \lambda^2 \dfrac{d w_{\mathrm{b}}}{dx} = 0$	$w_{\mathrm{b}} = 0; \dfrac{d^2 w_{\mathrm{b}}}{dx^2} = 0$
9	G-G	$\dfrac{d w_{\mathrm{b}}}{dx} = 0; \dfrac{d^3 w_{\mathrm{b}}}{dx^3} + \lambda^2 \dfrac{d w_{\mathrm{b}}}{dx} = 0$	$\dfrac{d w_{\mathrm{b}}}{dx} = 0; \dfrac{d^3 w_{\mathrm{b}}}{dx^3} + \lambda^2 \dfrac{d w_{\mathrm{b}}}{dx} = 0$
10	G-C	$\dfrac{d w_{\mathrm{b}}}{dx} = 0; \dfrac{d^3 w_{\mathrm{b}}}{dx^3} + \lambda^2 \dfrac{d w_{\mathrm{b}}}{dx} = 0$	$w_{\mathrm{b}} = 0; \dfrac{d w_{\mathrm{b}}}{dx} = 0$

*SS, simply supported or hinged–hinged or pinned–pinned.
**C, clamped.
***F, free.
****G, guided.

To conclude this section, a column with general boundary conditions is presented in Fig. 6.6.

Defining the following variables as

$$\overline{k}_1 = \frac{k_1}{\overline{D}_{11}}; \ \overline{k}_2 = \frac{k_2}{\overline{D}_{11}}; \ \overline{k}_{\theta_1} = \frac{k_{\theta_1}}{\overline{D}_{11}}; \ \overline{k}_{\theta_2} = \frac{k_{\theta_2}}{\overline{D}_{11}} \tag{6.24}$$

---

6 Some of the boundary conditions and their relevant buckling loads are also presented in Table 6.1.

Table 6.3: Buckling loads and relevant buckling modes of laminated composite columns using CLT approach.

No.	Name	Characteristic equation	Critical buckling load	Mode shape
1	SS-SS	$\sin(\lambda L) = 0$ $\lambda L = n\pi$	$(\overline{N}_{xx})_{cr} = \dfrac{\pi^2}{L^2} D_{11}$	$\sin\left(\dfrac{\pi x}{L}\right)$
2	C-C	$\lambda L \sin(\lambda L) = 2[1 - \cos(\lambda L)]$ $\lambda L = 2\pi, 8.987, 4\pi, .$	$(\overline{N}_{xx})_{cr} = 4\dfrac{\pi^2}{L^2} D_{11}$	$1 - \cos\left(\dfrac{2\pi x}{L}\right)$
3	C-F	$\cos(\lambda L) = 0$ $\lambda L = (2n - 1)\pi/2$	$(\overline{N}_{xx})_{cr} = \dfrac{\pi^2}{4L^2} D_{11}$	$1 - \cos\left(\dfrac{\pi x}{2L}\right)$
4	F-F	$\sin(\lambda L) = 0$ $\lambda L = n\pi$	$(\overline{N}_{xx})_{cr} = \dfrac{\pi^2}{L^2} D_{11}$	$\sin\left(\dfrac{\pi x}{L}\right)$
5	SS-C	$\tan(\lambda L) = \lambda L$ $\lambda L = 1.430\pi, 2.459\pi, \ldots$	$(\overline{N}_{xx})_{cr} = 2.045\dfrac{\pi^2}{L^2} D_{11}$	$\sin(\alpha x) + \alpha L\left[1 - \cos(\alpha x) - \dfrac{x}{L}\right]$ while $\quad \alpha = 1.4318\dfrac{\pi}{L}$
6	SS-F	$\sin(\lambda L) = 0$ $\lambda L = n\pi$	$(\overline{N}_{xx})_{cr} = \dfrac{\pi^2}{L^2} D_{11}$	$\sin\left(\dfrac{\pi x}{L}\right)$
7	G-F	$\cos(\lambda L) = 0$ $\lambda L = (2n - 1)\pi/2$	$(\overline{N}_{xx})_{cr} = \dfrac{\pi^2}{4L^2} D_{11}$	$\cos\left(\dfrac{\pi x}{2L}\right)$
8	G-SS	$\cos(\lambda L) = 0$ $\lambda L = (2n - 1)\pi/2$	$(\overline{N}_{xx})_{cr} = \dfrac{\pi^2}{4L^2} D_{11}$	$\cos\left(\dfrac{\pi x}{2L}\right)$
9	G-G	$\sin(\lambda L) = 0$ $\lambda L = n\pi$	$(\overline{N}_{xx})_{cr} = \dfrac{\pi^2}{L^2} D_{11}$	$\cos\left(\dfrac{\pi x}{L}\right)$
10	G-C	$\sin(\lambda L) = 0$ $\lambda L = n\pi$	$(\overline{N}_{xx})_{cr} = \dfrac{\pi^2}{L^2} D_{11}$	$1 - \cos\left(\dfrac{\pi x}{L}\right)$

Typical boundary conditions

Simply supported   Guided   Clamped   Free

Linear spring   Torsion spring
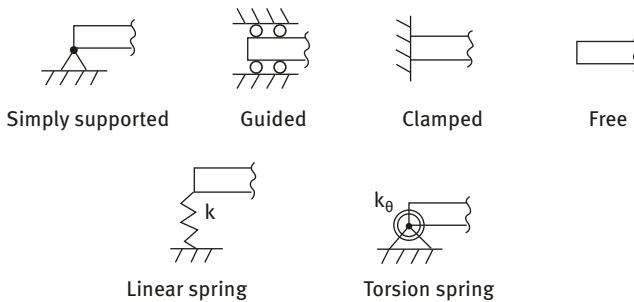
Fig. 6.5: Typical out-of-plane boundary conditions for laminated composite columns (and also isotropic columns) under axial compression.

Fig. 6.6: A typical laminated composite columns under axial compression having spring-based boundary conditions.[7]

where $\overline{D}_{11} \equiv D_{11} - \frac{B_{11}^2}{A_{11}}$ and k_1 and k_2 are linear springs, while $\overline{k}_{\theta_1}$ and $\overline{k}_{\theta_2}$ are torsion springs. The boundary conditions of the problem depicted in Fig. 6.6 are given by

$$\frac{d^3 w_{\rm b}(0)}{dx^3} + \lambda^2 \frac{d w_{\rm b}(0)}{dx} = -\overline{k}_1 \cdot w_{\rm b}(0) \quad \frac{d^2 w_{\rm b}(0)}{dx^2} = \overline{k}_{\theta_1} \frac{d w_{\rm b}(0)}{dx}$$

$$\frac{d^3 w_{\rm b}(L)}{dx^3} + \lambda^2 \frac{d w_{\rm b}(L)}{dx} = \overline{k}_2 \cdot w_{\rm b}(L) \quad \frac{d^2 w_{\rm b}(L)}{dx^2} = -\overline{k}_{\theta_2} \frac{d w_{\rm b}(L)}{dx}$$

$$(6.25)$$

Application of the boundary conditions to the general solution presented by eq. (6.19) yields the following characteristic equation (see details in [3]):

$$\left\{ -\left(\overline{k}_1 + \overline{k}_2\right)\lambda^6 + \left[\overline{k}_{\theta_1} \cdot \overline{k}_{\theta_2}\left(\overline{k}_1 + \overline{k}_2\right) + \overline{k}_1 \cdot \overline{k}_2 \cdot L\right]\lambda^4 + \overline{k}_{\theta_1} \cdot \overline{k}_{\theta_2}\left(\overline{k}_{\theta_1} + \overline{k}_{\theta_2} - \overline{k}_{\theta_1} \cdot \overline{k}_{\theta_2} \cdot L\right)\lambda^2 \right\} \sin(\lambda L)$$

$$+ \left\{ \left(\overline{k}_1 + \overline{k}_2\right)\left(\overline{k}_{\theta_1} + \overline{k}_{\theta_2}\right)\lambda^3 - \overline{k}_1 \cdot \overline{k}_2 \cdot L\left(\overline{k}_{\theta_1} + \overline{k}_{\theta_2}\right)\lambda^3 - 2 \cdot \overline{k}_1 \cdot \overline{k}_2 \cdot \overline{k}_{\theta_1} \cdot \overline{k}_{\theta_2} \cdot \lambda \right\} \cos(\lambda L)$$

$$+ \overline{k}_1 \cdot \overline{k}_2 \cdot \overline{k}_{\theta_1} \cdot \overline{k}_{\theta_2} \cdot \lambda = 0$$

$$(6.26)$$

Equation (6.26) can be used to solve not only problems involving boundary conditions with springs, but also classical boundary conditions. Letting the linear springs k_1 and k_2 tend to infinity (∞) while the torsional ones, $\overline{k}_{\theta_1}$ and $\overline{k}_{\theta_2}$, are set to zero, would lead to the classical hinged–hinged boundary conditions at both ends of the compressed beam. Similarly, setting all the springs to zero would yield free–free boundary conditions. Clamped boundary conditions can be obtained when both types of springs (linear and torsion) would tend to infinity.

6.2.3b Nonsymmetric laminate ($B_{11} \neq 0$)

To solve the case of a nonsymmetric laminate ($B_{11} \neq 0$), we can use eq. (6.15). The general solution can be written as

$$w_0(x) = C_1 \sin\left(\widehat{\lambda}x\right) + C_2 \cos\left(\widehat{\lambda}x\right) + C_3 x + C_4 \tag{6.27}$$

where

---

7 The drawing presented can also be suitable for a Bernoulli–Euler column.

$$\widehat{\lambda}^2 = \frac{\overline{N}_{xx}}{\left(D_{11} - \dfrac{B_{11}^2}{A_{11}}\right)} \tag{6.28}$$

The in-plane displacement will then be given as (see Appendix A)

$$u_0(x) = C_5 \sin\left(\widehat{\lambda}x\right) + C_6 \cos\left(\widehat{\lambda}x\right) + C_7 x + C_8 \tag{6.29}$$

where

$$
\begin{aligned}
C_5 &= -\frac{B_{11}}{A_{11}} \cdot \widehat{\lambda} \cdot C_2 \\
C_6 &= +\frac{B_{11}}{A_{11}} \cdot \widehat{\lambda} \cdot C_1
\end{aligned}
\tag{6.30}
$$

Solving for a hinged–hinged column (or pinned–pinned, or simply supported at both ends), with the following boundary conditions, two for the in-plane and four for the out-of-plane (see also Appendix A)

$$w_0(0) = 0; \quad M_{xx}(0) = 0 \quad \Rightarrow \quad -B_{11}\frac{du_0(0)}{dx} + D_{11}\frac{d^2w_0(0)}{dx^2} = 0 \tag{6.31}$$

$$w_0(L) = 0; \quad M_{xx}(L) = 0 \quad \Rightarrow \quad -B_{11}\frac{du_0(L)}{dx} + D_{11}\frac{d^2w_0(L)}{dx^2} = 0 \tag{6.32}$$

$$u_0(0) = 0 \tag{6.33}$$

$$A_{11}\frac{du_0(L)}{dx} - B_{11}\frac{d^2w_0(L)}{dx^2} = -\overline{N}_{xx} \tag{6.34}$$

yields the following eigenvalue:

$$\sin\left(\widehat{\lambda}L\right) = 0 \quad \Rightarrow \quad \widehat{\lambda}L = n\pi, \quad n = 1, 2, 3, 4, \ldots \tag{6.35}$$

which gives the critical buckling load per unit width having the following form:

$$\left(\overline{N}_{xx}\right)_{cr} = \frac{\pi^2}{L^2}\left(D_{11} - \frac{B_{11}^2}{A_{11}}\right) \tag{6.36}$$

The buckling shape will be like the symmetric case presented in Table 6.2, namely $\sin\left(\frac{\pi x}{L}\right)$. Note that as expected, the buckling load for a symmetric laminate will be higher than a nonsymmetric one, having the same number of layers. Tables 6.4 and 6.5 present the boundary conditions for the nonsymmetric case, while Table 6.6 gives the buckling loads and the associated buckling modes for the most used cases.

Table 6.4: Buckling of nonsymmetric laminated composite columns: out-of-plane boundary conditions using CLT approach.

No.	Name	Out-of-plane boundary conditions	
		$x = 0$	$x = L$
1	SS-SS[*]	$w_0 = 0$; $-B_{11}\dfrac{du_0}{dx} + D_{11}\dfrac{d^2 w_0}{dx^2} = 0$	$w_0 = 0$; $-B_{11}\dfrac{du_0}{dx} + D_{11}\dfrac{d^2 w_0}{dx^2} = 0$
2	C-C[**]	$w_0 = 0$; $\dfrac{dw_0}{dx} = 0$	$w_0 = 0$; $\dfrac{dw_0}{dx} = 0$
3	C-F[***]	$w_0 = 0$; $\dfrac{dw_0}{dx} = 0$	$-B_{11}\dfrac{du_0}{dx} + D_{11}\dfrac{d^2 w_0}{dx^2} = 0$ $-B_{11}\dfrac{d^2 u_0}{dx^2} + D_{11}\dfrac{d^3 w_0}{dx^3} + \overline{N}_{xx}\dfrac{dw_0}{dx} = 0$
4	F-F	$-B_{11}\dfrac{du_0}{dx} + D_{11}\dfrac{d^2 w_0}{dx^2} = 0$ $-B_{11}\dfrac{d^2 u_0}{dx^2} + D_{11}\dfrac{d^3 w_0}{dx^3} + \overline{N}_{xx}\dfrac{dw_0}{dx} = 0$	$-B_{11}\dfrac{du_0}{dx} + D_{11}\dfrac{d^2 w_0}{dx^2} = 0$ $-B_{11}\dfrac{d^2 u_0}{dx^2} + D_{11}\dfrac{d^3 w_0}{dx^3} + \overline{N}_{xx}\dfrac{dw_0}{dx} = 0$
5	SS-C	$w_0 = 0$ $-B_{11}\dfrac{du_0}{dx} + D_{11}\dfrac{d^2 w_0}{dx^2} = 0$	$w_0 = 0$; $\dfrac{dw_0}{dx} = 0$
6	SS-F	$w_0 = 0$; $-B_{11}\dfrac{du_0}{dx} + D_{11}\dfrac{d^2 w_0}{dx^2} = 0$	$-B_{11}\dfrac{du_0}{dx} + D_{11}\dfrac{d^2 w_0}{dx^2} = 0$ $-B_{11}\dfrac{d^2 u_0}{dx^2} + D_{11}\dfrac{d^3 w_0}{dx^3} + \overline{N}_{xx}\dfrac{dw_0}{dx} = 0$
7	G[***]-F	$\dfrac{dw_0}{dx} = 0$ $-B_{11}\dfrac{d^2 u_0}{dx^2} + D_{11}\dfrac{d^3 w_0}{dx^3} + \overline{N}_{xx}\dfrac{dw_0}{dx} = 0$	$-B_{11}\dfrac{du_0}{dx} + D_{11}\dfrac{d^2 w_0}{dx^2} = 0$ $-B_{11}\dfrac{d^2 u_0}{dx^2} + D_{11}\dfrac{d^3 w_0}{dx^3} + \overline{N}_{xx}\dfrac{dw_0}{dx} = 0$
8	G-SS	$\dfrac{dw_0}{dx} = 0$ $-B_{11}\dfrac{d^2 u_0}{dx^2} + D_{11}\dfrac{d^3 w_0}{dx^3} + \overline{N}_{xx}\dfrac{dw_0}{dx} = 0$	$w_0 = 0$; $-B_{11}\dfrac{du_0}{dx} + D_{11}\dfrac{d^2 w_0}{dx^2} = 0$
9	G-G	$\dfrac{dw_0}{dx} = 0$ $-B_{11}\dfrac{d^2 u_0}{dx^2} + D_{11}\dfrac{d^3 w_0}{dx^3} + \overline{N}_{xx}\dfrac{dw_0}{dx} = 0$	$\dfrac{dw_0}{dx} = 0$ $-B_{11}\dfrac{d^2 u_0}{dx^2} + D_{11}\dfrac{d^3 w_0}{dx^3} + \overline{N}_{xx}\dfrac{dw_0}{dx} = 0$
10	G-C	$\dfrac{dw_0}{dx} = 0$ $-B_{11}\dfrac{d^2 u_0}{dx^2} + D_{11}\dfrac{d^3 w_0}{dx^3} + \overline{N}_{xx}\dfrac{dw_0}{dx} = 0$	$w_0 = 0$; $\dfrac{dw_0}{dx} = 0$

[*]SS, simply supported, or hinged–hinged or pinned–pinned.
[**]C, clamped.
[***]F, free.
[***]G, guided.

Table 6.5: Buckling of nonsymmetric laminated composite columns: in-plane boundary conditions using CLT approach.

No.	Name	In-plane boundary conditions	
		$x = 0$	$x = L$
1	SS-SS	$u_0 = 0$	$A_{11}\dfrac{du_0}{dx} - B_{11}\dfrac{d^2w_0}{dx^2} = -\overline{N}_{xx}$
2	C-C	$u_0 = 0$	$A_{11}\dfrac{du_0}{dx} - B_{11}\dfrac{d^2w_0}{dx^2} = -\overline{N}_{xx}$
3	C-F	$u_0 = 0$	$A_{11}\dfrac{du_0}{dx} - B_{11}\dfrac{d^2w_0}{dx^2} = -\overline{N}_{xx}$
4	F-F	$A_{11}\dfrac{du_0}{dx} - B_{11}\dfrac{d^2w_0}{dx^2} = -\overline{N}_{xx}$	$A_{11}\dfrac{du_0}{dx} - B_{11}\dfrac{d^2w_0}{dx^2} = -\overline{N}_{xx}$
5	SS-C	$u_0 = 0$	$A_{11}\dfrac{du_0}{dx} - B_{11}\dfrac{d^2w_0}{dx^2} = -\overline{N}_{xx}$
6	SS-F	$u_0 = 0$	$A_{11}\dfrac{du_0}{dx} - B_{11}\dfrac{d^2w_0}{dx^2} = -\overline{N}_{xx}$
7	G-F	$u_0 = 0$	$A_{11}\dfrac{du_0}{dx} - B_{11}\dfrac{d^2w_0}{dx^2} = -\overline{N}_{xx}$
8	G-SS	$u_0 = 0$	$A_{11}\dfrac{du_0}{dx} - B_{11}\dfrac{d^2w_0}{dx^2} = -\overline{N}_{xx}$
9	G-G	$u_0 = 0$	$A_{11}\dfrac{du_0}{dx} - B_{11}\dfrac{d^2w_0}{dx^2} = -\overline{N}_{xx}$
10	G-C	$u_0 = 0$	$A_{11}\dfrac{du_0}{dx} - B_{11}\dfrac{d^2w_0}{dx^2} = -\overline{N}_{xx}$

6.3 Buckling of columns – FSDT approach

Buckling of columns using the first-order shear deformation theory (FSDT) (see also [2, 5, 8–19]) can be obtained using the equations presented in Chapter 2[8]:

$$A_{11}\left(\frac{d^2u_0}{dx^2} + \frac{d^3w_b}{dx^3}\right) + B_{11}\frac{d^2\phi_x}{dx^2} = 0 \tag{6.37}$$

$$KA_{55}\left(\frac{d^2w_b}{dx^2} + \frac{d\phi_x}{dx}\right) - \overline{N}_{xx}\frac{d^2w_b}{dx^2} = 0 \tag{6.38}$$

$$B_{11}\left(\frac{d^2u_0}{dx^2} + \frac{\partial^3w_b}{dx^3}\right) + D_{11}\frac{d^2\phi_x}{dx^2} - KA_{55}\left(\frac{dw_b}{dx} + \phi_x\right) = 0 \tag{6.39}$$

---

8 $w_0 = w_0^{\mathrm{p}} + w_b$ (w_0^{p} is the prebuckling deflection and w_b being the buckling deflection).

Table 6.6: Buckling loads and relevant buckling modes of laminated composite columns using CLT approach.

No.	Name	Characteristic equation	Critical buckling load per unit width	Mode shape
1	SS-SS	$\sin(\hat{\lambda}L) = 0; \quad \hat{\lambda}L = n\pi$	$(\bar{N}_{xx})_{cr} = \dfrac{\pi^2}{L^2}\bar{D}_{11}$ *	$\sin\left(\dfrac{\pi x}{L}\right)$
2	C-C	$\hat{\lambda}L\sin(\hat{\lambda}L) = 2\left[1 - \cos(\hat{\lambda}L)\right]$ $\hat{\lambda}L = 2\pi, 8.987, 4\pi,..$	$(\bar{N}_{xx})_{cr} = 4\dfrac{\pi^2}{L^2}\bar{D}_{11}$	$1 - \cos\left(\dfrac{2\pi x}{L}\right)$
3	C-F	$\cos(\hat{\lambda}L) = 0 \quad \hat{\lambda}L = (2n-1)\dfrac{\pi}{2}$	$(\bar{N}_{xx})_{cr} = \dfrac{\pi^2}{4L^2}\bar{D}_{11}$	$1 - \cos\left(\dfrac{\pi x}{2L}\right)$
4	F-F	$\sin(\hat{\lambda}L) = 0; \quad \hat{\lambda}L = n\pi$	$(\bar{N}_{xx})_{cr} = \dfrac{\pi^2}{L^2}\bar{D}_{11}$	$\sin\left(\dfrac{\pi x}{L}\right)$
5	SS-C	$\tan(\hat{\lambda}L) = \hat{\lambda}L$ $\hat{\lambda}L = 1.430\pi, 2.459\pi, \ldots$	$(\bar{N}_{xx})_{cr} = 2.045\dfrac{\pi^2}{L^2}\bar{D}_{11}$	$\sin(\alpha x) + \alpha L\left[1 - \cos(\alpha x)\right] - \dfrac{x}{L}$ while $\quad \alpha = 1.4318\dfrac{\pi}{L}$
6	SS-F	$\sin(\hat{\lambda}L) = 0$ $\hat{\lambda}L = n\pi$	$(\bar{N}_{xx})_{cr} = \dfrac{\pi^2}{L^2}\bar{D}_{11}$	$\sin\left(\dfrac{\pi x}{L}\right)$
7	G-F	$\cos(\hat{\lambda}L) = 0; \quad \hat{\lambda}L = (2n-1)\dfrac{\pi}{2}$	$(\bar{N}_{xx})_{cr} = \dfrac{\pi^2}{4L^2}\bar{D}_{11}$	$\cos\left(\dfrac{\pi x}{2L}\right)$
8	G-SS	$\cos(\hat{\lambda}L) = 0 \quad \hat{\lambda}L = (2n-1)\pi/2$	$(\bar{N}_{xx})_{cr} = \dfrac{\pi^2}{4L^2}\bar{D}_{11}$	$\cos\left(\dfrac{\pi x}{2L}\right)$
9	G-G	$\sin(\hat{\lambda}L) = 0$ $\hat{\lambda}L = n\pi$	$(\bar{N}_{xx})_{cr} = \dfrac{\pi^2}{L^2}\bar{D}_{11}$	$\cos\left(\dfrac{\pi x}{L}\right)$
10	G-C	$\sin(\hat{\lambda}L) = 0$ $\hat{\lambda}L = n\pi$	$(\bar{N}_{xx})_{cr} = \dfrac{\pi^2}{L^2}\bar{D}_{11}$	$1 - \cos\left(\dfrac{\pi x}{L}\right)$

$^*\bar{D}_{11} = \left(D_{11} - \dfrac{B_{11}^2}{A_{11}}\right)$.

Decoupling the equations leads to the following uncoupled ones[9] (see also [12, 13]):

$$\frac{d^4 w_b}{dx^4} + \Gamma^2 \frac{d^2 w_b}{dx^2} = 0 \tag{6.40}$$

$$\frac{d^3 \phi_x}{dx^3} + \Gamma^2 \frac{d^2 \phi_x}{dx} = 0 \tag{6.41}$$

$$\frac{d^4 u_0}{dx^4} + \Gamma^2 \frac{d^2 u_0}{dx^2} = 0 \tag{6.42}$$

where

$$\Gamma^2 = \frac{\overline{N}_{xx}}{\left(D_{11} - \frac{B_{11}^2}{A_{11}} \right) \left(1 - \frac{\overline{N}_{xx}}{KA_{55}} \right)} \quad \Rightarrow \quad \overline{N}_{xx} = \frac{\Gamma^2 \left(D_{11} - \frac{B_{11}^2}{A_{11}} \right)}{1 + \frac{\Gamma^2 \left(D_{11} - \frac{B_{11}^2}{A_{11}} \right)}{KA_{55}}} \tag{6.43}$$

Accordingly, the solutions for eqs. (6.40)–(6.42) have a form similar to that presented before, namely

$$w_b(x) = C_1 \sin(\Gamma x) + C_2 \cos(\Gamma x) + C_3 x + C_4 \tag{6.44}$$

$$\phi_x(x) = C_5 \sin(\Gamma x) + C_6 \cos(\Gamma x) + C_7 \tag{6.45}$$

$$u_0(x) = C_8 \sin(\Gamma x) + C_9 \cos(\Gamma x) + C_{10} x + C_{11} \tag{6.46}$$

One should note that the 11 constants (C_1–C_{11}) are not independent. Their dependency can be obtained by back-substituting the solutions (eqs. (6.44)–(6.46)) in the coupled equations (6.37) and (6.39) to yield the following five relations:

$$A_{11} \cdot C_8 + B_{11} \cdot C_5 = 0 \tag{6.47}$$

$$A_{11} \cdot C_9 + B_{11} \cdot C_6 = 0 \tag{6.48}$$

$$- B_{11} \cdot C_8 \cdot \hat{\lambda}^2 - D_{11} \cdot C_5 \cdot \hat{\lambda}^2 - KA_{55} \left(- C_2 \cdot \hat{\lambda} + C_5 \right) = 0 \tag{6.49}$$

$$- B_{11} \cdot C_9 \cdot \hat{\lambda}^2 - D_{11} \cdot C_6 \cdot \hat{\lambda}^2 - KA_{55} \left(C_1 \cdot \hat{\lambda} + C_6 \right) = 0 \tag{6.50}$$

$$- KA_{55} \cdot (C_3 + C_7) = 0 \quad \Rightarrow \quad C_3 + C_7 = 0 \tag{6.51}$$

These five relationships together with the six boundary conditions of the problem will provide the needed 11 equations with 11 unknowns, C_1–C_{11}. The six boundary conditions of the problem are (see also Chapter 2):

---

9 Note that to uncouple the equations one needs to neglect high-order terms like $\frac{d^3 w_b}{dx^3}$.

$$A_{11}\frac{du_0}{dx} + B_{11}\frac{d\phi_x}{dx} = -\overline{N}_{xx} \quad \text{or} \quad u_0 = 0 \tag{6.52}$$

$$KA_{55}\left(\frac{dw_b}{dx} + \phi_x\right) - \overline{N}_{xx}\frac{dw_b}{dx} = 0 \quad \text{or} \quad w_b = 0 \tag{6.53}$$

$$B_{11}\frac{du_0}{dx} + D_{11}\frac{d\phi_x}{dx} = 0 \quad \text{or} \quad \phi_x = 0 \tag{6.54}$$

Let us present the general case of a simply-supported laminated composite beam having the following boundary conditions:

$$u_0(0) = 0, \quad A_{11}\frac{du_0(L)}{dx} + B_{11}\frac{d\phi_x(L)}{dx} = -\overline{N}_{xx} \tag{6.55}$$

$$w_b(0) = 0, \quad w_b(L) = 0 \tag{6.56}$$

$$B_{11}\frac{du_0(0)}{dx} + D_{11}\frac{d\phi_x(0)}{dx} = 0, \quad B_{11}\frac{du_0(L)}{dx} + D_{11}\frac{d\phi_x(L)}{dx} = 0 \tag{6.57}$$

Solving for the 11 unknowns, C_1–C_{11}, we get the following results for the first four constants:

$$C_1 = \frac{B_{11}}{A_{11}}\frac{[1 - \cos(\Gamma L)]}{\sin(\Gamma L)}, \quad C_2 = \frac{B_{11}}{A_{11}}, \quad C_3 = 0, \quad C_4 = -\frac{B_{11}}{A_{11}}. \tag{6.58}$$

To obtain the buckling load, one should demand that $w_0(x) \to \infty$, leading to the same procedure applied for a general beam using the CLT approach. Observe that the constant C_1 leads to the following eigenvalue solution:

$$\sin(\Gamma L) = 0 \quad \Rightarrow \quad \Gamma L = n\pi, \quad n = 1, 2, 3, 4, \ldots \tag{6.59}$$

which leads to the critical buckling load per unit width having the following form:

$$(\overline{N}_{xx})_{cr} = \frac{\left(\frac{\pi}{L}\right)^2\left(D_{11} - \frac{B_{11}^2}{A_{11}}\right)}{1 + \frac{\left(\frac{\pi}{L}\right)^2\left(D_{11} - \frac{B_{11}^2}{A_{11}}\right)}{KA_{55}}} = \frac{\left[(\overline{N}_{xx})_{cr}\right]_{CLT}}{1 + \frac{\left[(\overline{N}_{xx})_{cr}\right]_{CLT}}{KA_{55}}} \tag{6.60}$$

If one defines the following term:

$$H \equiv \frac{\left[(\overline{N}_{xx})_{cr}\right]_{CLT}}{KA_{55}} \tag{6.61}$$

then eq. (6.60) can be written as

$$(\overline{N}_{xx})_{cr} = \frac{\left[(\overline{N}_{xx})_{cr}\right]_{CLT}}{1 + H} \tag{6.62}$$

The shape of the buckling will be $\sin\left(\frac{\pi x}{L}\right)$ like for the symmetric case, calculated using the CLT approach. One should notice that the buckling load calculated using FSDT approach is lower than the one calculated according to CLT. Like before, a nonsymmetric laminate would yield a even lower buckling load as compared with a symmetric one having the same layers. Some typical buckling loads are presented in Table 6.7.

Table 6.7: Buckling loads and relevant buckling modes of laminated composite columns using FSDT approach.

No.	Name	$\left[(\bar{N}_{xx})_{cr}\right]_{CLT}$	Critical buckling load per unit width	Mode shape
1	SS-SS	$(\bar{N}_{xx})_{cr} = \dfrac{\pi^2}{L^2}\bar{D}_{11}$ *	$(\bar{N}_{xx})_{cr} = \dfrac{\left[(\bar{N}_{xx})_{cr}\right]_{CLT}{}^{**}}{1+H}$	$\sin\left(\dfrac{\pi x}{L}\right)$
2	C-C	$(\bar{N}_{xx})_{cr} = 4\dfrac{\pi^2}{L^2}\bar{D}_{11}$	$(\bar{N}_{xx})_{cr} = \dfrac{\left[(\bar{N}_{xx})_{cr}\right]_{CLT}}{1+H}$	$1 - \cos\left(\dfrac{2\pi x}{L}\right)$
3	C-F	$(\bar{N}_{xx})_{cr} = \dfrac{\pi^2}{4L^2}\bar{D}_{11}$	$(\bar{N}_{xx})_{cr} = \dfrac{\left[(\bar{N}_{xx})_{cr}\right]_{CLT}}{1+H}$	$1 - \cos\left(\dfrac{\pi x}{2L}\right)$
4	F-F	$(\bar{N}_{xx})_{cr} = \dfrac{\pi^2}{L^2}\bar{D}_{11}$	$(\bar{N}_{xx})_{cr} = \dfrac{\left[(\bar{N}_{xx})_{cr}\right]_{CLT}}{1+H}$	$\sin\left(\dfrac{\pi x}{L}\right)$
5	SS-C	$(\bar{N}_{xx})_{cr} = 2.045\dfrac{\pi^2}{L^2}\bar{D}_{11}$	$(\bar{N}_{xx})_{cr} = \dfrac{\left[(\bar{N}_{xx})_{cr}\right]_{CLT}}{1+H}$	$\sin(\alpha x) + \alpha L\left[1 - \cos(\alpha x) - \dfrac{x}{L}\right]$ while $\quad \alpha = 1.4318\dfrac{\pi}{L}$
6	SS-F	$(\bar{N}_{xx})_{cr} = \dfrac{\pi^2}{L^2}\bar{D}_{11}$	$(\bar{N}_{xx})_{cr} = \dfrac{\left[(\bar{N}_{xx})_{cr}\right]_{CLT}}{1+H}$	$\sin\left(\dfrac{\pi x}{L}\right)$
7	G-F	$(\bar{N}_{xx})_{cr} = \dfrac{\pi^2}{4L^2}\bar{D}_{11}$	$(\bar{N}_{xx})_{cr} = \dfrac{\left[(\bar{N}_{xx})_{cr}\right]_{CLT}}{1+H}$	$\cos\left(\dfrac{\pi x}{2L}\right)$
8	G-SS	$(\bar{N}_{xx})_{cr} = \dfrac{\pi^2}{4L^2}\bar{D}_{11}$	$(\bar{N}_{xx})_{cr} = \dfrac{\left[(\bar{N}_{xx})_{cr}\right]_{CLT}}{1+H}$	$\cos\left(\dfrac{\pi x}{2L}\right)$
9	G-G	$(\bar{N}_{xx})_{cr} = \dfrac{\pi^2}{L^2}\bar{D}_{11}$	$(\bar{N}_{xx})_{cr} = \dfrac{\left[(\bar{N}_{xx})_{cr}\right]_{CLT}}{1+H}$	$\cos\left(\dfrac{\pi x}{L}\right)$
10	G-C	$(\bar{N}_{xx})_{cr} = \dfrac{\pi^2}{L^2}\bar{D}_{11}$	$(\bar{N}_{xx})_{cr} = \dfrac{\left[(\bar{N}_{xx})_{cr}\right]_{CLT}}{1+H}$	$1 - \cos\left(\dfrac{\pi x}{L}\right)$

* $\bar{D}_{11} = \left(D_{11} - \dfrac{B_{11}^2}{A_{11}}\right)$, ** $H \equiv \dfrac{\left[(\bar{N}_{xx})_{cr}\right]_{CLT}}{K A_{55}}$.

6.4 Buckling of plates

In contrast to the previous sections, which were dealing with a 1D structure, like columns or beams, plates are considered to be 2D entities, with the third dimension, the thickness, being much smaller than the other planar dimensions. Although the issue of stability of plates had been treated intensively in the literature (see for example [1, 4, 5, 20–37]) few closed-form solutions are available. Most of the buckling solutions are based on approximate methods, like Rayleigh–Ritz, Galerkin–Bubnov or extended Kantorovich methods (which will be presented in this chapter).

6.4.1 Buckling of isotropic plates

The results for isotropic plates to be presented in this section are based on the seminal work of Timoshenko and Gere [1]. The equation of motion for a thin isotropic plate (thickness, h) under in-plane loads (assuming the plate has some initial curvature due to those loads) is given by the following expression:

$$\frac{\partial^4 w(x,y)}{\partial x^4} + 2\frac{\partial^4 w(x,y)}{\partial x^2 \partial y^2} + \frac{\partial^4 w(x,y)}{\partial y^4} = \frac{1}{D}\left(N_x \frac{\partial^2 w(x,y)}{\partial x^2} + 2N_{xy}\frac{\partial^2 w(x,y)}{\partial x \partial y} + N_y \frac{\partial^2 w(x,y)}{\partial y^2}\right)$$
(6.63)

where N_x and N_y are compressive loads per unit length in the x and y directions of the plate (acting at the midplane), N_{xy} is the shear load per unit length and $D = \frac{Eh^3}{12(1-v^2)}$ is the bending rigidity of the plate, while E and v are its Young's modulus and Poisson's ratio, respectively.

Let us present the solution for simply-supported boundary conditions around all four sides of a thin plate having the length a, width b and thickness h, subjected to in-plane compression load N_x, while $N_y = N_{xy} = 0$, also known as the Navier method.[10] The out-of-plane displacement can be assumed to be

$$w(x,y) = \sum_{m=1}^{\infty}\sum_{n=1}^{\infty} \sin\frac{m\pi}{a}\sin\frac{n\pi}{b}$$
(6.64)

Note that the double series, representing the lateral deflection, satisfy both eq. (6.63) and the boundary conditions of the case, namely

$$w_0(x,0) = 0, \quad w_0(x,b) = 0, \quad w_0(0,y) = 0, \quad w_0(a,y) = 0$$
$$M_{xx}(0,y) = 0, \quad M_{xx}(a,y) = 0, \quad M_{yy}(x,0) = 0, \quad M_{yy}(x,b) = 0$$
(6.65)

---

10 Claude-Louis Navier (1785–1836).

where

$$M_{xx} = -D\left[\frac{\partial^2 w}{\partial x^2} + v\frac{\partial^2 w}{\partial y^2}\right], \quad M_{yy} = -D\left[\frac{\partial^2 w}{\partial y^2} + v\frac{\partial^2 w}{\partial x^2}\right] \tag{6.66}$$

Substituting eq. (6.64) into eq. (6.63) leads to the following expression:

$$N_x = \frac{\pi^2 a^2}{m^2}D\left[\left(\frac{m}{a}\right)^2 + \left(\frac{n}{b}\right)^2\right]^2 \tag{6.67}$$

To obtain the critical load, one should find the smallest value of N_x in eq. (6.67), which is easy to see that it will happen for $n = 1$, namely half-wave in the width direction (perpendicular do the applied in-plane load N_x). Therefore, the critical buckling load can be written as

$$(N_x)_{cr} = \frac{\pi^2}{m^2 b^2}D\left[\left(\frac{b}{a}\right)m^2 + \left(\frac{a}{b}\right)\right]^2 = k\frac{\pi^2}{b^2}D$$

$$k \equiv \frac{1}{m^2}\left[\left(\frac{b}{a}\right)m^2 + \left(\frac{a}{b}\right)\right]^2 \tag{6.68}$$

The variation of k with the aspect ratio a/b and the number of half-waves in the longitudinal direction, m, is presented in Fig. 6.7. The minimal value of k is 4, and it occurs at an integer value of the aspect ratio, a/b, with the critical buckling waves following the aspect ratio, in the longitudinal direction.
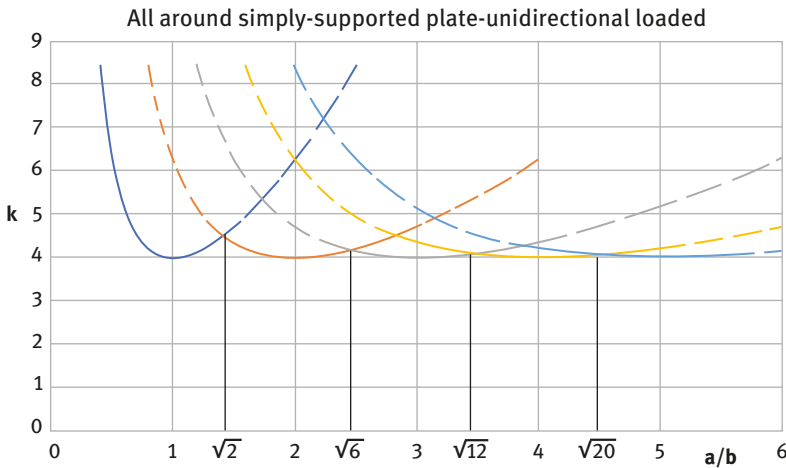

Fig. 6.7: All-around simply-supported thin plate loaded in the longitudinal direction – buckling factor, k, versus aspect ratio, a/b.

Other cases of interest would include plates with two opposite sides on simply-supported boundary conditions, while the other two sides have any combination of boundary conditions, with the axial compression load being applied on the simply-supported edges, also known as the Lévy method.[11] The general solution has the following form [1]:

$$w(x,y) = \sin\frac{m\pi}{a}[A_1 e^{-\alpha y} + A_2 e^{\alpha y} + A_3 \cos(\beta y) + A_4 \sin(\beta y)]$$

where

$$\alpha \equiv \sqrt{\left(\frac{m\pi}{a}\right)^2 + \sqrt{\frac{N_x}{D}\left(\frac{m\pi}{a}\right)^2}}, \quad \beta \equiv \sqrt{-\left(\frac{m\pi}{a}\right)^2 + \sqrt{\frac{N_x}{D}\left(\frac{m\pi}{a}\right)^2}}$$

(6.69)

The constants A_1–A_4 are to be determined by the application of proper boundary conditions, leading to the eigenvalue problem, which determines the critical buckling load (per unit width). Typical boundary condition for the unloaded edges of the plate are next given for clamped–clamped and free–free cases.

a. Clamped–clamped

$$w(x,0) = 0, \quad \frac{\partial w(x,0)}{\partial x} = 0, \quad w(x,b) = 0, \quad \frac{\partial w(x,0)}{\partial x} = 0 \qquad (6.70)$$

b. Free–free

$$\frac{\partial^2 w(x,0)}{\partial y^2} + v\frac{\partial^2 w(x,0)}{\partial x^2} = 0, \quad \frac{\partial^3 w(x,0)}{\partial y^3} + (2-v)\frac{\partial^3 w(x,0)}{\partial x^2 \partial y} = 0$$

$$\frac{\partial^2 w(x,b)}{\partial y^2} + v\frac{\partial^2 w(x,b)}{\partial x^2} = 0, \quad \frac{\partial^3 w(x,b)}{\partial y^3} + (2-v)\frac{\partial^3 w(x,b)}{\partial x^2 \partial y} = 0$$

(6.71)

Typical results for the common boundary conditions are presented in Fig. 6.8 (adopted from [38]).

Timoshenko and Gere [1] presented an expression for the case E (see Fig. 6.8) for long plates, having the following form:

$$k_c = 0.456 + \left(\frac{b}{a}\right)^2 \qquad (6.72)$$

More details about the buckling of flat isotropic plates, involving other in-plane loadings, bending and buckling of plates having elastic boundary conditions can be found in [1, 38].

---

11 Maurice Lévy (1838–1910), Comptes Rendus, vol. 129, 1899, pp. 535–539.
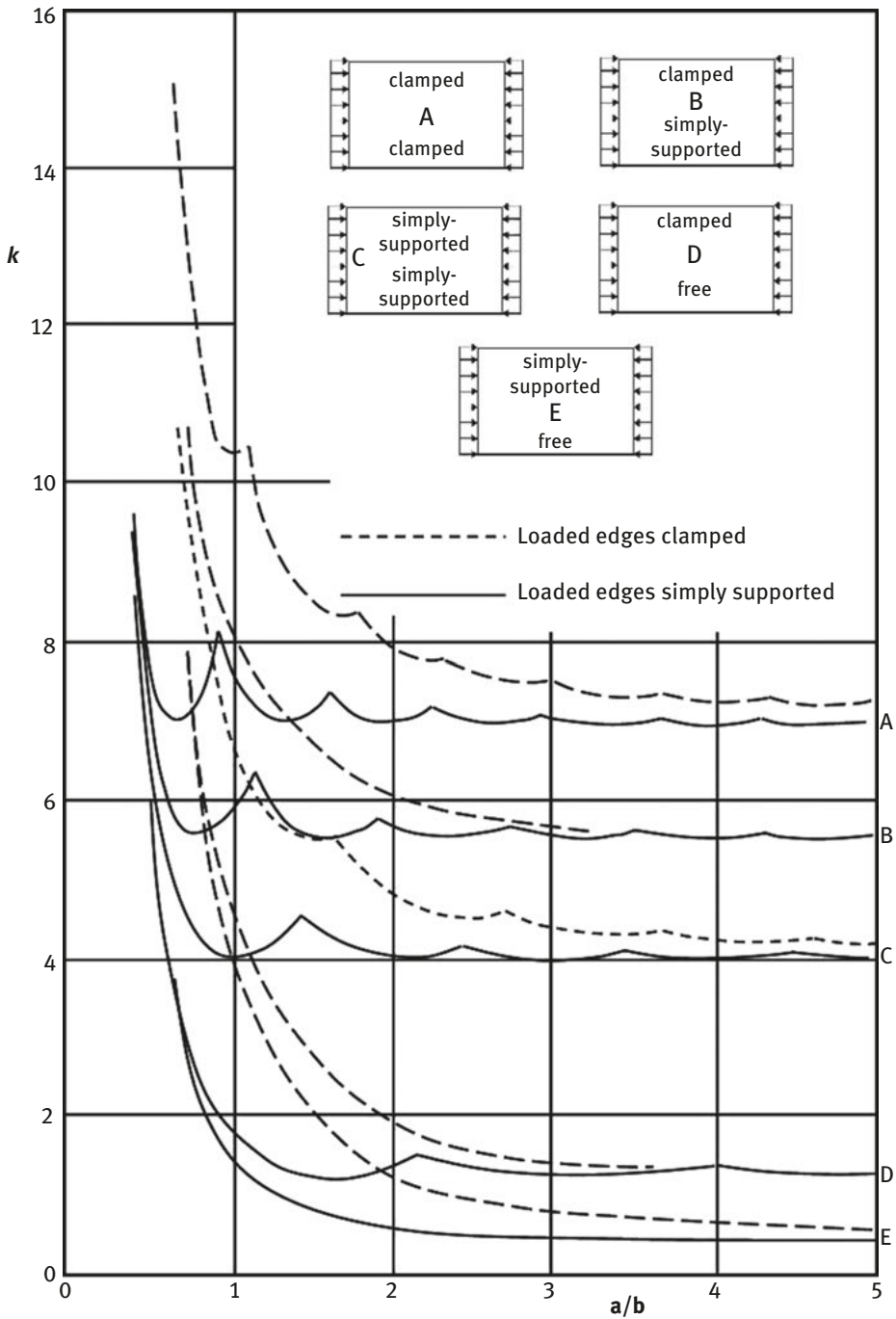
Fig. 6.8: Rectangular thin plates loaded in the longitudinal direction – buckling factor, *k*, versus aspect ratio, *a/b*, for various boundary conditions (adapted from [38]).

To conclude this section, we shall present the case of a rectangular flat isotropic plate under pure shear ($N_x = N_y = 0$, $N_{xy} \neq 0$), which was treated in [1, 38–42]. The equation of motion for this case is given by

$$\frac{\partial^4 w(x,y)}{\partial x^4} + 2\frac{\partial^4 w(x,y)}{\partial x^2 \partial y^2} + \frac{\partial^4 w(x,y)}{\partial y^4} = \frac{2N_{xy}}{D}\frac{\partial^2 w(x,y)}{\partial x \partial y} \tag{6.73}$$

Due to the mixed derivation on the right-hand side of eq. (6.73), no trigonometric solution for the deflection, w, is possible. The approximate solutions had been obtained using energy methods [1, 40]. Figure 6.9 presents the buckling coefficient, k_s, for a rectangular flat plate resting on simply-supported boundary conditions under shear stresses along its perimeter.

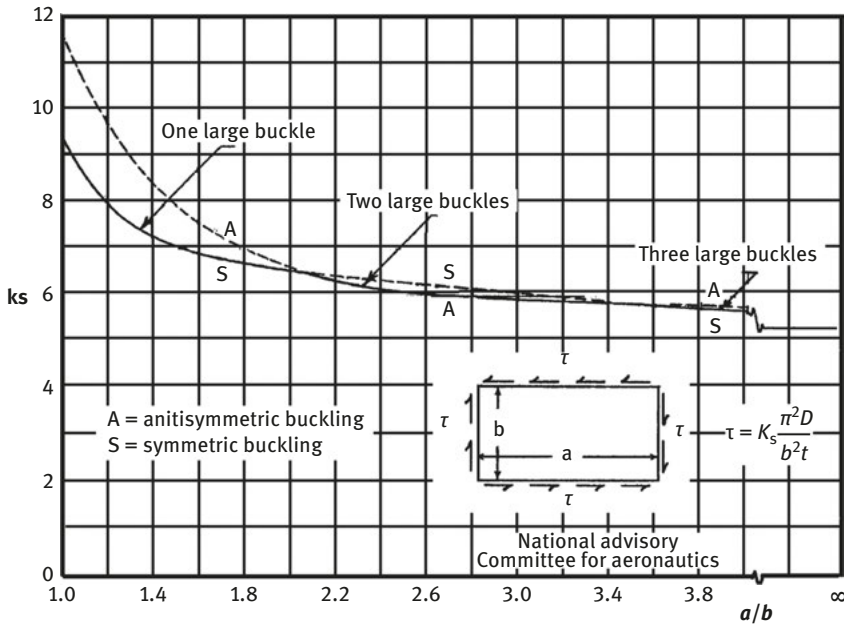**Fig. 6.9:** Rectangular thin plates loaded in pure shear-buckling factor, k, versus aspect ratio, a/b, for simply-supported boundary conditions (adapted from [40]).

From Fig. 6.9 one can obtain the buckling coefficient for infinitely long flat plates on simply-supported boundary conditions to yield

$$(\tau_{cr})_{SS} = k_s \frac{\pi^2 D}{b^2 h} = 5.35\frac{\pi^2 D}{b^2 h} \tag{6.74}$$

A similar expression is presented in [1] for infinitely long flat plates on clamped boundary conditions, namely

$$(\tau_{cr})_{clamped} = k_s \frac{\pi^2 D}{b^2 h} = 8.98 \frac{\pi^2 D}{b^2 h} \tag{6.75}$$

In the same reference [1], a general expression for the shear buckling coefficient, k_s, is presented for rectangular plates on simply-supported boundary conditions, starting with a $a/b = 1$ up to long infinite one, $a/b \to \infty$,

$$k_s = 5.35 + 4 \left(\frac{b}{a}\right)^2 \tag{6.76}$$

6.4.2 Buckling of orthotropic plates

Finding the buckling of orthotropic plates is more complicated as compared to the isotropic case and only few closed-form solutions are available for certain boundary conditions and layups. Other rigorous plate solutions can be found based on the Navier method, which treats rectangular plates on simply-supported boundary conditions all around it or the Lévy method suitable for plates with two opposite simply-supported edges, while the other two can have any combination of boundary conditions. Approximate solutions can be obtained using Rayleigh–Ritz, Galerkin-Bubnov or extended Kantorovich methods, all being based on energy approaches.

The first case to be presented is also called *special orthotropic plates* for which the bending–stretching coupling terms B_{ij} and the bending–twisting coefficients D_{16} and D_{26} are set to zero. This leads to the following equation, assuming constant in-plane compressive loads per unit width in the x and y directions, $\overline{N}_{xx}$ and $\overline{N}_{yy}$, respectively, and shear loads $\overline{N}_{xy}$:

$$D_{11} \frac{\partial^4 w_0}{\partial x^4} + 2(D_{12} + 2D_{66}) \frac{\partial^4 w_0}{\partial x^2 \partial y^2} + D_{22} \frac{\partial^4 w_0}{\partial y^4} = \overline{N}_{xx} \frac{\partial^2 w_0}{\partial x^2} + 2\overline{N}_{xy} \frac{\partial^2 w_0}{\partial x \partial y} + \overline{N}_{yy} \frac{\partial^2 w_0}{\partial y^2} \tag{6.77}$$

Note that the simply-supported boundary conditions presented in eq. (6.65), for the isotropic case, still hold; however, the expressions for the moments per unit width are for the orthotropic case:

$$M_{xx} = -\left[D_{11} \frac{\partial^2 w_0}{\partial x^2} + D_{12} \frac{\partial^2 w_0}{\partial y^2}\right], \quad M_{yy} = -\left[D_{12} \frac{\partial^2 w_0}{\partial x^2} + D_{22} \frac{\partial^2 w_0}{\partial y^2}\right], \quad M_{xy} = -2D_{66} \frac{\partial^2 w_0}{\partial x \partial y} \tag{6.78}$$

For the clamped boundary conditions along the plate's perimeter, eq. (6.70) presented for the isotropic case is valid also for the present orthotropic case. The issue

of free boundary conditions on all four sides of the plate, presented in eq. (6.71) for the isotropic case, is somehow more complicated and is presented as

$$M_{xx}(0, y) = 0, \quad M_{xx}(a, y) = 0, \quad M_{yy}(x, 0) = 0, \quad M_{yy}(x, b) = 0$$
$$V_y(0, y) = 0, \quad V_y(a, y) = 0, \quad V_x(x, 0) = 0, \quad V_y(x, b) = 0$$
(6.79)

where

$$V_x = \frac{\partial M_{xx}}{\partial x} + \frac{\partial M_{xy}}{\partial y} + \frac{\partial}{\partial x}\left(\overline{N}_{xy}\frac{\partial w_0}{\partial y} - \overline{N}_{xx}\frac{\partial w_0}{\partial x}\right) + \frac{\partial M_{xy}}{\partial y}$$
$$V_y = \frac{\partial M_{yy}}{\partial y} + \frac{\partial M_{xy}}{\partial x} + \frac{\partial}{\partial y}\left(\overline{N}_{xy}\frac{\partial w_0}{\partial x} - \overline{N}_{yy}\frac{\partial w_0}{\partial y}\right) + \frac{\partial M_{xy}}{\partial x}$$
(6.80)

Solving eq. (6.77) for a rectangular plate loaded in the x direction only ($\overline{N}_{xy} = \overline{N}_{yy} = 0$) for all-around simply-supported boundary conditions (eqs. (6.65) and (6.78)), which can be shown to be simplified yielding the following expressions:

$$w_0(x, 0) = \frac{\partial^2 w_0(x, 0)}{\partial x^2} = 0, \quad w_0(x, b) = \frac{\partial^2 w_0(x, b)}{\partial x^2} = 0$$
$$w_0(0, y) = \frac{\partial^2 w_0(0, y)}{\partial y^2} = 0, \quad w_0(a, y) = \frac{\partial^2 w_0(a, y)}{\partial y^2} = 0$$
(6.81)

and substituting the following out-of-plane deflection w_0, which satisfies the boundary conditions (eq. (6.81)), into eq. (6.77)

$$w_0 = A_{mn} \sin\frac{m\pi x}{a} \sin\frac{n\pi y}{b}, \quad m, n = 1, 2, 3, \ldots$$
(6.82)

where A_{mn} is a small arbitrary amplitude coefficient, which yields the following critical load per unit width (b being the width of the plate)

$$(\overline{N}_{xx})_{cr} = \pi^2\left[D_{11}\left(\frac{m}{a}\right)^2 + 2(D_{12} + 2D_{66})\left(\frac{n}{b}\right)^2 + D_{22}\left(\frac{n}{b}\right)^4\left(\frac{a}{m}\right)^2\right]$$
(6.83)

Equation (6.83) is a function of both m and n, which are the number of half-waves in the x and y directions, respectively. It is clearly that the minimum can be obtained for $n = 1$. Rearranging eq. (6.83) leads to the following expression:

$$\frac{K_x}{\pi^2} \equiv \frac{\overline{N}_{xx} \cdot b^2}{\pi^2 D_{22}} = \left[\frac{D_{11}}{D_{22}}\left(\frac{b}{a}\right)^2 m^2 + 2\left(\frac{D_{12}}{D_{22}} + 2\frac{D_{66}}{D_{22}}\right) + \left(\frac{a}{b}\right)^2\frac{1}{m^2}\right]$$
(6.84)

Equation (6.84) enables to find the lowest values for K_x as a function of the aspect ratio a/b and m for given values of D_{11}, D_{22}, D_{12} and D_{66}. Figure 6.10 presents the behavior of eq. (6.84) for three values of D_{11}/D_{22} assuming $(D_{12} + 2D_{66})/D_{22} = 1$. Similar curves would be achieved for other values of those parameters.
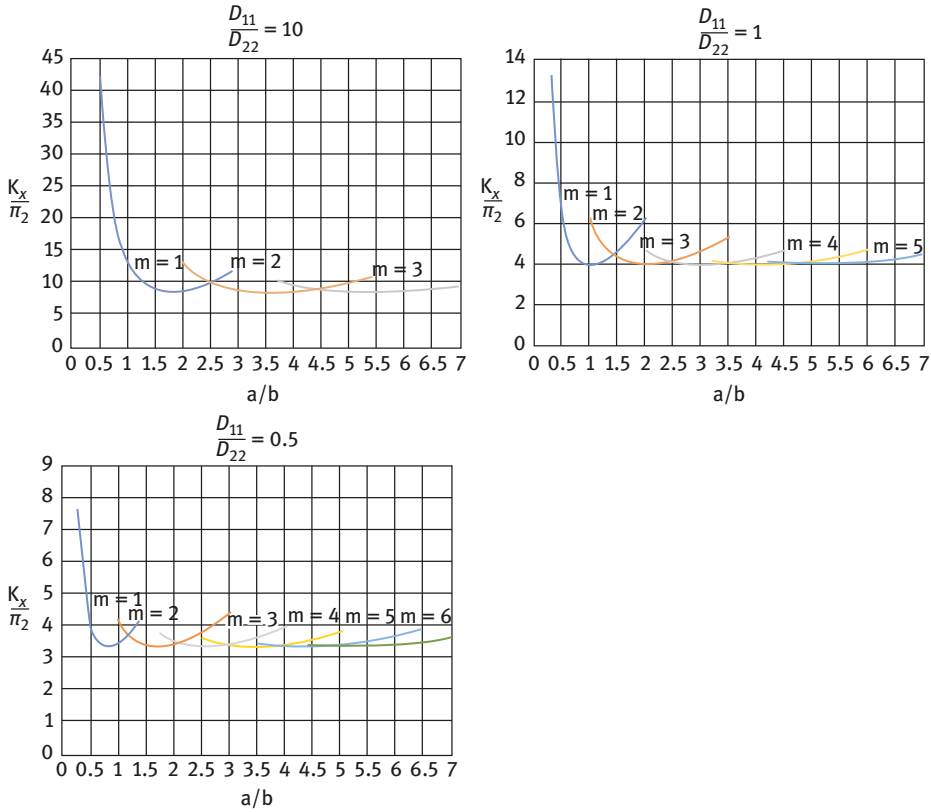
Fig. 6.10: Uniaxial buckling of a rectangular special orthotropic plate simply supported on all its sides for three values of D_{11}/D_{22} while $(D_{12} + 2D_{66})/D_{22} = 1$.

One should note that the minimum value for each curve generated by eq. (6.84) is found for a certain aspect ratio thus obtaining $(K_x/\pi^2)_{min}$

$$\frac{a}{b} = m \cdot \sqrt[4]{\frac{D_{11}}{D_{22}}} \Rightarrow \left(\frac{K_x}{\pi^2}\right)_{min} = 2\left(\sqrt{\frac{D_{11}}{D_{22}}} + \frac{D_{12}}{D_{22}} + 2\frac{D_{66}}{D_{22}}\right) \qquad (6.85)$$

The biaxial case, where only in-plane compressive forces $(\overline{N}_{xy} = 0)$ are applied in the x and y directions of an all-around simply-supported plate can also be solved, provided one can write $\kappa \equiv \overline{N}_{yy}/\overline{N}_{xx}$ (the y compression load is proportional to the x compression load). Then using eqs. (6.77) and (6.82) one obtains the expression for the critical buckling load, as

$$(\overline{N}_{xx})_{cr} = \pi^2 \frac{\left[D_{11}\left(\frac{m}{a}\right)^2 + 2(D_{12} + 2D_{66})\left(\frac{n}{b}\right)^2 + D_{22}\left(\frac{n}{b}\right)^4 \left(\frac{a}{m}\right)^2 \right]}{1 + \kappa\left(\frac{a}{b}\right)^2 \left(\frac{n}{m}\right)^2} \quad (6.86)$$

yielding as before the value of (K_x/π^2) as a function of the aspect ratio (a/b), stiffness $D_{11}, D_{12}, D_{22}, D_{66}$ and the half-waves in the x- and y-plate directions, m and n, respectively

$$\frac{K_x}{\pi^2} = \frac{\left[D_{11}\left(\frac{m}{a}\right)^2 + 2(D_{12} + 2D_{66})\left(\frac{n}{b}\right)^2 + D_{22}\left(\frac{n}{b}\right)^4 \left(\frac{a}{m}\right)^2 \right]}{1 + \kappa\left(\frac{a}{b}\right)^2 \left(\frac{n}{m}\right)^2} \quad (6.87)$$

Note that in contrast to the isotropic case, the assumption of $n = 1$ for the special orthotropic case of a plate under biaxial loads will not necessarily lead to the lowest value of the critical compression load, and therefore, its lowest value will be found after calculating the critical buckling loads for a few combinations of m and n.

The case of a special orthotropic rectangular plate on simply-supported boundary conditions under pure shear ($\overline{N}_{xy} \neq 0, \overline{N}_{xx} = 0, \overline{N}_{yy} = 0$) case is more complicated than the previous two ones. The equation to be solved is given by

$$D_{11}\frac{\partial^4 w_0}{\partial x^4} + 2(D_{12} + 2D_{66})\frac{\partial^4 w_0}{\partial x^2 \partial y^2} + D_{22}\frac{\partial^4 w_0}{\partial y^4} = 2\overline{N}_{xy}\frac{\partial^2 w_0}{\partial x \partial y} \quad (6.88)$$

There are no analytical solutions for this case, even for an all-around simply-supported rectangular plate. Bergmann and Reisner [30] assumed an infinitely long plate in the x-direction $(a/b \rightarrow \infty)$ with the D_{11} bending rigidity being neglected. The exact solution for this case, where simply-supported boundary conditions were assumed along the long edges, has the following form:

$$\frac{\overline{N}_{xy} \cdot b^2}{4\sqrt{[D_{22}(D_{12} + 2D_{66})]}} = 11.71 \quad (6.89)$$

Another solution for eq. (6.88) was given by Leissa [29], which has the following form:

$$w(x,y) = f(y)\exp\left(i\kappa\frac{x}{b}\right) \quad (6.90)$$

where $i = \sqrt{-1}$, b is the plate's width and κ is a wavelength constant to be determined. Substituting eq. (6.90) into eq. (6.88) yields

$$D_{11}\left(\frac{\kappa}{b}\right)^4 f(y) - 2(D_{12} + 2D_{66})\left(\frac{\kappa}{b}\right)^2 \frac{d^2 f(y)}{dy^2} + D_{22}\frac{d^4 f(y)}{dy^4} - 2i\overline{N}_{xy}\left(\frac{\kappa}{b}\right)\frac{df(y)}{dy} = 0 \quad (6.91)$$

The solution of eq. (6.91) has the following form:

$$f(y) = A_1 \exp\left(i\beta_1 \frac{y}{b}\right) + A_2 \exp\left(i\beta_2 \frac{y}{b}\right) + A_3 \exp\left(i\beta_3 \frac{y}{b}\right) + A_4 \exp\left(i\beta_4 \frac{y}{b}\right) \quad (6.92)$$

where β_1, β_2, β_3 and β_4 are the roots of the fourth-degree polynomial equation presented by eq. (6.91). Then the simply-supported boundary conditions are substituted at $y = 0$, b into eq. (6.92), leading to a fourth-order characteristic determinant, with κ and $\overline{N}_{xy}$ being free parameters. It was shown in [29] that the following parameter, $\sqrt{D_{11}/D_{22}}/[(D_{12} + 2D_{66})/D_{22}]$, determines the solution.

When only two opposite edges of a plate are on simply-supported boundary conditions, while the other two sides can be either clamped, free or any other combination of boundaries, the Lévy method can be applied to solve the buckling problem. Assuming the out-of-plane displacement has the following form

$$w_0(x, y) = G_n(x) \sin\frac{n\pi y}{b}, \quad n = 1, 2, 3 \quad (6.93)$$

and substituting into eq. (6.77), for constant in-plane loads, without shear-type ones ($\overline{N}_{xx} \neq 0$, $\overline{N}_{yy} \neq 0$, $\overline{N}_{xy} = 0$) yields

$$D_{11}\frac{d^4 G_n(x)}{dx^4} - \left[2(D_{12} + 2D_{66})\left(\frac{n\pi}{b}\right)^2 + \overline{N}_{xx}\right]\frac{d^2 G_n(x)}{dx^2} + \left(\frac{n\pi}{b}\right)^2\left[D_{22}\left(\frac{n\pi}{b}\right)^2 + \overline{N}_{yy}\right]G_n(x) = 0$$
$$(6.94)$$

The general solution for eq. (6.94) can be assumed to have the following form:

$$G_n(x) = A_1 \sinh(\lambda_1 x) + A_2 \cosh(\lambda_1 x) + A_3 \sin(\lambda_2 x) + A_4 \cos(\lambda_2 x) \quad (6.95)$$

where λ_1 and λ_2 are the roots of the following characteristic equation:

$$D_{11}\lambda^4 - \left[2(D_{12} + 2D_{66})\left(\frac{n\pi}{b}\right)^2 + \overline{N}_{xx}\right]\lambda^2 + \left[D_{22}\left(\frac{n\pi}{b}\right)^4 + \overline{N}_{yy}\left(\frac{n\pi}{b}\right)^2\right] = 0 \quad (6.96)$$

The roots of eq. (6.96) are given by

$$
\begin{aligned}
(\lambda_1)^2 &= \frac{1}{D_{11}}\left[B + \sqrt{B^2 - D_{11}C}\right] \\
(\lambda_2)^2 &= \frac{1}{D_{11}}\left[-B + \sqrt{B^2 - D_{11}C}\right]
\end{aligned}
\quad (6.97)
$$

where

$$B \equiv \left[(D_{12} + 2D_{66})\left(\frac{n\pi}{b}\right)^2 + \frac{\overline{N}_{xx}}{2}\right], \quad C \equiv \left[D_{22}\left(\frac{n\pi}{b}\right)^4 + \overline{N}_{yy}\left(\frac{n\pi}{b}\right)^2\right] \quad (6.98)$$

The constants A_1–A_4 are to be determined using the appropriate boundary conditions at $x = 0$, a, yielding the buckling load of the plate.

References

[1]   Timoshenko, S. P., and Gere, J.M. Elastic stability, 2nd, McGraw-Hill, New York, 1963, 541p.

[2]   Abramovich, H. Editor, Stability and Vibrations of Thin-Walled Composite Structures, Woodhead Publishing Series in Composites Science and Engineering, The Officers' Mess Business Centre, Royston Road, Duxford, CB22 4QH, Elsevier Ltd, United Kingdom, Copyright ©, 2017, 758p.

[3]   Simitses, G.J., An introduction to the elastic stability of structures, Prentice-Hall, Inc., Englewood Cliffs, New Jersey, 1976, 253p.

[4]   Reddy, J.N. Energy principles and variational methods in applied mechanics, 2nd, John Wiley, New York, 2002, 608p.

[5]   Brush, D.O., and Almroth, B.O. Buckling of bars, plates and shells, McGraw-Hill international student edition, New York (NY), USA. 1975, 379 pp.

[6]   Thompson, J.M.T., and Hunt, G.W. Elastic instability phenomena, John Wiley and Sons, Chichester, UK 1984, 216.

[7]   Johnson, J. B., Bryan, C. W., Turneaure, F. E., and Kinne, W. S. The theory and practice of modern framed structures-Designed for the use of schools and for engineers in professional practice, Part III: Design, New York, John Wiley & Sons, 1916, 565.

[8]   Whitney, J.M. Cylindrical bending of unsymmetrically laminated plates, Journal of Composite Materials, 3(4), 1969, 715–719.

[9]   Timoshenko, S. P. On the correction factor for shear of the differential equation for transverse vibrations of bars of uniform cross-section, Philosophical Magazine, 41(245), 1921, 744–746.

[10] Timoshenko, S. P. On the transverse vibrations of bars of uniform cross-section, Philosophical Magazine, 43(253), 1922, 125–131.

[11] Reissner, E. The effect of transverse shear deformation on the bending of elastic plates, Journal of Applied Mechanics, 12(2), 1945, A69–A77.

[12] Abramovich, H. Shear deformation and rotary inertia effects of vibrating composite beams, Composite Structures, 20, 1992, 165–173.

[13] Abramovich, H., and Hamburger, O. Vibration of a uniform cantilever Timoshenko beam with translational and rotational springs and with a tip mass, Journal of Sound and Vibration, 154 (1), 1992, 67–80.

[14] Abramovich, H. A note on experimental investigation on a vibrating Timoshenko cantilever beam, Journal of Sound and Vibration, 160(1), 1993, 167–171.

[15] Abramovich, H., and Livshits, A. Dynamic behavior of cross-ply laminated beams with piezoelectric layers, Composite Structures, 25(1–4), 1993, 371–379.

[16] Abramovich, H., and Livshits, A. Free vibrations of non-symmetric cross-ply laminated composite beams, Journal of Sound and Vibration, 176(5), 1994, 597–612.

[17] Abramovich, H. Thermal buckling of cross-ply composite laminates using a first-order shear deformation theory, Composites Structures, 28, 1994, 201–213.

[18] Abramovich, H. Deflection control of laminated composite beams with piezoceramic layers- closed form solutions, Composite Structures, 43, 1998, 217–231.

[19] Abramovich, H., Eisenberger, M., and Shulepov, O. Vibrations and buckling of cross-ply non-symmetric laminated composite beams, AIAA Journal, 34(5), 1996, 1064–1069. May.

[20] Timoshenko, S. P., and Woinowsky-Krieger, S. Theory of plates and shells, McGraw-Hill, New York, 1959, 580p.

[21] Reissner, E., and Stavsky, Y. Bending and stretching of certain types of heterogeneous aeolotropic elastic plates, Journal of Applied Mechanics, 28(3), 1961, 402–408.

[22] Dong, S.B., Pister, K.S., and Taylor, R.L. On the theory of laminated anisotropic shells and plates, Journal of Aerospace Sciences, 29(8), 1962, 969–975.

[23] Whitney, J.M., and Leissa, A.W. Analysis of heterogeneous anisotropic plates, Journal of Applied Mechanics, 36(2), 1969, 261–266.

[24] Reddy, J.N. Mechanics of laminated composite plates and shells- Theory and analysis, 2nd, CRC Press, Boca Raton, Florida, USA. 2004, 831p.

[25] Mindlin, R. D. Influence of rotatory inertia and shear on flexural motions of isotropic, elastic plates, ASME Journal of Applied Mechanics, 18(1), 1951, 31–38.

[26] Whitney, J.M. The effect of transverse shear deformation in the bending of laminated plates, Journal of Composite Materials, 3(4), 1969, 534–547.

[27] Whitney, J.M. Shear correction factors for orthotropic laminates under static load, Journal of Applied Mechanics, 40(1), 1973, 302–304.

[28] Reissner, E. Note on the effect of transverse shear deformation in laminated anisotropic plates, Computer Methods in Applied Mechanics and Engineering, 20, 1979, 203–209.

[29] Leissa, A. W., Buckling of laminated composite plates and shell panels, AFWAL-TR-85-3069, June 1985.

[30] Bergmann, S. and Reissner, H. Neuere probleme aus der flugzeugstatik uber die knickung von wellblechstreifen bei schubbeanspruchung, Zeitschrift fur Flugtechnik und Motorluftschiffahrt (Z.F.M.), 20(18), 1929, 475–481. September.

[31] Jones, R. M. Buckling and vibration of unsymmetrically laminated cross-ply rectangular plates, AIAA Journal, 11(12), 1973, 1626–1632.

[32] Whitney, J. M., A study of the effects of coupling between bending and stretching on the mechanical behavior of layered anisotropic composite materials, Ph.D. Dissertation, Ohio State University, 1968. Also Tech. Rept. AFML-TR-68-330, 80 pp., April 1969.

[33] Whitney, J. M., and Leissa, A. W. Analysis of heterogeneous anisotropic plates, Transactions ASME, Journal of Applied Mechanics, 36(2), 1969, 261–266.

[34] Whitney, J. M. Bending, vibrations, and buckling of laminated anisotropic rectangular plates, Wright Patterson AFBML, Ohio, Technical Report. AFML-TR-70-75, 1970, 35, Aug.

[35] Whitney, J. M. The effect of boundary conditions of the response of laminated composites, Journal of Composite Materials, 4, 1970, 192–203.

[36] Khdeir, A.A. Stability of antisymmetric angle-ply laminated plates, Journal of Engineering mechanics, 115(5), 1989, 952–962. May.

[37] Reddy, J.N., Khdeir, A.A., and Librescu, L. Lévy type solutions for symmetrically laminated rectangular plates using first order shear deformation theory, Journal of Applied Mechanics, 54, 1987, 740–742. September.

[38] Gerard, G., and Becker, H., Handbook of Structural Stability, PART I -Buckling of flat plates, NACA TN 3781, 106pp.

[39] Johns, D.J., Shear buckling of isotropic and orthotropic plates- A review, Aeronautical Research Council, R&M No. 3677, London: Her Majesty's Stationery Office, UK, March 1972, 37 pp.

[40] Stein, M., and Neff, J. Buckling stresses of simply supported rectangular flat plates in shear, NACA TN, 1222, 1947, March, 14.

[41] Batdorf, S.B., and Stein, M. Critical combinations of shear and direct stress for simply supported rectangular flat plates, NACA TN, 1223, 1947, March, 32.

[42] Whitney, J. M., and Pagano, N.J. Shear deformation in heterogeneous anisotropic plates, Journal of Applied Mechanics, 37(4), 1970, 1031–1036.

Appendix A: Nonsymmetric laminated composite beam – CLT approach

The two coupled equations of motion for a nonsymmetric laminated composite beam under compressive loads based on the CLT approach are

$$A_{11}\frac{d^2 u_0}{dx^2} - B_{11}\frac{d^3 w_0}{dx^3} = 0 \tag{A-1}$$

$$-B_{11}\frac{d^3 u_0}{dx^3} + D_{11}\frac{d^4 w_0}{dx^4} + \overline{N}_{xx}\frac{d^2 w_0}{dx^2} = 0 \tag{A-2}$$

Derivation with respect to x of eq. (A-1) and substituting in eq. (A-2) leads to the following decoupled equation:

$$-\frac{B_{11}}{A_{11}}\frac{d^4 w_0}{dx^4} + D_{11}\frac{d^4 w_0}{dx^4} + \overline{N}_{xx}\frac{d^2 w_0}{dx^2} = 0 \tag{A-3}$$

The solution of eq. (A-3) has the following general form:

$$w_0(x) = C_1 \sin\left(\widehat{\lambda}x\right) + C_2 \cos\left(\widehat{\lambda}x\right) + C_3 x + C_4 \tag{A-4}$$

where

$$\widehat{\lambda}^2 = \frac{\overline{N}_{xx}}{\left(D_{11} - \dfrac{B_{11}^2}{A_{11}}\right)} \tag{A-5}$$

Let us assume that the axial displacement $u_0(x)$ has the same form as the lateral displacement [8, 12–19, 26–28, 42], namely

$$u_0(x) = C_5 \sin\left(\widehat{\lambda}x\right) + C_6 \cos\left(\widehat{\lambda}x\right) + C_7 x + C_8 \tag{A-6}$$

The four constants in eq. (A-6) are connected to the four constants in eq. (A-4). By substituting eqs. (A-4) and (A-6) into eq. (A-1) we get the following relationships:

$$C_5 = -\frac{B_{11}}{A_{11}} \cdot \widehat{\lambda} \cdot C_2$$

$$C_6 = +\frac{B_{11}}{A_{11}} \cdot \widehat{\lambda} \cdot C_1 \tag{A-7}$$

The rest of the constants C_1, C_2, C_3, C_4, C_7 and C_8 will be determined using the six boundary conditions of the problem. For the case of simply supported at both ends of the column, the out-of-plane boundary conditions have the following expressions:

$$w_0(0) = 0, \quad M_{xx}(0) = 0 \quad \Rightarrow \quad -B_{11}\frac{du_0(0)}{dx} + D_{11}\frac{d^2w_0(0)}{dx^2} = 0 \qquad \text{(A-8)}$$

$$w_0(L) = 0, \quad M_{xx}(L) = 0 \quad \Rightarrow \quad -B_{11}\frac{du_0(L)}{dx} + D_{11}\frac{d^2w_0(L)}{dx^2} = 0 \qquad \text{(A-9)}$$

and the in-plane boundary conditions can be written (assuming that at $x = 0$ there is no axial displacement, while at the other end of the beam, at $x = L$, there is a compression load) as

$$u_0(0) = 0 \qquad \text{(A-10)}$$

$$A_{11}\frac{du_0(L)}{dx} - B_{11}\frac{d^2w_0(L)}{dx^2} = -\overline{N}_{xx} \qquad \text{(A-11)}$$

Applying the four out-of-plane boundary conditions (eqs. (A-8) and (A-9)) leads to the following four equations:

$$C_2 + C_4 = 0$$

$$\frac{B_{11}^2}{A_{11}} \cdot \widehat{\lambda}^2 \cdot C_2 - B_{11} \cdot C_7 - D_{11} \cdot \widehat{\lambda}^2 \cdot C_2 = 0$$

$$C_1 \sin\left(\widehat{\lambda}L\right) + C_2 \cos\left(\widehat{\lambda}L\right) + C_3 x + C_4 = 0 \qquad \text{(A-12)}$$

$$-\frac{B_{11}^2}{A_{11}} \cdot \widehat{\lambda}^2 \cdot C_2 \cdot \cos\left(\widehat{\lambda}L\right) - \frac{B_{11}^2}{A_{11}} \cdot \widehat{\lambda}^2 \cdot C_1 \cdot \sin\left(\widehat{\lambda}L\right) + B_{11} \cdot C_7$$

$$+ D_{11} \cdot \widehat{\lambda}^2 \cdot C_1 \cdot \sin\left(\widehat{\lambda}L\right) + D_{11} \cdot \widehat{\lambda}^2 \cdot C_2 \cdot \cos\left(\widehat{\lambda}L\right) = 0$$

Applying the two in-plane boundary conditions (eqs. (A-10) and (A-11)) yields

$$\frac{B_{11}}{A_{11}} \cdot \widehat{\lambda} \cdot C_1 + C_8 = 0$$

$$-B_{11} \cdot \widehat{\lambda}^2 \cdot C_2 \cdot \cos\left(\widehat{\lambda}L\right) - B_{11} \cdot \widehat{\lambda}^2 \cdot C_1 \cdot \sin\left(\widehat{\lambda}L\right) + A_{11} \cdot C_7$$

$$+ B_{11} \cdot \widehat{\lambda}^2 \cdot C_1 \cdot \sin\left(\widehat{\lambda}L\right) + -B_{11} \cdot \widehat{\lambda}^2 \cdot C_2 \cdot \cos\left(\widehat{\lambda}L\right) = -\overline{N}_{xx} \qquad \text{(A-13)}$$

$$\Rightarrow \quad C_7 = -\frac{\overline{N}_{xx}}{A_{11}}$$

Solving for the six constants we get the following results:

$$C_1 = \frac{B_{11}}{A_{11}}\frac{\left[\cos\left(\widehat{\lambda}L\right) - 1\right]}{\sin\left(\widehat{\lambda}L\right)}, \quad C_2 = \frac{B_{11}}{A_{11}}, \quad C_3 = 0$$

$$\text{(A-14)}$$

$$C_4 = -\frac{B_{11}}{A_{11}}, \quad C_7 = -\frac{\overline{N}_{xx}}{A_{11}}, \quad C_8 = -\widehat{\lambda}\frac{B_{11}^2}{A_{11}^2}\frac{\left[\cos\left(\widehat{\lambda}L\right) - 1\right]}{\sin\left(\widehat{\lambda}L\right)}.$$

To obtain the buckling load, one should demand that $w_0(x) \to \infty$, namely finding when one of the constants would tend to infinity. Observing the constant C_1 leads to the following eigenvalue solution

$$\sin\left(\widehat{\lambda}L\right) = 0 \quad \Rightarrow \quad \widehat{\lambda}L = n\pi, \quad n = 1, 2, 3, 4, \ldots \tag{A-15}$$

which leads to the critical buckling load per unit width, b, having the following form:

$$\left(\overline{N}_{xx}\right)_{\mathrm{cr}} = \frac{\pi^2}{L^2}\left(D_{11} - \frac{B_{11}^2}{A_{11}}\right) \tag{A-16}$$

The shape of the buckling will be $\sin\left(\frac{\pi x}{L}\right)$ like for the symmetric case.

One should note that the critical buckling load per unit width $\left(\overline{N}_{xx}\right)_{\mathrm{cr}}$ is influenced by the coupling coefficient B_{11}, presenting for nonsymmetric cases, a buckling load below that obtained for the symmetric case, having the same number of laminates.

For the clamped–clamped case the involved boundary conditions are

$$w_0(0) = 0, \quad \frac{dw_0(0)}{dx} = 0 \tag{A-17}$$

$$w_0(L) = 0, \quad \frac{dw_0(L)}{dx} = 0 \tag{A-18}$$

$$u_0(0) = 0, \quad A_{11}\frac{du_0(L)}{dx} - B_{11}\frac{d^2w_0(L)}{dx^2} = -\overline{N}_{xx} \tag{A-19}$$

Applying the boundary conditions yields the following characteristic equation:

$$\left(\widehat{\lambda}L\right) \cdot \sin\left(\widehat{\lambda}L\right) = 2\left[1 - \cos\left(\widehat{\lambda}L\right)\right] \quad \Rightarrow \quad \widehat{\lambda}L = 2\pi, 8.987, 4\pi, \ldots \tag{A-20}$$

with $C_1 = C_3 = C_4 = C_8 = 0$, $C_2 \neq 0$ and $C_7 = -\frac{\overline{N}_{xx}}{A_{11}}$. The critical buckling load per unit width can then be written as

$$\left(\overline{N}_{xx}\right)_{\mathrm{cr}} = \frac{4\pi^2}{L^2}\left(D_{11} - \frac{B_{11}^2}{A_{11}}\right) \tag{A-21}$$

The buckling shape can be written as

$$w_0(x) = C_2\left[\cos\left(\frac{2\pi x}{L}\right) - 1\right] \tag{A-22}$$

7 Vibrations of thin-walled structures

7.1 Introduction

This chapter is the complementary chapter to Chapter 6, which dealt with stability issues for isotropic and composite columns and plates. It is aimed at presenting the vibration analysis of isotropic and composite columns and plates based on the classical lamination theory (CLT) and the first-order shear deformation theory (FSDT) developed in Chapter 2. Some typical references dealing with 1D behavior characteristically to beams are given in ref. [1–17].

7.1.1 CLPT approach

As described in the previous chapter, the classical lamination plate theory (CLPT) is an extension of the well-known Kirchhoff–Love classical plate theory to be applied to laminated composite plates. The equations of motion are

$$\frac{\partial N_{xx}}{\partial x} + \frac{\partial N_{xy}}{\partial y} = I_0 \frac{\partial^2 u_0}{\partial t^2} - I_1 \frac{\partial^2}{\partial t^2} \left(\frac{\partial w_0}{\partial x} \right)$$

$$\frac{\partial N_{xy}}{\partial x} + \frac{\partial N_{yy}}{\partial y} = I_0 \frac{\partial^2 v_0}{\partial t^2} - I_1 \frac{\partial^2}{\partial t^2} \left(\frac{\partial w_0}{\partial y} \right)$$

$$\frac{\partial^2 M_{xx}}{\partial x^2} + 2\frac{\partial^2 M_{xy}}{\partial x \partial y} + \frac{\partial^2 M_{yy}}{\partial y^2} + \frac{\partial}{\partial x} \left(N_{xx} \frac{\partial w_0}{\partial x} + N_{xy} \frac{\partial w_0}{\partial y} \right) \qquad (7.1)$$

$$+ \frac{\partial}{\partial y} \left(N_{xy} \frac{\partial w_0}{\partial x} + N_{yy} \frac{\partial w_0}{\partial y} \right) = q + I_0 \frac{\partial^2 w_0}{\partial t^2} + I_1 \frac{\partial^2}{\partial t^2} \left(\frac{\partial u_0}{\partial x} + \frac{\partial v_0}{\partial y} \right)$$

$$- I_2 \frac{\partial^2}{\partial t^2} \left(\frac{\partial^2 w_0}{\partial x^2} + \frac{\partial^2 w_0}{\partial y^2} \right)$$

where q is the distributed pressure on the surface of the plate and the mass moments of inertia I_0, I_1 and I_2 are defined as

$$\left\{ \begin{array}{c} I_0 \\ I_1 \\ I_2 \end{array} \right\} = \int_{-h/2}^{+h/2} \left\{ \begin{array}{c} 1 \\ z \\ z^2 \end{array} \right\} \cdot \rho_0 \cdot dz \qquad (7.2)$$

where h is the total thickness of the plate and ρ_0 is the relevant density.

In eq. (7.1), N_{xx}, N_{xy}, N_{yy} are the force resultants per unit length and M_{xx}, M_{xy}, M_{yy} are the moment resultants per unit length defined as

$$\begin{Bmatrix} N_{xx} \\ N_{yy} \\ N_{xy} \end{Bmatrix} = \int_{-h/2}^{+h/2} \begin{Bmatrix} \sigma_{xx} \\ \sigma_{yy} \\ \tau_{xy} \end{Bmatrix} dz ; \quad \begin{Bmatrix} M_{xx} \\ M_{yy} \\ M_{xy} \end{Bmatrix} = - \int_{-h/2}^{+h/2} \begin{Bmatrix} \sigma_{xx} \\ \sigma_{yy} \\ \tau_{xy} \end{Bmatrix} \cdot z \cdot dz. \qquad (7.3)$$

In eq. (7.3), z is a coordinate normal to the surface of the plate, and σ_{xx} and σ_{yy} are the normal stresses in the x and y directions, respectively, while τ_{xy} is the shear stress.

The stress resultants N_{xx}, N_{xy}, N_{yy} and M_{xx}, M_{xy}, M_{yy} can be defined using the assumed displacements to yield:

$$\begin{Bmatrix} N_{xx} \\ N_{yy} \\ N_{xy} \end{Bmatrix} = \begin{bmatrix} A_{11} & A_{12} & A_{16} \\ A_{12} & A_{22} & A_{26} \\ A_{16} & A_{26} & A_{66} \end{bmatrix} \begin{Bmatrix} \dfrac{\partial u_0}{\partial x} + \dfrac{1}{2}\left(\dfrac{\partial w_0}{\partial x}\right)^2 \\ \dfrac{\partial v_0}{\partial y} + \dfrac{1}{2}\left(\dfrac{\partial w_0}{\partial y}\right)^2 \\ \dfrac{\partial u_0}{\partial y} + \dfrac{\partial v_0}{\partial x} + \dfrac{\partial^2 w_0}{\partial x \partial y} \end{Bmatrix} - \begin{bmatrix} B_{11} & B_{12} & B_{16} \\ B_{12} & B_{22} & B_{26} \\ B_{16} & B_{26} & B_{66} \end{bmatrix} \begin{Bmatrix} \dfrac{\partial^2 w_0}{\partial x^2} \\ \dfrac{\partial^2 w_0}{\partial y^2} \\ 2\dfrac{\partial^2 w_0}{\partial x \partial y} \end{Bmatrix}$$

$$(7.4)$$

$$\begin{Bmatrix} M_{xx} \\ M_{yy} \\ M_{xy} \end{Bmatrix} = \begin{bmatrix} B_{11} & B_{12} & B_{16} \\ B_{12} & B_{22} & B_{26} \\ B_{16} & B_{26} & B_{66} \end{bmatrix} \begin{Bmatrix} \dfrac{\partial u_0}{\partial x} + \dfrac{1}{2}\left(\dfrac{\partial w_0}{\partial x}\right)^2 \\ \dfrac{\partial v_0}{\partial y} + \dfrac{1}{2}\left(\dfrac{\partial w_0}{\partial y}\right)^2 \\ \dfrac{\partial u_0}{\partial y} + \dfrac{\partial v_0}{\partial x} + \dfrac{\partial^2 w_0}{\partial x \partial y} \end{Bmatrix} - \begin{bmatrix} D_{11} & D_{12} & D_{16} \\ D_{12} & D_{22} & D_{26} \\ D_{16} & D_{26} & D_{66} \end{bmatrix} \begin{Bmatrix} \dfrac{\partial^2 w_0}{\partial x^2} \\ \dfrac{\partial^2 w_0}{\partial y^2} \\ 2\dfrac{\partial^2 w_0}{\partial x \partial y} \end{Bmatrix}$$

$$(7.5)$$

where

$$A_{ij} = \sum_{k=1}^{N} \overline{Q}_{ij}^{(k)}(z_{k+1} - z_k); \quad B_{ij} = \frac{1}{2}\sum_{k=1}^{N} \overline{Q}_{ij}^{(k)}\left(z_{k+1}^2 - z_k^2\right); \quad D_{ij} = \frac{1}{3}\sum_{k=1}^{N} \overline{Q}_{ij}^{(k)}\left(z_{k+1}^3 - z_k^3\right)$$

$$(7.6)$$

with $\overline{Q}_{ij}^{(k)}$ being the lamina stiffness after transformation. Substituting eqs. (7.4) and (7.5) into eq. (7.1) leads to the equations of motion for a laminated composite plate expressed by the three assumed displacements (u_0, v_0 and w_0):

$$A_{11}\left(\frac{\partial^2 u_0}{\partial x^2} + \frac{\partial^3 w_0}{\partial x^3}\right) + A_{12}\left(\frac{\partial^2 v_0}{\partial x \partial y} + \frac{\partial^3 w_0}{\partial x \partial y^2}\right) + A_{16}\left(2\frac{\partial^2 u_0}{\partial x \partial y} + 3\frac{\partial^3 w_0}{\partial x^2 \partial y} + \frac{\partial^2 v_0}{\partial x^2}\right)$$

$$+ A_{26}\left(\frac{\partial^2 v_0}{\partial y^2} + \frac{\partial^3 w_0}{\partial y^3}\right) + A_{66}\left(\frac{\partial^2 u_0}{\partial y^2} + \frac{\partial^2 v_0}{\partial x \partial y} + 2\frac{\partial^3 w_0}{\partial x \partial y^2}\right) - B_{11}\frac{\partial^3 w_0}{\partial x^3} - B_{12}\frac{\partial^3 w_0}{\partial x \partial y^2} \qquad (7.7)$$

$$- 3B_{16}\frac{\partial^3 w_0}{\partial x^2 \partial y} - B_{26}\frac{\partial^3 w_0}{\partial y^3} - 2B_{66}\frac{\partial^3 w_0}{\partial x \partial y^2} = I_0\frac{\partial^2 u_0}{\partial t^2} - I_1\frac{\partial^3 w_0}{\partial x \partial t^2}$$

$$A_{22}\left(\frac{\partial^2 v_0}{\partial y^2} + \frac{\partial^3 w_0}{\partial y^3}\right) + A_{12}\left(\frac{\partial^2 u_0}{\partial x \partial y} + \frac{\partial^3 w_0}{\partial x^2 \partial y}\right) + A_{16}\left(\frac{\partial^2 u_0}{\partial x^2} + \frac{\partial^3 w_0}{\partial x^3}\right)$$

$$+ A_{26}\left(\frac{\partial^2 u_0}{\partial y^2} + 2\frac{\partial^2 v_0}{\partial x \partial y} + 3\frac{\partial^3 w_0}{\partial x \partial y^2}\right) + A_{66}\left(\frac{\partial^2 u_0}{\partial x \partial y} + \frac{\partial^2 v_0}{\partial x^2} + 2\frac{\partial^3 w_0}{\partial x^2 \partial y}\right) - B_{12}\frac{\partial^3 w_0}{\partial x^2 \partial y} \quad (7.8)$$

$$- B_{22}\frac{\partial^3 w_0}{\partial y^3} - B_{16}\frac{\partial^3 w_0}{\partial x^3} - 3B_{26}\frac{\partial^3 w_0}{\partial x \partial y^2} - 2B_{66}\frac{\partial^3 w_0}{\partial x^2 \partial y} = I_0\frac{\partial^2 v_0}{\partial t^2} - I_1\frac{\partial^3 w_0}{\partial y \partial t^2}$$

$$B_{11}\left(\frac{\partial^3 u_0}{\partial x^3} + \frac{\partial^4 w_0}{\partial x^4}\right) + B_{12}\left(\frac{\partial^3 v_0}{\partial x^2 \partial y} + \frac{\partial^3 u_0}{\partial x \partial y^2} + 4\frac{\partial^3 w_0}{\partial x^2 \partial y^2}\right) + B_{16}\left(3\frac{\partial^3 u_0}{\partial x^2 \partial y} + \frac{\partial^3 v_0}{\partial x^3} + 8\frac{\partial^4 w_0}{\partial x^3 \partial y}\right)$$

$$+ B_{22}\left(\frac{\partial^3 v_0}{\partial y^3} + 2\frac{\partial^4 w_0}{\partial y^4}\right) + B_{26}\left(\frac{\partial^3 u_0}{\partial y^3} + 3\frac{\partial^3 v_0}{\partial x \partial y^2} + 8\frac{\partial^4 w_0}{\partial x \partial y^3}\right) + 2B_{66}\left(\frac{\partial^3 u_0}{\partial x \partial y^2} + \frac{\partial^3 v_0}{\partial x^2 \partial y} + 4\frac{\partial^4 w_0}{\partial x^2 \partial y^2}\right)$$

$$- D_{11}\frac{\partial^4 w_0}{\partial x^4} - 2D_{12}\frac{\partial^4 w_0}{\partial x^2 \partial y^2} - D_{22}\frac{\partial^4 w_0}{\partial y^4} - 4D_{16}\frac{\partial^4 w_0}{\partial x^3 \partial y} - 4D_{26}\frac{\partial^4 w_0}{\partial x \partial y^3} - 4D_{66}\frac{\partial^4 w_0}{\partial x^2 \partial y^2} + P(w_0)$$

$$= q + I_0\frac{\partial^2 w_0}{\partial t^2} - I_2\frac{\partial^2}{\partial t^2}\left(\frac{\partial^2 w_0}{\partial x^2} + \frac{\partial^2 w_0}{\partial y^2}\right) + I_1\frac{\partial^2}{\partial t^2}\left(\frac{\partial u_0}{\partial x} + \frac{\partial v_0}{\partial y}\right)$$

$$(7.9)$$

where

$$P(w_0) = \frac{\partial}{\partial x}\left(N_{xx}\frac{\partial w_0}{\partial x} + N_{xy}\frac{\partial w_0}{\partial y}\right) + \frac{\partial}{\partial y}\left(N_{xy}\frac{\partial w_0}{\partial x} + N_{yy}\frac{\partial w_0}{\partial y}\right) \quad (7.10)$$

7.1.2 FSDPT approach

The first-order shear deformation plate theory (FSDPT) described in detail in Chapter 2 is an extension of the well-known Timoshenko beam theory and/or Mindlin–Reissner plate theory to be applied to laminated composite plates.

The equations of motion in terms of displacements for the FSDPT approach can be written as

$$A_{11}\left(\frac{\partial^2 u_0}{\partial x^2} + \frac{\partial^3 w_0}{\partial x^3}\right) + A_{12}\left(\frac{\partial^2 v_0}{\partial x \partial y} + \frac{\partial^3 w_0}{\partial x \partial y^2}\right) + A_{16}\left(2\frac{\partial^2 u_0}{\partial x \partial y} + 3\frac{\partial^3 w_0}{\partial x^2 \partial y} + \frac{\partial^2 v_0}{\partial x^2}\right)$$

$$+ A_{26}\left(\frac{\partial^2 v_0}{\partial y^2} + \frac{\partial^3 w_0}{\partial y^3}\right) + A_{66}\left(\frac{\partial^2 u_0}{\partial y^2} + \frac{\partial^2 v_0}{\partial x \partial y} + 2\frac{\partial^3 w_0}{\partial x \partial y^2}\right) + B_{11}\frac{\partial^2 \phi_x}{\partial x^2} + B_{12}\frac{\partial^2 \phi_y}{\partial x \partial y} \quad (7.11)$$

$$+ B_{16}\left(2\frac{\partial^2 \phi_x}{\partial x \partial y} + \frac{\partial^2 \phi_y}{\partial x^2}\right) + B_{26}\frac{\partial^2 \phi_y}{\partial y^2} + B_{66}\left(\frac{\partial^2 \phi_x}{\partial y^2} + \frac{\partial^2 \phi_y}{\partial x \partial y}\right) = I_0\frac{\partial^2 u_0}{\partial t^2} + I_1\frac{\partial^2 \phi_x}{\partial t^2}$$

$$A_{22}\left(\frac{\partial^2 v_0}{\partial y^2} + \frac{\partial^3 w_0}{\partial y^3}\right) + A_{12}\left(\frac{\partial^2 u_0}{\partial x \partial y} + \frac{\partial^3 w_0}{\partial x^2 \partial y}\right) + A_{16}\left(\frac{\partial^2 u_0}{\partial x^2} + \frac{\partial^3 w_0}{\partial x^3}\right)$$

$$+ A_{26}\left(\frac{\partial^2 u_0}{\partial y^2} + 2\frac{\partial^2 v_0}{\partial x \partial y} + 3\frac{\partial^3 w_0}{\partial x \partial y^2}\right) + A_{66}\left(\frac{\partial^2 u_0}{\partial x \partial y} + \frac{\partial^2 v_0}{\partial x^2} + 2\frac{\partial^3 w_0}{\partial x^2 \partial y}\right) + B_{12}\frac{\partial^2 \phi_x}{\partial x \partial y}$$

$$+ B_{22}\frac{\partial^2 \phi_y}{\partial y^2} + B_{16}\frac{\partial^2 \phi_x}{\partial x^2} + B_{26}\left(2\frac{\partial^2 \phi_y}{\partial x \partial y} + \frac{\partial^2 \phi_x}{\partial y^2}\right) + B_{66}\left(\frac{\partial^2 \phi_x}{\partial x \partial y} + \frac{\partial^2 \phi_y}{\partial x^2}\right) = I_0\frac{\partial^2 v_0}{\partial t^2} + I_1\frac{\partial^2 \phi_y}{\partial t^2}$$

$$(7.12)$$

$$KA_{44}\left(\frac{\partial^2 w_0}{\partial y^2} + \frac{\partial \phi_y}{\partial y}\right) + KA_{45}\left(\frac{\partial^2 w_0}{\partial x \partial y} + \frac{\partial \phi_y}{\partial x}\right) + KA_{45}\left(\frac{\partial^2 w_0}{\partial x \partial y} + \frac{\partial \phi_x}{\partial y}\right)$$

$$(7.13)$$

$$+ KA_{55}\left(\frac{\partial^2 w_0}{\partial x^2} + \frac{\partial \phi_x}{\partial x}\right) + \mathrm{P}(w_0) = q + I_0\frac{\partial^2 w_0}{\partial t^2}$$

$$B_{11}\left(\frac{\partial^2 u_0}{\partial x^2} + \frac{\partial^3 w_0}{\partial x^3}\right) + B_{12}\left(\frac{\partial^2 v_0}{\partial x \partial y} + \frac{\partial^3 w_0}{\partial x \partial y^2}\right) + B_{16}\left(2\frac{\partial^2 u_0}{\partial x \partial y} + \frac{\partial^2 v_0}{\partial x^2} + 3\frac{\partial^4 w_0}{\partial x^3 \partial y}\right)$$

$$+ B_{26}\left(\frac{\partial^2 v_0}{\partial y^2} + \frac{\partial^3 w_0}{\partial y^3}\right) + B_{66}\left(\frac{\partial^2 u_0}{\partial y^2} + \frac{\partial^2 v_0}{\partial x \partial y} + 2\frac{\partial^3 w_0}{\partial x \partial y^2}\right) + D_{11}\frac{\partial^2 \phi_x}{\partial x^2} + D_{12}\frac{\partial^2 \phi_y}{\partial x \partial y}$$

$$+ D_{16}\left(2\frac{\partial^2 \phi_x}{\partial x \partial y} + \frac{\partial^2 \phi_y}{\partial x^2}\right) + D_{26}\frac{\partial^2 \phi_y}{\partial y^2} + D_{66}\left(\frac{\partial^2 \phi_x}{\partial y^2} + \frac{\partial^2 \phi_y}{\partial x \partial y}\right) - KA_{55}\left(\frac{\partial w_0}{\partial x} + \phi_x\right)$$

$$(7.14)$$

$$- KA_{45}\left(\frac{\partial w_0}{\partial y} + \phi_y\right) = I_2\frac{\partial^2 \phi_x}{\partial t^2} + I_1\frac{\partial^2 u_0}{\partial t^2}$$

$$B_{12}\left(\frac{\partial^2 u_0}{\partial x \partial y} + \frac{\partial^3 w_0}{\partial x \partial y^2}\right) + B_{16}\left(\frac{\partial^2 u_0}{\partial x^2} + \frac{\partial^3 w_0}{\partial x^3}\right) + B_{22}\left(\frac{\partial^2 v_0}{\partial y^2} + \frac{\partial^3 w_0}{\partial y^3}\right)$$

$$+ B_{26}\left(\frac{\partial^2 u_0}{\partial y^2} + 2\frac{\partial^2 v_0}{\partial x \partial y} + 3\frac{\partial^3 w_0}{\partial x \partial y^2}\right) + B_{66}\left(\frac{\partial^2 v_0}{\partial x^2} + \frac{\partial^2 u_0}{\partial x \partial y} + 2\frac{\partial^3 w_0}{\partial x \partial y^2}\right)$$

$$+ D_{12}\frac{\partial^2 \phi_x}{\partial x \partial y} + D_{22}\frac{\partial^2 \phi_y}{\partial y^2} + D_{16}\frac{\partial^2 \phi_x}{\partial x^2} + D_{26}\left(\frac{\partial^2 \phi_x}{\partial y^2} + 2\frac{\partial^2 \phi_y}{\partial x \partial y}\right) + D_{66}\left(\frac{\partial^2 \phi_y}{\partial x^2} + \frac{\partial^2 \phi_x}{\partial x \partial y}\right)$$

$$(7.15)$$

$$- KA_{45}\left(\frac{\partial w_0}{\partial x} + \phi_x\right) - KA_{44}\left(\frac{\partial w_0}{\partial y} + \phi_y\right) = I_2\frac{\partial^2 \phi_y}{\partial t^2} + I_1\frac{\partial^2 v_0}{\partial t^2}$$

where $P(w_0)$ is given by eq. (7.10), u_0, v_0, w_0 are the displacements in the directions x, y and z, respectively, ϕ_x, ϕ_y are rotation about the x and y axes, respectively, and the various terms A_{ij}, B_{ij} and D_{ij} are defined in detail in Chapter 6.

7.2 Vibrations of columns – CLT approach

The equations of motion for calculating a general laminate column can be derived from eq. (7.1) by assuming that the displacement of the model is only a function of the x coordinate, yielding the following equations (v_0 is assumed to be zero):

$$A_{11}\left(\frac{\partial^2 u_0}{\partial x^2} + \frac{\partial^3 w_0}{\partial x^3}\right) - B_{11}\frac{\partial^3 w_0}{\partial x^3} = I_0\frac{\partial^2 u_0}{\partial t^2} - I_1\frac{\partial^3 w_0}{\partial x\partial t^2} \tag{7.16}$$

$$B_{11}\left(\frac{\partial^3 u_0}{\partial x^3} + \frac{\partial^4 w_0}{\partial x^4}\right) - D_{11}\frac{\partial^4 w_0}{\partial x^4} = q + \overline{P}(w_0) + I_0\frac{\partial^2 w_0}{\partial t^2} - I_2\frac{\partial^2}{\partial t^2}\left(\frac{\partial^2 w_0}{\partial x^2}\right) + I_1\frac{\partial^2}{\partial t^2}\left(\frac{\partial u_0}{\partial x}\right) \tag{7.17}$$

where

$$\overline{P}(w_0) = \frac{\partial}{\partial x}\left(N_{xx}\frac{\partial w_0}{\partial x}\right) \tag{7.18}$$

$$\begin{Bmatrix} I_0 \\ I_1 \\ I_2 \end{Bmatrix} = \int_{-h/2}^{+h/2} \begin{Bmatrix} 1 \\ z \\ z^2 \end{Bmatrix} \cdot \rho_0 \cdot dz \tag{7.19}$$

and h is the total thickness of the plate and ρ_0 is the relevant density.

To analyze the vibration problem of the columns, the lateral load q will be assumed to be zero while the axial compressive load, $\overline{P}(w_0)$ will be assumed to be non-zero. This leads to the following coupled equations:

$$A_{11}\left(\frac{\partial^2 u_0}{\partial x^2} + \frac{\partial^3 w_0}{\partial x^3}\right) - B_{11}\frac{\partial^3 w_0}{\partial x^3} = I_0\frac{\partial^2 u_0}{\partial t^2} - I_1\frac{\partial^2}{\partial t^2}\left(\frac{\partial w_0}{\partial x}\right) \tag{7.20}$$

$$B_{11}\left(\frac{\partial^3 u_0}{\partial x^3} + \frac{\partial^4 w_0}{\partial x^4}\right) - D_{11}\frac{\partial^4 w_0}{\partial x^4} = \overline{P}(w_0) + I_0\frac{\partial^2 w_0}{\partial t^2} - I_2\frac{\partial^2}{\partial t^2}\left(\frac{\partial^2 w_0}{\partial x^2}\right) + I_1\frac{\partial^2}{\partial t^2}\left(\frac{\partial u_0}{\partial x}\right) \tag{7.21}$$

7.2.1 Symmetric laminate (B_{11} = 0, I_1 = 0)

For the case of symmetric laminate, namely, B_{11} = 0, and I_1 = 0, the following single equation is obtained, while eq. (7.20) (assuming the term $\frac{\partial^3 w_0}{\partial x^3}$ is neglected) is solved independently

$$-D_{11}\frac{\partial^4 w_0}{\partial x^4} - \overline{N}_{xx}\frac{\partial^2 w_0}{\partial x^2} = I_0\frac{\partial^2 w_0}{\partial t^2} - I_2\frac{\partial^2}{\partial t^2}\left(\frac{\partial^2 w_0}{\partial x^2}\right) \tag{7.22}$$

Assuming that $w_0(x,t) = W(x)e^{i\omega t}$, where ω is the circular natural frequency and substituting into eq. (7.22) yields the following differential equation:

$$D_{11}\frac{d^4W}{dx^4} + \left(\overline{N}_{xx} + \omega^2 I_2\right)\frac{d^2W}{dx^2} - \omega^2 I_0 \cdot W = 0 \tag{7.23}$$

The solution of eq. (7.23) has the following general form:

$$W(x) = A_1 \sinh(\alpha_1 x) + A_2 \cosh(\alpha_1 x) + A_3 \sin(\alpha_2 x) + A_4 \cos(\alpha_2 x) \tag{7.24}$$

where A_1, A_2, A_3 and A_4 are constants to be determined using boundary conditions and the terms α_1 and α_2 are defined as

$$\alpha_1 = \sqrt{\frac{-(N_{xx} + \omega^2 I_2) + \sqrt{\left(\overline{N}_{xx} + \omega^2 I_2\right)^2 + 4D_{11}\omega^2 I_0}}{2D_{11}}}$$

$$\alpha_2 = \sqrt{\frac{(N_{xx} + \omega^2 I_2) + \sqrt{\left(\overline{N}_{xx} + \omega^2 I_2\right)^2 + 4D_{11}\omega^2 I_0}}{2D_{11}}} \tag{7-25}$$

To investigate the influence of the compression load, $\overline{N}_{xx}$ and the rotary inertia, I_2, on the natural frequency, the circular natural frequency squared (ω^2) is rewritten using eq. (7.25) to yield

$$\omega^2 = \frac{D_{11}\alpha_1^4 + \overline{N}_{xx}\alpha_1^2}{I_0 - I_2\alpha_1^2} = \alpha_1^4 \frac{D_{11}}{I_0} \frac{\left(1 + \frac{\overline{N}_{xx}}{D_{11}\alpha_1^2}\right)}{\left(1 - \frac{I_2}{I_0}\alpha_1^2\right)}$$

$$\omega^2 = \frac{D_{11}\alpha_2^4 - \overline{N}_{xx}\alpha_2^2}{I_0 + I_2\alpha_2^2} = \alpha_2^4 \frac{D_{11}}{I_0} \frac{\left(1 - \frac{\overline{N}_{xx}}{D_{11}\alpha_2^2}\right)}{\left(1 + \frac{I_2}{I_0}\alpha_2^2\right)} \tag{7.26}$$

The expressions in eq. (7.26) are the same, are the same and only one of the equations should be used , for instance when, α_2 is known. Also it is clear from eq. (7.26) (the second expression) that the compressive load $\overline{N}_{xx}$ reduces the natural frequency, and the same tendency is obtained by including the rotary inertia, I_2. Assuming $\overline{N}_{xx} = I_2 = 0$, one obtains the known frequency equation used by Bernoulli–Euler theory, namely

$$\omega^2 = \alpha_2^4 \frac{D_{11}}{I_0} \tag{7.27}$$

which holds true also for an isotropic column, by letting the bending stiffness, to be written as $D_{11} \equiv D = Eh^3/[12(1-v^2)]$, where E is the Young's modulus, v is the Poisson's ratio and h is the thickness of the column.

Let us show the application of boundary conditions in eq. (7.24) for the simply supported case. The boundary conditions for this case are

$$W(0) = 0; \quad M_{xx}(0) = 0 \quad \Rightarrow \quad \frac{d^2W(0)}{dx^2} = 0$$

$$W(L) = 0; \quad M_{xx}(L) = 0 \quad \Rightarrow \quad \frac{d^2W(L)}{dx^2} = 0 \tag{7.28}$$

Substituting the boundary conditions in eq. (7.24) yields a set of four equations with four unknowns, having the following matrix form:

$$\begin{bmatrix} 0 & 1 & 0 & 1 \\ 0 & \alpha_1^2 & 0 & -\alpha_2^2 \\ \sinh(\alpha_1 L) & \cosh(\alpha_2 L) & \sin(\alpha_2 L) & \cos(\alpha_2 L) \\ \alpha_1^2 \sinh(\lambda L) & \alpha_1^2 \cosh(\lambda L) & -\alpha_2^2 \sin(\alpha_2 L) & -\alpha_2^2 \cos(\alpha_2 L) \end{bmatrix} \begin{Bmatrix} C_1 \\ C_2 \\ C_3 \\ C_4 \end{Bmatrix} = \begin{Bmatrix} 0 \\ 0 \\ 0 \\ 0 \end{Bmatrix} \tag{7.29}$$

To obtain a unique solution, the determinant of the matrix appearing in eq. (7.29) must vanish. This leads to the following characteristic equation:

$$\sin(\alpha_2 L) = 0 \quad \Rightarrow \quad \alpha_2 L = n\pi, n = 1, 2, 3, 4\ldots \quad \Rightarrow \quad \alpha_2^2 = \frac{n^2\pi^2}{L^2} \tag{7.30}$$

Substituting the result of eq. (7.30) into the second expression of eq. (7.26) leads to the natural frequencies of a symmetric layered column, having a length L, under compressive load, including rotatory inertia on simply supported boundary conditions

$$\omega = \left(\frac{n\pi}{L}\right)^2 \sqrt{\frac{D_{11}}{I_0}} \sqrt{\frac{\left(1 - \frac{\overline{N}_{xx}}{D_{11}\left(\frac{n\pi}{L}\right)^2}\right)}{\left(1 + \frac{I_2}{I_0}\left(\frac{n\pi}{L}\right)^2\right)}}, \quad n = 1, 2, 3, 4, \ldots \tag{7.31}$$

Neglecting the rotatory inertial leads to the following expression:

$$\omega = \left(\frac{n\pi}{L}\right)^2 \sqrt{\frac{D_{11}}{I_0}} \sqrt{\left(1 - \frac{\overline{N}_{xx}}{D_{11}\left(\frac{n\pi}{L}\right)^2}\right)}, \quad n = 1, 2, 3, 4, \ldots \tag{7.32}$$

showing that the axial compression load reduces the natural frequencies of a column, while for the case of no axial compression, but including the rotatory inertia the expression has the following form:

$$\omega = \left(\frac{n\pi}{L}\right)^2 \sqrt{\frac{D_{11}}{I_0}} \sqrt{\frac{1}{\left(1 + \frac{I_2}{I_0}\left(\frac{n\pi}{L}\right)^2\right)}}, \quad n = 1, 2, 3, 4, \ldots \tag{7.33}$$

displaying the same tendency as before, namely the rotatory inertial tends to reduce the natural frequencies of the column. For the simple case of a column, without axial compression and rotatory inertia the expression for the natural frequencies is like for an isotropic case using the classical beam theory

$$\omega_n = \left(\frac{n\pi}{L}\right)^2 \sqrt{\frac{D_{11}}{I_0}}, \quad n = 1, 2, 3, 4, \ldots \tag{7.34}$$

Tables 7.1 and 7.2 present some of the most encountered column cases having various boundary conditions (see similar tables in Chapter 6). The various expressions given in Table 7.1 are for the case without axial compression load and neglecting the rotary inertia term. For this case, eq. (7.24) simplifies into the following equation:

$$W(x) = A_1 \sinh(\alpha_2 x) + A_2 \cosh(\alpha_2 x) + A_3 \sin(\alpha_2 x) + A_4 \cos(\alpha_2 x) \tag{7.35}$$

Table 7.1: Characteristic equations and eigenvalues for natural vibrations of laminated composite columns using CLT approach.

No.	Name	Characteristic equation	Eigenvalues
1	SS-SS[*]	$\sin(\alpha_2 L) = 0$ $(\alpha_2 L)_n = n\pi, \quad n = 1, 2, 3, \ldots$	$\omega_n = \left(\frac{n\pi}{L}\right)^2 \sqrt{\frac{D_{11}}{I_0}}$
2	C-C[**]	$\cos(\alpha_2 L)\cosh(\alpha_2 L) = 1$ $(\alpha_2 L)_n = 4.73004, 7.85321, 10.9956, \ldots \frac{(2n+1)\pi}{2}$	$\omega_1 = \left(\frac{4.73004}{L}\right)^2 \sqrt{\frac{D_{11}}{I_0}}$
3	C-F[***]	$\cos(\alpha_2 L)\cosh(\alpha_2 L) = -1$ $(\alpha_2 L)_n = 1.87510, 4.69409, 7.85340, \ldots \frac{(2n-1)\pi}{2}$	$\omega_1 = \left(\frac{1.87351}{L}\right)^2 \sqrt{\frac{D_{11}}{I_0}}$
4	F-F	$\cos(\alpha_2 L)\cosh(\alpha_2 L) = 1$ $(\alpha_2 L)_n = 4.73004, 7.85321, 10.9956, \ldots \frac{(2n+1)\pi}{2}$	$\omega_1 = \left(\frac{4.73004}{L}\right)^2 \sqrt{\frac{D_{11}}{I_0}}$
5	SS-C	$\tan(\alpha_2 L) = \tanh(\alpha_2 L)$ $(\alpha_2 L)_n = 3.9266, 7.0686, 10.2102, \ldots \frac{(4n+1)\pi}{4}$	$\omega_1 = \left(\frac{3.9266}{L}\right)^2 \sqrt{\frac{D_{11}}{I_0}}$
6	SS-F	$\tan(\alpha_2 L) = \tanh(\alpha_2 L)$ $(\alpha_2 L)_n = 3.9266, 7.0686, 10.2102, \ldots \frac{(4n+1)\pi}{4}$	$\omega_1 = \left(\frac{3.9266}{L}\right)^2 \sqrt{\frac{D_{11}}{I_0}}$
7	G[****]-F	$\tan(\alpha_2 L) = -\tanh(\alpha_2 L)$ $(\alpha_2 L)_n = 2.3650, 5.4978, 8.6394, \ldots \frac{(4n-1)\pi}{4}$	$\omega_1 = \left(\frac{2.3650}{L}\right)^2 \sqrt{\frac{D_{11}}{I_0}}$
8	G-SS	$\cos(\alpha_2 L) = 0 \ (\alpha_2 L)_n = (2n-1)\frac{\pi}{2} \quad n = 1, 2, 3, \ldots$	$\omega_n = \left[\frac{(2n-1)\pi}{2L}\right] \sqrt{\frac{D_{11}}{I_0}}$
9	G-G	$\sin(\alpha_2 L) = 0$ $(\alpha_2 L)_n = n\pi, \quad n = 1, 2, 3 \ldots$	$\omega_n = \left(\frac{n\pi}{L}\right)^2 \sqrt{\frac{D_{11}}{I_0}}$
10	G-C	$\tan(\alpha_2 L) = -\tanh(\alpha_2 L)$ $(\alpha_2 L)_n = 2.3650, 5.4978, 8.6394, \ldots \frac{(4n-1)\pi}{4}$	$\omega_1 = \left(\frac{2.3650}{L}\right)^2 \sqrt{\frac{D_{11}}{I_0}}$

[*]SS, simply supported; [**]C, clamped; [***]F, free; [****]G, guided.

Table 7.2: Mode shapes and their relevant eigenvalues for natural vibrations of laminated composite columns using CLT approach.

No.	Name	Mode shape	Eigenvalues
1	SS-SS	$W_n(x) = \sin\left(\dfrac{n\pi x}{L}\right)$	$\omega_n = \left(\dfrac{n\pi}{L}\right)^2 \sqrt{\dfrac{D_{11}}{I_0}}$
2[†]	C-C	$W_n(x) = \cosh\left[\dfrac{(\alpha_2 L)_n x}{L}\right] - \cos\left[\dfrac{(\alpha_2 L)_n x}{L}\right]$ $- \dfrac{\cosh\left[(\alpha_2 L)_n\right] - \cos\left[(\alpha_2 L)_n\right]}{\sinh\left[(\alpha_2 L)_n\right] - \sin\left[(\alpha_2 L)_n\right]} \left\{ \sinh\left[\dfrac{(\alpha_2 L)_n x}{L}\right] - \sin\left[\dfrac{(\alpha_2 L)_n x}{L}\right] \right\}$	$\omega_n = \left[\dfrac{(2n+1)\pi}{2L}\right]^2 \sqrt{\dfrac{D_{11}}{I_0}}$
3[†]	C-F	$W_n(x) = \cosh\left[\dfrac{(\alpha_2 L)_n x}{L}\right] - \cos\left[\dfrac{(\alpha_2 L)_n x}{L}\right]$ $- \dfrac{\cosh\left[(\alpha_2 L)_n\right] + \cos\left[(\alpha_2 L)_n\right]}{\sinh\left[(\alpha_2 L)_n\right] + \sin\left[(\alpha_2 L)_n\right]} \left\{ \sinh\left[\dfrac{(\alpha_2 L)_n x}{L}\right] - \sin\left[\dfrac{(\alpha_2 L)_n x}{L}\right] \right\}$	$\omega_n = \left[\dfrac{(2n-1)\pi}{2L}\right]^2 \sqrt{\dfrac{D_{11}}{I_0}}$
4[†]	F-F	$W_n(x) = \cosh\left[\dfrac{(\alpha_2 L)_n x}{L}\right] - \cos\left[\dfrac{(\alpha_2 L)_n x}{L}\right]$ $- \dfrac{\cosh\left[(\alpha_2 L)_n\right] - \cos\left[(\alpha_2 L)_n\right]}{\sinh\left[(\alpha_2 L)_n\right] - \sin\left[(\alpha_2 L)_n\right]} \left\{ \sinh\left[\dfrac{(\alpha_2 L)_n x}{L}\right] - \sin\left[\dfrac{(\alpha_2 L)_n x}{L}\right] \right\}$	$\omega_n = \left[\dfrac{(2n+1)\pi}{2L}\right]^2 \sqrt{\dfrac{D_{11}}{I_0}}$
5[†]	SS-C	$W_n(x) = \cosh\left[\dfrac{(\alpha_2 L)_n x}{L}\right] - \cos\left[\dfrac{(\alpha_2 L)_n x}{L}\right]$ $- \dfrac{\cosh\left[(\alpha_2 L)_n\right] - \cos\left[(\alpha_2 L)_n\right]}{\sinh\left[(\alpha_2 L)_n\right] - \sin\left[(\alpha_2 L)_n\right]} \left\{ \sinh\left[\dfrac{(\alpha_2 L)_n x}{L}\right] - \sin\left[\dfrac{(\alpha_2 L)_n x}{L}\right] \right\}$	$\omega_n = \left[\dfrac{(4n+1)\pi}{4L}\right]^2 \sqrt{\dfrac{D_{11}}{I_0}}$
6[†]	SS-F	$W_n(x) = \cosh\left[\dfrac{(\alpha_2 L)_n x}{L}\right] + \cos\left[\dfrac{(\alpha_2 L)_n x}{L}\right]$ $- \dfrac{\cosh\left[(\alpha_2 L)_n\right] + \cos\left[(\alpha_2 L)_n\right]}{\sinh\left[(\alpha_2 L)_n\right] + \sin\left[(\alpha_2 L)_n\right]} \left\{ \sinh\left[\dfrac{(\alpha_2 L)_n x}{L}\right] + \sin\left[\dfrac{(\alpha_2 L)_n x}{L}\right] \right\}$	$\omega_n = \left[\dfrac{(4n+1)\pi}{4L}\right]^2 \sqrt{\dfrac{D_{11}}{I_0}}$
7[†]	G-F	$W_n(x) = \cosh\left[\dfrac{(\alpha_2 L)_n x}{L}\right] - \cos\left[\dfrac{(\alpha_2 L)_n x}{L}\right]$ $- \dfrac{\cosh\left[(\alpha_2 L)_n\right] - \cos\left[(\alpha_2 L)_n\right]}{\sinh\left[(\alpha_2 L)_n\right] - \sin\left[(\alpha_2 L)_n\right]} \left\{ \sinh\left[\dfrac{(\alpha_2 L)_n x}{L}\right] - \sin\left[\dfrac{(\alpha_2 L)_n x}{L}\right] \right\}$	$\omega_n = \left[\dfrac{(4n-1)\pi}{4L}\right]^2 \sqrt{\dfrac{D_{11}}{I_0}}$
8	G-SS	$W_n(x) = \sin\left[\dfrac{(2n-1)\pi x}{2L}\right]$	$\omega_n = \left[\dfrac{(2n-1)\pi}{2L}\right]\sqrt{\dfrac{D_{11}}{I_0}}$
9	G-G	$W_n(x) = \cos\left(\dfrac{n\pi x}{L}\right)$	$\omega_n = \left(\dfrac{n\pi}{L}\right)^2 \sqrt{\dfrac{D_{11}}{I_0}}$
10[†]	G-C	$W_n(x) = \cosh\left[\dfrac{(\alpha_2 L)_n x}{L}\right] - \cos\left[\dfrac{(\alpha_2 L)_n x}{L}\right]$ $- \dfrac{\sinh\left[(\alpha_2 L)_n\right] + \sin\left[(\alpha_2 L)_n\right]}{\cosh\left[(\alpha_2 L)_n\right] - \cos\left[(\alpha_2 L)_n\right]} \left\{ \sinh\left[\dfrac{(\alpha_2 L)_n x}{L}\right] - \sin\left[\dfrac{(\alpha_2 L)_n x}{L}\right] \right\}$	$\omega_n = \left[\dfrac{(4n-1)\pi}{4L}\right]^2 \sqrt{\dfrac{D_{11}}{I_0}}$

[†]The expression for the eigenvalues is given for $n \gg 1$. For the first modes, see Table 7.1

7.2.2 Nonsymmetric laminate ($B_{11} \neq 0$, $I_1 \neq 0$)

To solve the case of a nonsymmetric laminate, it is easier to present eqs. (7.20) and (7.21) in a matrix form, where higher order terms are neglected, leading to

$$\begin{bmatrix} A_{11}\frac{\partial^2}{\partial x^2} & -B_{11}\frac{\partial^3}{\partial x^3} \\ -B_{11}\frac{\partial^3}{\partial x^3} & D_{11}\frac{\partial^4}{\partial x^4} + \overline{N}_{xx}\frac{\partial^2}{\partial x^2} \end{bmatrix} \left\{ \begin{array}{c} u_0(x,t) \\ w_0(x,t) \end{array} \right\} + \begin{bmatrix} -I_0 & I_1\frac{\partial}{\partial x} \\ I_1\frac{\partial}{\partial x} & I_0 - I_2\frac{\partial^2}{\partial x^2} \end{bmatrix} \frac{\partial^2}{\partial t^2} \left\{ \begin{array}{c} u_0(x,t) \\ w_0(x,t) \end{array} \right\} = \left\{ \begin{array}{c} 0 \\ 0 \end{array} \right\}$$

(7.36)

The matrix presentation in eq. (7.36) includes axial compression $\overline{N}_{xx}$, rotary inertia I_2, and the coupling mass moment of inertia I_1, which couples both structurally and dynamically the two assumed deflections, u_0 and w_0. There is no general solution for eq. (7.36). Only for simply supported boundary conditions we can present the natural frequencies of a non-symmetric beam in a closed form solution. For this case we assume that the deflections u_0 and w_0 have the following form:

$$\left\{ \begin{array}{c} u_0(x,t) \\ w_0(x,t) \end{array} \right\} = \left\{ \begin{array}{c} \sum\limits_{m=1}^{M} U_m \cos\left(\frac{m\pi x}{L}\right)e^{i\omega t} \\ \sum\limits_{m=1}^{M} W_m \sin\left(\frac{m\pi x}{L}\right)e^{i\omega t} \end{array} \right\} \equiv \left\{ \begin{array}{c} \sum\limits_{m=1}^{M} U_m \cos(\lambda x)e^{i\omega t} \\ \sum\limits_{m=1}^{M} W_m \sin(\lambda x)e^{i\omega t} \end{array} \right\}$$

(7.37)

where $i = \sqrt{-1}$, ω^2 is the circular natural frequency squared and $\lambda = m\pi/L$. Substituting eq. (7.37) into eq. (7.36) yields

$$\begin{bmatrix} A_{11}\lambda^2 & -B_{11}\lambda^3 \\ -B_{11}\lambda^3 & D_{11}\lambda^4 - \overline{N}_{xx}\lambda^2 \end{bmatrix} \left\{ \begin{array}{c} U_m \\ W_m \end{array} \right\} + \begin{bmatrix} -\omega^2 I_0 & \omega^2 I_1\lambda \\ \omega^2 I_1\lambda & -\omega^2\left(I_0 - I_2\lambda^2\right) \end{bmatrix} \left\{ \begin{array}{c} U_m \\ W_m \end{array} \right\} = \left\{ \begin{array}{c} 0 \\ 0 \end{array} \right\}$$

(7.38)

Then eq. (7.38) can be casted in the following form:

$$\begin{bmatrix} A_{11}\lambda^2 - \omega^2 I_0 & -B_{11}\lambda^3 + \omega^2 I_1\lambda \\ -B_{11}\lambda^3 + \omega^2 I_1\lambda & D_{11}\lambda^4 - \overline{N}_{xx}\lambda^2 - \omega^2\left(I_0 - I_2\lambda^2\right) \end{bmatrix} \left\{ \begin{array}{c} U_m \\ W_m \end{array} \right\} = \left\{ \begin{array}{c} 0 \\ 0 \end{array} \right\}$$

(7.39)

To obtain a unique solution, the determinant of the matrix in eq. (7.39) must vanish, leading to the following characteristic equation:

$$A\left(\omega^2\right)^2 + B\left(\omega^2\right) + C = 0$$

(7.40)

where

$$\begin{aligned} A &\equiv I_1^2\lambda^2 - I_0\left(I_0 - I_2\lambda^2\right) \\ B &\equiv A_{11}\lambda^2\left(I_0 - I_2\lambda^2\right) + I_0\left(D_{11}\lambda^2 - \overline{N}_{xx}\right)\lambda^2 - 2I_1 B_{11}\lambda^4 \\ C &\equiv \left[A_{11}\overline{N}_{xx} - \left(A_{11}D_{11} - B_{11}^2\right)\lambda^2\right]\lambda^4 \end{aligned}$$

(7.41)

Solution of eq. (7.40) would provide the natural frequency for the simply supported nonsymmetric case. For a symmetric case ($B_{11} = I_1 = 0$) eq. (7.39) will not be coupled and the result will be the expression presented in eq. (7.31).

Appendix A presents a procedure to solve the case of a non-symmetric beam having other boundary conditions.

7.3 Vibrations of columns – FSDT approach

As derived in Chapter 6, the equations of motion for a general laminate using the FSDT approach (see also [9–14]) can be written as (assuming $v_0 = \phi_y = 0$)

$$A_{11}\left(\frac{\partial^2 u_0}{\partial x^2} + \frac{\partial^3 w_0}{\partial x^3}\right) + B_{11}\frac{\partial^2 \phi_x}{\partial x^2} = I_0 \frac{\partial^2 u_0}{\partial t^2} + I_1 \frac{\partial^2 \phi_x}{\partial t^2} \tag{7.42}$$

$$KA_{55}\left(\frac{\partial^2 w_0}{\partial x^2} + \frac{\partial \phi_x}{\partial x}\right) - \overline{N}_{xx}\frac{\partial^2 w_0}{\partial x^2} = q + I_0 \frac{\partial^2 w_0}{\partial t^2} \tag{7.43}$$

$$B_{11}\left(\frac{\partial^2 u_0}{\partial x^2} + \frac{\partial^3 w_0}{\partial x^3}\right) + D_{11}\frac{\partial^2 \phi_x}{\partial x^2} - KA_{55}\left(\frac{\partial w_0}{\partial x} + \phi_x\right) = I_2 \frac{\partial^2 \phi_x}{\partial t^2} + I_1 \frac{\partial^2 u_0}{\partial t^2} \tag{7.44}$$

One should note that eqs. (7.42)–(7.44) are for the case of uniform properties along the beam. For the particular case of properties varying along the x coordinate of the beam, the reader is referred to [12–14]. To solve the vibration problem, the lateral load, q, is set to zero leading to the following three coupled equations of motion:

$$A_{11}\left(\frac{\partial^2 u_0}{\partial x^2} + \frac{\partial^3 w_0}{\partial x^3}\right) + B_{11}\frac{\partial^2 \phi_x}{\partial x^2} = I_0 \frac{\partial^2 u_0}{\partial t^2} + I_1 \frac{\partial^2 \phi_x}{\partial t^2} \tag{7.45}$$

$$KA_{55}\left(\frac{\partial^2 w_0}{\partial x^2} + \frac{\partial \phi_x}{\partial x}\right) - \overline{N}_{xx}\frac{\partial^2 w_0}{\partial x^2} = I_0 \frac{\partial^2 w_0}{\partial t^2} \tag{7.46}$$

$$B_{11}\left(\frac{\partial^2 u_0}{\partial x^2} + \frac{\partial^3 w_0}{\partial x^3}\right) + D_{11}\frac{\partial^2 \phi_x}{\partial x^2} - KA_{55}\left(\frac{\partial w_0}{\partial x} + \phi_x\right) = I_2 \frac{\partial^2 \phi_x}{\partial t^2} + I_1 \frac{\partial^2 u_0}{\partial t^2} \tag{7.47}$$

Assuming harmonic vibrations with a circular squared frequency, ω^2 and neglecting higher order terms we can rewrite eqs. (7.45)–(7.47) as

$$A_{11}\frac{d^2 U}{dx^2} + B_{11}\frac{d^2 \Phi}{dx^2} + \omega^2 I_0 U + \omega^2 I_1 \Phi = 0 \tag{7.48}$$

$$KA_{55}\left(\frac{d^2 W}{dx^2} + \frac{d\Phi}{dx}\right) - \overline{N}_{xx}\frac{d^2 W}{dx^2} + \omega^2 I_0 W = 0 \tag{7.49}$$

$$B_{11}\frac{d^2 U}{dx^2} + D_{11}\frac{d^2 \Phi}{dx^2} - KA_{55}\left(\frac{dW}{dx} + \Phi\right) + \omega^2 I_2 \Phi + \omega^2 I_1 U = 0 \tag{7.50}$$

For symmetric laminates, we can write the following expressions:

$$A_{11}\frac{d^2U}{dx^2} + \omega^2 I_0 U = 0 \tag{7.51}$$

$$KA_{55}\left(\frac{d^2W}{dx^2} + \frac{d\Phi}{dx}\right) - \overline{N}_{xx}\frac{d^2W}{dx^2} + \omega^2 I_0 W = 0 \tag{7.52}$$

$$D_{11}\frac{d^2\Phi}{dx^2} - KA_{55}\left(\frac{dW}{dx} + \Phi\right) + \omega^2 I_2 \Phi = 0 \tag{7.53}$$

One should note that for the symmetric case, the first equation eq. (7.51) is not coupled with the other two equations, eqs. (7.52) and (7.53), which are coupled and have to be solved together.

7.3.1 Symmetric laminate ($B_{11} = 0$, $I_1 = 0$)

First, we shall present a general solution for the symmetric case presented by the two coupled equations (7.52) and (7.53). The two equations are decoupled to yield uncoupled equations

$$\left[D_{11} - \frac{\overline{N}_{xx}}{KA_{55}}\right]\frac{d^4W}{dx^4} + \left\{\omega^2\left[\frac{D_{11}I_0}{KA_{55}} + \left(1 - \frac{\overline{N}_{xx}}{KA_{55}}\right)I_2 + \overline{N}_{xx}\right]\right\}\frac{d^2W}{dx^2} + \omega^2 I_0\left[\frac{I_2\omega^2}{KA_{55}} - 1\right]W = 0 \tag{7.54}$$

$$\left[D_{11} - \frac{\overline{N}_{xx}}{KA_{55}}\right]\frac{d^4\Phi}{dx^4} + \left\{\omega^2\left[\frac{D_{11}I_0}{KA_{55}} + \left(1 - \frac{\overline{N}_{xx}}{KA_{55}}\right)I_2 + \overline{N}_{xx}\right]\right\}\frac{d^2\Phi}{dx^2} + \omega^2 I_0\left[\frac{I_2\omega^2}{KA_{55}} - 1\right]\Phi = 0 \tag{7.55}$$

One should note that without axial compression, $\overline{N}_{xx} = 0$ eqs. (7.54) and (7.55) will have the following form which is similar to what is given in [10]

$$D_{11}\frac{d^4W}{dx^4} + \omega^2\left[\frac{D_{11}I_0}{KA_{55}} + I_2\right]\frac{d^2W}{dx^2} + \omega^2 I_0\left[\frac{I_2\omega^2}{KA_{55}} - 1\right]W = 0 \tag{7.56}$$

$$D_{11}\frac{d^4\Phi}{dx^4} + \omega^2\left[\frac{D_{11}I_0}{KA_{55}} + I_2\right]\frac{d^2\Phi}{dx^2} + \omega^2 I_0\left[\frac{I_2\omega^2}{KA_{55}} - 1\right]\Phi = 0 \tag{7.57}$$

The general solutions for eqs. (7.54) and (7.55) (as well as for eqs. (7.56) and (7.57)) have the following form:

$$W(x) = A_1\cosh(s_1 x) + A_2\sinh(s_1 x) + A_3\cos(s_2 x) + A_4\sin(s_2 x) \tag{7.58}$$

$$\Phi(x) = B_1\cosh(s_1 x) + B_2\sinh(s_1 x) + B_3\cos(s_2 x) + B_4\sin(s_2 x) \tag{7.59}$$

while the constants A_1, A_2, A_3, A_4 and B_1, B_2, B_3, B_4 are interconnected (by back-substituting eqs. (7.58) and (7.59) into the coupled equations (7.52) and (7.53) and have the following form:

$$B_1 = \frac{KA_{55} \cdot s_1}{D_{11} \cdot s_1^2 - KA_{55} + \omega^2 I_2} A_2 \equiv \alpha A_2 \tag{7.60}$$

$$B_2 = \frac{KA_{55} \cdot s_1}{D_{11} \cdot s_1^2 - KA_{55} + \omega^2 I_2} A_1 \equiv \alpha A_1 \tag{7.61}$$

$$B_3 = \frac{KA_{55} \cdot s_2}{\omega^2 I_2 - D_{11} \cdot s_1^2 - KA_{55}} A_4 \equiv \beta A_4 \tag{7.62}$$

$$B_4 = -\frac{KA_{55} \cdot s_2}{\omega^2 I_2 - D_{11} \cdot s_1^2 - KA_{55}} A_3 \equiv -\beta A_3 \tag{7.63}$$

and

$$s_1 = \sqrt{-\frac{b}{2a} + \frac{\sqrt{(b^2 - 4ac)}}{2a}} \tag{7.64}$$

$$s_2 = \sqrt{+\frac{b}{2a} + \frac{\sqrt{(b^2 - 4ac)}}{2a}} \tag{7.65}$$

where

$$a \equiv D_{11} - \frac{\overline{N}_{xx}}{KA_{55}}; b \equiv \omega^2 \left[\frac{D_{11} I_0}{KA_{55}} + \left(1 - \frac{\overline{N}_{xx}}{KA_{55}}\right) I_2 + \overline{N}_{xx} \right]; c \equiv \omega^2 I_0 \left[\frac{I_2 \omega^2}{KA_{55}} - 1 \right] \tag{7.66}$$

The remaining constants, A_1, A_2, A_3 and A_4 will be found after imposing the relevant boundary conditions.

The general boundary conditions for a nonsymmetric laminate are given in Table 7.3 and eq. (7.67).

Table 7.3: Out-of-plane boundary conditions for a nonsymmetric laminate column.

Name	Boundary conditions
Simply supported (or hinged) end	$W = 0$ and $B_{11} \dfrac{dU}{dx} + D_{11} \dfrac{d\Phi}{dx} = 0$
Clamped end	$W = 0$ and $\Phi = 0$
Free end	$B_{11} \dfrac{dU}{dx} + D_{11} \dfrac{d\Phi}{dx} = 0$ and $KA_{55} \left(\dfrac{dW}{dx} + \Phi \right) - \overline{N}_{xx} \dfrac{dW}{dx} = 0$
Guided end	$\Phi = 0$ and $KA_{55} \left(\dfrac{dW}{dx} + \Phi \right) - \overline{N}_{xx} \dfrac{dW}{dx} = 0$

The in-plane boundary condition for the nonsymmetric laminate is given as

$$A_{11}\frac{dU}{dx} + B_{11}\frac{d\Phi}{dx} = -\overline{N}_{xx} \quad \text{or} \quad U = 0 \tag{7.67}$$

One should note that for a symmetric case without axial compression load the expressions for the boundary condition simplify and are given in Table 7.4 and eq. (7.68).

Table 7.4: Out-of-plane boundary conditions for a symmetric laminate axial noncompressed column.

Name	Boundary conditions	
Simply supported (or hinged) end	$W = 0$ and	$\dfrac{d\Phi}{dx} = 0$
Clamped end	$W = 0$ and	$\Phi = 0$
Free end	$\dfrac{d\Phi}{dx} = 0$ and	$\dfrac{dW}{dx} + \Phi = 0$
Guided end	$\Phi = 0$ and	$\dfrac{dW}{dx} + \Phi = 0$

The in-plane boundary condition for the symmetric laminate axial noncompressed column is given as follows:

$$\frac{dU}{dx} = 0 \quad \text{or} \quad U = 0 \tag{7.68}$$

Table 7.5 presents the characteristic equations for various boundary conditions for symmetric laminate, axial noncompressed columns.

7.3.2 Nonsymmetric laminate ($B_{11} \neq 0$, $I_1 \neq 0$)

The way to solve a nonsymmetric laminate for the case of beams of columns, we shall follow the derivation performed by Abramovich and Livshits [17].

The equations of motion (7.45)–(7.47) will be presented in a matrix formulation (for $\overline{N}_{xx} = 0$) namely,

$$\begin{bmatrix} A_{11}\frac{\partial^2}{\partial x^2} & 0 & B_{11}\frac{\partial^2}{\partial x^2} \\[2mm] 0 & KA_{55}\frac{\partial^2}{\partial x^2} & KA_{55}\frac{\partial}{\partial x} \\[2mm] B_{11}\frac{\partial^2}{\partial x^2} & -KA_{55}\frac{\partial}{\partial x} & \left(D_{11}\frac{\partial^2}{\partial x^2} - KA_{55}\right) \end{bmatrix} \begin{Bmatrix} u_0(x,t) \\[2mm] w_0(x,t) \\[2mm] \phi_x(x,t) \end{Bmatrix}$$

$$+ \begin{bmatrix} -I_0 & 0 & -I_1 \\[2mm] 0 & -I_0 & 0 \\[2mm] -I_1 & 0 & -I_2 \end{bmatrix} \frac{\partial^2}{\partial t^2} \begin{Bmatrix} u_0(x,t) \\[2mm] w_0(x,t) \\[2mm] \phi_x(x,t) \end{Bmatrix} = \begin{Bmatrix} 0 \\[2mm] 0 \\[2mm] 0 \end{Bmatrix} \tag{7.69}$$

Table 7.5: Characteristic equations for natural vibrations of laminated composite columns using FSDT approach.

No.	Name	Boundary conditions		Characteristic equation
1	SS-SS[*]	$W(0) = 0$	$d\Phi(0)/dx = 0$	$\sin(s_2 L) = 0$
		$W(L) = 0$	$d\Phi(L)/dx = 0$	$(s_2 L)_n = n\pi, \quad n = 1, 2, 3, \ldots$
2	C-C**	$W(0) = 0$	$\Phi(0) = 0$	$2\alpha - 2\alpha \cos(s_2 L) \cosh(s_1 L) +$
		$W(L) = 0$	$\Phi(L) = 0$	$\left(\dfrac{\alpha^2 - \beta^2}{\beta}\right) \sin(s_2 L) \sinh(s_1 L) = 0$
3	C-F[***]	$W(0) = 0 \quad \Phi(0) = 0$		$\alpha[s_1(s_1 - \alpha) - s_2(s_2 + \beta)] +$
		$d\Phi(L)/dx = 0$		$\left[s_1 s_2 \left(\dfrac{\beta - \alpha^2}{\beta}\right) + \alpha(\beta s_2 - \alpha s_1)\right] \cosh(s_1 L) \cos(s_2 L) +$
		$dW(L)/dx + \Phi(L) = 0$		$-\alpha(2 s_1 s_2 + s_1 \beta + s_2 \alpha) \cosh(s_1 L) \cos(s_2 L) = 0$
4	F-F	$d\Phi(0)/dx = 0$		$2\alpha s_1(s_1 + \alpha) - 2 \cos(s_2 L) \cosh(s_1 L) +$
		$dW(0)/dx + \Phi(0) = 0$		$\dfrac{\beta^2 s_2^2(s_1 + \alpha)^2 - \alpha^2 s_1^2(s_2 + \beta)^2}{\beta s_2(s_2 + \beta)} \sin(s_2 L) \sinh(s_1 L) = 0$
		$d\Phi(L)/dx = 0$		
		$dW(L)/dx + \Phi(L) = 0$		
5	SS-C	$W(0) = 0$	$d\Phi(0)/dx = 0$	$\beta \tanh(s_1 L) = \alpha \tan(s_2 L)$
		$W(L) = 0$	$\Phi(L) = 0$	
6	SS-F	$W(0) = 0$	$d\Phi(0)/dx = 0$	$s_1 \alpha(s_2 + \beta) \tanh(s_1 L) = -s_2 \beta(s_1 + \alpha) \tan(s_2 L)$
		$d\Phi(L)/dx = 0$		
		$dW(L)/dx + \Phi(L) = 0$		
7	G[****]-F	$\Phi(0) = 0$		$s_1 \alpha(s_2 + \beta) \tan(s_2 L) = s_2 \beta(s_1 + \alpha) \tanh(s_1 L)$
		$dW(0)dx + \Phi(0) = 0$		
		$d\Phi(L)/dx = 0$		
		$dW(L)/dx + \Phi(L) = 0$		
8	G-SS	$\Phi(0) = 0$		$\cos(s_2 L) = 0 \ (s_2 L)_n = (2n - 1)\dfrac{\pi}{2} \quad n = 1, 2, 3, \ldots$
		$dW(0)dx + \Phi(0) = 0$		
		$W(L) = 0$	$d\Phi(L)/dx = 0$	
9	G-G	$\Phi(0) = 0$		$\sin(s_2 L) = 0$
		$dW(0)dx + \Phi(0) = 0$		$(s_2 L)_n = n\pi, \quad n = 1, 2, 3, \ldots$
		$\Phi(L) = 0$		
		$dW(L)dx + \Phi(L) = 0$		
10	G-C	$\Phi(0) = 0$		$\alpha \tanh(s_1 L) = -\beta \tan(s_2 L)$
		$dW(0)dx + \Phi(0) = 0$		
		$W(L) = 0$	$\Phi(L) = 0$	

[*]SS, simply supported; **C, clamped; [***]F, free; [****]G, guided.

The associated boundary conditions are given by eq. (7.63) and Table 7.3. Following [17], nondimensional displacements and beam's length are defined as

$$\{\overline{q}\} = \left\{u_0/L, w_0/L, \phi_x\right\}^T, \quad \xi \equiv x/L \tag{7.70}$$

yielding

$$\{q\} = \text{diagonal}\{L, L, 1\}\{\overline{q}\} \tag{7.71}$$

To obtain expressions for free vibrations, we assume that the solution for eq. (7.69) has the following form:

$$\{\overline{q}\} = \{U, W, \Phi\}^T e^{i\omega t} \equiv \{Q\} e^{i\omega t} \tag{7.72}$$

Substituting eq. (7.72) into eq. (7.69) leads to the following matrix equation:

$$\left[\begin{bmatrix} A_{11}\frac{\partial^2}{\partial x^2} & 0 & B_{11}\frac{\partial^2}{\partial x^2} \\ 0 & KA_{55}\frac{\partial^2}{\partial x^2} & KA_{55}\frac{\partial}{\partial x} \\ B_{11}\frac{\partial^2}{\partial x^2} & -KA_{55}\frac{\partial}{\partial x} & \left(D_{11}\frac{\partial^2}{\partial x^2} - KA_{55}\right) \end{bmatrix} + \omega^2 \begin{bmatrix} I_0 & 0 & I_1 \\ 0 & I_0 & 0 \\ I_1 & 0 & I_2 \end{bmatrix} \right] \begin{Bmatrix} L \cdot U \\ L \cdot W \\ \Phi \end{Bmatrix} = \begin{Bmatrix} 0 \\ 0 \\ 0 \end{Bmatrix} \tag{7.73}$$

Introducing nondimensional parameters and after some algebraic transformation, eq. (7.73) can be written as

$$\left[\begin{bmatrix} \zeta_1^2 & 0 & \zeta^2 \\ 0 & 1 & 0 \\ \zeta^2 b^2 & 0 & b^2 \end{bmatrix} \frac{\partial^2}{\partial \xi^2} + \begin{bmatrix} 0 & 0 & 0 \\ 0 & 0 & 1 \\ 0 & -1 & 0 \end{bmatrix} \frac{\partial}{\partial \xi} + \begin{bmatrix} p^2 & 0 & \eta^2 p^2 \\ 0 & b^2 p^2 & 0 \\ \eta^2 b^2 p^2 & 0 & (r^2 b^2 p^2 - 1) \end{bmatrix} \right] \begin{Bmatrix} U \\ W \\ \Phi \end{Bmatrix} = 0 \tag{7.74}$$

where the various parameters are defined as

$$p^2 \equiv \frac{\omega^2 I_0 L^4}{D_{11}}, \quad b^2 \equiv \frac{D_{11}}{KA_{55}L^2}, \quad \zeta^2 \equiv \frac{B_{11}L}{D_{11}}, \quad \zeta_1^2 \equiv \frac{A_{11}L^2}{D_{11}}, \quad r^2 \equiv \frac{I_2}{I_0 L^2}, \quad \eta^2 \equiv \frac{I_1}{I_0 L} \tag{7.75}$$

Assuming that the general solution for eq. (7.74) has the following form:

$$\{Q\} = \{\overline{Q}\} e^{im\xi} \tag{7.76}$$

with m being the eigenvalue and $\{\overline{Q}\}$ the eigenvector, substituting into eq. (7.74) leads to the following cubic algebraic equation:

$$As^3 + Bs^2 + Cs + D = 0, \quad s \equiv \frac{m^2}{p^2} \tag{7.77}$$

with

$$A \equiv \zeta_1^2 - \zeta^4, \quad B \equiv 1 + (r^2 + b^2)\zeta_1^2 - \zeta^2(2\eta^2 + \zeta^2 b^2),$$

$$C \equiv \zeta_1^2\left(r^2 b^2 - \frac{1}{p^2}\right) + (r^2 + b^2) - \eta^2(\eta^2 + 2\zeta^2 b^2), \tag{7.78}$$

$$D \equiv r^2 b^2 - \frac{1}{p^2} - b^2\eta^4$$

Solving eq. (7.77) we can write the general solution for eq. (7.74) in the following form (see a detailed discussion regarding the format of the solution in [17])

$$U = A_1\gamma\mu\sinh(m_1\xi) + A_2\gamma\mu\cosh(m_1\xi) + A_3\lambda\delta\sin(m_2\xi)$$

$$\quad - A_4\lambda\delta\cos(m_2\xi) + A_5\alpha\beta\sin(m_3\xi) - A_6\alpha\beta\cos(m_3\xi)$$

$$W = A_1\cosh(m_1\xi) + A_2\sinh(m_1\xi) + A_3\cos(m_2\xi)$$

$$\quad + A_4\sin(m_2\xi) + A_5\cos(m_3\xi) + A_6\sin(m_3\xi) \tag{7.79}$$

$$\Phi = - A_1\mu\sinh(m_1\xi) - A_2\mu\cosh(m_1\xi) - A_3\lambda\sin(m_2\xi)$$

$$\quad + A_4\lambda\cos(m_2\xi) - A_5\alpha\sin(m_3\xi) + A_6\alpha\cos(m_3\xi)$$

where the various terms in eq. (7.79) are defined as follows:

$$m_1 \equiv \sqrt{s_1}p, \quad m_2 \equiv \sqrt{-s_2}p, \quad m_3 \equiv \sqrt{-s_3}p$$

$$\gamma \equiv \frac{\zeta^2 s_1 + \eta^2}{\zeta_1^2 s_1 + 1}, \quad \delta \equiv \frac{\zeta^2 s_2 + \eta^2}{\zeta_1^2 s_2 + 1}, \quad \beta \equiv \frac{\zeta^2 s_3 + \eta^2}{\zeta_1^2 s_3 + 1} \tag{7.80}$$

$$\mu \equiv \frac{s_1 + b^2}{\sqrt{s_1}}p, \quad \lambda \equiv \frac{s_2 + b^2}{\sqrt{-s_2}}p, \quad \alpha \equiv \frac{s_3 + b^2}{\sqrt{-s_3}}p$$

Imposing the adequate boundary conditions would lead to the finding of both the eigenvalues (the natural frequencies) and the eigenvectors (the modes of vibration). For this problem six boundary conditions should be imposed as presented in Table 7.6.

One should note (see also [17]) that only for a column or a beam with two simply supported (hinged) movable ends, an analytical solution exists. The characteristic equation, obtained after demanding that the determinant of the coefficients in eq. (7.79) has the following form:

$$\sin(m_3)\sin(m_2) = 0 \tag{7.81}$$

The solutions for eq. (7.81) has two series: the first one having bending dominated vibrations

$$m_3 = k\pi, \quad k = 1, 2, 3, \dots, n \tag{7.82}$$

while the second series has longitudinal dominated vibrations

$$m_2 = k\pi, \quad k = 1, 2, 3, \dots, n \tag{7.83}$$

Table 7.6: Boundary conditions for the nonsymmetrical laminated columns using the FSDT approach.

Name	Boundary conditions
Clamped immovable end	$U = W = \Phi = 0$
Clamped movable end	$\zeta_1^2 \dfrac{dU}{d\xi} + \zeta^2 \dfrac{d\Phi}{d\xi} = W = \Phi = 0$
Simply supported immovable end	$\zeta^2 \dfrac{dU}{d\xi} + \dfrac{d\Phi}{d\xi} = W = U = 0$
Simply supported movable end	$\zeta^2 \dfrac{dU}{d\xi} + \dfrac{d\Phi}{d\xi} = W = \zeta_1^2 \dfrac{dU}{d\xi} + \zeta^2 \dfrac{d\Phi}{d\xi} = 0$
Free end	$\zeta^2 \dfrac{dU}{d\xi} + \dfrac{d\Phi}{d\xi} = \dfrac{1}{b^2}\left(\Phi + \dfrac{dW}{d\xi}\right) = \zeta_1^2 \dfrac{dU}{d\xi} + \zeta^2 \dfrac{d\Phi}{d\xi} = 0$

7.4 Vibrations of plates – CLPT approach

7.4.1 Simply supported special orthotropic plates

The first case to be solved is sometimes called *special orthotropic plates* for which the bending–stretching coupling terms B_{ij} and the bending–twisting coefficients D_{16} and D_{26} are set to zero. Then taking eq. (6.77) from Chapter 6 assuming symmetry ($B_{ij} = D_{16} = D_{26} = I_1 = 0$) and zeroing the in-plane and out-of-plane loads one obtains:

$$D_{11}\frac{\partial^4 w_0}{\partial x^4} + 2(D_{12} + 2D_{66})\frac{\partial^4 w_0}{\partial x^2 \partial y^2} + D_{22}\frac{\partial^4 w_0}{\partial y^4} + I_0\frac{\partial^2 w_0}{\partial t^2} - I_2\frac{\partial^2}{\partial t^2}\left(\frac{\partial^2 w_0}{\partial x^2} + \frac{\partial^2 w_0}{\partial y^2}\right) = 0$$

(7.84)

where I_0 and I_2 are defined in eq. (7.2). Let us assume the following solution for the out-of-plane displacement w_0 (tacitly assuming harmonic vibrations with a circular frequency ω)

$$w_0(x, y, t) = W_{mn}\sin\left(\frac{m\pi x}{a}\right)\left(\frac{n\pi y}{b}\right)e^{i\omega t}$$

(7.85)

where a is the length and b is the width of the plate having a total thickness of t, and substituting in eq. (7.84) we get

$$D_{11}\left(\frac{m\pi}{a}\right)^4 + 2(D_{12} + 2D_{66})\left(\frac{m\pi}{a}\right)^2\left(\frac{n\pi}{b}\right)^2 + D_{22}\left(\frac{n\pi}{b}\right)^4 - \omega^2\left\{I_0 + I_2\left[\left(\frac{m\pi}{a}\right)^2 + \left(\frac{n\pi}{b}\right)^2\right]\right\} = 0$$

(7.86)

The solution for eq. (7.86) has the following form, which presents the natural frequencies for a special orthotropic laminated plate

$$\omega_{mn}^2 = \left(\frac{\pi}{a}\right)^4 \frac{D_{11}m^4 + 2(D_{12} + 2D_{66})m^2 n^2 \left(\frac{a}{b}\right)^2 + D_{22}n^4 \left(\frac{a}{b}\right)^4}{I_0 + I_2 \left(\frac{\pi}{a}\right)^2 \left[m^2 + n^2 \left(\frac{a}{b}\right)^2\right]} \tag{7.87}$$

while the mode of vibration is given by

$$w_0(x, y) = W_{mn} \sin\left(\frac{m\pi x}{a}\right)\left(\frac{n\pi y}{b}\right) \tag{7.88}$$

One can see from eq. (7.87) that inclusion of the rotary inertia I_2 tends to reduce the natural frequencies. For a square plate, $a = b$, when neglecting the rotary inertia, the general frequency would show as

$$\omega_{mn}^2 = \frac{\pi^4}{I_0 a^4} \left[D_{11}m^4 + 2(D_{12} + 2D_{66})m^2 n^2 + D_{22}n^4\right] \tag{7.89}$$

The lowest frequency, sometimes called also the fundamental frequency, will occur at $m = n = 1$, namely for a rectangular plate we will have

$$\omega_{11}^2 = \frac{\pi^4}{I_0 a^4} \left[D_{11} + 2(D_{12} + 2D_{66})\left(\frac{a}{b}\right)^2 + D_{22}\left(\frac{a}{b}\right)^4\right] \tag{7.90}$$

7.4.2 Simply supported on two opposite edges of special orthotropic plates

Using the Lévy method[1] one can solve the vibrations of rectangular plates, where two opposite edges are on simply-supported boundary conditions, while the other two sides can be either clamped, free or any other combination of boundaries. Therefore the equilibrium equation, without in-plane loads, is given by eq. (7.84). The out-of-plane deflections can be written as

$$w_0(x, y, t) = W_m(x)\left(\frac{n\pi y}{b}\right)e^{i\omega t} \tag{7.91}$$

Substituting eq. (7.91) into (7.84) leads to the following differential equation:

$$D_{11}\frac{d^4 W_m}{dx^4} + \left[\omega^2 I_2 - 2(D_{12} + 2D_{66})\left(\frac{n\pi}{b}\right)^2\right]\frac{d^2 W_m}{dx^2} - \left\{\omega^2\left[I_0 + I_2\left(\frac{n\pi}{b}\right)^2\right] - D_{22}\left(\frac{n\pi}{b}\right)^4\right\}W_m = 0 \tag{7.92}$$

or

$$\widehat{a}\frac{d^4 W_m}{dx^4} + \widehat{b}\frac{d^2 W_m}{dx^2} - \widehat{c}W_m = 0 \tag{7.93}$$

---

[1] M. Lévy, Memoire sur la theorie des plaques elastiques planes, J Math Pures Appl, Vol.3, p. 219,1899.

where

$$\hat{a} \equiv D_{11}, \quad b \mathrel{\hat{=}} \omega^2 I_2 - 2(D_{12} + 2D_{66})\left(\frac{n\pi}{b}\right)^2, \quad c \equiv \omega^2\left[I_0 + I_2\left(\frac{n\pi}{b}\right)^2\right] - D_{22}\left(\frac{n\pi}{b}\right)^4 \quad (7.94)$$

The general solution of eq. (7.92) has the following form:

$$W(x) = A_1\sinh(\alpha_1 x) + A_2\cosh(\alpha_1 x) + A_3\sin(\alpha_2 x) + A_4\cos(\alpha_2 x) \quad (7.95)$$

where

$$s_1 = \sqrt{\frac{-\hat{b} + \sqrt{\hat{b}^2 + 4\hat{a}\hat{c}}}{2\hat{a}}}, \quad s_2 = \sqrt{\frac{\hat{b} + \sqrt{\hat{b}^2 + 4\hat{a}\hat{c}}}{2\hat{a}}} \quad (7.96)$$

Application of the boundary conditions in the x direction will lead to the natural frequencies and their associated mode shapes in the x direction.

References

[1]   Murty, A. V. K., and Shimpi, R. P. Vibrations of laminated beams, Journal of Sound and Vibration, 36(2), 1974, 273–284.
[2]   Teoh, L. S., and Huang, C. C. The vibration of beams of fiber-reinforced material, Journal of Sound and Vibration, 51(4), 1977, 467–473.
[3]   Chandrashekhara, K., Krishnamurthy, K., and Roy, S. Free vibration of composite beams including rotary inertia and shear deformation, Composite Structures, 14, 1990, 269–279.
[4]   Singh, G., Rao, G.V., and Iyengar, N.G.R. Analysis of the nonlinear vibrations of unsymmetrically laminated composite beams, AIAA Journal, 29(10), 1991, 1727–1735.
[5]   Krishnaswamy, S., Chandrashekhara, K., and Wu, W.Z.B. Analytical solutions to vibration of generally layered composite beams, Journal of Sound and Vibration, 159(1), 1992, 85–99.
[6]   Chandrashekhara, K., and Bangera, K.M. Free vibration of composite beams using a refined shear flexible beam element, Computers and Structures, 43(4), 1992, 719–727.
[7]   Kant, T., and Swaminathan, K. Analytical solutions for free vibration of laminated composite and sandwich plates based on a higher-order refined theory, Composite Structures, 53, 2001, 73–85.
[8]   Aagaah, M.R., Mahinfalah, M., and Jazar, G.N. Natural frequencies of laminated composite plates using third order shear deformation theory, Composite Structures, 72, 2006, 273–279.
[9]   Abramovich, H., and Hamburger, O. Vibration of a uniform cantilever Timoshenko beam with translational and rotational springs and with a tip mass, Journal of Sound and Vibration, 154(1), 1992, 67–80.
[10] Abramovich, H. Shear deformation and rotary inertia effects of vibrating composite beams", Composite Structures, 20, 1992, 165–173.
[11] Abramovich, H. A note on experimental investigation on a vibrating Timoshenko cantilever beam, Journal of Sound and Vibration, 160(1), 1993, 167–171.
[12] Abramovich, H. Thermal buckling of cross-ply composite laminates using a first-order shear deformation theory, Composites Structures, 28, 1994, 201–213.
[13] Abramovich, H. Deflection control of laminated composite beams with piezoceramic layers-closed form solutions, Composite Structures, 43, 1998, 217–231.

[14]   Abramovich, H., Eisenberger, M., and Shulepov, O. Vibrations and buckling of cross-ply non-symmetric laminated composite beams, AIAA Journal, 34(5), 1996, 1064–1069. May.
[15]   Abramovich, H., and Livshits, A. Free vibrations of non-symmetric cross-ply laminated composite beams, J. of Sound and Vibration, 176(5), 1994, 597–612.
[16]   Abramovich, H., and Livshits, A. Dynamic behavior of cross-ply laminated beams with piezoelectric layers, Composite Structures, 25(1-4), 1993, 371–379.
[17]   Abramovich, H., and Livshits, A. Free vibrations of non-symmetric cross-ply laminated composite beams, Journal of Sound and Vibration, 176(5), 1994, 597–612.

Appendix A: General solution for a nonsymmetrical beam resting on any boundary conditions

Using eq. (7.36), and assuming no axial compression is applied ($\overline{N}_{xx} = 0$), while $I_1 = 0$ (by placing the beam's coordinate system in the middle plane of the beam) and the rotary moment of inertia, assumed to be being negligible ($I_2 = 0$) we have the following matrix notation:

$$\begin{bmatrix} A_{11}\frac{\partial^2}{\partial x^2} & -B_{11}\frac{\partial^3}{\partial x^3} \\ -B_{11}\frac{\partial^3}{\partial x^3} & D_{11}\frac{\partial^4}{\partial x^4} \end{bmatrix} \begin{Bmatrix} u_0(x,t) \\ w_0(x,t) \end{Bmatrix} + \begin{bmatrix} -I_0 & 0 \\ 0 & I_0 \end{bmatrix} \frac{\partial^2}{\partial t^2} \begin{Bmatrix} u_0(x,t) \\ w_0(x,t) \end{Bmatrix} = \begin{Bmatrix} 0 \\ 0 \end{Bmatrix} \tag{A-1}$$

Assuming that the nondimensional displacements have the following form:

$$\begin{Bmatrix} \frac{u_0(x,t)}{L} \\ \frac{w_0(x,t)}{L} \end{Bmatrix} = \begin{Bmatrix} U(x)e^{i\omega t} \\ W(x)e^{i\omega t} \end{Bmatrix} \tag{A-2}$$

while the axial nondimensional axis being $\xi = x/L$ (L is the length of the beam) and substituting the nondimensional expressions of the two beam's displacements into eq. (A-1) we get

$$\begin{bmatrix} \zeta_1^2 \frac{d^2}{d\xi^2} + p^2 & -\zeta^2 \frac{d^3}{d\xi^3} \\ -\zeta^2 \frac{d^3}{d\xi^3} & \frac{d^4}{d\xi^4} - p^2 \end{bmatrix} \begin{Bmatrix} U(\xi) \\ W(\xi) \end{Bmatrix} = \begin{Bmatrix} 0 \\ 0 \end{Bmatrix} \tag{A-3}$$

where

$$p^2 \equiv \frac{\omega^2 I_0 L^4}{D_{11}}, \quad b^2 \equiv \frac{D_{11}}{KA_{55}L^2}, \quad \zeta^2 \equiv \frac{B_{11}L}{D_{11}}, \quad \zeta_1^2 \equiv \frac{A_{11}L^2}{D_{11}} \tag{A-4}$$

The characteristic equation of eq. (A-3) has the following form:

$$\left(\zeta_1^2 - \zeta^4\right)s^3 + s^2 - \frac{\zeta_1^2}{p^2}s - \frac{1}{p^2} = 0, \qquad s \equiv \frac{m^2}{p^2} \tag{A-5}$$

Solving eq. (A-5) we can write the general solution for (A-3) in the following form (see a detailed discussion regarding the format of the solution in [17])

$$U = A_1\gamma\mu\sinh(m_1\xi) + A_2\gamma\mu\cosh(m_1\xi) + A_3\lambda\delta\sin(m_2\xi)$$
$$- A_4\lambda\delta\cos(m_2\xi) + A_5\alpha\beta\sin(m_3\xi) - A_6\alpha\beta\cos(m_3\xi)$$
$$W = A_1\cosh(m_1\xi) + A_2\sinh(m_1\xi) + A_3\cos(m_2\xi)$$
$$+ A_4\sin(m_2\xi) + A_5\cos(m_3\xi) + A_6\sin(m_3\xi) \tag{A-6}$$

where the various terms in eq. (A-6) are defined as follows:

$$m_1 \equiv \sqrt{s_1}p, \qquad m_2 \equiv \sqrt{-s_2}p, \qquad m_3 \equiv \sqrt{-s_3}p$$

$$\gamma \equiv \frac{\zeta^2 s_1}{\zeta_1^2 s_1 + 1}, \quad \delta \equiv \frac{\zeta^2 s_2}{\zeta_1^2 s_2 + 1}, \qquad \beta \equiv \frac{\zeta^2 s_3}{\zeta_1^2 s_3 + 1} \tag{A-7}$$
$$\mu \equiv \sqrt{s_1}p, \quad \lambda \equiv \sqrt{-s_2}p, \qquad \alpha \equiv \sqrt{-s_3}p$$

Imposing the adequate boundary conditions would lead to the finding of both the eigenvalues (the natural frequencies) and the eigenvectors (the modes of vibration). For this problem six boundary conditions should be imposed at each end as presented in Table A.1.

Table A.1: Boundary conditions for a nonsymmetric laminate beam (CLT approach).

Name	Boundary conditions
Clamped immovable end	$U = W = \dfrac{dW}{d\xi} = 0$
Clamped movable end	$\zeta_1^2\dfrac{dU}{d\xi} - \zeta^2\dfrac{d^2W}{d\xi^2} = W = \dfrac{dW}{d\xi} = 0$
Simply supported immovable end	$U = W = \zeta^2\dfrac{dU}{d\xi} - \dfrac{d^2W}{d\xi^2} = 0$
Simply supported movable end	$\zeta^2\dfrac{dU}{d\xi} - \dfrac{d^2W}{d\xi^2} = W = \zeta_1^2\dfrac{dU}{d\xi} - \zeta^2\dfrac{d^2W}{d\xi^2} = 0$
Free end	$\zeta^2\dfrac{dU}{d\xi} - \dfrac{d^2W}{d\xi^2} = \zeta_1^2\dfrac{d^2U}{d\xi^2} - \zeta^2\dfrac{d^3W}{d\xi^3} = \zeta_1^2\dfrac{dU}{d\xi} - \zeta^2\dfrac{d^2W}{d\xi^2} = 0$

Appendix B: Matrix notation for the equilibrium equations using CLT approach

A convenient way of presenting the equilibrium equations at buckling and/or vibration is the following matrix form:

$$
\begin{bmatrix} \alpha_{11} & \alpha_{12} & \alpha_{13} \\ \alpha_{21} & \alpha_{22} & \alpha_{23} \\ \alpha_{31} & \alpha_{32} & [\alpha_{33}-N] \end{bmatrix} \left\{ \begin{array}{c} u(x,y,t) \\ v(x,y,t) \\ w_0(x,y,t) \end{array} \right\} + \frac{\partial^2}{\partial t^2} \begin{bmatrix} m_{11} & 0 & m_{13} \\ 0 & m_{22} & m_{23} \\ m_{13} & m_{23} & m_{33} \end{bmatrix} \left\{ \begin{array}{c} u(x,y,t) \\ v(x,y,t) \\ w_0(x,y,t) \end{array} \right\} = \left\{ \begin{array}{c} 0 \\ 0 \\ q \end{array} \right\}
$$

$$(B-1)$$

where the various operators are given by

$$
\alpha_{11} \equiv A_{11}\frac{\partial^2}{\partial x^2} + 2A_{16}\frac{\partial^2}{\partial x \partial y} + A_{66}\frac{\partial^2}{\partial y^2}
$$

$$
\alpha_{22} \equiv A_{22}\frac{\partial^2}{\partial y^2} + 2A_{26}\frac{\partial^2}{\partial x \partial y} + A_{66}\frac{\partial^2}{\partial x^2}
$$

$$
\alpha_{33} \equiv D_{11}\frac{\partial^4}{\partial x^4} + 4D_{16}\frac{\partial^4}{\partial x^3 \partial y} + 2(D_{12}+2D_{66})\frac{\partial^4}{\partial x^2 \partial y^2} + 4D_{26}\frac{\partial^4}{\partial x \partial y^3} + D_{22}\frac{\partial^4}{\partial y^4}
$$

$$
\alpha_{12} = \alpha_{21} \equiv A_{16}\frac{\partial^2}{\partial x^2} + (A_{12}+A_{66})\frac{\partial^2}{\partial x \partial y} + A_{26}\frac{\partial^2}{\partial y^2} \tag{B-2}
$$

$$
\alpha_{13} = \alpha_{31} \equiv -B_{11}\frac{\partial^3}{\partial x^3} - 3B_{16}\frac{\partial^3}{\partial x^2 \partial y} - (B_{12}+2B_{66})\frac{\partial^3}{\partial x \partial y^2} - B_{26}\frac{\partial^3}{\partial y^3}
$$

$$
\alpha_{23} = \alpha_{32} \equiv -B_{16}\frac{\partial^3}{\partial x^3} - (B_{12}+2B_{66})\frac{\partial^3}{\partial x^2 \partial y} - 3B_{26}\frac{\partial^3}{\partial x \partial y^2} - B_{22}\frac{\partial^3}{\partial y^3}
$$

$$
N \equiv \overline{N}_{xx}\frac{\partial^2}{\partial x^2} + 2\overline{N}_{xy}\frac{\partial^2}{\partial x \partial y} + \overline{N}_{yy}\frac{\partial^2}{\partial y^2}
$$

and

$$
m_{11} \equiv -I_0, \quad m_{22} \equiv -I_0, \quad m_{33} \equiv I_0 - I_2\left(\frac{\partial^2}{\partial x^2} + \frac{\partial^2}{\partial y^2}\right)
$$

$$
m_{13} \equiv I_1\frac{\partial}{\partial x}, \quad m_{23} \equiv I_1\frac{\partial}{\partial y}, \tag{B-3}
$$

Appendix C: The terms of the matrix notation for the equilibrium equations using FSDPT approach

$$
\begin{bmatrix}
\widehat{\alpha}_{11} & \widehat{\alpha}_{12} & 0 & \widehat{\alpha}_{14} & \widehat{\alpha}_{15} \\
\widehat{\alpha}_{21} & \widehat{\alpha}_{22} & 0 & \widehat{\alpha}_{24} & \widehat{\alpha}_{25} \\
0 & 0 & \widehat{\alpha}_{33} & \widehat{\alpha}_{34} & \widehat{\alpha}_{34} \\
\widehat{\alpha}_{41} & \widehat{\alpha}_{42} & \widehat{\alpha}_{43} & \widehat{\alpha}_{44} & \widehat{\alpha}_{45} \\
\widehat{\alpha}_{51} & \widehat{\alpha}_{52} & \widehat{\alpha}_{53} & \widehat{\alpha}_{54} & \widehat{\alpha}_{55}
\end{bmatrix}
\begin{Bmatrix}
U_{mn} \\
V_{mn} \\
W_{mn} \\
\overline{E}_{mn} \\
E_{mn}
\end{Bmatrix}
=
\begin{Bmatrix}
0 \\
0 \\
0 \\
0 \\
0
\end{Bmatrix}
\qquad\text{(C-1)}
$$

where

$$
\widehat{\alpha}_{11} \equiv A_{11}\left(\frac{m\pi}{a}\right)^2 + A_{66}\left(\frac{n\pi}{b}\right)^2 \qquad \widehat{\alpha}_{12} = \widehat{\alpha}_{21} \equiv (A_{12} + A_{66})\left(\frac{m\pi}{a}\right)\left(\frac{n\pi}{b}\right)
$$

$$
\widehat{\alpha}_{14} = \widehat{\alpha}_{41} \equiv B_{11}\left(\frac{m\pi}{a}\right)^2 + B_{66}\left(\frac{n\pi}{b}\right)^2 \qquad \widehat{\alpha}_{15} = \widehat{\alpha}_{51} \equiv (B_{12} + B_{66})\left(\frac{m\pi}{a}\right)\left(\frac{n\pi}{b}\right)
$$

$$
\widehat{\alpha}_{22} \equiv A_{66}\left(\frac{m\pi}{a}\right)^2 + A_{22}\left(\frac{n\pi}{b}\right)^2 \qquad \widehat{\alpha}_{24} = \widehat{\alpha}_{42} \equiv (B_{12} + B_{66})\left(\frac{m\pi}{a}\right)\left(\frac{n\pi}{b}\right)
$$

$$
\widehat{\alpha}_{25} = \widehat{\alpha}_{52} \equiv B_{66}\left(\frac{m\pi}{a}\right)^2 + B_{22}\left(\frac{n\pi}{b}\right)^2 \qquad \widehat{\alpha}_{33} \equiv K\left[A_{44}\left(\frac{n\pi}{b}\right)^2 + A_{55}\left(\frac{m\pi}{a}\right)^2\right]
$$

$$
- \overline{N}_{xx}\left(\frac{m\pi}{a}\right)^2 - \overline{N}_{yy}\left(\frac{n\pi}{b}\right)^2
$$

$$
\widehat{\alpha}_{34} = \widehat{\alpha}_{43} \equiv KA_{55}\left(\frac{m\pi}{a}\right) \qquad \widehat{\alpha}_{35} = \widehat{\alpha}_{53} \equiv KA_{44}\left(\frac{n\pi}{b}\right) \qquad \widehat{\alpha}_{44} \equiv D_{11}\left(\frac{m\pi}{a}\right)^2 + D_{66}\left(\frac{n\pi}{b}\right)^2 + KA_{55}
$$

$$
\widehat{\alpha}_{45} = \widehat{\alpha}_{54} \equiv (D_{12} + D_{66})\left(\frac{m\pi}{a}\right)\left(\frac{n\pi}{b}\right) \qquad \widehat{\alpha}_{55} \equiv D_{22}\left(\frac{n\pi}{b}\right)^2 + D_{66}\left(\frac{m\pi}{a}\right)^2 + KA_{44}
$$

$$
\text{(C-2)}
$$

8 Dynamic buckling of thin-walled structures

8.1 Introduction

This chapter deals with what is called in the literature "dynamic" buckling of columns and plates (metal and composite materials). First, the term "dynamic" buckling will be explained and defined followed by examples from the literature. Then the equations of motions for columns and plates will be presented, and numerical and experimental results of tests performed on columns, plates and shells will be highlighted.

The topic of applying an axially time-dependent load onto a column was studied for many years, thus inducing lateral vibrations and eventually causing the buckling of the column. Sometimes this is called *vibration buckling*, as proposed by Lindberg [1]. As it is described in his fundamental report [1], the axial oscillating load might lead to unacceptable large vibrations amplitudes at a critical combination of the frequency and amplitude of the axial load and the inherent damping of the column. This behavior is presented in Fig. 8.1a (adapted from [1]), where an oscillating axial load induces bending moments that cause lateral vibrations of the column. As described in [1], the column will laterally vibrate at large amplitude when the loading frequency will be twice the natural lateral bending frequency of the column. The term, *vibration buckling*, used by Lindberg, presents some kind of similarity to vibration resonance. However, in the case of vibration resonance the applied load is in the same direction as the motion, namely in our case lateral to the column, and the resonance will occur when the loading frequency equals the natural frequency of the column. This type of vibration buckling was called by Lindberg as *dynamic stability of vibrations induced by oscillating parametric loading*. This type of resonance is also called in the literature as *parametric resonance* (see an application of this type of dynamic stability in [2, 3]).

Another type of vibration type is sometimes also called pulse buckling, where the structure will be deformed to unacceptably large amplitudes as a result of a transient response of the structure to the dynamic axially applied load [1]. One should note that the sudden applied load might cause a permanent deformation due to plastic response of the column, a snap to a larger postbuckling deformation or simply a return to its undeform state. This is pictured in Fig. 8.1b (adapted from [1]) where the response of the column to a sudden short-time axial load is shown.

One should note that buckling will occur when an unacceptably large deformation or stress is encountered by the column. The column can withstand a large axial load before reaching the buckling condition, provided the load duration is short enough. Under an intense, short duration axial load, the column would buckle into a very high-order mode as shown in Fig 8.1b. Lindberg [1] claims that pulse buckling falls under the following mathematical definition: *dynamic response of structural*
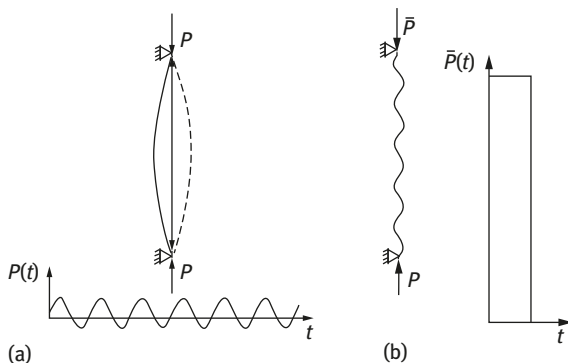
Fig. 8.1: (a) Buckling under parametric resonance and (b) pulse-type buckling.

systems induced by time-varying parametric loading. Throughout this chapter, the pulse buckling will be equivalent to dynamic buckling.

The dynamic buckling of structures has been widely addressed in the literature. It started with the famous paper by Budiansky and Roth [4], through Hegglin's report on dynamic buckling of columns [5] and continued with Budiansky and Hutchinson [6] and Hutchinson and Budiansky [7] in the mid-sixties. Then more structures have been addressed as presented in typical references [1, 2, 8–43].

One of the most intriguing and challenging things is to define a criterion to clearly define the critical load causing the structure to buckle under the subjected pulse loading. As presented by Kubiak [32] and also by Ari Gur [13, 19, 22] and others in [18, 20, 24–26] a new quantity is introduced called DLF (dynamic load factor) to enable the use of the dynamic buckling criteria. It is defined as

$$\text{DLF} \equiv \frac{\text{Pulse} \quad \text{Buckling} \quad \text{Quantity}}{\text{Static} \quad \text{Buckling} \quad \text{Quantity}} \equiv \frac{(P_{\text{cr}})_{\text{dyn.}}}{(P_{\text{cr}})_{\text{static}}} \tag{8.1}$$

According to Kubiak [32], the most popular criterion had been proposed by Volmir [10] for plates subjected to in-plane pulse loading. As quoted in [32], Volmir proposed the following criterion:

Dynamic critical load corresponds to the amplitude of pulse load (of constant duration) at which the maximum plate deflection is equal to some constant value k (k – half or one plate thickness).

Another very widely used criterion has been formulated and proposed by Budiansky and Hutchinson [6], based on an earlier work [4] and latter extended [7]. Originally, the criterion was formulated for shell-type structures but was used also for columns and plates. The criterion claims that "Dynamic stability loss occurs when the maximum deflection grows rapidly with the small variation of the load

amplitude." This criterion is schematically presented in Fig. 8.2b, where $R(\lambda, t)$ is the response of the simply nonlinear model assumed in [6] and presented also in Fig. 8.2a, and λ is the nondimensional applied dynamic pulse-type compressive load. Figure. 8.2c presents the application of the criterion for the axisymmetric dynamic buckling of clamped shallow spherical shells as presented in [4].
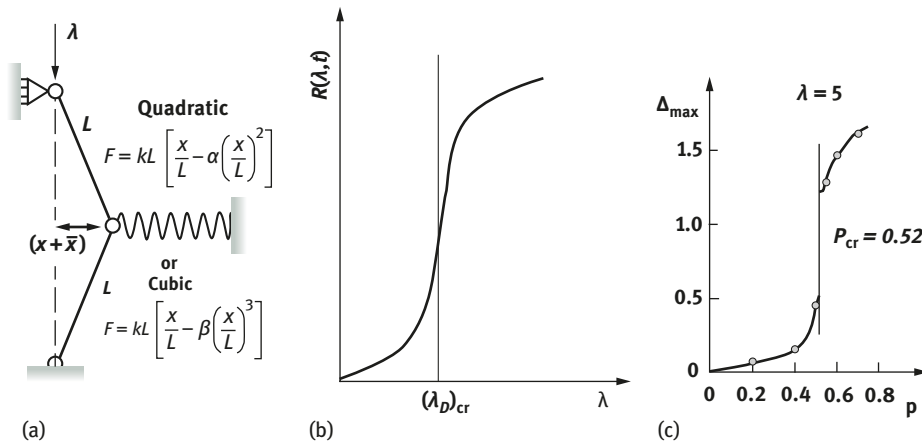
Fig. 8.2: (a) The nonlinear model (adapted from [6]), (b) the Budiansky and Hutchinson (B&H) schematic criterion (from [6]) and (c) the application of the B&H criterion to axisymmetric dynamic buckling of clamped shallow spherical shells ((adapted from [4]).

Other dynamic buckling criteria were suggested and applied by Ari-Gur and Simonetta in their manuscript [22]. They formulated four criteria presented schematically in Figs 8.3a–d. The first criterion (see Fig. 8.3a) correlates the maximum lateral deflection, W_m, to the pulse intensity defined as L_m. The first criterion is stated as "Buckling occurs when, for a given pulse shape and duration, a small increase in the pulse intensity causes a sharp increase in the rate of growth of the peak lateral deflection" [22]. The authors claim that this criterion can be used to both displacement and force loading types for a wide range of pulse frequencies; however, for very short pulse durations the results might be misleading. The reason for this is connected to the characteristics of the out-of-plane deflections which, for short pulse duration in the vicinity of buckling loads, turn out to have short wavelength patterns that are associated with smaller peak deflections. Therefore, the authors present the second criterion (Fig. 8.3b), which comes to answer the deficiency of the first criterion and is suitable to patterns of short-wavelength deflection shapes. It claims that "dynamic buckling occurs when a small increase in the pulse intensity causes a decrease in the peak lateral deflection" and is relevant to only impulsive loads and may be used in complimentary to the first criterion The last
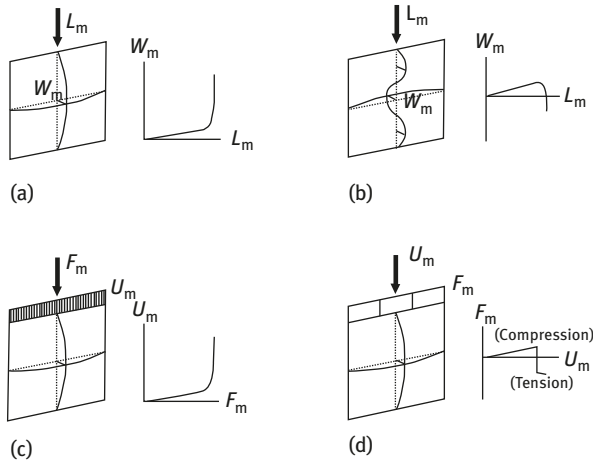
Fig. 8.3: Buckling criteria (adapted from [6]): (a) the first criterion, (b) the second criterion, (c) the third criterion and (d) the fourth criterion.

two criteria presented in [22] connect the intensity of the applied load versus the maximum response of the loaded edge, say at $x = 0$. According to the third buckling criterion (Fig. 8.3c), "buckling occurs when a small increase in the force intensity F_m causes a sharp increase in the peak longitudinal displacement U_m at $x = 0$." The buckling phenomenon under pulse loading is due to the diminishing of the structural resistance to an in-plane compressive load when the dynamic lateral deflections grow rapidly. The fourth buckling criterion associated with a displacement pulse (Fig. 8.3d) states that "buckling occurs when a small increase in the pulse displacement intensity U_m causes a transition of the peak reaction force F_m at $x = 0$ from compression to tension." This transition would come true, when the tensile force needed to keep the deforming structure at the prescribed U_m would be greater than the maximum compression at its loaded edge.

Another interesting criterion was suggested by Petry and Fahlbush [24], claiming that the Budiansky–Hutchinson criterion is very conservative for structures with stable postbuckling equilibrium path because it does not take into account load-carrying capacity of the structure. The criterion proposed is based on stress analysis and claims that "a stress failure occurs if the effective stress σ_E exceeds the limit stress of the material, σ_L; a dynamic response caused by an impact is defined to be dynamically stable if $\sigma_E \leq \sigma_L$ is fulfilled at every time everywhere in the structure." Using this criterion, which is claimed to be practical also for ductile materials (by using the yield stress σ_Y instead of σ_L), the DLF (see eq. (8.1)) is modified to

$$\mathrm{DLF} \equiv \frac{(N_F)_{\mathrm{dyn.}}}{(N_F)_{\mathrm{static}}} \tag{8.2}$$

where $(N_F)_{\text{dyn}}$ and $(N_F)_{\text{static}}$ are defined as the dynamic failure and static failure loads, respectively.

8.2 Dynamic buckling of columns

8.2.1 Dynamic buckling of columns using CLT

The column differential equations of motion under time-dependent axial compression, as presented in Fig. 8.4, are given by
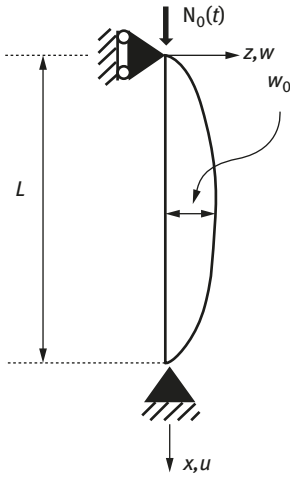
Fig. 8.4: A column with geometric initial imperfection, w_0, subjected to time-dependent axial compression ($N_0(t)$ is the axial compression at $x = 0$).

$$N_{x,x} = I_0 \ddot{u} - I_1 \ddot{w}_{,x} \tag{8.3}$$

$$[M_{x,x} + N_x \cdot w_{,x} + I_2 \cdot \ddot{w}_{,xx}] = I_0 \ddot{w} + I_1 \ddot{u}_{,x} \tag{8.4}$$

where

$$(I_0; I_1; I_2) = \rho \int\limits_{-h/2}^{h/2} (1; z; z^2) \, dz \tag{8.5}$$

and $()_{,x}$ is the first partial differentiation with respect to x, $\ddot{u}, \ddot{w}$ are the second partial differentiation of the axial and lateral displacements with respect to time, t, h is the total thickness of the column and ρ is the relevant densities for each layer in the laminate.

Assuming that the force and moment resultants can be written as a function of the strains and curvatures, according to the CLT approach we obtain

$$\left\{ \begin{array}{c} N_x \\ M_x \end{array} \right\} = \left[\begin{array}{cc} A_{11} & B_{11} \\ B_{11} & D_{11} \end{array} \right] \left\{ \begin{array}{c} \varepsilon_x \\ \kappa_x \end{array} \right\} \tag{8.6}$$

where

$$(A_{11};B_{11};D_{11}) = \int\limits_{-h/2}^{h/2} \overline{Q}_{11}\left(1;z;z^2\right) dz \tag{8.7}$$

and $\overline{Q}_{11}$ is the plane stress-reduced stiffness for each layer after transformation (for an exact expression, see Chapter 2). The strain displacements (u longitudinal displacement, w lateral displacement) relationships are

$$\left\{ \begin{array}{c} \varepsilon_x \\ \kappa_x \end{array} \right\} = \left\{ \begin{array}{c} u_{,x} + \frac{1}{2}\left(w_{,x}^2 - w_{0,x}^2\right) \\ -(w - w_0)_{,xx} \end{array} \right\} \tag{8.8}$$

Substitution of eqs. (8.6)–(8.8) into eqs (8.3) and (8.4) yields

$$A_{11}(u_{,xx} + w_{,x}\cdot w_{,xx} - w_{0,x}\cdot w_{0,xx}) - B_{11}(w - w_0)_{,xxx} = I_0\ddot{u} - I_1\ddot{w}_{,x} \tag{8.9}$$

$$A_{11}\left[(u_{,x}\cdot w_{,x})_{,x} + \frac{3}{2}w_{,x}^2\cdot w_{,xx} - w_{0,x}\left(w_{0,xx}\cdot w_{,x} - \frac{1}{2}w_{0,x}\cdot w_{,xx}\right)\right] + $$
$$B_{11}\left[u_{,xx} + w_{0,xx}(w - w_o)_{,x}\right]_{,x} - D_{11}[w - w_o]_{,xxxx} = I_0\ddot{w} + I_1\ddot{u}_{,x} \tag{8.10}$$

Assuming a symmetric laminate, $B_{11} = I_1 = 0$, then eqs. (8.9) and (8.10) are simplified to yield

$$A_{11}(u_{,xx} + w_{,x}\cdot w_{,xx} - w_{0,x}\cdot w_{0,xx}) = I_0\ddot{u} \tag{8.11}$$

$$A_{11}\left[(u_{,x}\cdot w_{,x})_{,x} + \frac{3}{2}w_{,x}^2\cdot w_{,xx} - w_{0,x}\left(w_{0,xx}\cdot w_{,x} - \frac{1}{2}w_{0,x}\cdot w_{,xx}\right)\right] - D_{11}[w - w_o]_{,xxxx} = I_0\ddot{w} \tag{8.12}$$

One should note that all the terms in eqs. (8.11) and (8.12) are a function of both x and t.

The associated boundary conditions (pinned-pinned or simply supported) for the symmetric laminate are

$$\text{Lateral deflection:} \quad w(0,t) = w(L,t) = 0 \tag{8.13}$$

$$\text{Bending moment:} \quad D_{11}\cdot w_{,xx}(0,t) = D_{11}\cdot w_{,xx}(L,t) = 0 \tag{8.14}$$

$$\text{Axial force:} \quad A_{11}\cdot u_{,x}(0,t) = N_x(0,t) = -N_0(t) = -N_0\sin\frac{\pi t}{T} \tag{8.15}$$

$$\text{Axial displacement:} \quad u_{,x}(L,t) = 0 \tag{8.16}$$

while the initial conditions assume that $w(x, 0) = w_0$ $w_{,x}(x, 0) = u(0, 0) = \dot{u}(0, 0) = 0$.

Note that eqs. (8.11) and (8.12) can be used for an isotropic column, by letting $A_{11} = EA$, the axial stiffness (E = Young's modulus and A = cross section of the column) and the bending stiffness, $D_{11} = Eh^3/[12(1 - v^2)]$.

The solution for the equations of motion (8.11) and (8.12) can be obtained using energy methods, like the Galerkin method, using the boundary and initial conditions presented in eqs. (8.13)–(8.16). To apply the Galerkin approach, one should assume displacements that satisfy the boundary conditions of the problem, namely for the present case the following functions will be assumed:

$$w(x, t) = A(t) \sin \frac{\pi x}{L}; \quad w_0(x) = A_0 \sin \frac{\pi x}{L}$$
$$u(x, 0) = B(t) \cos \frac{\pi x}{L}; \quad N_0(t) = N_0 \sin \frac{\pi t}{T}. \tag{8.17}$$

Multiplying eq. (8.11) by the expression for $u(x, 0)$ while eq. (8.12) is multiplied by $w(x, t)$ and integrating both from $x = 0$ till $x = L$, will exclude the x dependence, yielding two nonlinear time-dependent equations that have to be solved numerically.

For each value of N_o, the response of the beam w and u can be calculated for an assumed initial geometric imperfection, $w_0(x, t) = A_0 \sin \frac{\pi x}{L}$, where A_0 is a known amplitude (usually percentage of the columns thickness), for a constant time period T.

A typical drawing is presented in Fig. 8.5 (adapted from [18]). Calculating the dynamic buckling for each value of the $2T/T_b$ and dividing it by the static buckling load will yield the DLF for the tested or calculated case (see eq. (8.1).
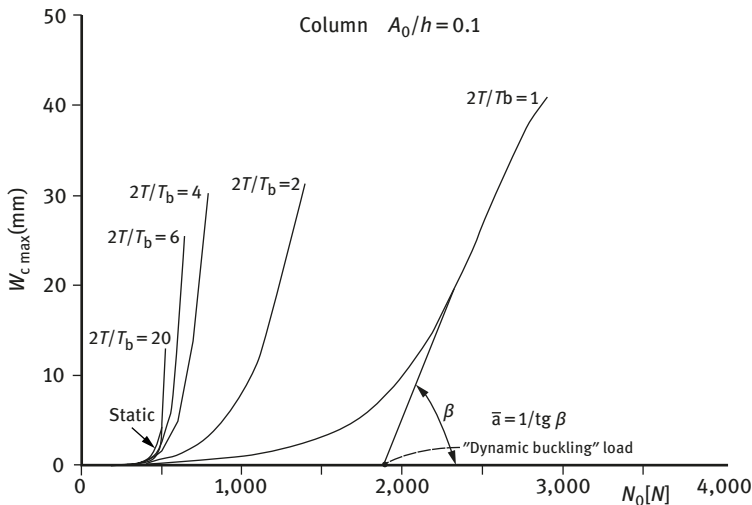
Fig. 8.5: The influence of the loading duration (T) on the columns response (adapted from [18]), T_b first natural period of the column, A_0 is the amplitude of the initial geometric imperfection.

8.2.2 Dynamic buckling of columns using FSDT

To solve the dynamic buckling of columns (see Fig. 8.4) using the FSDT we shall assume the following displacement field:

$$u_x(x, z, t) = u(x, t) + z\phi_x(x, t)$$
$$u_z(x, z, t) = w(x, t) - w_0(x)$$
(8.18)

where the assumed variables u and w are displacements in the x and z directions, of a point on the mid-plane of the plate (namely at $z = 0$), respectively, and ϕ_x is a rotation about the x-axis, while w_0 is the initial geometric imperfection of the column. The equations of motion can be written as (see Chapters 6 and 7)

$$N_{x,x} = I_0 \ddot{u} + I_1 \ddot{\phi}_x$$
$$Q_{x,x} + [N_x \cdot (w_{,x} - w_{0,x})]_{,x} = I_0 \ddot{w}$$
$$M_{x,x} - Q_x = I_2 \ddot{\phi}_x + I_1 \ddot{u}$$
(8.19)

In eq. (8.19), Q_x is the shear force or the transverse force resultant defined as

$$Q_x = K \int_{-h/2}^{+h/2} \tau_{xy} \cdot dz$$
(8.20)

where K is the shear correction coefficient computed by equating the strain energy due to transverse shear stresses to the strain energy due to true transverse shear as calculated by a 3D elasticity theory while τ_{xy} is the transverse shear stress. For a homogenous beam having a rectangular cross section, $K = 5/6$ (see Chapter 6). The force and moment resultants as a function of displacements are given by

$$\begin{Bmatrix} N_x \\ M_x \\ Q_x \end{Bmatrix} = \begin{bmatrix} A_{11} & B_{11} & 0 \\ B_{11} & D_{11} & 0 \\ 0 & 0 & KA_{55} \end{bmatrix} \begin{Bmatrix} u_{,x} + \frac{1}{2}(w_{,x}^2 - w_{0,x}^2) \\ \phi_{x,x} \\ \phi_x + w_{,x} - w_{0,x} \end{Bmatrix}$$
(8.21)

As assumed in Section 8.2.1, the strains have the following form:

$$\begin{Bmatrix} \varepsilon_x \\ \gamma_{xz} \end{Bmatrix} = \begin{Bmatrix} u_{x,x} + \frac{1}{2}(w_{,x}^2 - w_{0,x}^2) \\ u_{x,z} + u_{z,x} \end{Bmatrix} = \begin{Bmatrix} u_{,x} + \frac{1}{2}(w_{,x}^2 - w_{0,x}^2) + z\phi_{x,x} \\ \phi_x + w_{,x} - w_{0,x} \end{Bmatrix}$$
8.22

Substituting eq. (8.21) into eq. (8.19) yields the following equations of motion expressed by the three assumed displacements, $u(x, t)$, $w(x, t)$, $\phi_x(x, t)$ and the known initial geometric imperfection, $w_0(x)$ (see also a similar derivation in [25]):

$$A_{11}(u,_{xx} + w,_x \cdot w,_{xx} - w_{0,x} \cdot w_{0,xx}) + B_{11}\phi_{x,xx} = I_0\ddot{u} + I_1\ddot{\phi}_x$$

$$\left[A_{11}(u,_{xx} + w,_x \cdot w,_{xx} - w_{0,x} \cdot w_{0,xx}) + B_{11}\phi_{x,xx}\right](w,_x - w_{0,x}) +$$

$$\left[A_{11}\left(u,_x + \frac{1}{2}w,_x^2 - \frac{1}{2}w_{0,x}^2\right) + B_{11}\phi_{x,x}\right](w,_{xx} - w_{0,xx}) + KA_{55}(\phi_{x,x} + w,_{xx} - w_{0,xx}) = I_0\ddot{w}$$

$$B_{11}(u,_{xx} + w,_x \cdot w,_{xx} - w_{0,x} \cdot w_{0,xx}) + D_{11}\phi_{x,xx} - KA_{55}(\phi_x + w,_x - w_{0,x}) = I_2\ddot{\phi}_x + I_1\ddot{u}$$

$$(8.23)$$

For a symmetric layup, $B_{11} = I_1 = 0$, then eq. (8.23) are simplified to yield

$$A_{11}(u,_{xx} + w,_x \cdot w,_{xx} - w_{0,x} \cdot w_{0,xx}) = I_0\ddot{u}$$

$$\left[A_{11}(u,_{xx} + w,_x \cdot w,_{xx} - w_{0,x} \cdot w_{0,xx})\right](w,_x - w_{0,x}) +$$

$$\left[A_{11}\left(u,_x + \frac{1}{2}w,_x^2 - \frac{1}{2}w_{0,x}^2\right)\right](w,_{xx} - w_{0,xx}) + KA_{55}(\phi_{x,x} + w,_{xx} - w_{0,xx}) = I_0\ddot{w}$$

$$(8.24)$$

$$D_{11}\phi_{x,xx} - KA_{55}(\phi_x + w,_x - w_{0,x}) = I_2\ddot{\phi}_x$$

As in the previous section, one should note that all the terms in eq. (8.24) are a function of both x and t.

The associated boundary conditions (pinned–pinned or simply supported) for the symmetric laminate are

$$\text{Lateral deflection:} \quad w(0,t) = w(L,t) = 0 \qquad (8.25)$$

$$\text{Bending moment:} \quad D_{11} \cdot \phi_{x,x}(0,t) = D_{11} \cdot \phi_{x,x}(L,t) = 0 \qquad (8.26)$$

$$\text{Axial force:} \quad A_{11} \cdot u,_x(0,t) = N_x(0,t) = -N_0(t) = -N_0\sin\frac{\pi t}{T} \qquad (8.27)$$

$$\text{Axial displacement:} \quad u,_x(L,t) = 0 \qquad (8.28)$$

while the initial conditions assume that $w(x,0) = w_0$, $w,_x(x,0) = u(0,0) = \dot{u}(0,0) = 0$.

As before the analytic solution of the equations of motion cannot be obtained, therefore, energy methods like Galerkin method are suggested. Suitable assumed solutions for the case of simply supported boundary conditions are

$$u(x,0) = A(t)\cos\frac{\pi x}{L}, \quad w(x,t) = B(t)\sin\frac{\pi x}{L}, \quad \phi_x(x,t) = C(t)\cos\frac{\pi x}{L}$$

$$w_0(x) = A_0\sin\frac{\pi x}{L}, \quad N_0(t) = N_0\sin\frac{\pi t}{T} \qquad (8.29)$$

The procedure described before in Section 8.2 is again employed to obtain the response of the column to a pulse-type loading. As shown in Fig. 8.6, based on the
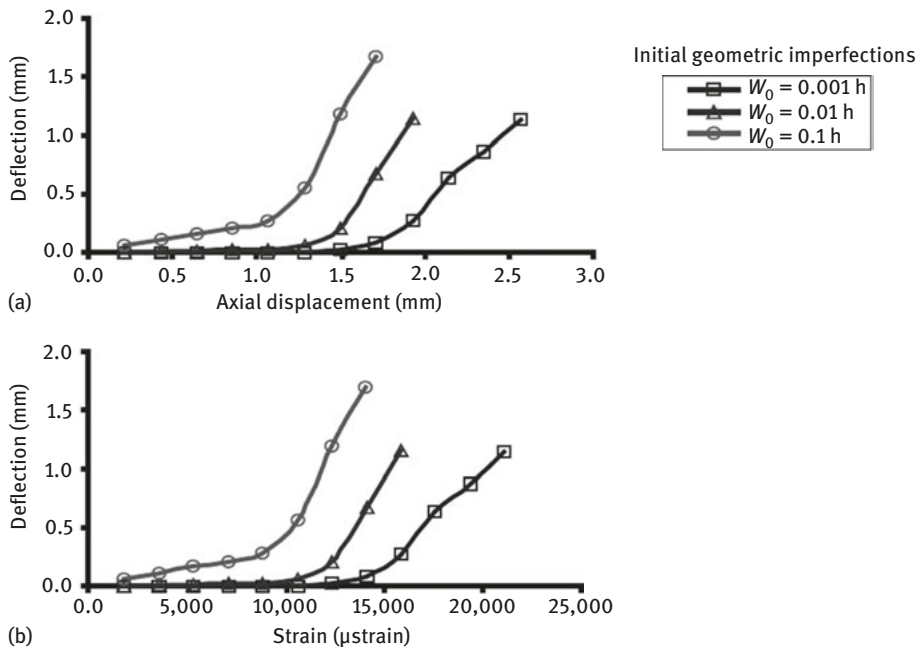
Fig. 8.6: The dynamic pulse buckling response of a column ($L = 150$ mm, width $= 20$ mm) for various initial geometric imperfections: (a) mid-span deflection versus maximal axial displacement at the impacted end; (b) mid-span deflection versus compressive strain at the neutral axis of the column mid-span (adapted from [25]).

results presented in [25], the response of the column has a similar behavior to what had been presented in Fig. 8.5. Note that in Fig. 8.6b, the compressive strain is a linear function of the applied axial compression load; therefore, it can be compared with what it is presented in Fig. 8.5.

8.3 Dynamic buckling of plates

The present derivation for the dynamic buckling of orthotropic rectangular plates under uniaxial loading is based on Ekstrom's fundamental study [11] presented already in 1973 using the models developed by Lekhnitskii for anisotropic plates [44]. Let us assume a simply-supported rectangular orthotropic plate uniaxially loaded as presented in Fig. 8.7. We choose the natural axes of the material to coincide with the coordinate axes leading to the following in-plane stress–strain relations
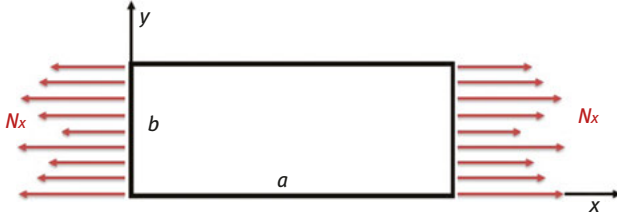
Fig. 8.7: A thin orthotropic plate uniaxial loaded.

$$\begin{Bmatrix} \sigma_x \\ \sigma_y \\ \tau_{xy} \end{Bmatrix} = \frac{1}{1 - \upsilon_{xy} \cdot \upsilon_{yx}} \begin{bmatrix} E_x & \upsilon_{xy}E_y & 0 \\ \upsilon_{yx}E_x & E_y & 0 \\ 0 & 0 & (1 - \upsilon_{xy} \cdot \upsilon_{yx})G_{xy} \end{bmatrix} \begin{Bmatrix} \varepsilon_x \\ \varepsilon_y \\ \gamma_{xy} \end{Bmatrix}$$

$$\equiv \begin{bmatrix} Q_{11} & Q_{12} & 0 \\ Q_{21} & Q_{22} & 0 \\ 0 & 0 & Q_{66} \end{bmatrix} \begin{Bmatrix} \varepsilon_x \\ \varepsilon_y \\ \gamma_{xy} \end{Bmatrix} \tag{8.30}$$

$$\begin{Bmatrix} \varepsilon_x \\ \varepsilon_y \\ \gamma_{xy} \end{Bmatrix} = \begin{bmatrix} \dfrac{1}{E_x} & -\dfrac{\upsilon_{xy}}{E_x} & 0 \\ -\dfrac{\upsilon_{yx}}{E_y} & \dfrac{1}{E_y} & 0 \\ 0 & 0 & \dfrac{1}{G_{xy}} \end{bmatrix} \begin{Bmatrix} \sigma_x \\ \sigma_y \\ \tau_{xy} \end{Bmatrix} \tag{8.31}$$

and

$$Q_{12} = Q_{21} \quad \Rightarrow \quad \upsilon_{yx} = \frac{E_x}{E_y} \upsilon_{xy} \tag{8.32}$$

The dynamic buckling problem can be solved assuming out-of-plane initial geometric imperfections (w_0), and therefore the strains will be assumed to have the following expressions:

$$\begin{Bmatrix} \varepsilon_x \\ \varepsilon_y \\ \gamma_{xy} \end{Bmatrix} = \begin{Bmatrix} \dfrac{\partial u}{\partial x} + \dfrac{1}{2}\left[\left(\dfrac{\partial w}{\partial x}\right)^2 - \left(\dfrac{\partial w_0}{\partial x}\right)^2\right] \\ \dfrac{\partial v}{\partial y} + \dfrac{1}{2}\left[\left(\dfrac{\partial w}{\partial y}\right)^2 - \left(\dfrac{\partial w_0}{\partial y}\right)^2\right] \\ \dfrac{\partial u}{\partial x} + \dfrac{\partial v}{\partial y} + \dfrac{\partial^2 w}{\partial x \partial y} - \dfrac{\partial^2 w_0}{\partial x \partial y} \end{Bmatrix} \tag{8.33}$$

where $w(x, y, t)$ is the total out-of-plane, $w_0 (x, y)$ is the initial out-of-plane geometric displacement and $u(x, y, t)$ and $v(x, y, t)$ are the in-plane displacements in the x and y directions, respectively.

The compatibility equation for the stress function $F(x, y, t)$ and the plate equations of motion (see [11, 44]) can be written as

$$\frac{1}{E_y} \cdot \frac{\partial^4 F}{\partial x^4} + \frac{1}{E_x} \cdot \frac{\partial^4 F}{\partial y^4} + 2\left(\frac{1}{2G_{xy}} - \frac{v_{xy}}{E_x}\right) = \left(\frac{\partial^2 w}{\partial x \partial y}\right)^2 - \left(\frac{\partial^2 w_0}{\partial x \partial y}\right)^2 + \frac{\partial^4 w_0}{\partial x^2 \partial y^2} - \frac{\partial^4 w}{\partial x^2 \partial y^2} \quad (8.34)$$

$$D_x \frac{\partial^4(w - w_0)}{\partial x^4} + 2(D_1 + 2D_{xy})\frac{\partial^4(w - w_0)}{\partial x^2 \partial y^2} + D_y \frac{\partial^4(w - w_0)}{\partial y^4} =$$

$$h\left[\frac{\partial^2 w}{\partial x^2} \cdot \frac{\partial^2 F}{\partial y^2} - 2\frac{\partial^2 w}{\partial x \partial y} \cdot \frac{\partial^2 F}{\partial x \partial y} + \frac{\partial^2 w}{\partial y^2} \cdot \frac{\partial^2 F}{\partial x^2} - \rho\frac{\partial^2 w}{\partial t^2}\right] \quad (8.35)$$

where h is the plate thickness and ρ is the plate density. The flexural densities of the plate are defined as follows:

$$D_x \equiv \frac{E_x h^3}{12(1 - v_{xy} v_{yx})}; \quad D_y \equiv \frac{E_y h^3}{12(1 - v_{xy} v_{yx})}; \quad D_{xy} = \frac{G_{xy} h^3}{12}$$

$$D_1 \equiv \frac{E_x v_{yx} h^3}{12(1 - v_{xy} v_{yx})} = \frac{E_y v_{xy} h^3}{12(1 - v_{xy} v_{yx})} \quad (8.36)$$

The out-of-plane boundary conditions of the present problem, assuming that the initially straight edges of the plate remain straight after buckling can be written as

$$@x = 0, a \quad w = w_0 = 0 \quad \text{and} \quad \frac{\partial^2 w}{\partial x^2} = \frac{\partial^2 w_0}{\partial x^2} = 0$$

$$@y = 0, b \quad w = w_0 = 0 \quad \text{and} \quad \frac{\partial^2 w}{\partial y^2} = \frac{\partial^2 w_0}{\partial y^2} = 0 \quad (8.37)$$

The in-plane boundary conditions have no restrain at $y = 0, b$ and in the x direction

$$@x = 0, a \quad \frac{1}{b}\int_0^b \sigma_x dy = \frac{1}{b}\int_0^b \frac{\partial^2 F}{\partial y^2} dy = -P$$

$$@y = 0, b \quad \frac{1}{a}\int_0^a \sigma_y dx = \frac{1}{a}\int_0^a \frac{\partial^2 F}{\partial x^2} dx = 0 \quad (8.38)$$

where P is the compression load acting on the plate.

The assumed solution for the w, and the initial geometric imperfection, w_0, have the following forms:

$$w(x, y, t) = A(t)\sin\frac{m\pi x}{a}\sin\frac{n\pi y}{b} \quad (8.39)$$

$$w_o(x, y, t) = A_o \sin\frac{m\pi x}{a}\sin\frac{n\pi y}{b} \quad (8.40)$$

One should note that the expressions in eqs. (8.39) and (8.40) satisfy the boundary conditions assumed above (eq. (8.37)). Substituting those equations in the compatibility equation leads to the following relationship between the stress function F and the displacements

$$\frac{1}{E_y} \cdot \frac{\partial^4 F}{\partial x^4} + \frac{1}{E_x} \cdot \frac{\partial^4 F}{\partial y^4} + 2\left(\frac{1}{2G_{xy}} - \frac{v_{xy}}{E_x}\right) = \frac{m^2 n^2 \pi^4}{2a^2 b^2}\left[\cos\frac{2m\pi x}{a} + \cos\frac{2n\pi y}{b}\right]\left(A^2 - A_0^2\right)$$

(8.41)

The solution for eq. (8.41), which also satisfies the in-plane boundary conditions, eq. (8.38), can be written as

$$F(x, y, t) = \left(A^2 - A_0^2\right)\left[\frac{a^2 n^2 E_y}{32 b^2 m^2}\cos\frac{2m\pi x}{a} + \frac{b^2 m^2 E_x}{32 a^2 n^2}\cos\frac{2n\pi y}{b}\right] - \frac{P}{2}y^2$$

(8.42)

Equation (8.42) is then inserted in eq. (8.34) yielding

$$\frac{\pi^4}{h}\left[D_x\frac{m^4}{a^4} + 2(D_1 + 2D_{xy})\frac{m^2 n^2}{a^2 b^2} + D_y\frac{n^4}{b^4}\right][A(t) - A_0] = \frac{m^2 \pi^2}{a^2}P(t) \cdot A(t)$$

$$-\rho\frac{d^2 A(t)}{dt^2} + \frac{\pi^4}{8}\left[\frac{m^4}{a^4}E_x\cos\frac{2n\pi y}{b} + \frac{n^4}{b^4}E_y\cos\frac{2m\pi x}{a}\right]\left[A^2(t) - A_0^2\right]A(t)$$

(8.43)

Note that eq. (8.43) is a nonlinear equation containing functions of the variables x, y and t. To eliminate the x, y dependency, the Galerkin method is applied which demands the multiplication of both sides of the equation by $\sin\frac{m\pi x}{a}\sin\frac{n\pi y}{b}\,dxdy$ and integrating over the middle plane of the plate yielding the following nonlinear time-dependent expression:

$$\frac{d^2 A(t)}{dt^2} + \frac{\pi^4}{\rho h}\left[D_x\frac{m^4}{a^4} + 2(D_1 + 2D_{xy})\frac{m^2 n^2}{a^2 b^2} + D_y\frac{n^4}{b^4}\right][A(t) - A_0]$$

$$-\frac{m^2 \pi^2}{a^2 \rho}P(t) \cdot A(t) + \frac{\pi^4}{24\rho}\left[\frac{m^4}{a^4}E_x + \frac{n^4}{b^4}E_y\right]\left[A^2(t) - A_0^2\right]A(t) = 0$$

(8.44)

where m and n are both odd integers. The time dependence of the term $P(t)$ is chosen according to its time dependence, namely for a step function $P(t) = P_0$ (constant), for an impulse $P(t) = P_0\delta(t)$ (where $\delta(t)$ is the Kronecker delta[1]) or any other

---

1 The function is 1 if the variables are equal, and 0 otherwise, namely:

$$\delta_{ij} = 0 \quad \text{if} \quad i \neq j$$

$$\delta_{ij} = 1 \quad \text{if} \quad i = j$$

time function. Equation (8.44) can be nondimensionalized (assuming $n = 1$) to yield the following expression (see discussion in [11]:)

$$
\frac{d^2\xi}{d\tau^2} + S\left[\frac{m^4 + 2R_{12}m^2\beta^2 + R_{22}\beta^4}{4}\left(\xi - \xi_0\right) - m^2\tau\xi\right.
$$

$$
\left. + \frac{(1 - \upsilon_{xy}\cdot\upsilon_{yx})}{8}\left(m^4 + R_{22}\beta^4\right)\left(\xi^2 - \xi_0^2\right)\xi\right] = 0
$$

(8.45)

where

$$
P_1 \equiv \frac{4D_x\pi^2}{a^2 h}; \quad \xi \equiv \frac{A}{h}; \quad \xi_0 \equiv \frac{A_0}{h}; \quad \beta \equiv \frac{a}{b}; \quad \tau \equiv \frac{P}{P_1} = \frac{c\cdot t}{P_1};
$$

$$
R_{12} \equiv \frac{D_1 + 2D_{xy}}{D_x}; \quad R_{22} \equiv \frac{D_y}{D_x} = \frac{E_y}{E_x}; \quad S \equiv \frac{P_1^3\pi^2}{c^2 a^2 \rho}.
$$

(8.46)

Equation (8.45) is solved using numerical methods for integration of nonlinear equations, like the famous Runge–Kutta methods.[2] Solutions for the response of the plate for various S values are presented in [11].

It is interesting to note that eq. (8.44) can be used to obtain the static plate buckling load and its natural frequencies, as well as the expression for large plate deflections.

Assuming the static case for a perfect plate,

$$
\frac{d^2 A(t)}{dt^2} = 0 \quad \text{and} \quad A_0 = 0
$$

(8.47)

and neglecting high-order terms like A^3, eq. (8.44) yields

$$
\frac{\pi^2}{h}\left[D_x\frac{m^4}{a^4} + 2\left(D_1 + 2D_{xy}\right)\frac{m^2 n^2}{a^2 b^2} + D_y\frac{n^4}{b^4}\right] - \frac{m^2}{a^2}P = 0
$$

(8.48)

The critical buckling load of the plate is obtained from eq. (8.48) by assuming $n = 1$, namely

$$
P_{cr} = \frac{\pi^2 D_x}{b^2 h}\left[\left(\frac{mb}{a}\right)^2 + \frac{2\left(D_1 + 2D_{xy}\right)}{D_x} + \frac{D_y}{D_x}\left(\frac{a}{mb}\right)^2\right]
$$

(8.49)

$$
\Rightarrow \quad (P_{cr})_{min.} \text{ occurs} \quad \text{when} \quad \frac{a}{b}\sqrt{\frac{D_y}{D_x}} = \text{integer}
$$

---

2 Runge–Kutta methods are a family of implicit and explicit iterative methods (including the Euler methods routine), used in temporal discretization for the approximate solutions of ordinary differential equations developed approx. in 1900 by C. Runge and M. W. Kutta.

Neglecting high-order terms like A^3, and assuming a perfect plate ($A_0 = 0$) eq. (8.44) is written as

$$\frac{d^2A(t)}{dt^2} + \frac{\pi^4}{\rho h}\left[D_x\frac{m^4}{a^4} + 2(D_1 + 2D_{xy})\frac{m^2n^2}{a^2b^2} + D_y\frac{n^4}{b^4}\right]A(t) - \frac{m^2\pi^2}{a^2\rho}P(t)\cdot A(t) = 0 \quad (8.50)$$

The second term in eq. (8.50) is the square of the natural frequency of the perfect plate, namely

$$\omega_{mn}^2 = \frac{\pi^4}{\rho h}\left[D_x\frac{m^4}{a^4} + 2(D_1 + 2D_{xy})\frac{m^2n^2}{a^2b^2} + D_y\frac{n^4}{b^4}\right] \quad (8.51)$$

Finally, assuming the static case, the expression for the postbuckling behavior for a perfect plate with large deflections is obtained from eq. (8.44), namely

$$\left\{\frac{\pi^4}{h}\left[D_x\frac{m^4}{a^4} + 2(D_1 + 2D_{xy})\frac{m^2n^2}{a^2b^2} + D_y\frac{n^4}{b^4}\right] - \frac{m^2\pi^2}{a^2}PA(t)\right\} + \frac{\pi^4}{24}\left[\frac{m^4}{a^4}E_x + \frac{n^4}{b^4}E_y\right]A^3 = 0$$

$$(8.52)$$

Equation (8.52) shows that the lateral deflection would be zero until the critical buckling load given by eq. (8.49) is reached. After that point, nonzero deflections are possible while the load–deflection relation is cubic.

For further references dealing with the behavior of plates under dynamic buckling, the reader is referred to [16–20, 22, 24, 32, 36].

The definition of the buckling loads for plates, both for a static and dynamic case is one of the often issues to be solved consistently. To assist the definition of the buckling load for a plate, a method is described in Appendix A, which can be easily applied for experimental and numerical data consisting of deflections versus applied load.

8.4 Dynamic buckling of thin-walled structures – numerical and experimental results

The dynamic buckling of thin-walled structures has been dealt in depth also from the experimental point of view, besides various calculations using different approaches. Figure. 8.8a presents a shallow clamped spherical cap loaded by a sudden rectangular pressure q applied at time $t = 0$ and held constant for a given period of time and then suddenly removed (as described in [4]). Typical numerical results are then shown in Fig. 8.8b, showing the reduction of the critical nondimensional pressure by the increasing the duration of the applied pressure (see other results in [4]). It is interesting to note that the static critical load, from a certain nondimensional time duration (in this case from approximately $\bar{\tau} = 3$) and the static
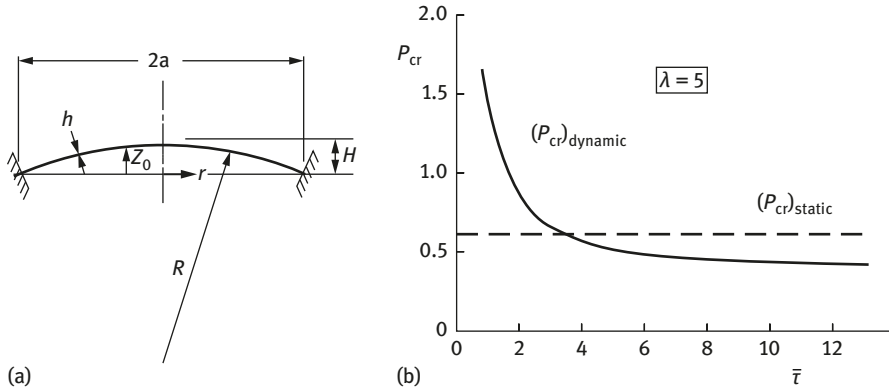
Fig. 8.8: (a) A clamped shallow spherical cap and (b) variation of the nondimensional critical pressure with nondimensional load duration (adapted from [4]).

critical pressure, is above the dynamic critical pressure, whereas for short time duration the dynamic critical load is higher than the static one, as is normally known for short duration loads. The various nondimensional terms used in Fig. 8.8 were defined in [4] as

$$\bar{\tau} = \frac{ct}{R}; \quad c = \sqrt{\frac{E}{\rho}}; \quad p = \frac{q}{q_0};$$

$$\lambda = 2\left[3\left(1 - \nu^2\right)\right]^{1/4} \left(\frac{H}{h}\right)^{1/2}; \quad q_0 = \frac{2E}{\left[3\left(1 - \nu^2\right)\right]^{1/2}} \left(\frac{h}{R}\right)^{1/2}$$

(8.53)

where E is the Young's modulus, ν is the Poisson's ratio and ρ is the density.

Similar results were reported in [24], where an isotropic plate (Fig. 8.9a) is suddenly loaded by a rectangular impulse and the response of the plate is presented using the term DLF as being defined in eq. (8.2) as a function of the nondimensional time duration, where T_s is the impact period and T_p is the natural period of the plate. As shown by other researchers, in the vicinity of $T_s/T_p = 1$, the term DLF is less than unity, implying that the static load is higher than the dynamic one. Shifting this period ratio toward 0.5 shows a rapid increase in the value of DLF, reaching a maximal value of 3.6 in the vicinity of $T_s/T_p = 0.1$ (approx.), namely as expected the plate can withstand high dynamic compressive stresses (3.6 the static buckling load of the plate) provided the time duration is very short. Impacting the plate with sinusoidal or triangular impulses displays the same behavior as the rectangular one (see Fig. 8.10 taken from [24]).

Experimental results for laminated composite plates under impulse-type uniaxial loading obtained by dropping masses and measuring the response using
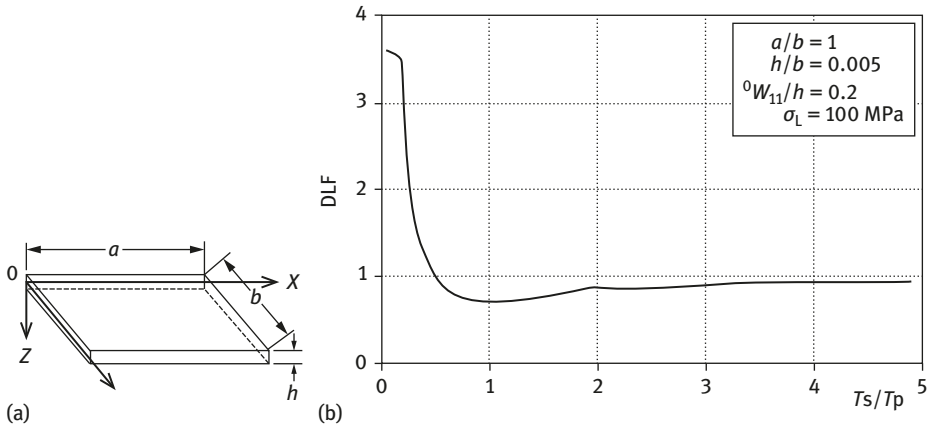
Fig. 8.9: (a) An isotropic flat plate and (b) variation of DLF with the nondimensional load duration (from [24]).
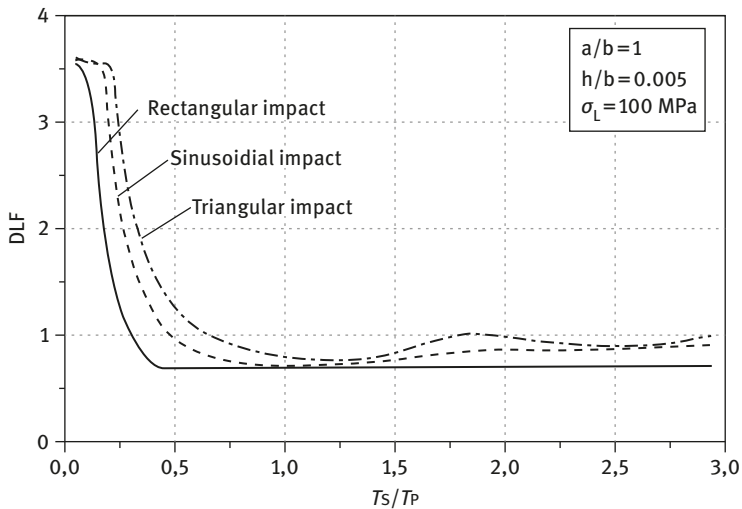
Fig. 8.10: Variation of DLF with the nondimensional load duration for three types of impulses [24].

a back-to-back strain gages bonded in the center of the plate is described in [20]. Figure. 8.11 presents the experimental variation of the DLF term defined as

$$\text{DLF} \equiv \frac{(\varepsilon_{cr})_{\text{dyn.}}}{(\varepsilon_{cr})_{\text{st.}}} \tag{8.54}$$
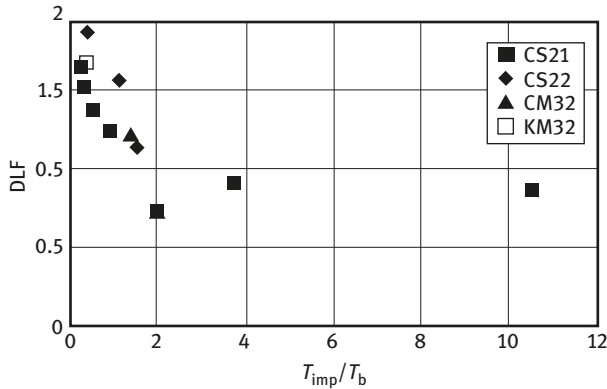
Fig. 8.11: Variation of DLF with the nondimensional load duration – experimental results (adapted from [20]).

as a function of the nondimensional period ratio T_{imp}/T_b, where T_{imp} is the period of the impact as measured by the bonded strain gages and T_b is the lowest natural frequency of the plate.

As shown before, DLF less than one was measured for some values of nondimensional period ratio, while for short periods, the DLF is higher than unity, reaching experimental values of up to 2. The properties of the specimens presented in Fig. 8.11 are summarized in Table 8.1, while the material properties are presented in Table 8.2 (using the data published in [20]). Table 8.3 presents additional data in the form of natural frequencies and static buckling strains as obtained during the tests described in [20]. One should note that except plate CM32, which was on clamped boundary conditions all around the perimeter of the plate, all the other plates had simply supported boundary conditions along the four edges of the plate.

Table 8.1: The properties of the tested plates (from [20]).

Specimen	Material	Lay-up	Total number of layers	Total thickness (measured) (mm)
CS21	Graphite-Epoxy HT-T300 (Torey)	$(\pm 45°, \pm 45°, \pm 45°)_{sym}$	12	1.63
CS22	Graphite-Epoxy HT-T300 (Torey)	$(\pm 45°, \pm 45°, \pm 45°)_{sym}$	12	1.63
CM32	Graphite-Epoxy HT-T300 (Torey)	$(0°, \pm 45°, 90°, \pm 45°, 0°)$	9	1.125
KM32	Kevlar (Dupont)	$(0°, \pm 45°, 90°, \pm 45°, 0°)$	9	1.125

Table 8.2: The material properties of the tested plates (from [20]).

Material	E_{11} (MPa)	E_{22} (MPa)	G_{12} (MPa)	v_{12}	v_{21}
Graphite-Epoxy HT-T300 (Torey)	122	8.55	3.88	0.32	0.022
Kevlar (Dupont)	70.8	5.5	2.o5	0.34	0.026

Table 8.3: The experimental results – the tested plates (from [20]).

Specimen	AR [$a \times b$] (mm^2)	f_{exp} (Hz)	$(\varepsilon_{cr})_{st.}$ (µs)
CS21	2 [150 × 300]	350	2600
CS22	2 [150 × 300]	250	2413
CM32[*]	1 [225 × 225]	393	90
KM32	1 [225 × 225]	186	400

[*]Nominal clamped boundary conditions

As the measured response of the plates was in the form of strains, measured by two back-to-back bonded strain gages, the compression strain ε_c and the bending strain ε_b were calculated[3] and the axial compression load and lateral out-of-plane deflection were replaced by the compression and bending strains, respectively.

The definition of the static load was performed using the modified Donell's approach, which was found to be the most appropriate for plates with initial geometric imperfections, w_0 (see a discussion in [45]), having the following expression:

$$\frac{\varepsilon_b}{\varepsilon_c} = \frac{\varepsilon_b + w_0}{(\varepsilon_{cr})_{st.} + a\left(\varepsilon_b^2 + 3\varepsilon_b w_0 + 2w_0^2\right)} \tag{8.55}$$

Using experimental data in the form of ε_b versus ε_c one can curve fit it using eq. (8.55) to yield the static buckling strain $(\varepsilon_{cr})_{st.}$ together with the initial geometric imperfection w_0 and the constant a. Based on the work performed in [18], the dynamic buckling strain $(\varepsilon_{cr})_{dyn.}$ is determined by curve fitting the following equation to the experimental data (ε_b vs. ε_c):

$$\frac{\varepsilon_b}{\varepsilon_c} = \frac{\varepsilon_b + w_0}{(\varepsilon_{cr})_{dyn.} + a\varepsilon_b} \tag{8.56}$$

---

3 $\varepsilon_c \equiv \frac{\varepsilon_1 + \varepsilon_2}{2}$; $\varepsilon_b \equiv \frac{\varepsilon_1 - \varepsilon_2}{2}$ where $\varepsilon_1, \varepsilon_2$ are the measured strains.

As for the static case, the two terms, the constant a and the initial geometric imperfection w_o are also determined from the curve fitting process, yielding consistent results as presented in [20].

A dynamic buckling investigation was numerically performed in [39] on a curved laminated composite stringer stiffened panel. Details of the actual model, the dimensions of the stringer, the FE model and the mode shape at $f = 424$ (Hz) (the lowest frequency of the panel) are presented in Fig. 8.12.
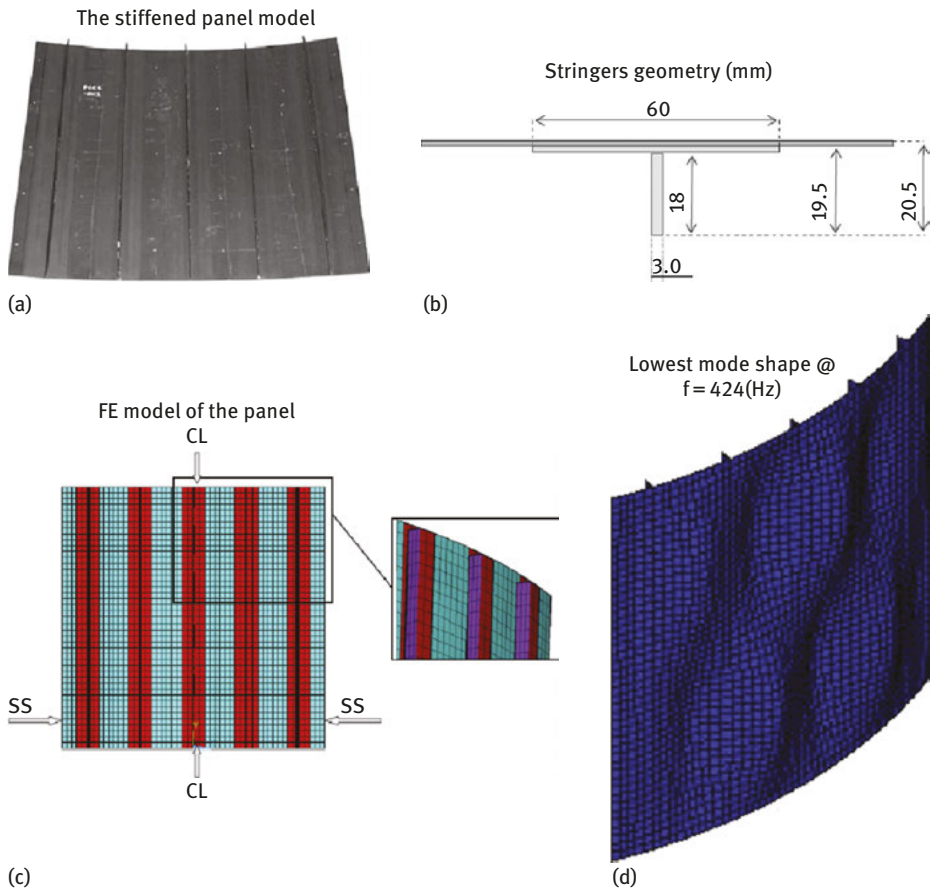
The stiffened panel model

Stringers geometry (mm)

(a)   (b)

(c)   (d)

Fig. 8.12: Dynamic buckling investigation of a curved laminated composite stringer stiffened panel: (a) the stringered panel model, (b) geometric dimensions of the stringer, (c) the FE model, (d) the lowest mode shape of the stringered panel @ $f = 424$ Hz (adapted from [39]).

The variation of the DLF (defined by eq. (8.1)) versus the nondimensional load duration is shown in Fig. 8.13, where T is the period of the applied load and

$T_b = 1/f_b = 2{,}358.5$ µs is the lowest natural period of the stringered panel ($f_b = 424$ Hz). As shown before for other structural cases, also for this stringered panel, the DLF is lower than unity in the vicinity of the lowest natural frequency of the specimen, returning to values above unity for very short periods, while for long periods of time, the DLF tends to unity.
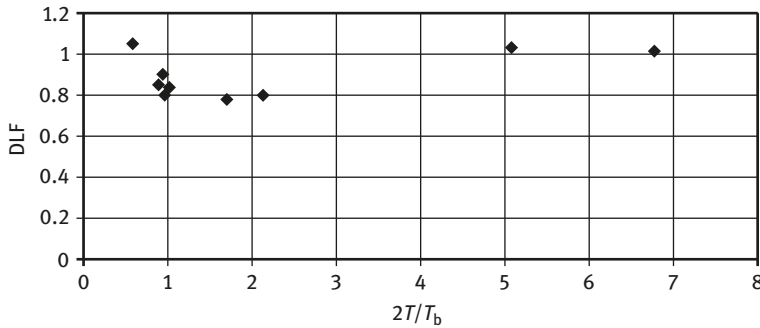
Fig. 8.13: Variation of DLF with the nondimensional load duration – experimental results (adapted from [39]).

Investigations of shells under dynamic-type loading have been performed by many investigators, like in [21, 23, 26, 27, 30, 31, 38, 46, 47]. A comprehensive experimental and numerical investigation was performed in the Ph.D. thesis written by Eglis [38], in which composite cylinders were subjected to gradually and suddenly applied axial compression loads, including half-sine-shaped pulse loads leading to the eventually dynamic buckling of the tested specimens. Figure 8.14 shows typical numerical and experimental results for the variation of the DLF with the loading period. The general trend presented in Fig. 8.14 is that the DLF is above unity for the tests performed on type 1 shells [38]. The mode shapes for loading periods less, equal and above the lowest natural frequency (the largest period) are presented in Fig. 8.15. At $T < \tau/2$, the shell buckling modes are similar to the static buckling mode, but with a larger number of longitudinal waves, at load duration $T = \tau/2$ the buckling mode starts to transform to an axisymmetric mode while for $T > \tau/2$ leads to axisymmetric buckling mode together with a slight drop of DLF at a load duration of $T = 2a/c$ (a is the shell length and c the speed of sound in the shell). The natural periods for RTU #16, RTU #4 and RTU #1–4 tested shells (see Fig. 8.14) were $\tau = 2.92$, 4.04 and 6.06 ms, respectively (see [38]).

Similar results are presented in [46], where numerical and experimental investigations of a composite laminated cylindrical shell under impulsive loading are presented. The tested shell (see Fig. 8.16a) had a laminate of $[0°, -45°, +45°]$, was nominally clamped at its edges, with a length of 230 mm (between the clamped edges), a diameter of 250 mm and manufactured from graphite-epoxy with the
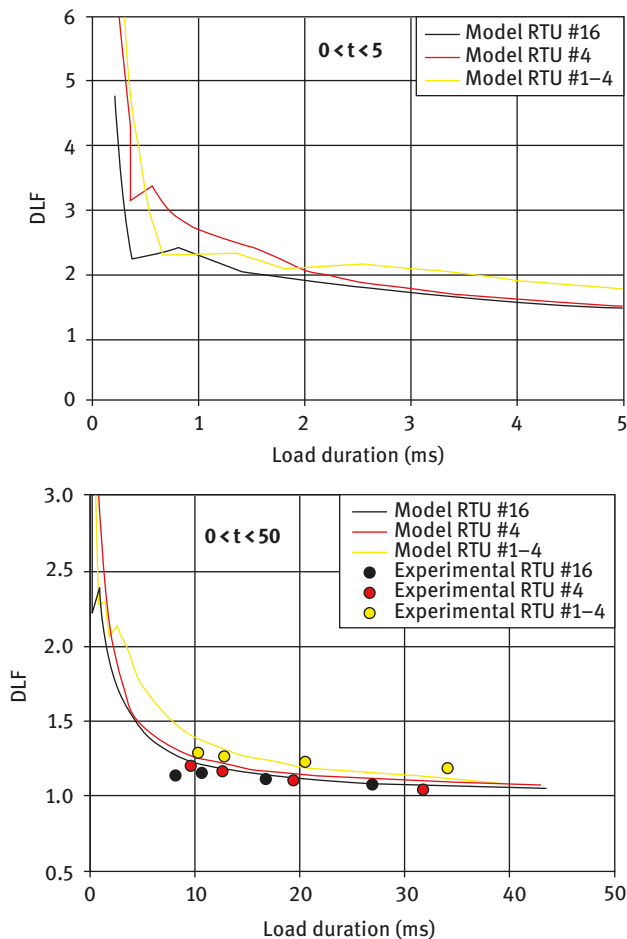
Fig. 8.14: Typical results from [38] – variation of DLF with load duration – experimental and numerical results of specimens type 1 (adapted from [38]).

following properties: E_{11} = 137.0 GPa, E_{22} = 9.81 GPa, G_{12} = 5.886 GPa and v_{12} = 0.34 and 0.125 mm layer thickness. The dynamic loading was calculated using a dropping mass on the end plate with a mass of 32 kg. The calculated shell static mode shape is presented in Fig. 8.16b, while the dynamic responses for 746 and 2,170 µs impact duration are shown in Fig. 8.16c and d, respectively. As expected the static and the dynamic modes have different patterns. The calculated DLF for numerical and experimental results is presented in Fig. 8.17 for various initial geometric imperfections. Although the experimental results do not go below DLF = 1, the numerical results show a DLF lower then unity in the vicinity of T/T_b = 1, for

$T < \tau/2$ $\quad\quad\quad$ $T = \tau/2$ $\quad\quad\quad$ $T > \tau/2$
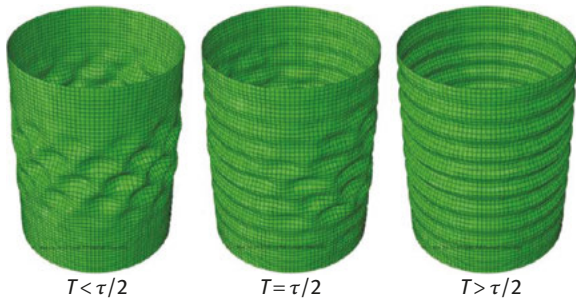
Fig. 8.15: Typical results from [38] – variation of dynamic buckling mode shapes (not to scale) with load duration (τ represents the longest natural bending period of the shell) – numerical results of specimen type 1 (adapted from [38]).
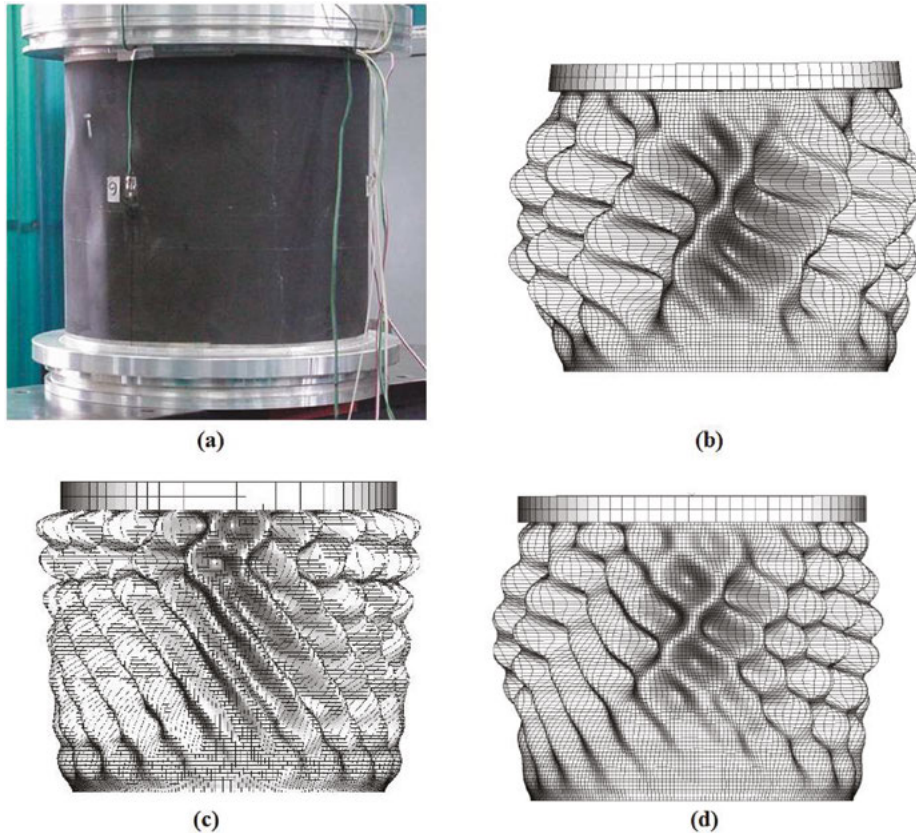
Fig. 8.16: Typical results from [46] – (a) the tested cylindrical shell, (b) the static mode shape, (c) dynamic mode shape @ 746 µs, (d) dynamic mode shape @ 2,170 µs (adapted from [46]).
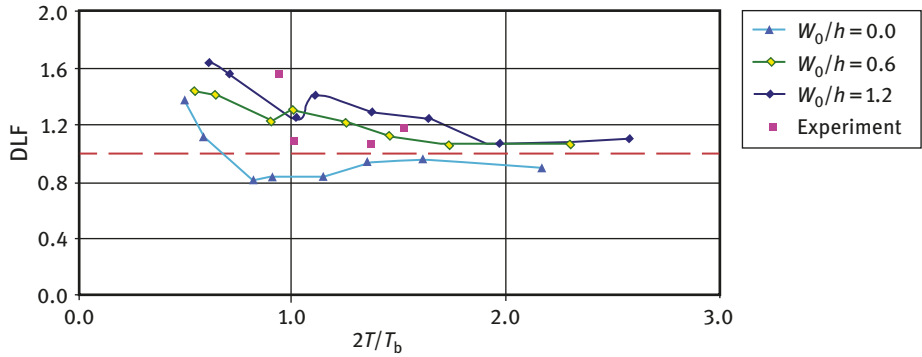
Fig. 8.17: DLF versus nondimensional impulse period ($T_b = 1/f_b$, where f_b is the lowest natural frequency of the shell) (adapted from [46]).

zero initial geometric imperfections, while for higher values of geometric imperfections, the DLF curve is higher the unity.

A recent research [47] presents similar results to those described in [46], for the behavior of composite cylindrical shells having laminates of [0°/90°/0°/90°/90°/0°/90°/0°] and [0°/0°/60°/−60°/−60°/60°/0°/0°] under various durations of load impulse. A step pulse was used for the compressive loading, while calculations using the ABAQUS/Standard code yielded a lowest natural frequency of 427 Hz and
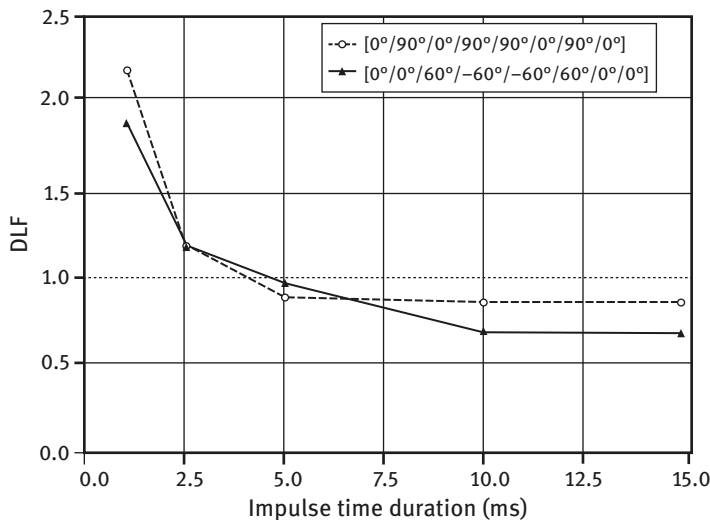
Fig. 8.18: DLF versus nondimensional impulse period ($T_b = 1/f_b$, where f_b is the lowest natural frequency of the shell) (adapted from [46]).

a static linear buckling load of 97.19 kN for the [0°/90°/0°/90°/90°/0°/90°/0] laminate and 120.39 kN for the [0°/0°/60°/–60°/–60°/60°/0°/0°] laminate. ABAQUS/Explicit was used for the dynamic buckling analysis of the shells under the impulsive loading. Figure. 8.18 presents the DLF, calculated using eq. (8.1), as a function of the period of the applied step impulse loading. For short periods the DLF is higher than unity, while from $T = 5$ ms it drops below unity for both laminates. As the largest natural period can be calculated to 2.342 ms, it again shows that in the vicinity of the lowest natural frequency the DLF might fall below unity also for laminated composite cylindrical shells.

References

[1]   Lindberg, H.E. Dynamic pulse buckling-theory and experiment, SRI International, DNA 6503H, Handbook, 333 Ravenswood Avenue, Menlo Park, California 94025, USA, 1983.

[2]   Simitses, G.J. Dynamic stability of suddenly loaded structures, Springer Verlag, 1990, New York, USA, 290p.

[3]   Chung, M., Lee, H.J., Kang, Y.C., Lim, W.-B., Kim, J. H., Cho, J.Y., Byun, W., Kim, S.J., and Park, S.-H. Experimental study on dynamic buckling phenomena for supercavitating underwater vehicle, International Journal of Naval Architecture and Ocean Engineering, 4, 2012, 183–198, http://dx.doi.org/10.2478/IJNAOE-2013-0089.

[4]   Budiansky, B., and Roth, R.S. Axisymmetric dynamic buckling of clamped shallow spherical shells, collected papers on instability of shell structures, NASA TN-D-1510, 761, 1962, 597–606.

[5]   Hegglin, B. Dynamic buckling of columns, SUDAER No. 129, June 1962, Department of Aeronautics & Astronautics, Stanford University, Stanford, California, USA, 55p.

[6]   Budiansky, B., and Hutchinson, J. W. Dynamic buckling of imperfection sensitive structures", Proceedings of the 11th International Congress of Applied Mechanics, pp. 636–651, Berlin, 1964. H. Götler, ed., Springer-Verlag, 1966.

[7]   Hutchinson, W. J., and Budiansky, B. Dynamic buckling estimates, AIAA Journal, 4(3), 1966, 525–530.

[8]   Lock, M.H. A study of buckling and snapping under dynamic load, Air Force Report No. SAMSO-TR-68-100, Aerospace Report No. TR-0158(3240-30)-3 December 1967, 55p.

[9]   Burt, J.A. Dynamic buckling of shallow spherical caps subjected to a nearly axisymmetric step pressure load, Master Thesis, Naval Postgraduate School, Monterey, California 93940, USA, Sept, 1971, Vol. 75, p.

[10] Volmir, S.A. Nonlinear dynamics of plates and shells, Science, 1972, Moscow, USSR.

[11] Ekstrom, R.E. Dynamic buckling of a rectangular orthotropic plate, AIAA Journal, 11(12), 1973, 1655–1659.

[12] Lee, L.H.N. Dynamic buckling of an inelastic column, International Journal of Solids and Structures, 17(3), 1981, 271–279.

[13] Ari-Gur, J., Weller T., and Singer J. Experimental and theoretical studies of columns under axial impact, International Journal of Solids and Structures, 18(7), 1982, 619–641.

[14] Lee, L.H.N., and Ettestad, K.L. Dynamic buckling of an ice strip by axial impact, International Journal of Impact Engineering, 1(4), 1983, 343–356.

[15] Gary, G. Dynamic buckling of an elastoplastic column, International Journal of Impact Engineering, 1(4), 1983, 357–375.

[16] Dannawi, M., and Adly. M. Constitutive equation, quasi-static and dynamic buckling of 2024-t3 plates – experimental result and analytical modelling, Journal de Physique Colloques, 49(C3), 1988, C3-575–C3-588.

[17] Birman, V. Problems of dynamic buckling of antisymmetric rectangular laminates, Composite Structures, 12(1), 1989, 1–15.

[18] Weller, T., Abramovich, H., and Yaffe, R. Dynamic buckling of beams and plates subjected to axial impact, Computers and Structures, 32(3–4), 1989, 835–851.

[19] Ari-Gur, J., and Hunt, D. H. Effects of anisotropy on the pulse response of composite panels, Composite Engineering (now Composites Part B), 1(5), 1991, 309–317.

[20] Abramovich, H., and Grunwald, A. Stability of axially impacted composite plates, Composite Structures, 32(1–4), 1995, 151–158.

[21] Schokker, A., Sridharan, S., and Kasagi, A. Dynamic buckling of composite shells, Computers and Structures, 59(1), 1996, 43–53.

[22] Ari-Gur, J., and Simonetta, R. Dynamic pulse buckling of rectangular composite plates, Composites Part B, 28, 1997, 301–308.

[23] Eslami, M. R., Shariyat, M., and Shakeri, M. Layerwise theory for dynamic buckling and postbuckling of laminated composite cylindrical shells, AIAA Journal, 36(10), 1998, 1874–1882.

[24] Petry, D., and Fahlbusch, G. Dynamic buckling of thin isotropic plates subjected to in-plane impact, Thin-Walled Structures, 38(3), 2000, 267–283.

[25] Zheng, Z., and Farid, T. Numerical studies on dynamic pulse buckling composite laminated beams subjected to an axial impact pulse, Composite Structure, 56(3), 2002, 269–277.

[26] Yaffe, R., and Abramovich, H. Dynamic buckling of cylindrical stringer stiffened shells, Computers & Structures, 81(9–11), 2003, 1031–1039.

[27] Chamis, C.C., and Abumeri, G.H. Probabilistic dynamic buckling of smart composite shells, NASA/TM-2003-212710, 2003.

[28] Zhang, Z. Investigation on dynamic pulse buckling and damage behavior of composite laminated beams subject to axial pulse, Ph.D. thesis, Faculty of Engineering, Civil Engineering, Dalhousie University, Halifax, Nova Scotia, Canada, 2003, 228 p.

[29] Lindberg, H.E. Little book of dynamic buckling, September, 2003, LCE Science/Software, 18388 Chaparral Drive Penn Valley, CA 95946–9234, USA.

[30] Bisagni, C. Dynamic buckling tests of cylindrical shells in composite materials, 24th International Congress of the Aeronautical Sciences (ICAS2004), 29 August-3 September, 2004, Yokohama, Japan.

[31] Bisagni, C. Dynamic buckling of fiber composite shells under impulsive axial compression, Thin Walled Structures, 43(3), 2005, 499–514.

[32] Kubiak, T. Dynamic buckling of thin-walled composite plates with varying widthwise material properties, International Journal of Solids and Structures, 42, 2005, 5555–5567.

[33] Ji, W., and Waas, A. M. Dynamic bifurcation buckling of an impacted column, International Journal of Engineering Science, 46(10), 2008, 958–967.

[34] Kubiak, T. Dynamic buckling estimation for beam-columns with open cross-sections, Paper No. 13, Proceedings of the Twelfth International Conference on Civil, Structural and Environmental Engineering Computing, B.H.V. Topping, L.F. Costa Neves and R.C. Barros, (Editors), 2009, Civil-Comp Press, Stirlingshire, Scotland.

[35] Jabareen, M., and Sheinman, I. Dynamic buckling of a beam on a nonlinear elastic foundation under step loading, Journal of Mechanics of Materials and Structures, 4(7–8), 2009, 1365–1373.

[36] Michalska, K.K. About some important parameters in dynamic buckling analysis of plated structures subjected to pulse loading, Mechanics and Mechanical Engineering, 14(2), 2010, 269–279.

[37] Mania, R.J. Membrane-flexural coupling effect in dynamic buckling of laminated columns, Mechanics and Mechanical Engineering, 14(1), 2010, 137–150.

[38] Eglitis, E. Dynamic buckling of composite shells, Ph.D. thesis, Riga Technical University, Faculty of Civil Engineering, Institute of Materials and Structures, 2011, Riga, Latvia, 172 p.

[39] Abramovich, H., and Less, H. Dynamic buckling of a laminated composite stringer-stiffened cylindrical panel", Composite Part B, 43(5), July 2012, 2348–2358.

[40] Landa, A. The buckling resistance of structures subjected to impulsive type actions, Master Thesis, Norwegian University of Science and Technology, Department of Marine Technology NTNU Trondheim, Norway, Feb, 2014, 104.

[41] Straume, J. G. Dynamic buckling of marine structures, Master Thesis, Norwegian University of Science and Technology, Department of Marine Technology NTNU Trondheim, Norway, June 2014, 148 p.

[42] Kuzkin, V.A. Structural model for the dynamic buckling of a column under constant rate compression, arXiv:1506.00427 [physics.class-ph],2015.

[43] Mouhata, O., and Abdellatif, K. Dynamic buckling of stiffened panels, The 5th International Conference of Euro Asia Civil Engineering Forum (EACEF-5), Procedia Engineering, Vol. 125, 2015, pp. 1001–1007.

[44] Lekhnitskii, S. G. Anisotropic plates, 2nd, translation from Russian, Gordon and Breach, New York, 1968.

[45] Abramovich, H., Weller, T., and Yaffe R. Application of a modified Donnell technique for the determination of critical loads of imperfect plates, Computers and structures, 37, 1990, 463–469.

[46] Abramovich, H., Weller, T., and Pevzner, P. Dynamic buckling behavior of thin walled composite circular cylindrical shells under axial impulsive loading, Proc. of AIAC-12, Twelfth Australian International Aerospace Congress, Melbourne, 19–22 March 2007

[47] Citra, V., and Priyadarsini, R.S. Dynamic buckling of composite cylindrical shells subjected to axial impulse, International Journal of Scientific & Engineering Research, 4(5), Issue 2013, 162–165.

Appendix A: Calculation of the critical buckling load of a uniaxial loaded plate from test results

One of the issues faced by a researcher is to correctly define the buckling load of a plate for the static and dynamic cases, based on experimental points obtained either by tests or numerically. The following method was already published and applied in [39] and is based on the work performed by Brown.[4] It was shown that for practical structural geometries and loading conditions, the following equation holds:

---

4 Brown, V.L., Linearized least-squared technique for evaluating plate-buckling loads, Journal Engineering Mechanics, Vol. 116, No. 5, pp.1050–1057, 1990.

$$\delta_i^2 - \delta_0^2 = \alpha^2 h^2 \theta = \alpha^2 h^2 \left[\frac{P_i}{P_{cr}} - 1 + \frac{\delta_0}{\delta_i} \right] \tag{A-1}$$

where δ_i is the lateral plate deflection due to corresponding in-plane loading P_i; δ_0 is the initial lateral plate deflection; h is the thickness of the plate and α is a constant accounting for the load configuration and boundary conditions. After some mathematical manipulations, eq. (A-1) can be rewritten as

$$P_i \delta_i = A_1 + A_2 \delta_i + A_3 \delta_i^3 \tag{A-2}$$

where

$$A_1 = -P_{cr}\delta_0; \quad A_2 = P_{cr} \left[1 - \frac{\delta_0^2}{\alpha^2 h^2} \right]; \quad A_3 = \frac{P_{cr}}{\alpha^2 h^2} \tag{A-3}$$

Equation (A-3) is presented in a suitable form for the application of the least square method to fit a curve to a series of given data points, P_i, δ_i. To do so, let us define the sum of the squares of the residuals for m data points as

$$\text{SUM} = \sum_{i=1}^{m} \left(P_i \delta_i - A_1 - A_2 \delta_i - A_3 \delta_i^3 \right)^2 \tag{A-4}$$

Taking partial derivatives of eq. (A-4) with respect to the coefficients A_1, A_2 and A_3 (see eq. (A-3)) and equating them to zero (thus minimizing the error) yields the following system of equations written in a matrix form:

$$\begin{bmatrix} m & \sum_{i=1}^{m} \delta_i & \sum_{i=1}^{m} \delta_i^3 \\ \sum_{i=1}^{m} \delta_i & \sum_{i=1}^{m} \delta_i^2 & \sum_{i=1}^{m} \delta_i^4 \\ \sum_{i=1}^{m} \delta_i^3 & \sum_{i=1}^{m} \delta_i^4 & \sum_{i=1}^{m} \delta_i^6 \end{bmatrix} \begin{Bmatrix} A_1 \\ A_2 \\ A_3 \end{Bmatrix} = \begin{Bmatrix} \sum_{i=1}^{m} P_i \delta_i \\ \sum_{i=1}^{m} P_i \delta_i^2 \\ \sum_{i=1}^{m} P_i \delta_i^4 \end{Bmatrix} \tag{A-5}$$

The three linear equations, presented in a matrix form in eq. (A-5), are then solved for the three unknowns A_1, A_2 and A_3. Substituting them into eq. (A-3) and the results in eq. (A-2) lead the following cubic equation for the single unknown P_{cr}:

$$P_{cr}^3 - A_2 P_{cr}^2 - A_1^2 A_3 = 0 \tag{A-6}$$

Solving eq. (A-6) will yield the buckling load of the plate based on the displacement–force curve, generated either by experiments or by numerical calculations.

9 Optimization of thin-walled structures

9.1 Introduction

The concept of design optimization is based on using a mathematical method to arrive at the best possible design according to a selected number of desirable features. Owing to the fact that design is a decision-making process, there is a possibility of superior, alternative designs that exist. The use of mathematical expressions of the relevant natural laws, empirically obtained relationships, experience and geometry are combined to obtain an abstract description of the artifact being designed [1]. These mathematical expressions can be used to analyze other possible designs and arrive at a more optimal solution [1]. The existence of multiple alternative designs obtainable from the mathematical model leads to the need to introduce criteria for comparing the alternative designs found from the mathematical model [1]. These criteria allow for the use of mathematical methods to find the optimal solution that satisfies all of the criteria. An important factor to consider during the optimization process is the prioritization of criteria, particularly for designs where multiple criteria are required to be optimized. In every design, the optimization of one criterion will have an impact on the other criteria. The prioritization of criteria allows the optimization process to be applied in a way which ensures that the more important criteria are optimized while the less important ones remain within the desired design constraints. An example of this can be seen in the aerospace structure field, where weight reduction, cost reduction and structural rigidity are generally prioritized, even though these criteria generally have a negative impact on each other. Additionally, the optimization of a structural design could negatively impact the design from another point of view, such as aerodynamics, where size, shape and surface conditions have higher priority. This example illustrates not only the complexity of optimizing a single component of a design, but ensuring that this optimization does not impact the overall design negatively. The example further illustrates the additional complexity in multidisciplinary optimization, particularly cases where optimization from the point of one design discipline negatively impacts that of another discipline requiring the introduction of trade-offs in the design. This high level of complexity has led to the logical exploitation of computers and software in order to allow for an increase in the speed, number of constraints and complexity of problems that can be simultaneously optimized. This has been exploited, particularly in recent years, where the drastic increase in computing power at a fraction of the historical cost has led to a plethora of optimization software [2]. This has led to a major challenge for researchers requiring them to design methods that can be implemented computationally by users with little knowledge of the source algorithms used by the software [2]. The results of an optimization method, whether manual, numerical or computational, are also highly dependent on the quality of the input model [1]. With the lack of obtainable

knowledge on the intricate workings of modern software packages, the quality [2], the general concepts, methods and procedures for optimization will be discussed in the next section.

9.2 The optimization process

The following sections will provide a brief introduction of the necessary vocabulary, concepts and the design process with the inclusion of optimization within the process.

9.2.1 Vocabulary and concepts

The first concepts that will be discussed are those of the design variable, the design parameter and the design constant. The design variables are made up of quantities by which the model can be described, which can vary during the optimization process [1, 3]. During the design optimization, the design variable is considered an input of the model, which can be varied in order to obtain an optimum solution. The design variables can either be classified as continuous (having any value within a range of values) or discrete (having specific values from a list of permissible values) [2]. There also exist design parameters that are quantities by which the model can be described which are set at a constant value during the optimization process. The choice of which quantities will be classified as variables or parameters is a subjective decision to be made by the designer [1]. The final type of quantity that can be used to describe a model is the design constants. These are constant values that are usually fixed by the underlying phenomenon instead of the model statement and are, therefore, uncontrollable by the designer, such as the gas constant [1]. These concepts can then be used to generate the objective or target function, which is discussed later.

The second concept that will be discussed is the objective function. The objective function is the specific criterion required to be optimized in order to characterize whether the design is the best one possible. It is a mathematical relation, which relates several model variables, parameters and constants as a function [4]. The purpose of any optimization problem is to find either a maximum or minimum value for the objective function, subject to the constraints of the problem that are further discussed below [4]. The formulation of the objective function is usually the most difficult part of the modeling process, with the mathematical relations attempting to describe the function of the model within the conditions imposed by its environment [4]. It must be noted that for a standard optimization problem it is possible, if not highly likely, that the objective "function" can be a system of algebraic or differential equations or even a computerized procedure or subroutine [1]. The objective function can also be written in terms of multiple variables that would then classify the problem as multicriteria optimization [2].

The problem constraints are a set of mathematical relations that limit the possible optimized solutions based on the requirements of the design. The constraints can either be inequality constraints (formulated using > or < criteria) or equality constraints. The points of the objective function that satisfy the constraints of the system are known as feasible design points, with all of the feasible design points making up the feasible region [3]. The feasible region will include a global minimum or maximum value of the objective function, which will be the optimized solution to the design problem. The feasible region can also include local minimum or maximum values, which give an optimized solution within a given range, however, will not be the most optimized solution within the entire feasible region. The minima or maxima that gives a global minimum or maximum value of the objective function will be the best optimized solution of the design problem [3].

When the objective function and all of the constraints of an optimization problem are linear with respect to the design variables, the optimization problem is said to be a linear problem [2]. These problems can be solved using a branch of mathematics known as linear programming [2]. If either the objective function or the constraints are nonlinear, the optimization problem is defined as a nonlinear problem.

The design problem can also be classified as constrained or unconstrained. Constrained design problems arise when explicit constraints are placed on the optimization variables. The constraints placed on the variables can be anything from simple bounds to a system of equalities and inequalities used to model highly complex relationships between variables in the mathematical model. These constraints can be linear, nonlinear or convex in nature and can be further defined by their smoothness, making them either differentiable or nondifferentiable.

The discussed vocabulary and concepts can now be used to describe the general procedure followed during design optimization and will be discussed in the following section.

9.2.1a The general design optimization process

The design process, while highly complex and variable in nature, will generally follow a specific set of steps, which can vary depending on the design itself. An example of a general procedure is shown in Fig. 9.1.

The optimization step, while always having been an important step in the past, has become the focus of much research in recent years, owing to the improvements in computing capabilities allowing for more complex optimization to be performed in a reduced amount of time. However, even with the increase in the number and complexity of methods for optimizing a design, the general procedure for optimization has remained similar.

The initial process of the optimization procedure is to set up the model, variables, parameters and constants. Once this has been set up, the objective function and constraints can be defined, usually in the following format [2]:
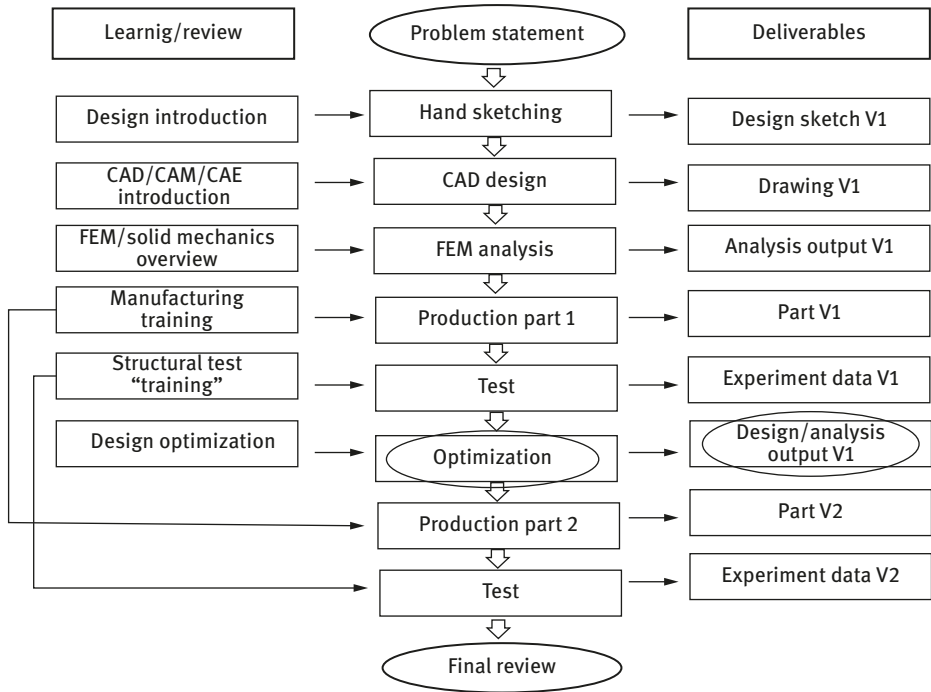
Fig. 9.1: Generalized design procedure.

$$\text{Minimize: } f(x) \quad \text{such that: } g(x) \geq 0, h(x) = 0 \tag{9.1}$$

where x represents the optimization variables, $f(x)$ is the objective function, which can be made up of more than a single function, $g(x)$ represents the inequality constraints and $h(x)$ represents the equality constraints. Once the objective function and constraints have been set up, the actual optimization process can begin. Using an initial design, an attempt is made to improve the design by adjusting the design variables using one of the methods described in the next section. By seeing if the objective function is larger/smaller, depending on if the objective function needs to be maximized/minimized, than the objective function of the previous design, the new design can be directly compared to the previous iteration to determine if it is a more optimized solution. This process is terminated when no improvement can be made in the design without violating any of the constraints [2] (see for example Fig. 9.2).

The procedure described earlier is a general approach to optimization, which is widely used in the industry and academy. There exist many different methods of implementing this procedure, which are discussed later in the report.

Minimize: $f(x)$
such that: $g(x) \geq 0$, $h(x) = 0$

Start — Choose an initial design (x_0)

Design improvement ← Computer simulation — Calculate $f(x), g(x), h(x)$

Change x

Converge ? — Does your design meet a termination criterion ?

N

Y

End
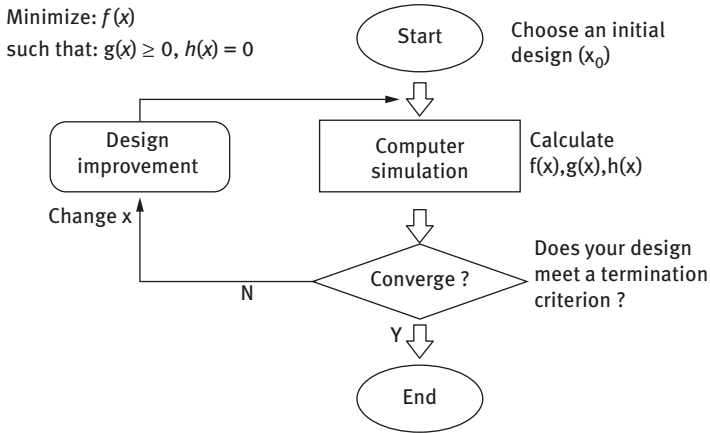
Fig. 9.2: Optimization process – a block diagram.

9.3 Structural optimization

The principal aim of structural design is to create a structure that can carry the expected load in an efficient way [5]. This leads to a design that uses the least amount of material in order to carry the predicted loads in order to maximize its efficiency. The aim of using a minimum amount of material is usually synonymous by ensuring that the weight of the structure is minimized [5]. The optimization process is a useful tool for optimization of structures, particularly in the aerospace field where lightweight yet rigid structures are required.

Structural optimization is usually split into three main sections: size optimization, shape optimization and topology optimization. While the first two sections are easily explained in their naming, topology optimization attempts to distribute the least amount of material within a specified available area [6].

The main constraint for structural optimization is usually the required load, which the structure needs to carry; however, in real design problems, a multitude of other constraints, such as maximum deformation, fatigue requirements, damage resistance, buckling requirements and natural frequency of the structure can be included in the optimization procedure [5].

9.4 Multidisciplinary and multiobjective design optimization

In order to obtain a design solution for many existing problems, it is usually necessary to solve the problem using a number of disciplines. It is very common for the optimization of one subsystem within a design, or even the optimization of a single subsystem from the point of view of a single discipline, to negatively

impact the optimization of another subsystem or the subsystem being optimized from the point of view of another discipline. A classic example of this is the design of an aircraft wing, where from a structural point of view the designer would prefer a thicker wing cross section with internal structural strengthening, whereas from an aerodynamics point of view a very thin wing is more optimal. Both of these requirements are also not optimal for the design of the systems that are stored in the wing which require adequate space to be placed throughout the wing. It can be seen that if the wing was to be optimized by prioritizing a single discipline's requirements it would negatively impact the design of the wing and the aircraft as a whole. It is for this reason that multidisciplinary design optimization exists; to ensure that the entire design is optimized incorporating all of the relevant disciplines simultaneously. As expected, the inclusion of multiple disciplines within the simultaneous optimization problem significantly increases the complexity of the optimization problem.

The need for multidisciplinary optimization leads to the requirement to use a multiobjective design optimization method. These processes use multiple objective functions in order to find an optimum design [1]. It is generally impossible to arrive at an optimal design for every objective function, as objective functions are usually competing, which introduces the need for trade-offs within the optimization process [1]. The objective functions, relevant criteria, parameters and constants can be represented in a vector form and require specialized mathematics and optimization techniques to solve the optimization problem with the feasible solutions making up an attainable set instead of a region [1]. Another approach that is taken to solve a multiobjective design optimization problem is to represent the objective function as a single scalar equation, which contains weighted contributions from all of the objectives [3].

A majority of methods that use the vector form attempt to find the Pareto optimal point. The Pareto efficiency, named after the Italian engineer and economist Vilfredo Pareto who used the concept for economic efficiency and income distribution, is a concept that looks for a Pareto optimal point, where any change to one objective cannot be made without negatively affecting another objective [3]. A Pareto improvement exists if another optimal design point occurs, where an improvement can be made to one objective without negatively affecting, but not necessarily improving, any other objectives [3]. The set of all Pareto-efficient design points, usually depicted graphically, is called a Pareto set or frontier and is shown in Fig. 9.3.

The example in Fig. 9.3 shows a production-possibility frontier, where the frontier and the area left and below it is a continuous room of choices. The brown points are examples of Pareto optimal choices of production. Points off the frontier, such as *K* and *L*, are not Pareto efficient.

There are multiple methods for solving a single scalar setup, which heavily vary in their approach. While most of these methods are based on methods using calculus or numerical solving techniques [3], there is no simple procedure from
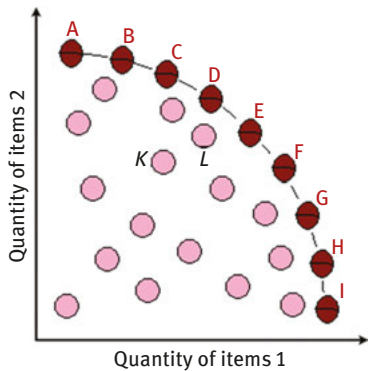
Fig. 9.3: An example of Pareto set.

which they all stem from; therefore, these methods, as well as other methods in general, will be discussed individually in the next section.

9.5 Methods of optimization

The previous section discussed the general approaches and definitions with regard to the optimization of a design solution. This section will use these approaches and concepts in order to discuss a selection of methods that are used for optimal design analysis. While a multitude of methods do exist, relying on calculus or numerical methods to obtain a solution, they all require some form of repetition or iteration. While defining a good mathematical model and objective functions from the start can greatly reduce the number of iterations required to arrive at a solution, the specific abilities of computers to perform billions of calculations in each second have made them a requirement for efficient implementation of any of the methods mentioned in what follows below [3, 5]. While the simpler techniques can be done manually, it is vastly more inefficient than a computerized solution while limiting the complexity of the problem that can be solved.

The following sections are split into general categories of methods for solving optimization problems with specific examples of methods that fit into each category given.

9.6 Classical optimization techniques

The classical optimization techniques are a set of methods that have been developed from differential calculus and are, therefore, very useful for obtaining optimal solutions for functions that are continuous and differentiable [7]. The methods are analytic in nature and use calculus methods to find the optimal points for the

objective function. Many practical problems involve objective functions that are not continuous or differentiable, limiting the number of scenarios to which classical optimization techniques can be applied [7]. The classical techniques, however, are also the basis for the numerical methods used to obtain solutions for practical problems. The classical optimization techniques can be used to find an optimal solution for single-variable functions, multivariable unconstrained functions and multivariable constrained functions with both equality- and inequality-type constraints [7]. Classical optimization methods usually lead to a set of nonlinear, simultaneous equations whose solution is required to obtain the optimum point, with the possibility of these equations being difficult to solve. The necessary and sufficient conditions required to use classical optimization techniques on each of the previously mentioned categories are presented below:

For single-variable optimization problems, the first necessary condition is that at a local minimum/maximum point within the range of the objective function with a dependence on only a single variable in which optimization is being performed, the first derivative of the function will be equal to zero [7]. This theorem does not state that all points that have a gradient equal to zero are minimum/maximum points as they can also be stationary points. A sufficient condition for classifying a minimum/maximum for this class of optimization problem states that if

$$f'(x^*) = f''(x^*) = \cdots = f^n(x^*) = 0 \text{ and } f^n(x^*) \neq 0 \qquad (9.2)$$

Then the point is a minimum if the final derivative is greater than zero and n is even; it is a maximum point if the final derivative is negative and n is even and neither a maximum or minimum if n is odd [7]. These two theorems can be used to prove a local minimum/maximum point in a classical optimization technique.

The requirements for multivariable problems, both constrained and unconstrained, are immensely more complicated than those for single-variable problems and will therefore not be discussed in this chapter, particularly owing to the superiority of numerical methods when solving these problems. It is for this reason that numerical optimizations methods, particularly with the use of computers, are preferred for solving both complex single-variable problems and multivariable problems. Numerical methods, however, are usually based on classical methods but introduce an iterative estimation process to solve the problem instead of finding actual solutions for the problem.

9.7 Numerical methods of optimization

Numerical methods in mathematics are a highly useful tool for optimization problems. They use approximation methods to arrive at a solution to problems that are too complex for or cannot be solved using classical methods. A numerical method

generally uses an initial value for the solution of a problem and, using a variation of developed techniques, iteratively changes the solution until it converges on a solution approximately equal to the actual solution. The iterative nature of these methods makes computers highly suitable tools for running these methods until a solution is reached. There is usually a trade-off between computational complexity and convergence speed when utilizing these methods. These methods are also useful, as a solution can be found without large amounts of analysis needing to be performed manually by the user. However, as with all numerical methods, the ability and speed of the method to converge to a realistic answer depends heavily on the model and the input by the user, as well as the starting feasible point used by the solver.

Many numerical methods and solvers exist for optimization problems. A few examples are next given and discussed in the following sections.

9.7.1 Linear programming

Linear programming is a method where the objective function and all of the equality and inequality constraints are linear with respect to the design variable. Owing to its early conception and relative simplicity, linear programming has been applied to an immeasurable number of optimization problems [7]. The relative simplicity of the objective function and constraints usually allows for a graphical solution to simpler real-world optimization problems. An example of the geometric solution is shown in Fig. 9.4.
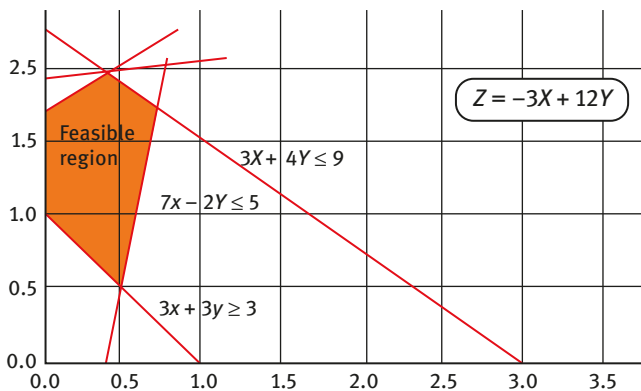
Fig 9.4: Typical graphical solution to linear programming.

A method of solving a linear programming problem, known as the simplex method, utilizes the fact that if an optimum solution exists, it will be represented by a vertex of the feasible region. This allows for the selection of an optimal point from the set

of all of the possible feasible points as the optimal point will be found on a vertex of the feasible region [7]. While examining each feasible point individually is inefficient, the simplex method improves the efficiency by only looking for a point that reduces the value of the objective function until a minimum is found [7].

The simplex method, while improving efficiency compared to checking each individual feasible point, still requires large amounts of computing power and memory to run; particularly for multivariable optimization processes. Other methods, such as the revised simplex method, dual simplex method and Karmarkar's interior method, can further improve efficiency of the linear programming solution method; however, they are still relatively computationally expensive and will not be discussed in this chapter [7].

9.7.2 Integer programming

Integer programming is similar to linear programming except some or all of the variables are constrained to take on integer values. These possible variable values are not continuous and while it is possible to use a linear programming approach and round off the answer, this approach can lead to violations of the constraints [7]. This is the only difference between linear programming and integer programming. Integer programming is useful for optimization problems, where the variables cannot physically take on a value that is not an integer. An example of that would be a number of a certain product produced or number of people in a workforce. The integer variable can also represent a decision in which case it can only be represented by a 0 or a 1. This is known as binary integer programming. While there are some applications in engineering design, integer programming is more useful in fields such as production planning, scheduling and cellular networks.

9.7.3 Nonlinear programming

Nonlinear programming is used to solve general optimization problems, where either the objective function or the constraints are nonlinear. While it is possible to use classical optimization techniques to solve specific nonlinear problems, a large portion of them do not contain closed-form solutions to the problem requiring a numerical solving method to be implemented [7]. It is also possible, in some specific circumstances, to linearize any nonlinear components within the optimization model setup; however, this can result in a loss of generality of the model and the subsequent solution. Specific solution methods exist for different types of nonlinear programming problems, which usually depend on the type of nonlinear programming problem and the way in which the objective function or the constraints are characterized.

9.7.4 Quadratic programming

Quadratic programming is a type of nonlinear programming used for optimization problems, where the objective function contains quadratic terms while the constraints are linear. Some examples of methods that are used to solve quadratic programming optimization problems are the interior point's method, active set method, augmented Lagrangian method, conjugate gradient method and an extension of the simplex method that is used to solve linear programming problems [7]. They have been successfully used in specific applications such as financial portfolio optimization, power generation optimization for electrical utilities and in engineering design optimization.

9.7.5 Stochastic programming

Stochastic programming is used to optimize cases in which some of the variables depend on random variables. These methods are usually based on statistical analysis with the randomness of the variables originating from a number of sources. Examples of real-world applications for optimization using stochastic programming include material properties (owing to variations in test results for the same material), dimensions of parts within a permissible range and flight loads placed on aircraft structures during operation [7]. Stochastic programming problems can be divided into stochastic linear, geometric dynamic or nonlinear programming problems [7]. Using classical optimization techniques, the approach usually involves converting stochastic programming problems into equivalent deterministic problems, which are then solved using the relevant numerical technique for the type of deterministic problem obtained [8]. These techniques use classical statistical techniques in place of calculus techniques to model the optimization problem.

9.7.6 Dynamic programming

Dynamic programming uses the approach of dividing the optimization problem into smaller optimization problems. This optimization method is particularly useful for engineering design of subsystems that all need to be optimized, where, owing to the need to make decisions sequentially at different stages of the design process (known as multistage decision problems), it is impossible to optimize the overall design as any changes would change the succeeding decisions that would be inefficient and impractical [7]. The dynamic programming optimization technique decomposes a multistage decision process into a sequence of single-stage decision problems, optimizing each stage individually [7]. The optimization technique used at each stage, whether classical, differential calculus, nonlinear programming or any other

numerical method, is irrelevant to the overall process [7]. While it is possible to solve multistage decision problems using classical methods, it requires the number of variables to be small and the functions to be continuous and differentiable [7]. The use of nonlinear programming techniques can solve more difficult multistage decision problems; however, particularly with the introduction of randomness to the variables, a majority of the problems become unsolvable. Dynamic programming can handle all of these complexities, owing to the procedure of breaking down the optimization problem into smaller optimization problems while being able to vary the optimization technique used at each stage according to which the technique is most efficient and appropriate. Another advantage of dynamic programming is its ability to be used to optimize infinite or continuous problems as the optimization occurs at each decision point whether there are a finite or infinite number of them. An example of this would be a missile system following a target where, even though the time frame is finite, the number of decisions made by the missile system is continuous as the target movement is measured and relayed to the missile system. A negative aspect of using dynamic programming is the "curse of dimensionality," a term that refers to the arising of various phenomena when organizing and analyzing data in high-dimensional spaces such as the ones needed for dynamic programming.

9.8 Advanced optimization techniques

The need for advanced optimization techniques arises out of the requirement to solve difficult optimization problems such as those that include multimodality, dimensionality and differentiability, which are usually associated with large-scale problems [9]. Traditional methods such as those previously discussed tend to fail for large-scale problems particularly if the objective function or the constraints are nonlinear. The previous methods also generally rely on obtaining information regarding the gradient of the function that is problematic if the function is not differentiable. Previously mentioned optimization techniques also tend to fail if there are many local maxima/minima [9]. It is for these reasons that more capable and robust optimization methods have become the focus of recent research. A large portion of these techniques are inspired by naturally occurring systems. A selection of techniques is discussed in the following sections.

9.8.1 Hill climbing

Hill climbing is a graph search algorithm, where a successor node is extended from the current path which is closer to the solution than the end of the current path. The hill climbing technique starts at a random solution in the feasible region and iteratively moves from a current solution to a better neighboring solution in the

feasible space until a local optimum is reached [10]. The algorithm will only accept a downhill movement, where the quality of the neighboring solution is better than the current one, which can lead to the algorithm getting stuck on a local maxima/minima instead of the global optimal point [10]. Attempts to improve the method have led to other methods such as simulated annealing, Tabu search (TS),[1] greedy randomize adaptive search procedure, variable neighborhood search, guided local search and iterated local search, all of which attempt to overcome the problem of stagnation on local optimum points instead of global ones [10]. Hill climbing is used in artificial intelligence in order to reach a goal state from a starting node.

9.8.2 Simulated annealing

The inspiration for the simulated annealing method comes from the metallurgical process of annealing, where the heating and cooling of a metal increases the crystal sizes and reduce defects. The heating allows the atoms within the crystal lattices to detach and wonder from their position while the controlled cooling allows for the possibility of their finding of a configuration with a lower internal energy than the initial one.

The simulated annealing method compares each point within a feasible region to the state of a physical system where the function to be minimized is interpreted as the internal energy of the system in the current state. The method then attempts to bring the system from an arbitrary starting point to one with minimum internal energy, therefore, finding an optimal point in the feasible space. In order to simulate the annealing process, a temperature-like parameter is introduced and is controlled using the Boltzmann's probability distribution [7]. The accuracy of the solution obtained is unaffected by the chosen starting point with the only effect being on computational effort required to solve the problem [7]. The method can be used for mixed-integer, discrete and continuous problems.

9.8.3 Genetic algorithms

Genetic algorithms (GAs) are optimization methods inspired by evolutionary genetics, making use of concepts such as inheritance, mutation, selection and crossover. They are usually implemented as computer simulations in which a population of abstract representations ("chromosomes") of feasible solutions ("individuals") evolve toward

---

1 TS is a global optimization algorithm and a metaheuristic or metastrategy for controlling an embedded heuristic technique. TS is a parent for a large family of derivative approaches that introduce memory structures in metaheuristics, such as reactive TS and parallel TS (from www.cleveralgorithms.com/nature-inspired/stochastic/tabu_search.html).

a better solution. The initial population is completely random with improvements occurring in generations. The fitness of the whole population within each generation is evaluated with select individuals chosen stochastically according to their fitness and modified by being mutated or recombined to form a new population, which is then used in the next iteration of the algorithm.

GAs are best suited to design problems with mixed continuous–discrete variables and discontinuous design spaces, which would be computationally expensive for standard nonlinear techniques [7]. Standard nonlinear techniques tend to find local optimum points, whereas GAs have a high probability of finding global optimal points. GAs do not rely on the gradient of the objective function but rather on the value of the objective function itself [7].

9.8.4 Ant colony optimization

The ant colony optimization method is inspired by the foraging process of ants. In reality, ants initially wonder randomly in search of food sources. When they find food, they return to the colony leaving a pheromone trail leading to the food source. Any other ants that come across the trail are likely to stop traveling randomly and follow the pheromones to the food source leaving their own pheromone trail thereby strengthening the trail. Owing to evaporation, the longer it takes for another ant to travel down the trail the less strong the pheromone trail will be causing a short path to a food source to have a stronger trail. The evaporation also stops convergence on a specific food source allowing for full exploration of the solution. When one ant finds a good and short path to a food source, the other ants are more likely to follow this path. If the path leads to a good food source, the number of ants on this path increases until all of the ants follow a single path. Simulating this search pattern within a feasible region allows for an optimum solution to be found. The simulation can be run continuously and react to real-time changes. This method of optimization is applicable to optimization in fields such as network routing and urban transport systems.

9.8.5 Neural network optimization

Neural network optimization methods are inspired by the large computational power of the nervous system and its ability for parallel processing [7]. A neural network is a massively parallel network of interconnected simple processors ("neurons") in which each neuron accepts the inputs from other neurons and computed an output that is sent to the output nodes. The network of processors maps an input vector from one space to another with the mapping being learnt instead of specified [7]. The network is described by individual processors, the network

connectivity, the weighting of the connections between the processors and the activation function of each processor. The network can be trained by minimizing the mean squared error (MSE) between the actual output and the target output for all the input parameters by adjusting the weighting values in order to determine the optimal weighting values that lead to an optimum association of the input and output [7]. There are multiple methods and architectures of the neural network that can be used to solve optimization problems.

9.9 Gradient-based methods

Another way of classifying optimization methods is by separating the methods based on their approach to solving the optimization problem. Gradient-based methods use differential calculus to check the gradient of an objective function while moving from point to point in a feasible region until a gradient of zero (indicating a minimum/maximum point) is found. Gradient-based methods can be applied to both constrained and unconstrained problems. During each iteration of a gradient-based method, both the search direction and the step size between each iteration are required to be calculated. The different gradient-based methods, some of which are discussed below, are categorized by the method in which they compute the search direction. A problem with gradient-based methods arises from the need to determine if a point with a zero gradient is a global or local maximum/minimum point.

9.9.1 Unconstrained methods

These methods are applied to optimization problems without any constraints on the possible values of the optimization variables. The first gradient-based method for unconstrained problems, which will be discussed, is the steepest descent method.

The steepest descent method uses the theory that, for a differentiable function, the value of the function will decrease faster if the negative gradient of the function at a test point is used to determine the direction to the next test point until a minimum value is found [2]. In order to find the minimum point along this direction, a line search is then performed on the line in that direction [5]. By using the positive gradient for the method, a local maximum can be found instead of a minimum. A graphical representation of the method is presented in Fig. 9.5.

The steepest descent method is not very efficient for many problems and can suffer a condition known as zigzagging, which increases the time it takes for the method to converge on a solution. A method that attempts to correct for this error is the conjugate gradient method. The conjugate gradient method is an improvement of the steepest descent method, where the history of the gradients is taken into
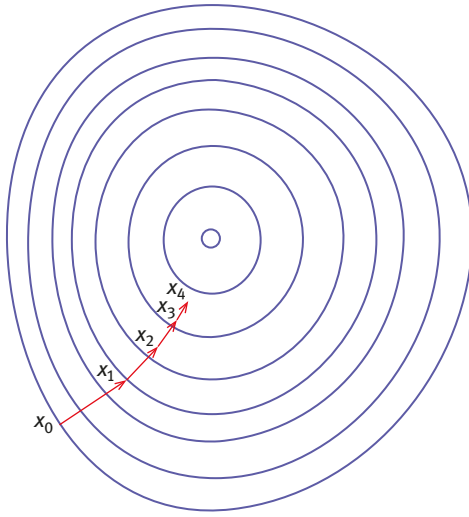
Fig. 9.5: Steepest descent method.

account when calculating the direction of the movement. This improves the efficiency of the method, which result in a decrease in convergence time [5].

Another related pair of gradient-based methods for unconstrained problems are the Newton method and the quasi-Newton method. The Newton method uses the value of the Jacobian or the Hessian matrix, a matrix of the second derivatives of the objective function at a specific point, at each iteration to numerically determine the minimum/maximum value of the problem [5]. However, calculating the Jacobian or Hessian can be computationally expensive at each iteration with the possibility of divergence being introduced to the problem. In order to overcome this, the quasi-Newton method uses estimates of the Hessian matrix, which are improved with the results from each iteration, to calculate a new search direction instead of the actual optimum point in each iteration [5].

9.9.2 Constrained methods

Some examples of gradient-based methods for constrained problems are the simplex method, sequential linear programming (SLP) method, sequential quadratic programming method, exterior penalty method, interior penalty method, generalized reduced gradient method, method of feasible directions and mixed integer programming which will be briefly discussed below.

Sequential or successive linear programming is a gradient-based method for approximately solving nonlinear optimization problems by reducing the problem

using linearization to a series of linear approximations of the nonlinear optimization problem [2]. This method is particularly useful when the computation of the constraints, objective function and its derivatives are much larger than the calculation costs of the optimization operations, such as the search direction or step size [2]. The approximation involved in each cycle of the linear programming optimization generally results in a solution which is not the optimum solution; however, the solution will be more optimal than the initial design analyzed. The method is then repeated on the new solution, creating a sequence of linear programming problems giving this method its name [2].

Sequential or successive quadratic programming has the same concept of an SLP; however, it is applied to optimization problems with nonlinear quadratic approximations of the objective function instead of linearizing the objective function.

Penalty-based methods are used to convert a constrained problem into an effectively unconstrained problem by introducing a penalty term into the objective function, which ensures that the original constraints are either not violated or a solution that does violate them is penalized [5]. The method is repeated with decreasing penalty terms, producing a solution that approaches the optimal solution of the original constrained problem [5]. These methods are used for their simplicity and their ability to be applied to equality and inequality problems for both linear and nonlinear optimization problems [9]. The method does rely on iteration and is, therefore, more computationally expensive than the more sophisticated constraint following methods [5]. The exterior penalty method is a method that applies a penalty to a solution violating any of the problem constraints [2]. This method applies penalties only if the point is found on the exterior of the feasible domain meaning that the method approaches the optimization problem from the unfeasible region and moves toward the feasible region. The interior penalty method uses a similar approach to the exterior penalty method; however, this method is restricted to solutions that are found in the feasible region only [5].

Generalized reduced gradient methods use the concept of projecting the search direction into the feasible region at a tangent to the constraints of the optimization problem [2]. They are suitable for large-scale, nonlinear structural optimization problems [11]. The method uses the addition of slack variables to inequality constraints to transform them to equality constraints while maintaining the total number of variables in the optimization problem, making the method completely general in terms of its application [11]. The method then uses the equalities to express the part of the variables, called basic variables, in terms of the remaining nonbasic variables in a manner similar to the simplex method [11]. This reduces the problem to a series of problems with only upper and lower bounds, which are then solved sequentially with all of the constraints being treated in the same manner [5, 11]. Using the derivatives of the constraints, a reduced gradient in the basic variables is found from which the search direction is calculated with nonbasic variables that need to remain positive or zero throughout the optimization procedure [5]. A line search method is then

used in the direction calculated with a new reduced gradient when a nonbasic variable reaches zero [5].

The methods of feasible directions are specifically aimed at nonlinear optimization problems with inequality constraints [5]. These methods solve the problem of directions tangent to nonlinear constraints of an optimization problem causing a departure from the true constraints [5]. In these methods, the search direction is allowed to point at an angle into the feasible region [5]. The use of these methods ensures that the next solution considered during the optimization process is within the feasible region [1].

9.10 Heuristic methods

Heuristic methods are methods that rely on rules of thumb instead of established mathematical procedures to arrive at a near-optimum solution. These methods often use algorithms that were inspired by nature and are useful for solving large complex optimization problems. They are also able to circumvent the problem of getting stuck on local optimum points instead of global ones, usually by incorporating some form of randomness within the algorithm. Heuristic methods are generally faster and more efficient than traditional methods by sacrificing optimality, precision, accuracy or completeness for speed. A few of the heuristic methods have been discussed in a previous section of advanced optimization techniques. Another example of a heuristic method, the TS, is discussed below.

9.10.1 Tabu search

The TS method uses the premise of a local search technique, starting at a point and proceeding iteratively from one point to another local point until a termination criterion is met. Unlike the gradient descent method, the TS can move to a neighbor solution that is inferior to the current solution point while selecting the move from point to point using a modified neighborhood which helps in avoiding getting stuck at local minima/maxima. The method uses both short-term and long-term memory structures in order to construct the modified neighborhoods. This leads to the neighborhood being dynamic rather than static, such as in local search methods. The most common memory structure used in TSs is that of recency-based memory.[2] This memory structure records information about solution properties that change

---

2 The first item in a list is initially distinguished from previous activities as important (primacy *effect*) and may be transferred to long-term *memory* by the time of recall. Items at the end of the list are still in short-term *memory* (*recency effect*) at the time of recall.

when moving from point to point. Recency-based memory structures keep track of solution properties that have changed in the recent past, labeling some solution properties as Tabu active. When a solution contains Tabu-active elements, these solutions become Tabu (or Taboo), removing them from the modified neighborhood and preventing them from being revisited. The use of adaptive memory creates a balance between search intensification and diversification. Intensification strategies modify search rules to encourage more move combinations and solution features which were seen to be historically good while diversification strategies attempt to incorporate new attributes and attribute combinations that were not previously part of the previously generated solutions.

9.11 Optimization of topology of aerospace structures

The design of a structure usually requires optimization of three parameters of the structure: size, shape and topology. The optimization of the structure size attempts to find the optimum thickness distribution of components within the design which is based on the desire to minimize or maximize a physical quantity such as peak stress, deflection or a multitude of other parameters [6]. The main feature of size optimization is that the domain of the design model is fixed throughout the optimization procedure [6]. Shape optimization problems use the design domain as the optimization variable in an attempt to find the optimum shape of this domain [6]. Topology optimization of solid structures attempts to optimize the features of the structure such as the number and location and shape of holes and the connectivity of the design domain [6]. Figure 9.6 presents a schematic example of the above three types of structural optimizations.

Topology optimization assists with ensuring that a design has a minimum weight and that all components of the design are carrying maximum load so that no material is wasted in terms of the potential load-carrying capabilities [8]. This has led to vast improvements in the field since the early 2000s in both research and applications, as the optimization of the distribution of material and the load paths in the structure are of vast importance in all fields, particularly the aerospace field [8].

A topology optimization problem is generally defined using the design loads, possible support conditions, the available domain size for the structure and the required holes or solid sections for other design considerations as constraints for the problem [6]. The constraints are used to optimize the distribution of the available material in the fixed domain size, usually by using a distribution function instead of a standard parametric function [6]. Topology optimization methods are focused on deciding whether a point in the design domain should contain material (a material point) or should not contain any material (a void) [6]. This led to the consideration of topology optimization as a binary optimization problem with a point in the design domain either containing material or not which would usually require an
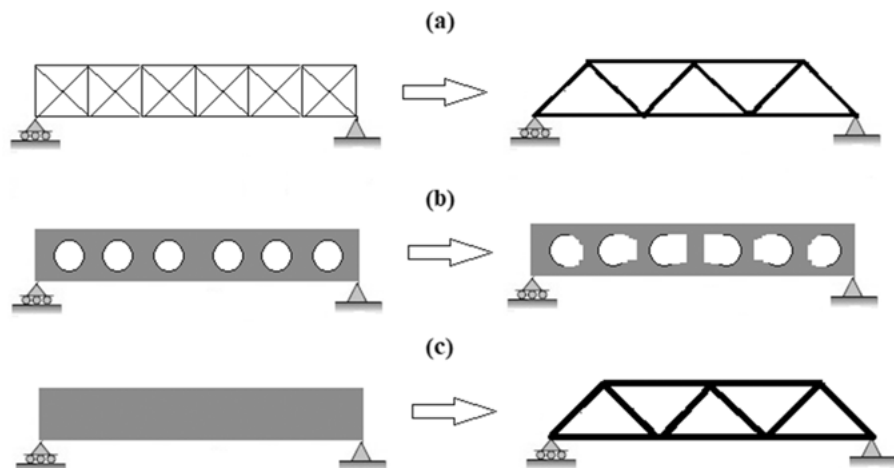
Fig. 9.6: Types of structural optimization problems: (a) truss structure sizing optimization, (b) shape optimization, (c) topology optimization (left: initial problem; right: optimized solution) (adapted from [10]).

integer programming approach to solve [8], resulting in computationally expensive methods to solve such large-scale integer programming problems and, therefore, limited the success of applicable methods. This also led to the development of multiple methods that approached an optimization problem from different perspectives in order to avoid these problems [8]. The sections below discuss a selection of methods developed within the last 20 years in order to optimize topology problems in the structural field. The number of methods developed over the last 20 years are immense and it is for that reason that this chapter will only focus on a select few methods that were considered to have made important advances in the field of topology optimization.

9.12 History of topology optimization

The first description of structural optimization was presented by Anthony G.M. Michell, an Australian mechanical engineer [12]. The field of structural optimization was only focused on and further developed nearly 50 years later with the invention of electronic computers, allowing for a great increase in efficiency of all procedures [13]. The success of topology optimization, even with the use of computer solutions, was limited until the late 1980s as the problem was approached as a binary optimization problem, which required large amounts of computing power and precluded the use of gradient free algorithms [8]. The first major improvement was made by Bendsöe and Kikuchi in 1988 when they proposed a homogenization-based method [14], which was

the basis for the density-based methods discussed in the next section. The homogenization method uses density variables, which are linked to specific microstructure models, in order to optimize global structural performance. The density variable of each cell within the design domain is then modified iteratively in order to optimize the topology. Figure 9.7 displays schematically the different microstructure cells that were used for the optimization procedure.
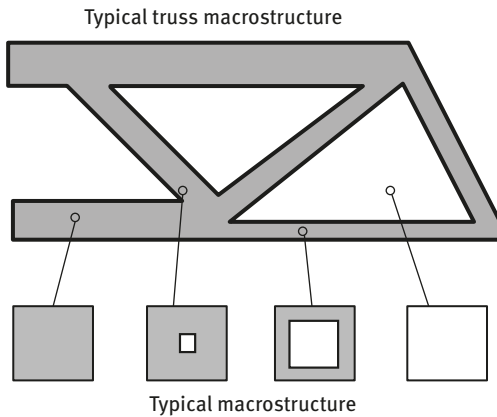
Fig. 9.7: The homogenization method cell structures (adapted from [8]).

The original homogenization method is extremely mathematically complicated, which prevents its general application. This led to the density-based methods to be presented and discussed in the next section.

9.13 Density-based methods

Density-based methods are the most widely used methods for topology optimization [15]. These methods operate by discretizing a fixed domain into finite elements and minimizing an objective function by deciding whether each element should contain materials or remain empty (void). The constraints are usually placed on the amount of material that is utilized. To avoid a challenging large-scale integer programming problem, discrete variables are replaced by continuous variables and iteratively driven to a discrete solution by the use of an interpolation function, which interprets the continuous design variables as the material density of each element [15]. This is because the general discretized problems lack a solution [16] as for many problems the addition of more holes will decrease the objective function and, therefore, the optimum solution for the discretized design domain is dependent on the number of divisions of the domain (mesh dependence) [13]. The first density-based

method introduced was the simplified isotropic with penalizations (SIMP) method [17] and will be discussed below.

The SIMP method was first introduced by Bendsøe [17] as an improvement of the previously devised homogenization method [14]. Its purpose was to artificially reduce the complexity of the homogenization method while improving the convergence of the binary topology optimization problem [13]. The SIMP method was physically justified by Bendsøe and Sigmund [18].

The SIMP method makes the use of a power law relation to apply a penalization parameter onto the density design variable that is multiplied onto a material property (such as material stiffness, cost or conductivity) [13, 18]. The simplicity of the SIMP method has led to its widespread use both in industry and academia. The choice of the penalization parameter has a major impact on the quality of the solution obtained using the SIMP method, possibly causing either grayscale or convergence problems [13]. The experimentally verified value for the penalization parameter is a value of 3, which ensures physical realizability of elements with intermediate densities [18] and has been shown to make density gradients equal to topological derivatives for elasticity problems [19]. The penalization parameter, however, will only work correctly when the volume of the material is constrained, either as a direct constraint or indirectly through another constraint [13].

The SIMP method, while being simple and efficient to implement compared to the homogenization method, does have some shortfalls. When looking at the well-posedness of the SIMP method, when the penalization parameter is greater than 1, there is no guarantee that a solution to the optimization problem can be found [6]. Therefore, the use of numerical methods to solve the optimization problem, such as FEA=Finite Element Analysis, introduces the possibility of mesh dependence of the solution [20]. Another problem is the possibility of the checkerboard phenomenon, where the optimum solution has adjacently varying material-filled elements and voids creating a checkerboard pattern. This is often seen in topology optimization problems particularly when lower-ordered finite elements are used to discretize the design domain [20]. An example of the checkerboard phenomenon is presented in Fig. 9.8.

Another problem is the possible existence of intermediate density values in the optimization solution, where the element has a density value that is neither 0 nor 1 and is therefore neither a pure solid-filled element nor a void [20].

The problems associated with the SIMP method have led to modified versions of the penalization method being developed, such as the rational approximation of material properties (RAMP) method [19] and the SINH method [21, 22]. Unlike the SIMP method, the RAMP method has nonzero sensitivity (gradient) at zero density [23], rectifying numerical problem in regions with low-density values in the presence of design-dependent loading [15]. The RAMP method was introduced in order to alleviate nonconcavity of the original SIMP method [24] ensuring convergence to a fully binary solution. This feature does not play a major role in practical examples. The SINH
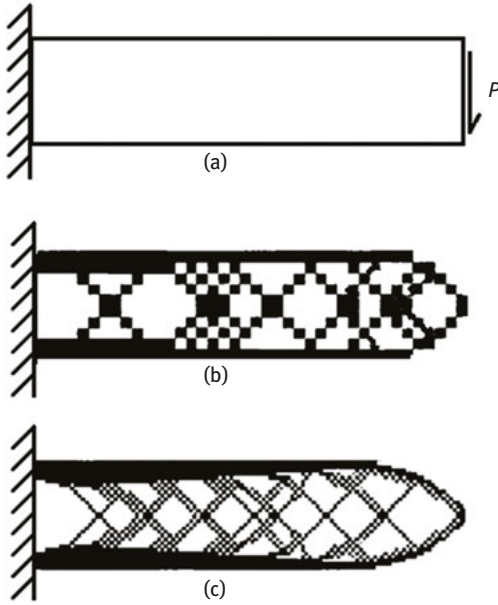
Fig. 9.8: Typical example of the checkerboard problem: (a) initial structure, (b) coarse optimization and (c) finer optimization (adapted from [6]).

method uses cost penalization, as cost can represent material weight, in order to penalize material volume instead of material parameters as seen in the previous two methods [15]. The various expressions for the three methods, the SIMP, the SINH and the RAMP, are described in the following equations, where p or q is the penalization parameter (with multiple values shown in Fig. 9.9) and ρ is the density variable:

$$SIMP: \quad \zeta(\rho) = \rho^p$$

$$SINH: \quad \zeta_1(\rho) = \frac{1 - \sinh[p(1-\rho)]}{\sinh(\rho)}$$

$$\zeta_2(\rho) = \rho \tag{9.3}$$

$$RAMP: \quad \zeta(\rho) = \frac{\rho}{1 + q(1-\rho)}$$

This results in intermediate density cells carrying more volume with respect to the loading than either material filled cells or voids, reducing the number of intermediate cells in the optimization problem [15]. A comparison of the results for the three methods in shown in Fig. 9.9.

In general, density-based methods are represented by smooth, differentiable problems that are easily solvable by gradient-based methods [25, 26], the method of moving asymptotes [27] or other mathematical programming-based methods [13].
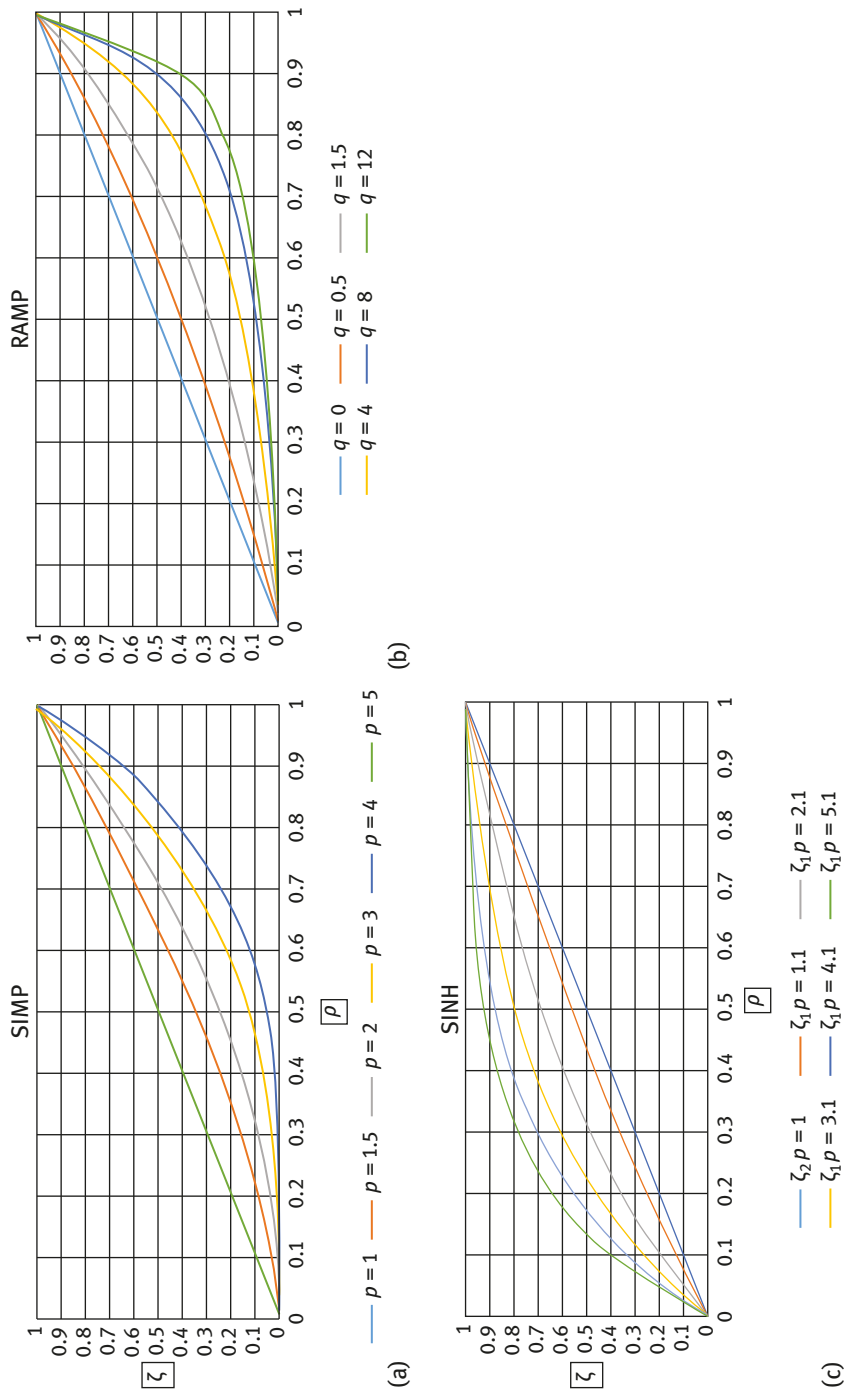
Fig. 9.9: Comparison between (a) SIMP, (b) RAMP and (c) SINH methods (adapted from [15]).

The use of these optimization methods also allow for the systematic and straight-forward inclusion of any additional global constraints; however, when including local constraints, parametrization problems, particularly in stress constrained problems, may cause great difficulty when solving real problems [28].

9.14 Hard-kill methods

Hard-kill methods optimize a topology problem by incrementally adding or removing a material to a design domain, with the choice of the location to add or remove material being dictated by the heuristic method [15]. The heuristic analyses may or may not be based on the sensitivity information in the design domain which, unlike the density-based methods, is never relaxed [15]. A problem with hard-kill methods is the possibility that the solution that is obtained may be nonoptimal when the methods are implemented and used inadequately, particularly when a prescribed boundary support is broken during optimization of a statically indeterminate structure resulting in a completely changed structure from the initially defined one [29]. By far the most popular and widely implemented hard-kill method is the evolutionary structural optimization (ESO) method and its derivatives which are discussed in more detail in the following section.

9.14.1 Evolutionary structural optimization methods

The first developed evolutionary method was the ESO method. The ESO method is based solely on the heuristic-based removal of material from an optimization design by gradually removing redundant or inefficient material from the structure until an optimal solution was found by achieving the presumed volume constraint [30]. This is achieved by calculating a criteria function, also known as a sensitivity number, for each element in the model, with the removal of elements having low sensitivity numbers [15]. Early versions of ESO were devised for use with FEA analyses for stress-based, stiffness or displacement problems using an iteratively increasing rejection ratio to remove increasing amounts of inefficient material from the FEA model until an optimum solution is reached [31]. An example of an ESO stiffness topology optimization process for a Michell-type structure[3] with two simple supports is shown in Fig. 9.10.

---

3 A. G. M. Michell formulated the criteria to be satisfied by all least-volume trusses with equal tensile and compressive yield stresses (see Michell, A. G. M., The limits of economy of material in frame-structures, Philosophical Magazine, 8 (47), 1904, pp.589–597).
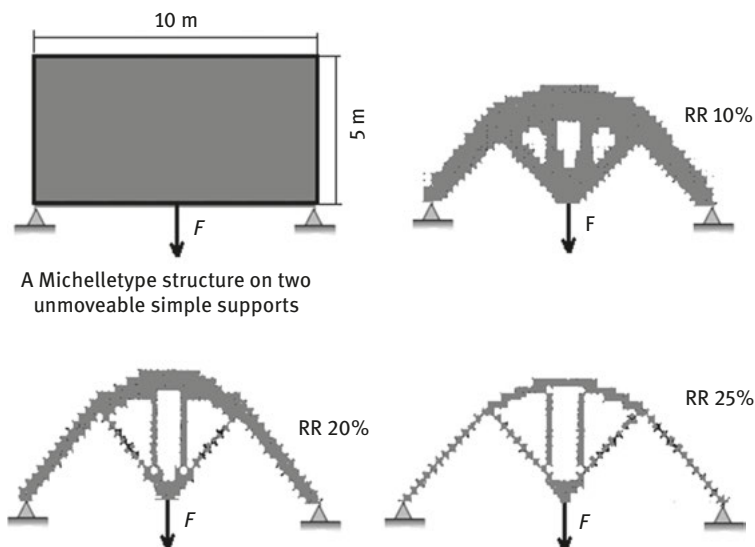
Fig. 9.10: ESO topologies with varying rejection rates (RR) (adapted from [30]).

A major disadvantage in the ESO method comes from the way in which it is implemented. The method removes material, or volume, iteratively until with the removal of any more material, a constraint is no longer satisfied. This, however, does not necessarily give an optimum solution as a material that has been removed in earlier iterations could be required for a more optimum design at a later stage in the process when other elements of a material have been removed [31]. This removed material cannot be recovered by using the ESO method. The early implementation of the ESO method also ignored many numerical problems that arose, such as checkerboarding, owing to its being a heuristic method. These deficiencies in the method led to the development of the bidirectional ESO (BESO) method.

The BESO method is an attempt to correct the disadvantage of not being able to reintroduce the removed material in the ESO method by simultaneously removing and adding material at each iteration of the optimization problem. A method for the removal and addition of elements was first designed in 1998 [32] and was applied for a stress-based optimization problem [33] and for a stiffness optimization problem [34] using FEA model bases. The method developed in the stiffness optimization problem [34] uses a linear extrapolation of the displacement field in the FEA model to estimate the sensitivity numbers of void elements, allowing the removal of elements with the lowest sensitivity numbers and the replacement of void elements with the highest sensitivity numbers. The method that makes use of the rejection ratio for the removal of a material and an inclusion ratio for addition of a material, both of them are not in relation to each other [31]. The selection of these values directly impact the ability of the method to arrive at an optimum solution. The BESO

method can be applied to initial full designs, an initial guess design and can even be used for 3D optimization.

The BESO method is a widely used optimization method mainly owing to its ability to obtain converged, checkerboard free, mesh-independent solutions for a multitude of designs with comparable optimal solutions to the SIMP method, as shown in Fig. 9.11, with the ability to start from a smaller than the domain guessed initial design, saving the computational time.

Optimization using SIMP

Optimization using BESO
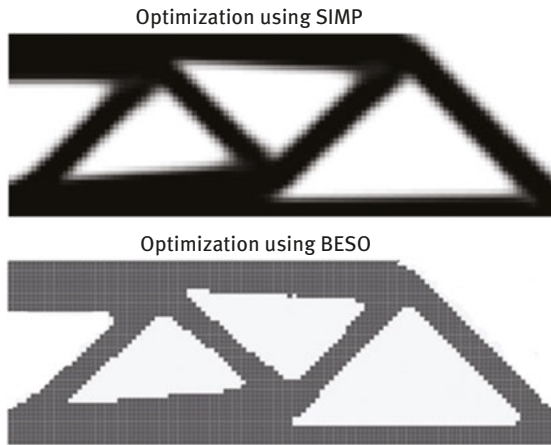
Fig. 9.11: Comparison of beam optimization using BESO and SIMP methods (adapted from [31]).

The BESO method, however, has been shown to be incorrect for specific optimization problems bringing the validity of the method into question [35]. While overcoming some shortfalls of the ESO method, the BESO method still has some common problems. The methods are fully heuristic; therefore, there is no mathematical proof that the obtained solution is the optimal one. Both the ESO and BESO methods rely on selecting the best solution by comparing a large number of intuitively generated solutions, reducing the efficiency of the methods heavily. Both methods have many cases where the solution obtained is not the optimal solution or, in particular cases, where they are completely broken down [35]. These problems have led to a large number of debates in the academic world on the validity of ESO/BESO methods, particularly when compared to SIMP methods [35].

9.15 Boundary variation methods

Boundary variation methods are a relatively recent addition to the topology optimization field, having been adapted from shape optimization techniques. Compared to

density-based methods, they use implicit functions to define structural boundaries instead of explicit parameterizations of the design domain. Boundary variation techniques generally have the advantage of producing very well-defined results, having little need for post optimization processing or interpretation of results [15]. These methods are also distinguished from the shape optimization methods on which they are based as they allow for the movement of structural boundaries as well as the addition, removal and merging of voids within the model, making these methods as topological optimization methods [15]. There are two prominent boundary variation methods being researched, which will be discussed in the following sections.

9.15.1 Level-set methods

In level-set methods the boundary of the design is defined by the zero-level contour of the level-set function while the structure is defined by the domain where the level-set function takes positive values. The shape of the geometric boundary is modified by controlling the motion of the level set according to optimization conditions and the physical problem by using the shape sensitivities of the objective function until a convergence criterion is met.

The conventional level-set approach, developed from the work of Wang et al. [36], uses the concept of the link between the velocity of the points on the structural boundary, the design sensitivity, the structural optimization process and the level-set method for boundary definition. Concurrently, a mathematical framework linking the velocity of the level-set boundaries to an adjoint shape sensitivity analysis for a stiffness optimization problem was developed [37–39]. These two direct methods are limited by their inability to create new holes in the level-set function away from the free boundary, which typically represent the outside of the design domain, and that they both are extremely dependent on the initial state of the design problem. This led to the inclusion of topological derivatives, representing the change in objective function with the introduction of infinitesimally small holes, in subsequent methods in order to allow for the nucleation of holes at any point in the design domain [39–41]. More recently, Dunning and Kim [42] make use of a secondary level-set function instead of topological derivatives to introduce holes. James and Martins [43] proposed using an extension of the conventional level-set method on body-fitted finite mesh models, allowing the design domain to be irregularly shaped.

The conventional level-set formulations make use of an explicit numerical method for solving the Hamilton–Jacobi partial differential equation (PDE) that controls the structural boundary. A problem associated with explicit numerical methods is that their convergence is dependent on the time step size chosen for the method. Additionally, the explicit method often causes the need to reinitialize the level-set function when they become too steep or too flat. This reduces the computational efficiency of the method. This has led to the development of a number of

alternative level-set function methods that use alternative strategies to solve the Hamilton–Jacobi PDE. These methods will not be discussed in this chapter as they are too numerous both in types and methods of solving the PDE.

Level-set methods have some advantages when compared with other topology optimization methods. Checkerboarding can be significantly reduced, the optimal shape and topology can be obtained simultaneously and the handling of any topology-dependent loads is more easily implemented when using level-set methods while the method is more versatile compared to the density-based methods [20, 44]. However, the level-set methods have their own distinct disadvantages. They have a slow convergence rate, particularly when using a Hamilton–Jacobi-based level-set method, and the required topology changes can only be obtained by pinching or merging of the boundaries in the original form with complicated workarounds required adding voids in the problem [20]. In general, there is large potential for the use of level-set methods; however, currently, the majority of uses are in research and not commercial applications.

9.15.2 Phase field method

The phase field method for topology optimization is based on theories that were originally developed as a method to represent the surface dynamics of phase-transition phenomena such as solid–liquid transitions [45, 46]. While this method has been utilized in many fields, such as diffusion, crack propagation and multiphase flow, the method can also be applied to topology optimization problems. The method begins by specifying a phase field function over a design domain that is composed of two phases with a continuously varying boundary region between the phases having a thin finite thickness. This setup is shown in Fig. 9.12.
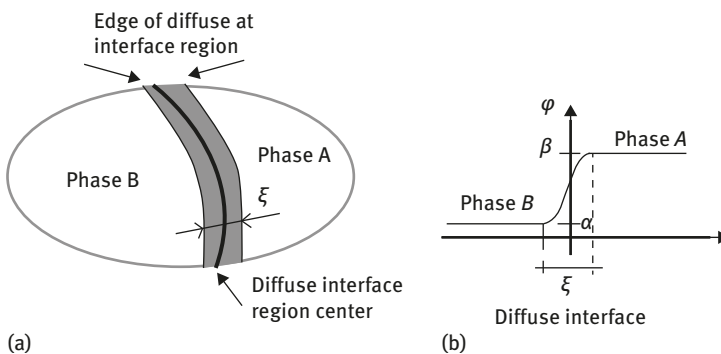
Fig. 9.12: (a) A 2D domain represented by a phase field function, and (b) a 1D representation of the phase field function (adapted from [46]).

In phase field topology optimization this region defines structural boundaries and is modified by dynamic evolution equations of the phase field function. The main difference between the level-set and phase field methods lies in the fact that in the phase field method the boundary interface between phases is not tracked throughout optimization as it is when using level-set methods. The governing equations of phase transition are solved over the complete design domain without previous information about the location of the phase interface. In addition, phase field methods do not require the re-initialization step of level-set functions [15], which reduces the complexity of the problem [47]. Phase field methods, like level-set methods, have the advantage of being able to simultaneously solve shape and topology optimization problems [47]. However, it has been observed that phase field methods are dependent on the initial shape of the design model as well as the mesh size and number of iterations of the method on the optimization problem [47]. An example of these effects is shown in Fig. 9.13.
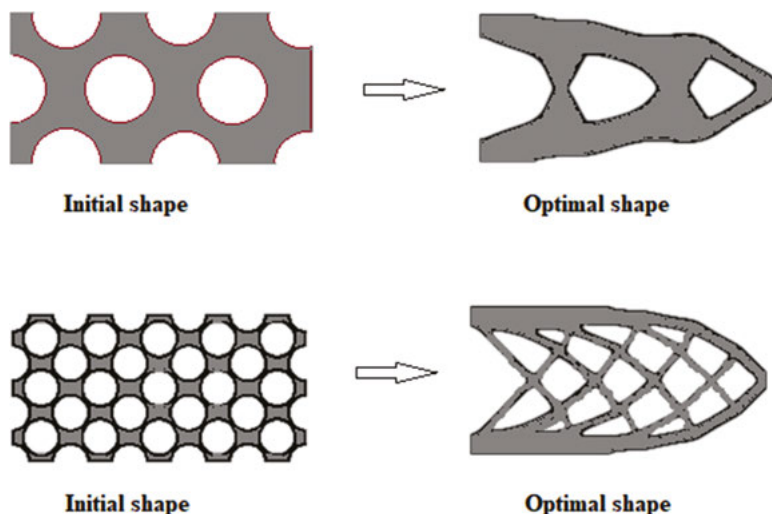
Fig. 9.13: Effect of initial shape to obtain the optimal shape using the phase field optimization (adapted from [47]).

Initial work began on the phase field method in 2003 by Bourdin and Chambolle [48] with further developments being made from 2004 onward. However, because of the later start date as well as relatively less research being performed on phase field methods, the field has remained in the academic sphere and has not been widely applied in real-world applications. Additionally, the computational costs of the phase field method are relatively high, reducing the current applications of the method [49]. The flexibility of the approach has the potential to allow for modeling coupled

systems, not only focusing on a pure structural optimization problem, giving the method a large potential for future research [49].

9.16 Recently developed methods

The field of topology optimization is a vast topic. While shape and size optimization problems have been developed further than topology optimization, mainly due to the complexity of topology optimization comparatively, the possible benefits of a topologically optimized design outweigh those from size or shape optimization. Additionally, with the increased computing power available today, computationally expensive methods are becoming easier, quicker and cheaper to run while yielding better results. It is for these reasons that research into new, more efficient methods that give improved optimization results is a focus of the field of topology optimization. While many different new methods of topology optimization have been proposed, one of the most promising and easy-to-implement methods is a bio-inspired cellular division-based method which is discussed as follows.

9.16.1 Bio-inspired cellular division-based method

In 2010, Kobayashi proposed a topology optimization method inspired by the cellular division process in living organisms that is capable of generating discrete and continuum-like structures [49]. The method uses a developmental program to implicitly govern topology layout development in stages. The method, when driven by a GA, assigns a set of rules called a Lindenmayer or map-L system[4] which define the tasks of the developmental program as the design variables for the optimization problem [15]. By controlling these developmental rules, a diverse set of topological designs may be generated with few design variables [15].

An advantage of the method is its ability to couple easily onto the existing finite element tools to develop a topology optimization capability. Similar to ESO methods, this is done by using simple pre-processing and post-processing operations especially if the design is a multiphysics one. The method also produces topologically optimal solutions that are immediately ready to undergo shape and sizing optimization processes and has the potential for these optimization processes to be performed simultaneously with the topology optimization process [15]. However, the use of a GA as a

---

4 L-systems were introduced and developed in 1968 by Aristid Lindenmayer, a Hungarian theoretical biologist and botanist at the University of Utrecht. He used L-systems to describe the behavior of plant cells and to model the growth processes of plant development.

basis of the method immediately ensures that it is more computationally expensive than the most gradient-based methods.

The map-L systems are a type of grammar system capable of acting as rewriting systems that can generate developmental programs to describe the construction of a natural engineered system [51]. The maps are analogous to cellular layers with the regions representing the cells and the edges in the walls of the cells. A series of production rules can then be applied in order to govern the processes that construct the map leading to complex topology being obtained. An example of the execution of a production rule is shown in Fig. 9.14.
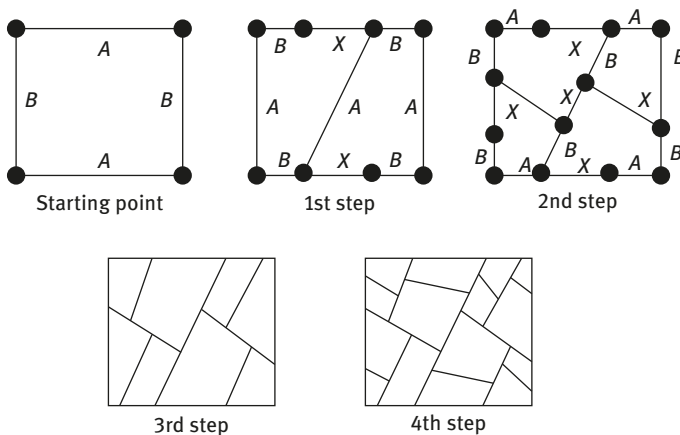
Fig. 9.14: The first four steps in a cellular division process (adapted from [52]).

More complex topologies can be obtained by utilizing additional rules and not just the division rule shown in Fig. 9.14. The geometry can also be stretched and superimposed onto nonrectangular domains that can also undergo shape changes. However, it must be noted that topologies generated by the map-L system have no physical or structural meaning and as such the geometry must be interpreted into a structural element [15]. Reference [53] presents the topology of a structure defined by the map-L system, projected onto a nonrectangular domain and interpreted into a 3D wing and spar layout for an aircraft component.

Topology optimization is performed by encoding the map-L system into a binary representation to use in a GA. A number of parameters that affect the topology are controlled by the optimizer, including those that control the growth and dynamics of the development, the developmental rules and the definition of the overall geometry or physical properties of the design model. The GA is, therefore, able to modify both the initial map and the rules that create the topology according to some fitness function.

The implicit representation of topology found in the GA of this method differs from the explicit representation, where a single design variable for each finite element corresponds to the genome that is utilized in other GA topology optimization methods. It is this representation that allows for fewer design variables and more design freedom while avoiding other issues such as maintaining domain connectivity throughout the evolution process [15].

9.17 Applications in the aerospace field

Having discussed a multitude of methods for topology optimization, the following section will look at some real-life applications of topology optimization in the aerospace field and, where possible, will give examples of the specific topology optimization methods discussed in the previous section.

9.17.1 General topology optimization applications

This section contains some general examples of topology optimization for structural components in the aerospace field. A majority of the examples are presented as graphical results and have limited information on the method of optimization used, usually because the design process relied on optimization software where the specific method of optimization was not attainable.

When optimizing aircraft components, a vast majority of the optimization problems are either minimum compliance (stiffest design) problems or minimum weight designs. Optimizing topology has a great effect on both cases with some stating that out of the three structural optimization categories, this will have the greatest impact on the design.

9.17.2 Applications of density-based methods

A good example of topology optimization using a density-based method is observed in the optimization problem for an engine pylon of a large cargo aircraft [8]. The optimization was performed in order to comply with stiffness, strength and weight requirements of the design. The first consideration was to define the design and nondesign domains based on multiple restriction imposed on the structure from sources such as aerodynamic restrictions and manufacturing restrictions.

The next consideration was the predicted flight loads. The entire envelope of predicted flight loads was analyzed with 24 possibly critical cases chosen for the topology optimization of the pylon, leading to the use of a polynomial interpolation model to incorporate all the loading cases and boundary conditions. The

implemented topology optimization method was an extended formulation of the SIMP method.

Another use of density-based topology optimization is to solve aeroelastic problems. The first work to tackle this problem used a 3D Euler solver, linear finite element models and additional sensitivity analyses to design wing stiffeners for minimizing mass with constraints given by the values of the drag, lift and deflection [54]. While the chapter did reach a final design, the focus was on developing a methodology for similar problems and, as such, the pictures of the results are not presented here.

9.17.3 Applications of hard-kill methods

Hard-kill methods have been utilized far less frequently than density-based methods. This is partially owing to their fully heuristic nature and the possibility for presenting a nonoptimum result as an optimum one. However, there have still been attempts to use these methods in optimizing aircraft structures. An example of the optimization of an aircraft bulkhead component using a modified ESO method [55] is presented below.

The paper focuses on improving the optimization of the design of a bulkhead in an F/A 18 fighter aircraft. The goal was to produce a lighter bulkhead for the aircraft while satisfying the geometric, functional and strength requirements. A finite element analysis of the half symmetric 3D model of the current bulkhead was first performed. The von Mises stress was then taken as the ESO criterion. The ESO algorithm was used to reduce the weight of the structure by removing the inefficient material. At each optimization cycle, a finite element analysis was performed using NE-NASTRAN (a FE code). The optimization algorithm was then employed to modify the topology based on the von Mises stress field. At each iteration, an element of the structure was removed only if the calculated current von Mises stress was less than a reference value. The topology optimization presented in [55] succeeds in removing the material from regions not in the primary load path. This has led to a lower weight design with a more even distribution of the von Mises stresses.

9.17.4 Applications of boundary variation methods

The use of boundary variation methods in aerospace fields appears to be very limited. NASA has researched the optimization of a 3D wing for different purposes, with an example focusing on aeroelastic constraints [56] and another focusing on a common research model wing [57]. The example described later is focused on the topology optimization of a reinforced wing box for enhanced roll maneuvers [58].

The chapter looks for a solution to maximize aileron reversal speed of a wing torsion box by reinforcing the upper skin of the wing. A spectral level-set topology optimization method was used to solve the design problem. The results showed that similar topology optimum results were obtained for different initial conditions. Therefore,, for any of the four initial setups, the final optimal solution is similar for all cases. This was considered a successful implementation of the optimization method; showing some form of independence between the initial setup and the solution.

9.17.5 Applications of bio-inspired cellular division-based method

While the bio-inspired division-based method is relatively new, there have been a few attempts to use the method for topology optimization in aircraft structures, such as the optimization of aircraft lifting surface [57] and the aeroelastic optimization of flapping wing venation [58]. The example below is for the topology optimization of a component in a jet engine [59]. The topology optimization of a bracket for drawing bars of a reverse device was performed using a software-based implementation of the bio-inspired cellular division-based method. Because the method was implemented using a software-based optimizing tool, the details of the method are scarce in the chapter.

The optimization procedure resulted in a weight saving of nearly 20% of the part being built out of steel powder by a selective laser melting method in order to be tested mechanically.

9.18 Conclusions

The field of optimization in general and particularly for structures is a vast one, which is continuously growing. Having been developed from mathematical first principles, most methods became practical and feasible after the introduction of the computer, which allowed for iterative procedures to be performed economically and quickly while increasing the complexity of the calculations that could be handled. With the continued increase in computational power and the focused research on both improving current methods and developing new methods, the field of optimization is continuously expanding and improving. The obvious benefits of design optimization to design solutions and procedures are numerous. Not only can a design save on material and cost while ensuring that any part of the structure that is inefficient is removed, but the ability to run optimization simulations before having to manufacture test items is increasing the overall efficiency of the design process continuously.

The chapter has covered some background to design optimization and some general optimization techniques while focusing on topology optimization methods

and their applicability in the aerospace field. However, the amount of information contained within this chapter is just a small part of the immense field that is design optimization.

To enhance the optimization method applicability, Appendix A presents a method to design optimized structures using the response surface methodology (RSM) approach, as authored by Dr Kaspars Kalnins, from Riga Technical University, Latvia.

References

[1]   Papalambros, P. Y., and Wilde, D. J. Principles of Optimal Design, Modeling and Computation, 2nd, Cambridge, The Press Syndicate of the University of Cambridge, 2000, 416p.

[2]   Haftka, R.T., Gürdal, Z., and Kamat, M.P. Elements of Structural Optimization, 2nd revised, Springer-Science+Business Media, B.V., 1992, 410p.

[3]   Adeli, H. editor, Advances in Design Optimization, Chapman and Hall, London, UK. 1994, 590p.

[4]   Majid, K.I. Optimum Design of Structures, London: Newnes-Butterworths, 1974, 264p.

[5]   Rothwell, A. Optimization Methods in Structural Design, © Springer International Publishing AG 2017, Gewerbestrasse 11, 6330 Cham, Switzerland, 2017, 314p.

[6]   Sigmund, O., and Bendsøe M.P. Topology Optimization: Theory, Methods and Applications. Berlin and Heidelberg: Springer-Verlag, 392p.

[7]   Rao, S. S. Engineering Optimization: Theory and Practice. s.l.: John Wiley & Sons, Inc., 2009 814p.

[8]   Zhu, J.-H., Zhang, W.-H., and Xia L. Topology optimization in aircraft and aerospace structures design, Archives of Computational Methods in Engineering, 23, 2015, 595–622.

[9]   Rao, R.V., and Savsani, V.J. Mechanical Design Optimization Using Advanced Optimization Techniques. s.l.: Springer, 2012, 233p.

[10] Al-Betar, M.A. β -Hill climbing: an exploratory local search, Neural Computing and Applications, 28(1), 2017, 153–168.

[11] Lasdon, L.S., Fox, R.L. and Ratner, M.W. Nonlinear optimization using the generalized reduced gradient method, RAIRO – Operations Research – Recherche Opérationnelle, 8(V3), 1974, 73–103.

[12] Michell, A.G.M. The limits of economy of material in frame-structures, Philosophical Magazine, 8, 2010, 589–597. doi: 10.1080/14786440409463229.

[13] Sigmund, O., and Maute, K. Topology optimization approaches, Structural and Multidisciplinary Optimization, 48, 2013, 1031–1055.

[14] Bendsøe, M.P., and Kikuchi, N. Generating optimal topologies, Computer Methods in Applied Mechanics and Engineering, 71, 1988, 197–224.

[15] Deaton, J. D., and Grandhi, R.V. A survey of structural and multidisciplinary continuum topology optimization: post 2000, Structural and Multidisciplinary Optimization, Springer–Verlag New York, Inc. Secaucus, NJ, USA, Vol. 49, 2014, 1–38.

[16] Sigmund, O., and Petersson, J. Numerical instabilities in topology optimization: a survey on procedures dealing with checkerboards,mesh-dependencies and local minima, Structural Optimization, 16(1), 1998, 68–75.

[17] Bendsøe, M.P. Optimal shape design as a material distribution problem, Structural Optimization, 1, 1989, 193–202.

[18] Bendsøe, M.P., and Sigmund, O. Material interpolation schemes in topology optimization, Archive of Applied Mechanics, 69, 1999, 635–654.

[19]   Stolpe, M., and Svanberg, K. An alternative interpolation scheme for minimum compliance optimization, Structural and Multidisciplinary Optimization, 22, 2001, 116–124.

[20]   Guo, X., and Cheng, G.-D. Recent development in structural design and optimization, Acta Mechanica Sinica, 26(2010), 2010, 807–823.

[21]   Bruns, T.E. A reevaluation of the SIMP method with filtering and an alternative formulation for solid–void topology optimization, Structural and Multidisciplinary Optimization, 30, 2005, 428–436.

[22]   Zhou, M., and Rozvany G. I. N. The COC algorithm, Part II: Topological, geometrical and generalized shape optimization, Computer Methods in Applied Mechanics and Engineering, 89, 1991, 309–336.

[23]   Pedersen, N.L. Maximization of eigenvalues using topology optimization, Structural and Multidisciplinary Optimization, 20, 2000, 2–11.

[24]   Stolpe, M., and Svanberg, K. On the trajectories of penalization methods for topology optimization, Structural and Multidisciplinary Optimization, 21, 2001, 128–139.

[25]   Sigmund, O. A 99 line topology optimization code written in Matlab. 2, s.l.: Springer, 2001, Structural and Multidisciplinary Optimization, 21, 2001, 120–127.

[26]   Andreassen, E., Clausen, A., Schevenels, M., Lazarov, B.S., and Sigmund, O. Efficient topology optimization in MATLAB using 88 lines of code, Structural and Multidisciplinary Optimization, 43(1), 2011, 1–16. doi: 100.1007/s00158-010-0594-7.

[27]   Krister, S. The method of moving asymptotes—a new method for structural optimization, International Journal for Numerical Methods in Engineering, 24, 1987, 358–373. doi: 10.1002/nme.1620240207.

[28]   Duysinx, P., and Bendsoe, M.P. Topology optimization of continuum structures with local stress constraints, Numerical Methods in Engineering, 43, 1998, 1453–1478.

[29]   Huang, X., and Xie, Y. M. A new look at ESO and BESO optimization methods, Structural and Multidisciplinary Optimization, 35, 2008, 89–92.

[30]   Xie, Y.M., and Steven, G.P. A simple evolutionary procedure for structural optimization, Computers & Structures, 49, 1993, 885–896.

[31]   Huang, X and Xie, M. Evolutionary Topology Optimization of Continuum Structures: Methods and Applications, Wiley, Chichester, United Kingdom, 2010, 238p.

[32]   Querin, O.M., Steven, G.P., and Xie, Y.M. Evolutionary structural optimisation (ESO) using a bidirectional algorithm, Engineering Computations, 15(8), 1998, 1031–1048. doi: 10.1108/02644409810244129.

[33]   Querin, O.M., Young, V., Steven, G.P. and Xie, Y.M., Computational efficiency and validation of bi-directional evolutionary structural optimisation, Computer Methods in Applied Mechanics and Engineering, Vol. 189, Issue 2, 2000, pp. 559–573.

[34]   Yang, X. Y., Xei, Y. M., Steven, G. P., and Querin O. M. Bidirectional evolutionary method for stiffness optimization, AIAA Journal, 37(11), 1999, 1999, 1483–1488. doi: 10.2514/2.626.

[35]   Rozvany, G.I.N. A critical review of established methods of structural topology optimization, Structural and Multidisciplinary Optimization, 37, 2008, 217–237. doi: 10.1007/s00158-007-0217-0.

[36]   Wang, M.Y., Wang, X., and Guo, D. A level set method for structural topology optimization, Computer Methods in Applied Mechanics and Engineering, 192, 2003, 227–246.

[37]   Allaire, G., Jouve, F., and Toader, A.-M. A level-set method for shape optimization, 2002, Comptes Rendus Mathematique, 334(12), 2002, 1125–1130.

[38]   Allaire, G., Jouve, F., and Toader, A.-M. Structural optimization using sensitivity analysis and a level-set method, Journal of Computational Physics, 194, 2004, 363–393.

[39]   Blank, L., Garcke, H., Sarbu, L., Srisupattarawanit, T., Styles V., and Voigt, A. Phase-field approaches to structural topology optimization, Constrained Optimization and Optimal Control

for Partial Differential Equations, Leugering, G., Engell, S., Griewank, A., Rannacher, R., Schulz, V., Ulbrich, M. and Ulbrich, S., Eds., Birkhäuser, Basel, Switzerland. 2012, 245–256.

[40] Burger, M., Hackl, B., and Ring, W. Incorporating topological derivatives into level set methods, Journal of Computational Physics, 194, 2004, 344–362.

[41] He, L., Kao, C.-Y., and Osher, S. Incorporating topological derivatives into shape derivatives based level set methods, Journal of Computational Physics, 225, 2007, 891–909. doi: 10.1016/j.jcp.2007.01.003.

[42] Dunning, P.D., and Kim, H.A. A new hole insertion method for level set based structural topology optimization, Numerical Methods in Engineering, 93, 2012, 118–134. doi.org/ 10.1002/nme.4384.

[43] James, K., and Martins J.R.R.A. An isoparametric approach to level set topology optimization using a body-fitted finite-element mesh, Computers & Structures, Vols, 90–91, 2012, 97–106.

[44] Chen, L.Q. Phase-field models for microstructure evolution, Annual Review of Materials Research, 32, 2002, 113–140.

[45] McFadden, G.B. Phase-field models of solidification, Contemporary Mathematics, 306, 2002, 107–146.

[46] Takezawa, A., Nishiwaki, S., and Kitamura, M. Shape and topology optimization based on the phase field method and sensitivity analysis, Journal of Computational Physics, 229, 2010, 2697–2718.

[47] Blaise B., and Antonin, C. Design-dependent loads in topology optimization, ESAIM: Control, Optimisation and Calculus of Variations, 9, 2003, 19–48.

[48] Bourdin, B., and Chambolle, A. Design-dependent loads in topology optimization, ESAIM: Control, Optimisation and Calculus of Variations, 9, 2003, 19-48.

[49] Kobayashi, M. H. On a biologically inspired topology optimization method, Communications in Nonlinear Science and Numerical Simulation, 15, 2010, 787–802.

[50] Nakamura, A., Lindenmayer, A., and Aizawa, K. Some systems for map generation, The Book of L., Springer, Berlin, Heidelberg, 1986, 323–332. doi.org/10.1007/978-3-642-95486-3_26.

[51] Kolonay, R.M., and Kobayashi, M.H. Optimization of aircraft lifting surfaces using a cellular division method, Journal of Aircraft, 52(2), 2015, 2051–2063.

[52] Krog, L., Tucker, A., and Rollema, G., Application of topology, sizing and shape optimisation methods to optimal design of aircraft components, Proc. of the 3rd Altair UK HyperWorks users Conference, Airbus UK Ltd., Copyright Altair Engineering, Inc., 2002.

[53] Maute, K., and Allen, M. Conceptual design of aeroelastic structures by topology optimization, Structural and Multidisciplinary Optimization, 27(1–2), 2004, 27–42. doi.org/ 10.1007/s00158-003-0362-z.

[54] Dunning, P.D., Stanford, B.K., and Kim, A.K., Level-set topology optimization with aeroelastic constraints. 56th AIAA/ASCE/AHS/ASC Structures, Structural Dynamics, and Materials Conference, AIAA SciTech Forum, AIAA 2015-1128, 2015, doi.org/10.2514/ 6.2015-1128.

[55] Dunning, P.D., Stanford, B.K., and Kim, A.K., Aerostructural level set topology optimization for a common research model wing, 10th AIAA Multidisciplinary Design Optimization Conference, AIAA SciTech Forum, AIAA 2014–0634, 2014, doi.org/10.2514/ 6.2014-0634.

[56] Gomes, A.A., and Suleman, A. Topology optimization of a reinforced wing box for enhanced roll maneuvers, AIAA Journal, 46(3), 2008, 548–556.

[57] Kolonay, M.R., and Kobayashi, M.H. Optimization of aircraft lifting surfaces using a cellular division method, Journal of Aircraft, 52(6), 2015, 2051–2063. doi.org/10.2514/1. C033138.

[58] Stanford, B., Beran, P., and Kobayashy, M.H. Aeroelastic optimization of flapping wing venation: A cellular division approach, AIAA Journal, 50(4), 2012, 938–951. doi.org/10.2514/1. J051443.

[59] Faskhutdinov, R.N., Dubrovskaya, A.S., Dongauzer, K.A., Maksimov, P.V., and Trufanov. N.A., Topology optimization of a gas-turbine engine part, IOP Conference Series: Materials Science and Engineering, Vol. 177, 2017, 012077, doi:10.1088/1757-899X/177/1/012077.

Appendix A: Response surface methodology

K. Kalinin

Riga Technical University, Latvia

RSM can be summarized as a collection of statistical tools and techniques for constructing and exploring an approximate functional relationship between a response variable and a set of design variables [1]. RSM has been widely used to simulate and analyze complex engineering problems in different industrial applications (see [2, 3]). The strategy used in RSM is to utilize approximation models, which are often referred to as metamodels or surrogate models, as they provide a model of the model, replacing the expensive simulation analyses during the process. This approximate functional relationship is typically constructed in the form of a low-order polynomial, referred to as a response surface (RS) approximation. RSM was originally developed for constructing and exploring approximate response functions based on physical experiments and results in smooth approximate response functions, thus effectively filtering out any noise.

RSM includes methods for selecting data points where the experiments should be evaluated, a process known as statistical design of experiments (DoE) (as in [4, 5]); methods for solving the unknown coefficients of an RS approximation; and methods for evaluating the accuracy of the resulting RS approximation. The unknown coefficients of an RS approximation are estimated from experimental data points by means of a process known as regression. These coefficients are estimated in such a way as to minimize the sum of the squares of the error terms, the so-called least squares criterion (e.g. [1, 6–8] with more than 300-year long history).

An alternative to least squares is maximum likelihood estimation method requiring an assumption about the probability distribution of the disturbance term. It is commonly assumed that the disturbances are identically and independently distributed normal variables with zero mean and constant variance.

An important research issue related to metamodeling is how to achieve good accuracy in a metamodel with a reasonable number of sample points and the distribution of the sample points in the domain of interest. This sampling technique is

often referred to as a design of computer experiments (DoCE), and is implemented into numerical analysis in order to reduce the number of simulation runs without decreasing the accuracy of the metamodel.

The stages of metamodeling (see Fig. A1) can be considered as follows [9–11]:

– Development and experimental verification of a representative finite element model
– Formulation of the domain of interest and selection of variables to be used in approximation of sampled data responses
– Elaboration of space-filled experiment designs to determine sample points for which deterministic computer simulation is performed
– Building the approximating function (parametric or nonparametric approximations) employing the data set of deterministic computer experiment (or alternatively employing a combined data set of numerical and physical experimental data)
– Screening, parametric sensitivity analysis and validation of metamodel
– Design optimization and derivation of design guidelines

It should be noted that all of these metamodeling stages can easily be extended by additive user-defined functions or methods, though the so-called curse of dimensionality is the limiting factor for application of the methodology to engineering processes and problems.

A1 Design of experiments and design of computer experiments

An experiment can be defined as a test or series of tests on a process or system that is performed in order to study the relationship between the input variables and the output responses of the process. In any experiment, the results and conclusions that can be drawn depend to a large extent on the manner in which the data are collected [12]. In this context, the objectives of any experiment may be outlined as follows:

– determining which of the input variables, x, is most influential on the response, y;
– determining where to set the influential x's so that y is almost always near the desired nominal value;
– determining where to set the influential x's so that variability in y is small.

In attempting to fulfill these objectives, engineers and scientists frequently use a best-guess approach; however, this is limited by the technical or theoretical knowledge of the experimenter. The one-factor-at-a-time approach is an alternative approach that is also extensively used in practice, though this is limited to problem
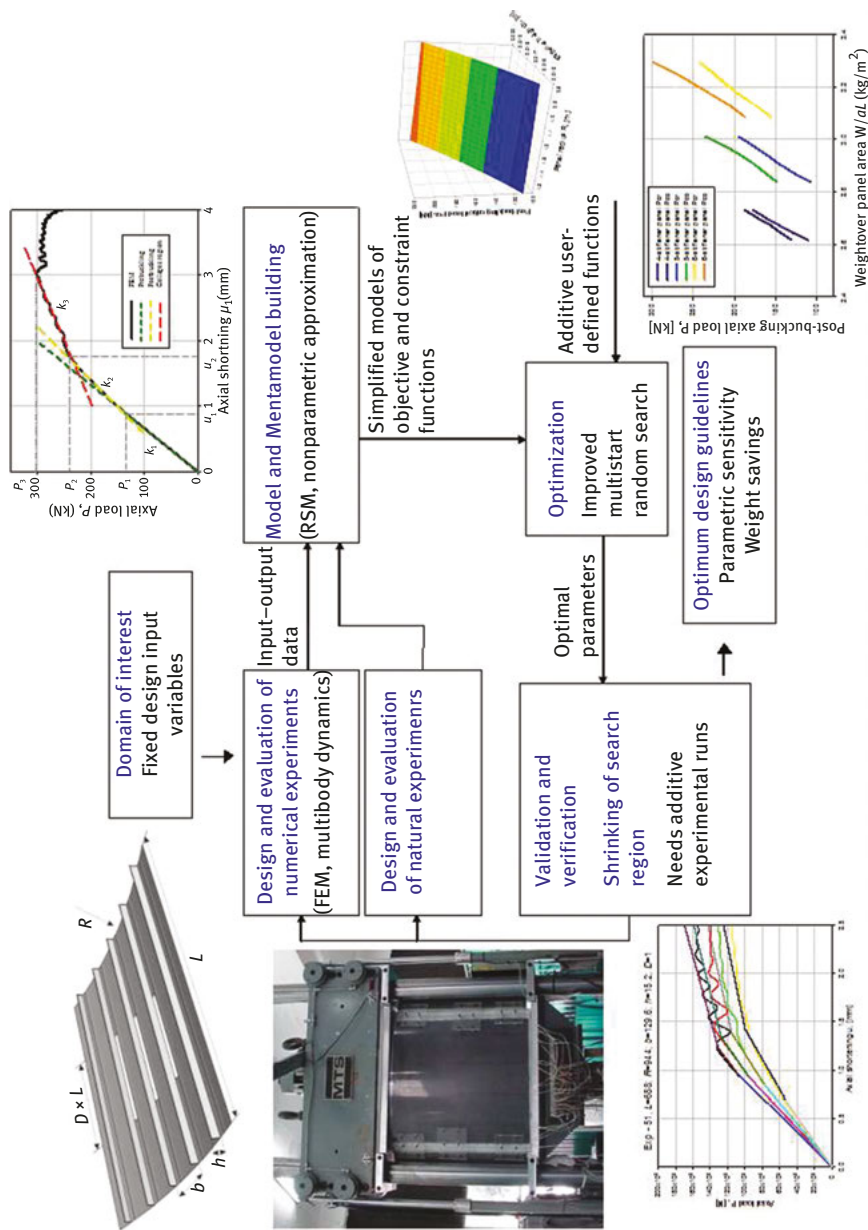
Fig. A1: Response surface flowchart example, to be used for optimization of a stiffened shell design.

dimensions and fails to consider any possible interaction between input factors. So, there is an obvious need for an experimentation strategy, or an approach for DoE.

There is also an important distinction between physical experiments and computer experiments, so that separate experimentation strategies have been developed for DoCE. While physical experiments have statistical experimental error, numerical analysis is deterministic and results are obtained with 100% repetition and no statistical variance of model parameters (see [13, 14]), though there is numerical noise due to calculation or discretization errors (see, e.g., [15]). Many researchers (see [16–18]) argue that classical experimental designs are not well suited for sampling deterministic computer experiments, and Sacks et al. [17] state that the "classical notions of experimental blocking, replication and randomisation are irrelevant" when it comes to deterministic computer experiments that have no random error. This means that designs for deterministic computer experiments should "fill the space" of experiment design as opposed to possessing properties for estimating the variability in the data. Currently there is a wide range of literature concerning different methods for DoCE (as in [4, 5]), which include many approaches for space-filling designs. It should be noted that the first space-filling design criterion [13, 19] for numerical experiments was proposed at Riga Technical University.

In this section the key concepts of DoE and DoCE are summarized, which includes the classical DoE and Latin hypercube (LH) design. This is followed by discussion on the techniques of space-filling and sequential design, which were developed for DoCE with LH designs.

A1.1 Classical design of experiments

Classical experimental designs are so named because they have been developed for what are considered to be the more "classical" applications of RS metamodeling: physical experiments, which are plagued by variability and random error (see [6–8, 20, 21]. Among these designs, the full-factorial, central composite and Box–Behnken designs (BBD) are well known and are easily generated, and a more detailed description of these types of designs can be found in literature [21, 22].

In box-like design spaces, the range of a design variable between the upper and lower limit is typically divided into levels, and experiments are run only at the particular levels of the design variables. A full-factorial design contains all the combination of the different levels of all the design variables that are also commonly called factors. It is easy to understand that even with a modest number of factors, the full-factorial design approach becomes unreasonable in solving practical problems, as the number of experimental runs becomes very large and can be an order of magnitude greater than the number of parameters to be estimated. The number of experiments required by a factorial design is $l^{n_{dv}}$, where n_{dv} is the

number of design variables and l is the number of levels per design variable. There are several special cases of the factorial design that are important to discuss because they are widely used and because they form the basis of other designs of considerable practical value. The most important of these is perhaps the $2^{n_{dv}}$ factorial design. Figure A2 shows a two-level factorial design for three design variables that is a 2^3 factorial design. Note that in the figure the location of experiments is denoted by black dots.

This design is particularly useful in the early stages of experimental work when only the different impact of the design variables on the results is of interest.
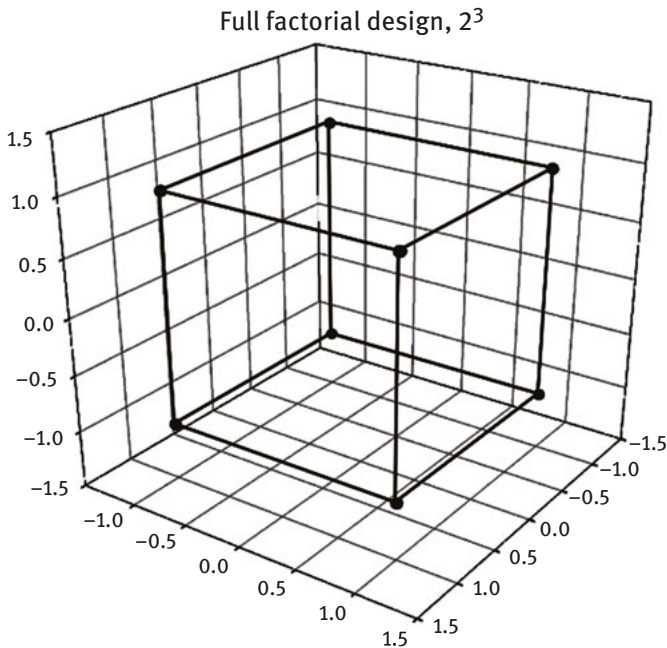
Fig. A2: Full-factorial design, $2^n = 2^{3.}$

Because there are only two levels per design variable, only a linear RS or at most the mixed terms of a quadratic RS approximation (first-order interactions) can be obtained from the $2^{n_{dv}}$ factorial design. The limitation of linear approximation inhibits the use of $2^{n_{dv}}$ factorial designs for many problems. When the true function that is being approximated by the RS approximation is expected to have considerable curvature, designers often apply $3^{n_{dv}}$ factorial design. The $3^{n_{dv}}$ factorial designs allow an estimation of all the terms of a quadratic RS approximation. Also, RS approximations obtained from $3^{n_{dv}}$ factorial designs are generally accurate because

they avoid extrapolation. An example of a $3^{n_{dv}}$ factorial design for a three-variable case with a total of 27 experiments is shown in Fig. A3.

Factorial design, 3^3
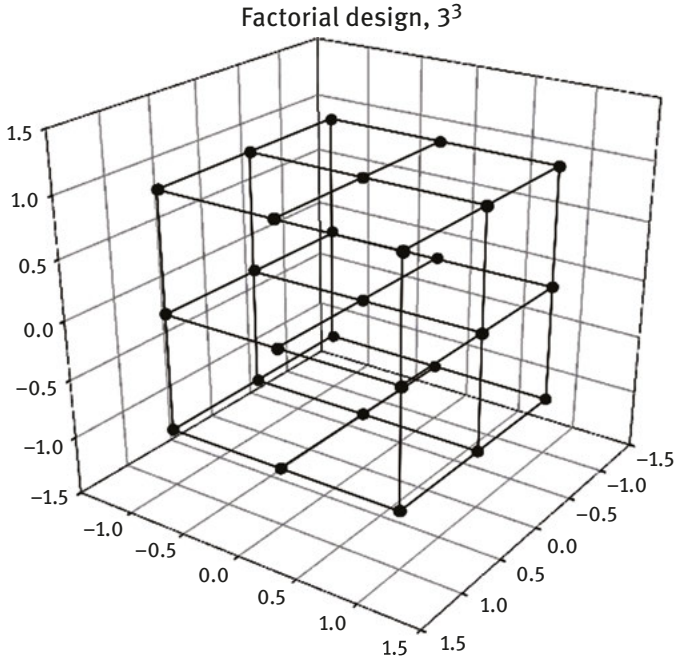
Fig. A3: Full-factorial design, $3^n = 3^3$.

A central composite design (CCD) is a combination of $2k$ factorial points, $2k$ star points and a center point for k factors as shown in Fig. A4. CCDs are the most widely used experimental design for fitting second-order RSs [1]. Different CCDs are defined by varying the distance from the center of the design space to the star points, and include:

- ordinary central composite design – star points are placed at a distance of $\pm a$ ($a > 1$) from the center with the cube points placed at ±1 from the center;
- face-centered central composite design – star points are positioned on the faces of the cube;
- inscribed central composite design – star points are positioned $\frac{1}{a}$ from the center with the cube points placed at ±1.

It should be noted that experiments in center point are replicated at least three to five times in order to estimate the variance of output y.

Central composite design
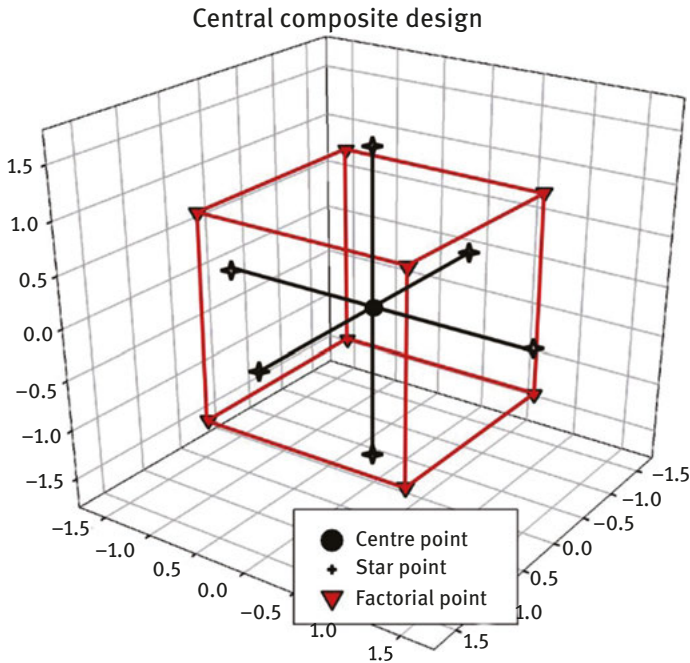
Fig. A4: Central composite design.

A BBD is formed by combining $2k$ factorial and incomplete block designs and is an important alternative to CCDs because they require only three levels of each factor [8]. The BBD are found by perturbing combinations of two variables in turn, and adding to this n_c replicates of the nominal design. When the experiments are numerical in nature, instead of repeating the nominal design experiment slight perturbations are needed. The two variables vary from their nominal value to a low and high level, respectively, in all four possible ways. As there are different ways to select two variables out of n_{dv}, a particular BBD consists of totally $2n_{dv}(n_{dv} - 1) + n_c + 1$ points. This arrangement of the BBDs allows the number of design points to increase at the same rate as the number of polynomial coefficients. For a large number of variables, the amount of points asymptotically approaches four times the number of terms required for a quadratic polynomial fit. As an example, a seven-variable BBD with no center-point replication holds 85 designs, nearly half of the 143 runs required by the CCD and only a fraction of the 2,187 needed for a full $3^{n_{dv}}$-level factorial design. The inevitable drawback of a BBD is that corner regions of the domain are poorly represented; therefore, corner approximations are based on extrapolation rather that interpolation. As a result, Myers et al. [1] warn that these designs should not be used when accurate predictions at the extremes (i.e., the
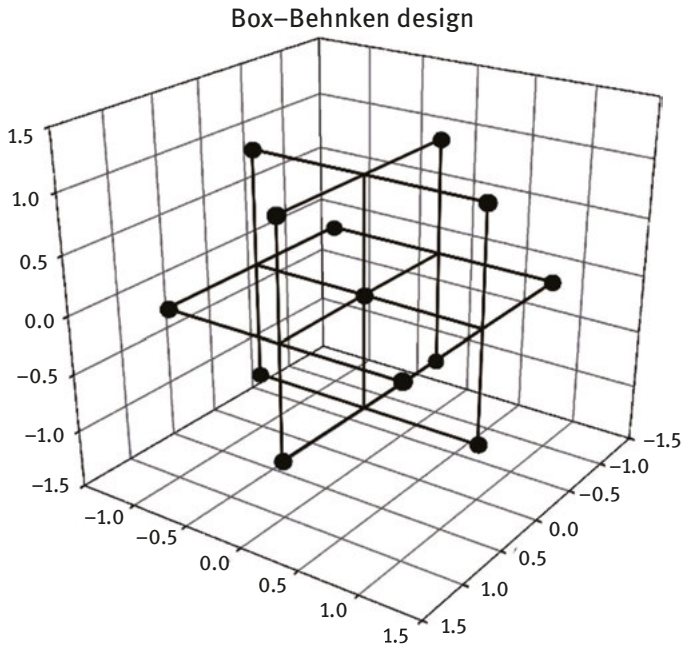
Fig. A5: Box–Behnken design.

corners) are important. An example for 13-point BBD for three factors is shown in Fig. A5.

A1.2 Latin hypercube designs

LH design was first proposed by Audze and Eglājs [13] and later McKay et al. [23] formulated the term Latin hypercube. In the context of statistical sampling, a square grid containing sample positions is a Latin square only if there is only one sample in each row and each column. An LH is the generalization of this concept to an arbitrary number of dimensions, whereby each sample is the only one in each axis-aligned hyperplane containing it (see Fig. A6). When sampling a function of m variables, the range of each variable is divided into n equally probable intervals,
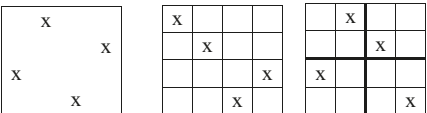
Fig. A6: A comparison between random sampling, LH sampling and orthogonal LH sampling.

where n-sample points are then placed to satisfy the LH requirements. Note that this forces the number of divisions, n, to be equal for each variable. Also note that this sampling scheme does not require more samples for more dimensions, and this independence is one of the main advantages of LH sampling.

Another advantage of LH designs is that random samples can be taken one at a time, with regard to the samples that have already been taken. Orthogonal sampling adds the requirement that the entire sample space must be sampled evenly. Although more efficient, orthogonal sampling strategy is more difficult to implement since all random samples must be generated simultaneously. A 2D comparison in Fig. A6 demonstrates the difference between random sampling, LH sampling and orthogonal LH sampling, and is explained as follows:

a) In random sampling new sample points are generated without taking into account the previously generated sample points. Thus, one does not necessarily need to know beforehand how many sample points are needed.
b) In LH sampling one must first decide how many sample points to use and for each sample point remember in which row and column the sample point was taken.
c) In orthogonal LH sampling, the sample space is divided into equally probable subspaces, where Fig. A6 shows four subspaces. All sample points are then chosen simultaneously making sure that the total ensemble of sample points is an LH sample and that each subspace is sampled with the same density.

In other words, LH sampling ensures that the ensemble of random numbers is a good representative of the real variability, whereas traditional random sampling is just an ensemble of random numbers without any guarantees. However, there is a general belief that the distribution of points in the design space should be regulated by a certain criterion, detailed in the following section, and therefore the distribution will be regular and experiments can be used not only for parametric approximations but also for nonparametric approximations.

A1.3 Space-filling criteria

Numerous space-filling experimental designs have been developed in an effort to provide more efficient and effective means for sampling deterministic computer experiments based on LH, as discussed previously. Different space-filling criteria for LH designs were proposed by many authors: maximin LH [24], minimal integrated MSE (IMSE) designs [17], orthogonal array-based LH designs [25], orthogonal LH [26], IMSE and optimal LH [27].

Historically, the first space-filling experimental design criterion for numerical experiments was proposed by Riga Technical University researcher Vilnis Eglājs and published in 1977 [13], which is referred to as Eglajs or Audze–Eglais uniformity criterion [28]. For the analysis of deterministic computer experiments, Eglājs

proposed the principle that the number of levels for each factor is equal to the number of runs and each level is used only once. In the situation when the response depends mainly on one factor (the number of which is unknown before experimentation) this principle provides the maximum amount of information about this dependency. Later McKay et al. [23] introduced the name "Latin Hypercube" for DoEs of this type and showed that random LHs give better accuracy for the Monte Carlo integration than pseudorandom samples. The second principle proposed in Audze and Eglājs [13, 19] was that the experiments must fill the area of interest as uniformly as possible. For the measure of the uniformity, Audze and Eglājs [13] introduced the first space-filling criterion – the potential energy criterion

$$\Phi_{\text{Eglājs}} = \sum_{i=1}^{m} \sum_{j=i+1}^{m} \frac{1}{d_{ij}^2} \tag{A-1}$$

where m is the number of experimental points (runs) and d_{ij} is the Euclidean distance between points i and j. The LH designs with minimal value of the criterion (A-1) have good space-filling properties; however, the experimental points tend to spread out to the corners of the unit cube. Audze and Eglājs [13] also proposed the first coordinate exchange algorithm for construction of LHs with minimal value of the potential energy criterion. Morris and Mitchell [29] introduced a generalization of Eglājs criterion:

$$\Phi_{\text{Morris – Mitchell}} = \left[\sum_{i=1}^{n-1} \sum_{j=i+1}^{n} \frac{1}{d_{ij}^p} \right]^{1/p} \tag{A-2}$$

where

$$d(x_i, x_j) = d_{ij} = \left[\sum_{k=1}^{m} \left| x_{ik} - x_{jk} \right|^t \right]^{1/t}, \ t = 1 \text{ or } 2 \tag{A-3}$$

The other category of space-filling designs are constructed by algorithmic approaches under certain optimality criteria, such as minimax and maximin designs [30]. The initial results on minimax and maximin distance designs were developed by Johnson et al. [24], and as they are based on the same principle, they are referred to as the MinDist criterion.

The MinDist criterion [24] seeks to maximize the minimum distance between any pair of points in the design:

$$\Phi_{\text{MinDist}} = \min_{u, v = 1, \dots, n} \sum_{i=1}^{m} \left(x_{ui} - x_{vi} \right)^2 \tag{A-4}$$

The entropy criterion was first proposed by Shewry and Wynn [31] and then used by Currin et al. [32]. The application of the entropy criterion for designs in unit cube $[0, 1]^m$ is equivalent to the minimization of $E = - \log|C|$, where C is the $n \times n$ covariance matrix of the design with elements:

$$\Phi_{\text{Entropy}} = \exp\left\{ -\Theta \sum_{u=1}^{m} \left| x_{iu} - x_{ju} \right|^{q} \right\}, \ 0 < q \leq 2 \tag{A-5}$$

Where $i, j = 1, \ldots, n$. The mostly used value of the parameter q is 2 [33], so the correlation between two points is a function of their Euclidean distance L_2, and Θ is set equal to 2.

Another measure used in constructing designs is the discrepancy $(D_c)^2$ [34−−37]. The discrepancy measures how much the empirical distribution of the design points departs from the uniform distribution; in other words, the criterion averages the squared difference in the cumulative density function [38], and so minimum discrepancy designs are often called uniform designs. The discrepancy has been used to construct space-filling designs in computer experiments [28], and to construct designs for evaluating multiple integrals. Fang and Wang [34] gave the details of uniform designs and described several examples of discrepancy measurement. Uniform designs are a class of designs based on statistical applications of a number of theoretical methods [34]:

$$\Phi_{(D_C)^2} = \left(\frac{13}{12}\right)^m - \frac{2}{n} \sum_{u=1}^{n} \prod_{i=1}^{m} \left[1 + \frac{1}{2} \left| x_{ui} - 0.5 \right| - \frac{1}{2} \left| x_{ui} - 0.5 \right|^2 \right] +$$
$$+ \frac{1}{n^2} \sum_{u=1}^{n} \sum_{v=1}^{n} \prod_{i=1}^{m} \left[1 + \frac{1}{2} \left(\left| x_{ui} - 0.5 \right| + \left| x_{vi} - 0.5 \right| - \left| x_{ui} - x_{vi} \right| \right) \right] \tag{A-6}$$

The MSE criterion, as suggested by Fang and Wang [34] and Auzins [34], would give the root mean squared distance between the mesh points in design space R^m and the nearest point from experimental design D:

$$\Phi_{\text{MSE}} = \sqrt{ \left(\frac{1}{N}\right) \sum_{v=1}^{N} \min_{u=1,\ldots,n} \left[\sum_{i=1}^{m} \left(w_{vi} - x_{ui} \right)^2 \right] } \tag{A-7}$$

Where w_v are points from a large sample in design space R^m, $v = 1, \ldots, m$, m is the number of points of the experimental design and n is the number of mesh points. Designs optimized according to the MSE criterion give points uniformly distributed in the design space and tend to minimize the expected MSE of the nonparametric approximations [14, 34, 39]). According to any criterion, to search for the optimal LH DoE is a very difficult task, though this can be achieved with methods of discrete optimization − coordinate exchange, multistart, threshold or simulated annealing methods ([1, 33, 37, 40]). Comparisons of the different types of space-filling experimental designs are few, and often the novel space-filling design being described is compared against LH designs and random sampling [27], though rarely are space-filling designs compared with each other. Simpson [14, 18] gives a comparison of wide variety of space-filling designs against themselves and classical experimental designs. In a paper by Auzins [33] a comparison was given of many metamodeling test problems where experimental designs are sampled according to an optimality

criterion and space-filling criteria such as MSE, Eglājs criterion, entropy criterion and discrepancy criterion. It is the decision of the author to state that in the case of second-order local polynomial approximation the use of the MSE criterion would be preferable, as it gives good accuracy of metamodels and the finding of optimal designs using the proposed algorithm is less difficult than optimization according to other criteria.

Further comparison of the various approaches is given below, where Fig. A7 shows several 3D 20-factor plans of experiments with different space-filling criteria, and Table A1 presents a comparison of different space-filling criteria and designs.

A1.4 Sequential design

Sequential designs can be obtained in a traditional way by adding new experimental points to the existing design created with space-filling criteria. These designs are called "adaptive," when the information about responses in previously created experimental points is used. Such designs are commonly needed when the initial amount of the sampling points is insufficient in order to derive a required level of approximation error. To obtain a sequential design from a fixed-size design space, Auzins et al. [33, 41–43], used the point arranging method. According to this method, first, an optimal LH design with large number of runs must be built. Then the point that gives the minimal worsening of optimality criterion by its elimination is moved out from the n-run design to build an n–1-run design. In this work and in [37], also the cross-validation approach was used where a point with the largest prediction error is selected as the new sample point. An accurate and efficient assessment of the prediction error must be made in light of the fact that in usual engineering optimization tasks several responses must be simultaneously approximated. A validation test was performed by Janushevskis et al. [39] and Auzins et al. [41–43], where the point in which the largest prediction error occurs for some test functions (six-hump camel, Branin) was directly added, and the authors found that maximal prediction error measures decreased when using fixed-size experimental designs or sequential designs without adaptation.

Sequential design of sample point addition is required in order to manage the fact that at the start of an experiment the optimal number of runs for metamodel building is unknown, but adding additional runs to an existing data set damages the uniformity of LHs. The classical hierarchical quasirandom sequences, which allow adding new sample points (experimental runs, trials), like Halton [44] and Sobol [45] sequences, give highly correlated components for four, five or more dimensions. Good results are given by adaptive experimental designs, in which the approximation or optimization information obtained from previous experimental runs is used for the choice of additional runs. However, this approach loses effectiveness in the practical engineering case when several responses must be simultaneously observed and used in optimization for quality criterion and constraint functions. In this work a recently
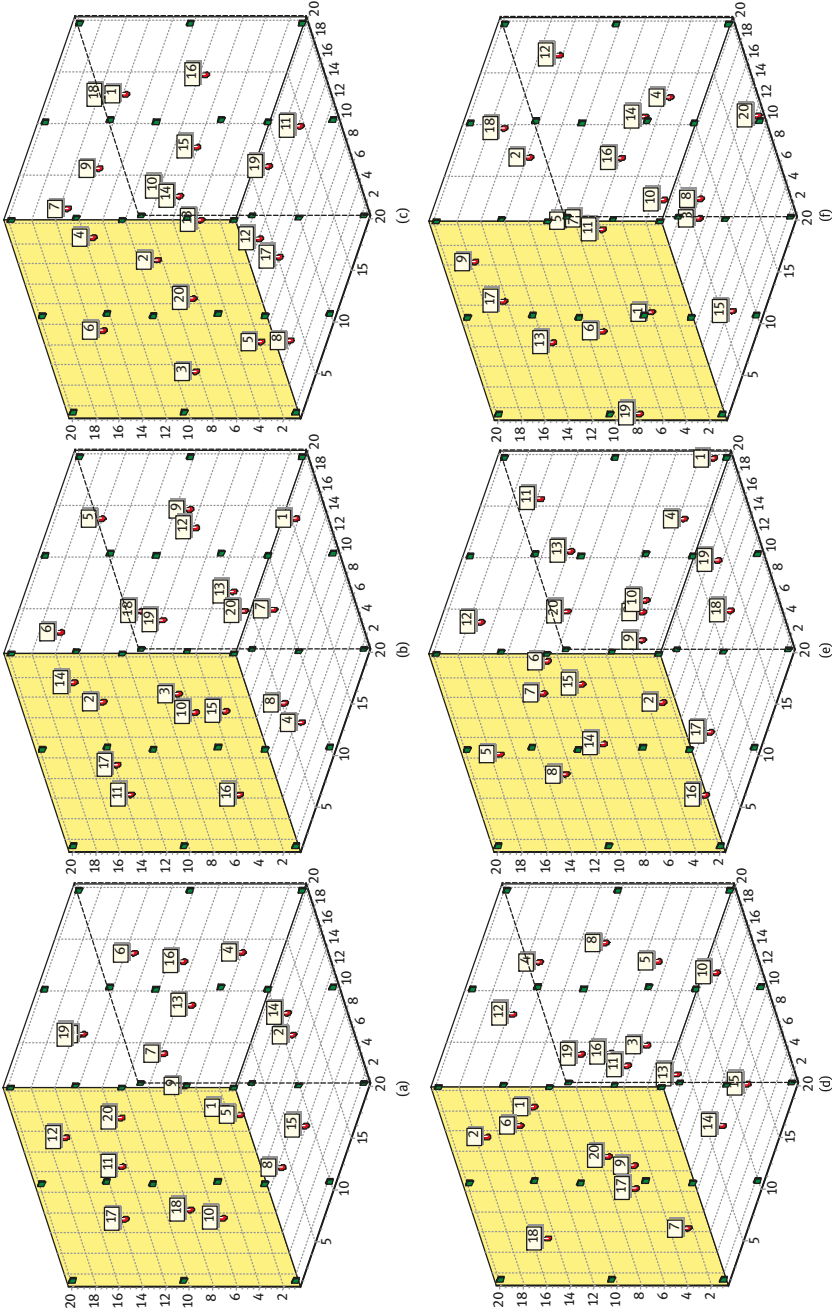
Fig. A7: Three-dimensional 20-variable designs of experiments using space-filling criteria: Eglājs (a), Morris–Mitchell (b), MinDist (c), entropy (d), discrepancy (e) and MSE (f).

Table A1: Comparison of different space-filling criterions and design.

	Eglājs	Morris–Mitchell	MinDist	Entropy	Discrepancy	MSE
Eglājs Φ_{Eglajs}	10.906*	11.043	11.083	11.004	11.236	11.202
MinDist $\Phi_{MinDist}$	0.394	0.372	0.424*	0.337	0.302	0.307
MinDist between points	5–7	12–19	10–15	13–15	1–16	4–16
Entropy $\Phi_{Entropy}$	11.606	11.350	11.538	10.983*	12.486	11.799
Discrepancy $\Phi_{(D_c)^2}$	0.00342	0.00363	0.00424	0.00366	0.00301*	0.00453
MSE Φ_{MSE}	0.4135	0.4154	0.4113	0.4133	0.4293	0.4084*
D^2	194,194	555,769	344,326	830,173	579,277	375,989
D^3	0	8.28	0.01	134.19	0.02	0.06

developed approach for the creation of hierarchical degrees of freedom (DoEs) and the modification of a local polynomial approximation method is applied for the first time to engineering applications, and this approach has been shown to give almost the same or better accuracy of prediction than metamodels built with adaptive sampling methods and other nonparametric approximations.

The sequential design approach applied in this work is based on a compromise between space uniformity and subspace uniformity, including the uniformity of 1D projections, being used to build a combined criterion for any known criterion as the weighted sum of criteria for entire space and subspaces. For example, when we are interested in the uniformity of space filling of the entire space of all 1D projections and all 2D subspaces, we can build the combined criterion

$$\Phi_{comb} = \Phi + \frac{a}{m}\sum_{k=1}^{m}\Phi_k + \frac{2b}{m(m-1)}\sum_{k=1}^{m-1}\sum_{j=k+1}^{m}\Phi_{kj} \tag{A-8}$$

where Φ_k, Φ_{kj} are filling quality criterions for 1D and 2D subspaces, and a, b are weighting coefficients for 1D and 2D uniformity, respectively. For example, using criteria (A-7) and (A-8), we can build the complex criterion

$$\Phi_{complex} = \left[\sum_{i=1}^{N-1}\sum_{j=i+1}^{N}\left[\frac{1}{\sum_{k=1}^{m}|x_{ik}-x_{jk}|}\right]^p + \frac{a}{m}\sum_{i=1}^{N-1}\sum_{j=i+1}^{N}\sum_{k=1}^{m}\left[\frac{1}{|x_{ik}-x_{jk}|}\right]^p \right.$$
$$\left. + \frac{2b}{m(m-1)}\sum_{i=1}^{N-1}\sum_{j=i+1}^{N}\sum_{k=1}^{m-1}\sum_{l=k+1}^{m}\left[\frac{1}{|x_{ik}-x_{jk}|+|x_{il}-x_{jl}|}\right]^p\right]^{1/-p} \tag{A-9}$$

In order to apply this equation, the weighting coefficients need to be determined. Using large values of weighting coefficients a, we can obtain LHs with a nearly uniform distribution. The analysis of the problem can be facilitated by an approximate expression, which describes the dependency of the optimal criteria (A-7) and (A-8) values on the number of runs N and the number of factors m. Figure A8 shows this dependence graphically for $p = 50$, $t = 1$, $20 \leq N \leq 200$ and $1 \leq m \leq 6$.
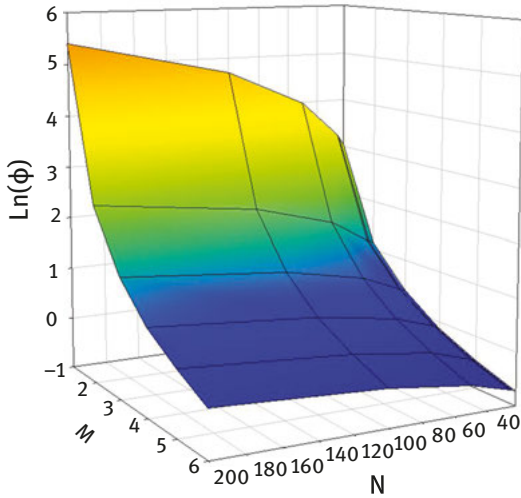
Fig. A8: Optimal values of criterion presented in eqs. (A-7) and (A-8).

Good approximation for the dependency of the optimal criterion values on the number of runs N and number of factors (variables) m gives the expression

$$\Phi_p^{Optimal} = \left(1 + \sqrt{(m-1)(0.04778 + 0.000422N)}\right)(Nm)^{1/p}\left(N^{1/m} - 1\right) \tag{A-10}$$

This equation can be used for the control of the choice of the weighting coefficients a, b in the complex criterion (A-9).

The nonadaptive sequential design was implemented into the program code Relax [33]. Figure A9 gives an example of the use of this code for the optimization of a 2-factor 41-run design, obtained by adding one point at a time according to criterion (A-5), beginning from a 13-run optimal LH design. As further example of the use of the program in three dimensions, Fig. A10 shows the sequential design for a 3-factor 125-run experiment.
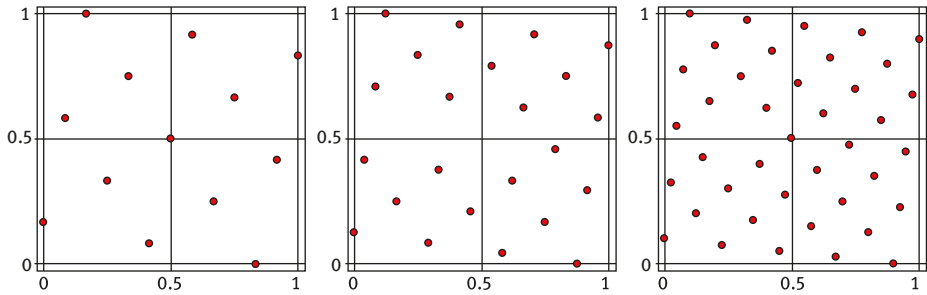
Fig. A9: Fixed-size Latin hypercubes optimized according to eqs. (A-9) and (A-10), $p = 50$.

A1.5 Fitting an approximation to given data

In this section, methods for determining an accurate RS for a given experimental data set are discussed. It is assumed that a relationship describing the performance measure of a phenomenon that it is under investigation exists, and that this relationship is a function of the design variables. It is important to note that this relationship does not have to be known explicitly or even be possible to be known exactly. The response that is to be approximated is denoted as y or $\hat{F}(x)$, and in principle can represent any measurable quantity such as stresses, critical force, deflection and structural eigenfrequencies.

In statistics, regression analysis is used to model relationships between random variables, determine the magnitude of the relationships between variables and can be used to make predictions based on the approximated models. Least square regression is one of the simplest, which is the most applicable and widely used methodologies for derivation of functional dependencies.

A1.5.1 Polynomial approximations

Low-order polynomial approximations are the most widely used and are described in every statistics book, and implemented in every statistics program. First-, second- and third-order polynomials can be expressed as follows:

$$\hat{F}(x) = b_0 + \sum_{i=1}^{m} b_i x_i \tag{A-11}$$

$$\hat{F}(x) = b_0 + \sum_{i=1}^{m} b_i x_i + \sum_{i=1}^{m} \sum_{j=i}^{m} b_{ij} x_i x_j \tag{A-12}$$

$$\hat{F}(x) = b_0 + \sum_{i=1}^{m} b_i x_i + \sum_{i=1}^{m} \sum_{j=i}^{m} b_{ij} x_i x_j + \sum_{i=1}^{m} \sum_{j=i}^{m} \sum_{k=j}^{m} b_{ijk} x_i x_j x_k \tag{A-13}$$
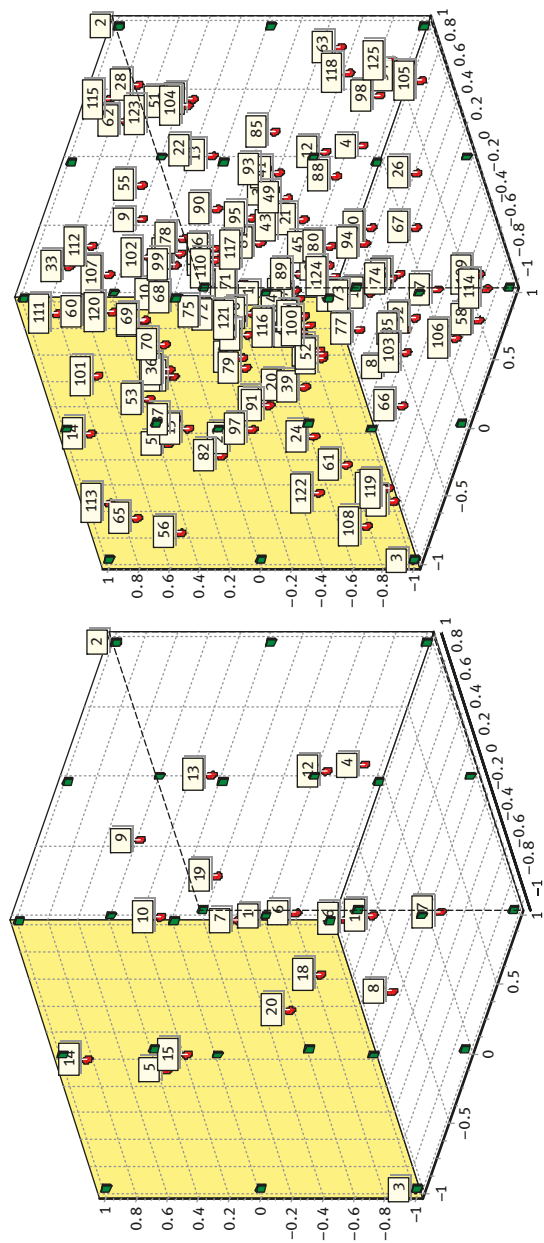
Fig. A10: Comparison of three-dimensional sequential design of 20 (left figure) and 125 factors (right figure).

where m is total amount of variables; b_0 b_i b_{ij} b_{ijk} are the unknown coefficients of the regression functions.

As stated by Myers and Montgomery [46], there is a considerable practical experience indicating that second-order models work well in solving real RS problems. In general, it is thought that third- and higher order polynomials can over-fit data, consequently avoiding construction of global behavior of the parameters. On the contrary, first-order polynomials are too simple and give prediction errors too high for use in science and engineering. In this chapter, a linear model will be used in order to derive parametric sensitivities and weight-saving parametric analysis, and third-order approximations will be compared with second-order and nonparametric approximations for RSs.

A1.5.2 Partial polynomial approximations

In general, design variables in engineering problems are not equally distributed. For example, in the analysis of simple beam bending, beam length, height and thickness have different effects on the response. Moreover, commonly response parameters are affected by only some of the input variables, and the irrelevant parameters become approximation noise that decreases prediction accuracy. In light of this, it seems reasonable to use partial polynomials instead of full-order polynomial approximations. In such an assumption, polynomial parameters are used adequately with relevance to the input variables [47, 48]. However, one of the drawbacks for partial polynomials is the difficulty in selecting the essential parameters for an approximation function in the case of using nonorthogonal terms.

By generalizing the idea of polynomials, the nonlinear regression function is the linear combination of any kind of function. Such a model is written as follows:

$$\hat{F}(x) = b_0 F_0(x_1, x_2, \ldots, x_D) + b_1 F_1(x_1, x_2, \ldots, x_D) + \cdots + b_{m-1} F_{m-1}(x_1, x_2, \ldots, x_D)$$

(A-14)

where $F = \{F_i\}$ is a set of linearly independent functions consisting exclusively of m functions.

An exhaustive search of the space is impractical, as there exist 2^M possible subsets of functions. The problem of function selection is to take a set of candidate functions and select a subset with the best performance. Eglājs [19] proposed the algorithm of selection of the terms for nonpolynomial regression function. In this work also the "correlation" approach for the optimal choice of the number of terms was proposed. This approach needs no additional experimental runs for the estimation of best choice of regression function but may give wrong results in some cases.

The selection procedure can provide better regression accuracy due to finite sample size effects – irrelevant functions may negatively affect the accuracy of regression [49–51]. In addition, reducing the number of functions may help decrease the cost of acquiring data and might make the regression models easier to understand.

One strategy is to normalize variables in scaled $[-1, 1]^m$ space and eliminate the regression parameters that have the least importance, therefore, decreasing the approximation prediction error. This approach is the most simple and practical; however, variations of different parametrical interdependencies cannot be realized.

A more efficient approach conducts the search by considering local changes to the current set of attributes, selecting one and then iterating. For instance, the hill climbing approach considers both adding and removing functions at each decision point, which lets one retract an earlier decision without keeping explicit track of the search path. Within these options, one can consider all states generated by the operators and then select the best, or one can simply choose the first state that improves accuracy over the current set. A convenient paradigm for viewing the function selection approach is that of heuristic search, with each state in the search space specifying a subset of the possible functions. Two of the most promising sequential search algorithms are those proposed by Russel and Norvig [52], namely, the sequential forward floating selection (SFFS) algorithm and the sequential backward floating selection (SBFS) algorithm. They improve the standard SFS (Sequential Floating Selection) and SBS (Sequential Backward Selection) techniques by dynamically changing the number of features included (SFFS) or removed (SBFS) at each step and by allowing the reconsideration of the features included or removed at the previous steps.

Another effective algorithm is random mutation hill climbing (RMHC) [53]. RMHC is a stochastic meta-algorithm. It simply runs an outer loop over hill climbing that stochastically iterates in any direction as long as it is possible to increase the value of the criterion function. Each step of the outer loop chooses a random initial condition x_0 to start hill climbing. The best x_m is kept: if a new run of hill climbing produces a better x_m than the stored state, it replaces the stored state.

A1.5.3 Nonparametric approximations

Nonparametric approximations such as multivariate adaptive regression splines (MARS), radial basis functions (RBF) and krigings are recognized as the most precise for different orders of nonlinearity and problem scale response approximations, though by definition nonparametric approximations do not generate any tangible function. In design optimization, all nonparametric approximations are supreme over polynomial functions, though on the other hand implementation of response functions in different tools requires more advanced skills in statistics. Comparative studies of metamodeling techniques under multiple modeling criteria were performed by Jin et al. [37] providing insightful observations into performance of various metamodeling techniques under different testing problems. The comparative study presented three common advantages for polynomial regression models and MARS: they both have a good transparency, which means it is easy to obtain the contributions of each input factor and the interaction among them; both

methods take the least amount of time for model building and; both methods are resistant to numerical noise from the input data.

A methodology comparable to MARS is that of locally weighted polynomial regression (LOESS). In LOESS, originally proposed by Cleveland [53] and further developed by Cleveland and Devlin [54] and Cleveland and Grosse [55], at each point in the data set a low-degree polynomial is fit to a subset of the data, with explanatory variable values near the point whose response is being estimated. The polynomial is fit using weighted least squares, giving more weight to points near the point whose response is being estimated and less weight to points further away. The value of the regression function for the point is then obtained by evaluating the local polynomial using the explanatory variable values for that data point. The LOESS fit is complete after regression function values have been computed for each of the N data points. Many of the details of this method, such as the degree of the polynomial model and the weights, are flexible. The range of choices for each part of the method and typical default values are briefly discussed in the following paragraph. LOESS is an efficient method that makes use of small data sets to share the ability to provide different types of easily interpretable statistical intervals for estimation, prediction, calibration and optimization.

To predict the value of the response function at point x, we use a second-order locally weighted polynomial approximation:

$$\hat{F}(x) = \beta_0 + \sum_{j=1}^{m} \beta_j x_j + \sum_{i=1}^{m} \sum_{k=j}^{m} \beta_{jk} x_j x_k \tag{A-15}$$

Unlike global (parametric) approximation the coefficients β depend on x and are calculated by minimizing the weighted least squares

$$\beta = \arg \min_{\beta} \sum_{j \in N_x} w(x - x^j) \times (F^j - \beta_0 - \sum_{i=1}^{m} \beta_i x_{ji} - \sum_{i=1}^{m} \sum_{k=1}^{m} \beta_{ik} x_i^j x_k^j)^2 \tag{A-16}$$

Where $\beta_0, \beta_i, \beta_{ik}$ are coefficients of the local quadratic approximation, N_x is the set of the nearest neighbors of the point x. Here we use a constant number of neighbors – bandwidth N_t. The weight function w depends on the Euclidean distance (in scaled $[-1, 1]^m$ space) between the points of interest x and the points of observation x^j. Let u be

$$u = (x, x^j) = \left\| \frac{x - x^j}{x - x^q} \right\| \tag{A-17}$$

where x^q is the furthest point in the neighborhood of point x. An often-used weight function is the tricube function $(1 - u^3)^3$ [34, 40]; however, investigations in this work showed that a more accurate local approximation model can be obtained using a weight function of $(1 - u)^4$. Also in this work the Gaussian weight function

$$w(x, x^j) = \exp\left(-\alpha u^2\right) \tag{A-18}$$

is used to achieve a very accurate and smooth fit. In general, the Gaussian weight function with constant value $\alpha = 1/2$ is used in local approximations varying only the optimum bandwidth value. In this work, the Gaussian weight function was used with a particular weight function of fixed bandwidth value $N_t = N$, controlling the selection of the optimal fitting coefficient α. If the coefficient value is set to zero, then the global instead of the local parametric approximation is evaluated.

A main advantage of weighted least squares in comparison with other methods is the ability to handle regression situations in which the data points are of varying quality [56]. If the standard deviation of the random errors in the data is not constant across all levels of the explanatory variables, using weighted least squares with weights that are inversely proportional to the variance at each level of the explanatory variables yields the most precise parameter estimates possible. However, the biggest and largely unknown disadvantage of weighted least squares is the fact that when the weights are estimated from small numbers of replicated observations, the results of an analysis can be very badly and unpredictably affected. This is especially likely to be the case when the weights for extreme values of the predictor or explanatory variables are estimated using only a few observations. Therefore, it is recommended to remain aware of this potential problem, and to only use weighted least squares when the weights can be estimated precisely relative to one another [57, 58].

A1.6 Evaluation of metamodel prediction accuracy

The accuracy of an RS approximation is expressed in terms of various error terms and statistical parameters that are representative of the predictive capabilities of the approximation [1]. Traditionally, the statistical DoE is performed using a minimum-variance criterion that assumes all errors to be random errors of variance, as shown in Table A2.

When finite element codes are used, the random errors associated with uncertainties of testing and measuring can be disregarded; therefore, for evaluation of approximation prediction accuracy different error estimation criteria should be used. A bootstrap or jackknife [59] error estimation methodology is one of the most promising methods; however, for effective application of these error estimation methodologies the amount of testing samples is not reasonable in engineering problems. The most effective approach for prediction accuracy can be a leave-one-out cross-validation error approach [52], in which each single experiment in turn removed from the data set, and the result for this removed experiment is estimated using the approximation built from the remaining data. Using this approach, the choice between polynomial approximations of full, partial and locally weighted

Table A2: Error measures for accuracy assessment.

Name	Equation	
Max. absolute error	$\max \left| F_i - \hat{F}_i \right|$	(A-19)
Average absolute error	$\dfrac{1}{n} \sum_{i=1}^{n} \left| F_i - \hat{F}_i \right|$	(A-20)
Mean square error	$\dfrac{1}{n} \sum_{i=1}^{n} \left(F_i - \hat{F}_i \right)^2$	(A-21)
Root mean square error	$\sqrt{\dfrac{\sum_{i=1}^{n} \left(F_i - \hat{F}_i \right)^2}{n}} = \sqrt{\mathrm{MSE}}$	(A-22)
Relative root mean square error	$100\% \sqrt{\dfrac{\mathrm{MSE}}{\mathrm{Variance}}} = 100\% \sqrt{\dfrac{\frac{1}{n} \sum_{i=1}^{n} \left(F_i - \hat{F}_i \right)^2}{\frac{1}{n} \sum_{i=1}^{n} \left(F_i - \bar{F} \right)^2}}$	(A-23)

different order polynomial functions can be evaluated. The standard deviation of approximation can be written in the form

$$\sigma = \sqrt{\frac{\sum_{i=1}^{N} \left(F(x^i) - \hat{F}(x^i) \right)^2}{N}} \tag{A-24}$$

The relative (percentage) standard deviation is calculated as

$$\sigma_\% = 100\% \frac{\sigma}{\sqrt{\dfrac{\sum_{i=1}^{N} \left(F(x^i) - \bar{F} \right)^2}{N}}} = 100\% \frac{\sigma}{\mathrm{STD}} \tag{A-25}$$

where $\bar{F}$ is the mean of observed response values and STD stands for standard deviation from the mean value of experimental responses. This measure shows the degree to which the standard deviation of approximation is smaller in comparison with the approximation using a constant value.

The leave-one-out cross-validation error is calculated as

$$\sigma_{\mathrm{cr}} = \sqrt{\frac{\sum_{i=1}^{N} \left(\hat{F}_{-i} - F_i \right)^2}{N}} \tag{A-26}$$

where $\hat{F}_{-i}$ denotes the prediction of the response of x^i using the metamodel created with $N-1$ sample points and point i removed ($i = 1,2,\ldots,N$).

Similarly, the cross-validation leave-one-out percentage error [33, 39] is calculated as

$$\sigma_{\mathrm{cr/STD\%}} = 100\% \cdot \frac{\sigma_{\mathrm{cr}}}{\mathrm{STD}} \tag{A-27}$$

or alternatively the standard deviation mean value can be used

$$\sigma_{\mathrm{cr/MEAN\%}} = 100\% \cdot \sqrt{\left(\frac{(1/n)\sum_{i=1}^{n} \left(\hat{F}_{-i} - F_i \right)^2}{(1/n)\sum_{i=1}^{n} F_i} \right)} \tag{A-28}$$

Usually leave-one-out cross-validation error gives an overvaluation of the prediction error, though it has the singular benefit of being able to estimate the prediction error without additional experimental runs. Various statistical tools are available in order to evaluate the predictive capabilities of an RS approximation from the data used to generate them (MiniTab, Design Expert and Modefrontier). In this dissertation the calculation of cross-validation percentage error was performed using EDAOpt, a program developed at Riga Technical University, Machine and Mechanism Dynamics Research Laboratory [39, 41–43], and FUNSEL [50, 60].

A1.7 Sensitivity analysis of metamodels

Sensitivity analysis methods can be classified in a variety of ways. In a report by Frey and Patil [61], they are classified as (1) mathematical, (2) statistical and (3) graphical. In this classification, the focus is on sensitivity analysis techniques applied in addition to the fundamental modeling technique. For example an analyst may be required to perform a deterministic analysis, in which case a mathematical method, such as nominal range sensitivity, can be employed to evaluate sensitivity. Alternatively, an analyst may perform a probabilistic analysis, using either frequentist or Bayesian frameworks, in which case statistical-based sensitivity analysis methods can be used [62, 6, 63–65].

Mathematical methods assess the sensitivity of a model output to the range of variation of an input. These methods typically involve calculating the output for a few values of an input that represent the possible input range [66]. These methods do not address the variance in the output due to the variance in the inputs, but they can assess the impact of range of variation in the input values on the output [67]. In some cases, mathematical methods can be helpful in screening the most important inputs [68], which can also be used for verification and validation [69] and to identify inputs that require further data acquisition or research [70].

Statistical methods involve running simulations in which inputs are assigned probability distributions and assessing the effect of input variance on the output distribution [71, 72]. Depending on the method, one or more inputs are varied at a time. Statistical methods allow one to identify the effect of interactions among multiple inputs. The range and relative likelihood of inputs can be propagated using a variety of techniques such as Monte Carlo simulation, LH sampling and other methods. The sensitivity of the model results to individual inputs or groups of inputs can

be evaluated by a variety of techniques, with Cullen and Frey [62], Fontaine and Jacomino [73] and Andersson et al. [71], all giving examples of the application of statistical methods. The statistical methods evaluated include regression analysis, analysis of variance, RS methods, Fourier amplitude sensitivity test and mutual information index.

Graphical methods give a representation of sensitivity in the form of graphs, charts or surfaces. Generally, graphical methods are used to give visual indication of how an output is affected by variation in inputs [74]. Graphical methods can be used as a screening method before further analysis of a model or to represent complex dependencies between inputs and outputs [75]. Graphical methods can be used to complement the results of mathematical and statistical methods for better representation [76, 77].

A1.8 Metamodels in optimization

RS approximations are often used to replace constraints or objective functions in optimization problems. Optimization problems, however, have the general tendency of exploiting weaknesses in the formulation of RS. In terms of RS approximation, the optimizer tends to drive the optimum design toward regions where the approximations are inaccurate. Due to the similarities between detailed numerical simulations and physical experiments, there has recently been growing interest in using RS approximations within structural optimization. When using polynomial RS approximations, in addition to providing the designer with an overall perspective of the response, spurious local minima resulting from human and numerical errors are eliminated by using the least squares method to formulate smooth low-order polynomials.

In recent years, many researchers have exploited the advantages of using conventional (second-order polynomial) RS approximations that are more global in nature to integrate numerical analyses in an optimization environment. For example, in a monograph by Schmidt and Launsby [3] a manufacturing process of forging hammer and molding casting was optimized using a response approach. Similarly, using GAs a design and optimization procedure of laminated composite materials was compiled by Gürdal et al. [78]. Additionally, Thacker and Wu [79] used RS approximations to reduce the computational cost associated with reliability-based optimization problems using probabilistic methods, while Harrison et al. [80] and Sellar and Batill [81] reduced the cost of designing a stiffened composite panel using a GA. RBF formulated by GA in combination with neural network approximations was used in post-buckling optimization of composite stiffened panels by Bisagni and Lanzi [82]. Giunta et al. [15], Kaufman et al. [83] and Venter and Haftka [84] showed that RS approximations are valuable in solving optimization problems with nonsmooth functional behavior, as numerical noise is filtered out from the resulting approximate response function. Additionally, Mistree et al. [85] made extensive use of the global perspective of the

response over the design space provided by global RS approximations, while Barthelemy and Haftka [86] used RS approximations to meet the organizational challenge posed by multidisciplinary optimization problems. More specifically, Ragon et al. [87] used RS approximations as a simple yet flexible interface between the global and local design codes in the design of a large airplane wing structure. Rodríguez et al. [88] applied the approach to multidisciplinary design optimization, constructing local RS approximations in a sequential manner based on design points evaluated at the discipline level of the current design cycle. With few exceptions [89], almost all the standard applications of RS approximations in structural optimization employ quadratic approximations, which still do not provide fully global approximations. For further details, Haftka and Gürdal [90] gave a wide overview of engineering problems optimized using RS methodology, and also provided some of the benchmark cases frequently validated in structural design optimization.

References

[1]   Meyer R.H., and Nachtsheim C.J. The coordinate-exchange algorithm for constructing exact optimal experimental designs, Technometrics, 37, 1995, 60–69.

[2]   Evans, M. Optimisation of manufacturing processes: A response surface approach, Maney Publishing, 2003, 320p.

[3]   Schmidt, S.R., and Launsby, R.G. Understanding industrial design experiments, Air Academy Press, 4th, 1994, 768p.

[4]   Wu C.F., Hamada M. Experiments – planning, analysis, and parameter design optimization, John Wiley & Sons, Inc., 2000, 624p.

[5]   Santner, T.J., Williams, B.J., and Notz, W.I. The design and analysis of computer experiments, Springer Verlag, New York, 2003, 203p.

[6]   Box, G.E.P., and Tiao, G.C., Bayesian inference in statistical analysis, John Wiley and Sons Inc., New York, 1992, 608p.

[7]   Box, G.E.P., and Draper, N.R. On minimum-point second-order designs, Technometrics, 16, 1974, 613–616.

[8]   Box, G.E.P., and Benhken, D.W. Some new three level designs for the study of quantitative variables, Technometrics, 2, 1960, 455–476.

[9]   Rikards, R., Abramovich, H., Auzins, J., Korjakins, A., Ozolinsh, O., Kalnins, K., and Green, T. Surrogate models for optimum design of stiffened composite shells, Composite Structures, Elsevier, 63, 2004, 243–251.

[10] Rikards, R., Kalnins, K., and Ozolinsh O., Delamination and skin-stringer separation analysis in composite stiffened shells, Topping, B.H.V. and Mota Soares, C.A. (editors), Computational Structures Technology, Proc. of 7th Int. Conf., Lisbon, 7–9 September 2004, Stirling, Civil-Comp Press: 47, 2004.

[11] Rikards, R., Auzins, J., and Kalnins, K. Surrogate modeling in design optimization of stiffened composite shells, Neittaanmäki, P., Rossi, T., Majava, K. and Pironneau, O, editors, Proc. European Congress on Computational Methods in Applied Sciences and Engineering, ECCOMAS-04, Jyväskylä, 24–28 July, 2004, CD-ed, 14, pages, 2004.

[12] Montgomery, D.C. Design and analysis of experiments, Wiley and Sons Ltd., New York, 1997, 478p.

[13] Audze, P., and Eglājs, V. New approach for planning out of experiments, Problems of Dynamics and Strength, Vol. 35, 1977, pp.104–107, Zinatne, Riga (in Russian).

[14] Simpson, T.W. A concept exploration method for product family design, Ph.D. thesis, Georgia Institute of Technology, Georgia, USA, 1998.

[15] Giunta, A.A., Balabanov, V., Haim, D., Grossman, B., Mason, W.H., Watson, L.T., and Haftka, R. T. Wing design for a high-speed civil transport using a design of experiments methodology, Proc. of the 6th AIAA/NASA/ISSMO Symposium on Multidisciplinary Analysis and Optimization, 4–6 September, 1996, Bellevue, Washington, Paper No.96–4001, Part 1: 168–183.

[16] Sacks, J., Schiller, S.B., and Welch W.J. Designs for computer experiments, Technometrics, 34, 1989, 15–25.

[17] Sacks, J., Welch, W.J., Mitchell, T.J., and Wynn, H.P. Design and analysis of computer experiments, Statistical Science, 4(4), 1989, 409–435.

[18] Simpson, T.W., Peplinski, J., Koch, P.N., and Allen, J.K. On the use of Statistics in design and the implications for deterministic computer experiments, Design Theory and Methodology – DTM'97, ASME Paper, No.DETC97/DTM-3881, Sacramento, CA, 1997. Eglājs, 1981

[19] Eglājs, V. Approximation of data by multi-dimensional equation of regression, Problems of Dynamics and Strength, Vol. 39, Zinatne, Riga (in Russian), 1981, 120–125.

[20] Draper, N.R., and Lin, D.K.J. Small response-surface designs, Technometrics, 32, 1990, 187–194.

[21] Myers, R.H., Montgomery, D.C., and Anderson-Cook, C.M. Response surface methodology : Process, and product optimization using designed experiments, 4th, Wiley, 2016, 856p.

[22] Vitali, R., Haftka, R.T., and Sankar, B.V. Correction response surface design of stiffened composite panel with a crack, AIAA/ASME/ASCE/ AHS/ASC Structures, Structural Dynamics and Material Conference Paper AIAA No.99–1313, Proceedings, St Louis, Missouri, 1999.

[23] McKay, M.D., Beckman, R.J., and Conover, W.J. A comparison of three methods for selecting values of input variables in the analysis of output from a computer code, Technometrics, 21, 1979, 239–245.

[24] Johnson, M.E., Moore, L.M., Ylvisaker, D. Minimax and maximin distance designs, Journal of Statistical Planning and Inference, 26, 1990, 131–148.

[25] Tang, B. Orthogonal array-based Latin hypercubes, Journal of the American Statistical Association, 88, 1993, 1392–1397.

[26] Ye, K.Q. Column orthogonal Latin hypercubes and their application in computer experiments, Journal of American Statistical Association, 93, 1998, 1430–1439.

[27] Park, J.S. Optimal Latin-hypercube designs for computer experiments, Journal of Statistical Planning and Inference, 39(1), 1994, 95–111.

[28] Bates, S.J., Sienz, J., and Langley, D.S. Formulation of the Audze–Eglais uniform Latin hypercube design of experiments, Journal of Advances in Engineering Software, 34(8), 2003, 493–506.

[29] Morris. M.D., and Mitchell, T.J. Exploratory designs for computational experiments, Journal of Statistical Planning and Inference, 43(3), 1995, 381–402.

[30] Hardin, R.H., and Sloane, N.J.A. A new approach to the construction of optimal designs, Journal of Statistical Planning and Inference, 37, 1993, 339–369.

[31] Shewry, M., and Wynn, H.P. Maximum entropy sampling, Journal of Applied Statistics, 14, 1987, 165–170.

[32] Currin, C., Mitchell, T.J., Morris, M., and Ylvisaker, D. Bayesian prediction of deterministic functions with applications to the design and analysis of computer experiments, Journal of American Statistics Association, 86, 1991, 953–963.

[33] Auzins, J. Direct optimization of experimental designs, 10th AIAA/ISSMO Multidisciplinary Analysis and Optimization Conference, AIAA paper, No.2004–4578, Albany, NY, 28 Aug.-2 Sep. 2004.

[34] Fang, K.T., and Wang, Y. Number-theoretic methods in statistics, Chapman & Hall, London, 1994, 344p.

[35] Fang, K., Ma, X., and Winker P. Centered L2-discrepancy of random sampling and Latin hypercube design and construction of uniform designs, Mathematics of Computation, 71, 2002, 275–296.

[36] Fang, K., Lu, X., and Winker, P. Lower bounds for centered and wrap-around L2-discrepancies and construction of uniform design by threshold accepting, Journal of Complexity, 19, 2003, 692–711.

[37] Jin, R., Chen, W., and Simpson T. Comparative studies of metamodeling techniques under multiple modelling criteria, 8th AIAA/NASA/USAF/ISSMO Symposium on Multidisciplinary Analysis and Optimization, Long Beach, CA, USA, AIAA Paper AIAA-2000–4801, 2000.

[38] Hickernell, F.J. A generalized discrepancy and quadrature error bound, Mathematics of Computation, 67, 1998, 299–322.

[39] Janushevskis, A., Akinfiev, T., Auzins, J., and Boyko, A. "A comparative analysis of global search procedures", Proceedings of the Estonian Academy of Sciences, 10(4), 2004, 236–250.

[40] Ma, C.X., and Fang, K.T. A new approach to construction of nearly uniform designs, International Journal of Materials and Product Technology, 20, 2004, 115–126.

[41] Auzins, J., Janushevskis, A., and Rikards R. Software tools for experimental design, metamodeling and optimization, Book of Abstracts, Aifantis, E.C. (Ed.), 5th Euromech Solid Mechanics Conf. ESMC, 5 August, 2003, Giapoulis, Thessaloniki, Greece, Vol. 182, 2003.

[42] Auzins, J., Kalnins, K., and Rikards, R. Sequential design of experiments for metamodeling and optimization, Proc. of 6th World Congress of Structural and Multidisciplinary Optimization, 30 May – 03 June 2005, Rio de Janeiro, Brazil, 2005.

[43] Auzins, J., Janushevskis, J., Kalnins, K., and Rikards R. Sequential metamodeling techniques for structural optimization, Proc. of Intern. Conf. TCN CAE –05, 5–8 October 2005, Lecce, Italy, CD-ed.: 20 pages, 2005 b.

[44] Halton, J.H. On the efficiency of certain quasi-random sequences of points in evaluating multi-dimensional integrals, Numerische Mathematik, 2, 1960, 84–90.

[45] Sobol, I.M. The distribution of points in a cube and approximate evaluation of integrals, Zhurnal Vychislitel'noi Matematiki i Matematicheskoi Fiziki, 7, 1967, 784–802.
in Russian.

[46] Myers, R.H., and Montgomery, D.C. Response surface methodology: Process and product optimization using designed experiments, John Wiley and Sons, New York, 1995, 690p.

[47] Antony J. Design of experiments for engineers and scientists, Butterworth-Heinemann, 2003, 190p.

[48] Minitab – User Manual Version 8.30, http://www.mscsoftware.com, 2006.

[49] Vapnik, N.V. Statistical learning theory, John Wiley, 1998, 768p.

[50] Jekabsons, G. Heuristic approach for nonlinear multiple regression analysis, Master thesis, RTU, Riga, Latvia, 2005.

[51] Russell, S.J., and Norvig, P. Artificial intelligence: A modern approach, 3rd, Prentice-Hall, Upper Saddle River, New Jersey, 1995, 1132p.

[52] Kohavi, R. A study of cross-validation and bootstrap for accuracy estimation and model selection, in Mellish, C.S. (editor), Proceedings of IJCAI-95, Montreal, Canada, 1995, pp.1137–1143, Los Altos, CA: Morgan Kaufmann.

[53] Cleveland, W.S. Robust locally weighted regression and smoothing scatterplots, Journal of the American Statistical Association, 74, 1979, 829–836.

[54] Cleveland, W.S., and Devlin, S.J. Locally weighted regression: An approach to regression analysis by local fitting, Journal of the American Statistical Association, 83, 1988, 596–610.

[55] Cleveland, W.S., and Grosse E. Computational methods for local regression, Statistics and Computing, 1, 1991, 47–62.

[56] Croarkin, C. NIST/SEMATECH, e-Handbook of Statistical Methods, http://www.itl.nist.gov/handbook/, 2006.

[57] Carroll, R.J., and Ruppert, D. Transformation and weighting in regression, Chapman and Hall, New York, 1988, 264p.

[58] Ryan, T.P. Modern regression methods, Wiley, New York, 1997, 515p.

[59] Shao, J., and Tu, D. The Jackknife and bootstrap, Springer Series in Statistics, 1995, 446p.

[60] Jēkabsons, G., and Lavendels, J. Labākā aproksimanta izvēle iespējamo variantu kopā, Computer Science, Vol. 5/18, Scientific Proceedings of Riga Technical University, Riga, 2004, 24–31.

[61] Frey, H.C., and Patil, S. Identification and review of sensitivity analysis methods, Proc. of NCSU/USDA Workshop on Sensitivity Analysis Method, 2001.

[62] Cullen, A.C., and Frey, H.C. Probabilistic techniques in exposure assessment, Plenum Press, New York, 1999, 336p.

[63] Saltelli, A. Tarantola, S., and Chan, K. A quantitative, model independent method for global sensitivity analysis of model output, Technometrics, 41(1), 1999, 39–56.

[64] Saltelli, A. Chan, K., and Scott, E.M. Sensitivity analysis, John Wiley and Sons, Ltd., West Sussex, England, 2009, 494p.

[65] Weiss, R. An approach to Bayesian sensitivity analysis, Journal of the Royal Statistical Society Series B-Methodological, 58(4), 1996, 739–750.

[66] Salehi, F., Prasher, S.O., Amin, S., Madani, A., Jebelli, S.J., Ramaswamy, H.S., and Drury, C. T. Prediction of annual Nitrate-N losses in drain outflows with artificial neural networks, Transactions of the ASAE, 43(5), 2000, 1137–1143.

[67] Morgan, M.G., and Henrion, M. Uncertainty: A guide to dealing with uncertainty in quantitative risk and policy analysis, Cambridge University Press, Cambridge, NY, 1990, 332p.

[68] Brun, R., Reichert, P., and Kunsch, H.R. Practical identifiability analysis of large environmental simulation models, Water Resources Research, 37(4), 2001, 1015–1030.

[69] Wotawa, G., Stohl, A., and Kromp, K.H. Estimating the uncertainty of a Lagrangian photochemical air quality simulation model caused by inexact meteorological input data, Reliability Engineering & System Safety, 57(1), 1997, 31–40.

[70] Ariens, G.A., van Mechelen, W., Bongers, P.M., Bouter L.M., and van der Wal, G. Physical risk factors for neck pain, Scandinavian Journal of Work Environment & Health, 26(1), 2000, 7–19.

[71] Andersson, F.O., Aberg, M., and Jacobsson, S.P. Algorithmic approaches for studies of variable influence, contribution and selection in neural networks, Chemometrics and Intelligent Laboratory Systems, 51(1), 2000, 61–72.

[72] Neter, J., Kutner, M.H., Nachtsheim, C.J., and Wasserman, W. Applied linear statistical models, 4th, WCB McGraw-Hill, Chicago, IL, 1996, 1408p.

[73] Fontaine, T.A., and Jacomino, V.M.F. Sensitivity analysis of simulated contaminated sediment transport, Journal of the American Water Resources Association, 33(2), 1997, 313–326.

[74] Geldermann, J. and Rentz, O. Integrated technique assessment with imprecise information as a support for the identification of best available techniques (BAT), OR Spektrum, 23(1), 2001, 137–157.

[75] McCamley, F., and Rudel, R.K. Graphical sensitivity analysis for generalized stochastic dominance, Journal of Agricultural and Resource Economics, 20(2), 1995, 403–403.

[76] Stiber, N.A., Pantazidou, M., and Small, M.J. Expert system methodology for evaluating reductive dechlorination at TCE sites, Environmental Science and Technology, 33(17), 1999, 3012–3020.

[77] Critchfield, G.C., and Willard, K.E. Probabilistic analysis of decision trees using Mote Carlo simulation, Medical Decision Making, 6(1), 1986, 85–92.

[78] Gürdal, Z., Haftka, R., and Hajela, P. Design and optimization: Laminated composite materials, Wiley and Sons Ltd., New York, 1999, 352p.

[79] Thacker, B.H., and Wu, Y.T. A new response surface approach for structural reliability analysis, Proc. of the 33rd AIAA/ASME/ASCE/AHS/ASC Structures, Structural Dynamics and Materials Conference, 13–15 April, 1992, Dallas, Texas, Paper No.92–2408, Part 2: 586–593.

[80] Harrison, P.N., Le Riche, R., and Haftka, R.T. Design of stiffened composite panels by genetic algorithm and response surface approximations, Proc. of the 36th AIAA/ASME/ASCE/AHS/ASC Structures, Structural Dynamics, and Materials Conference, 10–13 April 1995, New Orleans, Louisiana, Paper No.95–1163, Part 1: 58–65.

[81] Sellar, R.S.,and Batill, S.M. Concurrent subspace optimization using gradient-enhanced neural network approximations, Proc. of the 6th AIAA/NASA/ISSMO Symposium on Multidisciplinary Analysis and Optimization, 4–6 September 1996, Bellevue, Washington, Paper No.96–4019, Part 1: 319–330.

[82] Bisangi, C., and Lanzi, L. Post-buckling optimization of composite stiffened panels using neural networks, Composites Structures, 58, 2002, 237–247.

[83] Kaufman, M., Balabanov, V., Burgee, S.L., Giunta, A.A., Grossman, B., Mason, W.H., Watson, L.T., and Haftka, R.T. Variable-complexity response surface approximations for wing structural weight in HSCT design, Journal of Computational Mechanics, 18(2), 1996, 112–126.

[84] Venter, G., and Haftka, R.T. Minimum-bias based experimental design for constructing response surfaces in structural optimization, Proc. of the 38th AIAA/ASME/ASCE/AHS/ASC Structures, Structural Dynamics, and Materials Conference, 7–10 April 1997, Kissimmee, Florida, Paper No.97–1053, Part 2: 1225–1238.

[85] Mistree, F., Patel, B., and Vadde, S. On modeling objectives and multilevel decisions in concurrent design, Advances in Design Automation, Gilmore, B.J., Hoeltzel, D., Dutta, D. and Eschenauer, H. Eds., ASME, New York, 1994, 151–161. ASME DE-Vol. 69–2.

[86] Barthelemy, J.F.M., and Haftka, R.T. Approximation concepts for optimum structural design-A review, Structural Optimization, 5(3), 1993, 129–144.

[87] Ragon, S., Gürdal, Z., Haftka, R.T., and Tzong, T.J. Global/local structural wing design using response surface techniques, Proc. of the 38th AIAA/ASME/ASCE/AHS/ASC Structures, Structural Dynamics, and Materials Conference, 7–10 April 1997, Kissimmee, Florida, Paper No.97–1051, Part 2: 1204–1214.

[88] Rodríguez, J.F., Renaud, J.E., and Watson, L.T. Trust region augmented Lagrangian methods for sequential response surface approximation and optimization, Proc. of the 1997 ASME Design Engineering Technical Conferences, 14–17 September 1997, Sacramento, California, Paper No.DETC97DAC3773.

[89] Houten, M.H., Schoofs, A.J.G., and van Campen, D.H. Response surface techniques in structural optimization, 1st World Congress of Structural and Multidisciplinary Optimization, 28 May- 2 June 1995, Gosler, Germany, pp. 89–94.

[90] Haftka, R., and Gürdal, Z. Elements of structural optimization, 3rd, Kluwer Academic Publishers, 1992, 468p.

10 Structural health monitoring (SHM)

10.1 Introduction

Structural health monitoring (SHM) is an emerging technique developed from nondestructive testing (NDT),[1] which combines advanced sensing technology with intelligent algorithms to interrogate the structural "health" condition of a given structure. Unlike conventional maintenance procedures based on NDTs, the SHM system, also known as health and usage monitoring system, makes the embedded/bonded sensors an integral part of the structure and operates with a minimal manual intervention. The potential benefits of using an SHM system might include improved reliability and safety and reduced operating costs [1]. Furthermore, when used to monitor new manufacturing processes, SHM-based procedures might also improve the design and ensure the quality of the products [2]. The field of SHM is considered to emerge from another relatively new field of smart structures, and includes various disciplines such as materials, fatigue, NDT, sensors, signal processing, communication systems and decision-making processes. It is an interdisciplinary field, with a very active research community (a dedicated journal on this field being well evaluated by the scientists[2]), with industrial deployments being demonstrated as very effective.

A typical SHM system consists of three key subsystems: diagnosis, damage prognosis (DP) and predictive maintenance (PM) (see Fig. 10.1). Diagnosis deals with the sensing mechanism, which usually relies on active or passive in situ sensors. The sensors can be either wired or wireless, covering a large area of inspection on the monitored structure. Usually the measurements are recorded and logged, in real time or periodically as part of the maintenance policy, using a centralized analysis station.

DP involves taking the data acquired from the diagnosis subsystem and performing analysis that combines damage evolution models with probability of detection models. The purpose of DP is to assess the structural integrity of the structure and its remaining lifetime under assumed operational and service conditions. Relying on the DP, the prevailing scheduled maintenance policy of the structure can be replaced by PM, also known as condition-based maintenance (CBM), which allows scheduling and optimizing the corrective maintenance actions required in order to ensure the structural integrity of an aircraft or any other system.

---

1 NDT is a wide group of analysis techniques used in science and technology industry to evaluate the properties of a material, component or system without causing damage. The terms nondestructive examination (NDE), nondestructive inspection (NDI) and nondestructive evaluation (NDE) are alternative terms.

2 Structural Health Monitoring, https://journals.sagepub.com/home/shm.
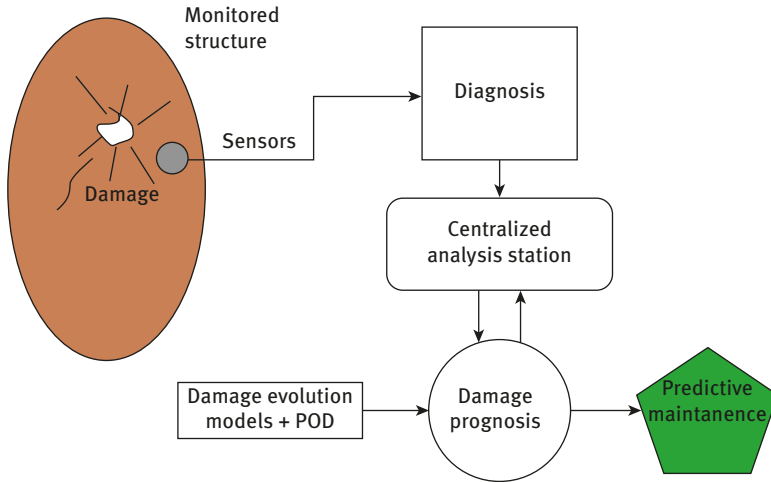
Fig. 10.1: A schematic typical SHM system.

10.1.1 Diagnosis

As stated earlier, the diagnosis subsystem refers to the sensing mechanism existing in every SHM system. The sensors constantly record at least one parameter related to the monitored structure, which is expected to obtain irregular values in the case of structural integrity deterioration. Electrical conductivity, mechanical strain, mechanical stiffness and wave propagation characteristics are few examples of parameters that can be monitored over time, each by its own sensing mechanism.

The literature divides the sensor mechanism into two categories: passive and active sampling.

Passive sampling-based sensors operate by detecting responses due to perturbations of ambient conditions in the monitored structure, without using any external source of energy. This category includes pressure-sensitive polymers, shape memory alloys (SMAs), comparative vacuum monitoring (CVM) sensors, which can passively detect crack propagation. Another type of passive sensing, considered to be much more advanced than the previous examples, is the acoustic emission (AE) measurement using piezoelectric wafers.

Active sampling-based sensors require externally supplied energy in order to function. This energy can be in the form of mechanical stress or electromagnetic waves. This category includes the electrical and magnetic impedance sensors, piezoelectric wafer-active sensors (PWAS) and optical fiber sensors (OFS), which require an external laser for taking measurements.

Appendix A presents the various sensors and the way they operate.

10.1.2 Damage prognosis

DP attempts to forecast the structural integrity of an aircraft structural component by assessing its current damage state, estimating the future loading environments, and then performing a prediction, through simulations and past experience, of the remaining applicable lifetime of the component. There are two main approaches for conducting DP as part of SHM. The first is to monitor load sequences/cycles, which are then used to estimate the assumed accumulated fatigue damages. The other way is to use the diagnosis system to directly determine the occurrence, size and location of the damages in the structural component, and then to constantly estimate its remaining lifetime. The former approach of DP is based on operating load monitoring (OLM), and the latter one is based on a process called pattern recognition (PR). This section briefly introduces both of the DP approaches and the relevant terminology associated with them. Even though the latter approach, which deals with the identification and classification of the actual damage, is considered more advanced and attractive, these two approaches are presented for a better understanding of the full picture.

10.1.2a Operating load monitoring

Loads can be monitored only through the parameters describing them. Here (again) there are two approaches. Loads monitoring can be performed globally by analyzing the flight parameters recorded in the flight data recorder, which is found in almost every aircraft. Flight parameters such as height, speed, acceleration, position of control surfaces and flap positions determine the aerodynamic forces acting on the aircraft structure. Using the manufacturer-supplied strength reports, numeric simulations and several assumptions, the loads acting on the aircraft can be indirectly deduced and monitored during the aircraft lifetime.

The second approach, which is much more "straightforward," is based on taking local measurements of the mechanical strain at several discrete points. The data are analyzed and directly converted, usually through a preliminary calibration test, to the aerodynamic loads acting on the aircraft. Both ways have their advantages and disadvantages. The former approach involves much less data processing issues, but demands full information regarding the aircraft structure, which is (intentionally) not always provided by the aircraft manufacturer. On the other hand, the latter approach only requires a fundamental knowledge regarding the structural loads acting on the monitored structure in order to adequately place the sensors on the aircraft components. However, it demands a large amount of data processing, in direct relationship to the number of the sensors. An OLM system allows the identification of unusual flight events that could lead to a static failure, and the estimation of the number of load cycles leading to a fatigue failure. Therefore, loads monitoring can assist the operator to indirectly forecast damages before occurrence, and thus to define a more effective maintenance policy.

10.1.2b Pattern recognition (PR)

A number of definitions can be proposed to define damage. Intuitively, damage is a material, structural or functional failure. Therefore, one of the fundamental assumptions taken while designing SHM system is that material or structural failure in a structure will lead to a change in its static and/or dynamic behavior. In other words, one can think of the data recorded, containing the static and/or dynamic information of a structure, as describing its "healthy" pattern, and a change in this recorded pattern may be associated with the existence of a new damage. This approach is known in the professional jargon as "statistical pattern recognition[3]."

PR, originally a term borrowed from "Machine Learning," describes the ability to (automatically) recognize patterns in multivariable data sets [3]. The notion of PR appears in many literature sources in the context of damage identification and classification. As explained earlier, after having the ability to identify and classify all types of damages in a structure, the step toward having DP abilities is quite small. Here, three types of the most common applications of PR are introduced and briefly discussed.

10.1.2c A strain measurement under constant static loading

Consider a "healthy" structural component, that is, without any significant damage, which is subjected to a constant static loading. As a result, a mechanical strain field develops in the structural component, obeying Hooke's law. As long as the component remains "healthy," and after the cancellation of all environmental effects, the same external static loading will lead to the same corresponding mechanical strain field. Monitoring the mechanical strain field, either using local strain sensors [strain gauges, fiber Bragg gratings (FBGs), PZTs, etc.] or a distributed sensing (optical fiber backscattering), allows the location of areas in a component that might have been damaged.

10.1.2d Modal analysis

Modal analysis relates to the dynamic properties of a structure under vibrational excitation. The dynamic properties of a structure are determined by how it responds to forced and free vibrations. Forced vibrations occur when the structure is forced to vibrate at a particular frequency by a periodic input of force. Free vibrations are caused by a one-time excitation. In this case, the structure vibrates in one or more particular frequencies that are called natural frequencies/resonant frequencies. Since the resonant frequencies do not depend on the external one-time excitation, they can be thought of a unique pattern of the structure, which can be monitored.

---

3 From the writer's point of view, the word "statistical" can be omitted since there are several SHM applications that do not necessarily involve statistics.

Williams and Messina [4] formulated a correlation coefficient that compares the resonant frequencies of a structure with a finite element model (FEM)-based prediction for damage identification and localization purposes. For that, they defined a damage index, δD_i, which represents a linear stiffness reduction in the i element of the model. Thus, the fractional change in the k resonant frequency, δf_k can be described as follows:

$$\delta f_k = \sum_{i=1}^{m} \frac{\delta f_k}{\delta D_i} \delta D_i \tag{10.1}$$

where i and m represent the element index and the total number of elements, respectively, and the expression

$$\frac{\delta f_k}{\delta D_i} = \frac{\{\phi_k\}^T [K_i] \{\phi_k\}}{8\pi^2 \{\phi_k\}^T [M_i] \{\phi_k\}} \tag{10.2}$$

is the sensitivity of the k frequency to the damage index at the i element, $\{\phi_k\}$ being the k mode shapes, $[M_i]$ and $[K_i]$, respectively, the mass and stiffness matrices of the element i.

Williams and Messina conducted several experiments on aluminum rods and compared the predicted changes in the resonant frequencies, δf, to the actual changes measured in the experiments, Δf, by using the cross-correlation technique:

$$C = \frac{\left| \{\Delta f\}^T \{\Delta f\} \right|^2}{\left[\{\Delta f\}^T \{\Delta f\} \right] \cdot \left[\{\Delta f\}^T \{\Delta f\} \right]} \tag{10.3}$$

where C represents the cross-correlation coefficient that takes the value of 1.0 in the case of a perfect match between the model and experiment, and 0.0 in the case of a mismatch. They found that 10–15 resonant frequencies are needed to provide sufficient information about a damage. Furthermore, they also suggested a couple of techniques to improve the accuracy of the damage estimation. Additional information can be found in their paper [4].

Many other works based on a modal analysis have been conducted in the past two decades, demonstrating creative ideas to identify, classify and even predict damages. However, the major challenge in this kind of PR technique is related to damage sensitivity. Modal analysis is in fact a global method, and is therefore limited to the identification of local damage, which affects the dynamic behavior of the entire monitored structure [5]. In other words, damage must have become more significant before being identifiable. This is an issue especially in composite-based components. For example, a minor delamination, which does not necessarily affect the global dynamic response of the structural component, may lead to a structural failure. This issue requires further investigation.

10.1.2d Principal component analysis

Principal component analysis (PCA) is another familiar PR-based technique. This technique involves multivariable analysis, which reduces complex data sets to a lower dimension, thereby revealing simplified patterns, which are often hidden in the complexity of the raw data. Generally, PCA enables to determine the more important patterns in the measured data, which provides more information regarding the structural integrity of the component under test.

A fundamental PCA of a multiple sensor-based SHM system can be described in three main stages: First, it is necessary to normalize and arrange the collected data in a $[m \times n]$ matrix A, which represents the measurements acquired from n sensors in m experimental trials. Experimental trial is defined as a measurement taken from each sensor at a specific moment. The next stage is the calculation of the covariance matrix, symbolized by C_A, which measures the degree of linear relationship within the data set among all possible pairs of the sensors. C_A is calculated as follows (T stands for "transpose"):

$$C_A = \frac{1}{m-1} A^T A \tag{10.4}$$

In the last stage, the eigenvectors and eigenvalues of the covariance matrix are derived using the following relation:

$$C_A \cdot V = V \cdot \Lambda \tag{10.5}$$

where the eigenvectors of C_A are the columns of V, and the eigenvalues are the diagonal elements of Λ (the off-diagonal elements are zero). The columns of the matrix V are arranged according to the corresponding eigenvalues in descending order. The principal components are defined as the eigenvectors of the covariance matrix scaled by their corresponding eigenvalues.

10.1.3 Predictive maintenance

As stated at the beginning of the present chapter, once the DP stage was executed, the prevailing scheduled maintenance policy of the monitored structure or the monitored system can be replaced by a PM, also known as CBM. This will allow scheduling and optimizing the corrective maintenance actions required in order to ensure the structural integrity of the monitored system or structure. The benefits from applying the PM are:

a. Reduced maintenance time- automatic reports for strategic maintenance scheduling and pro-active repairs, can lead to a reduction of up to 20–50% in maintenance time, yielding a decrease in overall maintenance costs.

b. Better efficiency- insights based on analytical procedures would improve the overall equipment effectivity, by reducing/ unnecessary maintenance procedures,

leading to extended system life and enabling the application of root cause system analysis to pinpoint issues ahead of failure.

c. Improved customer satisfaction- providing the customer with automatic alerts for parts to be replaced in parallel with timely maintenance services, would lead to a better predictability of the product thus boosting the satisfaction of the customers.

d. Competitive advantage- a company applying the PM would be seem as a strong one with costumers continuously appreciating it due to its reliable and better products.

e. Additional revenues- a company can earn additional revenues by offering its PM digital services to their customers, thus generating a new growth engine for the company.

10.2 Applications

The use of SHM in industry is somehow restricted to two main sectors: the aerospace and the civil engineering, although other sectors also use the method (naval engineering and car industry). In the present chapter we shall address the aerospace and the civil engineering sectors.

Beside industry, the academy is very active in the SHM area, delivering many new manuscripts on advanced topics of this research area. To familiarize with the topic applications, the reader is referred to the various reviews [5–8].

10.2.1 Aerospace applications

The aerospace sector demands high reliability for its vehicles, therefore the SHM was first introduced in this industry. References [9–28] are only typical manuscripts, written on SHM issues. The increasing use of laminated composite materials in the various passenger aircraft, lead to numerous papers on how to increase the reliability of those structures. Scala et al. [9] present a report on the use of AE method to monitor and thus ensure the structural integrity of an aircraft. Staszewski et al. [10] address the issue of impact being inflicted to a composite made structure. The research presents the use of an active approach, 3-D laser vibrometry, to scan the structure and by revealing the change in the Lamb wave response amplitudes, the severity of the local delamination can be estimated. An additional approach, the authors called "passive means" involves the use of an array of piezoelectric patches, serving as sensors, to detect the waves being caused by an applied impact on the composite structure. Using

Genetic Algorithms,[4] the authors succeeded in locating the impact. Giurgiutiu et al. [11], use PWAS to monitor the onset and the progress of fatigue cracks and corrosion in aging aircraft structure. The electromechanical (EM) impedance technique is used to detect near field damage, while the wave propagation approach is applied for far-field damage detection. Heida and Platenkamp [12] derived in-service NDT guidelines for aerospace structures made of composite materials, mainly carbon fiber reinforced structures. They recommend using tap test to detect and find the size and depth of the damage due to impact, delaminations and debonds. The application of the shearography[5] and thermography[6] methods seemed to be less applicable due to its poor-to-moderate capability to characterize a defect, when compared to ultrasonic inspection. However, the authors recommend the use of noncontact techniques, like thermography, for special shape configurations like curved panels and/or repaired structures, and for detection of water entry in honeycomb structures.

Giurgiutiu and Soutis [13] recommend the use of enhanced SHM to increase the reliability and integrity of composite structures, while Assler and Telgkamp [14] from Airbus advocate the use of smart structures approach, in the design phase of an aircraft, thus enabling SHM during the manufacturing and operation phases of the vehicle. Finlayson [15] present the use of AE and acousto-ultrasonic NDT methods to monitor the health of aerospace structures. Pieczonka et al. [16] present a theoretical and experimental study for detection of damage. They used guided ultrasonic waves together with 3d laser Doppler[7] vibrometry. The Lamb waves are excited by surface bonding piezoelectric actuators. Comparing between in-plane and out-of-plane wave vector components leads to the reliable detection of the structural damage. D'Angelo and Rampone [17] address the diagnosis issue within the SHM approach. They present a high-performance computing parallel implementation of a novel learning algorithm, U-BRAIN,[8] allowing them to process multiparameter data involved in composite specimen testing. They claim that their approach yielded a "defect classifier in aerospace structures." A different approach is

---

4 Genetic algorithm is a method that is used to optimize a given problem and is based on natural selection, the same process that drives biological evolution. The genetic algorithm repeatedly modifies a population of individual solutions.

5 Shearography, sometimes called speckle pattern shearing interferometry, is an NDT approach like holographic interferometry. It uses coherent light or coherent soundwaves yielding strain measurement output of the measured structure.

6 Thermography is an NDT approach that uses infrared cameras usually to detect radiation in the long-infrared range of the electromagnetic spectrum due to changes in the measured specimen.

7 Doppler vibrometry is a scientific instrument used to make noncontact vibration measurements of a surface using a laser .

8 U-BRAIN (*U*ncertainty-managing *B*atch *R*elevance-based *A*rtificial *IN*telligence) is designed for learning DNF Boolean formulas from partial truth tables, possibly with uncertain values or missing bits.

presented by Oliver [18], in his Ph.D. thesis for the diagnosis issue. He developed and validated a damage identification approach based on a statistical least-squares damage identification algorithm based on concepts of parameter estimation and model update. The data used by the algorithm is the frequency response function-based residual force vectors coming from the distributed vibration measurements, which is updating a FEM through statistically weighted least-squares minimization leading to the location and the size of the damage, its uncertainty and a new updated model.

Boukabache et al. [19] designed an advanced sensor, based on a piezoelectric transducer, capable of generating Lamb waves (shear type waves) and measuring those waves to detect the damage and its severity. In addition, the manuscript presents an analog interface procedure for the measurements and an experimental validation of the new sensor.

Wandowski et al. [20] checked three NDT methods to assess the integrity of composite aerospace structures. They used laboratory samples made of CFRP (carbon fiber reinforced polymer) and GFRP (glass fiber reinforced polymer). The application of the EM impedance method on CFRP specimens revealed the delamination by measuring the real part of the impedance, namely the resistance. The delamination caused the shifting of some resonance frequencies, which could be detected by the resistance characteristics. The second method applied was laser vibrometry, a noncontact NDT technique. They had used two types of waves, standing (vibration-based application) and propagating (guided wave-based application) ones. The third method was Terahertz spectroscopy, using electromagnet radiation in the range of 01–3 THz. The GFRP specimens were scanned yielding B scans and C scans, from which the delamination could be located.

Diamanti and Soutis [21] used the Lamb waves NDT technique to monitor the composite layers of an aerospace structure, to ensure no delamination was developed, thus increasing the reliability of structures. Baker et al. [22] address another important issue, namely the patched cracks in an aircraft structure. Monitoring the health of the patch was done in their study using strain gages, although they had evaluated also the use of Bragg grating optical fibers. Maier et al. [23] address the same topic also in their report on SHM of repairs. The state of the art to detect cracks, delamination, impacts and corrosion of aircraft structures using AE, acoustic ultrasonic, phase array ultrasonic fiber Bragg gratings and CVM is outlined and discussed. Schnars and Henrich [24] give a review of the application of various NDT methods in the composite aerospace structures. Manual and automatic ultrasonic measurement using either single element transducers or phase array detectors applying pulse echo or transmission modes is highlighted in their report. Other NDT methods, like resonance methods, shearography and thermography, mentioned earlier in this chapter are also described. Laser ultrasonic method is recommended for contactless measurements of composite structures. Hsu [25] addresses also the application of NDT methods, for composite structures. The focus is on the practice applications of those methods.

Chang and Lan [26] address the issue of SHM being applied on aging transport aircraft, which experienced severe atmospheric turbulence. Due to the lack of knowledge on the structural flexibility of those old structural parts, the structural response is achieved using the fuzzy logic modeling of the aerodynamic loads.

Finally, Terroba et al. [27] present a research study on the measurement of the structural integrity of a target drone equipped with four fiber Bragg grating sensors. The system was found to be reliable and can detect barely visible structural damage in the high-loaded front fuselage of the drone.

10.2.2 Civil applications

Spencer et al. [28] present a short review of the use of smart sensors technology for SHM of civil engineering structures like bridges, highways and buildings. They define a smart sensor as a MEMS[9] sensor with wireless capabilities. Various aspects of the use and the respective hardware are outlined. Swartz et al. [29] address the same topic of the use of smart sensors. Wireless sensors serve as the basic means to monitor the health of civil structures. Their sensors would include accelerometers, strain gages, geophones, whose data have to be transmitted to a central computer for further analysis. Typical results for wind turbines structures and bridges are presented.

Sun et al. [30] review the smart sensing technologies available for SHM of civil engineering structures. Typical sensors as fiber optic, piezoelectric transducers, magnetostrictive transducers and self-diagnostic fiber reinforced composite are cited as good candidates to measure the health of the structure monitored. Typical laboratory and on-site applications of those sensors are evaluated and compared.

Yi et al. [31] apply a hybrid method named optimal sensor placement strategy to optimize the number of sensors and their locations on a monitored structure. The on-site use of the method on a high TV tower (Guangzhou New TV Tower, China) proved to be effective with a friendly software interface. Yi et al. [32] also studied the use of global positioning system to monitor the displacement of high-rise structures due to wind, thermal variation and earthquake-induced responses.

Dhakal et al. [33] review wired and wireless technologies, with subtechniques like impedance-based, nondestructive evaluation using vibration signature, limit strain measurement, data fusion method and inverse method and their applications in civil infrastructures like buildings, bridges and towers.

Kim et al. [34] present an interesting technique to digital processing of images containing actual cracks and differ them from crack-like noise pattern like dark

---

9 MEMS – microelectrical mechanical system.

shadows, stains, lumps and holes, characteristic of concrete structures. The technique is based on machine learning process.

Li et al. [35] also use the learning machine process to accurately monitor the displacement of a deep foundation pit at early construction stage and predict its behavior with time.

Qu et al. [36] present a new approach of using an amplitude-adaptive wavelet transform, to detect deep or shallow delaminations in a concrete slab, using the impact echo experimentally recorded. The authors report good results for the civil structures they had tested.

10.2.3 General applications

Various NDT methods are found in the literature. Park et al. [37] review the piezoelectric impedance-based health monitoring method, while Oromiehie et al. [38] use the Bragg grating sensors to characterize process-induced defects in automated fiber placement manufacturing of composites. Cha and Wang [39] improved the learning machine method by adding an unsupervised mode, as it requires only enough intact states at the training of the machine. A novel detection-based structural damage localization using a density peak-based fast clustering algorithm is described in detail. The same topic, the use of machine learning, is addressed by Demarie and Sabia [40] for long-term SHM and Jin and Jung [41] in their study.

Other topics like guided wave excitation in composite plates [42], the use of fuzzy c-means clustering algorithm to detect double defects in plates [43], damage-scattered wave extraction in an integral stiffened isotropic plate [44] and the use of changes in the curvature mode shapes of the monitored structure to detect damage [45] are worth to be mentioned to show the diversibility of the SHM method.

10.3 Monitoring natural frequencies of composite beams for detection of damage

This section is aimed at providing the insight of a method to monitor the natural frequencies to detect a damage in a given structure as elaborated by Penias and Abramovich [46], in the first author master thesis.

The numerical study was performed on a rectangular beam, with a high length-to-width ratio (1:20) (see fig. 10.2 for beam's geometry). The beam was constructed of 16 Graphite-Epoxy As4–12k/E7K8 layers (see Fig. 10.3 for the beams' cross section).

The cantilever beam's first 10 natural frequencies and their associated mode shapes were calculated numerically, using the ANSYS FE code. Delamination was created by changing the boundary condition of certain elements (by choice) to
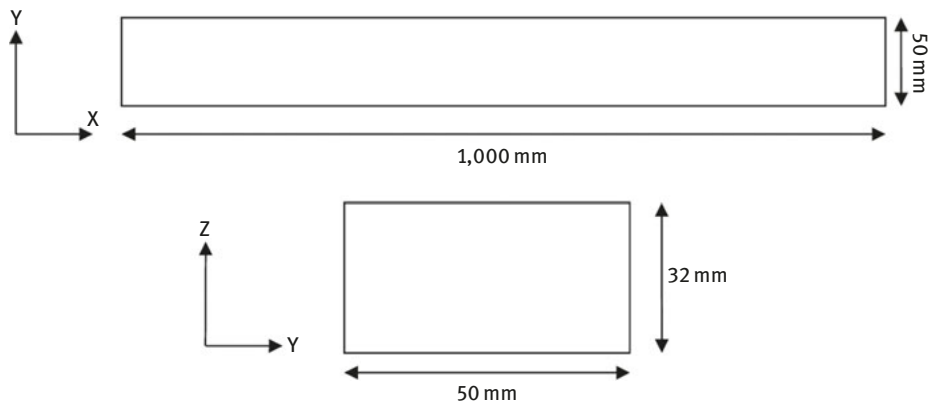
Fig. 10.2: The geometry of the beam's model.
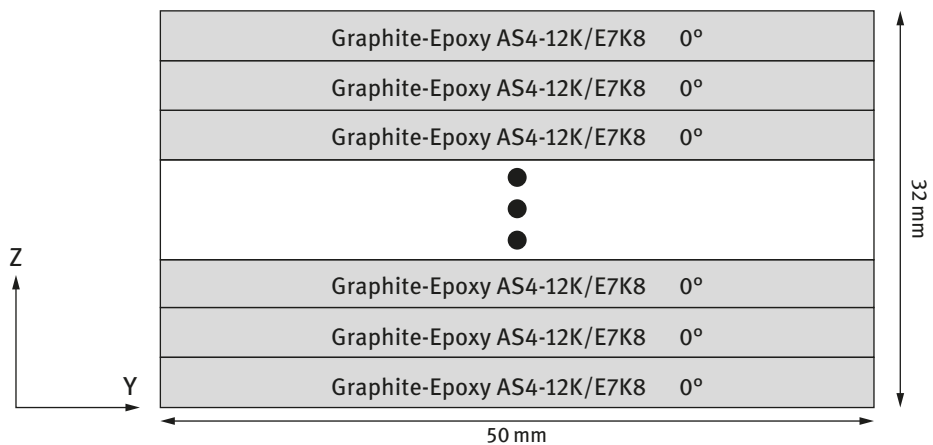
Fig. 10.3: The model's cross section.

"unbounded," thus creating a perfect delamination. A typical delamination, which was implemented in the beam between various layers, is displayed in Fig. 10.4.

Numerical results show that the natural frequencies around the Z-axis (sideway bending) remain the same (as expected); therefore, those modes were disregarded. The natural modes around the X-axis (torque) and the Y-axis (bending) show decrease in the natural frequencies as the delamination is closer to the mid-layer of the beam (Figs. 10.5 and 10.6).

Delamination of different sizes were considered, all symmetric with respect to the X-axis. The numeric results show that, as expected, the natural frequencies in the bending and torque modes decrease with the increase in the delamination size.
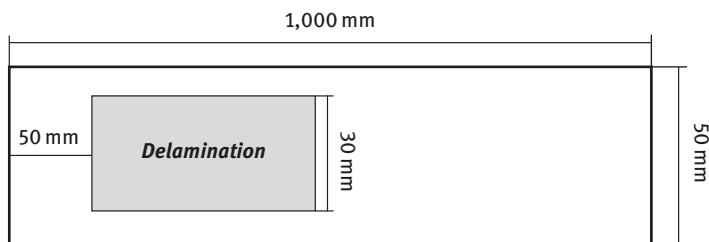
Fig. 10.4: The delamination model (not to scale).

Figure 10.7 shows the results for delamination of different sizes and different layers, for the fourth bending mode and second torque mode as typical examples (all modes showed the same behavior).

To determine the effect of delamination's location, a delamination, with fixed sizes, was implemented in different locations (along the *X*-axis) in the mid-layer of the beam (see Fig. 10.8). The results for the first four bending modes, presented in Fig. 10.9, display various behaviors of the natural frequency as the delamination change its location (Fig. 10.9).

The results, presented in Fig.10.9, show that the change in the natural frequencies for every bending mode resembles its mode shape, which indicated that the change in the natural frequency is affected by the movement of the delaminated area with respect to the mode shape.

A similar investigation was performed for the *Y*-axis, for which different delaminations were inspected in various ways (Fig. 10.10) – symmetric and nonsymmetric with respect to the *Y*-axis. Results presented in Fig. 10.11 show that the bending modes (e.g., fourth mode) are not influenced by the delamination location along the *Y*-axis, and the change in the natural frequency was dictated only by the size of the delamination. On the other hand, torque modes (see, e.g., second mode) display a noticeable difference between symmetric and nonsymmetric delaminations (as expected) along the *Y*-axis.

Additional parameters were investigated, such as the type of the material used, the influence of the width of the beam, the influence of the boundary conditions and various other laminates. The results are found in [46].

To validate the numerical model, an experimental campaign was performed on four specimens, with their geometry presented in Fig. 10.12.

The specimens that were clamped at one end and freed at the other end were excited using a shaker table. The response measured by accelerometer bonded on the specimens was recorded using a PC. Typical results are shown in Fig. 10.13 [46]. Although the four tested specimens were not 100% identical, the results present a detectable reduction in the natural frequencies.
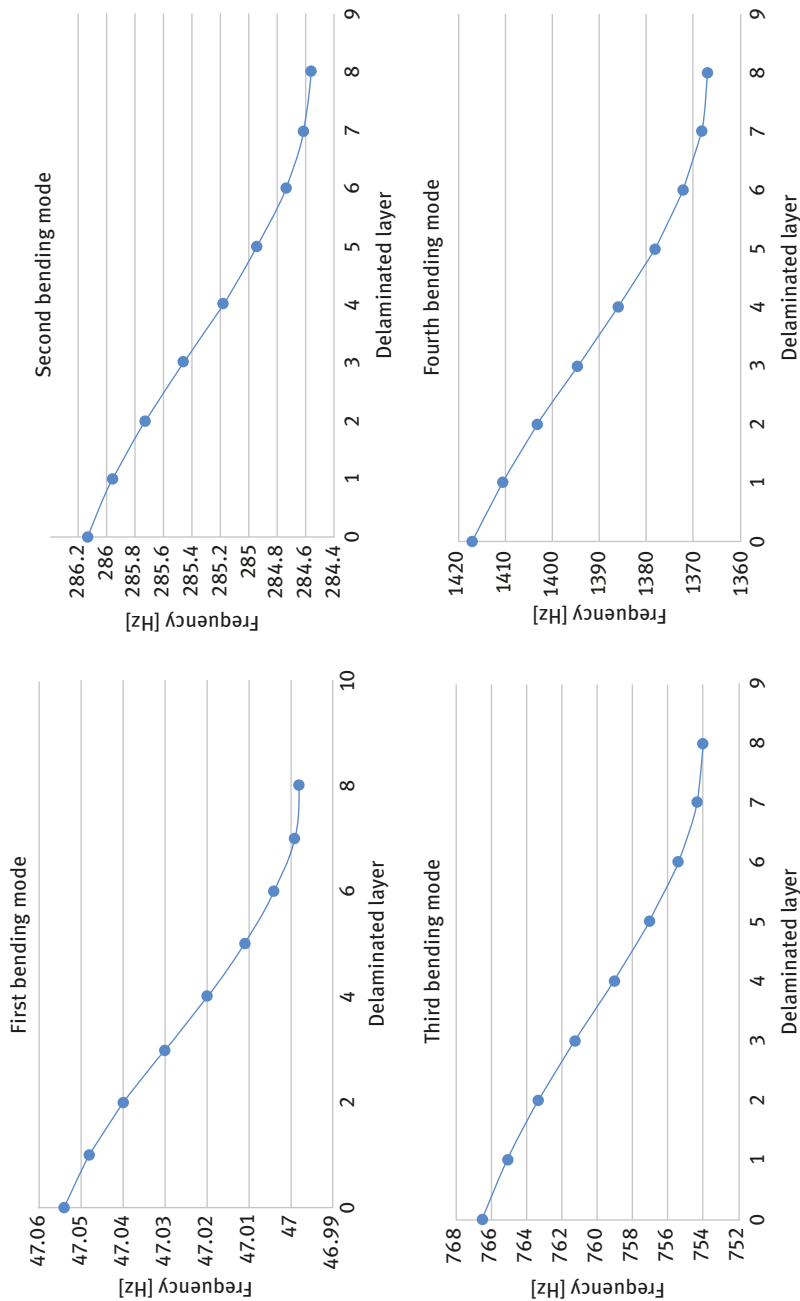
Fig. 10.5: The first four bending modes – natural frequencies for different delamination layers.
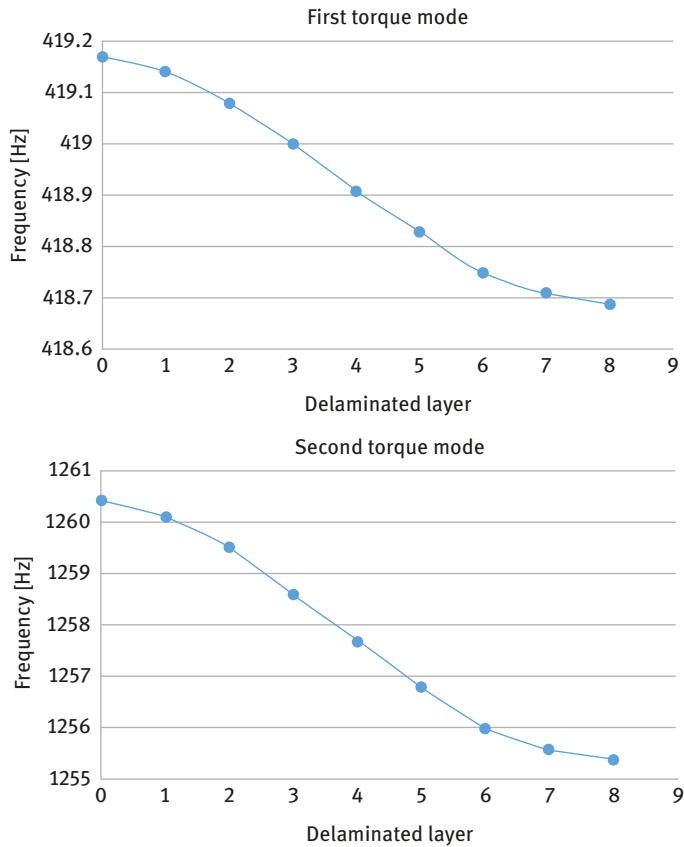
Fig. 10.6: The first two torque modes – natural frequencies for different delamination layers.

The conclusions from the study were:

a. The effect of delamination on the bending and torque modes of natural frequencies is larger, as the delamination is closer to the midlayer of the beam.

b. Natural bending and torque frequencies are reduced, as the delamination is larger.

c. Bending frequencies are affected by the delamination's size only. Torque frequencies are affected by the deviation of the delamination from the symmetry line of the specimen.

d. The variation of the natural bending frequencies change with the location of the delamination on the *X*-axis. The frequency change plot resembles the relevant mode shape.

e. Delamination in laminated composite beams has a significantly larger effect on their natural frequencies when compared with delaminated isotropic materials.

Fourth bending mode frequency vs. delaminated area for different layers

(a)

Second torque mode frequency vs. delaminated area for different layers

(b)
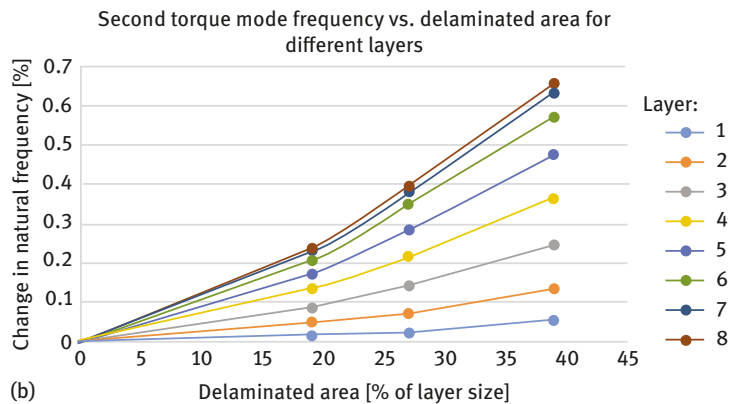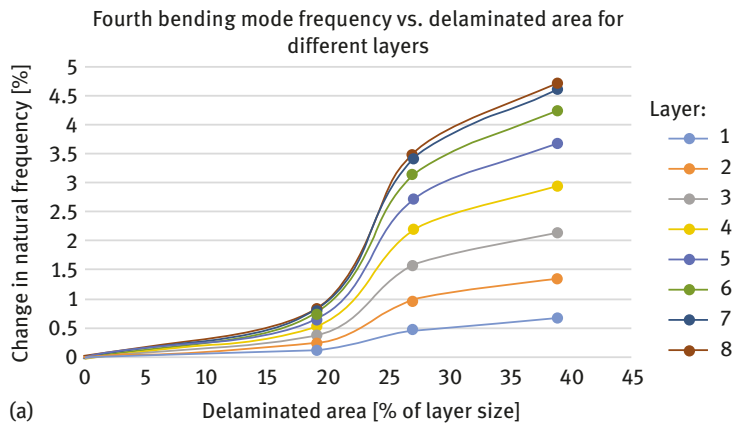
Fig. 10.7: Change in frequency with change in delamination area and delamination layer: (a) fourth bending mode and (b) second torque mode.
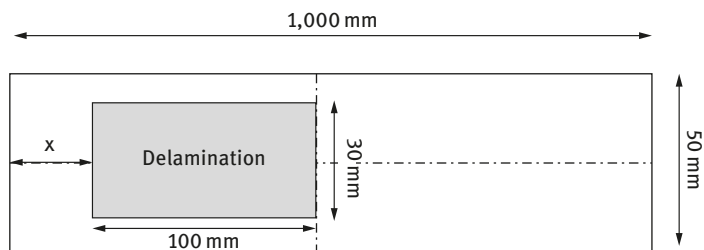
Fig. 10.8: Delamination location along the *X*-axis (*X* symbolizes the distance from the beam's edge).
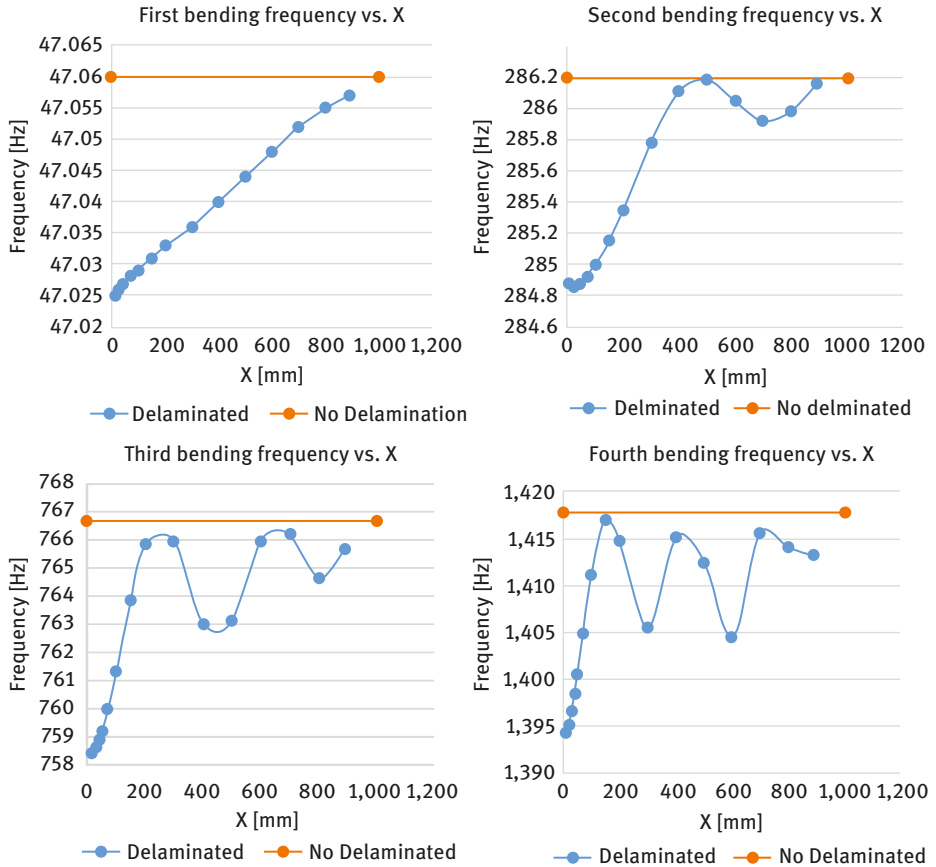
Fig. 10.9: Natural frequencies for different value of *X* – the first four bending modes.

f. Clamped–clamped beams tend to show a more significant change in their natural frequencies compared with cantilever and simply supported beams.

g. Tests performed on four specimens, with and without damage, showed the reduction in the natural frequencies due to the presence of delaminations.

All the above conclusions show that a simple measurement of the first few bending and torque natural frequencies of a beam might provide a lot of information regarding the presence of a delamination:

– Delaminated layer – by the change in bending mode frequencies
– Delamination size – by change in both torque and bending modes
– Delamination location:
    – Along the *X*-axis – by difference between different bending modes
    – Along the *Y*-axis – by change in the torque modes
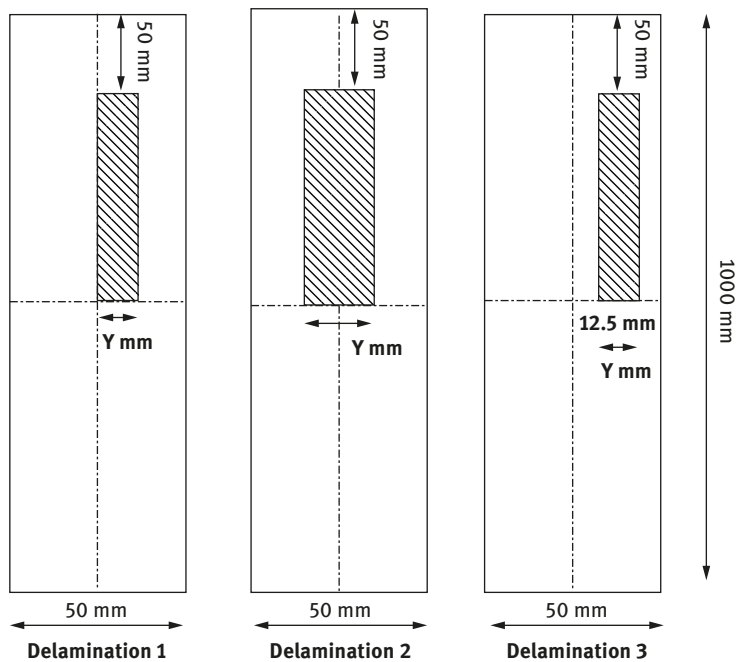
Fig. 10.10: The geometry for the various delaminations used in the *Y*-axis direction.
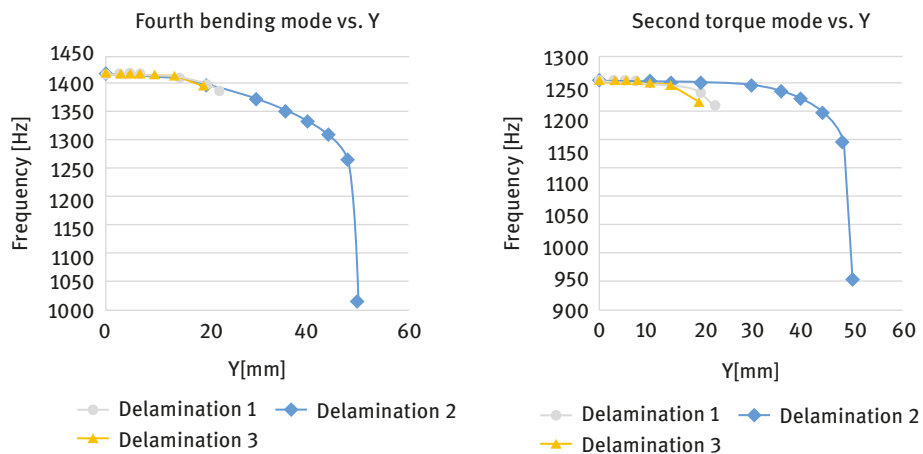
Fig. 10.11: The change in the fourth bending and second torque modes for different *Y* values.
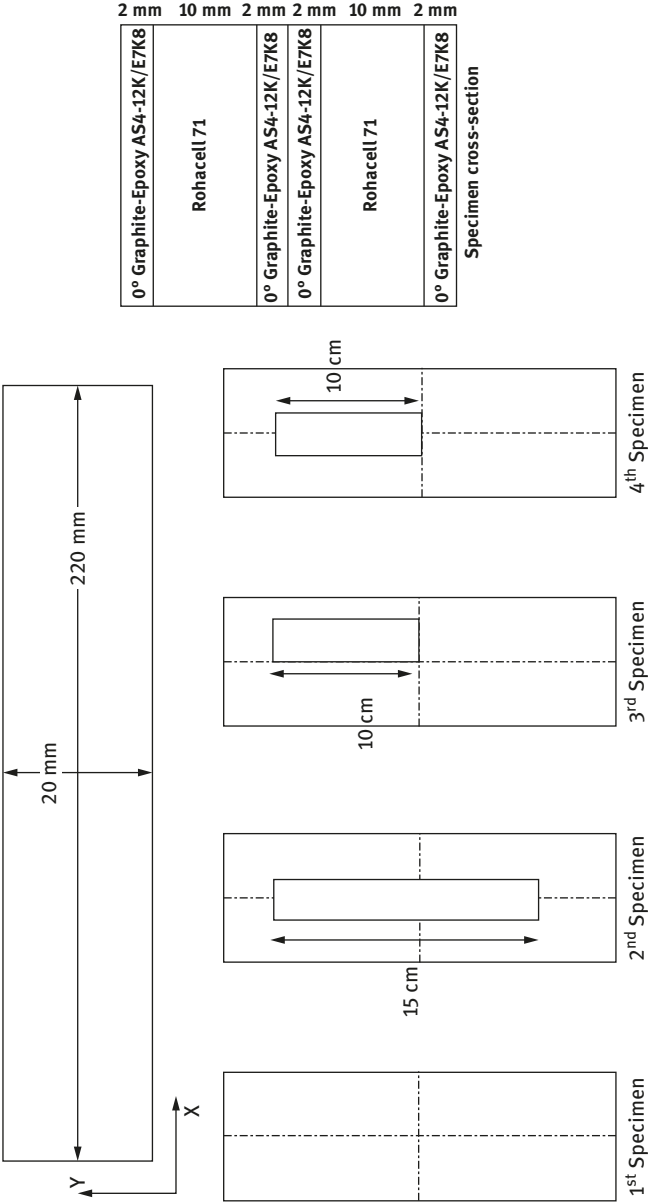
Fig. 10.12: The geometry of the experimental specimens.
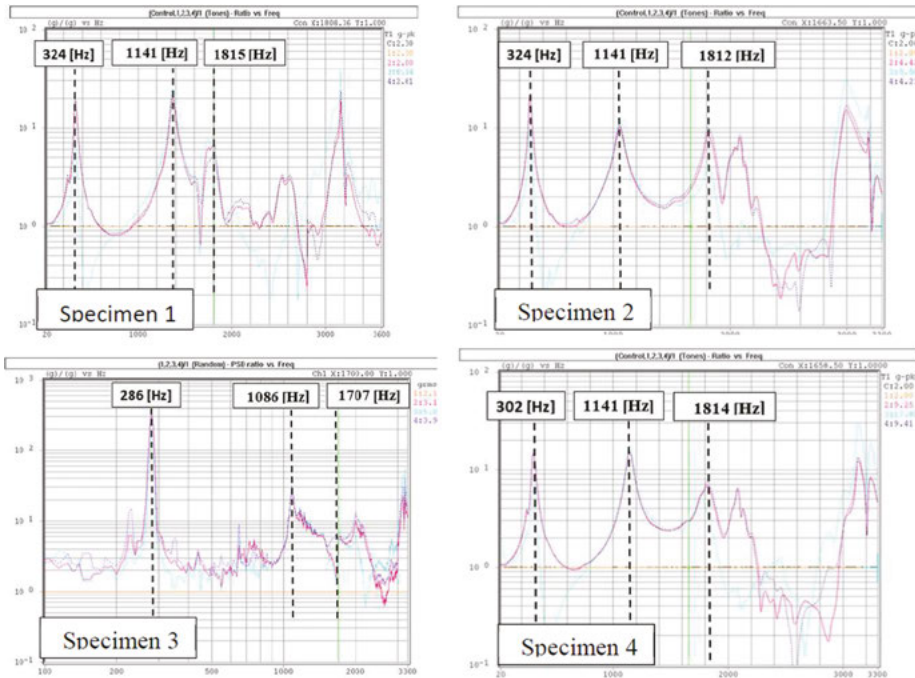
Fig. 10.13: The first experimental natural frequencies for the four tested specimens.

To increase the chances of detecting delaminations in laminated composite beams, it is recommended to clamp the beam at its both sides.

References

[1] Cai, J., Qiu, L., Yuan, S., Shi, L., Liu, P.P., and Liang, D. Structural health monitoring for composite materials, Ch. 3 in Composites and Their Applications, Hu, N, editor, INTECHOPEN, 2012, 25 p. doi: 10.5772/3353.

[2] De Baere, D., Strantza, M., Hinderdael, M., Devesse, W., and Guillame, P., Effective structural health monitoring with additive manufacturing," in EWSHM – 7th European Workshop on Structural Health Monitoring, July 8–11, 2014, La Cité, Nantes, France, 10p.

[3] Jain, A. K., Duin, R. P. W., and Mao, J. Statistical pattern recognition, a review, IEEE Transactions on Pattern Analysis and Machine Intelligence, 22(1), 2000, 4–37.

[4] Messina, A., E. Williams, J., and Contursi, T. Structural damage detection by a sensitivity and statistical-based method, Journal of Sound and Vibration, 216(5), 1998, 791–808.

[5] Sohn, H., Farrar, C.R., Hemez, F., Shunk, D.D., Stinemates, D.W., Nadler, B.R., and Czarnecki, J.J. A review of structural health monitoring literature 1996–2001, Los Alamos National Laboratory, LA-13976-MS Feb, 2004, 311p.

[6] Farrar, C.R., and Worden, K. An introduction to structural health monitoring, Philosophical Transactions of the Royal Society A, 365, 2007, 303–315. doi: 10.1098/rsta.2006.1928.

[7]   Del Grosso, A.E. Structural health monitoring: research and practice, Proc. of the 2nd Conference on Smart Monitoring, Assessment and Rehabilitation of Civil Structures (SMAR2013), Ilki, A., editor, 9–11 Sept, 2013, Istanbul Turkey.

[8]   Kim, J.-T., Sim, S.-H., Cho, S., Yun, C.-B., and Min, J. Recent R&D activities on structural health monitoring in Korea, Structural Monitoring and Maintenance, 3(1), 2016, 91–114. doi: 10.12989/smm.2016.3.1.091

[9]   Scala, C.M., Bowles, S.J., and Scott, I.G. The development of acoustic emission for structural integrity monitoring of aircraft (U), Department of Defense, Defense, Science and Technology Organization, Aeronautical Research Laboratory, Melbourne, Victoria, Australia, Aircraft materials Report, Vol. 120, 1989, 34p.

[10]   Staszewski, W.J., Mahzan, S., and Traynor, R. Health monitoring of aerospace composite structures- Active and passive approach, Composite Science and Technology, 69, 2009, 1678–1685.

[11]   Giurgiutiu, V., Zagrai, A., and Bao, J.J. Piezoelectric wafer embedded active sensors for aging aircraft structural health monitoring, Structural Health Monitoring, 1(1), 2002, 41–61.

[12]   Heida, J.H., and Platenkamp, D. J. In-service inspection guidelines for composite aerospace structures, 18th World Conference on Nondestructive Testing, 16–20 April, 2012, Durban, South- Africa, 14p.

[13]   Giurgiutiu, V., and Soutis, C. Enhanced composites integrity through structural health monitoring, Applied Composite Materials, 19(5), 2011, 813–829. doi: 10.1007/s10443-011-9247-2.

[14]   Assler, H., and Telgkamp, J. Design of aircraft structures under special consideration of NDT, 9th European Conference on NDT (ECNDT 2006), Berlin, Germany, Sept. 25–29, 2006.

[15]   Finlayson, R.D., Friesel, M., Carlos, M., Cole, P., and Lenain, J.C. Health monitoring of aerospace structures with acoustic emission and acousto-ultrasonics, Insight, 43(3), 2001, 4p.

[16]   Pieczonka, Ł., Ambroziński, Ł., Staszewski, W.J., Barnoncel, D., and Pérès, P. Damage detection in composite panels based on mode-converted Lamb waves sensed using 3D laser scanning vibrometer, Optics and Lasers in Engineering, 99, 2017, 80–87. doi: 10.1016/j. optlaseng.2016.12.017.

[17]   D'Angelo, G., and Rampone, S. Diagnosis of aerospace structure defects by a HPC implemented soft computing algorithm, 2014 IEEE Metrology for Aerospace (MetroAeroSpace 2014), Benevento, Italy, June 29–30, 2014, 5p., doi: 10.1109/MetroAeroSpace.2014.6865959.

[18]   Oliver, J.A. Frequency response function based damage identification for aerospace structures, Ph.D. thesis, University of California, San Diego, CA, 2015, 583p.

[19]   Boukabache, H., Escriba, C., and Fourniols, J.-Y. Toward smart aerospace structures: Design of a piezoelectric sensor and its analog interface for flaw detection, Sensors, 14, 2014, 20543–20561. doi: 10.3390/s141120543.

[20]   Wandowski, T., Malinowski, P., Radzienski, M., Opoka, S., and Ostachowicz, W. Assessment methods for composite aerospace structures, in Proc. of 7th ECCOMAS Thematic Conference on Smart Structures and Materials (SMART 2015), Araújo, A.L., Mota Soares, C.A., et al. editors, @IDMEC 2015, 15p.

[21]   Diamanti, K., and Soutis, C. Structural health monitoring techniques for aircraft composite structures, Progress in Aerospace Sciences, 46, 2010, 342–352.

[22]   Baker, A., Rajic, N., and Davis, C. Towards a practical structural health monitoring technology for patched cracks in aircraft structure, Composite: Part A, 40, 2009, 1340–1352.

[23]   Maier, A., Benassi, L., and Stolz, C. Structural health monitoring of repairs, NATO Research and Technology Organization, RTO-EN-AVT-156, Battle Damage Repair Techniques and Procedures on Air Vehicles-Lessons Learned and Prospects, May 2010, URL: http://www.rta. nato.int/pubs/rdp.asp?RDP=RTO-EN-AVT-156, Apr. 5, 2011.

[24] Schnars, U., and Henrich, R. Application of NDT methods on composite structures in aerospace industry, in CDCM 2006-Conference on Damage in Composite materials, 2006, Online-Proc. on ndt.net. 18./19.09.2006, Germany, 8p.

[25] Hsu, D.K. Nondestructive inspection of composite structures: Methods and practice, 17th World Conference on Nondestructive Testing, 25–28 Oct. 2008, Shanghai, China, 14p.

[26] Chang, R.C., and Lan, C.E. Structural health monitoring of transport aircraft with fuzzy logic modelling, Mathematical Problems in Engineering, 2013, 2013, Article ID 640852, 11p. doi: 10.1155/2013/640852.

[27] Terroba, F., Fr vel, M., and Atienza, R. Structural health and usage monitoring of an unmanned turbojet target drone, Structural Health Monitoring, 18(2), 2018, 635–650. doi: 10.1177/1475921718764082.

[28] Spencer, Jr., B.F., Ruiz-Sandoval, M., and Kurata, N. Smart sensing technology for structural health monitoring, 13th World Conference on Earthquake Engineering (WCEE), Vancouver, B.C., Canada, Aug. 1–6, 2004, Paper # 1791, 13p.

[29] Swartz, R.A., Zimmerman, A., and Lynch, J.P. Structural health monitoring system with the latest information technology, Proc. of 5th Infrastructure & Environmental Management Symposium, Yamaguchi, Japan, Sept. 28, 2007, 28p.

[30] Sun, M., Staszewski, W.J., and Swamy, R.N. Smart sensing technologies for structural health monitoring of civil engineering structures, Advances in Civil Engineering, 2010, 2010, Article ID 724962, 13p. doi: 10.1155/2010/724962.

[31] Yi, T.-H., Li, H.-N., and Gu, M. Optimal sensor placement for structural health monitoring based on multiple optimization strategies, Structural Design of Tall and Special Buildings, 20(7), 2011, 881–900. doi: 10.1002/tal.712

[32] Yi, T.-H., Li, H.-N., and Gu, M. Recent research and applications of GPS-based monitoring technology for high-rise structures, Structural Control and Health Monitoring, 20(5), 2013, 649–670.

[33] Dhakal, D.R., Neupane, K., Thapa, C., and Ramanjaneyulu, G.V. Different techniques of structural health monitoring, International Journal of Civil, Structural, Environmental and Infrastructure Engineering Research and Development (IJCSEIERD), 3(2), 2013, 55–66.

[34] Kim, H., Ahn, E., Shin, M., and Sim, S.-H. Crack and non-crack classification from concrete surface images using machine learning, Structural Health Monitoring, 2018, 1–14. doi: 10.1177/1475921718768747.

[35] Li, X., Liu, X., Li, C.Z., Hu, Z., Shen, G.Q., and Huang, Z. Foundation pit displacement monitoring and prediction using least squares support vector machines based on multi-point measurement, Structural Health Monitoring, 2018, 1–10. doi: 10.1177/1475921718767935.

[36] Qu, H., Li, T., and Chen, G. Adaptive wavelet transform: Definition, parameter optimization algorithms, and application for concrete delamination detection from impact echo responses, Structural Health Monitoring, 2018, 1–10. doi: 10.1177/1475921718776200.

[37] Park, G., Sohn, H., Farrar, C.R., and Inman, D.J. Overview of piezoelectric impedance-based health monitoring and path forward, The Shock and Vibration Dogest, 55(6), 2003, 451–463.

[38] Oromiehie, E., Prusty B.G., Compston, P., and Rajan, G. Characterization of process-induced defects in automated fiber placement manufacturing of composite using Bragg grating sensors, Structural Health Monitoring, 15(6), 2016, 706–714. doi: 10.1177/1475921716685935.

[39] Cha, Y.-J., and Wang, Z. Unsupervised novelty detection-based structural damage localization using a density peaks-based fast clustering algorithm, Structural Health Monitoring, 17(2), 2017, 313–324. doi: 10.1177/1475921717691260.

[40] Demarie, G.V., and Sabia, D. A machine learning approach for the automatic long-term structural health monitoring, Structural Health Monitoring, 2018, 1–19. doi: 10.1177/1475921718779193.

[41] Jin, S.-S., and Jung, H.-J. Vibration-based damage detection using online learning algorithm for output-only structural health monitoring, Structural Health Monitoring, 17(4), 2018, 727–746. doi: 10.1177/1475921717717310.

[42] Mei, H., and Giurgiutiu, V. Guided wave excitation and propagation in damped composite plates, Structural Health Monitoring, 2018, 1–25. doi: 10.1177/1475921718765955.

[43] Chen, S., Zhou, S., Chen, C., Li, Y., and Zhai, S. Detection of double defects for plate-like structures based on a fuzzy c-means clustering algorithm, Structural Health Monitoring, 2018, 1–10. doi: 10.1177/1475921718772042.

[44] He, J., Leser, P.E., Leser, W.P., and Yuan, F.-G. IWSHM 2017: damage-scattered wave extraction in an integral stiffened isotropic plate: a baseline-substraction-free approach, Structural Health Monitoring, 17(6), 2018, 1365–1376. doi: 10.1177/1475921718769232.

[45] Pandey, A. K., Biswas, M., and Samman, M. M. Damage detection from changes in curvature mode shapes, Journal of Sound and Vibration, 145(2), 1991, 321–332.

[46] Penias, S., and Abramovich, H. Monitoring natural frequencies of composite structures as a means to detect defects, M.Sc. Thesis (in Hebrew), Faculty of Aerospace Engineering, Technion, I.I.T., Vol. 32000, Haifa, Israel, 2017, 110p.

Appendix A: Passive and active sensors

A1 Passive sensors

A1.1 Pressure-sensitive polymers

Pressure-sensitive polymers are materials that will change their properties due to applied stress. Two types that are discussed here are pressure-sensitive paint (PSP) and pressure-sensitive film (PSF).

A1.1.1 Pressure-sensitive paint

PSP has been around for some time (see [1–11]. PSP was developed at NASA to enable better measurements of the drag loadings on airfoils. The technology behind PSP is based on the sensitivity of certain luminescent molecules to the presence of oxygen. Using a process called oxygen quenching, the fluorescence of the molecules change as a function of the pressure in oxygen molecules. The measurement system, depicted in Fig. A1 consists of a light source to excite the oxygen and the luminescence molecules contained in the paint layer, and a photodetector to detect the long-wavelength emission to be translated into pressure applied on the paint.
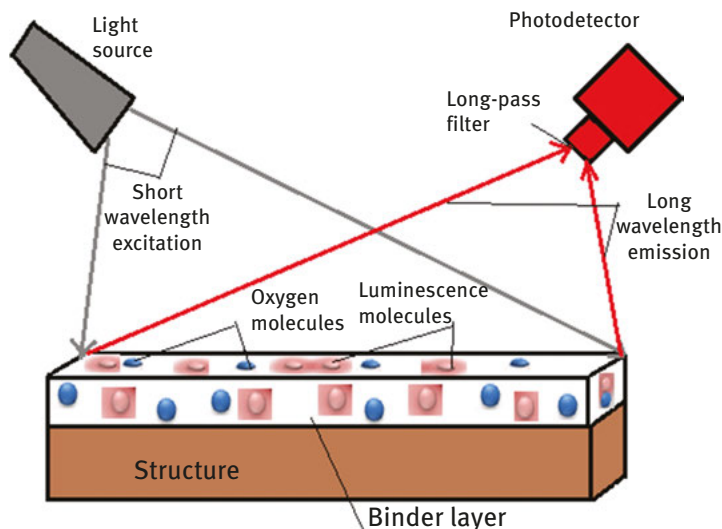
Fig. A1: – A schematic PSP test setup.

A1.1.2 Pressure-sensitive film

PSF is based on a simple but reliable technology. The film consists of a microencapsulated color layer and a color-developing layer sandwiched between two polyester layers as presented in Fig. A2. When a defined pressure is exceeded, the microcapsules would break and would react with the adjacent color-forming layer leading to a change in the film color. The color presented is monochromatic but the shading of the color will indicate pressure level. A calibration table is supplied by the manufacturing of the film (see, e.g., Fuji company[10]). One should note that the measurement of the pressure is not continuous, and the change in color is at discrete levels of pressure, causing the user to use various PSFs for different load levels, and also the films come in a variety of pressure ranges (0.05–300 MPa).

A1.2 Shape memory alloys

SMAs are materials that "would remember" their original shape and go back to their original shape after deformation under a stimulus in the form of heating/cooling and/or application of mechanical stresses. Probably, the most known SMA is the one abbreviated as NITINOL (Nickel Titanium Naval Ordnance Laboratory) developed by William Buehler and Frederick Wang of the US Naval Ordnance

---

10 http://www.fujifilm.com/products/prescale/prescalefilm/#See_All.
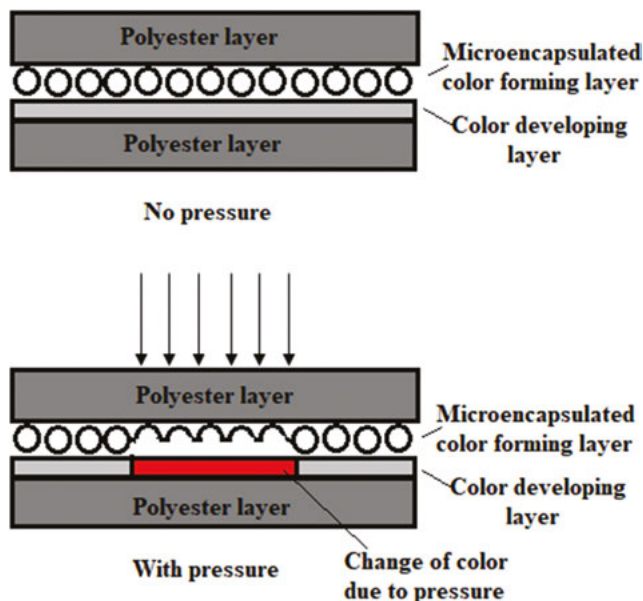
Fig. A2: – A schematic PSF way of activating due to the application of pressure on the film.

Laboratory in 1962 [12]. Some SMAs can go back to a shape different from their original shape under a stimulus, thus holding two different shapes and are called two-way SMAs.

SMAs have two different phases with different crystal structures leading to large different properties: martensite, a low-temperature phase; and austenite, a high-temperature phase. Contrary to a typical transformation that involves the diffusion of atoms, the phase change in SMAs occurs by a shear lattice distortion, which makes the change reversible.

SMAs also show a property called pseudoelasticity sometimes, whereby they show almost rubber-like mechanical behavior. SMAs can produce a large deformation compared to most other metals. Due to their lattice structure, the pseudoelasticity property enables the SMA to recover from relatively large strains (up to 7%), although some hysteresis can be experienced. This dissipation of energy by SMAs finds applications in vibration dampers.

Their property of changing structural phases from martensite to austenite and vice versa, applying mechanical stress, allows the use of SMA as sensors to mechanical loads.

A1.3 Comparative vacuum monitoring

CVM offers a novel application for in situ, real-time monitoring of crack initiation and/or propagation. CVM measures the differential pressure between very small diameter tubes containing a low vacuum alternating with similar tubes at atmosphere in a simple manifold-type structure. A schematic picture of the sensor, manufactured by the SMS Company[11] mounted on a structural part containing a crack is shown in Fig. A3.
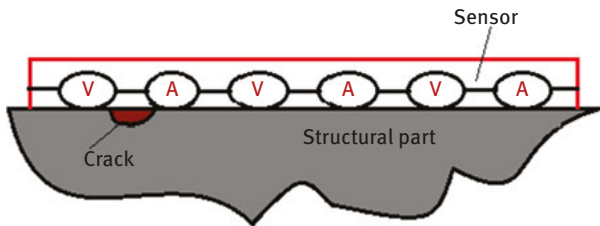
Fig. A3: A schematic drawing of the sensing of the crack using CVM (V, vacuum pressure; A, atmospheric pressure).
Note that an increase in ΔP pressure (between the vacuum and the atmospheric pressures) would be measured when a crack would cross two adjacent channels, one at vacuum (V) and the second one at atmospheric (A) pressure. As schematically shown in Fig. A3, any shape development of a flaw will cause a flow of air from the atmosphere to the vacuum channel, through the passage between them. A transducer would be used to measure the fluid flow between the small tubes; the rate of fluid flow would be an indication of the size of the flaw.

The CVM system consists of three primary components: a sensor, a fluid flow meter and a stable source of low vacuum. As no adhesive is needed, the method utilizes a direct measurement of the test surface making it a part of the sensor, thus resulting in a high reliability [13, 14] and built-in fail-safe mechanisms.

A1.4 Acoustic emission

AE is the phenomenon of sound and ultrasound stress wave radiation in structures, which undergo deformation or fracture processes. When a structure is subjected to an external stimulus (change in pressure, load or temperature), localized AE sources trigger the release of stress waves that propagate to the surface. These stress waves are recorded by several sensors, and then are analyzed in order to locate and classify these AE sources (see Fig. A4).

---

11 www.smsystems.com.au/.
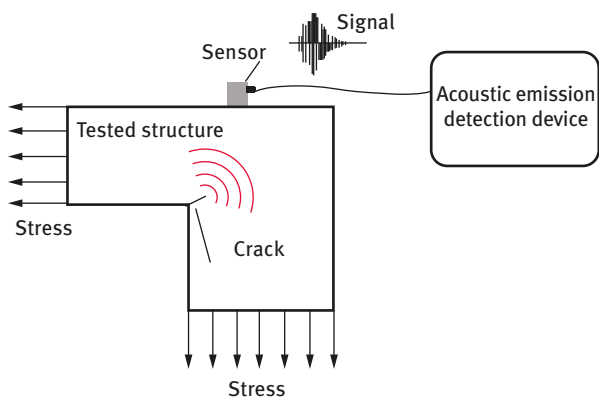
Fig. A4: Schematic of AE source, a crack, triggered due to an external stress, detected and transmitted to a centralized device prior to further analysis.

Common examples of AE sources can be growth of cracks, slip and dislocation movements, melting and phase transformations in metals. In composites, matrix cracking, fiber breakage and delamination are typical modes of failure and each contributes its own unique AE (see [15]).

AE sensing is considered to be *passive* since the only energy required for activating the sensors is supplied by the wave signal, which is spontaneously released in the case of existence of damage/discontinuity in the *loaded* structure. AE usually provides an immediate indication relating to the risk of failure of a component. In addition, using multiple AE sensors, a large area of inspection can be monitored. These sensors can even be permanently mounted for applications demanding periodic inspections, saving the need for preliminary preparations.

However, AE-based systems can only qualitatively gauge how much damage is contained in a structure. In order to obtain quantitative results about size, depth and overall acceptability of a part, other sensing techniques should be involved.

Another aspect that should be mentioned is how to define a loading procedure, which ensures optimal damage identification. Currently, there is no standard, which gives certain guidelines regarding the loading procedures, and therefore most of the applications today are based on the accumulated experience of the designers. The loading procedure becomes a challenge mostly in the case of large aircraft components, which are assembled on aircrafts. It will be interesting and feasible to investigate new techniques for implementing *local* loading, that is, loading only area of interests instead of all the aircraft. Such techniques can be based on either dynamic or thermal loading. Usually, the sensors utilized for AE are piezoelectric (see Fig. A5).

Fig. A5: Acoustic emission piezoelectric sensor from Fuji Ceramics Corporation.[12]

A2 Active sensors

A2.1 Electrical impedance

The sensor is capable of measuring the changes in the impedance of the tested specimen and thus provide adequate output to correlate the measured change in the impedance to the size of the flaw. Depending on the application, a change in the resistivity, capacitance or inductance (the structure's impedance, Z) of the tested structure in the presence of a flaw can be detected, providing the intact structure was previously measured.

A2.2 Magnetic impedance

The magnetoimpedance sensor is based on the change in the complex impedance (Z) that ferromagnetic conductors experience (like amorphous micro wires) when an external magnetic field (H) is applied and a high frequency (ω) alternating current flows through them. The sensor is applied on the tested structure, and due to external disturbances and/or flaws, it will change its magnetic impedance, thus

---

12 www.fujicera.co.jp/en/product/ae/.

measuring the reason for its change. Note that the method would require a reference data, for the undisturbed, perfect structure.

A2.3 Piezoelectric wafer active

The brothers Jacque and Pierre Curie first discovered piezoelectricity at the end of the nineteenth century, who demonstrated it on crystals of tourmaline, quartz, topaz, cane sugar and Rochelle salt [12]. The word *Piezoelectricity* comes from the Greek word *piesi*, which means *pressure*, and *electricity*, which implies the production of electricity resulting from the pressure. Piezoelectric materials, whether inherently piezoelectric or artificially poled, can be used to convert mechanical energy to electrical energy and vice versa. The constitutive equations describing these materials are written as follows:

$$S = s^E T + d^t E$$
$$D = dT + \varepsilon^T E$$

(A-1)

where S is the mechanical strain, E is the electric field, T is the mechanical stress, D is the electrical displacement (all these variables are second-order tensors in the general case); d^t, s^E and ε^T, respectively, represent the matrix of the transpose piezoelectric effect, the mechanical compliance tensor (obtained at $E = 0$) and the permittivity (obtained at $T = 0$). This EM coupling property enables the utilization of these unique materials both as strain sensors and mechanical actuators. The voltage–strain curve does not exhibit linear behavior in its entire range. However, there is always a linear part in the curve used in practice for the sensing.

Piezoelectric ceramics, also called piezoceramics, is a subgroup of piezoelectric materials, which exhibit simultaneous actuator and sensor behavior, and therefore, are particularly attractive for diagnosis systems especially in the form of PWAS, which can be permanently attached to the structure [12]. The main advantage of PWAS over conventional ultrasonic probes is in their small size, lightweight, low-profile and inexpensive cost. In addition, their frequency bandwidth is several orders of magnitude larger than that of conventional modal analysis equipment, permitting effective modal diagnosis in a relatively wide frequency band. The diagnosis process can be described as follows: The PWAS transmitter generates Lamb waves in the structure [16]. The generated Lamb waves travel through the structure and are reflected or diffracted by the structural boundaries, discontinuities and damage. The waves arrive at the PWAS receiver, where they are transformed into electrical signals. Using at least two PWAS, one can detect structural anomalies, that is, cracks, corrosions, delaminations and other damage [17]. PWAS can be used in several sensing applications as shown in Fig. A6.
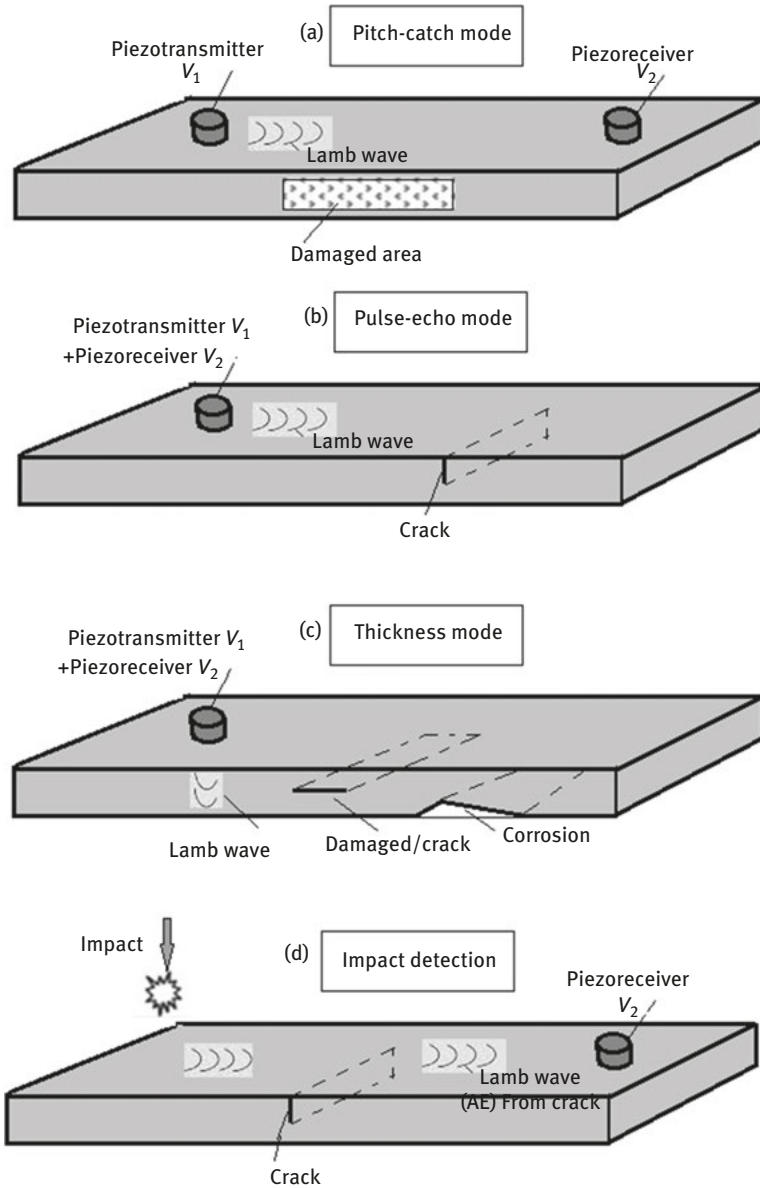
Fig. A6: Implementations of PWAS as traveling wave transducers for damage detection:
(a) pitch-catch mode, (b) pulse-echo mode, (c) thickness mode and (d) detection of impacts and
acoustic emission (AE) (adapted from [11]).

Since the PWAS sensing technology has been found to be useful for detecting
damages in composites, much effort has been recently invested in the qualification

of this technology. This effort includes the investigation of sensor transduction under mechanical static and cyclic loading [18] and its reliability over time [19].

A2.4 Optical fiber

Among the available sensing technologies, the use of OFS to implement SHM appears quite attractive. Optical fibers are flexible, passive, tolerant to environmental conditions and insensitive to electromagnetic disturbances. In addition, due to their small diameter, it can be easily embedded within composite materials. The most common implementation of a fiber optic-based SHM system involves one of the two sensing principles: site-specific sensing, performed by using FBG sensors, or distributed sensing, performed by using Rayleigh backscattering.

A.2.4.1 Fiber Bragg grating

Site-specific sensing using FBG sensors allows the measurement of mechanical strain and temperature changes in several locations along an optical fiber. An FBG sensor is a type of *distributed Bragg reflector*[13] constructed in a short segment of optical fiber, which reflects a *particular* wavelength of light and transmits all others (see Fig. A7). This particular wavelength reflected, called the Bragg wavelength, is given as follows:

$$\lambda_B = 2n_e\Lambda \tag{A-2}$$

where n_e is the effective refractive index characterizing the FBG, and Λ represents the grating period. The linear dependence of the reflected wavelength λ_B on the grating period Λ enables to easily deduce changes in the grating period Λ by measuring the reflected wavelength λ_B.

An external mechanical load or temperature change causes a uniform change in the grating period Λ, resulting in a shift in the reflected wavelength λ_B. By measuring the difference in the reflected wavelength λ_B, the strain and the temperature of the optical fiber at the FBG location can be derived by using the following relation:

$$\frac{\Delta\lambda_B}{\lambda_B} = C_s\varepsilon + C_T\Delta T = (1 - P_e)\varepsilon + (\alpha_\Lambda + \alpha_n)\Delta T$$

where

$$(1 - P_e) = C_S \quad (\alpha_\Lambda + \alpha_n) = C_T$$

$$\tag{A-3}$$

---

13 A structure formed from multiple layers of alternating materials with varying refractive indices.
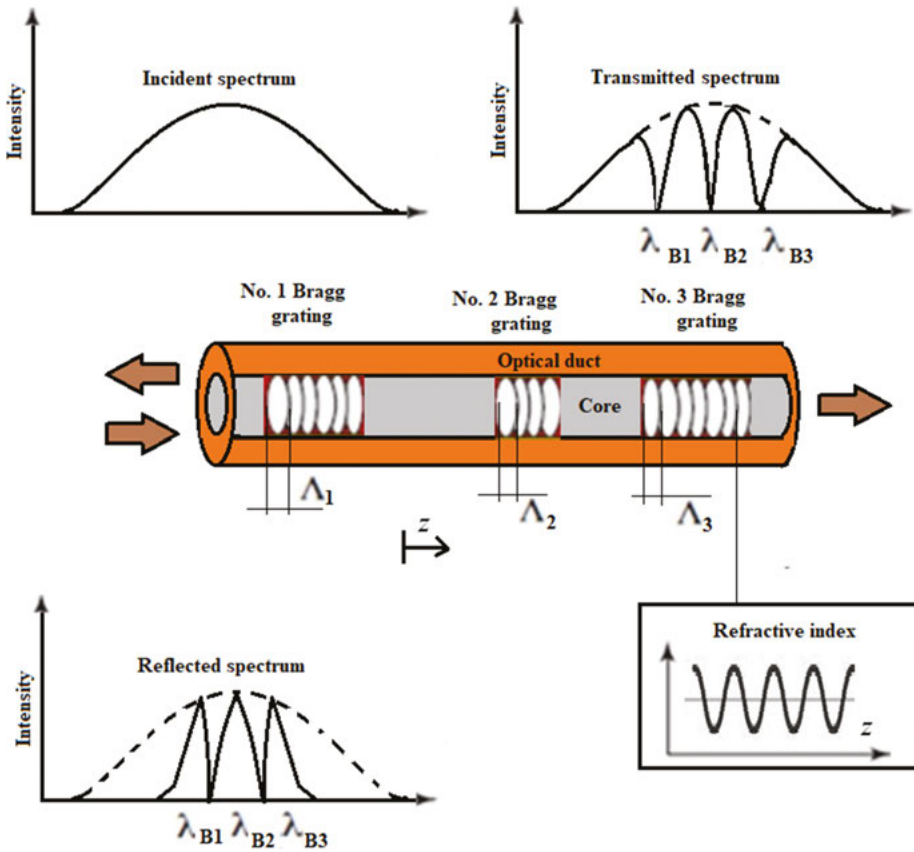
Fig. A7: Optical fiber containing several FBG sensors (each sensor reflects a particular wavelength of light only), depending on its grating period [14].

where C_s is the strain coefficient that is related to the strain optic coefficient P_e and C_T is the coefficient of temperature, obtained by the summation of the optical fiber core thermal expansion coefficient, α_Λ, and the thermo-optic coefficient α_n.

A.2.4.2 Rayleigh backscattering distributed strain sensing

Rayleigh backscattering in an optical fiber caused by random fluctuations in the refractive index profile along the length of the fiber. For a given fiber, the scatter amplitude as a function of distance is a random but fixed property. Similar to FBG sensors, external stimulus such as mechanical strain or change in the temperature causes a shift in the local reflected spectrum [20]. In data processing, the complex data acquired from the optical fiber are divided into interval length, also called "sensor length," which are separated in a constant predefined gap. The shift in the

reflected spectrum is calculated upon each "sensor length" separately and independently. Thus, the optical fiber can be modeled as a series of weak FBG sensors, which are placed side by side in a constant predefined gap (see Fig. A8). The predefined length of the sensors and the gap between the sensors, respectively, affect the spectral resolution and the signal-to-noise ratio. Therefore, these two parameters should be optimized to obtain the desired spatial resolution with maximum measurement accuracy.
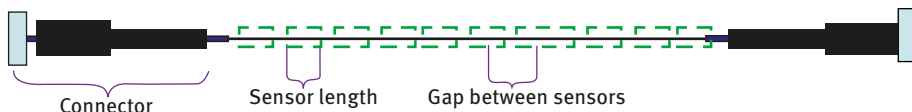
Fig. A8: A schematic drawing of an optical fiber, virtually divided into intervals, representing the sensors along the optical fiber that are separated by a constant gap.

Additional information associated with Rayleigh-distributed strain and temperature sensing can be found in Ref. [21].

References

[1]   Kavandi, J. Callis, J., Gouterman, M., Khalil, G., Wright, D., and Green, E. Luminescence barometry in wind tunnels, Review of Scientific Instruments, 61(11), 1990, 3340–3347.

[2]   Morris, M.J., Benne, M.E., Crites, R.C., and Donovan, J.F. Aerodynamic measurements based in photoluminescence, presented at the 31st Aerospace Sciences Meeting and Exhibit, Reno, NV, Jan. 11–14, 1993, Paper 93–0175.

[3]   McLachlan, B., and Bell, J. Pressure-sensitive in aerodynamic testing, Experimental Thermal and Fluid Science, 10(4), 1995, 470–485.

[4]   Liu, T., Campbell, B., Burns, S., and Sullivan, J. Temperature and pressure-sensitive luminescent paints in aerodynamics, Applied Mechanical Reviews, 50(4), 1997, 227–246.

[5]   Liu, T., and Sullivan, J.P. Pressure and Temperature Sensitive Paints, Berlin, Springer-Verlag, 2005, 292p.

[6]   Lakowicz J.R. Principles of Fluorescence Spectroscopy, 3rd, New York, Kluwer Academic/ Plenum Publishers, 1999, 795636p.

[7]   Engler, R., and Klein, C. DLR PSP System: Intensity and lifetime measurements, in Proc. 17th International Congress on Instrumentation in Aerospace Simulation Facilities, Pacific Grove, CA, USA, 1997, pp. 46–56.

[8]   Holmes, J. Analysis of radiometric, lifetime and fluorescent imaging for pressure sensitive paint, Aeronautical Journal, 102(1014), 1998, 189–194.

[9]   Bell, J.H., Schairer, T.E., Hand, L.A., and Mehta, R.D. Surface pressure measurements using luminescent coatings, Annul Review of Fluid Mechanics, 33, 2001, 155–206.

[10]   Mitsuo, K., Egami, Y., Asai, K., Suzuki, H., and Mizushima, H. Development of lifetime imaging system for pressure-sensitive paint, presented at the 22nd AIAA Aerodynamic

Measurement Technology and Ground Testing Conference, St. Louis, MO, June 24–26, 2002, Paper 2002–2909.

[11] Watkins, A.N., Jordan, J.D., Leighty, B.D., Ingram, J.L., and Oglesby, D.M. Development of next generation lifetime PSP imaging systems, Proc. 20th Int. Congr. Instrumentation in Aerospace Facilities, Gottingen, Germany, 2003, pp. 372–382.

[12] Abramovich, H. Intelligent Materials and Structures, ©, Walter de Gruyter GmbH, Berlin/ Boston, 2016, 386 p.

[13] Stehmeier, H., and Speckmann, H. Comparative Vacuum Monitoring (CVM)-Monitoring of fatigue cracking in aircraft structures, 2nd European Workshop on Structural Health Monitoring, Munich, Germany, July 7–9, 2004, 9p.

[14] Roach, D. Real time crack detection using mountable comparative vacuum monitoring sensors, Smart Structures and Systems, 5(4), 2009, 317–328.

[15] Professionals & Educators, Introduction to Acoustic Emission testing, Education Resource Center, 2014. [Online]. Available: https://www.nde-ed.org/EducationResources.

[16] Kessler, S.S., Spearing S.M., and Soutis C. Damage detection in composite materials using Lamb wave methods, Smart Materials and Structures, 11(2), 2002, 269–278.

[17] Giurgiutiu, V. Structural damage detection with piezoelectric wafer active sensors, Journal of Physics Conference Series, 305, 2011, 012123, 10p.

[18] Abramovich, H., Tsikchotsky, E., and Klein, G. An experimental investigation on PZT behavior under mechanical and cycling loading, Journal of the Mechanical Behavior of Materials, 22(3–4), 2013, 129–136.

[19] Bach, M., Dobmann, N., Eckstein, B., Moix-Bonet, M., and Stolz, C. Reliability of co-bonded piezoelectric sensors on CFRP structures, 9th International Workshop on Structural Health Monitoring, Sept 10–12, Stanford University, CA, USA, 2013, 9p.

[20] Kreger, S. T., Gifford, D. K., Froggatt, M. E., Soller, B. J., and Wolfe, M. S. High resolution distributed strain or temperature measurements in single- and multi-mode fiber using swept-wavelength interferometry, Optical Fiber Sensors, Technical Digest (CD) (optical Society of America), 2006, paper ThE42.

[21] Samiec, D. Distributed fiber-optic temperature and strain measurement with extremely high spatial resolution, Photonik International, 2012, 10–13.

Index